

**From Spins to Solutions**  
**Expanding the Horizons of Electron Spin**  
**Resonance (ESR) Spectroscopy**

Dissertation  
zur Erlangung des Grades  
des Doktors der Naturwissenschaften  
der Naturwissenschaftlich-Technischen Fakultät  
der Universität des Saarlandes

von  
Haakon Tassilo Adam Wiedemann

Saarbrücken

November 2024

Tag des Kolloquiums: 11.04.2025

Dekan: Prof. Dr.-Ing. Dirk Bähre

Berichterstatter: Prof. Dr. Christopher W.M. Kay  
Prof. Dr. Gregor Jung

Akad. Mitglied: Dr. Bernd Morgenstern

Vorsitz: Prof. Dr. Dominik Munz





はるばるとこころつといてはなさかる。

(Harubaru to kokoro tsudoite hana sakaru)

When distant minds come together, cherries blossom.

- Inscription on the monument dedicated to those who came from Japan to the University College London (UCL) in 1863 and 1865, unveiled by His Excellency Mr Hiroshi Kitamura, Ambassador of Japan, on 2nd September 1993.





## Acknowledgements

As I reflect on the journey that has led me to this moment, I am reminded of the generations before me whose perseverance and determination laid the foundation for my path. My great grandfather *Harald Foss* from southern Norway, was a whale catcher on the polar sea on a ship called *Sevilla* in the 1930th years. His ship went to the arctic sea and he sailed for 10 years on this ship, until he could finally buy a farm called *Hallingsrud*. My great grandfather was a pioneer, a fighter and had the goal in life to become a farmer. Afterwards, my grandfather *Erling Bøe* was also taught how to be a farmer. My mother, *Inger-Helene*, grew up on a farm called *Langeröd* in southern Norway and had to learn how to cultivate and earn crops and how to take care of animals together with her brother *Svein* and her sisters *Torill* and *Anita*. The family from my father's side originates from the old country of Yugoslavia and my ancestors from the *Lukisz* family used to work on a farm or in a bakery. Shortly after the war my ancestors moved towards Germany and ended up in Bavaria where my grandmother *Anna Wiedemann* is living to this day. It was in Germany where my parents met, each bringing their own experiences and determination into my upbringing. Their stories, resilience, and unwavering support instilled in me the belief that no goal is too far to reach if you work for it. When I first heard that earning a PhD in chemistry meant years of dedication and hard work, I could not help but be inspired. Sometimes I like to think that my great grandfather *Harald* had the same thought on his whale catcher ship on the ocean. His vision kept him going through the hardships of the sea, just as my vision of earning a PhD has driven me through the challenges of academia. It is a similar journey of persistence, where the goal—whether it be a farm or a doctoral degree—is the reward for years of struggle. I am also curious to see what the future brings after that goal, also for my descendents. I would like to encourage them in the same way as my parents did. With that my greatest thanks goes to both my parents *Inger-Helene* and *Peter* who are amazing in what they do and I can always rely on them. My two brothers also helped massively even when they don't think of their support as that great. I have to give the same gratitude to my two younger brothers *Timon* and *Stian* and my grandmother *Anna Wiedemann*. Furthermore, I want to thank my step-parents *Nicole* and *Andreas* for their support. My family kept me sane during all the stress and hard work of this thesis as well as my personal life.

I owe a great deal to my supervisor, *Prof. Dr. Christopher W.M. Kay*, whose mentorship and guidance have shaped my research and personal growth. I am grateful for the opportunity to work on interdisciplinary and challenging projects, and for his consistent support,

including the chance to travel to conferences and experience the world—especially the unforgettable trip to Japan. His belief in me, starting with my bachelor thesis, has been a constant source of motivation.

I also want to thank my scientific advisor, *Prof. Dr. Gregor Jung*, for his interest in my work and his encouraging discussions about my future. I will always remember our conversations with fondness.

My heartfelt thanks goes to my appreciated and experienced collaborators from whom I was really able to learn a lot and earned a deeper understanding for associated fields of science. I would like to acknowledge all the past and current colleagues from the research groups, the Department of Physical Chemistry and our workshop members for the very pleasant and supporting working environment. This includes *Dr. Daniel Rauber, Dr. Christoph Zollitsch, Dr. Klaus Hollemeyer, Dr. Clemens Matt, Petra Theobald, Rudolf Richter, Jens Wiegert, Dina Klippert, Kevin Staudt, Stefan Ruloff, Maxim Neuberger, Jonas Bach, Daniel Schroeder, Lukas Schank, Eva Steuer, Robin Pilger, Ruwen Schank* and *Maximilian Frisch*. I really enjoyed talking and exchanging knowledge about spectroscopy as well as other topics. I want to mention especially *Dr. Christoph Zollitsch, Maxim Neuberger* and *Jonas Bach* with whom I could really exchange deeper discussions about spectroscopy and I consider them the greatest colleagues one can have. Moreover, I want to express a deep thanks to *Rehani Perera* with whom I share a lot of good memories regarding our collaborative biological project.

I am also thankful to my colleagues from the chemistry didactics field that helped me a lot in understanding the art of teaching which I enjoyed to implement in the supervision of experiments for undergraduate students. Especially appreciated are *Dr. Johann Seibert, Dr. Vanessa Lang, Dr. Sabine Fey, Laura Mallwitz, Annika Eichinger, Luca Deeg* and *Janica Schumacher*.

I owe a special thanks to my best friend *Stavroula Pachoula*, a highly talented and brilliant synthetic chemist who supported and guided me during these three PhD years and before that time.

Lastly, I want to express my love and gratitude to my cat, *Sada*, whose quiet companionship and daily greeting at the door never failed to lift my spirits.

As I look toward the future, I am reminded of my great-grandfather, *Harald*, a true explorer of the oceans. Like him, I am eager to embark on the next phase of my journey, curious about the "whales" that await me in the vast ocean of life. I hope that, like him, I can continue to explore, push boundaries, and never lose sight of the goals that drive me forward.

# Table of contents

<b>Kurzzusammenfassung</b>	<b>xi</b>
<b>Abstract</b>	<b>xiii</b>
<b>Motivation and aim of the thesis</b>	<b>xv</b>
<b>1 Introduction</b>	<b>1</b>
1.1 Electron Spin Resonance . . . . .	1
1.1.1 Resonance and Precession . . . . .	3
1.1.2 Hyperfine Interaction . . . . .	4
1.2 Continuous Wave (CW) ESR techniques . . . . .	9
1.2.1 Conventional CW ESR . . . . .	9
1.2.1.1 CW ESR Instrumentation . . . . .	9
1.2.2 Power Saturation . . . . .	11
1.2.3 Spin Trapping Technique . . . . .	16
1.2.4 Transient EPR . . . . .	20
1.2.4.1 TR-EPR Experimental Setup . . . . .	20
1.2.4.2 Description of TR-EPR spectroscopy . . . . .	23
1.3 Pulse ESR Methods . . . . .	29
1.3.1 Relaxation Time Measurement . . . . .	29
1.3.1.1 Spin-Spin Relaxation Time $T_2$ . . . . .	33
1.3.1.2 Spin Lattice Relaxation Time $T_1$ . . . . .	34
1.3.2 Electron Nuclear Double Resonance (ENDOR) . . . . .	36
1.3.3 Pulsed Electron Electron Double Resonance (PELDOR) . . . . .	40
<b>2 Experimental Setup</b>	<b>45</b>
2.1 Spectrometers . . . . .	45
2.1.1 X-Band (9 - 10 GHz) . . . . .	45
2.1.2 Q-Band (33 - 35 GHz) . . . . .	47
2.2 Temperature Control . . . . .	48
2.3 Optical Excitation . . . . .	49
<b>3 Main part</b>	<b>51</b>
3.1 Contributions to Chemical Science . . . . .	52

---

3.1.1	Stable Radicals . . . . .	52
3.1.1.1	Aluminum Complex . . . . .	54
3.1.1.2	TiO <sub>2</sub> and Nb <sub>2</sub> O <sub>5</sub> Nanoparticles . . . . .	62
3.1.1.3	Atomic Hydrogen ENDOR Manuscript . . . . .	75
3.1.2	Short-lived Radicals . . . . .	84
3.1.2.1	LaCoO <sub>4</sub> Nanoparticles . . . . .	85
3.1.2.2	LaCoO <sub>3</sub> /Graphene Nanoparticles . . . . .	99
3.1.3	Light-induced Radicals . . . . .	115
3.1.3.1	Aluminum Porphyrine TR-EPR . . . . .	117
3.2	Contributions to Physical Science . . . . .	130
3.2.1	Microwave Resonators . . . . .	132
3.2.1.1	High Performance MW Resonators . . . . .	132
3.2.1.2	MASER Resonator . . . . .	142
3.3	Contributions to Biological Science . . . . .	148
3.3.1	Membrane Proteins . . . . .	150
3.3.1.1	Structural Rearrangement of Hairpin Protein . . . . .	150
<b>4</b>	<b>Conclusion</b>	<b>169</b>
4.1	First section of the Conclusion . . . . .	169
4.2	Second section of the Conclusion . . . . .	171
<b>5</b>	<b>Scientific Contributions</b>	<b>181</b>
5.1	Publications of Haakon T.A. Wiedemann in peer-reviewed Journals . . . . .	181
5.2	Contributions of Haakon T.A. Wiedemann at Scientific Conferences . . . . .	182
5.3	Other Contributions of Haakon T.A. Wiedemann . . . . .	183
	<b>References</b>	<b>185</b>
	<b>Appendix A Supporting Information</b>	<b>193</b>

# Kurzzusammenfassung

Die Elektronenspinresonanz (ESR)-Spektroskopie kombiniert experimentelle und theoretische Ansätze im Feld der Magnetresonanz. Verschiedene Studien werden im Folgenden aufgelistet.

Untersuchungen zur Radikalbildung in einem Aluminiumkomplex, der mechanochemischen Reduktion von Metalloxiden und der dipolaren Kopplung von Wasserstoffatomen, konnte das Verständnis katalytischer Prozesse und molekularer Wechselwirkungen vertiefen. Forschungen zu neuartigen  $\text{LaCoO}_4$  und  $\text{LaCoO}_4$ /Graphen Nanopartikeln beleuchten deren katalytische Reaktivität, während Arbeiten zu Aluminiumporphyrin die Rolle von Jahn-Teller-Verzerrungen in der Kinetik von Triplett-Zuständen aufzeigen. Diese bieten Einblicke in das dynamische Verhalten von Radikalspezies.

Optimierte Mikrowellen-ESR-Resonatoren zeigen eine hohe Korrelation zwischen Simulationen und Experimenten und die Resonatorperformance konnte erheblich verbessert werden. Weiterführende Untersuchungen zur MASER-Kopplung hinterfragen bestehende Annahmen und tragen zu Fortschritten in der Mikrowellentechnologie und deren Anwendungen bei.

Eine weitere Studie zu einem Membranprotein im endoplasmatischen Retikulum kombiniert experimentelle und computergestützte Daten und liefert integrative Einblicke in die Proteindynamik. Sie beleuchtet zudem breitere Implikationen für die strukturelle Biologie und die Funktionalität von Membranproteinen. Diese Dissertation vertieft die Anwendungen und theoretischen Grundlagen der ESR-Spektroskopie und ebnet den Weg für interdisziplinäre Fortschritte in den Wissenschaften der Chemie, Physik und Biologie und innovativen Anwendungen.



# Abstract

Electron spin resonance (ESR) spectroscopy combines experimental and theoretical approaches in the field of magnetic resonance. Various studies are listed in the following.

Exploring the radical formation in an aluminum complex, the mechanochemical reduction of metal oxides, and the dipolar coupling of hydrogen atoms, enhances the understanding of catalytic processes and molecular interactions. Research on novel  $\text{LaCoO}_4$  and  $\text{LaCoO}_4$ /graphene nanoparticles investigate their catalytic reactivity, while work on aluminum porphyrine reveals the role of Jahn-Teller distortions in triplet state kinetics, offering insights into the dynamic behavior of radical species and their implications for material design.

Optimized microwave (MW) ESR resonator designs demonstrate high simulation-to-experiment correlation and lead to a significantly improved resonator performance. Further research on the coupling situation in a MASER challenges existing assumptions, contributing to advancements in MW technologies and their applications.

Another study of a membrane protein in the endoplasmic reticulum combines experimental and computational data, offering integrative insights into protein dynamics and shedding light on broader implications for structural biology and membrane protein functionality. This thesis deepens ESR spectroscopy's applications and theoretical foundations, paving the way for interdisciplinary progress in science and innovative applications. It advances understanding in chemistry, physics, and biology, driving innovation in molecular dynamics and magnetic resonance.



# Motivation and aim of the thesis

The pursuit of a PhD is more than an academic endeavor, it is a profound journey marked by curiosity, discovery, and the desire to contribute meaningfully to the scientific community. A cumulative PhD thesis, composed of a series of interconnected studies, embodies this journey through a comprehensive exploration of a focused research area in the three disciplines of chemistry, physics and biology. This cumulative PhD thesis comprises eight distinct, yet interrelated publications and one unpublished manuscript that explore key challenges and advancements in the field of electron spin resonance (ESR, also called: electron paramagnetic resonance, EPR) spectroscopy. This approach not only showcases the depth and breadth of the research conducted, but also highlights the progression of ideas, methodologies, and innovations that culminate in significant scientific contributions.

In the realm of spectroscopy in physical chemistry, the need for advanced understanding and novel solutions is ever-growing. This thesis is motivated by the pressing challenges and intriguing questions that define this scientific field. By addressing issues through a series of systematic investigations, this work aims to push the boundaries of current knowledge and provide a foundation for future research and applications. The cumulative nature of this thesis allows for a thorough examination of ESR spectroscopy from multiple perspectives, fostering a comprehensive understanding that is greater than the sum of its parts.

The motivation for this cumulative PhD thesis stems from a deep curiosity about ESR spectroscopy since the beginning of my academic career and the recognition of its potential impact on the chemical, physical and biological sciences. Each study within this thesis builds upon previous findings, creating a cohesive narrative that underscores the interconnectedness of scientific inquiry. The iterative process of hypothesis, simulation, experimentation, and analysis not only advances our understanding of magnetic resonance and paramagnetism in ESR spectroscopy, but also demonstrates the evolution of research skills and intellectual growth.

Additionally, this thesis is driven by the aspiration to contribute to the field of magnetic resonance in a meaningful way. By addressing key questions and developing innovative approaches, the research presented herein aims to provide insights that are both academically significant and practically relevant for the scientific fields of chemistry, physics and biology. The motivation extends beyond mere academic curiosity. It is about making a tangible impact on the scientific community. Whether through improving existing technologies, characterizing reactions or catalytic pathways, or enhancing theoretical

frameworks, the work aims to bridge the gap between theoretical research and real-world applications.

The interdisciplinary nature of ESR spectroscopy also fuels the motivation behind this thesis. The convergence of the scientific disciplines of chemistry, physics and biology often leads to groundbreaking discoveries and novel solutions. By integrating concepts and methods from various ESR techniques, this research not only aims to solve complex problems, but also to open new avenues for future investigations. The synergy of interdisciplinary approaches is a driving force behind the innovative aspects of this work, highlighting the importance of collaboration and cross-disciplinary thinking in advancing science.

Furthermore, the process of conducting this research has been a journey of personal and professional growth. The challenges faced, the skills acquired, and the knowledge gained throughout this PhD journey are invaluable. This thesis reflects a commitment to rigorous scientific inquiry, a dedication to overcoming obstacles, and a passion for contributing to the collective understanding of ESR spectroscopy. My scientific journey throughout this PhD began with novel stable radicals, works on potential quantum bit (qubit) molecules, scientific studies on catalytic active nanoparticles, optimisation of resonators, observing light-induced triplet states and finally elucidating structural properties of membrane protein samples. The experiences and lessons learned during this journey will continue to shape my future endeavors and drive my contributions to the scientific community.

Ultimately, this work is motivated by the belief that rigorous scientific research can drive progress and innovation. By contributing to the fields of chemistry, physics and biology in ESR spectroscopy, this cumulative PhD thesis is meant to inspire future researchers and make a lasting impact on the scientific and broader communities. Through dedication, perseverance, and a passion for discovery, this thesis represents a significant step forward in the ongoing quest to unravel the complexities of our world. My hope is that the insights gained and the methodologies developed will serve as a catalyst for further research, sparking new questions and driving continued advancements in the field.

# Chapter 1

## Introduction

### 1.1 Electron Spin Resonance

Electrons are independent particles and belong to the family of leptons. They have a (resting) mass, charge and spin and are point-like (no spatial expansion). The spin represents the intrinsic angular momentum, which can correspond figuratively to the idea of an intrinsic rotation [1].

The angular momentum of the electron can be defined either by the orbital angular momentum  $\vec{L}$  or the intrinsic angular momentum  $\vec{S}$ . The intrinsic angular momentum of the electron paired with the charge of the electron generates a magnetic moment, which can be expressed by the following equation [2]<sup>1</sup>:

$$\hat{\mu}_{e,S} = -\mu_B \cdot g_e \cdot \frac{\hat{S}}{\hbar} \quad (1.1)$$

where  $\hat{\mu}_{e,S}$  is the magnetic moment of the electron,  $\mu_B$  is the Bohr magneton,  $g_e$  is the Landé factor,  $\hat{S}$  is the spin operator of the electron and  $\hbar$  is the reduced Planck constant. The Landé factor  $g_e = 2.0023193$  for an electron is the quotient of the magnitude of the measured magnetic moment and the magnitude of the magnetic moment that would theoretically be expected for the given angular momentum according to classical physics [3].

If an external magnetic field is applied to this system, it interacts with the unpaired electron and the magnetic moment of the electron aligns itself in different spin settings in the direction of the applied magnetic field. The spin vector for a  $\hat{S} = 1/2$  system can be aligned parallel or antiparallel to the magnetic field. The two orientations have two different energy values derived by solving the Schrödinger equation, resulting in an energy splitting between the two energy levels. This effect is called the Zeeman effect [2].

The externally applied magnetic field allows the quantum mechanical energy operator, the Hamilton operator, to be set up for an unpaired electron:

---

<sup>1</sup>Notation: SI units are used in every formulatory derivation. Operators are indicated with a hat (e.g.  $\hat{\mathcal{H}}$ ) and vectorial variables are indicated with an arrow (e.g.  $\vec{S}$ ).

$$\hat{\mathcal{H}} = -\hat{\mu}_{e,S} \cdot \vec{B}_0 \quad (1.2)$$

where  $\hat{\mathcal{H}}$  is the Hamilton operator and  $\vec{B}_0$  is the magnetic field strength. Substituting equation (1.1) into equation (1.2) gives the following expression for the electron Zeeman Hamilton operator:

$$\hat{\mathcal{H}}_{\text{EZ}} = \frac{\mu_B \cdot g_e}{\hbar} \cdot \hat{S} \cdot \vec{B}_0 \quad (1.3)$$

To obtain the energy, the expectation value of the Hamilton operator must be calculated. For this instance, solely the spin vector of the electron must be taken into account. Since apart from physical constants, only the component in the z-direction of the magnetic field is considered here, which is by convention the z-direction and allows the expectation value derivation of Eq.(1.3) [2]<sup>2</sup> to:

$$\begin{aligned} \langle \hat{\mathcal{H}}_{\text{EZ}} \rangle &\propto \langle S, m_S | \hat{S}_z | S, m_S \rangle \\ \text{with } \hat{S}_z | S, m_S \rangle &= m_S \hbar \\ \langle \hat{\mathcal{H}}_{\text{EZ}} \rangle &\propto \langle S, m_S | m_S \hbar | S, m_S \rangle \\ &\propto m_S \hbar \langle S, m_S | S, m_S \rangle \\ &\propto m_S \hbar \end{aligned} \quad (1.4)$$

S is the spin quantum number, and the magnetic quantum number  $m_s$  can take values in the range of  $[-S, -S+1, \dots, S-1, S]$ . For a free electron with  $S = 1/2$  and in its eigenbasis  $m_s = [-1/2, 1/2]$  the expectation value of Eq.(1.3) yields the Zeeman equation:

$$\begin{aligned} E &= \frac{\mu_B \cdot g_e}{\hbar} \cdot m_S \cdot \hbar \cdot B_0 \\ E &= \mu_B \cdot g_e \cdot m_S \cdot B_0 \end{aligned} \quad (1.5)$$

Using the possible values for  $m_s$ , two energy states are identified:

$$E_{\pm\frac{1}{2}} = \pm \frac{1}{2} \cdot \mu_B \cdot g_e \cdot B_0 \quad (1.6)$$

The two energy eigenvalues  $E_{+\frac{1}{2}}$  and  $E_{-\frac{1}{2}}$  can be extracted from equation (1.6) and their energy difference  $\Delta E$  can be calculated:

<sup>2</sup>Notation: The relation of  $\langle S, m_S | S, m_S \rangle$  is orthonormic and hence, equals 1.

$$\Delta E = E_{+\frac{1}{2}} - E_{-\frac{1}{2}} = \mu_B \cdot g_e \cdot B_0 \quad (1.7)$$

The two electron spin states are separated by  $\Delta E$ , the energy required to induce a transition between the two states. The visualisation and further explanation will be illustrated in the following chapter.

### 1.1.1 Resonance and Precession

The previous chapter explained how the energy levels of the electron with one magnetic spin moment and their energy difference arise. This transition energy can be supplied in the form of electromagnetic radiation of the appropriate microwave (MW) frequency. This results in a resonant transition, which can be described by the following equation:

$$\Delta E = h \cdot \nu_{\text{Larmor}} = \mu_B \cdot g_e \cdot B_0 \quad (1.8)$$

where  $h$  is the Planck constant and  $\nu_{\text{Larmor}}$  is the resonance frequency. This equation is called the ‘fundamental equation of ESR spectroscopy’ [4], as spins can only be excited by electromagnetic radiation with the resonance frequency  $\nu_{\text{Larmor}}$  [5].  $\vec{\mu}_{e,S}$  and the spin vector  $\vec{S}$  perform precessional movements around the z-axis but point in opposite directions due to the negative charge of the electron (see g-factor in Eq.(1.1)) [6].

In Figure 1.1, the precession movement of several spin vectors around the external magnetic field  $B_0$  is illustrated by blue arrows that circle around the z-axis (magnetic field axis, labelled  $B_0$ ) on the surface of a double cone. The magnetization vector, as a sum of all spin vectors, is illustrated as a bold, red arrow pointed in the +z-direction in this case. This magnetization vector will be important in the usage of the pulsed ESR technique discussed in later chapters.

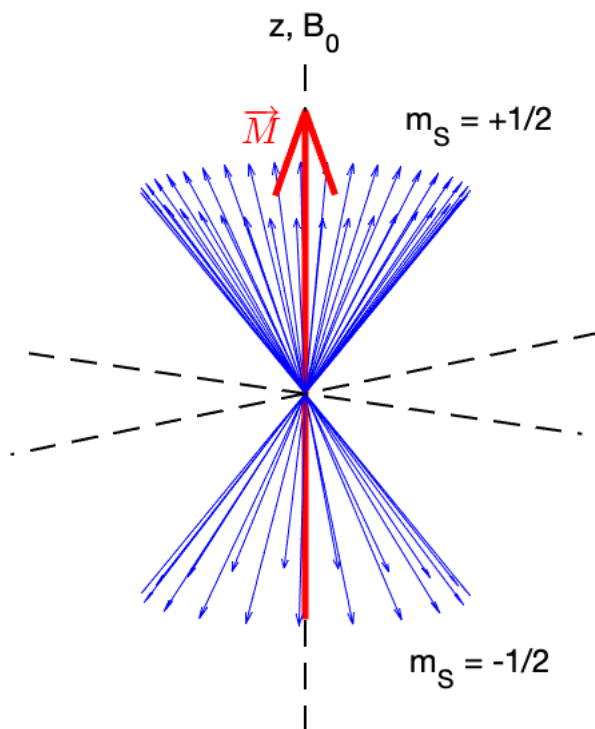


**Fig. 1.1** Precession of the electron spin vectors around an external magnetic field  $B_0$  on the z-axis. The smaller arrows (blue) represent the two different possibilities of spin alignment and they represent single spins. The upwards pointing arrows resemble the parallel alignment of the  $S_z$  spin component ( $m_S = +\frac{1}{2}$ ) while the downwards pointing arrows resemble the antiparallel alignment of the  $S_z$  spin component ( $m_S = -\frac{1}{2}$ ). The magnetization vector (red) as a sum of all spin vectors is illustrated as a bold arrow pointed in the +z-direction in this case.<sup>3</sup>

### 1.1.2 Hyperfine Interaction

At the end of the last chapter, the precession of fermions parallel or antiparallel with respect to an external magnetic field is illustrated. Although electron spin resonance is mainly concerned about the electron spin, nuclear spins in close vicinity have an influence on the electron spin state, too. This results in a hyperfine interaction between electron spins and nuclear spins. In the quantum chemical description of spin resonance a matrix representation of the operators and Hamiltonians is chosen, due to its convenient and compact notation. The spin operator consists of the so-called Pauli spin matrices which can be derived from the Lie algebra description in group theory of the special unitary group of degree 2,  $SU(2)$  [7]. The Pauli spin matrices  $\sigma_x$ ,  $\sigma_y$  and  $\sigma_z$  together with the unitary matrix  $\mathbb{1}_2$  can be described as:

<sup>3</sup>Derived from [8].

$$\sigma_x = \begin{pmatrix} 0 & 1 \\ 1 & 0 \end{pmatrix} \quad \sigma_y = \begin{pmatrix} 0 & -i \\ i & 0 \end{pmatrix} \quad \sigma_z = \begin{pmatrix} 1 & 0 \\ 0 & -1 \end{pmatrix} \quad \text{with } \mathbb{1}_2 = \begin{pmatrix} 1 & 0 \\ 0 & 1 \end{pmatrix} \quad (1.9)$$

Each Pauli matrix is Hermitian, and together with the identity matrix  $\mathbb{1}_2$ , the Pauli matrices form a basis for the real vector space of 2 x 2 Hermitian matrices. The properties of Hermitian matrices are the following[2]:

- The elements of the principal diagonal of a hermitian matrix are all real numbers.
- Every hermitian matrix is a normal matrix, such that the adjoint  $M^\dagger = M$ .
- The sum of any two hermitian matrices is hermitian.
- The inverse of a hermitian matrix is a hermitian.
- The product of two hermitian matrices is hermitian.
- The determinant of a hermitian matrix is real.

In quantum mechanics Hermitian matrices are fundamental because they describe operators with real eigenvalues. An eigenvalue  $a$  of an operator  $\hat{M}$  on some quantum state  $|\psi\rangle$  is one of the possible measurement outcomes of the operator.

Each Pauli matrix is related to an angular momentum operator that corresponds to an observable describing a fermion, in each of the three spatial directions x, y and z. In order to describe the effect of spins and their interaction on the total energy of a system, one has to take into account their effect on the Hamiltonian.

In order to describe the hyperfine interaction with the electron spin  $\hat{S}$  and nuclear spin  $\hat{I}$  operators the Pauli spin matrices described earlier are used. The respective  $\hat{S}_x$ ,  $\hat{S}_y$  and  $\hat{S}_z$  operators are derived by multiplying the Pauli spin matrices by the factor  $\frac{\hbar}{2}$ .

$$\hat{S}_x = \frac{\hbar}{2} \begin{pmatrix} 0 & 1 \\ 1 & 0 \end{pmatrix} \quad \hat{S}_y = \frac{\hbar}{2} \begin{pmatrix} 0 & -i \\ i & 0 \end{pmatrix} \quad \hat{S}_z = \frac{\hbar}{2} \begin{pmatrix} 1 & 0 \\ 0 & -1 \end{pmatrix} \quad (1.10)$$

The total number of states in a coupled system is  $(2S+1) \cdot (2I+1)$ , which for  $S = \frac{1}{2}$  and  $I = \frac{1}{2}$  yields four states in total. The following equation (1.11) describes the total Hamiltonian for the resulting hyperfine interaction.

$$\hat{\mathcal{H}} = \hat{\mathcal{H}}_{\text{EZ}} + \hat{\mathcal{H}}_{\text{NZ}} + \hat{\mathcal{H}}_{\text{HF}} \quad (1.11)$$

The Hamiltonian consists of the sum of three contributions, the electron Zeeman interaction  $\hat{\mathcal{H}}_{EZ}$ , the nuclear Zeeman interaction  $\hat{\mathcal{H}}_{NZ}$  and the interspin hyperfine interaction  $\hat{\mathcal{H}}_{HF}$ . Expanding each contribution of Zeeman interaction (see Eq.(1.2)) and describing each hyperfine interaction in all three spatial directions yields equation 1.12. Note that only the Zeeman splitting for the z-component is considered here, similar to the description of two electron spins in a magnetic field.

$$\begin{aligned}\hat{\mathcal{H}} &= -\hat{\mu}_{e,S} \cdot \hat{B}_0 - \hat{\mu}_{N,I} \cdot \hat{B}_0 + \hat{S} \cdot \sum_i A_i \cdot \hat{I}_i \\ \hat{\mathcal{H}} &= -\mu_B \cdot g_e \cdot \frac{\hat{S}_z}{\hbar} \cdot B_0 + \mu_N \cdot g_N \cdot \frac{\hat{I}_z}{\hbar} \cdot B_0 + A \cdot \frac{\hat{S}}{\hbar} \cdot \frac{\hat{I}}{\hbar}\end{aligned}\tag{1.12}$$

where  $\mu_B$  is the Bohrmagneton,  $\mu_N$  is the nuclear magneton,  $g_e$  is the free electron Lande-factor,  $g_N$  is the nuclear Lande-factor,  $B_0$  is the magnetic field strength and  $A$  is the hyperfine coupling constant<sup>4</sup>.

Eq.(1.10) forms the eigenbasis of any spin 1/2 particle. The hyperfine interaction links two spins together and hence the eigenbasis of the whole system is 4-dimensional. The spin operators are expanded, using the direct product (mathematical kronecker product:  $A \otimes B$ ):<sup>5</sup>:

<sup>4</sup>Notation: the minus sign of the magnetic moment of the nuclear spin is positive as a consequence of the opposite charge in a nucleus.

<sup>5</sup>The third part of the Hamiltonian (hyperfine interaction) usually has the hyperfine splitting constant  $A$  in units of Hertz (Hz). In order to change the units of the first two Zeeman terms of the Hamiltonian we inserted an extra  $\frac{1}{\hbar}$  before the Kronecker product in the second line of Eq.(1.13).

$$\begin{aligned}
\hat{\mathcal{H}} &= -\mu_B g_e B_0 \cdot \frac{\hat{S}_z}{\hbar} \otimes \mathbb{1}_2 + \mu_N g_N B_0 \cdot \mathbb{1}_2 \otimes \frac{\hat{I}_z}{\hbar} + A \cdot \left[ \frac{\hat{S}_x}{\hbar} \otimes \frac{\hat{I}_x}{\hbar} + \frac{\hat{S}_y}{\hbar} \otimes \frac{\hat{I}_y}{\hbar} + \frac{\hat{S}_z}{\hbar} \otimes \frac{\hat{I}_z}{\hbar} \right] \\
\hat{\mathcal{H}} &= -\mu_B g_e B_0 \cdot \frac{1}{2} \begin{pmatrix} 1 & 0 \\ 0 & -1 \end{pmatrix} \otimes \begin{pmatrix} 1 & 0 \\ 0 & 1 \end{pmatrix} \frac{1}{\hbar} + \mu_N g_N B_0 \cdot \frac{1}{2} \begin{pmatrix} 1 & 0 \\ 0 & 1 \end{pmatrix} \otimes \begin{pmatrix} 1 & 0 \\ 0 & -1 \end{pmatrix} \frac{1}{\hbar} \\
&\quad + \frac{A}{4} \cdot \left[ \begin{pmatrix} 0 & 1 \\ 1 & 0 \end{pmatrix} \otimes \begin{pmatrix} 0 & 1 \\ 1 & 0 \end{pmatrix} + \begin{pmatrix} 0 & -i \\ i & 0 \end{pmatrix} \otimes \begin{pmatrix} 0 & -i \\ i & 0 \end{pmatrix} + \begin{pmatrix} 1 & 0 \\ 0 & -1 \end{pmatrix} \otimes \begin{pmatrix} 1 & 0 \\ 0 & -1 \end{pmatrix} \right] \\
\hat{\mathcal{H}} &= -\mu_B g_e B_0 \cdot \frac{1}{2\hbar} \begin{pmatrix} 1 & 0 & 0 & 0 \\ 0 & 1 & 0 & 0 \\ 0 & 0 & -1 & 0 \\ 0 & 0 & 0 & -1 \end{pmatrix} + \mu_N g_N B_0 \cdot \frac{1}{2\hbar} \begin{pmatrix} 1 & 0 & 0 & 0 \\ 0 & -1 & 0 & 0 \\ 0 & 0 & 1 & 0 \\ 0 & 0 & 0 & -1 \end{pmatrix} \\
&\quad + \frac{A}{4} \cdot \left[ \begin{pmatrix} 0 & 0 & 0 & 1 \\ 0 & 0 & 1 & 0 \\ 0 & 1 & 0 & 0 \\ 1 & 0 & 0 & 0 \end{pmatrix} + \begin{pmatrix} 0 & 0 & 0 & -1 \\ 0 & 0 & 1 & 0 \\ 0 & 1 & 0 & 0 \\ -1 & 0 & 0 & 0 \end{pmatrix} + \begin{pmatrix} 1 & 0 & 0 & 0 \\ 0 & -1 & 0 & 0 \\ 0 & 0 & -1 & 0 \\ 0 & 0 & 0 & 1 \end{pmatrix} \right]
\end{aligned} \tag{1.13}$$

Extracting  $a = \frac{\mu_B g_e B_0}{2\hbar}$  and  $b = \frac{\mu_N g_N B_0}{2\hbar}$  yields

$$\hat{\mathcal{H}} = \begin{pmatrix} \frac{A}{4} - a + b & 0 & 0 & 0 \\ 0 & -\frac{A}{4} - a - b & \frac{A}{2} & 0 \\ 0 & \frac{A}{2} & -\frac{A}{4} + a + b & 0 \\ 0 & 0 & 0 & \frac{A}{4} + a - b \end{pmatrix}$$

To extract magnetic field dependent energy eigenvalues out of the 4x4-matrix of  $\hat{\mathcal{H}}$ , the matrix has to be diagonalized first. One possible diagonalization is given in Eq.1.14:

$$\hat{\mathcal{H}} = \begin{pmatrix} -\frac{A}{4} - \frac{(A^2 + 4a^2 + 8ab + 4b^2)^{\frac{1}{2}}}{2} & 0 & 0 & 0 \\ 0 & -\frac{A}{4} + \frac{(A^2 + 4a^2 + 8ab + 4b^2)^{\frac{1}{2}}}{2} & 0 & 0 \\ 0 & 0 & \frac{A}{4} + a - b & 0 \\ 0 & 0 & 0 & \frac{A}{4} - a + b \end{pmatrix} \tag{1.14}$$

**Table 1.1** Constants used for the diagonalization of the Hamiltonian 4x4-matrix of the interaction of an electron with a nucleus.

Constant (abbreviation)	Value	Unit
Electron g-factor ( $g_e$ )	2.0023	-
Nuclear g-factor ( $g_N$ )	5.5858	-
Bohr Magneton ( $\mu_B$ )	$9.27 \cdot 10^{-24}$	$\text{J}\cdot\text{T}^{-1}$
Nuclear Magneton ( $\mu_N$ )	$5.05 \cdot 10^{-27}$	$\text{J}\cdot\text{T}^{-1}$
Planck-constant ( $h$ )	$6.67 \cdot 10^{-34}$	Js

Implementing the constants (see table 1.1) and using an exemplary hyperfine splitting constant  $A$  of 20 MHz obtains a dependence of each energy eigenvalue against the magnetic field. The plot of all four energy levels is displayed in Fig. 1.2. Here, there are two plots illustrated. The left side (Fig. 1.2(a)) shows all four energy eigenvalues in colored lines as a function of the rising magnetic field. There are also four dashed, black lines illustrated showing the energy splitting extracted by the Hamiltonian only taking into account the hyperfine interaction of the z-component and leaving out the x- and y-component in the third part of the Hamiltonian. Upon higher fields ( $B > 2$  mT) it is demonstrated that the four eigenvalues for both cases, z-component hyperfine interaction and x-,y- and z-component hyperfine interaction, overlap. Hence, we can approximate mainly contribution of the z-component of spins in higher fields. This is called the high-field approximation [3].

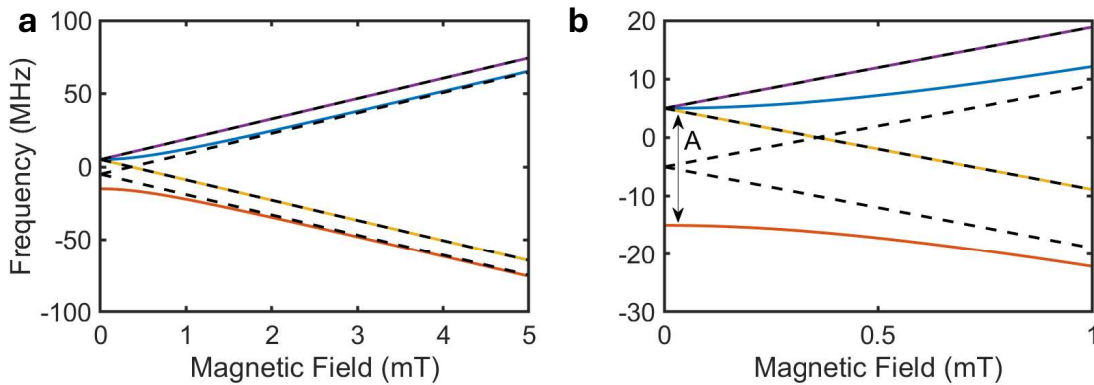


**Fig. 1.2** (a) Energy levels plotted against magnetic field in units of MHz. The four colored lines represent the eigenvalues extracted by diagonalizing the 4x4-matrix of the Hamiltonian. The four black dashed lines represent the high-field approximation by only taking into account the z-component hyperfine interaction without the x- and y-contribution in the Hamiltonian. (b) Smaller field range of (a) to showcase the zero field splitting (hyperfine splitting constant  $A = 20$  MHz displayed by a double-headed arrow at 0 mT).

The right side (Fig. 1.2(b)) shows the part below 1 mT of the energy splitting derived by the Hamiltonian. Here, it is evident that two colored lines start with a slight curvature (blue and orange) while the other two colored lines (purple and yellow) are perfectly overlapping with their black-dashed high-field approximated counterparts.

This showcases the hyperfine interaction of the two spins. The curvature comes from the contribution of mixed states (e.g.  $|\alpha\beta\rangle$  and  $|\beta\alpha\rangle$  or also called  $|\uparrow\downarrow\rangle$  and  $|\downarrow\uparrow\rangle$ ). Because we have to derive these mixed states by linear combination of pure states (e.g.  $|\alpha\alpha\rangle$  and  $|\beta\beta\rangle$  or also called  $|\uparrow\uparrow\rangle$  and  $|\downarrow\downarrow\rangle$ ), we obtain a slight curvature due to the off-diagonal contributions in the 4x4-matrix of the Hamiltonian before the diagonalization [3].

The double arrow on the right side shows the hyperfine splitting constant of  $A = 20$  MHz derived by three states starting at  $+\frac{A}{4}$  while the fourth state starting at  $-\frac{3A}{4}$  at a magnetic field of 0 mT.

The ESR transitions can now be observed by changing the electron spin. Hence, the two possible transitions are derived from the orange line to the blue line and from the yellow line to the purple line.

## 1.2 Continuous Wave (CW) ESR techniques

Continuous wave electron spin resonance (CW ESR) spectroscopy is a powerful technique used to study the magnetic properties of paramagnetic species by observing their interaction upon microwave (MW) radiation with an external magnetic field. This method involves the continuous application of MW radiation to a sample while varying the magnetic field to induce resonance conditions. CW ESR is instrumental in investigating the electronic structure, local environment, and dynamics of radicals, transition metal complexes, and other paramagnetic entities. In this thesis, we focus on the conventional aspects of CW ESR, as well as specialized techniques such as power saturation, spin traps and transient ESR, to comprehensively explore their applications and advancements in understanding paramagnetic systems.

### 1.2.1 Conventional CW ESR

#### 1.2.1.1 CW ESR Instrumentation

Several spectroscopic methods in ESR are used to characterise and spectroscopically investigate paramagnetic species. These are briefly summarised in the following chapters in order to be able to proceed to the evaluation of the published results. In this chapter,

conventional CW ESR spectroscopy will be explained in more detail before moving on to the power saturation technique.

To explain the principle of CW ESR spectroscopy in more detail, the theoretical background will be explained using a schematic example.

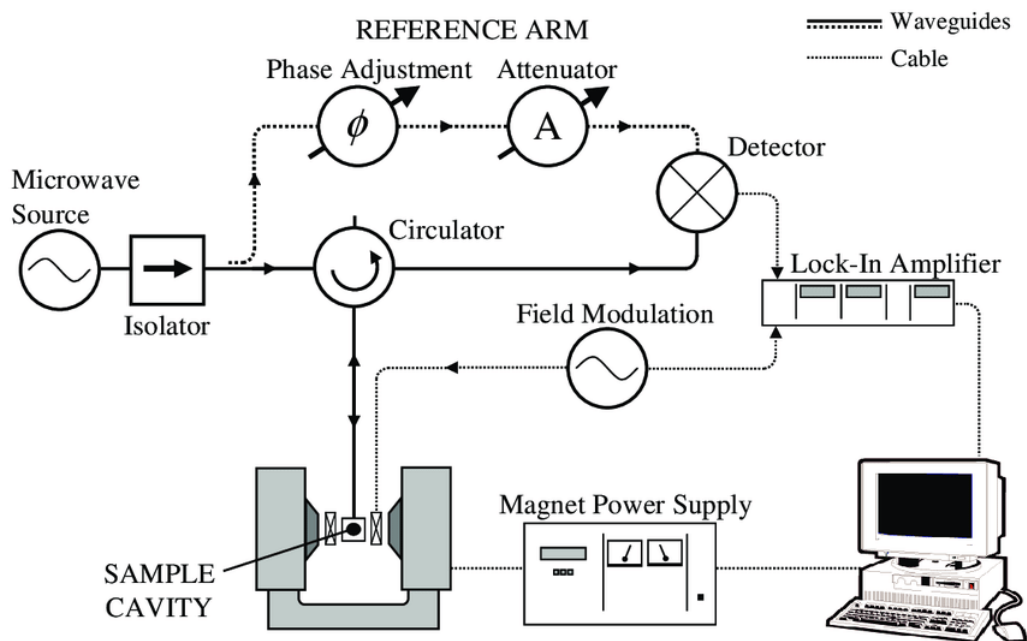


**Fig. 1.3** Schematic representation of an ESR spectrometer where microwave radiation is supplied from the microwave source and gets redirected through the circulator, resonator and reference arm until the reflected microwaves get detected at the detector and are processed at the digitizer and computer. An electro magnet supplies a homogeneous  $B_0$  magnetic field at the sample positioned in the cavity. [9]

Figure 1.3 shows a schematic diagram of the setup of an ESR spectrometer. The microwave radiation is generated by a microwave source in the microwave bridge, such as a Gunn diode or a klystron, and is guided through a reference arm and a sample pathway.

The microwave radiation in the sample arm is guided by a circulator via a waveguide into the resonator where the sample of interest is located. The circulator works in such a way that it only transmits radiation in an anti-clockwise direction, for example from the microwave source to the resonator, as well as radiation from the resonator to the detector. MW radiation could also be transmitted by reflections back to the microwave source, but this is prevented by an isolator connected between the microwave source and the circulator. This isolator only allows electromagnetic radiation to pass in one direction, so that radiation is only transmitted towards the circulator [9].

The electromagnet ensures a homogeneous magnetic field in the area of the sample of interest and is supplied with the necessary current by the magnet power supply. The homogeneous magnetic field results from the special design of the electro magnet, as the distance between the two coils corresponds to the inner radius of each individual coil.

The used CW ESR resonator setup can either consist of a dielectric resonator (sapphire,  $\text{Al}_2\text{O}_3$ ) within a shielded resonator (cavity) or a split-ring resonator. Both resonator topologies build up a standing microwave field inside the resonator,  $B_1$ , which is perpendicular to the outer static magnetic field generated by the electro magnet,  $B_0$ .

If the electromagnetic radiation is absorbed by a magnetic transition at the sample, when the resonance condition is fulfilled (see Eq.(1.8)), less energy is available in the resonator. However, it is not the absorbed radiation that is measured, but the reflected radiation at the resonator. Hence, during continuous microwave irradiation, the detected signal gets mixed with a reference signal. When there is no ESR transition happening, the detector shows no signal because it is 180 degrees phase-shifted to the reference signal. If a resonant magnetic transition is achieved, both signals will not cancel each other and a signal gets detected. This signal is plotted in the console against the magnetic field and can be read out on the computer [10].

### 1.2.2 Power Saturation

Most paramagnetic samples can be saturated with the power levels available in commercial ESR spectrometers. If quantitation of spin concentration or the power saturation of spins is the goal of the experiment, it is necessary to acquire the ESR spectrum at a microwave power level well below the significant saturation of the ESR spectrum. In the absence of saturation the ESR signal increases linearly with  $B_1$ . The resonator efficiency to convert microwave power to  $B_1$  is dependent on e.g. the resonator design or the quality factor ( $\nu_{Res}/\Delta\nu$ ).

If there is no unresolved hyperfine splitting, the relationship between linewidth,  $B_1$  and relaxation times (will be discussed in the next chapter) is:

$$(\Delta B_{PP})^2 = \frac{4}{3\gamma^2 T_2^2} \cdot (1 + \gamma^2 B_1^2 T_1 T_2) \quad (1.15)$$

where  $B_{PP}$  is the peak-to-peak line width,  $\gamma$  is the electron gyromagnetic ratio,  $T_1$  the spin-lattice relaxation time and  $T_2$  the spin-spin relaxation time. If the  $B_1$  field is small enough that the  $\gamma^2 B_1^2 T_1 T_2$  product term is  $\lll 1$ , the signal is unsaturated. Furthermore we can define the saturation factor:

$$s = \frac{1}{(1 + \gamma^2 B_1^2 T_1 T_2)} \quad (1.16)$$

For microwave power levels below saturation,  $s = 1$ . In general it is useful to know the relationship of  $B_1$  at the sample and the incident microwave power. A series of measurements at different power levels is called a progressive power saturation study. Species with shorter relaxation times can be characterized by CW methods better than by pulse ESR methods.

One example of the power saturation experiment is the derivation of relaxation behaviour of a spin-label introduced in membrane proteins.

The motivation to study membrane proteins lies within their central regulatory role in cellular signaling pathways. The use of site-directed spin labeling (see Fig. 1.4 a) and power saturation is a powerful tool to study protein-membrane interactions. This approach was pioneered by studies of transmembrane proteins, membrane-binding peptides, and peripheral proteins in the working groups of Hubbell, Cafiso, and Robinson [11–16].

The reaction mechanism of site-directed spin labelling is displayed in Fig. 1.4a [17]. Here, (1-Oxyl-2,2,5,5-tetramethyl-3-pyrroline-3-methyl)methanethiosulfonate (MTSSL) is used as a stable radical to be attached to thiole groups in the protein at positions of interest. It is possible to use natural occurring cysteine residues with thiole groups or the other possibility is to employ mutagenesis to change amino acids selectively to cysteine in order to be able to attach MTSSL. The CW ESR spectra of MTSSL-labelled proteins already incorporate important information of the mobility of the MTSSL spin label (depicted in Fig. 1.4b) [17]. Here, the CW ESR spectrum undergoes a broadening due to anisotropy caused by the mobility of the spin label, especially in proteins embedded in membranes. In frozen solution, the spin label will be fully immobilized.

Several studies have used a combination of site-directed spin labeling and ESR power saturation methods to define the membrane-docking depths and geometries of several functionally important peripheral signaling proteins [18–22]. This method, termed the ESR membrane depth measurement, first introduces a spin label to selected positions on the protein of interest. Afterwards the depth of the spin label in the membrane is measured by monitoring its rate of collisions with extrinsic paramagnetic probes. The information provided by a sufficiently large library of spin label positions includes the identification of the protein residues and secondary structure elements that interact with the membrane, and their depth of penetration into the membrane. This information in turn enables the development of a structural model that describes the depth to which the protein penetrates into the bilayer environment, as well as the angle of the docked protein relative to the membrane surface.

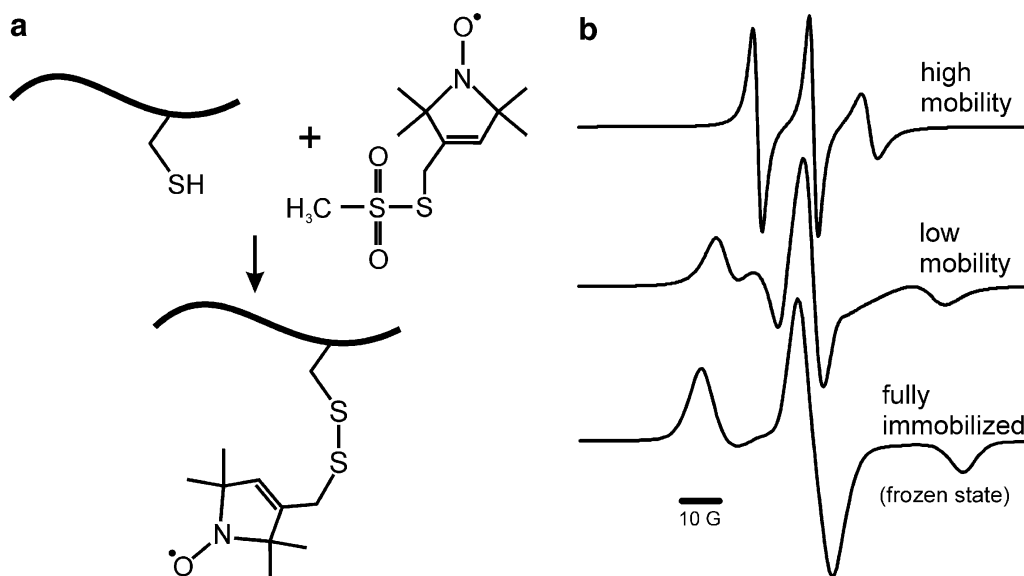


**Fig. 1.4** (a) Example showcasing the site-directed spin labelling approach of single-cysteine mutants. Here, the reaction with MTSSL (S-(1-oxyl-2,2,5,5-tetramethyl-2,5-dihydro-1H-pyrrol-3-yl)methyl methanesulfonylthioate) yields a relatively long-lived radical attached to the backbone of the protein. (b) The CW ESR spectra of MTSSL-labelled proteins incorporate important information of the mobility of the MTSSL spin label. The CW ESR spectrum undergoes a broadening due to anisotropy caused by the mobility of the spin label, while in frozen solution, the spin label will be fully immobilized. [17]

The main advantage of this method is that it can be carried out under physiological temperature and ionic conditions using small amounts of protein (~1 nmol). Analysis of these proteins by the ESR membrane depth method can differentiate membrane-docking geometries and can provide further structural explanations for the function of membrane proteins.

An example on how this technique works and how the membrane depth parameter can be extracted will be illustrated in the following figures 1.5 and 1.6.

Fig. 1.5 shows the CW ESR spectra acquired at different MW power values for a single-cysteine mutant of a model membrane protein with MTSL-spin label attached [23]. Using the power saturation technique one has to extract the peak-to-peak amplitude of the central resonance line. On the first glance it is visible that the central signal rises with increasing microwave power until it reaches a saturation point and then decreases again [23].

If this procedure is done for the three several conditions, a supply of compressed air or with high purity  $N_2(g)$  or incubated overnight with NiEDDA (Nickel Ethylenediamine-N,N-

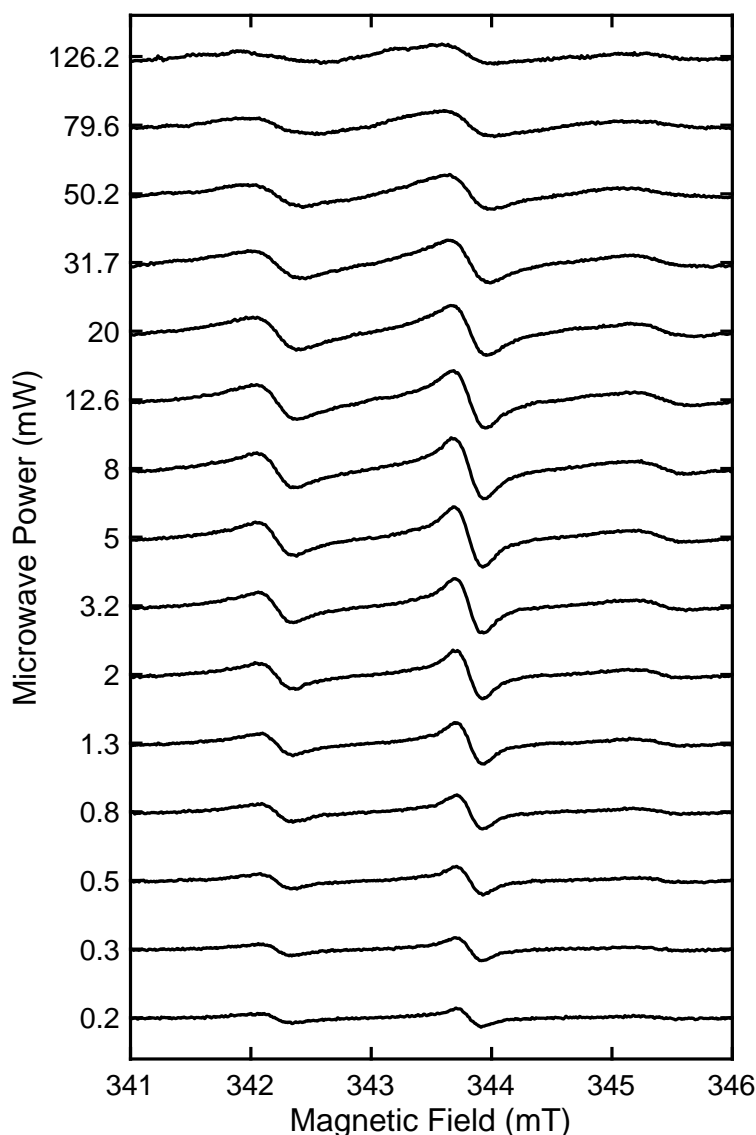


**Fig. 1.5** Stacked illustration of several CW ESR spectra acquired during the power saturation experiment. The microwave power is changed in 2dB power steps (y-axis) and an ESR spectrum gets acquired. Typically, the ESR spectrum reaches a saturation point (here: 8 mW) of signal intensity. After this point, the ESR signal intensity gets lower again.

diacetic acid) purged with  $N_2(g)$ , the penetration of a relaxing agent ( $O_2(g)$  or NiEDDA) can be monitored throughout the protein.

The three mentioned conditions on an example system for a model protein are shown in the following Fig. 1.6. Power saturation curves were plotted for the peak-to-peak amplitude of the central ESR line as a function of the square root of the incident microwave power ( $P$ ).

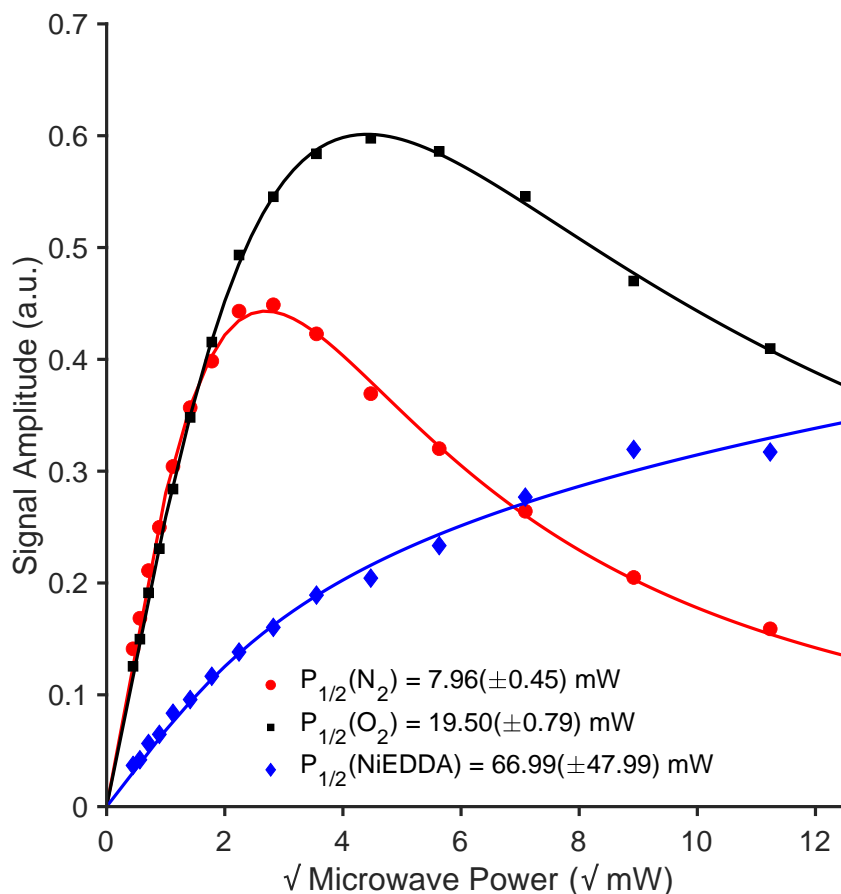


**Fig. 1.6** Signal amplitude of power saturation experiments during several conditions (nitrogen: red, oxygen: black, NiEDDA: blue) of a model membrane protein. The signal intensity of the central ESR line is plotted against the square root of incident MW power.

The data points were then fitted using the following equation 1.17:

$$A = I\sqrt{P} \left[ 1 + \frac{(2^{1/\epsilon} - 1)P}{P_{1/2}} \right]^{-\epsilon} \quad (1.17)$$

where  $A$  is the central line amplitude,  $I$  is a dimensionless scaling factor,  $P$  is the microwave power and  $P_{1/2}$  is the power where the first derivative amplitude is reduced to half with respect to its unsaturated value. The parameter  $\epsilon$  is a measure of the homogeneity of saturation of the resonance line. For homogeneous and inhomogeneous saturation curves,  $\epsilon$  is 1.5 and 0.5 respectively.  $\epsilon$  is approximately close to 1.5 under  $\text{N}_2(\text{g})$  for natural relaxation conditions and  $\epsilon$  decreases with higher collision rates [11, 23, 24].

The depth parameter was calculated using the following equation 1.18 where  $P_{1/2}(\text{O}_2)$ ,  $P_{1/2}(\text{N}_2)$  and  $P_{1/2}(\text{NiEDDA})$  are the corresponding power values where the ESR central line amplitude is reduced to half of its hypothetical unsaturated value [11, 23, 24].

$$\Phi = \ln \left[ \frac{\Delta P_{1/2}(\text{O}_2)}{\Delta P_{1/2}(\text{NiEDDA})} \right] = \ln \left[ \frac{P_{1/2}(\text{O}_2) - P_{1/2}(\text{N}_2)}{P_{1/2}(\text{NiEDDA}) - P_{1/2}(\text{N}_2)} \right] \quad (1.18)$$

Using this simple MW power saturation CW ESR method allows the monitoring of the spin-label position throughout a membrane protein embedded in a specific environment. This method was mainly used in a project of describing a membrane protein conformational shift upon changing lipid environment from bilayer to monolayer and can be further employed to other similar proteins embedded in lipid membranes (see chapter 3).

### 1.2.3 Spin Trapping Technique

The direct observation of transient and reactive radicals poses a significant challenge due to their short lifetimes and low concentrations. To overcome these obstacles, spin trapping has emerged as a pivotal method in ESR spectroscopy, enhancing the detection and analysis of elusive radical species [25–27].

Spin traps are stable molecules that react with short-lived radicals (often reactive oxygen species, ROS) to form long-lived radical adducts, which are more easily detected and can be analyzed by ESR spectroscopy. This technique not only extends the lifespan of the radical species but also provides structural insights into the nature of the original radicals and allows kinetic postulations about the radical formation pathway. The application of spin traps thus bridges the gap between the fleeting existence of transient radicals and the robust analytical capabilities of ESR spectroscopy [28–30].

In this section, the fundamental principles and practical applications of spin traps in ESR spectroscopy will be explained. Furthermore, the chemistry of spin trapping agents and their reaction mechanisms with various radical species will be shown. Through presented case studies and recent advancements, we illustrate how spin traps have significantly expanded the analytical scope of ESR spectroscopy, facilitating groundbreaking research in the reaction pathway of nanoparticles used in degrading microplastics in water [31] (see chapter 3).

The reaction mechanism of the spin trapping technique is schematically shown in Fig. 1.7(a). When a short-lived free radical is generated in a system (e.g.  $\cdot\text{R}_2$ ), it reacts with the spin trap to form a long-lived spin adduct. The spin trap typically contains a reactive double bond (often a nitroso or a nitron compound) that can readily react with the

radical. This reaction between the spin trap and the radical results in a new species (the spin adduct) that contains an unpaired electron, which is stable enough to be detected by ESR spectroscopy.

The spin adducts have characteristic ESR spectra that provide information about the nature of the trapped radical. By analyzing the hyperfine splitting patterns and  $g$ -values in the ESR spectrum, one can infer details about the original free radical, such as its identity and environment. A few examples of spin traps are illustrated in Fig. 1.7(b). Usually spin traps contain the nitron functionality, such as DMPO, PBN and DEPMPO but other functionalities allow hints to other reaction mechanisms, e.g. TEMP as a probe to investigate the formation of singlet oxygen as a ROS [31].

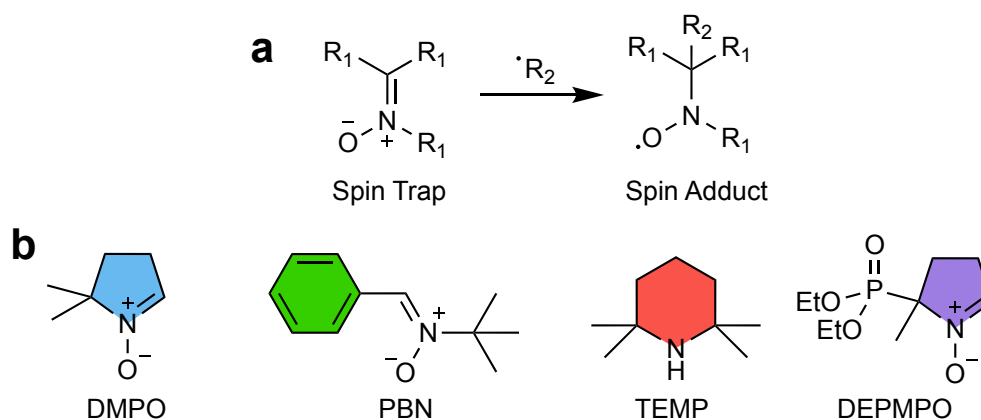


**Fig. 1.7** (a) Schematic illustration of the formation of detectable spin adducts after the reaction of a spin trap with a short-lived radical species  $\cdot R_2$ . (b) A collection of commonly spin trap examples with the nitron functionality (5,5-Dimethyl-1-pyrroline N-Oxide (DMPO, blue),  $\alpha$ -Phenyl-N-tButylnitron (PBN, green) and 5-(Diethoxyphosphoryl)-5-methyl-1-pyrroline N-Oxide (DEPMPO, purple)) and others (2,2,6,6-Tetramethylpiperidine (TEMP, red)).

In order to investigate the reaction pathway of the radical scavenging process of spin traps, an example using DMPO will be shown. The next Fig. 1.8 shows the detection scheme how the radical adduct will be formed in the subsequent reaction of DMPO with generated hydroxide radicals. The spin trap DMPO yields no ESR signal and is ESR silent. After reacting with the short-lived hydroxide radicals the relatively stable radical adduct DMPOOH (right side of Fig. 1.8) is formed which is ESR active, yielding the ESR spectra depicted in Fig. 1.9.

Here, the typical DMPOOH spectrum is visible as pseudo-quartett yielded by coupling of the electron with nitrogen and the nearest hydrogen (depicted on the right side of Fig. 1.8). In order to allow assumptions about the radical formed upon the reaction



investigation into their magnetic properties and reaction behaviors also allowing kinetic predictions, significantly expanding the scope of ESR applications. A few examples of the usage of this technique are displayed in several scientific works in the beginning of chapter 3.

### 1.2.4 Transient EPR

Some common methods using CW ESR spectroscopy were described in the last sections. Transient EPR (TR-EPR) spectroscopy is another strong CW ESR technique that was first introduced in the 1970s by the working groups of Kim [32] and Weissman [32]<sup>6</sup>.

This technique has proven to be a very useful method for the observation of light-induced, short-lived paramagnetic species [33–36]. These include triplet states and radical pairs whose lifetimes range from a few nanoseconds to several microseconds. The latest developments using this technique have been in the areas of detecting radical pairs in the electron transfer processes in proteins [37–41] and in donor-acceptor electron transfer models [42–46]. Furthermore higher multiplet states (e.g. quartet or quintet states) can be observed [47–51].

The following describes the experimental procedure in more detail by exemplary showing the investigation of the photo-excited triplet state in pentacene-doped p-terphenyl crystals [52].

#### 1.2.4.1 TR-EPR Experimental Setup

The experimental setup of a TR-EPR spectrometer is shown schematically in Fig. 1.10.

The schematic in Fig. 1.10 shares several similarities with the conventional CW ESR spectrometer (see Fig. 1.3). To enable a time-resolved detection and the excitation of photo-sensitive states, the TR-EPR setup is additionally equipped with an oscilloscope and a pulse laser. Similar to conventional CW ESR, microwaves are continuously applied to the resonator. Samples under investigation are generally non-magnetic in their ground state. An excitation via a short, high power laser pulse creates short-lived paramagnetic excited states.

After the generation of a paramagnetic species (in this example: pentacene triplet state), a time-dependent EPR signal is recorded in the oscilloscope, representing the decay of the excited state (see Fig. 1.13). Pentacene (see Fig. 1.12 for chemical structure) has received a lot of attention in TR-EPR spectroscopy in recent decades. The origin lies in the magnetic and electronic properties after light-induced excitation [54, 55]. The long triplet lifetime of several microseconds makes pentacene a well suited molecule for the acquisition of triplet spectra. Therefore, modifications of pentacene have already been investigated by EPR spectroscopy as possible organic semiconductors [56–58].

---

<sup>6</sup>Notation: Since both terms, ESR (electron spin resonance) and EPR (electron paramagnetic resonance) describe the phenomenon of magnetic resonance, the term EPR will be used in this section to differentiate TR-EPR from conventional CW ESR methods.

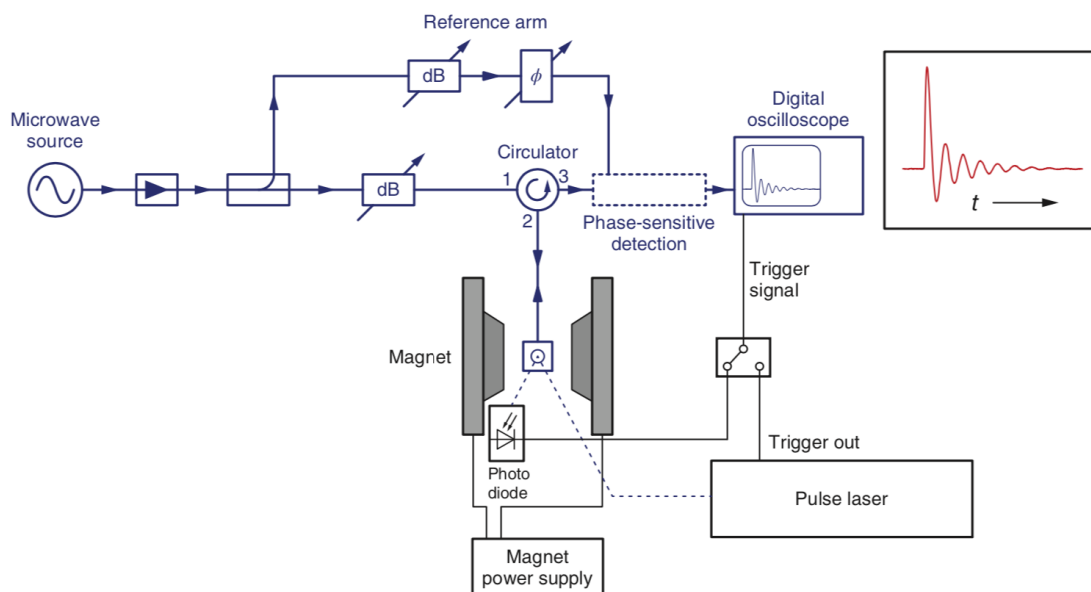


**Fig. 1.10** Scheme of a TR-EPR spectrometer where MW radiation is supplied from the microwave source and gets redirected through the circulator, resonator, reference arm until the detection by a digital oscilloscope will be acquired. The oscilloscope gets triggered by either a photodiode or a trigger signal coming from the Q-Switch synchronization of a pulsed laser which is used to generate a photo-induced triplet state. [53]

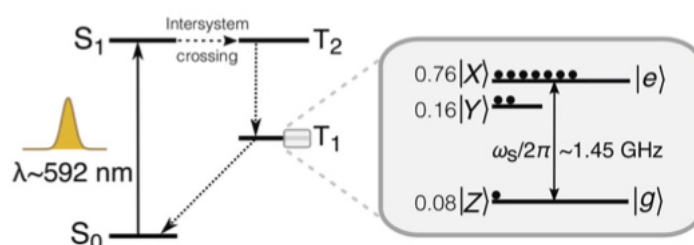


**Fig. 1.11** Simplified Jablonski diagram of the light-induced excitation (592 nm) of pentacene from the singlet ground state  $S_0$  to the excited singlet state  $S_1$ . The excitation is followed by an intersystem crossing (ISC) transition into the triplet state  $T_2$  with subsequent relaxation into the triplet state  $T_1$ . [59]

Fig. 1.11 shows the schematic Jablonski diagram, which illustrates the optical excitation pathway from the singlet ground state  $S_0$  to the excited singlet state  $S_1$ . The excitation is followed by an intersystem crossing (ISC) transition to the triplet state  $T_2$  with subsequent relaxation into the triplet state  $T_1$  [59]. On the right-hand side of Fig. 1.11, the triplet

population is also shown, which showcases a spin-polarized population (population does not occupy according to Boltzman's principle) after the ISC.

The time-dependent EPR signal after laser excitation is obtained at a fixed magnetic field strength  $B_0$  without applying magnetic field modulation.

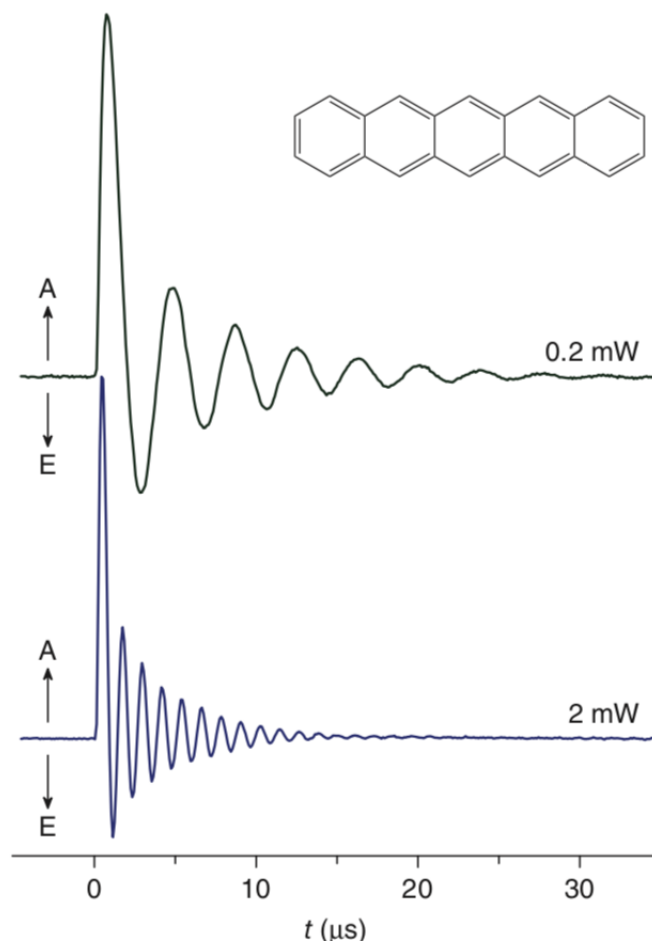


**Fig. 1.12** Simulated, transient nutations of the triplet state of a pentacene crystal ( $S=1$ ). Absorptive signals (A) and emissive signals (E) show the relaxation behaviour of the net magnetization vector  $\vec{M}$ . The visible oscillations in time are also called Torrey oscillations [60] or  $B_1$  oscillations of the magnetization vector around  $B_1$ . The nutation frequency  $\omega_1$  is proportional to the square root of incident microwave power. [53]

The time dependent signal (so called 'transients' [53], visible on Fig. 1.12) is acquired as a function of  $B_0$ , resulting in a time/magnetic field map of the EPR signal (see Fig. 1.13).

These transient time traces can show oscillations, also called nutations (visible in Fig. 1.12). These nutations can be very helpful for determining the relaxation behaviour and lifetime of the irradiated chromophore within the resonator [53]. Furthermore, the

conversion factor  $\Lambda$  can be calculated, a measure for the resonator efficiency to convert the incoming microwave power into a  $B_1$  magnetic field to interact with the sample. An example for this use is explained in one of the presented scientific works in the next chapter.

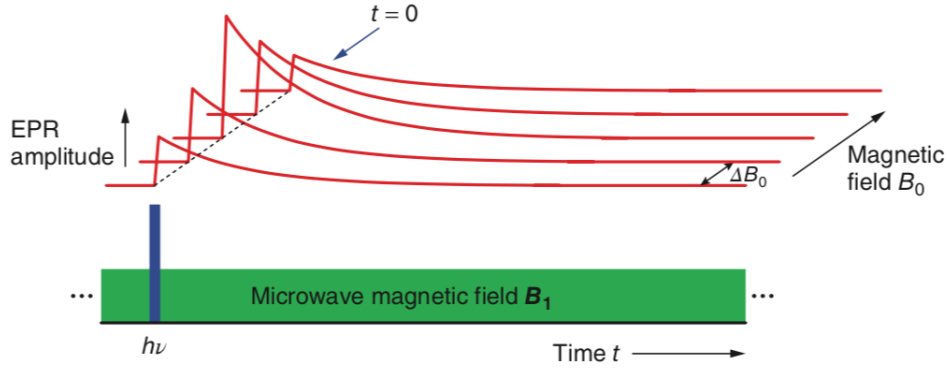


**Fig. 1.13** Schematic representation of the TR-EPR data acquisition. Different time traces (red lines) are recorded upon against the magnetic field ( $\Delta B_0$ ). The starting point of signal acquisition is the laser pulse trigger signal  $h\nu$  (blue bar). [53]

#### 1.2.4.2 Description of TR-EPR spectroscopy

The quantum mechanical description of the TR-EPR experiment can be described with the help of Bloch's equations established in a reference frame rotating with  $\omega_{MW}$  [61–63]:

$$\begin{aligned}
 \frac{dM_x}{dt} &= \Delta\omega M_y(t) - \frac{M_x(t)}{T_2} \\
 \frac{dM_y}{dt} &= \Delta\omega M_x(t) - \frac{M_y(t)}{T_2} - \omega_1 M_z(t) \\
 \frac{dM_z}{dt} &= \omega_1 M_y(t) + \frac{M_0 - M_z(t)}{T_1} \\
 \Delta\omega &= \omega - \omega_0
 \end{aligned}
 \tag{1.19}$$

Here  $M_{x,y,z}$  stands for the corresponding x-, y-, z-components of the macroscopic magnetisation vector of the sample,  $T_1$  is the longitudinal or spin-lattice relaxation time

and  $T_2$  is the transverse or spin-spin relaxation time which will be discussed in the next chapter more thoroughly [63].

With a solution for  $M_y(\omega_0, t)$ , the signal amplitude  $S(t)$  results in:

$$S(t) = \int_{-\infty}^{\infty} f(\omega_0) M_y(\omega_0, t) d\omega_0 \quad (1.20)$$

where  $f(\omega_0)$  is a frequency distribution function. When solving Eq.(1.20), the oscillatory solution can be selected for solids since most triplet states are measured in frozen solution state below the freezing point of their respective solvent, as a crystal or as a powder [64]:

$$\omega_1^2 > \frac{1}{4} \left( \frac{1}{T_1} - \frac{1}{T_2} \right)^2 \quad (1.21)$$

For solids,  $T_2 \ll T_1$  and therefore the condition from Eq.1.21 is reduced to  $|\omega_1| \gg \frac{1}{T_2}$  and the following equation is obtained by inserting  $|\omega_1|$  into Eq.(1.20):

$$S(t) = -M_0 \int_{-\infty}^{\infty} f(\omega_0) \frac{\omega_1}{\omega_{\text{eff}}} \sin(\omega_{\text{eff}} t) \cdot \exp\left(-\frac{2\omega_{\text{eff}}^2 - \omega_1^2}{2\omega_{\text{eff}}^2 T_2} \cdot t\right) d\omega_0 \quad (1.22)$$

with  $\omega_{\text{eff}} = \gamma B_{\text{eff}}$ . With an analytical integration for a broad Gaussian line, the following term is obtained [64]:

$$S(t) \propto -M_0 \omega_1 J_0(\omega_1 t) \exp\left(-\frac{t}{2T_2}\right) \quad (1.23)$$

$J_0$  is the zero-order Bessel function, which is a solution of the second-order linear differential equation [65]. The transient nutation is mainly determined by this zero-order Bessel function, multiplied by an exponential decay function [64, 66].

The transient time traces are a representation of the precession vector of the magnetisation  $\vec{M}_{eq}$  around the magnetic field component of the microwave radiation  $B_1$ . The frequency of these oscillations,  $\omega_1$ , depends on the strength of the  $B_1$  field [67]. The Torrey oscillations (visible in Fig. 1.12) only become visible, when the spin-spin relaxation is very small  $\omega_1 \gg \frac{1}{T_2}$ . This is the case, for example when paramagnetic molecules are held spatially fixed, for example in crystalline compounds. If the spin-spin relaxation is very fast, the Torrey oscillations will dissipate and can be recorded with poor resolution. To obtain the nutation frequency  $\omega_1$ , a Fourier transformation of the transient nutation is required [67].

Fig. 1.12 shows two nutations of a pentacene crystal at different microwave power values (0.2 mW and 2 mW). The nutation frequency  $\omega_1$  of both oscillations is propor-

tional to the square root of the irradiated microwave power and can be described by equation 1.24 [53].

$$B_1 = \Lambda \cdot \sqrt{Q \cdot P} = \frac{\omega_1}{\sqrt{2} \cdot \gamma_e} \quad (1.24)$$

Where  $\Lambda$  is the conversion factor,  $Q$  the quality factor and  $P$  the radiated microwave power. If equation 1.24 is now rearranged, the conversion factor can be determined:

$$\Lambda = \frac{\omega_1}{\gamma_e \cdot \sqrt{2} \cdot \sqrt{Q \cdot P}} \quad (1.25)$$

The factor  $\sqrt{2}$  in equation 1.25 takes into account the fact that the measured sample (pentacene) is a triplet state and not a doublet state. This means that the conversion factor can be determined for a given resonator configuration and quantifies the efficiency of irradiated microwave power to  $B_1$  magnetic field conversion.

The greater the conversion factor, the higher the conversion of microwave radiation into a oscillating magnetic field  $B_1$ . A high conversion factor is therefore desirable, to achieve the greatest possible interaction between microwaves and the paramagnetic sample. One example for the use of the conversion factor enhancement will be discussed in the scientific works following the theoretical description.

A further description of the Hamilton operator allows deeper knowledge about the excited triplet state. As TR-EPR spectra of triplet states of organic molecules, are usually dominated by the zero-field splitting (ZFS) interaction, the Hamiltonian  $\hat{\mathcal{H}}$  used to describe the system is dramatically reduced since all other contributions, including hyperfine interactions with nearby nuclei, can be considered as small perturbations that can be accounted for (inhomogeneous) line broadening [68]. The only contributions to be considered are the Hamiltonian for the electron Zeeman interaction,  $\hat{\mathcal{H}}_{EZ}$ , and for the ZFS interaction,  $\hat{\mathcal{H}}_{ZFS}$ :

$$\hat{\mathcal{H}} = \hat{\mathcal{H}}_{EZ} + \hat{\mathcal{H}}_{ZFS} = -\mu_B \cdot g_e \cdot \frac{\hat{S}_z}{\hbar} \cdot B_0 + \hat{\mathbf{S}}\mathbf{D}\hat{\mathbf{S}} \quad (1.26)$$

where  $g_e$  is the g-factor,  $\mu_B$  is the Bohr magneton,  $B_0$  the magnetic field,  $\hat{S}_z$  the electron spin operator in the z-direction,  $\hat{\mathbf{S}}$  the electron spin operator in all directions and  $\mathbf{D}$  is the ZFS tensor. The ZFS Tensor  $\mathbf{D}$  is given by [68]:

$$\mathbf{D} = \begin{pmatrix} D_x & 0 & 0 \\ 0 & D_y & 0 \\ 0 & 0 & D_z \end{pmatrix} = \begin{pmatrix} -\frac{1}{3}D + E & 0 & 0 \\ 0 & -\frac{1}{3}D - E & 0 \\ 0 & 0 & \frac{2}{3}E \end{pmatrix} \quad (1.27)$$

where  $D$  and  $E$  are the ZFS parameters that can be evaluated from the experimental spectra. Since the ZFS Tensor  $\mathbf{D}$  is traceless ( $D_x + D_y + D_z = 0$ ), the remaining degrees of freedom can be completely described by the ZFS parameters  $D$  and  $E$ . They are related to the eigenvalues of the  $\mathbf{D}$  tensor and can be assigned as [68]:

$$D = \frac{3}{2}D_z \quad E = \frac{D_x - D_y}{2} \quad (1.28)$$

Experimentally assigning the signs of  $D$  and  $E$  is demanding, and therefore, absolute values are usually given. A method to quantify the signs of  $D$  and  $E$  could be realised via quantummechanical calculations or via ODMR (optically detected magnetic resonance) techniques [53]. A visual representation of the yielded TR-EPR spectra depending on the ZFS parameter is illustrated in Fig. 1.14. Depending on the rhombicity, three general cases can be distinguished. The intermediate case (blue, central TR-EPR spectrum in Fig. 1.14(b)) is the situation for  $0 < |E| < |D|/3$  found mostly and allowing to extract absolute values for  $D$  and  $E$  even graphically from the spectra. An example for that situation can be seen on photo-excited porphycene or porphyrine derivates (the molecular structure of porphycene as an exemplary is shown beside the TR-EPR spectrum on Fig. 1.14(b)) [69].

Proceeding from this situation, the spectra can show either the fully axial case with  $|E| = 0$  (Fig. 1.14(c)) or the fully rhombic case with  $|E| = |D|/3$  (Fig. 1.14(a)). As  $2|E|$  is defined as the separation of the energy values of  $D_x$  and  $D_y$  in the fully axial case with  $|E| = 0$ , the respective lines in the spectrum collapse. As an example for this situation, the thoroughly described photo-excited triplet state of pentacene can be used (Fig. 1.14(c)) [52].

The other extreme, the fully rhombic case with  $|E| = |D|/3$ , results in the two innermost lines of the EPR spectrum to fall on top of each other and to cancel each other out. The other lines collapse as well, but on the outermost position usually referred to as  $D_z$  (Fig. 1.14(a), top, red line). An example for this situation is illustrated by a BODIPY (boron-dipyrromethene) dye compound shown on the right side of Fig. 1.14(a). Fully axial triplet spectra are rare, as they require a particular high symmetry of the excited state [68], e.g.

pentacene. These three characteristic situations with exemplary molecular examples are depicted in the following Fig. 1.14.

In conclusion, transient EPR spectroscopy is a strong tool for studying the dynamic behavior of paramagnetic species and short-lived intermediates in matrices and participating in chemical reactions. By providing time-resolved insights into electron spin states, TR-EPR helps investigating reaction mechanisms, energy transfer processes, and molecular interactions. A few scientific examples of the usage of this technique are shown in chapter 3 on a metal porphyrine triplet states and the evaluation of resonator optimizations.

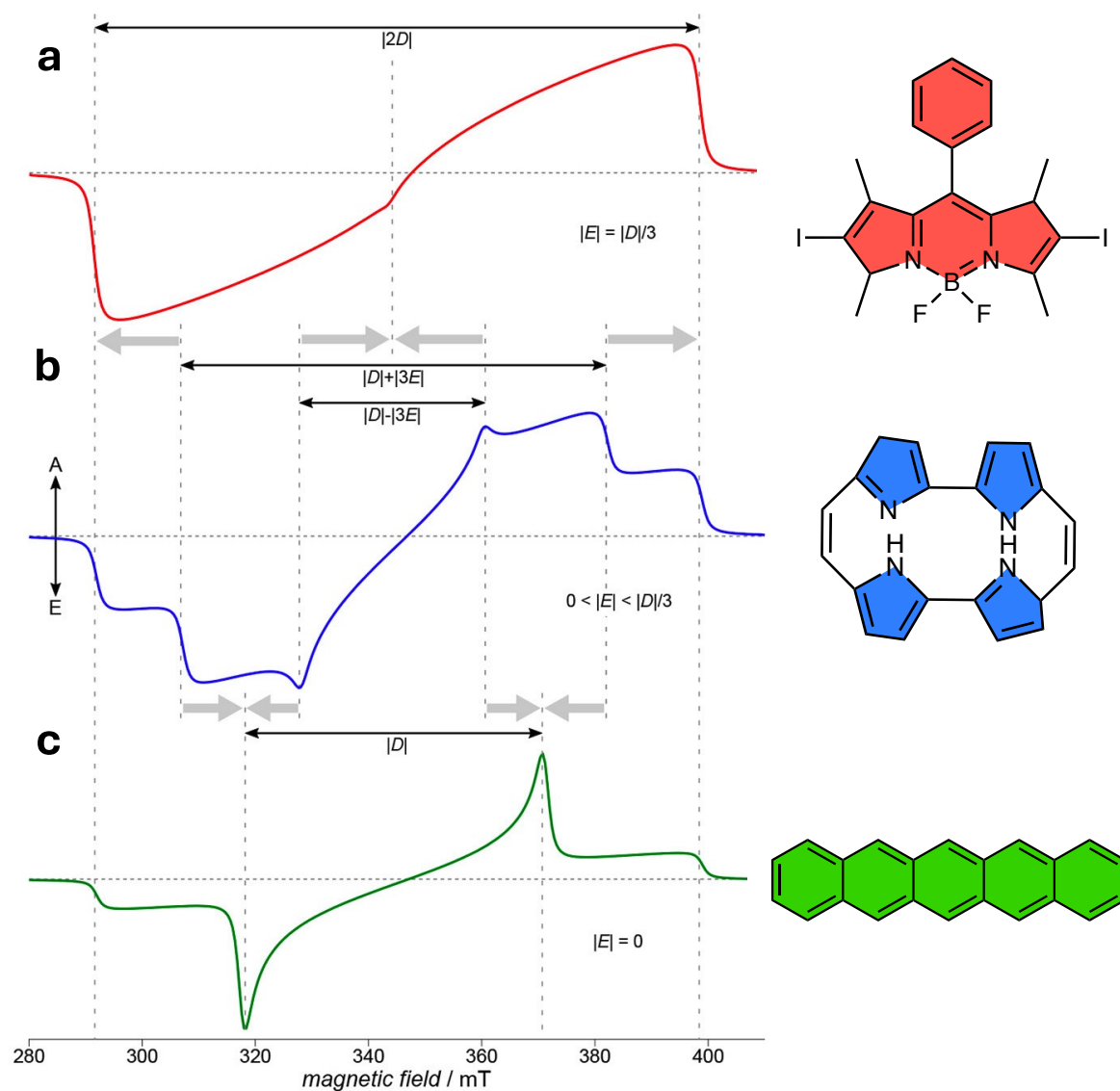


**Fig. 1.14** Exemplary TR-EPR spectra of (photo-generated) triplet states. The three characteristic situations for the ratio of the two parameters  $D$  and  $E$  are shown here: (a) the fully rhombic case (top, red) with a BODIPY (boron-dipyrromethene) derivate as example [69], (b) an intermediate case (blue, centre) with porphycene as an exemplary [70] and a fully axial case (green, bottom) with pentacene as already showcased [52]. The intermediate case (b) depicts all three principal axes of the  $\hat{D}$  tensor in the spectrum. This case is not fulfilled for either fully axial or fully rhombic situations (a) and (c). Whereas assigning  $D_x$  and  $D_y$  is usually not possible to derive from the spectra, the  $D_z$  position is always assigned to the shoulders furthest apart in the spectrum. [52, 53, 68–70]

## 1.3 Pulse ESR Methods

The first two sections described CW ESR techniques which were used in this collection of scientific projects. Nevertheless, the investigation of structure and dynamic properties are often limited in CW ESR due to the spectral and time resolution. One possibility to overcome these challenges is the application of microwave pulses. Unlike its continuous-wave counterpart, pulse ESR uses short, intense bursts of microwave radiation to interrogate the magnetic properties of electron spins, providing higher resolution and sensitivity. This method allows scientists to unravel the complexities of molecular structures, dynamics, and interactions with exceptional precision. This section will shed light on the application of simple and advanced pulse ESR sequences to detect relaxation times, to obtain structural information and to extract distance distributions of electron spins [3].

### 1.3.1 Relaxation Time Measurement

Relaxation time measurement via pulse ESR spectroscopy is a crucial technique for understanding the dynamic behavior of electron spins in paramagnetic systems. This process involves determining the timescales in which electron spins return to equilibrium after being perturbed by a microwave pulse. As already mentioned in the theoretical description of transient EPR for simplicity reasons we are using the Bloch equations in a rotating reference frame to model the influence of MW pulses on the spins (Eq. (1.19)). Electron spins can orientate themselves parallel or antiparallel to an outer magnetic field (typically oriented in the z-direction). Generally, in pulse ESR spectroscopy samples with  $10^{12} - 10^{16}$  spins are used, thus a vector describing the majority of spins is feasible. The sum or ensemble  $\vec{M}$  of all magnetic moments  $\vec{m}_i$  is given by:

$$\vec{M} = \sum \vec{m}_i \quad (1.29)$$

A visual representation of the magnetization vector  $\vec{M}$  is illustrated in Fig. 1.15. Here, the majority of spins or spin packets  $\vec{m}_i$  are orientated parallel to the outer magnetic field given by  $B_z$  demonstrated by the bright red vector  $\vec{M}$ . This vector  $\vec{M}$  is rotating with the Larmor frequency:

$$\omega_L = \frac{g_e \mu_B B_z}{\hbar} \quad (1.30)$$

This rotation process happens upon application of an outer magnetic field  $B_0$  on the sample of interest without microwave radiation. Further irradiation with short microwave

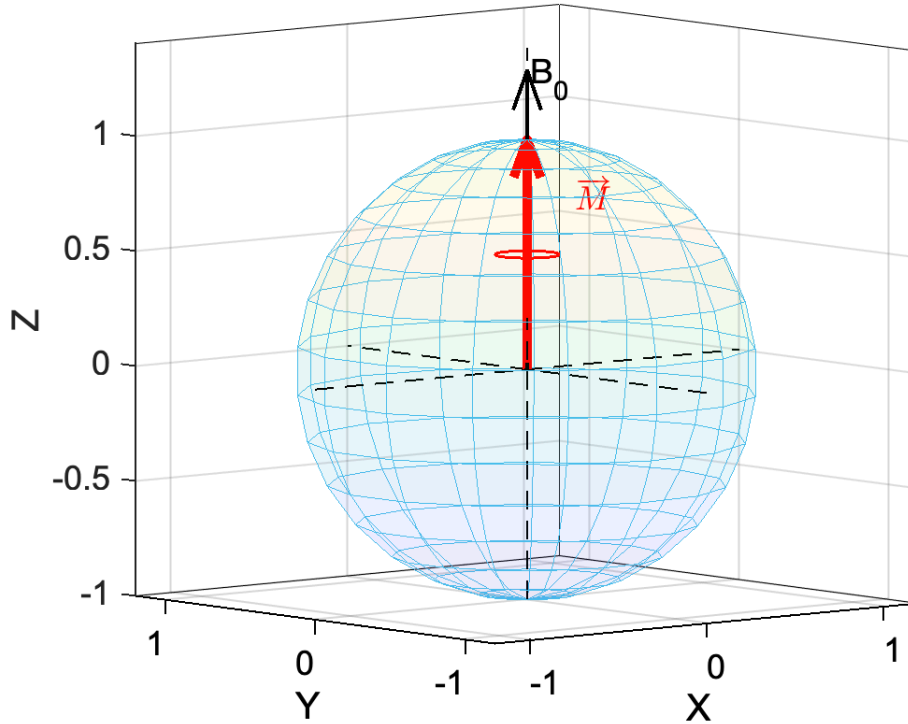


**Fig. 1.15** Simulated precession movement of the magnetization vector  $\vec{M}$  around the outer magnetic field  $B_0$  in the  $z$ -direction. The vector  $\vec{M}$  is precessing with the Larmor frequency  $\omega_L$  (depicted by the red circle) in the laboratory frame.

pulses allows to perturb this equilibrium state of  $\vec{M}$ . MW pulses can be described by their magnetic field component  $B_1$  [71].

Depending on how long the microwave irradiation lasts, in other words, how long the length of the applied microwave pulse is chosen, the magnetization vector  $\vec{M}$  will be disturbed by a Rabi frequency  $\omega_R$  (see Eq.(1.31)) to precess around the new magnetic field vector  $B_1$  depicted in Fig. 1.16.

$$\omega_R = \frac{g_e \mu_B B_1}{\hbar} \quad (1.31)$$

The lengths of the applied microwave pulses are often abbreviated by their resulting rotation angle on  $\vec{M}$ . The most important microwave pulses are described as a  $\pi/2$  pulse (90 degrees rotation angle resulting in  $\vec{M}$  positioning in the  $x$ - $y$ -plane) and a  $\pi$ -pulse (180 degree rotation angle resulting in  $\vec{M}$  positioning in the  $-z$  direction). These two pulses are important for the description of the next two subchapters in regards to the relaxation time  $T_1$  and  $T_2$  measurement. A detailed description how the perturbation

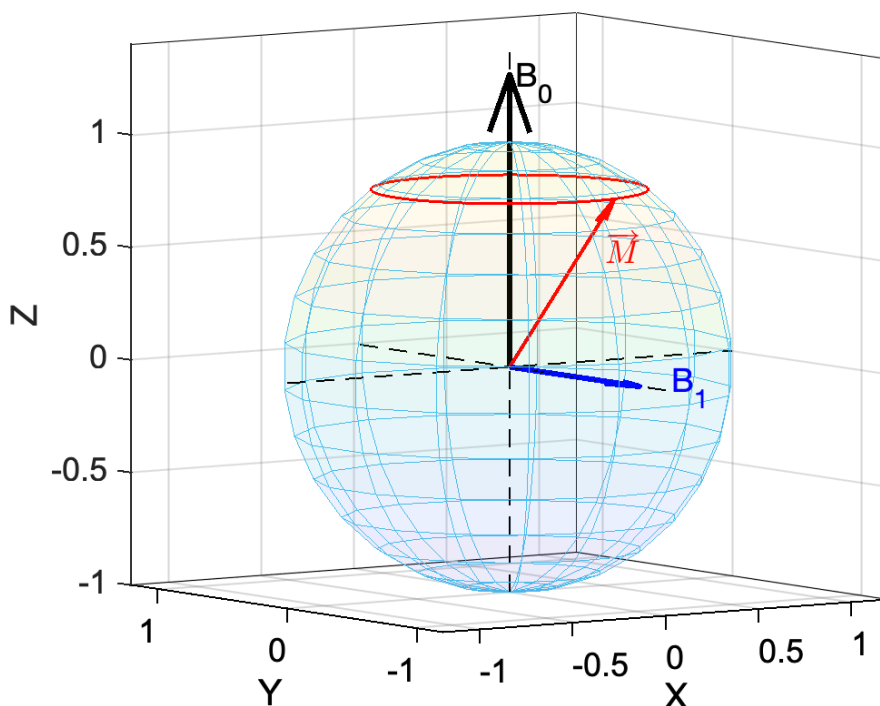


**Fig. 1.16** Simulated precession movement of a single magnetization vector  $\vec{M}$  around the outer magnetic field  $B_0$  (black) in the z-direction. The vector  $\vec{M}$  is precessing with the Larmor frequency  $\omega_L$  (red) upon irradiation with microwaves which generate an oscillating magnetic field  $B_1$  (blue). The projection of the precession movement in the x- and y-direction is illustrated as a red line on the Bloch sphere.

and relaxation process is affecting  $\vec{M}$  will be described using Bloch spheres in the next paragraphs supporting Fig. 1.17.

Fig. 1.17 illustrates how the application of microwave pulses yields a detectable voltage signal, the so-called Hahn-Echo [3]. The pulse pattern of a  $\pi/2$  pulse followed by a  $\pi$ -pulse after the time interval  $\tau$  is called the Hahn-Echo pulse sequence. This sequence generates a spin echo signal which consists of a rising and then falling free induction decay (FID) signal. The origin of this FID signal lies within relaxation mechanisms. In order to further describe the origin of this spin-echo-signal, the next paragraphs will describe the mechanisms upon excitation and relaxation after applying the Hahn-Echo pulse pattern sequence.

The mechanism of excitation pulses and subsequently relaxation of the perturbed spin system can be described using the following steps:

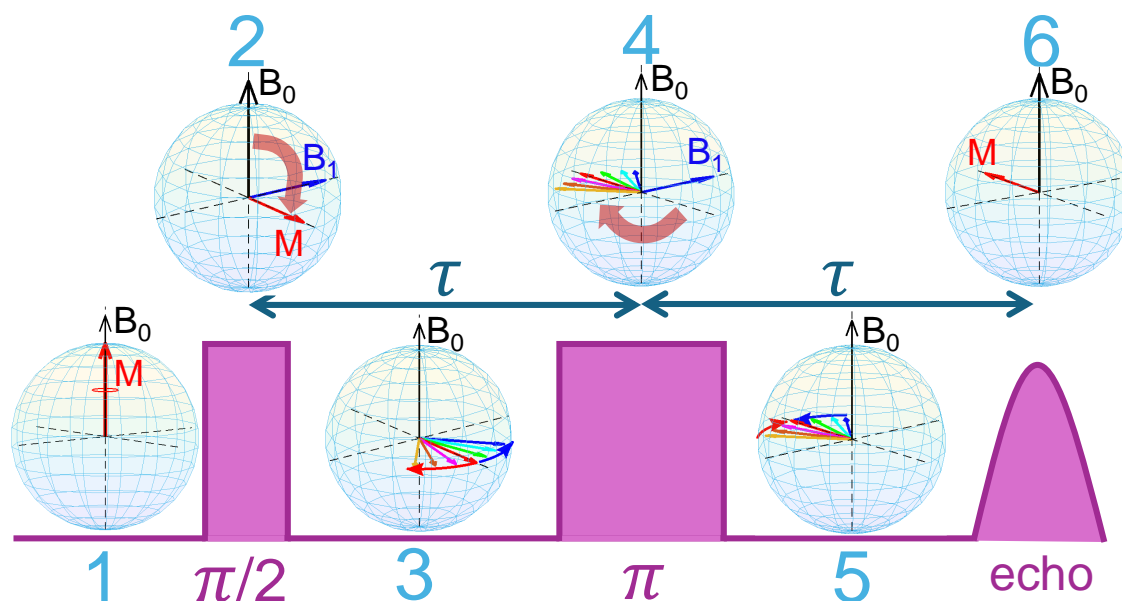


**Fig. 1.17** Stimulated spin echo yielded by applying the Hahn-Echo sequence on a paramagnetic sample of interest in a resonant magnetic field. 1 - Ground state magnetization vector  $\vec{M}$ , 2 -  $\vec{M}$  in the +y-direction after  $\pi/2$  pulse, 3 - Unfolding of the  $\vec{M}$  due to relaxation processes, 4 - 180 degree spin flip after  $\pi$ -pulse, 5 - Refocusing of  $\vec{M}$ , 6 - Combination of spin vectors after  $2\tau$  yielding the spin-echo-signal.

1 - The spin vectors create a magnetization vector  $\vec{M}$  upon applying an external field,  $B_0$ , with the orientation of  $\vec{M}$  in the +z direction. This is the ground state of the spin system which will be perturbed by high-power microwave pulses.

2 - Directly after applying the  $\pi/2$  pulse in the +x direction (direction of  $B_1$ ),  $\vec{M}$  will be precessing around the +x-direction until it positions itself in the +y-direction.

3 - Due to field inhomogeneities and/or impurities in the sample as well as magnetic couplings to other spins, electron spins will exhibit a distribution of Larmor frequencies, instead of a single frequency. Hence, there will be some spin vectors with a faster  $\omega_L$  (depicted by the red, orange and yellow vectors) and some spin vectors with a slower  $\omega_L$  (green and blue vectors). The equilibrium magnetization  $\vec{M}$  will be fanning out in the x-y-plane during the time  $\tau$  between the first two pulses.

4 - The second  $\pi$ -microwave pulse flips every spin vector around 180 degrees in the x-y-plane while the radial speed of propagation of the spin vectors is maintained.

5 - After the second microwave pulse, the spin vectors maintain their direction of propagation in the x-y-plane.

6 - After exactly the time interval  $2\tau$  the slow and fast  $\omega_L$  spin vectors recombine in the -y-direction, yielding a measurable voltage signal, the so-called spin echo. The relaxation mechanisms will be discussed in the next chapters.

### 1.3.1.1 Spin-Spin Relaxation Time $T_2$

The spin-spin relaxation time  $T_2$ , also called transversal relaxation time, describes the relaxation mechanisms of electron spins in the x-y-plane after the application of a microwave pulse on a spin system in a magnetic field. Sometimes it is also called phase memory time,  $T_M$ , since it can be used to describe how long information can be stored in the selected spin system until the information will be lost during relaxation processes. This feature is important for modern information storage technologies such as quantum bits (qubit) [72–74]. A scientific example where  $T_M$  on a possible qubit system could be prolonged using deuterated solvent as environment will be discussed in the next chapter 3.

The mechanism of the  $T_2$  relaxation time can be described with flip-flop transitions between electron spins. When an electron spin A interacts with an electron spin B in near proximity, a transition can happen where both spins change their respective magnetic quantum number (e.g.  $\uparrow_A \downarrow_B \rightarrow \downarrow_A \uparrow_B$ ). Angular momentum is preserved during that transition but another effect takes place: The system loses coherence and hence, the ensemble magnetization vector  $\vec{M}$  will be lower in intensity. If the time between two pulses is long enough, the magnetization will be equally distributed in both directions and hence, no coherence (no spin echo after the Hahn-Echo sequence) is observed.

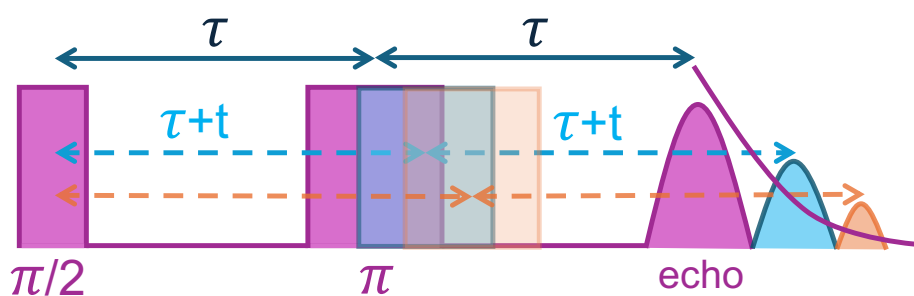


**Fig. 1.18** Schematic representation of the delayed Hahn-Echo sequence, the  $T_2$  relaxation time measurement. Firstly, a Hahn-Echo sequence will be applied (purple bars). Afterwards, the time between the two pulses will be prolonged by the time  $t$  (blue bars). At the end the time will be prolonged even further until there is almost no spin echo visible (orange bars).

In order to monitor and measure the  $T_2$  relaxation time, a time-delayed Hahn-Echo pulse sequence can be used. The measurement principle is schematically shown in

Fig. 1.18. Here, a first Hahn-Echo sequence will be employed (purple bars) to observe a spin echo. The next measurement will prolong the time between the  $\pi/2$ -pulse and the  $\pi$ -pulse with the time  $t$  (blue bars). The resulting spin echo will be smaller and can be observed after the time  $2\tau + 2t$ . This principle will be repeated for longer interpulse delay times  $\tau + t$  (orange bars) until the spin system will lose the coherence completely and no spin echo will be observed.

The resulting exponential decay curve (purple curve in Fig. 1.18) follows the equation [3]:

$$M_z = M_0 \cdot \exp\left(-\frac{2t}{T_2}\right) \quad (1.32)$$

where  $M_z$  is the integrated spin echo signal,  $M_0$  is a scaling factor,  $2t$  the time prolonging step size and  $T_2$  the spin-spin relaxation time. This relaxation mechanism as already explained happens in the transversal (x-y-) plane without taking into account the relaxation of the spin system in the ground state where  $\vec{M}$  will be positioned along the z-axis again. This relaxation process will be discussed in the next chapter.

An example on how the spin spin relaxation time can be implemented in a scientific workflow is illustrated in the physical contributions of chapter 3 regarding the pulse ESR performance of optimized MW resonators.

### 1.3.1.2 Spin Lattice Relaxation Time $T_1$

The spin lattice relaxation time,  $T_1$ , is also called the longitudinal relaxation time since it describes the relaxation of  $\vec{M}$  towards the thermal equilibrium aligned in the z-direction of the spin system. In order to determine this relaxation mechanism, a 3-pulse inversion recovery pulse sequence can be used. The pulse sequence is schematically illustrated in the following Fig. 1.19.

Here, a  $\pi$ -pulse inverts the magnetization  $\vec{M}$  to the -z-direction in the beginning. Shortly afterwards, a Hahn-Echo detection sequence is employed yielding a negative spin echo signal (purple sequence). In the second pulse sequence, the interpulse time  $\tau$  of the Hahn-Echo sequence stays unchanged while the time between the first  $\pi$ -inversion pulse and the Hahn-Echo sequence is prolonged by  $T + t$  (blue sequence). The resulting spin echo will be smaller in intensity because upon prolonging the time between the  $\pi$ -inversion pulse and the Hahn-Echo sequence, the spin system already relaxed to some extent towards the +z-direction, yielding a smaller absolute value of  $\vec{M}$  vector in the x-y-plane. When the time between the first two pulses is prolonged even further, the resulting spin echo will be positive again. When the time  $t$  is long enough the spin system will be in

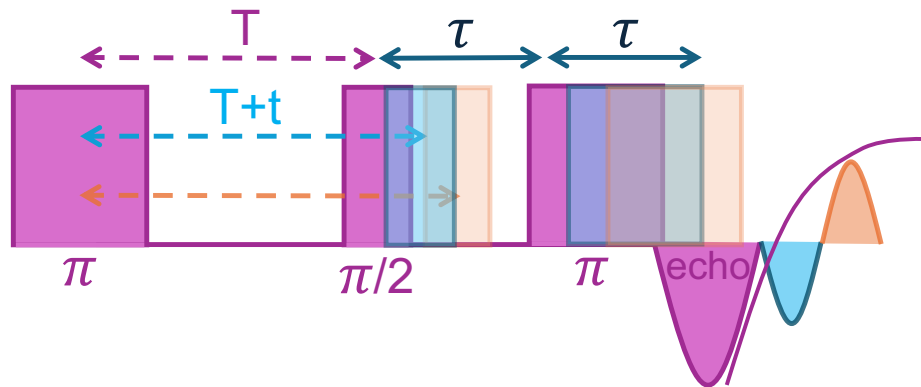


**Fig. 1.19** Schematic representation of the 3-pulse inversion recovery sequence, the  $T_1$  relaxation time measurement. Firstly, a  $\pi$ -pulse followed by a Hahn-Echo sequence will be applied resulting in a negative spin echo signal (purple sequence). Afterwards, the time between the first two pulses will be prolonged by the time  $t$  (blue sequence). At the end the time will be prolonged even further until the spin echo is positive again (orange sequence).

the ground state again upon detecting the spin echo with the Hahn-Echo sequence. The resulting saturation curve (purple curve in Fig. 1.19) can be described by:

$$M_z = M_0 \cdot \left( 1 - \exp\left(-\frac{t}{T_1}\right) \right) \quad (1.33)$$

where  $M_z$  is the integrated spin echo signal,  $M_0$  is the scaling factor,  $t$  the time prolonging step size and  $T_1$  the spin lattice relaxation time.

### 1.3.2 Electron Nuclear Double Resonance (ENDOR)

In contrast to the relaxation time measurements described in previous sections, electron nuclear double resonance (ENDOR) spectroscopy is a well established pulse ESR technique for measuring nuclear transition frequencies of paramagnetic compounds. A description of the basic principle of pulse ENDOR will be provided as well as a discussion of the details in the two standard pulse schemes, Davies and Mims ENDOR, which are based on polarization transfers by RF (radio frequency) pulses [3, 75–77].

Polarization is generated or shifted via transfer of populations between electron and nuclear transitions. The following Fig. 1.20 illustrates the pulse sequence for the Davies ENDOR technique. During the preparation period (Fig. 1.20 a), nuclear polarization is created by a single MW pulse. In the subsequent mixing period (Fig. 1.20 b), the nuclear polarization is changed by one or several selective RF pulses. Finally, during the detection period (Fig. 1.20 c), the nuclear polarization is transferred back to electron coherence and can be observed as an echo of the electron spins [3].

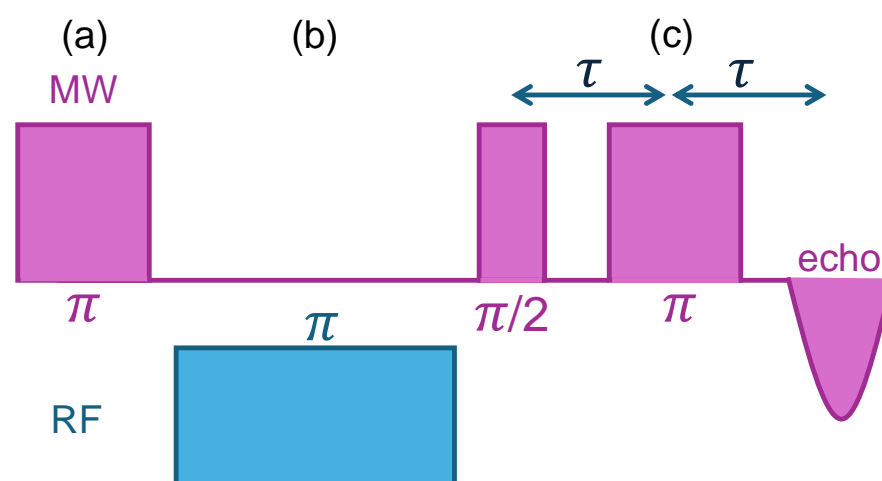


**Fig. 1.20** Schematic representation of the Davies ENDOR sequence. Firstly, the preparation period (a) creates a nuclear polarization by a single MW  $\pi$ -pulse. In the subsequent mixing period (b), the nuclear polarization is changed by a selective RF pulse. Finally, during the detection period (c), the nuclear polarization is transferred to electron coherence and can be observed as an electron spin echo signal. [3]

To further describe the polarization transfers, a simplified model for a four-level energy system will be used as exemplary depiction. Here, the four energy levels correspond to an electron spin ( $S = 1/2$ ) hyperfine coupled to a nuclear spin ( $I = 1/2$ ). For a magnetic field large enough to tune the Zeeman interactions dominant over the hyperfine interaction, four pure spin states form. These four energy levels (1-4 in Fig. 1.21) are depicted by boxes

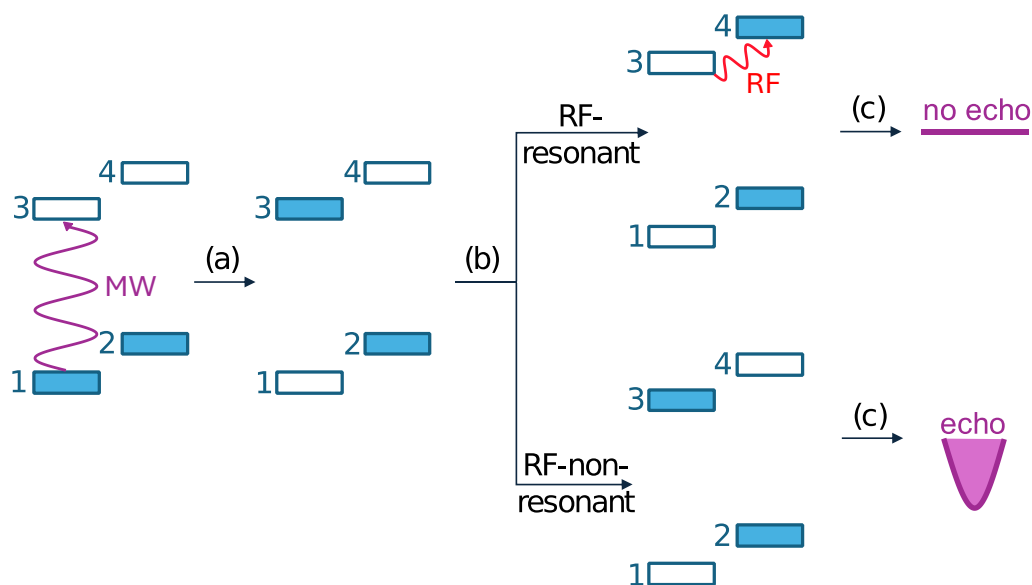


**Fig. 1.21** Energy level model of the Davies ENDOR pulse sequence for a four-level system. The left side depicts the ground state where the two lowest energy levels 1 and 2 are mostly populated (filled boxes) and the higher energy levels 3 and 4 are mostly unpopulated (empty boxes). (a) The first MW  $\pi$ -pulse allows one electron transition to switch the population from 1 to 3. After this partial population inversion two pathways can happen during the mixing period: (b) Resonant nuclear transition (upper trace), the absorption of the RF pulse allows the population transfer from energy level 3 to 4. (c) In the following detection period no spin echo will be observed. Other possible pathway: RF pulse is not on resonance with a nuclear transition. The resulting detection period with a Hahn-Echo sequence will result in detecting a negative spin echo. [3]

which can be differentiated by their respective color, empty boxes describe unpopulated energy levels, filled boxes represent populated energy levels [3].

Fig. 1.21 shows the influence of the polarization transfer happening after every pulse period. The system is initially in the ground state. The population of the lower energy levels (1,2) are Boltzman distributed, while the splitting to the higher energy levels (3,4) are assumed unpopulated ( $k_B T \ll E_{(1-3/2-4)}$ ). After the first MW  $\pi$ -pulse resonant with the transition 1- $\rightarrow$ 3 (see (a) in Fig. 1.21) population will be transferred from energy level 1 to 3. After this population inversion two pathways can happen during the mixing period (b).

If the RF pulse is resonant with a nuclear transition (upper trace in Fig. 1.21), the absorption of the RF pulse allows the population to transfer from energy level 3 to 4. In the following detection period (c) resonant with 1- $\rightarrow$ 3, no spin echo will form, as 3 was depopulated by the resonant RF pulse.

The other possible pathway after the mixing period is the application of a non-resonant RF pulse, leaving the populations unchanged to the preparation period. The resulting detection period will result in a negative spin echo, similar to the inversion recovery measurement required to measure  $T_1$ .

By observing the integrated echo signal as a function of the RF frequency allows the detection of nuclear spin transitions, via a reduction of the echo signal intensity.

Since the Davies ENDOR sequence is using mostly MW  $\pi$ -pulses, it is more selective towards high hyperfine couplings  $> 2$  MHz [3]. To resolve smaller hyperfine couplings between nuclei, the more selective Mims ENDOR sequence was developed. The Mims ENDOR pulse sequence is illustrated in Fig. 1.22.

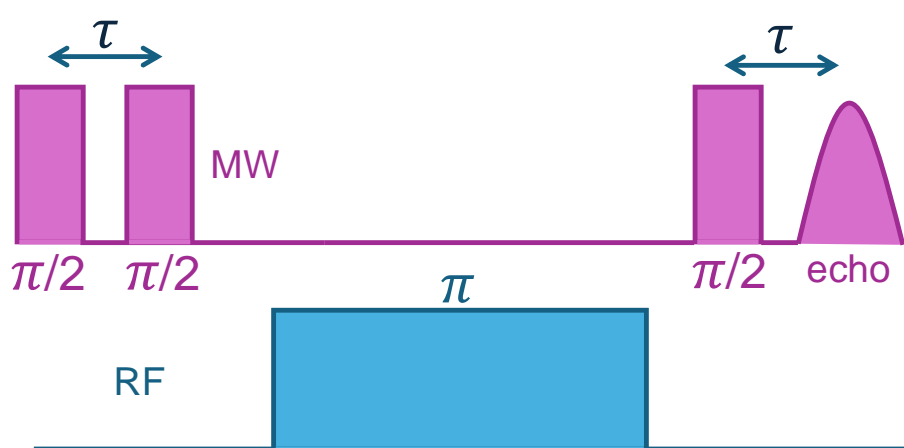


**Fig. 1.22** Schematic representation of the Mims ENDOR sequence. Firstly the preparation period (a) creates a nuclear polarization by two MW  $\pi/2$  pulses. In the subsequent mixing period (b), the nuclear polarization is changed by a selective RF pulse. Finally, during the detection period (c), the nuclear polarization is transferred to electron coherence and can be observed as an electron spin echo signal. [3]

Here, three MW  $\pi/2$ -pulses are used which are more selective. The higher selectivity arises from the usage of MW  $\pi/2$  pulses which transfer the magnetization in the x-y-plane where  $\vec{M}$  can interact more with nearby nuclei. The second MW  $\pi/2$  pulse transfers the coherence into the population [3]. Here, in comparison with the Davies ENDOR sequence, we observe a positive spin echo if the nuclear transition is non-resonant with the RF pulse. When the RF pulse is able to induce a nuclear transition (on resonance) there is no spin echo detectable.

An exemplary system where Mims-ENDOR was employed is illustrated in chapter 3. There, temperature dependent ENDOR measurements were employed to investigate

the structural influence on the spin-spin relaxation time,  $T_2$ , of a quantum bit (qubit) molecule.

In general, ENDOR spectroscopy is a vital technique for probing the interactions between electron spins and nearby nuclear spins in paramagnetic systems. By providing high-resolution information about the local environment of unpaired electrons, ENDOR helps reveal fine details of molecular structures and bonding interactions. This makes it invaluable in studying complex systems and processes where detailed knowledge of electron-nuclear couplings is essential.

### 1.3.3 Pulsed Electron Electron Double Resonance (PELDOR)

The techniques of pulsed ESR spectroscopy have been pivotal in investigating the structural and dynamic properties of paramagnetic species in chemical and biological systems [78–81]. Within this domain, pulsed electron-electron double resonance (PELDOR), also known as double electron-electron resonance (DEER), has emerged as a powerful tool for investigating the spatial arrangements and distances between paramagnetic centers. PELDOR is particularly valuable in the study of macromolecular complexes, where it can provide insights into conformational changes, intermolecular interactions, and the assembly of multi-subunit structures [82–86].

PELDOR exploits the interaction between electron spins to measure distances typically in the range of 1.5 to 5 nanometers [22]. By applying a series of microwave pulses, PELDOR can selectively manipulate and detect spin pairs and from analyzing their interaction strength, a distance distribution is derived. This capability is crucial for understanding the three-dimensional architecture of biological systems and the mechanisms underlying their function [86].

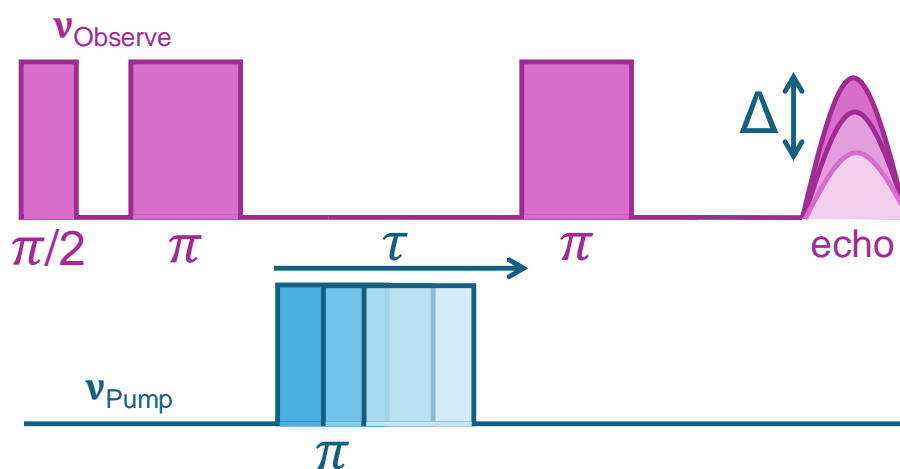


**Fig. 1.23** Schematic representation of the 4-pulse PELDOR sequence. Firstly, three MW pulses at the observe frequency ( $\nu_{\text{Observe}}$ ) create a spin echo. Another MW  $\pi$ -pulse at another MW pump frequency ( $\nu_{\text{Pump}}$ ) will be irradiated, furthermore exciting nearby spins. The spin echo irradiated by the initial MW frequency, will be modulated ( $\Delta$ ) by the dipolar coupling of two nearby electron spins upon moving the pump-pulse along the time scale of  $\tau$ . [3]

The earliest developments were initially generated with a three pulse PELDOR sequence. Due to losses in the early time intervals (short distances, low modulation depth) the theoretical description will advance directly towards the more popular and more

commonly used four pulse PELDOR sequence [3]. Fig. 1.23 illustrates the pulse pattern of the 4-pulse PELDOR sequence. Here, the resulting spin echo arises from a three-pulse MW pulse sequence with a fixed probe frequency ( $\nu_{\text{Probe}}$ ). Another MW  $\pi$ -pulse with a pump frequency ( $\nu_{\text{Pump}}$ ) is applied, exciting a second subset of spins, the so-called B spins. The spin echo irradiated by the initial MW frequency, will be modulated by the dipolar coupling of two nearby A and B spins through systematically delaying the pump pulse by time  $\tau$ , depicted in Fig. 1.23. The reason behind this phenomenon lies within the  $\pi$ -pulse at  $\nu_{\text{Pump}}$  which shifts the A spins off resonance by  $\pm\omega_{dd}$ . After the refocussing period, the transverse magnetisation is off by  $\pm\omega_{dd} \cdot t$  leading to a modulation of the spin echo [86–88]. The separate excitation of A and B spins results in individual phases. The interference is observed as a modulation in the spin echo intensity [3]. Since the timing of the pulse sequence for the A spins is unchanged, the variation of the spin echo is not influenced by the transverse relaxation time  $T_2$  [3].

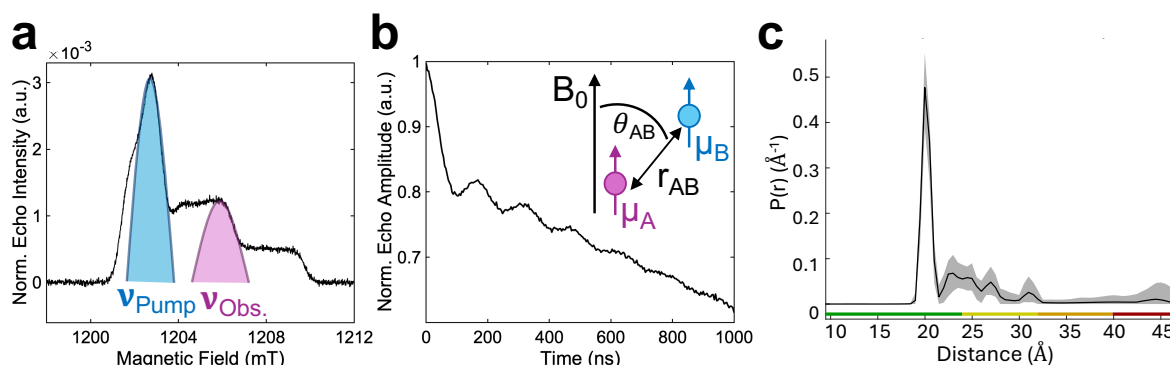


**Fig. 1.24** Measurement principle description of the 4-pulse PELDOR sequence of a polymer example system consisting of two nitroxide spin labels separated by 2.1-2.2 nm. (a) Echo-detected field sweep (EDfS) spectrum showing the excitation profiles of the observe and pump frequency. (b) PELDOR trace showcasing the modulated echo amplitude against the temporal position of the pump pulse. Upper left inset: scheme of the dipolar coupling between the A and B spins in near proximity. (c) Distance distribution after regularization of the acquired PELDOR trace in (b) with an average distance for the polymer system of 2.1-2.2 nm. [3]

The measuring principle will be further described using an exemplary sample. Fig. 1.24 (a) shows the echo-detected field sweep (EDfS) spectrum acquired of a PELDOR standard sample (polymer consisting of two nitroxide spin labels separated by 2.1-2.2 nm). The excitation of the B spins (blue part in Fig. 1.24(a)) is responsible for the modulation of the spin echo acquired at the magnetic field of the A spins (pink part in Fig. 1.24(a)). A scheme of the dipolar coupling between the A and B spins in near proximity is depicted in the upper left corner of Fig. 1.24(b).

The decaying oscillation in Fig. 1.24(b) shows a PELDOR trace acquired at low temperatures (80 K) for the described polymer sample. There, the modulation of the acquired spin echo is clearly visible as a decaying oscillation function. The dipolar Hamiltonian is given by:

$$\hat{\mathcal{H}}_{\text{dd}} = \omega_{ee} \hat{S}_z^A \hat{S}_z^B \quad (1.34)$$

where  $\omega_{\text{dd}}$  is the dipole-dipole coupling and  $\hat{S}_z^{A,B}$  the respecting spin operators for the A and B spins. The dipole-dipole coupling can be furthermore described as [3, 89]:

$$\omega_{\text{dd}} = \frac{\mu_0 g_A g_B \beta_e^2}{4\pi \hbar} \cdot \frac{1}{r_{\text{AB}}^3} \cdot (3 \cos^2(\theta_{\text{AB}}) - 1) \quad (1.35)$$

where  $\mu_0$  is the magnetic constant,  $g_A$  and  $g_B$  are the  $g$  values of the two spins,  $\mu_B$  is the Bohr magneton,  $\hbar$  is the reduced Planck constant,  $r_{\text{AB}}$  is the inter-spin distance, and  $\theta_{\text{AB}}$  is the angle between the inter-spin vector and the magnetic field (inset of Fig. 1.24(b)). The antiproportional correlation between the frequency of the spin echo modulation and the interspin-distance  $r_{\text{AB}}$  is evident in Eq.(1.35).

In order to obtain a probability distribution  $P(r)$  of distances  $r_{\text{AB}}$  in a doubly spin-labeled molecule or protein, the goal is measuring isolated spin pairs. In reality, even at the lowest accessible concentrations, dipolar coupling to spins in other molecules is not negligible. As a result, the overall dipolar signal has to take into account the intramolecular contribution  $V_{\text{intra}}(t)$  of the A-B spin-pair and the intermolecular contribution  $V_{\text{inter}}(t)$  from B spins in other molecules:

$$V(t) = V_{\text{intra}}(t) V_{\text{inter}}(t) \quad (1.36)$$

For molecules homogeneously distributed in all three dimensions,  $V_{\text{inter}}(t)$  is determined by the overall spin concentration and the fraction of spins inverted by the pump pulse  $\lambda$ :

$$V_{\text{inter}}(t) = V_{t=0} \exp\left(-\frac{ct\lambda}{1.0027 \text{ mmol L}^{-1} \mu\text{s}}\right) \quad (1.37)$$

where the numerical constant is  $1.0027 \text{ mmol L}^{-1} \mu\text{s} = 2\pi g_A g_B \mu_B 2\mu_0 N_A / (9\sqrt{3}\hbar)$ , with  $N_A$  being the Avogadro constant. For homogeneous distributions with lower dimension  $d$ , the intermolecular contribution is a stretched exponential function  $\exp(-(kt)d/3)$  with fractal dimension  $d$ , e.g.,  $d \sim 2$  for systems embedded in lipid bilayers and  $d = 3$  for the homogeneous three-dimensional distribution typically encountered for soluble proteins [90–92]. If possible, the signal is recorded such that the dipolar modulation is completely

damped at time  $2t_{max}/3$ , allowing robust separation of the intermolecular contributions [93–95].

After acquiring the modulated spin echo signal displayed in Fig. 1.24(b), the time domain data will be converted into distance distributions. Since distance distributions are much more instructive than the average distance (e.g. multiple distinct conformations) a preprocessing via regularisation is often used. Approaches like Thikonov-regularisation and/or comparison with already existing databanks stabilise the distance distributions and provide an optimal compromise between quality of fit  $\rho$  and smoothness  $\eta$ . An example is illustrated in Fig. 1.24(c) where the average distance for the polymer system of 2.1-2.2 nm could be reproduced.

The technique's sensitivity to long-range distance constraints complements other structural biology methods such as X-ray crystallography, nuclear magnetic resonance (NMR) spectroscopy, and cryo-electron microscopy (cryo-EM) [86]. Unlike these methods, PELDOR does not require crystalline samples or isotopic labeling, and it can be performed in a variety of environments, including solutions, membranes, and even within cells. This versatility enhances its applicability across a broad spectrum of scientific inquiries [3].

The exploration of PELDOR within ESR spectroscopy underscores its profound impact on structural biology and materials science. As a sophisticated technique capable of measuring distances between paramagnetic centers with high precision, PELDOR has proven indispensable for investigating the spatial arrangements and dynamic behaviors of complex molecular systems. PELDOR is applied in the ongoing research towards the investigation of a membrane protein which will be discussed in the biological contribution of chapter 3. Throughout this thesis, we have delved into the fundamental principles of PELDOR, examined its methodological advancements, and highlighted its diverse applications in probing the architecture of proteins, nucleic acids, and a macromolecule as an example.



# Chapter 2

## Experimental Setup

### 2.1 Spectrometers

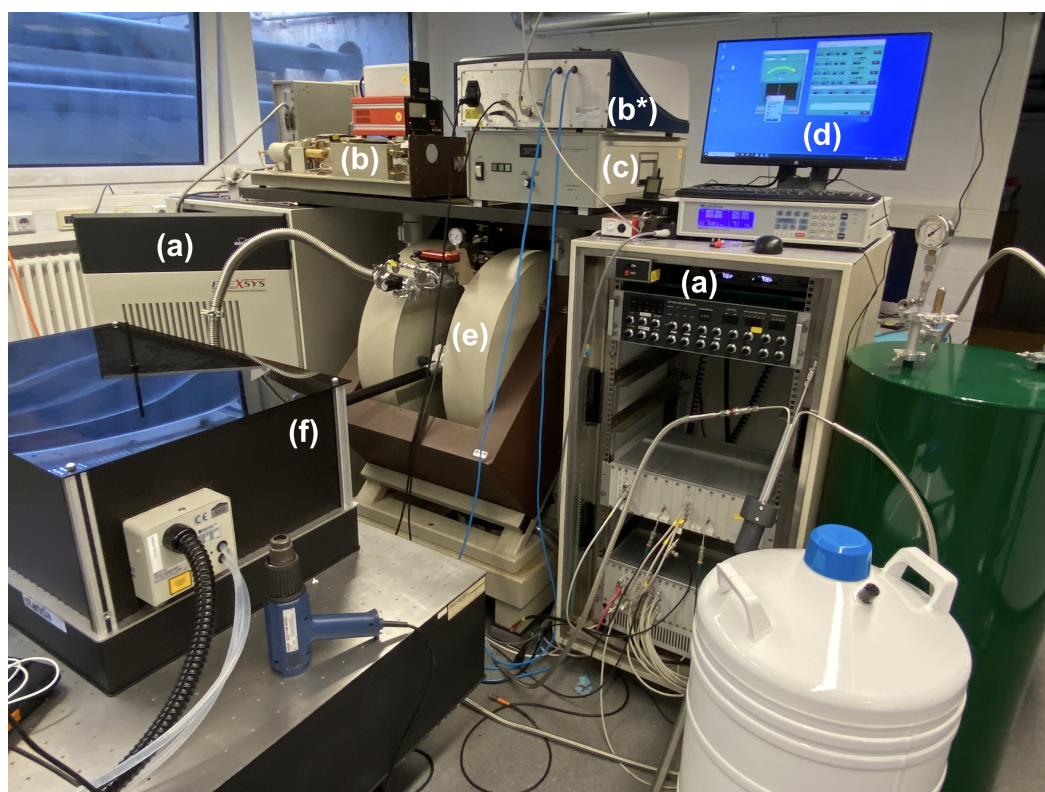
#### 2.1.1 X-Band (9 - 10 GHz)

Fig. 2.1 illustrates the experimental setup of the continuous wave (CW) EMX X-band ESR spectrometer equipped with the console (a), microwave bridge (b), Helmholtz coils (c) and data acquisition software at a computer (d).



**Fig. 2.1** Experimental setup of the continuous wave (CW) EMX X-band ESR spectrometer with console (a), microwave bridge (b), Helmholtz coils (c) and data acquisition software at a computer (d). [96]

In pulsed operation, the pulsed X-band E580 ESR spectrometer was used, depicted in Fig. 2.2. Here, the spectrometer consists of additional parts including two consoles (a), microwave bridge (b), external microwave EMX bridge (b\*), 1 kW Traveling-wave tube (TWT) microwave amplifier (c), closed-cycle Helium cryostat temperature control unit (d), Helmholtz coils (e) and laser beam pathway (f). The external microwave EMX bridge (b\*) was used because the continuous irradiation of the new EMX bridge provides a better stability during longer irradiation periods, hence for CW purposes, the new EMX bridge was used.



**Fig. 2.2** Experimental setup of the pulsed X-band E580 ESR spectrometer with console (a), microwave bridge (b), external microwave EMX bridge (b\*), microwave amplifier (c), closed-cycle Helium cryostat temperature control unit (d), Helmholtz coils (e) and laser beam pathway (f). [97]

### 2.1.2 Q-Band (33 - 35 GHz)

Fig. 2.3 illustrates the experimental setup of the pulsed Q-band SuperQ E580 ESR spectrometer with the console (a), microwave bridge (b), 300 W TWT microwave amplifier (c), closed-cycle Helium cryostat temperature control unit (d), Helmholtz coils (e), 250 W radio frequency amplifier (f) and laser beam pathway (g). The radio frequency (RF) amplifier was necessary to provide RF irradiation in ENDOR measurements.

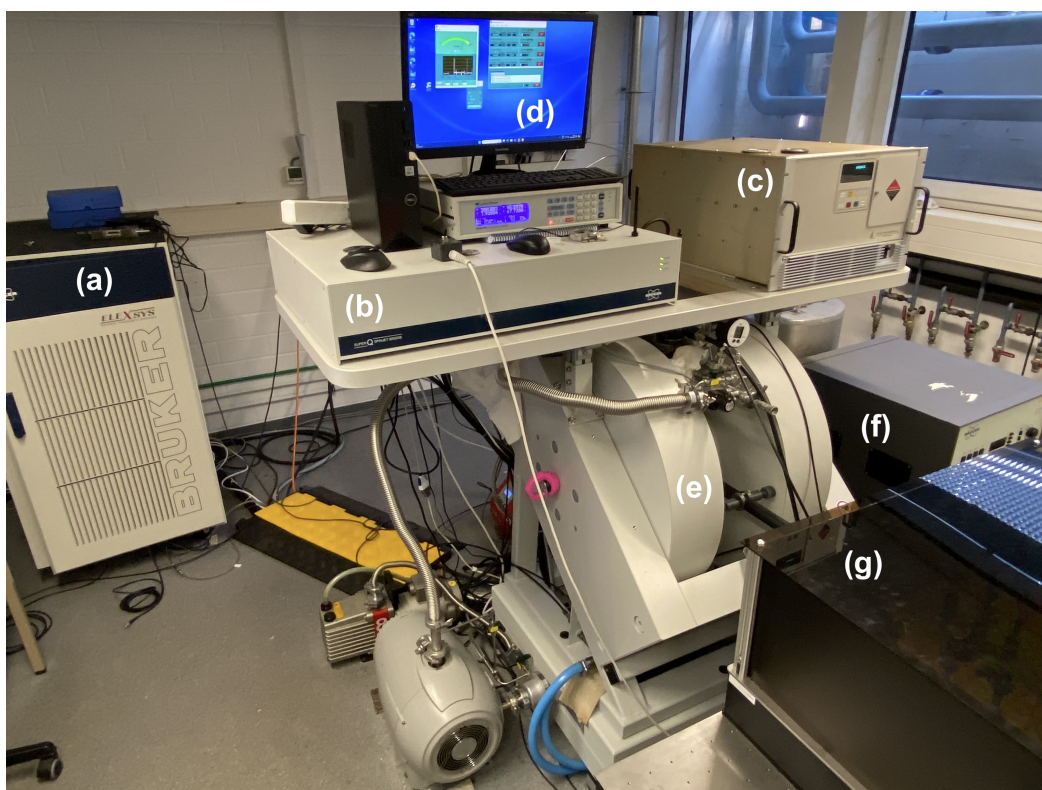


**Fig. 2.3** Experimental setup of the pulsed Q-band SuperQ E580 ESR spectrometer with console (a), microwave bridge (b), 300 W microwave amplifier (c), closed-cycle Helium cryostat temperature control unit (d), Helmholtz coils (e), 250 W radio frequency amplifier (f) and laser beam pathway (g). [98]

## 2.2 Temperature Control

In order to be able to measure at low temperatures, the operated resonators were inside a variable temperature insert (VTI), which can be constantly surrounded by helium in a closed-cycle Helium cryostat (Cryogenic Limited) and thus temperatures of down to Millikelvin can be achieved (see figure 2.4). The closed-cycle Helium cryostat consists of a variable temperature insert (VTI) (a), external Helium gas inlet (b), optical window (c) and cooling head (d).

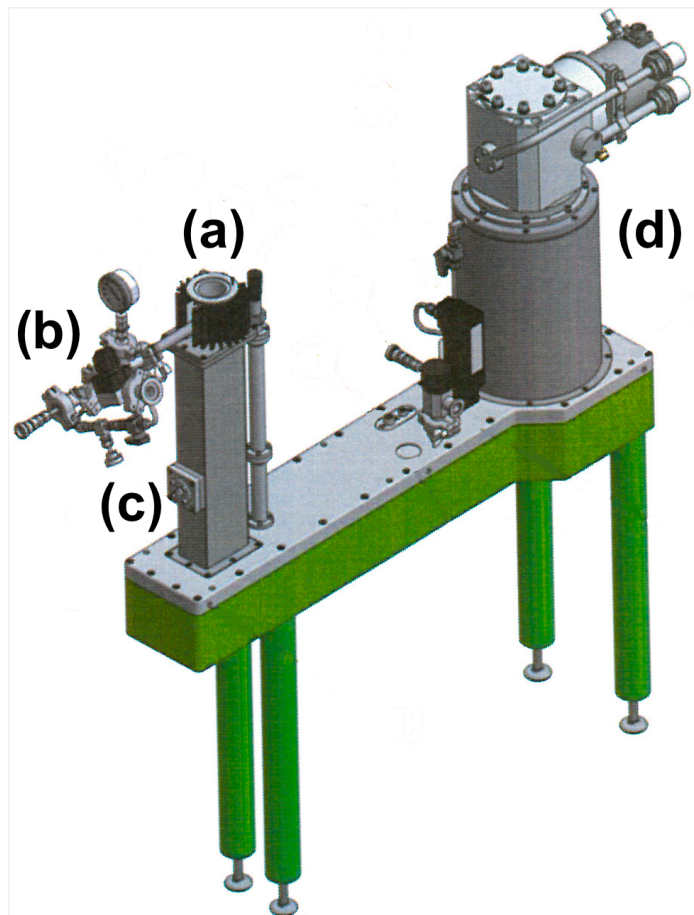


**Fig. 2.4** Scheme of the closed-cycle Helium cryostat with variable temperature insert (VTI) (a), external Helium gas inlet (b), optical window (c) and cooling head (d). [99]

## 2.3 Optical Excitation

Several experiments described in the scientific works in chapter 3 required laser excitation on the sample of interest for TR-EPR purposes. Fig. 2.5 illustrates the experimental setup of pulsed laser excitation on a rigid laser desk. The laser excitation components consist of the laser pathway towards the pulsed Q-band spectrometer (a), an optical parametric oscillator (OPO) to convert the input laser wavelength of 355 nm to a range of 400 - 800 nm (b), pulsed excitation laser (Lumibird) (c), the laser pathway towards the pulsed X-band spectrometer (d) and the console and water supply of the pulsed laser (e).

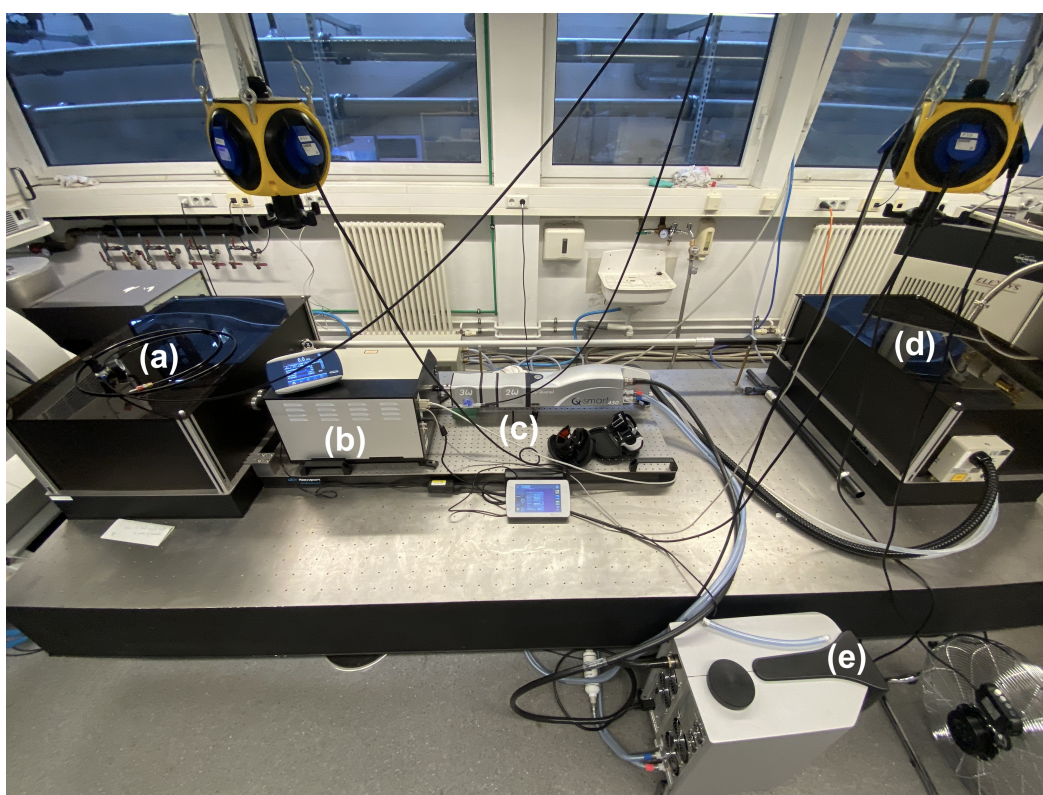


**Fig. 2.5** Scheme of the laser excitation used in the described scientific works. It consists of the laser pathway towards the pulsed Q-band spectrometer (a), an optical parametric oscillator (OPO) to convert the input laser wavelength of 355 nm to a range of 400 - 800 nm (b), pulsed excitation laser (Lumibird) (c), the laser pathway towards the pulsed X-band spectrometer (d) and the console and water supply of the pulsed laser (e). [100]



# Chapter 3

## Main part

The focus of this PhD thesis lies within spectroscopy in the field of physical chemistry. The following chapter is secluded in contributions of scientific works in the three domains of chemical, physical and biological sciences. The scientific works will also have a small introduction to explain their relevance to the respective scientific field. Furthermore, the used ESR technique will be briefly mentioned before it will be explained more thoroughly in the conclusion. The next section will show the scientific works in the discipline of chemistry. The section starts with several stable radicals which will be introduced and their magnetic properties before moving on to novel, catalytically active nanoparticles and the usage of spin traps to investigate the reaction pathways. Afterwards, a light-induced radical system will be presented.

The next section illustrates two examples about more physical viewpoints on the optimisation of a commercially available MW resonator and the implementation of previous findings on a MASER resonator. Here, the focus lies more within the experimental setup and the optimisation of MW conversion inside of ESR resonators.

The last section showcases an example on the usage of ESR spectroscopy in the realm of structural biology. Here, the power saturation technique will be shown as a strong tool for the evidence of the structural rearrangement of a model protein system which was predicted by computational methods.

All in all, this chapter illustrates the interdisciplinary nature of ESR spectroscopy through all scientific domains of chemistry, physics and biology.

## **3.1 Contributions to Chemical Science**

### **3.1.1 Stable Radicals**

This subsection will showcase a few examples of stable radicals, starting off with a study on an inorganic, paramagnetic aluminum complex and the time dependent radical formation. The CW ESR spectra simulation could provide evidence for the spin density derived by theoretical calculations. Furthermore, the reactivity towards a reducing agent could be monitored via ESR spectra acquisition.



## 3.1.1.1 Aluminum Complex



## Organometallic Chemistry

How to cite:

International Edition: doi.org/10.1002/anie.202217184

German Edition: doi.org/10.1002/ange.202217184

Evidence of Al<sup>II</sup> Radical Addition to Benzene

Debdeep Mandal, T. Ilgin Demirer, Tetiana Sergeieva, Bernd Morgenstern,  
Haakon T. A. Wiedemann, Christopher W. M. Kay, and Diego M. Andrada\*

**Abstract:** Electrophilic Al<sup>III</sup> species have long dominated the aluminum reactivity towards arenes. Recently, nucleophilic low-valent Al<sup>I</sup> aluminyl anions have showcased oxidative additions towards arenes C–C and/or C–H bonds. Herein, we communicate compelling evidence of an Al<sup>II</sup> radical addition reaction to the benzene ring. The electron reduction of a ligand stabilized precursor with KC<sub>8</sub> in benzene furnishes a double addition to the benzene ring instead of a C–H bond activation, producing the corresponding cyclohexa-1,3(or1,4)-dienes as Birch-type reduction product. X-ray crystallographic analysis, EPR spectroscopy, and DFT results suggest this unprecedented reactivity proceeds through a stable Al<sup>II</sup> radical intermediate, whose stability is a consequence of a rigid scaffold in combination with strong steric protection.

## Introduction

The preference of aluminum to adopt its oxidation state Al<sup>III</sup> has been extensively exploited in the design of trivalent species as Lewis acid catalysts in various organic transformations.<sup>[1]</sup> In contrast, and despite significant progress in the field, low oxidation states such as Al<sup>II</sup> and Al<sup>I</sup> are still considered exotic, and their applications are considerably less numerous.<sup>[2]</sup> Efforts in this area have been driven by their proven potential to replace transition metals in various catalytic cycles involving bond activation processes.<sup>[3]</sup>

The first Al<sup>I</sup> species was reported more than thirty years ago by Schnöckel in the form of a tetrameric species (**I**), which upon thermal conditions, dissociates into its monomeric units.<sup>[4]</sup> The isolation of the pure monomeric form has been accomplished by increasing the steric demand AlCp<sup>R</sup> (Cp<sup>R</sup> = C<sub>5</sub>H<sub>2</sub>tBu<sub>3</sub>).<sup>[5]</sup> Ten years later, the first monomeric neutral Al<sup>I</sup> compound (**II**) was isolated and characterized by Roesky.<sup>[6]</sup> The bulky β-diketiminato (NacNac) supporting ligand was the key to providing enough electronic and steric protection to the aluminum center. Over the years, this compound has evolved from a lab curiosity into a valuable reagent, given its ability to participate in various bond activations via oxidative addition.<sup>[7]</sup> In 2018, the groups of Aldridge and Goicoechea expanded the scope by synthesizing the anionic Al<sup>I</sup> nucleophilic species, aluminyl anions (**III**), which demonstrate unprecedented reactivity in the oxidative addition on non-polarized C–H and C–C bonds of aromatic hydrocarbons (Scheme 1). Since then, several amido- and alkyl-substituted aluminyl compounds have been prepared and their reactivity has been explored.<sup>[8]</sup> Recently, examples of neutral mono-coordinated aluminyl Al<sup>I</sup> compounds **IV–V** have been reported by Liu, Hinz, and Power taking advantage of sterically demanding carbazolyl and terphenyl ligands respectively.<sup>[9]</sup>

The exotic reactivity of aluminyl anions is currently in the spotlight for the activation of small molecules. Notably, the reaction outcome sharply depends on the nature of the counter cation and its coordination nature with the anionic moiety.<sup>[10]</sup> The extent of the interaction between the cation and the flanking aryl substituents plays a crucial role in the formation of aluminyl species.<sup>[8c,f,11]</sup> In this vein, we envisage that bulky silyl groups, instead of aromatic groups, may provide sufficient kinetic stability to isolate Al<sup>II</sup> radical species, preventing ionic interactions in favor of aluminyl anions. Compared to Al<sup>I</sup>, dicoordinated Al<sup>II</sup> radicals are even rarer. This is partially due to the inherent instability of mononuclear neutral Al<sup>II</sup>/Al<sup>I</sup> radical species, which prefers to dimerize forming Al–Al single bonded compounds, **VI–IX**.<sup>[8h,k,12]</sup> Thus, a suitable ligand that not only stabilizes the elusive Al<sup>II</sup> radical but also avoids dimerization is indispensable for the successful isolation of aluminum radical species. To date, only a few examples **X–XI**<sup>[13]</sup> are known for neutral monomeric aluminum radicals, using cyclic(alkyl)-(amino)carbene (CAAC) as stabilization units of the radical centers.

Herein, we report on the unusual *trans* 1,4-addition of two aluminum(II) species to a benzene furnishing a 1,4-cyclohexadiene system as a Birch-type reduction reaction product (Scheme 1). The Birch reduction of aromatic

[\*] Dr. D. Mandal, T. I. Demirer, Dr. T. Sergeieva, Dr. B. Morgenstern, Dr. D. M. Andrada

General and Inorganic Chemistry Department, University of Saarland

Campus C4.1, 66123 Saarbrücken (Germany)

E-mail: diego.andrada@uni-saarland.de

H. T. A. Wiedemann, Prof. Dr. C. W. M. Kay

Physical Chemistry Department, University of Saarland

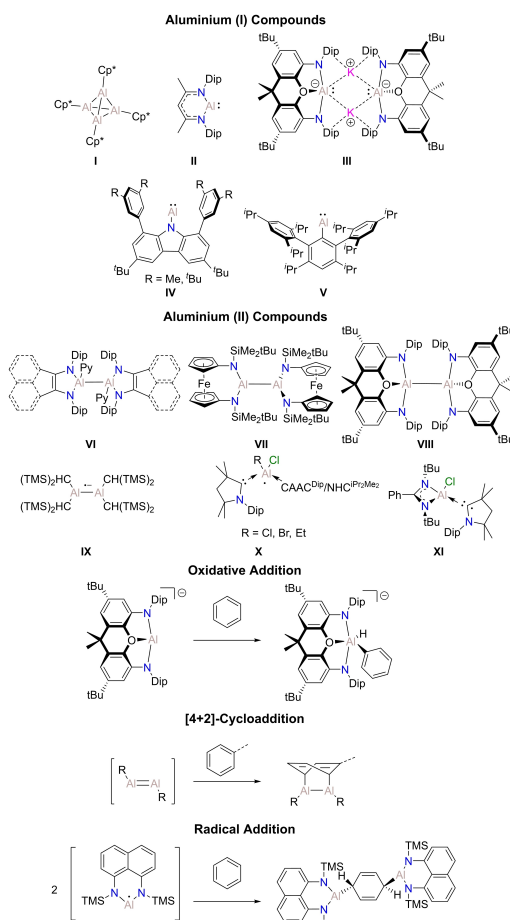
Campus B2.2, 66123 Saarbrücken (Germany)

Prof. Dr. C. W. M. Kay

London Centre for Nanotechnology, University College London

17-19 Gordon Street, London WC1H 0AH (UK)

© 2023 The Authors. Angewandte Chemie International Edition published by Wiley-VCH GmbH. This is an open access article under the terms of the Creative Commons Attribution License, which permits use, distribution and reproduction in any medium, provided the original work is properly cited.



**Scheme 1.** Selected structures of Al<sup>I</sup> and Al<sup>II</sup> compounds. Oxidative addition, [4+2]-cycloaddition, and radical addition. R: Ar<sup>\*</sup> = 2,6-Dip<sub>2</sub>C<sub>6</sub>H<sub>3</sub>, Ar<sup>\*\*</sup> = 2,6-Dip<sub>2</sub>-4-TMS-C<sub>6</sub>H<sub>2</sub>, Bbp = 2,6-[CH-(TMS)]<sub>2</sub>C<sub>6</sub>H<sub>3</sub>, Tbp = 2,6-[CH-(TMS)]<sub>2</sub>-4-tBu-C<sub>6</sub>H<sub>2</sub> [Dip = 2,6-(iPr)<sub>2</sub>C<sub>6</sub>H<sub>3</sub>, TMS = Trimethylsilyl].

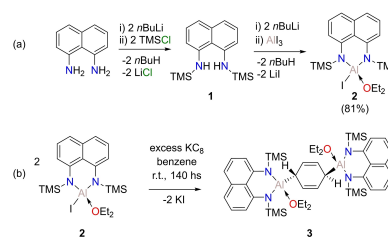
compounds is well-established in organic chemistry to produce *cis* and/or *trans* 1,4-disubstituted-cyclohexadienes as hydro, alkyl or silyl derivatives.<sup>[14]</sup> The groups of Power and Tokito have described a *cis* 1,4-addition to toluene and benzene via [4+2]-cycloaddition of a transient dialuminene compound,<sup>[15]</sup> which has been later stabilized as a dianion<sup>[16]</sup> or by coordination to Lewis bases.<sup>[17]</sup> The group of Harder has shown that the combination of the nucleophilic Al<sup>I</sup> compound (**II**) with the highly Lewis acidic (NacNac)Ca<sup>+</sup> analogue reduces benzene.<sup>[18]</sup> Notably, the isolobal Mg compound can also undergo a Birch-type benzene reduction, when the dimerization of the intermediate Mg<sup>I</sup> radical is prevented by a super bulky spectator ligand ((HC[C(Me)N-[2,6-(3-pentyl)-phenyl]]<sub>2</sub>)<sub>2</sub>) and a coordinating species, TME-

DA (N,N,N',N'-tetramethylethylenediamine).<sup>[19]</sup> In the course of the development of this work, the group of Braunschweig reported a similar outcome, in which the aluminum center is coordinated to an *N*-heterocyclic carbene (NHC) and stabilized by a redox-active ferrocenyl substituent.<sup>[20]</sup> Although it was not possible to isolate or characterize a radical addition to arenes, the authors proposed a plausible radical-based mechanism. We now provide compelling evidence of an in situ generated diamino-substituted Al<sup>II</sup> radical as a key reactive species for such Birch-type reduction of aromatic molecule.

## Results and Discussion

Bis(silylamido)naphthalene derivatives have been recently established as attractive ligands given their unexpectedly high degree of thermodynamic and kinetic stability.<sup>[21]</sup> This framework provides a characteristic interplay between steric repulsion and dispersive attraction, allowing the isolation of exotic chemical bonds.<sup>[22]</sup> Thus, the *N*-trimethylsilyl substituted diamino naphthyl amine has been chosen as the supporting ligand for synthesizing the aluminum precursor. Compound **2** was prepared in 81% yield from a salt metathesis reaction of the respective dilithiated ligand with AlI<sub>3</sub> (Scheme 2a). The molecular structure of compound **2** exhibits a tetra-coordinated aluminum atom located out of the naphthalene plane (Figure 1).<sup>[23]</sup> The diethylether molecule coordinates to the acidic aluminum center with a bond length of 1.884(4) Å, which is in the range of an Al–O single bond (1.89 Å).<sup>[24]</sup> This structure is reminiscent to the aluminum iodide stabilized by xanthene ligand (precursor of compound **III**), but the rigid structure carries a longer Al–O bond length (1.967(2) Å).<sup>[8a]</sup> The Al–N bond lengths are 1.797(5) and 1.803(5) Å, fall in between the typical Al–N single and double bonds (1.97 and 1.73 Å, respectively),<sup>[24]</sup> indicative of a weak N π-donation. The nitrogen atoms are planar (Σ<sub>z</sub> = 359.5), underlining that the location of the aluminum is a consequence of the relatively small bonding pocket of the ligand, i.e. 2.06 Å compared to the xanthene scaffold 4.55 Å in **III**.<sup>[25]</sup> Note that precursor **III** analogue has longer Al–N bond lengths (1.847(2) Å).<sup>[8a]</sup>

In order to prepare the corresponding Al<sup>II</sup> radical or alumanyl Al<sup>I</sup> anion species, we attempted various reducing conditions. The reduction of **2** with conventional reducing



**Scheme 2.** (a) Synthesis of **1** and **2**. (b) Reduction of **2** with excess of KC<sub>8</sub>.

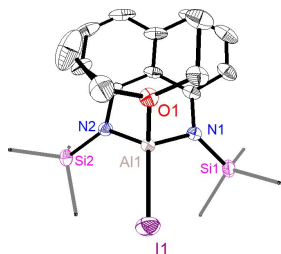


**Figure 1.** Molecular structure of **2** in the solid state as determined by X-ray crystallography. Thermal ellipsoids set at 50% probability. Hydrogen atoms were omitted for clarity. Selected experimental bond lengths (Å) and bond angles (°): Al1–N1 1.797(5), Al1–N2 1.803(5), Al1–O1 1.884(4), Al1–I1 2.520(2), N1–Si1 1.739(5), N2–Si2 1.742(5), N2–Al1–N1 103.7(2), N1–Al1–I1 118.2(2), N2–Al1–I1 124.0(2).

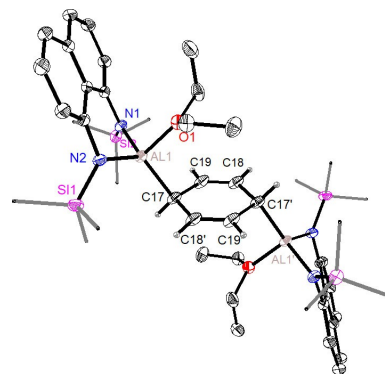


**Figure 2.** Molecular structure of **3** in the solid state as determined by X-ray crystallography. Thermal ellipsoids set at 50% probability. Nonessential hydrogen atoms were omitted for clarity. Selected experimental and theoretical [TPSSH/def2-SVP] bond lengths (Å) and bond angles (°): Al1–N1 1.8293(8) [1.848], Al1–N2 1.8319(8) [1.850], Al1–O1 1.9151(7) [1.971], Al1–C17 1.9925(9) [2.016], C17–C19 1.503(1) [1.506], C18–C19 1.333(2) [1.349], N1–Al1–N2 101.56(2) [101.7], N1–Al1–C17 121.19(8) [124.4], N1–Al1–C17 124.49(2) [123.0].

agents like metallic Mg, K(mirror), or  $\text{KC}_8$  in ethereal solvents (THF, diethyl ether) afforded either an unidentified mixture or decomposition products. Also, reduction of compound **2** with equimolar Jones  $\text{Mg}^{\text{I}}$  reagent or cobaltocene ( $\text{Co}(\text{Cp})_2$ ) led to no reaction in benzene solution. While reducing **2** with one equivalent of  $\text{KC}_8$  led to incomplete reduction even after several days, stirring a reaction mixture containing compound **2** with an excess of  $\text{KC}_8$  (2 equivalents) at room temperature in benzene for 140 hs gave rise to complete conversion (Scheme 2a). The initially expected formation of an aluminyl anion or dialumane species could rapidly be ruled out based on the NMR spectra indicating the occurrence of six new protons symmetrically distributed. In  $^1\text{H}$  NMR, alongside the expected trimethylsilyl groups ( $\delta(^1\text{H})=0.44$  ppm (s)) and the coordinated diethyl ether ( $\delta(^1\text{H})=3.79$  (sept) and  $0.40$  ppm(t)), two distinctive singlets at 5.89 (4H) and 2.37 (2H) ppm were observed. In confirmation of the  $^1\text{H}$  NMR data, the  $^{13}\text{C}$  NMR spectrum shows two new signals at chemical shifts of 124.6 and 29.9 ppm. These NMR spectroscopic data compare favorably with the reported quinoid type benzene moiety suggesting a Birch-type reduction product of benzene.<sup>[14a, 19, 20]</sup>

After the filtration of the insoluble precipitate from the reaction mixture, an orange solution was obtained. Pale yellow crystals of **3** were grown from concentrated solution after 1 week at 4 °C and the structure was confirmed by X-ray diffraction (Figure 2). As predicted from the  $^1\text{H}$  NMR chemical shifts, a benzene molecule reacts with two molecules of reduced intermediate of compound **2**, and the resulting molecule **3** exhibits a  $C_i$  symmetry. While the tetra-coordinated environment around aluminum center from compound **2** is preserved, the bond lengths with the surrounding atoms become longer in **3**, probably because of the steric repulsion with the new  $\text{C}_6\text{H}_6$  moiety. In this sense, the Al–N bonds to the supporting ligands in **3** (1.8293(8) Å) are longer than in **2**. Also, the coordinating ether molecule has a 1.9151(7) Å bond length, while the distortion degree ( $\Sigma_g=347$ ) supports a weak interaction ( $D_e=29.1$  and  $25.6$  kcal mol $^{-1}$  for **2** and **3**, respectively). The bond lengths

between the aluminum atom and the carbon atom of the benzene (1.9925(9) Å) in **3** are slightly shorter than the expected Al–C single bond (2.01 Å),<sup>[24]</sup> and also than those reported for the Birch reduction by Brand et al. 2.060(3)/2.073(3) Å,<sup>[18]</sup> by Dhara et al. 2.064(3)/2.059(3) Å,<sup>[20]</sup> and also from the products resulting from the [4+2]-cycloaddition, i.e. 2.000(2)/2.003(2) Å,<sup>[15a]</sup> and 2.028(5)/2.020(5) Å.<sup>[15b]</sup> As in the case of compound **2**, the Al atom in **3** remains out of the plane of the ligand. Notably, the C18–C19 bond length of 1.333(2) Å is comparable to the double bond (1.34 Å), while the C17–C19 bond length of 1.503(1) indicates a C–C single bond (1.50 Å).

The new adduct **3** is indefinitely stable at ambient temperature in the solid state under argon atmosphere. Notably, the addition of the aluminum units to the benzene ring in the 1,4 fashion leading to the quinoid type of structure through de-aromatization benzene can only be explained by the presence of an in situ generated  $\text{Al}^{\text{I}}$  radical species.<sup>[14b]</sup> We explored the reaction paths using density functional theory (DFT) at the PCM(benzene)-TPSSH/def2-TZVPP/TPSSH/def2-SVP level of theory (see Supporting Information for further details). Figure 3 shows the computed reaction profiles along with some key optimized structures. The reaction starts with one electron reduction of compound **2**, with the elimination of iodine in the form of  $\text{KI}$  to generate a new radical species **INT1**, where the ether molecule is coordinated. The corresponding radical anion of **2** is computed as an unstable species which is prone to the elimination of iodine ( $\Delta G=-11.4$  kcal mol $^{-1}$ ). The strength of the bond between Al and O in **INT1** is significantly reduced, and its release is endergonic by 2.6 kcal mol $^{-1}$ , forming the radical species **INT3**. Despite not being experimentally observed, both **INT1** and **INT3** can dimerize to form their respective dialumane **D1** and **D2** since the

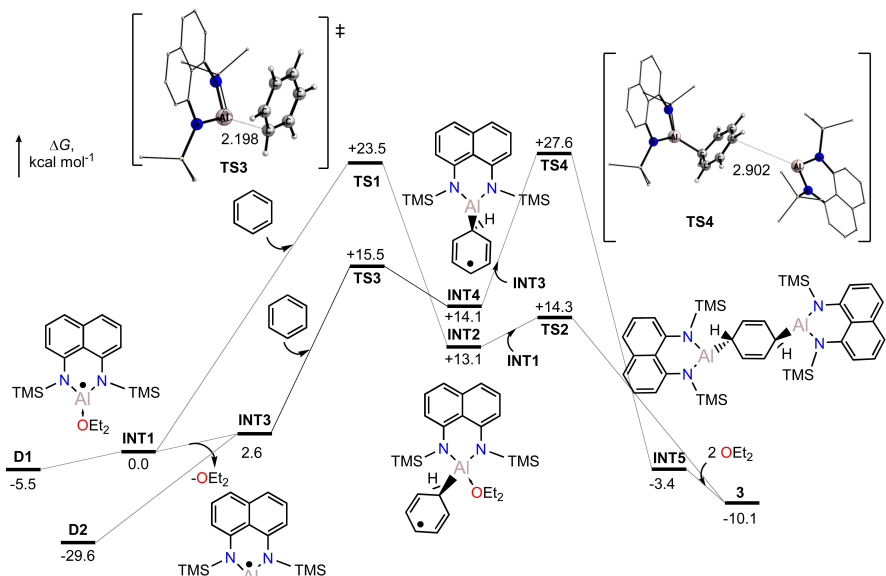


**Figure 3.** Gibbs free energy ( $\Delta G$  in  $\text{kcal mol}^{-1}$ ) profile at the PCM(benzene)-TPSSH/def2-TZVPP//TPSSH/def2-SVP level of theory for the reduction of **2** in benzene solvent. Transition state structures are shown, where nonessential hydrogens were omitted for clarity.

process is exergonic by 5.5 and 29.6  $\text{kcal mol}^{-1}$ , respectively. The monomer and dimer species can exist in equilibrium.<sup>[26]</sup> Nonetheless, the probability of meeting a benzene solvent molecule is higher than meeting another **INT1** or **INT3** to dimerize, similar to the situation of a heterobimetallic Ca/Al Birch-reduction.<sup>[18]</sup> Thus, the radical addition to a molecule of benzene is the first step of the reaction. While the most stable radical species **INT1** requires 23.5  $\text{kcal mol}^{-1}$ , the corresponding addition from **INT3** has lower energy barrier 15.5  $\text{kcal mol}^{-1}$ . The energy needed to form the intermediate **INT2** and **INT4** is 13.1 and 14.1  $\text{kcal mol}^{-1}$ , respectively. The formed intermediates are thermodynamically unfavored, and they can easily collapse back to **INT1** or **INT3**, as the difference in energy to **TS3** is very small. However, in a high-pressure regime where molecular collisions are efficient enough to cool the otherwise rovibrationally hot intermediates, causing it to be in thermal equilibrium with the environment. To produce the observed product **3**, a second **INT1** or **INT3** must meet **INT2** or **INT4**. The second step of the reaction course is computed to be fast when the ether molecule is coordinated **TS3**, while the **INT4** and **INT3** react via **TS4** with a Gibbs energy of 27.6  $\text{kcal mol}^{-1}$  relative to the reactants. The overall thermodynamics of the reaction is favorable by 10.1  $\text{kcal mol}^{-1}$ . Potentially, different isomers are possible according to the position and geometry of the second radical addition. Our calculations suggest the observed *trans*- structure in **3** as the most stable isomer (see Figure S32).

The optimized structure for **3** is in good agreement with the crystal structure (Figure 2). The calculated NPA charge

of +2.14 (Al) is in line with previously assigned of  $\text{Al}^{\text{III}}$ .<sup>[18]</sup> The total charge on the  $\text{C}_6\text{H}_6^{2-}$  fragment ( $-1.37 e$ ) is in agreement with its strongly reduced nature. While the C atoms directly attached to the Al atoms bear a (C18/C19 =  $-0.89 e$ ), the vinylic C atoms has only (C18/C19 =  $-0.22 e$ ). The chemical bond Al–C is rather ionic (Figure S33 and Table S5) with a Wiberg bond order of 0.41 au.

Noteworthy, the experimental conditions and the computational calculations agree on a rather slow reduction process under the given conditions. The rate-determining step is computed as the first step consisting of the radical addition of aluminum species to the benzene molecule with an energy of 15.5  $\text{kcal mol}^{-1}$ , and a second step with 13.5  $\text{kcal mol}^{-1}$ . Therefore, this result predicts the presence of long-living and relatively stable radical species **INT1–4** in solution. In order to prove the radical addition reaction, we recorded the time dependence of the reduction of **2** with continuous wave (cw) EPR spectroscopy at X-band frequencies. For that, dry  $\text{C}_6\text{H}_6$  was added to the solid mixture of compound **2** and  $\text{KC}_8$  (1:2.2 ratio) at room temperature under inert conditions. An aliquot of reaction mixture (supernatant solution) was transferred into a quartz EPR tube at various time intervals. The aliquot was then diluted with dry  $\text{C}_6\text{H}_6$ , and the EPR spectra were measured. This procedure was repeated over several days. Figure 4a shows the experimentally obtained EPR spectra together with their simulations.

All EPR spectra are dominated by the sextet that results from the coupling of the unpaired electron with the aluminum center ( $^{27}\text{Al}$ , 100% natural abundance,  $I=5/2$ ).

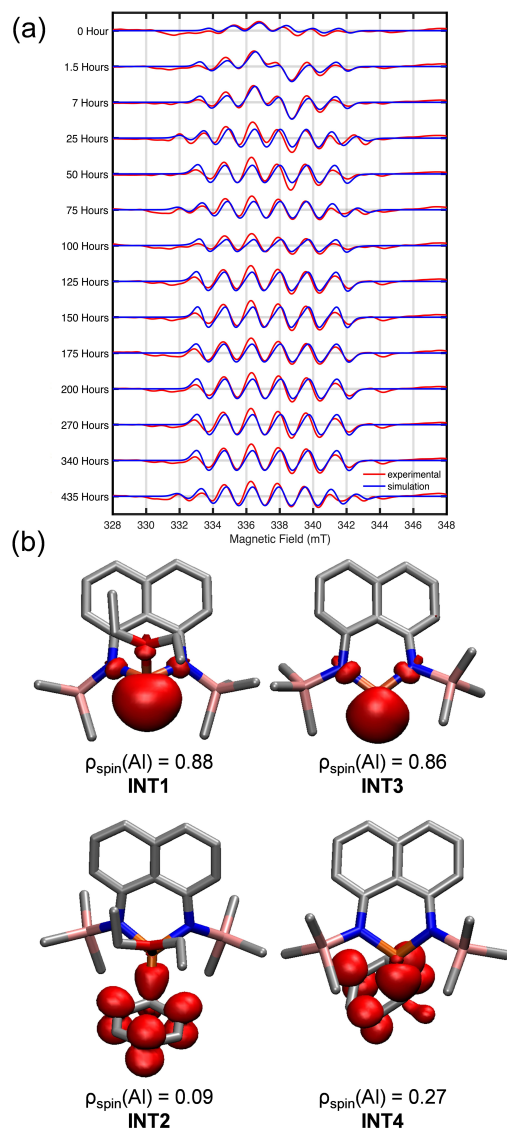


**Figure 4.** (a) EPR spectra of (1 : 2) reduction reaction between compound **2** and  $\text{KC}_8$  at various time intervals. Simulation parameters:  $g_{\text{iso}} = 2.0057$ ,  $A_{\text{iso}}(^{27}\text{Al}) = 1.63$  mT. (b) Spin density (isovalue 0.004 a.u.) and Mulliken spin-density plots of **INT1–4**. H atoms have been omitted for clarity.

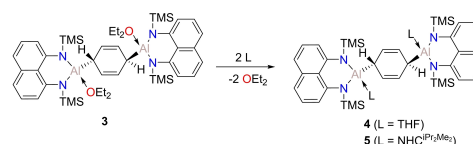
At early times, our simulations suggest the presence of two species with  $g_{\text{iso}}$  of 2.0057 and 2.0051 and isotropic hyperfine couplings ( $hfc$ ),  $A_{\text{iso}}(^{27}\text{Al})$  of 1.63 mT and 1.54 mT, respectively. However, on a longer times scale, the EPR radical formation corresponds mainly to one species ( $g_{\text{iso}}$  of 2.0057 and  $A_{\text{iso}}(^{27}\text{Al})$  of 1.63 mT), probably **INT3** or **INT4**. The

magnitude of the  $hfc$ s in this species is significantly larger than those reported for metal-base spin aluminum radicals such as  $[\text{R}_2\text{AlAIR}_2]^{\bullet-}$  (1.11 mT),<sup>[27]</sup> and carbene-stabilized aluminum radicals (0.93–1.25 mT).<sup>[13a,c]</sup> In contrast, aluminum radical complexes with ligand-based spin have smaller  $A(^{27}\text{Al})$  values (0.13–0.46 mT).<sup>[28]</sup> The  $hfc$ s of Al centered radicals strongly depend on the  $s$ -orbital character via pyramidalization.<sup>[29]</sup> For instance, the radical anion  $[\text{AlH}_3]^{\bullet-}$  displays an isotropic  $hfc$  of 15.4 mT with a deviation from planarity of  $\Sigma_s = 331.8^\circ$ , while the  $[\text{Al}(\text{SiMetBu}_2)_3]^{\bullet-}$  which is more planar  $\Sigma_s = 358.4^\circ$  exhibits a  $hfc$  of 6.2 mT.<sup>[30]</sup> Furthermore, the resulting cyclohexadienyl radical adduct from the  $[\text{AlH}_3]^{\bullet-}$  addition to benzene affords an  $A_{\text{iso}}(^{27}\text{Al})$  of 5.4 mT.<sup>[29]</sup> The stronger participation of the  $s$ -orbital character has also been suggested as responsible for the higher  $hfc$ s of  $[\text{R}_2\text{AlAIR}]^{\bullet}$  ( $A_{\text{iso}}(^{27}\text{Al})$  of 2.18 and 1.89 mT), compared to the aforementioned  $[\text{R}_2\text{AlAIR}_2]^{\bullet-}$ .<sup>[31]</sup> Figure 4b shows the calculated spin density of the main radical species **INT1–4**. In general, the calculations indicate the presence of an unpaired electron mainly located at the aluminum atom, with a small contribution of the nitrogen atoms of the supporting ligand (Table S7). EPR calculations provided an estimated  $hfc$  of 36.6 mT and 41.8 mT for **INT1** and **INT3**, respectively, in line with the strong  $s$ -orbital character of the unpaired electron. On the other hand, the **INT2** and **INT4** display a smaller  $hfc$ , namely 7.7 mT and 8.8 mT, respectively. Note, that the predicted  $hfc$ s depend on a rather flat potential energy surface.

The manipulation of adduct **3** in different solvents indicated that the ether molecule can be easily exchanged. Therefore, we envisioned the use of stronger  $\sigma$ -donors such NHC or CAAC for stabilizing the radical species and re-aromatizing the benzene molecule. However, the reaction process led only to a ligand exchange with 1,3-diisopropyl-4,5-dimethylimidazol-2-ylidene ( $\text{NHC}^{\text{IPr}_2\text{Me}_2}$ ), while  $\text{CAAC}^{\text{Dip}}$  shows no reaction (Scheme 3).

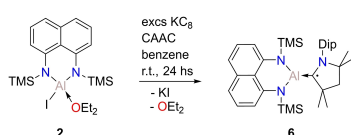
Furthermore, all our attempts to isolate the radical species or activate different aromatic compounds such as toluene, xylene and biphenyl with the in situ generated  $\text{Al}^{\text{II}}$  radical were unsuccessful. In contrast to former benzene reductions,<sup>[15b,18]</sup> leaving a  $\text{C}_6\text{D}_6$  solution of compounds **3**, **4**, or **5** at room temperature does not lead to any detectable decrease of the NMR signals corresponding to the  $\text{C}_6\text{H}_6$  moiety. This observation holds even after heating for 24 hrs at 60 °C, thus indicating the intermolecular exchange of the  $\text{C}_6\text{H}_6$  molecule is not possible.

The low reactivity of the radical intermediate is advantageous for the EPR detection, but the lifetime measurements by other spectroscopic methods like UV/Vis are precluded



**Scheme 3.** Ligand exchange reaction of **3**.

by the absorption of **2**. Additionally, due to the reaction setup, TEMPO cannot be used as radical scavenger. Instead, to trap or examine the transient radical, we conducted the reduction of **2** with  $\text{KC}_8$  in the presence of 1 equiv of  $\text{CAAC}^{\text{Dip}}$  in benzene at room temperature, which afforded a deep yellow solution (Scheme 4). The related product is NMR silent, and unfortunately, despite numerous crystallization attempts no crystals could be obtained. Nonetheless, the formation of **6** was confirmed by liquid injection field desorption/ionization-mass spectrometry showing a peak at  $m/z$  613.38  $[\text{LAl}(\text{cAAC})]^+$  (Figure S25). Although the ether



**Scheme 4.** Reduction of **2** with excess of  $\text{KC}_8$  in the presence of  $\text{CAAC}^{\text{Dip}}$ .

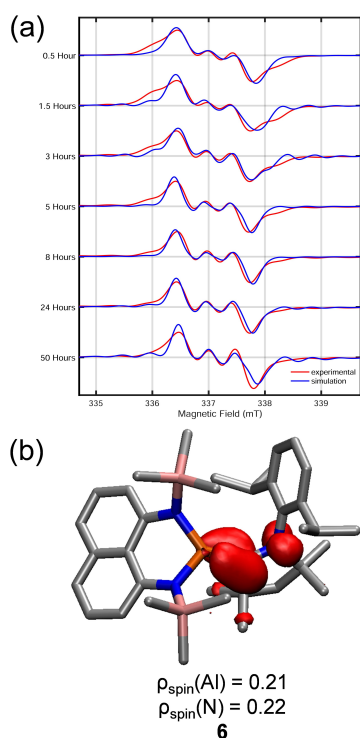


**Figure 5.** (a) EPR spectra of (1:2) reduction reaction of compound **2** with  $\text{KC}_8$  in the presence of  $\text{CAAC}^{\text{Dip}}$  at various time intervals. Simulation parameters, **6**:  $g_{\text{iso}} = 2.0026(3)$  (2.00261),  $A_{\text{iso}}(^{27}\text{Al}) = 0.47$  mT (0.34 mT),  $A_{\text{iso}}(^{14}\text{N}) = 0.48$  mT (0.62 mT);  $[\text{CAAC}^{\text{Dip}}]^{\cdot-}$ :  $g_{\text{iso}} = 2.0033(2)$ ,  $A_{\text{iso}}(^{14}\text{N}) = 0.48$  mT,  $A_{\text{iso}}(^1\text{H}) = 0.21$  mT. (b) Spin density (isovalue 0.003 a.u.) and Mulliken spin-density plots of **6**. H atoms have been omitted for clarity.

molecule could bind to the Al center, our calculations suggest a very weak coordination energy ( $D_e = 11.6$  kcal mol $^{-1}$ ).

We were also able to monitor the progress of this reaction via EPR spectroscopy. In this case, the EPR spectra show a broad four-line asymmetric signal shape (Figure 5a). The simulations suggest the occurrence of two species. At short reaction time (1.5 hrs), a radical with  $g = 2.0033(2)$  and  $A(^{14}\text{N}) = 0.48$  mT is the major radical species, probably the  $\text{CAAC}^{\text{Dip}}$  radical anion. A minor component increases with time, with  $g = 2.0026(3)$  and  $A_{\text{iso}}(^{27}\text{Al}) = 0.47$  mT. Our theoretical calculations suggest a  $hfc$  of **6** of  $A_{\text{iso}}(^{27}\text{Al}) = 0.34$  mT (Figure 5b). This result is in good agreement with previous ligand-base radical of aluminum **XI** with a experimental  $A_{\text{iso}}(^{27}\text{Al}) = 0.93$  mT.<sup>[13c]</sup>

## Conclusion

In conclusion, we have described a new reaction mode of aluminum(II) species. In great contrast to the well-known  $\text{Al}^{\text{III}}$  and  $\text{Al}^{\text{I}}$  reactions towards arenes, the designed aluminum complex produces a stable radical intermediate upon reduction, leading to a Birch reduction type reaction. This unusual behavior is a consequence of the rigid scaffold of the supporting ligand in combination with silyl protecting groups. Thus, the absence of protecting aromatic substituent on the neighboring nitrogen atoms prevents the formation of an ionic pair between a putative aluminyl anion and counter cations, leaving room for an aluminum radical. Current efforts are directed at the isolation and further spectroscopic characterization of the aluminum radical.

## Acknowledgements

The work at University of Saarland has been supported by the ERC StG (EU805113). DM thanks the Alexander von Humboldt Foundation for the postdoctoral fellowship. DMA thanks Prof. Dr. Scheschkewitz for his kind support. All authors gratefully acknowledge the suggestions from M.Sc. S. Danés and M.Sc. E. Sabater. Instrumentation and technical assistance for this work were provided by the Service Center Mass Spectrometry and the Service Center X-ray Diffraction, with financial support from Saarland University and the German Science Foundation (project number INST 256/506-1). EPR spectroscopy was performed on spectrometers purchased with support of the State of Saarland and the German Science Foundation (project number INST 256/535-1) Open Access funding enabled and organized by Projekt DEAL.

## Conflict of Interest

The authors declare no conflict of interest.



### Data Availability Statement

The data that support the findings of this study are available in the supplementary material of this article.

**Keywords:** Aluminum · EPR Spectroscopy · Low-Valent Compounds · Radicals · Structure Elucidation

- [1] a) T. Krahl, E. Kemnitz, *Catal. Sci. Technol.* **2017**, *7*, 773–796; b) T. Krahl, E. Kemnitz, *J. Fluorine Chem.* **2006**, *127*, 663–678; c) S. Saito, in *Main Group Metals in Organic Synthesis*, Wiley-VCH, Weinheim, **2004**, pp. 189–306; d) G. A. Olah, V. P. Reddy, G. K. S. Prakash, in *Kirk-Othmer Encyclopedia of Chemical Technology*, Wiley, Hoboken, **2000**; e) V. P. Reddy, G. K. S. Prakash, in *Kirk-Othmer Encyclopedia of Chemical Technology*, Wiley, Hoboken, **2000**, pp. 1–49.
- [2] a) P. P. Power, *Nature* **2010**, *463*, 171–177; b) M. Melaimi, R. Jazzar, M. Soleilhavoup, G. Bertrand, *Angew. Chem. Int. Ed.* **2017**, *56*, 10046–10068; *Angew. Chem.* **2017**, *129*, 10180–10203; c) R. L. Melen, *Science* **2019**, *363*, 479–484; d) Y. Su, R. Kinjo, *Chem. Soc. Rev.* **2019**, *48*, 3613–3659; e) C. Weetman, S. Inoue, *ChemCatChem* **2018**, *10*, 4213–4228; f) P. Bellotti, M. Koy, M. N. Hopkinson, F. Glorius, *Nat. Chem. Rev.* **2021**, *5*, 711–725.
- [3] a) C. Weetman, H. Xu, S. Inoue, in *Encyclopedia of Inorganic and Bioinorganic Chemistry*, Wiley, Hoboken, **2011**, pp. 1–20; b) K. Hobson, C. J. Carmalt, C. Bakewell, *Chem. Sci.* **2020**, *11*, 6942–6956.
- [4] a) C. Dohmeier, C. Robl, M. Tacke, H. Schnöckel, *Angew. Chem. Int. Ed. Engl.* **1991**, *30*, 564–565; *Angew. Chem.* **1991**, *103*, 594–595; b) H. Sitzmann, M. F. Lappert, C. Dohmeier, C. Üffing, H. Schnöckel, *J. Organomet. Chem.* **1998**, *561*, 203–208.
- [5] A. Hofmann, T. Tröster, T. Kupfer, H. Braunschweig, *Chem. Sci.* **2019**, *10*, 3421–3428.
- [6] C. Cui, H. W. Roesky, H.-G. Schmidt, M. Noltemeyer, H. Hao, F. Cimpoesu, *Angew. Chem. Int. Ed.* **2000**, *39*, 4274–4276; *Angew. Chem.* **2000**, *112*, 4444–4446.
- [7] Y. Liu, J. Li, X. Ma, Z. Yang, H. W. Roesky, *Coord. Chem. Rev.* **2018**, *374*, 387–415.
- [8] a) J. Hicks, P. Vasko, J. M. Goicoechea, S. Aldridge, *Nature* **2018**, *557*, 92–95; b) M. M. D. Roy, J. Hicks, P. Vasko, A. Heilmann, A.-M. Baston, J. M. Goicoechea, S. Aldridge, *Angew. Chem. Int. Ed.* **2021**, *60*, 22301–22306; *Angew. Chem.* **2021**, *133*, 22475–22480; c) R. J. Schwamm, M. D. Anker, M. Lein, M. P. Coles, *Angew. Chem. Int. Ed.* **2019**, *58*, 1489–1493; *Angew. Chem.* **2019**, *131*, 1503–1507; d) R. J. Schwamm, M. P. Coles, M. S. Hill, M. F. Mahon, C. L. McMullin, N. A. Rajabi, A. S. S. Wilson, *Angew. Chem. Int. Ed.* **2020**, *59*, 3928–3932; *Angew. Chem.* **2020**, *132*, 3956–3960; e) M. J. Evans, M. D. Anker, M. G. Gardiner, C. L. McMullin, M. P. Coles, *Inorg. Chem.* **2021**, *60*, 18423–18431; f) T. X. Gentner, M. J. Evans, A. R. Kennedy, S. E. Neale, C. L. McMullin, M. P. Coles, R. E. Mulvey, *Chem. Commun.* **2022**, *58*, 1390–1393; g) S. Kurumada, S. Takamori, M. Yamashita, *Nat. Chem.* **2020**, *12*, 36–39; h) K. Koshino, R. Kinjo, *J. Am. Chem. Soc.* **2020**, *142*, 9057–9062; i) S. Grams, J. Eysel, J. Langer, C. Färber, S. Harder, *Angew. Chem. Int. Ed.* **2020**, *59*, 15982–15986; *Angew. Chem.* **2020**, *132*, 16116–16120; j) S. Kurumada, K. Sugita, R. Nakano, M. Yamashita, *Angew. Chem. Int. Ed.* **2020**, *59*, 20381–20384; *Angew. Chem.* **2020**, *132*, 20561–20564; k) I. L. Fedushkin, M. V. Moskalev, A. N. Lukoyanov, A. N. Tishkina, E. V. Baranov, G. A. Abakumov, *Chem. Eur. J.* **2012**, *18*, 11264–11276.
- [9] a) J. D. Queen, A. Lehmann, J. C. Fetting, H. M. Tuononen, P. P. Power, *J. Am. Chem. Soc.* **2020**, *142*, 20554–20559; b) X. Zhang, L. L. Liu, *Angew. Chem. Int. Ed.* **2021**, *60*, 27062–27069; *Angew. Chem.* **2021**, *133*, 27268–27275; c) A. Hinz, M. P. Müller, *Chem. Commun.* **2021**, *57*, 12532–12535.
- [10] a) J. Hicks, P. Vasko, J. M. Goicoechea, S. Aldridge, *J. Am. Chem. Soc.* **2019**, *141*, 11000–11003; b) J. Hicks, P. Vasko, J. M. Goicoechea, S. Aldridge, *Angew. Chem. Int. Ed.* **2021**, *60*, 1702–1713; *Angew. Chem.* **2021**, *133*, 1726–1737; c) J. Hicks, P. Vasko, A. Heilmann, J. M. Goicoechea, S. Aldridge, *Angew. Chem. Int. Ed.* **2020**, *59*, 20376–20380; *Angew. Chem.* **2020**, *132*, 20556–20560.
- [11] S. Grams, J. Mai, J. Langer, S. Harder, *Dalton Trans.* **2022**, *51*, 12476–12483.
- [12] a) P. Henke, T. Pankewitz, W. Klopfer, F. Breher, H. Schnöckel, *Angew. Chem. Int. Ed.* **2009**, *48*, 8141–8145; *Angew. Chem.* **2009**, *121*, 8285–8290; b) V. A. Dodonov, W. Chen, L. Liu, V. G. Sokolov, E. V. Baranov, A. A. Skatova, Y. Zhao, B. Wu, X.-J. Yang, I. L. Fedushkin, *Inorg. Chem.* **2021**, *60*, 14602–14612; c) Y. Zhao, Y. Liu, L. Yang, J.-G. Yu, S. Li, B. Wu, X.-J. Yang, *Chem. Eur. J.* **2012**, *18*, 6022–6030; d) W. Uhl, *Z. Naturforsch. B* **1988**, *43*, 1113–1118.
- [13] a) B. Li, S. Kundu, A. C. Stückl, H. Zhu, H. Keil, R. Herbst-Irmer, D. Stalke, B. Schwederski, W. Kaim, D. M. Andrada, G. Frenking, H. W. Roesky, *Angew. Chem. Int. Ed.* **2017**, *56*, 397–400; *Angew. Chem.* **2017**, *129*, 407–411; b) S. Kundu, S. Sinhababu, S. Dutta, T. Mondal, D. Koley, B. Dittrich, B. Schwederski, W. Kaim, A. C. Stückl, H. W. Roesky, *Chem. Commun.* **2017**, *53*, 10516–10519; c) M. M. Siddiqui, S. Banerjee, S. Bose, S. K. Sarkar, S. K. Gupta, J. Kretsch, N. Graw, R. Herbst-Irmer, D. Stalke, S. Dutta, D. Koley, H. W. Roesky, *Inorg. Chem.* **2020**, *59*, 11253–11258; d) B. Li, B. L. Geoghegan, H. M. Weinert, C. Wolper, G. E. Cutsail, S. Schulz, *Chem. Commun.* **2022**, *58*, 4372–4375.
- [14] a) P. W. Rabideau, Z. Marcinow, The Birch Reduction of Aromatic Compounds. In *Organic Reactions*, **2004**, pp. 1–334, <https://doi.org/10.1002/0471264180.or042.01>; b) H. E. Zimmerman, *Acc. Chem. Res.* **2012**, *45*, 164–170.
- [15] a) R. J. Wright, A. D. Phillips, P. P. Power, *J. Am. Chem. Soc.* **2003**, *125*, 10784–10785; b) T. Agou, K. Nagata, N. Tokitoh, *Angew. Chem. Int. Ed.* **2013**, *52*, 10818–10821; *Angew. Chem.* **2013**, *125*, 11018–11021.
- [16] R. J. Wright, M. Brynda, P. P. Power, *Angew. Chem. Int. Ed.* **2006**, *45*, 5953–5956; *Angew. Chem.* **2006**, *118*, 6099–6102.
- [17] a) P. Bag, A. Porzelt, P. J. Altmann, S. Inoue, *J. Am. Chem. Soc.* **2017**, *139*, 14384–14387; b) C. Weetman, A. Porzelt, P. Bag, F. Hanusch, S. Inoue, *Chem. Sci.* **2020**, *11*, 4817–4827.
- [18] S. Brand, H. Elsen, J. Langer, W. A. Donaubauer, F. Hampel, S. Harder, *Angew. Chem. Int. Ed.* **2018**, *57*, 14169–14173; *Angew. Chem.* **2018**, *130*, 14365–14369.
- [19] T. X. Gentner, B. Rösch, G. Ballmann, J. Langer, H. Elsen, S. Harder, *Angew. Chem. Int. Ed.* **2019**, *58*, 607–611; *Angew. Chem.* **2019**, *131*, 617–621.
- [20] D. Dhara, F. Fantuzzi, M. Härterich, R. D. Dewhurst, I. Krummenacher, M. Arrowsmith, C. Prankevicus, H. Braunschweig, *Chem. Sci.* **2022**, *13*, 9693–9700.
- [21] N. J. Roberts, E. R. Johnson, S. S. Chitnis, *Organometallics* **2022**, *41*, 2180–2187.
- [22] a) K. M. Marczenko, J. A. Zurakowski, K. L. Bamford, J. W. M. MacMillan, S. S. Chitnis, *Angew. Chem. Int. Ed.* **2019**, *58*, 18096–18101; *Angew. Chem.* **2019**, *131*, 18264–18269; b) K. M. Marczenko, S. S. Chitnis, *Chem. Commun.* **2020**, *56*, 8015–8018; c) A. Koner, T. Sergeieva, B. Morgenstern, D. M. Andrada, *Inorg. Chem.* **2021**, *60*, 14202–14211.
- [23] Deposition numbers 2193647 (for 2), 2193648 (for 3), 2193649 (for 4), and 2193650 (for 5) contain the supplementary crystallographic data for this paper. These data are provided free of charge by the joint Cambridge Crystallographic Data



- Centre and Fachinformationszentrum Karlsruhe Access Structures service.
- [24] P. Pyykko, *J. Chem. Phys. A* **2015**, *119*, 2326–2337.
- [25] P. Federmann, T. Bosse, S. Wolff, B. Cula, C. Herwig, C. Limberg, *Chem. Commun.* **2022**, *58*, 13451–13454.
- [26] a) P. P. Power, *Chem. Rev.* **2003**, *103*, 789–810; b) J. Moilanen, P. P. Power, H. M. Tuononen, *Inorg. Chem.* **2010**, *49*, 10992–11000.
- [27] W. Uhl, A. Vester, W. Kaim, J. Poppe, *J. Organomet. Chem.* **1993**, *454*, 9–13.
- [28] W. Kaim, *J. Am. Chem. Soc.* **1984**, *106*, 1712–1716.
- [29] J. R. M. Giles, B. P. Roberts, *J. Chem. Soc. Chem. Commun.* **1981**, 1167–1168.
- [30] M. Nakamoto, T. Yamasaki, A. Sekiguchi, *J. Am. Chem. Soc.* **2005**, *127*, 6954–6955.
- [31] N. Wiberg, T. Blank, W. Kaim, B. Schwederski, G. Linti, *Eur. J. Inorg. Chem.* **2000**, 1475–1481.

Manuscript received: November 22, 2022

Accepted manuscript online: January 3, 2023

Version of record online: ■ ■ ■ ■ ■

### 3.1.1.2 $\text{TiO}_2$ and $\text{Nb}_2\text{O}_5$ Nanoparticles

The next scientific work illustrates a more efficient way to reduce metal oxides using a mechanochemical reduction approach instead of commonly used high temperature reductions. Here, low temperature ESR studies have been employed to investigate the hyperfine structure of the unpaired electron at the  $\text{Ti}^{3+}$  and  $\text{Nb}^{4+}$  centres.

# Black Titania and Niobia within Ten Minutes – Mechanochemical Reduction of Metal Oxides with Alkali Metal Hydrides

Anna Michaely,<sup>[a]</sup> Oliver Janka,<sup>[a]</sup> Elias C. J. Giebelmann,<sup>[a]</sup> Robert Haberkorn,<sup>[a]</sup> Haakon T. A. Wiedemann,<sup>[b]</sup> Christopher W. M. Kay,<sup>[b, c]</sup> and Guido Kickelbick\*<sup>[a]</sup>

**Abstract:** Partially or fully reduced transition metal oxides show extraordinary electronic and catalytic properties but are usually prepared by high temperature reduction reactions. This study reports the systematic investigation of the fast mechanochemical reduction of rutile-type TiO<sub>2</sub> and H-Nb<sub>2</sub>O<sub>5</sub> to their partially reduced black counterparts applying NaH and LiH as reducing agents. Milling time and oxide to reducing agent ratio show a large influence on the final amount of reduced metal ions in the materials. For both oxides LiH shows a higher reducing potential than NaH. An intercalation of Li<sup>+</sup> into the structure of the oxides was

proven by PXRD and subsequent Rietveld refinements as well as <sup>6</sup>Li solid-state NMR spectroscopy. The products showed a decreased band gap and the presence of unpaired electrons as observed by EPR spectroscopy, proving the successful reduction of Ti<sup>4+</sup> and Nb<sup>5+</sup>. Furthermore, the developed material exhibits a significantly enhanced photocatalytic performance towards the degradation of methylene blue compared to the pristine oxides. The presented method is a general, time efficient and simple method to obtain reduced transition metal oxides.

## Introduction

The partial reduction of transition metal oxides (TMO) results in an increase in oxygen vacancies and subsequently in materials with altered electronic properties compared to the original oxides, leading to extraordinary changes in their chemical and physical behavior.<sup>[1]</sup> A prominent example is the so-called black titania, which was first obtained by Chen et al. via hydrogenation of TiO<sub>2</sub> for 5 days.<sup>[2]</sup> Due to the introduction of defects and the partial reduction of the Ti<sup>4+</sup> cations, the material exhibits enhanced photocatalytic activities compared to the pristine oxide. Since then, defect engineering by full or partial

reduction of metal ions has become a growing field of research. Today black Nb<sub>2</sub>O<sub>5-x</sub>,<sup>[3]</sup> ZrO<sub>2-x</sub>,<sup>[4]</sup> WO<sub>3-x</sub>,<sup>[5]</sup> V<sub>2</sub>O<sub>5-x</sub>,<sup>[6]</sup> and MoO<sub>3-x</sub><sup>[7]</sup> are other prominent examples of this class of materials. Compared to the pristine oxides, the defect-rich counterparts usually exhibit enhanced light absorption<sup>[4]</sup> as well as improved photocatalytic<sup>[6,8]</sup> and photoelectrochemical (PEC)<sup>[3,9]</sup> performance. Besides gas phase hydrogenation,<sup>[2,8b]</sup> they can also be prepared by annealing at high temperatures in an oxygen-deficient atmosphere,<sup>[10]</sup> or via chemical reductions, for example, with Mg,<sup>[11]</sup> Al,<sup>[3]</sup> or NaBH<sub>4</sub>.<sup>[8a,12]</sup> Mechanochemical reduction can lower the required temperatures and therefore the energy consumption in the preparation of such materials. Furthermore, mechanochemical reactions are often faster and additional defects are introduced solely by the impact of the ball milling process, which can also increase the chemical reactivity of the final material. To the best of our knowledge, few mechanochemical approaches for the partial reduction of transition metal oxides have been investigated. Often, the reduction is carried out using highly reactive alkali metals, such as Na<sup>[13]</sup> or Li<sup>[14]</sup> or non-conventional hydrides such as TiH<sub>2</sub>.<sup>[15]</sup>

In our study, we used LiH and NaH as readily available alkali metal hydrides and powerful reducing agents in the fast solventless mechanochemical reduction of TiO<sub>2</sub> and Nb<sub>2</sub>O<sub>5</sub> at room temperature. While Li<sup>+</sup> (76 pm) has a smaller cationic radius compared to Na<sup>+</sup> (102 pm),<sup>[16]</sup> NaH exhibits a lower enthalpy of formation and hence a lower stability and thus higher reactivity of NaH (−56.3 kJ mol<sup>−1</sup>) compared to LiH (−90.5 kJ mol<sup>−1</sup>).<sup>[17]</sup> It can therefore be expected that both hydrides have a different reactivity for the reduction of TMO or reaction behavior such as the involvement of the alkali metal ion during the reaction, which is systematically studied below.

[a] A. Michaely, Dr. O. Janka, E. C. J. Giebelmann, Dr. R. Haberkorn, Prof. Dr. G. Kickelbick  
Inorganic Solid-State Chemistry  
Saarland University  
Campus, Building C4.1, 66123 Saarbrücken (Germany)  
E-mail: guido.kickelbick@uni-saarland.de

[b] H. T. A. Wiedemann, Prof. Dr. C. W. M. Kay  
Physical Chemistry and Didactics of Chemistry  
Saarland University  
Campus, Building B2.2, 66123 Saarbrücken (Germany)

[c] Prof. Dr. C. W. M. Kay  
University College London  
London Centre for Nanotechnology  
17–19 Gordon Street, London WC1H 0AH (UK)

Supporting information for this article is available on the WWW under <https://doi.org/10.1002/chem.202300223>

© 2023 The Authors. Chemistry - A European Journal published by Wiley-VCH GmbH. This is an open access article under the terms of the Creative Commons Attribution Non-Commercial License, which permits use, distribution and reproduction in any medium, provided the original work is properly cited and is not used for commercial purposes.

TiO<sub>2</sub> was chosen for the experiments as it is the most studied oxide for photocatalysis and defect engineering. A lot of studies use anatase-type TiO<sub>2</sub> (*I4<sub>1</sub>/amd*) or commercially available P25 due to their high photocatalytic activity. We chose the photocatalytically less active rutile<sup>[18]</sup> modification (*P4<sub>2</sub>/mnm*) for our study because it has higher mechanical stability than anatase.<sup>[19]</sup> Similar to TiO<sub>2</sub>, H-Nb<sub>2</sub>O<sub>5</sub> is also a stable wide-band gap *n*-type semiconductor with  $E_g = 3.1$  eV. It is mainly investigated for use in sensors and numerous electronic devices, but there also some reports on the application of Nb<sub>2</sub>O<sub>5</sub> in dye-sensitized solar cells<sup>[20]</sup> and other photocatalytic applications.<sup>[21]</sup> Thus, it is worth to further investigate Nb<sub>2</sub>O<sub>5</sub> as a potentially promising alternative for TiO<sub>2</sub> for photocatalytic applications. In the following, the influence of the type of reducing agent, milling time and composition on the photocatalytic activity of mechanochemically prepared TiO<sub>2</sub> and Nb<sub>2</sub>O<sub>5</sub> is systematically investigated.

## Results and Discussion

### Crystal chemistry

It is known from the literature that the reduction of oxides with LiH at high temperatures can lead to the incorporation of Li into the oxides, for example, in the reaction of LiH with BaTiO<sub>3</sub><sup>[22]</sup> or Sr<sub>2</sub>MnO<sub>4</sub>.<sup>[23]</sup> Therefore, it seems possible that Li is also to some extent inserted into TiO<sub>2</sub> and Nb<sub>2</sub>O<sub>5</sub> during the mechanochemical reduction. To facilitate the following discussion about the possible Li intercalation, the crystal chemistry of (lithiated) TiO<sub>2</sub> and Nb<sub>2</sub>O<sub>5</sub> will be discussed briefly.

Rutile-type TiO<sub>2</sub> crystallizes in the tetragonal crystal system with space group *P4<sub>2</sub>/mnm* with lattice parameters of  $a = 458.0$  pm and  $c = 297.0$  pm.<sup>[24]</sup> In the crystal structure, each Ti<sup>4+</sup> cation is octahedrally surrounded by oxide anions. These TiO<sub>6</sub> octahedra form chains along [001] via *cis*-edge sharing, the remaining two corners are linked to adjacent strands. Upon insertion of Li, either the tetra- or octahedral sites are occupied (Figure 1a). Using neutron diffraction measurements, Borghols et al. showed that the rutile structure is retained up to a maximum of Li<sub>0.07</sub>TiO<sub>2</sub> ( $a = 461.9$  pm,  $c = 295.4$  pm).<sup>[25]</sup> It was shown that the occupation of the tetrahedral sites is energetically favored at low temperatures (10 K), while the occupation of the octahedral sites becomes more favorable at room temperature. For even higher Li contents, for example, Li<sub>0.5</sub>Ti<sub>0.5</sub>O the cubic NaCl-type structure (*Fm $\bar{3}$ m*,  $a = 414.0$  pm)<sup>[26]</sup> is observed.<sup>[27]</sup> Both Li and Ti are octahedrally coordinated by the oxide anions and share the Wyckoff position *4a* (Figure 1b).

For Nb<sub>2</sub>O<sub>5</sub> several polymorphs, depending on the synthesis temperature, have been reported. The monoclinic high temperature phase H-Nb<sub>2</sub>O<sub>5</sub> crystallizes with space group *P2/m* and lattice parameters of  $a = 1933.0$  pm,  $b = 382.3$  pm,  $c = 2032.2$  pm and  $\beta = 115.8$ .<sup>[28]</sup> The Wadsley-Roth phase consists of blocks formed by 3×5 and 3×4 [NbO<sub>6</sub>] octahedra. These are connected by common corners within a block; however, edge sharing is observed between these entities. Finally, the tetrahedrally coordinated niobium site in H-Nb<sub>2</sub>O<sub>5</sub> is only half-occupied.<sup>[29]</sup> Different lithiated Nb-oxides have been described

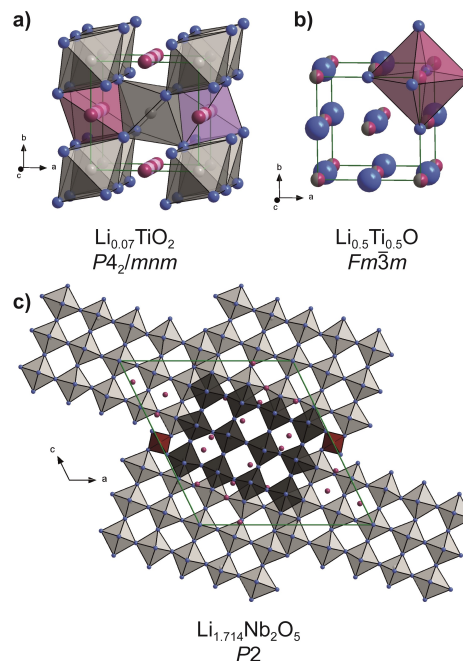


**Figure 1.** (a) Crystal structure of lithiated rutile-type Li<sub>0.07</sub>TiO<sub>2</sub>.<sup>[25]</sup> Tetrahedrally coordinated Li atoms are shown in purple, octahedrally coordinated Li atoms are pink, Ti atoms are shown in grey and oxygen atoms in blue. (b) Crystal structure of NaCl-type Li<sub>0.5</sub>Ti<sub>0.5</sub>O.<sup>[26]</sup> Li atoms are purple, Ti atoms are shown in grey and oxygen atoms in blue. (c) Crystal structure of lithiated H-Nb<sub>2</sub>O<sub>5</sub>.<sup>[30]</sup> The 3×4 block of octahedrally coordinated Nb atoms in H-Nb<sub>2</sub>O<sub>5</sub> is shown in dark grey, the 3×5 block in light grey, the tetrahedrally coordinated Nb atoms are drawn in red. The space groups are given.

for example, by Cava et al.<sup>[28]</sup> who identified five cavities in H-Nb<sub>2</sub>O<sub>5</sub>. Catti and Ghaani<sup>[30]</sup> characterized lithiated H-Nb<sub>2</sub>O<sub>5</sub> (Li<sub>1.714</sub>Nb<sub>2</sub>O<sub>5</sub>) via neutron diffraction experiments and localized the Li<sup>+</sup> cations in four-fold nonplanar, distorted tetrahedral and distorted square-pyramidal voids (Figure 1c), in line with the positions proposed by Cava et al. However, the localization of the Li atoms leads to a reduction in symmetry (*P2*,  $a = 1913.2$  pm,  $b = 413.5$ ,  $c = 2014.2$  pm,  $\beta = 119.57$ ).<sup>[30]</sup>

### Optical color change after ball milling

The partial reduction of TiO<sub>2</sub> and Nb<sub>2</sub>O<sub>5</sub> by a mechanochemical route was performed by milling the TMO with *n* equivalents of LiH and NaH ( $n = 0.5, 1$  and  $2$ ) for 10, 30, and 60 min at a fixed milling speed of 300 rpm. In the following, the samples are denoted as *NM<sub>n</sub>:m:t*. The first letter being T for TiO<sub>2</sub> or N for Nb<sub>2</sub>O<sub>5</sub>, the second letter corresponds to the alkali metal hydride (N=NaH, L=LiH), while *n* and *m* represent the number of equivalents of TiO<sub>2</sub>/Nb<sub>2</sub>O<sub>5</sub> and the hydride, respectively. Finally, *t* represents the milling time in minutes.

After only 10 minutes of ball milling at room temperature, a visually perceptible color change of the powders from white to light gray in the case of  $\text{TiO}_2$  or brownish-gray to dark blue-black for  $\text{Nb}_2\text{O}_5$  was observed. The obtained coloration is clearly depending on the amount of hydride added (Figure 2). The observed coloration of the samples after ball milling is most likely caused by the reduction of  $\text{Ti}^{4+}$  to  $\text{Ti}^{3+}$ <sup>[31]</sup> and of  $\text{Nb}^{5+}$  to  $\text{Nb}^{4+}$ <sup>[32]</sup>. However, for reasons of electroneutrality, the reduction must be either accompanied by the intercalation of alkali metal ions or the formation of oxygen vacancies, which also can give rise to color centers.<sup>[10b]</sup> Also a combination of both effects seems possible. Therefore, ball milling of the oxides in the presence of the reducing agents should produce various types of defects in the compounds. For both oxides, the milled powders have a darker color when LiH was used as the reducing agent compared to samples reduced under the same conditions applying NaH. Usually, NaH would be expected to have a higher reductive power and therefore we expected the darker color in the corresponding samples. This assumption is based on the size difference of the alkali metal ions ( $\text{Li}^+$ : 76 pm,

$\text{Na}^+$ : 102 pm)<sup>[16]</sup> and on the lower enthalpy of formation and thus also the lower stability and thus higher reactivity of NaH ( $-56.3 \text{ kJ mol}^{-1}$ ) compared to LiH ( $-90.5 \text{ kJ mol}^{-1}$ ).<sup>[17]</sup> It has already been reported that Li-containing reducing agents can behave differently due to the incorporation of Li into the oxide,<sup>[22]</sup> which could also be the reason for the apparent higher reactivity of LiH in our study.

With the EASY GTM system for the Fritsch Pulverisette 7 premium line, we can monitor the development of temperature and pressure in the grinding bowl. A continuous increase in pressure up to several bar can be observed, which is due to the development of hydrogen with increasing milling time. At the same time, the temperature also increases, but remains below 35 °C (Figure S1, Supporting Information).

#### Powder X-ray diffraction analysis

Powder X-ray diffraction (PXRD) patterns were recorded to gain a better understanding of the processes during ball milling and

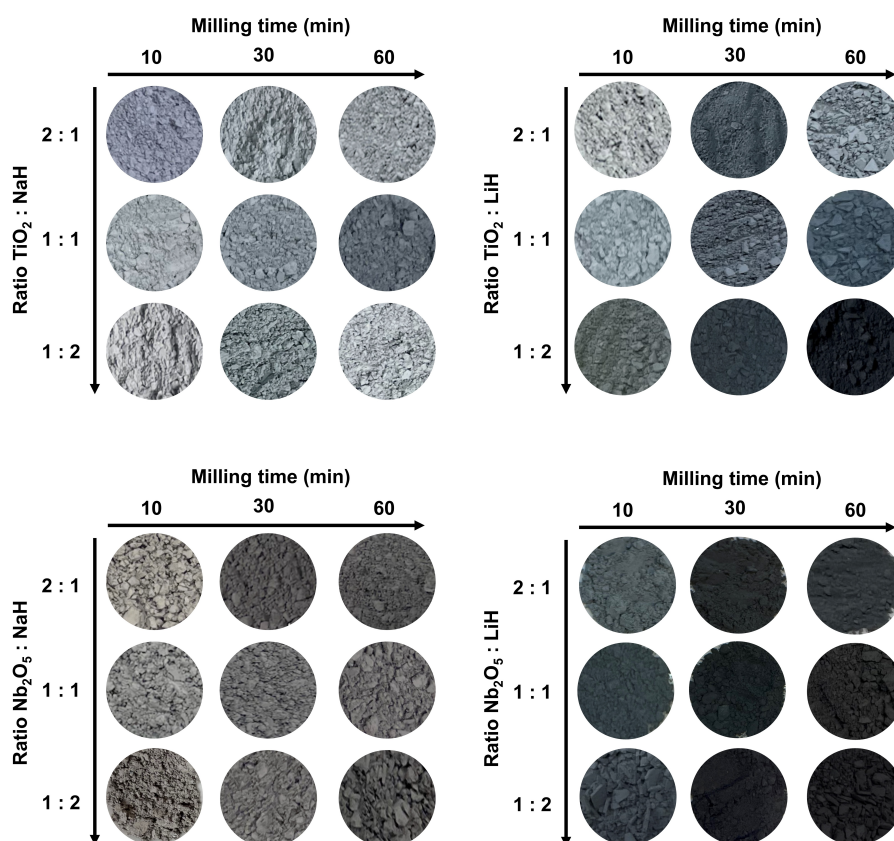


**Figure 2.** Photographs of reduced  $\text{TiO}_2$  and  $\text{Nb}_2\text{O}_5$  obtained after milling with NaH and LiH at various molar ratios between 10 and 60 min at a constant milling speed of 300 rpm.

to analyze possible changes in the crystal structure due to the partial reduction. No significant changes in the PXRD patterns are observed after milling  $\text{TiO}_2$  (rutile,  $P4_2/mnm$ ) with NaH (NaCl-type,  $Fm\bar{3}m$ ). The observed powder pattern still corresponds to rutile-type  $\text{TiO}_2$ . Contrary, the reflections at around 27.4 (110) and 54.0  $2\theta$  (211) show a strong asymmetry after ball milling with LiH (NaCl-type,  $Fm\bar{3}m$ ) caused by an increasing amount of disorder due to the reaction with LiH (Figure 3a). Both reflections are dominated by changes of the  $a$  lattice parameter of  $\text{TiO}_2$ , indicating that the structural changes such as the intercalation of  $\text{Li}^{+}$  and the formation of oxygen vacancies mainly influence the  $ab$ -plane.<sup>[34]</sup> To accommodate for these structural changes in the Rietveld refinement, a multi-fraction model with different fractions of rutile-type  $\text{TiO}_2$  was used (Figure S2-6, Supporting Information). Moreover, the reflections at  $\sim 44$  (200) and  $\sim 63$   $2\theta$  (220) are significantly broadened due to an overlap with newly emerging reflections corresponding to the cubic  $\text{Li}_{0.5}\text{Ti}_{0.5}\text{O}$  phase with a rock salt-type structure ( $Fm\bar{3}m$ ) (Figure S6, Supporting Information) exhibiting titanium in the oxidation state +III. This observation is in line with the formation of  $\text{Li}_{0.5}\text{Ti}_{0.5}\text{O}$  when rutile-type  $\text{TiO}_2$  is lithiated via more conventional reagents such as  $n\text{-BuLi}$ <sup>[33b]</sup> or hydrothermally with  $\text{LiOH}$ <sup>[35]</sup> but can also be achieved by grinding the oxide with  $\text{Li}$ <sup>[33b]</sup>.

The fraction of  $\text{Li}_{0.5}\text{Ti}_{0.5}\text{O}$  increases with longer milling time and higher amounts of initial LiH (Figure 3b), for example from 9 to 44 wt% after milling with 2 equiv. LiH for 10 and 60 min, respectively. The increase of the Li-containing phase with increasing milling time was proven by the determination of the Li to Ti ratio by ICP-MS measurements. After milling  $\text{TiO}_2$  for 10 and 60 min with 2 equiv. LiH, a molar Li:Ti ratio of 0.08:1 and 0.38:1 was determined. These results are in good agreement with the results of the Rietveld refinements, which gave an overall composition of  $\text{Li}_{0.09(1)}\text{TiO}_2$  and  $\text{Li}_{0.36(1)}\text{TiO}_2$  for the samples TL\_1:2\_10 and TL\_1:2\_60, respectively. The presence of Li inside the sample is further proven by  $^6\text{Li}$  solid-state NMR (see below). In contrast, no sodiation was observed in  $\text{TiO}_2$  reduced with NaH after reduction, possibly due to the larger radius of

$\text{Na}^+$  compared to  $\text{Li}^+$ . A similar change in color and lithiation was also observed after ball milling anatase-type  $\text{TiO}_2$  ( $I4_1/amd$ ) with LiH. In addition to the transformation of anatase into the orthorhombic high-pressure form ( $\alpha\text{-PbO}_2$ -type,  $Pbcn$ ), which is known to occur during milling,<sup>[36]</sup> orthorhombic  $\text{Li}_{0.5}\text{TiO}_2$  ( $Imma$ ) was also formed (Figure S12, Supporting Information).

For  $\text{Nb}_2\text{O}_5$ , no significant changes in the crystal structure are observed by PXRD measurements after milling with both hydrides. The observed diffraction patterns still correspond to monoclinic  $\text{H-Nb}_2\text{O}_5$  ( $P2/m$ ) regardless of the reducing agent and milling time (Figure S13a, Supporting Information). However, the unit cell volumes revealed an increase for  $\text{Nb}_2\text{O}_5$  upon reduction with LiH, whereas no significant increase was observed for NaH (Figure S13b, Supporting Information). Only lithiated, but no sodiated  $\text{Nb}_2\text{O}_5$  phases have been reported in the literature, where the crystal system was maintained during the intercalation of the alkali metal ions,<sup>[30]</sup> which is again due to a smaller ionic radius of  $\text{Li}^+$  compared to  $\text{Na}^+$ .<sup>[16]</sup> Hence, the increase of the unit cell volume of several  $\text{\AA}^3$  can be attributed to an intercalation of  $\text{Li}^+$ ,<sup>[28,30]</sup> whose presence is also proven by  $^6\text{Li}$  solid-state NMR (see below). Based on the increase of the unit cell volume of LiH reduced samples, a sample composition between  $\text{Li}_{0.02(1)}\text{Nb}_2\text{O}_5$  and  $\text{Li}_{0.25(1)}\text{Nb}_2\text{O}_5$  was calculated (Table S2, Supporting Information).

Elemental analysis (CHN) of sample TL\_1:2\_60 revealed that no significant amount of hydrogen is found, indicating that no hydrogen is introduced into the crystal structure. Therefore, no Ti–OH or Ti–H bonds are formed, as it is sometimes reported for black titania prepared by hydrogenation.<sup>[2,37]</sup> However, the formation of these bonds strongly depends on the synthesis conditions<sup>[1]</sup> and open questions about the actual structure remain.<sup>[38]</sup> Since no significant hydrogen concentration was detectable, the hydride ion will most likely transfer one or two electrons to the oxide<sup>[39]</sup> during the ball milling process, followed by the reduction of  $\text{Ti}^{4+}/\text{Nb}^{5+}$  to  $\text{Ti}^{3+}/\text{Nb}^{4+}$  along with the formation of oxygen vacancies or the insertion of  $\text{Li}^+$  to respect charge neutrality. It is also possible that the mechanochemical reduction process follows an even more complicated reaction mechanism,<sup>[23]</sup> but no experimentally proven mechanistic details can be given currently.

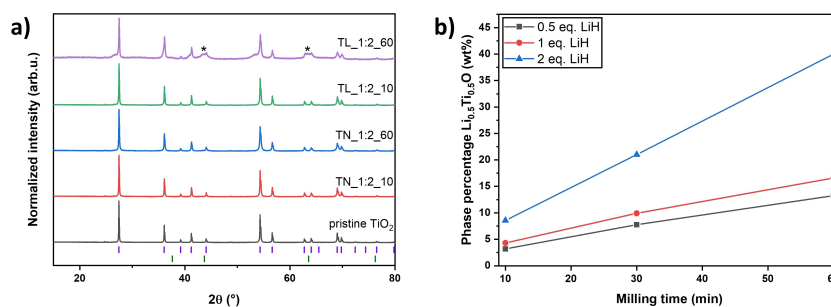


**Figure 3.** (a) PXRD patterns of pristine and reduced titania. Violet ticks indicate the Bragg positions of rutile-type  $\text{TiO}_2$  ( $P4_2/mnm$ ) and green ones of  $\text{Li}_{0.5}\text{Ti}_{0.5}\text{O}$  ( $Fm\bar{3}m$ ). The position of the most intense reflections of the latter are marked with asterisks. (b) Phase percentage of  $\text{Li}_{0.5}\text{Ti}_{0.5}\text{O}$  versus milling time and LiH amount, obtained by Rietveld refinement.

### TGA measurements

In a next step, TGA measurements were performed to investigate the re-oxidizability of the samples by heating them under nitrogen to 600 C followed by heating under synthetic air to 900 C to see if a reoxidation, which is accompanied by a mass increase, takes place.<sup>[40]</sup> After the thermal treatment, all samples turned white again due to the reoxidation of  $Ti^{3+}/Nb^{4+}$  to  $Ti^{4+}/Nb^{5+}$  during the formation of alkali metal titanates or niobates and/or the refilling of oxygen vacancies.<sup>[7,41]</sup> In most samples, no significant mass gain was observed, most likely due to the low degree of reduction. Only for TL\_1:2\_60 and NL\_1:2\_60 a mass gain of 1.4 and 0.7% due to the uptake of oxygen was observed, respectively (Figure S14, Supporting Information). PXRD measurements confirmed that in all samples the reoxidation of  $Ti^{3+}$  and  $Nb^{4+}$  to  $Ti^{4+}$  and  $Nb^{5+}$  occurred. While samples with a lower degree of reduction or samples reduced via NaH were simply reoxidized to  $TiO_2$  and  $Nb_2O_5$ , lithium titanates and niobates such as  $Li_4Ti_5O_{12}$  ( $Fd\bar{3}m$ )<sup>[42]</sup> and  $LiNb_3O_8$  ( $P2_1/c$ )<sup>[43]</sup> were formed from higher reduced samples

(Figure S15, Supporting Information). The color change of  $TiO_2$  if heated under air in absence of a sodiation reaction (Figure S16, Supporting Information) leads to the conclusion, that oxygen defects according to  $TiO_{2-x}$  can form in principle. However, since the formation of the before mentioned Li-titanates and Li-niobates can also only occur upon oxygen uptake, a differentiation between reduction via lithium intercalation and reduction due to oxygen vacancies is not possible.

### $^6Li$ solid-state NMR experiments

Solid-state MAS NMR investigations of  $^6Li$  or  $^7Li$  nuclei are a powerful technique to probe the local environment of the  $Li^+$  ions in their respective host structures as for example shown for  $TiO_2$ .<sup>[44]</sup> And although the differences in the chemical shifts are small ( $\delta = -1$  to 1 ppm), a site assignment was possible. Figure 4a shows a comparison of the  $^6Li$  MAS NMR spectra of the LiH reduced  $TiO_2$  samples after 10, 30 and 60 minutes of milling. The presence of a resonance near  $\delta \sim 1$  ppm clearly

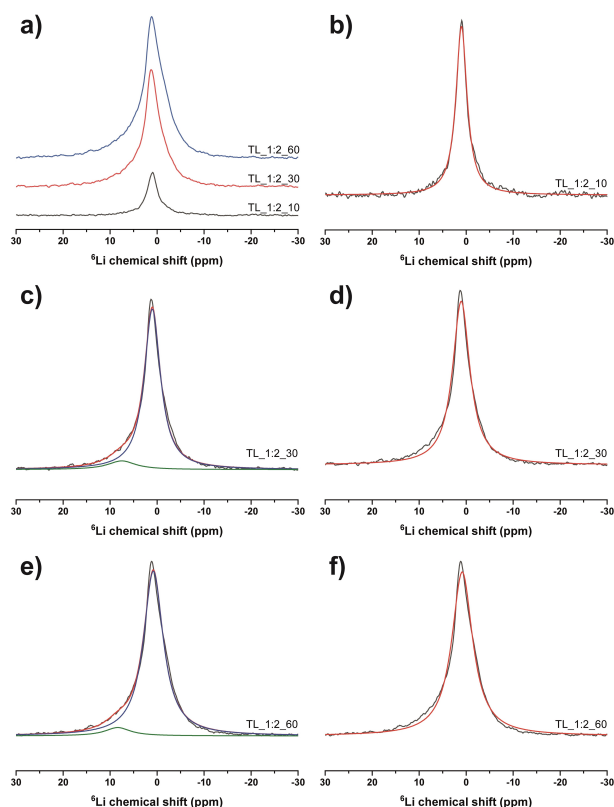


**Figure 4.** (a)  $^6Li$  MAS NMR spectra of  $TiO_2 + LiH$  (1:2) after ball-milling of 10 (grey), 30 (red) and 60 (blue) minutes. (b, d, f) Individual  $^6Li$  MAS spectra for the given ball milling times fitted with a single Gaussian-Lorentz line.  $^6Li$  MAS spectra for  $TiO_2 + LiH$  after a milling time of (c) 30 and (e) 60 minutes fitted with two lines. Spectra are plotted in black; red lines are the fitting curves; the blue and green lines indicate the individual spectral components.

proves the presence of Li in the solid. The increasing intensity of the NMR signal is proportional to the milling times suggesting that more Li is present in the samples since the measurement conditions for the NMR spectra (number of scans, acquisition time, pulse sequence, delay time) were kept the same for all samples. In addition, the full width at half maximum (FWHM) of the signal increases with prolonged milling times (Table S5, Supporting Information), indicating higher structural disorder. A deeper analysis of the individual spectra using the DMFit software program package showed that the line shape varies significantly. Gaussian-Lorentz fit functions were used for analysis of the asymmetry of the peaks (Figure 4b, d, f and Table S5, Supporting Information). All samples show a broad asymmetric signal over the range from  $-5$  up to  $9$  ppm. The maximum of the resonance can be observed around  $\delta \sim 1$  ppm, which is typical for ionic, diamagnetic Li species.<sup>[45]</sup> For the reduced samples with a milling time of 10 minutes, the line shape can be described well with a single line fit. In contrast, single line fits applied to the spectra obtained from the longer milled samples (30 and 60 min) show a rather bad agreement with the experimental data. The intensity profile, especially at higher and lower frequencies, cannot be described in a satisfactory way. Especially the intensity in the region between  $5$  to  $8$  ppm seems to be caused by a signal caused by at least one other Li species. The addition of a second signal (Gaussian-Lorentz function) indicated that this resonance is centered around  $\delta = 8.4$  ppm, however, an extremely large FWHM is found (Figure 4c, e).

When comparing this data to the literature<sup>[44a-d]</sup> it becomes clear that the presented spectra are rather broad and featureless. Even in ball-milled samples of Li-titanates, synthesized by a high temperature solid-state approach, structural information about the location of the Li ions within the structures could be obtained due to sharp lines and the sensitivity of  $^6\text{Li}$  to the structural and electronic environment.<sup>[44e]</sup> This is in total contrast to the measurements performed here because no detailed insight about the coordination of Li in the structure could be obtained. Therefore, it can be concluded that these systems exhibit significant disorder resulting in many different crystallographic Li sites, which leads to a large variation of the Li–O bond lengths and in turn to the observed line broadening.

The broad resonance with its large shift of  $\delta \sim 8$  ppm, though disagrees with the previously mentioned NMR studies. However, NMR investigations on paramagnetic  $\text{LiCoO}_2$  reported resonance shifts of up to  $17$  ppm.<sup>[45]</sup> The intermetallic compound  $\text{Li}_4\text{Pt}_3\text{Si}$  shows even resonance shifts of up to  $\sim 120$  ppm.<sup>[46]</sup> Here the nuclear magnetic moment interacts with the magnetic moment of the Co atoms in the case of  $\text{LiCoO}_2$  or the conduction electrons of  $\text{Li}_4\text{Pt}_3\text{Si}$  leading to these drastic shifts known as Knight shifts. Since the reduced  $\text{TiO}_2$  shows a black color, but is not metallic in nature, the signal at  $\delta \sim 8$  ppm could be explained from the interactions of the paramagnetic  $\text{Ti}^{3+}$  centers with the Li nuclei similar to  $\text{LiCoO}_2$ .<sup>[45]</sup> This hypothesis is further strengthened by the fact that the signal at  $\delta \sim 8$  ppm increases in intensity with prolonged ball milling time and the recorded electron paramagnetic resonance (EPR) spectra (see below). Finally, the  $^6\text{Li}$  NMR spectrum of LiH reduced  $\text{Nb}_2\text{O}_5$  (1:2 ratio) after 60 min ball milling was exemplarily also fitted with a single Gaussian-Lorentz line (Figure S17, Supporting Information). The main resonance shows a chemical shift around  $\delta \sim 1$  ppm with a comparable FWHM (Table S5, Supporting Information).

#### Electron paramagnetic resonance spectroscopy

EPR spectroscopy was used to detect and further investigate the presence of unpaired electrons at the  $\text{Ti}^{3+}$  and  $\text{Nb}^{4+}$  centers. According to Chester et al., the hyperfine structure of their niobium-doped rutile only showed hyperfine splitting at temperatures below  $25$  K.<sup>[47]</sup> Therefore, the EPR experiments were conducted at  $10$  K. EPR experiments above  $10$  K showed a broad signal without hyperfine lines, which was a first qualitative evidence for the presence of unpaired electrons in both reduced titania and niobia samples. The observed EPR signal (Figure 5) could be caused by paramagnetic oxygen vacancies  $V_{\text{O}}$ , as well as  $\text{Ti}^{3+}$  and other lower valence Ti species, as documented for many oxide materials.<sup>[48]</sup> The formation of unpaired electrons during the mechanochemical reduction of  $\text{TiO}_2$  with LiH could be confirmed, while the NaH reduced  $\text{TiO}_2$  only showed a weak intensity signal. To differentiate and compare the different ball milling times, the peak areas of the

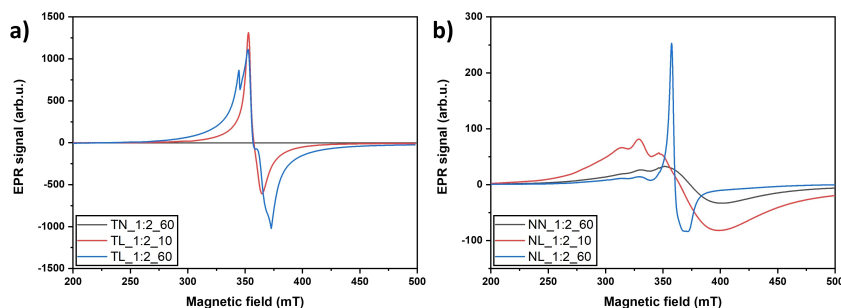


**Figure 5.** Continuous wave (CW) EPR spectra of NaH (black line) and LiH (blue and red lines) reduced (a)  $\text{TiO}_2$  and (b)  $\text{Nb}_2\text{O}_5$  samples.

reduced oxides were compared. As expected, for samples obtained after prolonged milling, the peak area increases with milling time.<sup>[14]</sup> Thus, the longer the milling time, the more  $\text{Ti}^{4+}$  ions are reduced to  $\text{Ti}^{3+}$ , which is accompanied by the formation of oxygen vacancies or the intercalation of Li.

The formation of unpaired electrons during the mechanochemical reduction of  $\text{Nb}_2\text{O}_5$  with LiH/NaH could be confirmed as well, but with lower intensities and peak areas and thus, fewer paramagnetic species. The  $\text{Nb}^{4+}$  concentration shows the same time dependency as in titania with a higher formation of oxygen vacancies and Li intercalation with prolonged milling duration. Theoretically, a total of ten instead of the three visible lines would be expected for  $^{93}\text{Nb}^{4+}$  due to hyperfine coupling since niobium has a nuclear spin of  $9/2$  (100% natural abundance). Similarly, a total of six lines is expected for  $^{47}\text{Ti}^{3+}$  ( $I=5/2$ , 7.4% natural abundance) and eight lines for  $^{49}\text{Ti}^{3+}$  ( $I=7/2$ , 5.4% natural abundance) but  $\sim 87\%$  of the Ti centers have no spin, and therefore no coupling. The total number of lines does not match the expectation, but hyperfine splitting constants could be derived from the visible peaks. For the  $\text{TiO}_2/\text{LiH}$  system, 7.9 mT and for the  $\text{Nb}_2\text{O}_5/\text{LiH}$  system, 17.8 mT, were extracted.

### Raman spectroscopy

In order to further investigate the structural changes, Raman spectra were recorded. Both pristine and reduced titania show the typical Raman signals of rutile at 143, 240, 446 and  $609\text{ cm}^{-1}$ , which can be assigned to the Raman modes  $B_{1g}$ , second-order scattering,  $E_g$  and  $A_{1g}$  (Figure 6a).<sup>[49]</sup> Similarly, the typical Raman bands of monoclinic  $\text{H-Nb}_2\text{O}_5$ , namely Nb–O–Nb angle-deformations between  $160$  to  $300\text{ cm}^{-1}$ , transverse optic modes (TO) originating from symmetric stretching of  $\text{NbO}_6$  octahedra between  $600$  and  $700\text{ cm}^{-1}$  and the longitudinal optic mode (LO) of  $\text{NbO}_6$  edge-shared octahedra at around  $990\text{ cm}^{-1}$  were observed for all  $\text{Nb}_2\text{O}_5$  samples (Figure 6b).<sup>[50]</sup> No major changes are observed for NaH reduced oxides in both cases, suggesting that only minor structural changes, for example introduction of oxygen defects, occurred during the mechanochemical reduction. In case of LiH reduced  $\text{TiO}_2$  a redshift of up to  $10\text{ cm}^{-1}$  of the multi-photon band at around  $230\text{ cm}^{-1}$  and a blueshift of  $15\text{ cm}^{-1}$  of  $E_g$  is observed, while a red shift of up to  $8\text{ cm}^{-1}$  occurred of the LO mode of the symmetric Nb–O stretching of LiH reduced  $\text{Nb}_2\text{O}_5$ . Furthermore, the Raman bands become more broadened the more reduced the samples are due to the increase of structural disorder for example, due to Li intercalation<sup>[51]</sup> or formation of other defects during the ball milling process.<sup>[52]</sup>

Compared to the pristine oxides, all reduced samples exhibit a significantly stronger absorption in the visible region

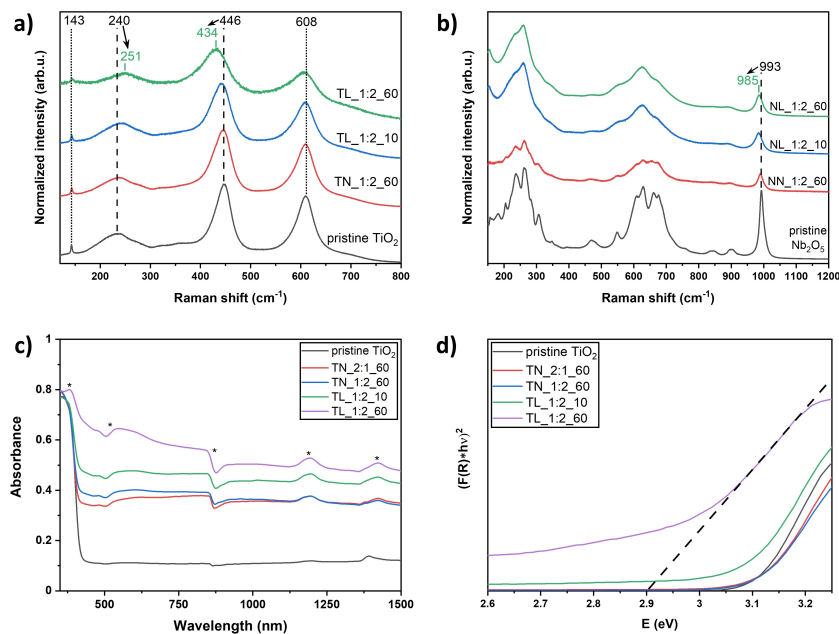


**Figure 6.** Raman spectra of pristine (black) and with 2 equiv. NaH (60 min, red) and LiH (10 min, blue; 60 min, green) reduced (a)  $\text{TiO}_2$ , and (b)  $\text{Nb}_2\text{O}_5$ , (c) DRS-UV-Vis absorbance spectra and (d) Kubelka-Munk plot of pristine and reduced  $\text{TiO}_2$ . Lamp, detector, and filter changes in c) are marked with an asterisk, the evaluation of the band gap is shown by the dashed line in d).

(Figure 6c) as shown via the UV-Vis diffuse reflectance spectra (DRS). A clear correlation between the color of the samples and the absorbance of visible light was observed. The values of the optical band gaps and their changes during the reduction were obtained based on the Kubelka-Munk function  $F(R)$  and the Tauc relationship  $(F(R)h\nu)^{\frac{1}{n}} = A(h\nu - E_g)$  with  $h\nu$  being the photon energy,  $A$  is a proportionality constant,  $E_g$  the band gap energy and  $n$  a parameter depending on the type of band gap. For direct allowed electronic transitions  $n$  equals  $\frac{1}{2}$  and for indirect allowed transitions  $n$  equals 2.<sup>[53]</sup> According to literature, rutile-type  $\text{TiO}_2$  and monoclinic  $\text{H-Nb}_2\text{O}_5$  both have a direct band gap.<sup>[54]</sup> In both cases, the optical band gap of the reduced oxides is significantly lowered (up to 0.4 eV compared to the pristine oxide) due to the partial reduction and introduction of defects (Figure 6d, Figure S18, Table S6, Supporting Information).<sup>[14]</sup>

#### Photocatalytic degradation experiments

Often, a reduction in the band gap and absorption properties over a wider range of wavelengths leads to improved (photo-generated) charge carrier properties and higher photocatalytic activity.<sup>[14]</sup> To evaluate the photocatalytic activities of the reduced oxides compared to the pure oxides, the photochemical degradation of methylene blue (MB), commonly used in tests of the photocatalytic activity of heterogeneous catalysts

and found as a pollutant in the wastewater of the textile industry, was studied.<sup>[55]</sup> For the experiments under UV irradiation, a light source emitting 365 nm was used, while the wavelengths emitted by the visible light source range from 400 to 700 nm with the strongest irradiance being at around 450 and 550 nm. Blank experiments show that without the addition of a catalyst, the photobleaching of MB is only minimal (Figure 7). Overall, no enhancement is observed for NaH reduced  $\text{TiO}_2$  and  $\text{Nb}_2\text{O}_5$  samples, possibly due to the small degree of reduction. In contrast, all LiH reduced samples exhibit an improved performance compared to the pristine oxides. When visible light was used for the degradation experiments, about 33% of the MB was degraded after 5 h using untreated rutile-type  $\text{TiO}_2$  was used as catalyst. When a LiH reduced  $\text{TiO}_2$  sample was used milled for 10 and 60 min, a significant increase to 45 and 70% of the degraded MB was observed in the same period (Figure 7a). Due to the successful introduction of defects and the partial reduction of  $\text{Ti}^{4+}$  to  $\text{Ti}^{3+}$ , the synthesized materials even show a higher photocatalytic activity under visible light compared to the commercially available and widely used photocatalyst Evonik P25 (Figure 7a), which consists of both anatase and rutile  $\text{TiO}_2$ . In the case of  $\text{H-Nb}_2\text{O}_5$  only a slight enhancement of the photocatalytic performance of the LiH reduced sample obtained after 10 min of milling ( $C_t/C_0 = 0.69$ ) was observed compared to pristine  $\text{H-Nb}_2\text{O}_5$  ( $C_t/C_0 = 0.72$ ). LiH treated  $\text{Nb}_2\text{O}_5$  obtained after 60 min of ball milling in contrast shows a significant improvement since a MB con-

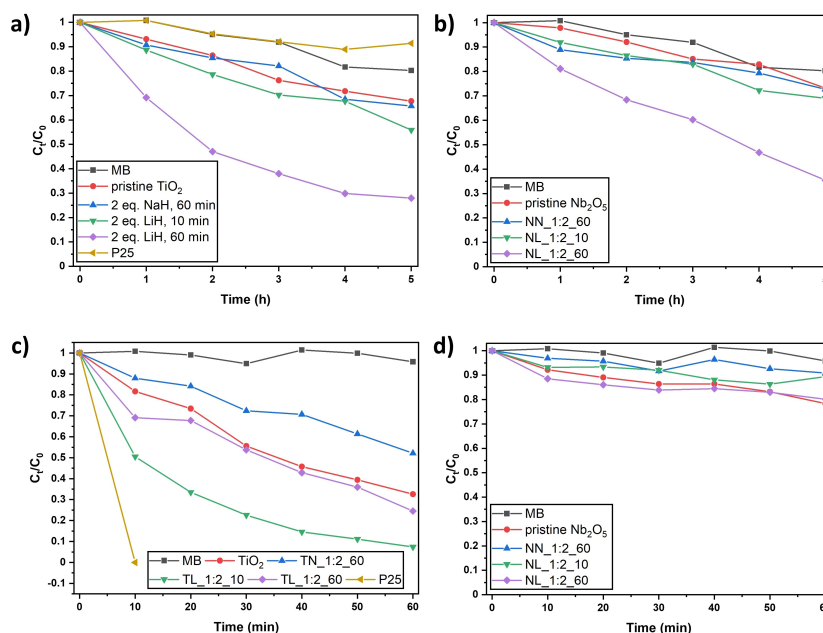


**Figure 7.** Photocatalytic degradation of methylene blue (MB) (a), (b) under visible light and (c), (d) under UV (365 nm) light without catalyst (black), with pristine titania and niobia (red) and with reduced titania and niobia (blue: NaH, 60 min; green: LiH, 10 min; purple: LiH, 60 min) and with commercially available P25 (yellow). Note the different time scales between (a, b) and (c, d).

version of 65% was achieved after 5 h of irradiation (Figure 7b). It can therefore be concluded that longer milling times and thus a higher degree of reduction for the LiH reduced samples favor the degradation of MB using visible light. In contrast, under irradiation with UV light (365 nm) a complete discoloration of the MB solution was achieved after only 60 min using the LiH reduced titania sample obtained after 10 min of milling ( $C_t/C_0 = 0.07$ ). Interestingly, both pristine rutile  $\text{TiO}_2$  and the LiH reduced sample (60 min) exhibit a lower photocatalytic activity in the UV range (Figure 7c). In comparison to the standard photocatalyst P25, our prepared materials show a somewhat lower photocatalytic activity since a complete discoloration of the MB solution can be achieved with these tailor-made materials after only 10 min with P25 under UV irradiation (Figure 7b). This is attributed to the fact that our sample still predominately composed of photocatalytically less active rutile. As for the niobia samples, both pristine and reduced niobia show almost no activity in the UV range (Figure 7d), which makes the reduced titania samples the more suitable for photocatalytic applications, especially in the UV range.

To exclude that the enhancement of the photocatalytic properties only originates from ball milling,  $\text{TiO}_2$  was milled for 60 min and its photocatalytic activity was measured under both UV and visible light. In general, mechanochemistry is a suitable method for the preparation of catalysts.<sup>[56]</sup> While some publications report an enhancement of the photocatalytic activity of oxides,<sup>[57]</sup> sulfides<sup>[58]</sup> or composite materials<sup>[59]</sup> depending on the milling conditions, no enhancement was observed compared to pristine rutile-type  $\text{TiO}_2$  in the present case (Figure S19, Supporting Information), in contrast to the already active anatase phase cited above. This shows that the mechanochemical reaction with the alkali metal hydrides is the main reason for the faster MB degradation. The higher activity of the synthesized materials can be ascribed to the presence of defects such as  $\text{Ti}^{3+}/\text{Nb}^{4+}$ , resulting in a smaller band gap and consequently a better absorption of light, as well as a probable reduction of the recombination rate of photogenerated electron-hole pairs.<sup>[11a,14]</sup>

In literature, there are some reports on the use of rock salt-type  $\text{Li}_{0.5}\text{Ti}_{0.5}\text{O}$  as a catalyst for the photocatalytic dye

degradation<sup>[35a]</sup> and hydrogen generation.<sup>[60]</sup> Since the compounds formed during ball milling of  $\text{TiO}_2$  and LiH,  $\text{Li}_{0.5}\text{Ti}_{0.5}\text{O}$  was prepared via a solid-state reaction under argon using  $\text{TiO}_2$  and 2 equiv. LiH (Figure S20, Supporting Information). The reaction mixture was heated to 600 °C for 60 min. Afterwards, the obtained material was washed with  $\text{NH}_4\text{Cl}/\text{MeOH}$  and MeOH. As a proof of concept that not all measured effects of reduced titania samples are caused by  $\text{Li}_{0.5}\text{Ti}_{0.5}\text{O}$ , its photocatalytic activity was compared with the photocatalytic activity of TL\_1:2\_60 under visible light irradiation and with TL\_1:2\_10 under UV (365 nm) irradiation. As shown in Figure 8,  $\text{Li}_{0.5}\text{Ti}_{0.5}\text{O}$  performs slightly better under visible irradiation than TL\_1:2\_60 but shows a poor performance under UV irradiation. This suggests that not all observed effects originate from the presence of  $\text{Li}_{0.5}\text{Ti}_{0.5}\text{O}$  such as the good MB degradation ability under UV light of our synthesized material, but it seems that  $\text{Li}_{0.5}\text{Ti}_{0.5}\text{O}$  might be especially beneficial for an effective MB degradation under visible light irradiation.

## Conclusion

In summary, a simple and rapid room temperature mechanochemical process was developed for the reduction of rutile-type  $\text{TiO}_2$  and  $\text{H-Nb}_2\text{O}_5$  using alkali metal hydrides. Depending on the synthesis conditions (type and amount of reducing agent and milling duration), samples with a color ranging from light gray to blue to gray and black were obtained. In general, longer milling times and higher amounts of the reducing agent resulted in a higher degree of reduction of the transition metal ions. After reduction using NaH, no significant changes in the crystal structure were observed from PXRD measurements, but the formation of cubic  $\text{Li}_{0.5}\text{Ti}_{0.5}\text{O}$  and the intercalation of Li was observed for  $\text{TiO}_2$  and  $\text{Nb}_2\text{O}_5$  when reduced with LiH. The intercalation may occur due to the smaller radius of  $\text{Li}^+$  compared to  $\text{Na}^+$ . The band gap of the ball milled transition metal oxides decreased by up to 0.4 eV, while more paramagnetic centers were formed with longer milling time, as shown by EPR spectroscopy.  $^6\text{Li}$  NMR spectroscopic investigations clearly demonstrate that the samples contain significant

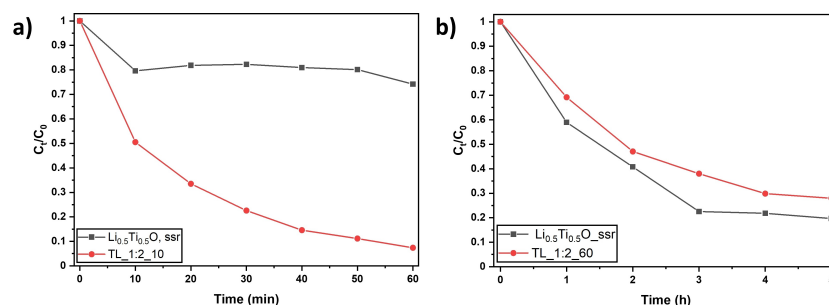


**Figure 8.** Photocatalytic degradation of MB with  $\text{Li}_{0.5}\text{Ti}_{0.5}\text{O}$  prepared by solid state reaction and LiH reduced titania (60 min and 10 min) under (a) visible and (b) UV (365 nm) light.

amounts of disorder since the signals are featureless. In the case of LiH reduced TiO<sub>2</sub> milled for 30 or 60 min, a second signal arises that could be attributed to the interaction of the paramagnetic Ti<sup>3+</sup> ions with the Li nucleus. Raman spectroscopy revealed an increase in structural disorder due to the formation of defects. These are more pronounced when LiH is used, as indicated by the darker color of the reduced oxides. Due to these defects, a significantly better photocatalytic performance of the synthesized materials compared to the pristine oxides was achieved under illumination with both UV and visible light.

## Experimental Section

**Materials:** Nb<sub>2</sub>O<sub>5</sub> (ChemPur, Karlsruhe, Germany, 99.98%), TiO<sub>2</sub> (Alfa Aesar GmbH, Karlsruhe, Germany, 99.5%), LiH (Alfa Aesar GmbH, Karlsruhe, Germany, 99.4%), and NaH (Merck, Darmstadt, Germany, > 98%) were used without further purification and stored in a glovebox under argon atmosphere. All solids have been characterized by powder X-ray diffraction before use.

**Synthetic procedures:** The syntheses were performed in a planetary ball mill Pulverisette 7 premium line (Fritsch, Idar-Oberstein, Germany) using ZrO<sub>2</sub> grinding jars with a volume of 45 mL and 180 Y-stabilized ZrO<sub>2</sub> milling balls with a diameter of 5 mm. All syntheses were performed under inert gas by filling and closing the milling jars in an argon filled glovebox. For the ball milling experiments 3.00 g of Nb<sub>2</sub>O<sub>5</sub> (11.29 mmol, 1 equiv.) or TiO<sub>2</sub> (37.6 mmol, 1 equiv.) were milled with *n* equiv. of LiH or NaH (*n* = 0.5, 1 and 2). The milling speed was set to 300 rpm, and the milling time was varied from 10 to 30 to 60 min.

Afterwards, the samples were washed with 0.1 M NH<sub>4</sub>Cl/MeOH and MeOH under argon several times to remove unreacted alkali metal hydrides as well as side products. Both solvents were degassed with argon for 1 h beforehand. After centrifugation, samples were dried in a vacuum oven at 80 °C and stored in an argon-filled glovebox.

**Testing of the photocatalytic activity:** The photocatalytic experiments were performed in an EvoluChem™ PhotoRedOx Box (HepatoChem, Beverly, USA) equipped with 2 × 20 ml sample holder, an EvoluChem 365PF lamp (365 nm) for testing the photocatalytic activity in the UV region and an EvoluChem 6200PF lamp (cold white) for the Vis region.

In a typical methylene blue (MB) degradation experiment, 15 mg of catalyst (1 mg/ml) were added to 15 mL of an aqueous MB solution (20 ppm). After stirring for 30 min in the dark, the suspensions were irradiated. After certain time intervals, 0.4 ml of suspension were periodically sampled and centrifuged to separate the photocatalyst from the solution. The MB solution was then diluted by a factor of 2 before the concentration of MB was measured by UV-Vis spectroscopy (PerkinElmer Inc., Shelton, USA).

**Characterization:** Powder X-ray diffraction (PXRD) patterns were recorded on a D8-A25-Advance diffractometer (Bruker AXS, Karlsruhe, Germany) under ambient conditions in Bragg-Brentano  $\theta$ - $\theta$  geometry (goniometer radius 280 mm) with Cu K $\alpha$ -radiation ( $\lambda$  = 154.0596 pm). A 12  $\mu$ m Ni foil served as a K $\beta$  filter at the primary beam side. At the primary beam side, a variable divergence slit was mounted and a LYNXEYE detector with 192 channels at the secondary beam side. Experiments were carried out in a  $2\theta$  range of 7 to 120 with a step size of 0.013° and a total scan time of 2 h. Rietveld refinements of the recorded diffraction patterns was

performed using TOPAS 5.0 (Bruker AXS, Karlsruhe, Germany) software.<sup>[61]</sup> Crystallographic structure and microstructure were refined, while instrumental line broadening was included in a fundamental parameters approach.<sup>[62]</sup> The mean crystallite size  $\langle L \rangle$  was calculated as the mean volume weighted column height derived from the integral breadth. Crystal structure data were obtained from the Pearson's Crystal database.<sup>[63]</sup>

Electron paramagnetic resonance (EPR) spectra were recorded using a Bruker Elexsys E580 X-band spectrometer with a Bruker ER 4118X-MD5 resonator. All shown EPR spectra were recorded at 10 K using a closed cycle cryostat (Cryogenic CF VTC).

For the acquisition of the Raman spectra, a Raman microscope LabRAM HR Evolution HORIBA Jobin Yvon A (Longmujeau, France) with a 633 nm He-Ne Laser (Melles Griot, IDEX Optics and Photonics, Albuquerque, USA) and an 1800 lines/mm grating was used.

UV-Vis diffuse reflectance spectra were recorded on a Perkin Elmer Lambda 750 spectrometer (PerkinElmer Inc., Shelton, USA) equipped with a 100 mm integration sphere from 290 to 1500 nm with a 2 nm increment and an integration time of 0.2 s. BaSO<sub>4</sub> was used as the white reference.

Thermogravimetric analyses (TGA) were performed on a TG F1 Iris (Netzsch Gerätebau GmbH, Selb, Germany). The samples were first heated from room temperature to 600 °C under nitrogen flow (40 mL min<sup>-1</sup>) followed by heating to 900 °C under synthetic air (40 mL min<sup>-1</sup>, N<sub>2</sub>/O<sub>2</sub> 4:1). The heating rate was set to 20 K min<sup>-1</sup>.

<sup>6</sup>Li single-pulse excitation magic angle spinning (SPE MAS) NMR spectra were recorded at 58.91 MHz on a Bruker AV400WB spectrometer (Bruker, Karlsruhe, Germany) at 298 K in standard ZrO<sub>2</sub> rotors with a diameter of 4 mm. A spinning rate of 13 kHz and a relaxation delay of 3 s were applied. Solid LiCl was used as an external reference with a chemical shift of 0 ppm. Spectra were recorded using the TopSpin software.<sup>[64]</sup> Fitting of the spectra was performed using the DMFit software program package.<sup>[65]</sup>

The elemental quantification was conducted via inductively coupled plasma mass spectrometry (ICP-MS) with a commercial ICP-MS system (8900 Triple Quad and SPS4 autosampler, Agilent, Santa Clara, USA). Stock solutions of single element ICP-MS standards of Li<sup>+</sup> (Merck Millipore, Darmstadt, Germany), Ti<sup>4+</sup> (VWR, Radnor, USA) and Sc<sup>3+</sup> (Merck Millipore, Darmstadt, Germany) were used. The detector dwell time was 100  $\mu$ s, the repetition was 3 times, and the measured isotopes were <sup>7</sup>Li in no-gas mode and <sup>47</sup>Ti using He as collision gas as well as <sup>45</sup>Sc (all used modes) as internal standard. For the ICP-MS measurements, the washed samples were dissolved in H<sub>2</sub>SO<sub>4</sub> (Fisher Chemical, Loughborough, United Kingdom,  $\geq 95\%$ ).

Elemental analysis was performed using a Vario Micro Cube CHN analyzer (Elementar, Langensfeld, Germany).

## Acknowledgements

We thank Dr. Kristina Brix for the ICP-MS, Dr. Petra Herbeck-Engel for Raman, Dr. Clemens Matt for EPR and Dr. Michael Zimmer for NMR measurements. Instrumentation and technical support for this work were provided by the Service Center NMR at UdS, with financial support from Saarland University and German Science Foundation DFG. Additionally, instrumentation and technical assistance were provided by the Service Center X-ray Diffraction, with financial support from Saarland University

and German Science Foundation (project number INST 256/349-1). Open Access funding enabled and organized by Projekt DEAL.

### Conflict of Interest

The authors declare no conflict of interests.

### Data Availability Statement

The data that support the findings of this study are available in the supplementary material of this article.

**Keywords:** black niobia · black titania · hydrides · mechanochemistry · solid-state reactions

- [1] X. Chen, L. Liu, F. Huang, *Chem. Soc. Rev.* **2015**, *44*, 1861–1885.
- [2] X. Chen, L. Liu, P. Y. Yu, S. S. Mao, *Science* **2011**, *331*, 746–750.
- [3] a) H. Cui, G. Zhu, Y. Xie, W. Zhao, C. Yang, T. Lin, H. Gu, F. Huang, *J. Mater. Chem. A* **2015**, *3*, 11830–11837; b) W. Zhao, W. Zhao, G. Zhu, T. Lin, F. Xu, F. Huang, *Dalton Trans.* **2016**, *45*, 3888–3894.
- [4] A. Sinhamahapatra, J.-P. Jeon, J. Kang, B. Han, J.-S. Yu, *Sci. Rep.* **2016**, *6*, 27218.
- [5] T. Matsukawa, T. Ishigaki, *Dalton Trans.* **2021**, *50*, 7590–7596.
- [6] A. Badreldin, M. D. Imam, Y. Wubulikasimu, K. Elsaid, A. E. Abusrafa, P. B. Balbuena, A. Abdel-Wahab, *J. Alloys Compd.* **2021**, *871*, 159615.
- [7] H.-S. Kim, J. B. Cook, H. Lin, J. S. Ko, S. H. Tolbert, V. Ozolins, B. Dunn, *Nat. Mater.* **2017**, *16*, 454–462.
- [8] a) H. Tan, Z. Zhao, M. Niu, C. Mao, D. Cao, D. Cheng, P. Feng, Z. Sun, *Nanoscale* **2014**, *6*, 10216–10223; b) L. Han, Z. Ma, Z. Luo, G. Liu, J. Ma, X. An, *RSC Adv.* **2016**, *6*, 6643–6650.
- [9] Z. Wang, C. Yang, T. Lin, H. Yin, P. Chen, D. Wan, F. Xu, F. Huang, J. Lin, X. Xie, M. Jiang, *Energy Environ. Sci.* **2013**, *6*, 3007–3014.
- [10] a) S.-T. Myung, M. Kikuchi, C. S. Yoon, H. Yashiro, S.-J. Kim, Y.-K. Sun, B. Scrosati, *Energy Environ. Sci.* **2013**, *6*, 2609–2614; b) B. Santara, P. K. Giri, K. Imakita, M. Fujii, *Nanoscale* **2013**, *5*, 5476–5488.
- [11] a) A. Sinhamahapatra, J.-P. Jeon, J.-S. Yu, *Energy Environ. Sci.* **2015**, *8*, 3539–3544; b) M. Ye, J. Jia, Z. Wu, C. Qian, R. Chen, P. G. O'Brien, W. Sun, Y. Dong, G. A. Ozin, *Adv. Energy Mater.* **2017**, *7*, 1601811.
- [12] W. Fang, M. Xing, J. Zhang, *Appl. Catal. B* **2014**, *160–161*, 240–246.
- [13] M. Zhang, Q. Pei, W. Chen, L. Liu, T. He, P. Chen, *RSC Adv.* **2017**, *7*, 4306–4311.
- [14] G. Ou, Y. Xu, B. Wen, R. Lin, B. Ge, Y. Tang, Y. Liang, C. Yang, K. Huang, D. Zu, R. Yu, W. Chen, J. Li, H. Wu, L.-M. Liu, Y. Li, *Nat. Commun.* **2018**, *9*, 1302.
- [15] X. Zhou, N. Liu, J. Schmidt, A. Kahnt, A. Osvet, S. Romeis, E. M. Zolnhofer, V. R. R. Marthala, D. M. Guld, W. Peukert, M. Hartmann, K. Meyer, P. Schmuki, *Adv. Mater.* **2017**, *29*, 1604747.
- [16] R. D. Shannon, *Acta Crystallogr. Sect. A* **1976**, *32*, 751–767.
- [17] C. E. Housecroft, A. G. Sharpe, *Inorganic Chemistry*, Pearson Education Limited, **2008**, p. 279.
- [18] J. Zhang, P. Zhou, J. Liu, J. Yu, *Phys. Chem. Chem. Phys.* **2014**, *16*, 20382–20386.
- [19] R. Ren, Z. Yang, L. L. Shaw, *J. Mater. Sci.* **2000**, *35*, 6015–6026.
- [20] A. Le Viet, R. Jose, M. V. Reddy, B. V. R. Chowdari, S. Ramakrishna, *J. Phys. Chem. C* **2010**, *114*, 21795–21800.
- [21] K. Su, H. Liu, Z. Gao, P. Fornasiero, F. Wang, *Adv. Sci.* **2021**, *8*, 2003156.
- [22] H. Guo, A. Jaworski, Z. Ma, A. Slabon, Z. Bacsik, R. Nedumkandathil, U. Häussermann, *RSC Adv.* **2020**, *10*, 35356–35365.
- [23] B. C. Hernden, J. A. Lussier, M. Bieringer, *Inorg. Chem.* **2015**, *54*, 4249–4256.
- [24] G. Greenwood, *Phil. Mag.* **1924**, *48*, 654–663.
- [25] W. J. H. Borghols, M. Wagemaker, U. Lafont, E. M. Kelder, F. M. Mulder, *Chem. Mater.* **2008**, *20*, 2949–2955.
- [26] D. W. Murphy, R. J. Cava, S. M. Zahurak, A. Santoro, *Solid State Ionics* **1983**, *9–10*, 413–417.
- [27] M. Vijayakumar, S. Kerisit, C. Wang, Z. Nie, K. M. Rosso, Z. Yang, G. Graff, J. Liu, J. Hu, *J. Phys. Chem. C* **2009**, *113*, 14567–14574.
- [28] R. J. Cava, D. W. Murphy, S. M. Zahurak, *J. Electrochem. Soc.* **1983**, *130*, 2345–2351.
- [29] C. Valencia-Balvin, S. Pérez-Walton, G. M. Dalpian, J. M. Osorio-Guillén, *Comput. Mater. Sci.* **2014**, *81*, 133–140.
- [30] M. Catti, M. R. Ghaani, *Phys. Chem. Chem. Phys.* **2014**, *16*, 1385–1392.
- [31] C. Dwivedi, T. Mohammad, V. Kumar, V. Dutta, *Vacuum* **2020**, *182*, 109612.
- [32] H. Schäfer, R. Gruhn, F. Schulte, *Angew. Chem. Int. Ed.* **1966**, *5*, 40–52; *Angew. Chem.* **1966**, *78*, 28–41.
- [33] a) M. V. Koudriachova, N. M. Harrison, S. W. de Leeuw, *Phys. Rev. B* **2002**, *65*, 235423; b) E. Baudrin, S. Cassaignon, M. Koelsch, J.-P. Jolivet, L. Dupont, J.-M. Tarascon, *Electrochem. Commun.* **2007**, *9*, 337–342.
- [34] H. Li, Y. Guo, J. Robertson, *J. Phys. Chem. C* **2015**, *119*, 18160–18166.
- [35] a) H.-D. Yang, Y.-Y. Kang, P.-P. Zhu, Q.-W. Chen, L. Yang, J.-P. Zhou, *J. Alloys Compd.* **2021**, *872*, 159759; b) D. R. Zhang, H. L. Liu, R. H. Jin, N. Z. Zhang, Y. X. Liu, Y. S. Kang, *J. Ind. Eng. Chem.* **2007**, *13*, 92–96.
- [36] J. Chaudhuri, M. L. Ram, B. K. Sarkar, *J. Mater. Sci.* **1994**, *29*, 3484–3488.
- [37] a) X. Chen, L. Liu, Z. Liu, M. A. Marcus, W.-C. Wang, N. A. Oyler, M. E. Grass, B. Mao, P.-A. Glans, P. Y. Yu, J. Guo, S. S. Mao, *Sci. Rep.* **2013**, *3*, 1510; b) Z. Wang, C. Yang, T. Lin, H. Yin, P. Chen, D. Wan, F. Xu, F. Huang, J. Lin, X. Xie, M. Jiang, *Adv. Funct. Mater.* **2013**, *23*, 5444–5450; c) Z. Zheng, B. Huang, J. Lu, Z. Wang, X. Qin, X. Zhang, Y. Dai, M.-H. Whangbo, *Chem. Commun.* **2012**, *48*, 5733–5735.
- [38] X. Liu, G. Zhu, X. Wang, X. Yuan, T. Lin, F. Huang, *Adv. Energy Mater.* **2016**, *6*, 1600452.
- [39] a) R. Nedumkandathil, A. Jaworski, J. Grins, D. Bernin, M. Karlsson, C. Eklöf-Österberg, A. Neagu, C.-W. Tai, A. J. Pell, U. Häussermann, *ACS Omega* **2018**, *3*, 11426–11438; b) Y. Kobayashi, Z. Li, K. Hirai, C. Tassel, F. Loyer, N. Ichikawa, N. Abe, T. Yamamoto, Y. Shimakawa, K. Yoshimura, M. Takano, O. J. Hernandez, H. Kageyama, *J. Solid State Chem.* **2013**, *207*, 190–193.
- [40] B. Oberhausen, G. Kickelbick, *Nanoscale Adv.* **2021**, *3*, 5589–5604.
- [41] S. Zhang, G. Liu, W. Qiao, J. Wang, L. Ling, *J. Colloid Interface Sci.* **2020**, *562*, 193–203.
- [42] A. Deschanvres, B. Raveau, Z. Sekkal, *Mater. Res. Bull.* **1971**, *6*, 699–704.
- [43] B. M. Gatehouse, P. Leverett, *Acta Crystallogr. Sect. C* **1972**, *1*, 83–86.
- [44] a) S. Britto, M. Leskes, X. Hua, C.-A. Hébert, H. S. Shin, S. Clarke, O. Borkiewicz, K. W. Chapman, R. Seshadri, J. Cho, C. P. Grey, *J. Am. Chem. Soc.* **2015**, *137*, 8499–8508; b) M. Wagemaker, R. van de Krol, A. P. M. Kentgens, A. A. van Well, F. M. Mulder, *J. Am. Chem. Soc.* **2001**, *123*, 11454–11461; c) K. Hoshina, Y. Harada, H. Inagaki, N. Takami, *J. Electrochem. Soc.* **2014**, *161*, A348–A354; d) M. Vijayakumar, S. Kerisit, K. M. Rosso, S. D. Burton, J. A. Sears, Z. Yang, G. L. Graff, J. Liu, J. Hu, *J. Power Sources* **2011**, *196*, 2211–2220; e) D. Becker, R. Haberkorn, G. Kickelbick, *Inorganics* **2018**, *6*, 117.
- [45] C. Pan, Y. J. Lee, B. Ammundsen, C. P. Grey, *Chem. Mater.* **2002**, *14*, 2289–2299.
- [46] a) R. Pöttgen, T. Dinges, H. Eckert, P. Sreeraj, H.-D. Wiemhöfer, *Z. Phys. Chem.* **2010**, *224*, 1475–1504; b) T. Dinges, R.-D. Hoffmann, L. van Wüllen, P. Henry, H. Eckert, R. Pöttgen, *J. Solid State Electrochem.* **2011**, *15*, 237–243.
- [47] P. F. Chester, *J. Appl. Phys.* **1961**, *32*, 866–868.
- [48] Y. Su, J. Lang, L. Li, K. Guan, C. Du, L. Peng, D. Han, X. Wang, *J. Am. Chem. Soc.* **2013**, *135*, 11433–11436.
- [49] S. P. S. Porto, P. A. Fleury, T. C. Damen, *Phys. Rev.* **1967**, *154*, 522–526.
- [50] A. A. McConnell, J. S. Aderson, C. N. R. Rao, *Spectrochim. Acta Part A* **1976**, *32*, 1067–1076.
- [51] V. V. Strelchuk, S. I. Budzulyak, I. M. Budzulyak, R. V. Illytsyy, V. O. Kotsyubynskyy, M. Y. Segin, L. S. Yablou, *Semicond. Phys. Quantum Electron. Optoelectron.* **2010**, *13*, 309–313.
- [52] S. K. Gautam, F. Singh, I. Sulania, R. G. Singh, P. K. Kulriya, E. Pippel, *J. Appl. Phys.* **2014**, *115*, 143504.
- [53] S. Landi Jr., I. R. Segundo, E. Freitas, M. Vasilevskiy, J. Carneiro, C. J. Tavares, *Solid State Commun.* **2022**, *341*, 114573.
- [54] a) Y. Jia, M. Zhong, F. Yang, C. Liang, H. Ren, B. Hu, Q. Liu, H. Zhao, Y. Zhang, Y. Zhao, *J. Phys. Chem. C* **2020**, *124*, 15066–15075; b) S. Sathasivam, B. A. D. Williamson, S. A. Althabaiti, A. Y. Obaid, S. N. Basahel, M. Mokhtar, D. O. Scanlon, C. J. Carmalt, I. P. Parkin, *ACS Appl. Mater. Interfaces* **2017**, *9*, 18031–18038; c) I. Erdem, H. H. Kart, *Mater. Sci. Semicond. Process.* **2014**, *28*, 59–65; d) M. Landmann, E. Rauls, W. G. Schmidt, *J. Phys. Condens. Matter.* **2012**, *24*, 195503.
- [55] P. O. Oladoye, T. O. Ajiboye, E. O. Omotola, O. J. Oyewola, *Results Eng.* **2022**, *16*, 100678.

- [56] A. P. Amrute, J. De Bellis, M. Felderhoff, F. Schüth, *Chem. Eur. J.* **2021**, *27*, 6819–6847.
- [57] K. Saitow, T. Wakamiya, *Appl. Phys. Lett.* **2013**, *103*, 031916.
- [58] W. Ashraf, A. Khan, S. Bansal, M. Khanuja, *Physica E Low Dimens. Syst. Nanostruct.* **2022**, *140*, 115152.
- [59] a) M. Ye, J. Pan, Z. Guo, X. Liu, Y. Chen, *Nanotechnol. Rev.* **2020**, *9*, 558–567; b) J. Zhou, M. Zhang, Y. Zhu, *Phys. Chem. Chem. Phys.* **2015**, *17*, 3647–3652.
- [60] M. K. Kim, W. H. Sim, M. Choi, H. Lim, Y. Kwon, H. M. Jeong, *Catal. Today* **2021**, *359*, 23–27.
- [61] Bruker AXS, *Topas 5*, Karlsruhe, Germany, **2014**.
- [62] R. W. Cheary, A. A. Coelho, J. P. Cline, *J. Res. Natl. Inst. Stand. Technol.* **2004**, *109*, 1–25.
- [63] P. Villars, K. Cenzual, Pearson's Crystal Data: Crystal Structure Database for Inorganic Compounds (on DVD), Release 2022/23, ASM International®, Materials Park, Ohio, USA
- [64] Bruker Corp., *Topspin 2.1*, Karlsruhe, Germany, **2008**.
- [65] D. Massiot, F. Fayon, M. Capron, I. King, S. Le Calvé, B. Alonso, J.-O. Durand, B. Bujoli, Z. Gan, G. Hoatson, *Magn. Reson. Chem.* **2002**, *40*, 70–76.

---

Manuscript received: January 23, 2023

Accepted manuscript online: February 10, 2023

Version of record online: ■■■

**3.1.1.3 Atomic Hydrogen ENDOR Manuscript**

This subsection embodies an unpublished manuscript about the investigation of the dipolar interaction between a 1s electron in atomic hydrogen ( $^1\text{H}$ ) with distant nuclei. Here, the possible qubit candidate  $^1\text{H}@\text{POSS}$  is investigated. It could be shown that changing the environment of that system to deuterated environment, the phase memory time could be prolonged, hence the qubit performance enhanced. The origin of that enhancement was investigated by temperature dependent ENDOR measurements.

PCCP

ARTICLE TYPE

Cite this: DOI: 00.0000/xxxxxxxxx

## Exploring the dipolar interaction of the 1s electron in atomic hydrogen with distant nuclei<sup>†</sup>

Haakon Tassilo Adam Wiedemann,<sup>\*a</sup> Maxim Neuberger,<sup>a</sup> Jonas Nicolas Bach,<sup>a</sup> Daniel Schroeder,<sup>a</sup> Eva Steuer,<sup>a</sup> Ruwen Schank,<sup>a</sup> George Mitrikas,<sup>b</sup> and Christopher William Michael Kay<sup>a,c</sup>Received Date  
Accepted Date

DOI: 00.0000/xxxxxxxxx

Pulsed electron paramagnetic resonance (EPR) spectroscopy, in which the microwave (MW) irradiation is applied in the form of short pulses, comprises many advanced methods for the measurement of dynamic effects and the determination of weak hyperfine interactions between the unpaired electron and distant magnetic nuclei. These methods are typically applied for the measurement of the electron spin coherence time of molecular magnets or encaged paramagnetic atoms, and their evaluation as potential quantum bits (qubits) in the field of spin-based quantum computing. In addition, electron nuclear double resonance spectroscopy (ENDOR) can provide information on the local environment of the paramagnetic centre and is thus well suited for structural studies in systems lacking long-range order on length scales that are not easily accessible by other techniques. Here we describe encaged atomic hydrogen as a promising potential qubit system implemented in two matrix systems (protiated and deuterated tetrahydrofuran/toluene (5:1) solvent mixture). We found a phase memory time,  $T_M$ , enhancement in one of our systems and could postulate structural evidence by temperature dependent ENDOR measurements. Our results demonstrate how small changes inside the environment of a potential qubit system can enhance  $T_M$ .

### 1 Introduction

Quantum computers have already been introduced in the late years of the 20th century and may speed up solutions to particular mathematical problems but struggle to yield computational advantage for practical tasks<sup>1</sup>. The development of superior quantum computers arose interest in recent years since IBM introduced the first commercially available quantum computer in 2019<sup>2</sup>. The performance of quantum computers depend highly on the properties of its quantum bits (qubits)<sup>3</sup>. In this context, the phase memory time,  $T_M$ , is a figure of merit for the stability of a qubit which should be as long as possible<sup>3</sup>. Atomic hydrogen (<sup>1</sup>H) encaged in polyhedral oligosilsesquioxanes (POSS) has been studied as a promising candidate for quantum computing devices for many years since its first identification in 1994<sup>4</sup> with phase memory times up to 13.9  $\mu$ s reported by Mitrikas et al. in

2021<sup>5–7</sup>. To enhance the  $T_M$  of this potential qubit candidate, several approaches have been developed. One of these approaches includes derivatives of <sup>1</sup>H@POSS such as replacing the centre hydrogen with deuterium which already enhances the  $T_M$  up to 60.8  $\mu$ s or exchanging the trimethyl groups of the silsesquioxane cage corners with deuterated trimethyl groups which enhances  $T_M$  to 35.1  $\mu$ s<sup>7</sup> or by dynamical decoupling with the Carr-Purcell-Meiboom-Gill (CPMG) sequence<sup>8</sup>.

Electron paramagnetic resonance (EPR) spectroscopy is an important analytical tool in this manner. The encaged hydrogen atom as the simplest paramagnetic atom with a 1s electron and a spin of  $S = 1/2$  coupled to the proton nuclear spin of  $I = 1/2$  exhibits a very large hyperfine coupling constant of 1420.41 MHz<sup>7</sup>. Continuous wave (CW) and pulse EPR spectroscopy can be applied to study the spin coherence time and structural properties of this potential qubit system. As previously mentioned, changing the environment around the electron spin as natural quantum object can enhance the phase memory time<sup>7</sup>.

Here, we exploit the qubit performance and dipolar interaction of the 1s electron upon examining the <sup>1</sup>H@POSS construct in different environments. Our approach included the identification whether the phase memory time can be prolonged upon diluting the pristine powder of <sup>1</sup>H@POSS in a tetrahydrofuran (THF) / toluene (5:1) mixture and the deuterated solvent mixture. The

<sup>a</sup> Department of Chemistry, Saarland University, Saarbruecken, 66123, Saarland, Germany. Tel: +49 681 3022741; E-mail: haakon.wiedemann@uni-saarland.de

<sup>b</sup> Institute of Materials Science, NCSR Demokritos, Athens, Aghia Paraskevi Attikis 15310, Greece.

<sup>c</sup> London Centre of Nanotechnology, University College London, London, WC1H 0AH, United Kingdom.

<sup>†</sup> Electronic Supplementary Information (ESI) available: [details of any supplementary information available should be included here]. See DOI: 10.1039/cXCP00000x/

solvents were chosen in respect to the solubility of  $^1\text{H}@POSS$  in THF and toluene as a supporting chemical to help in the crystallization process. Furthermore, we applied the electron nuclear double resonance (ENDOR) method to shed light on the temperature dependence and the distance derivation of the dipolar interaction in the structure of the three tested systems (pristine powder, diluted in THF/toluene (5:1) and diluted in deuterated THF/toluene (5:1))<sup>9</sup>.

## 2 Experimental

### 2.1 Sample preparation

Octakis (dimethylsilyloxy) silsesquioxane ( $\text{Si}_8\text{O}_{12}(\text{OSiMe}_2\text{H})_8$ , CAS 125756-69-6), THF ( $\text{C}_4\text{OH}_8$ , CAS 109-99-9), toluene ( $\text{C}_7\text{H}_8$ , CAS 108-88-3),  $\text{d}_8$ -THF ( $\text{C}_4\text{OD}_8$ , CAS 1693-74-9) and  $\text{d}_8$ -toluene ( $\text{C}_7\text{D}_8$ , CAS 2037-26-5) were purchased from Sigma-Aldrich and used without further purification. Atomic hydrogen encapsulation was performed with  $\gamma$ -irradiation using a cave-type  $^{60}\text{Co}$  source at a dose rate of  $5.5 \text{ Gy min}^{-1}$ . 200 mg of POSS powder mixed with 36 mg of iodine  $\text{I}_{2(s)}$  (acting as a radical scavenger<sup>10</sup>) were placed in a vial and irradiated for 13.8 days resulting in a total dose of 109.4 kGy. After  $\gamma$ -irradiation the powder was purified by the precipitation method using methanol to remove iodine. The process was repeated several times until a clear methanol solution was observed. The recovered H@POSS-containing powder was dried under reduced pressure (101 mbar) for 1 h and was transferred into an EPR quartz tube.

### 2.2 Pulsed EPR spectroscopy

EPR measurements at Q-band were carried out on a Bruker ELEXSYS E580E SuperQ FT Pulse-EPR spectrometer equipped with a Bruker EN 5107D2 Q-band ENDOR resonator. Low temperature measurements were performed with a closed-cycle helium cryostat from Cryogenic (at temperatures between 10 and 300 K). The temperature was stabilized with an Oxford ITC4 temperature controller within 0.1 K. The relaxation measurements were performed at the low-field EPR transition. The shot repetition rate was properly adjusted in every measurement in order to avoid saturation.

Echo-detected field sweep (EDFS) detected EPR spectra were measured by varying the magnetic field while applying the two-pulse Hahn-Echo sequence  $\pi/2 - \tau - \pi - \tau - \text{echo}$  with  $\pi/2 = 16 \text{ ns}$  and  $\pi = 32 \text{ ns}$  gaussian pulses.

The electron spin-lattice relaxation times  $T_1$  were measured by inversion recovery with the pulse sequence  $\pi - \tau - \pi/2 - t - \pi - t - \text{echo}$ . The lengths of the MW  $\pi/2$  and  $\pi$  gaussian pulses were 16 and 32 ns, respectively, and the interpulse delay  $t = 1000 \text{ ns}$ . For each trace, 50 data points were collected with an appropriate time increment  $\tau$  to ensure complete magnetization recovery.

The phase memory times  $T_M$  were measured by the delayed two-pulse Hahn-Echo sequence  $\pi/2 - \tau - \pi - \tau - \text{echo}$  with  $\pi/2 = 16 \text{ ns}$  and  $\pi = 32 \text{ ns}$  gaussian pulses and  $\tau$  varying.

Electron-nuclear double resonance spectroscopy (ENDOR) experiments were performed with the Mims-ENDOR pulse sequence  $\pi/2 - \tau - \pi/2 - \tau - \pi(RF) - \tau - \pi/2 - \tau - \text{echo}$ ; ( $\pi/2 = 12 \text{ ns}$ , ( $\pi = 24 \text{ ns}$ ,  $\tau = 4 \mu\text{s}$ ,  $t_1 = 48 \text{ ns}$ ,  $t_2 = 96 \text{ ns}$  with

$\pi/2 = 16 \text{ ns}$  gaussian pulses,  $\pi(RF) = 8000 \text{ ns}$  radio frequency (RF) pulse,  $\tau = 500 \text{ ns}$  and 48 - 52 MHz RF range<sup>11</sup>. The ENDOR spectra were 3000 times averaged and each trace 8 MHz RF span was covered with 801 points around the Larmor frequency of the  $^1\text{H}$  nucleus in Q-band.

### 2.3 Data manipulation

The data were processed with the program MATLAB 9.10 (The MathWorks, Natick, MA).  $T_1$  relaxation times were determined by fitting the time traces with single exponential functions, whereas for obtaining  $T_M$  a stretched exponential function was appropriate.

The CW- and edfs-detected field-swept EPR spectra were plotted and simulated with the EasySpin package<sup>12</sup>.

## 3 Results and discussion

### 3.1 Pulsed EPR spectroscopy

#### 3.1.1 Echo-detected field sweep and FID detected EPR spectrum

Fig. 1 shows a schematic representation of the atomic structure of the  $^1\text{H}@POSS$  powder. The first descriptive measurements of the presented samples were echo-detected field sweep (edfs) measurements on the pristine powder. The Q-band echo-detected field sweeps (EDFS) are illustrated in the supporting information. All EDFS spectra show a hyperfine coupling of 50.6 mT corresponding to 1418 MHz as already described in the literature for X-band frequencies<sup>6</sup>. The FID detected EPR spectra show similar results although they differ slightly from the hyperfine coupling derived in X-band frequencies (see supporting information).

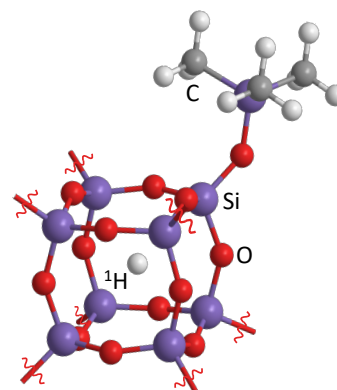


Fig. 1 Schematic representation of the structure of one  $^1\text{H}@POSS$  cage. Here, atomic hydrogen with the 1s electron (white sphere) is centered inside the POSS cage. The POSS cage contains eight silicon corners (purple spheres) bridged by eight oxygen atoms (red spheres). Attached to each silicon corner is a Trimethyl-silyl (TMS) group connected by one oxygen (red sphere) and three methyl groups with carbon atoms shown as grey spheres. The scheme shows only one corner attachment, the other seven are omitted for simplicity.

The EDFS spectra acquired in Q-band show only absorptive features with a splitting visible between the electron and the proton.

The coupling of the electron with  $^{29}\text{Si}$  ( $I = 1/2$ ) nuclei in the silsesquioxane cage corners is rather small ( $A_{29\text{Si}} = -1.76$  MHz) and lies within the linewidth of the resonance line for the coupling of the electron with the proton as already described by Mitrikas et al.<sup>13</sup>. The simulated EPR parameters by simulation with easypin are given in the supporting information (SI).

Taken together, these first validations of paramagnetic atomic hydrogen led to the question whether it is possible to alternate the spin relaxation behaviour and hence, the potential qubit performance, by substituting the intermolecular relaxation environment of the pristine powder with a solvent and deuterated solvent. The next chapter will discuss the relaxation times of these three configurations around the atomic hydrogen system before going more into detail towards the structural investigation of dipolar distances through ENDOR spectroscopy.

### 3.1.2 Spin-lattice relaxation time $T_1$ and phase memory time $T_M$

The spin lattice relaxation time,  $T_1$ , was measured for all three environments at different temperatures. All  $T_1$  measurement series show a single exponential character of the echo recovery (see SI). The temperature dependence between the three investigated environments show small differences. The two lowest temperatures of 10 K and 20 K could not be acquired since the spectrometer memory time was insufficient to measure  $T_1$  of the powder sample and the deuterated sample even though an external trigger waveform generator was used. Since qubit operation at these temperatures is not feasible, further investigations were not pursued. At higher temperatures over 100 K, only the  $T_2$  relaxation times of the powder sample could be identified due to the fact that the dissolved samples undergo the phase transition from frozen solution, quasi solid state, to solution state above 100 K where no spin echo could be detected.

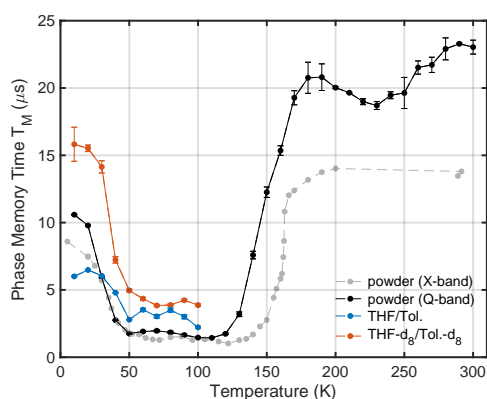


Fig. 2 Temperature dependence of the phase memory time  $T_M$  for  $^1\text{H}$  encaged in POSS cages as powder in Q-band (black), dissolved in protiated THF/toluene (5:1) (blue) and dissolved in deuterated THF/toluene (5:1) (orange) over the temperature range of 10 - 300 K.

The temperature dependent  $T_M$  values for the powder sample displayed as black in Fig. 2 are in good agreement with previ-

ously published results of X-band frequencies by Mitrikas et al. in 2021 (displayed as grey in Fig. 2)<sup>7</sup>. We see a first  $T_M$  decrease upon heating up from cryogenic temperatures to 120 K similar as already measured in X-band frequencies<sup>7</sup>. Afterwards, the  $T_M$  increases, as already described by Mitrikas et al. due to a dynamic process of the methyl group rotation which contributes to the electron spin dephasing<sup>7</sup>.

When the powder is dissolved in a THF/toluene (5:1) mixture, no  $T_M$  enhancement is visible (displayed as blue in Fig. 2). At lower temperature ( $< 30$  K) even a decrease in  $T_M$  is observed. At higher temperature (30 – 100 K) the  $T_M$  curve shows a similar dependence with slightly higher  $T_M$  values visible compared to the powder species.

We compared these results with dissolving the powder in a deuterated THF/toluene (5:1) mixture (displayed as orange in Fig. 2). There we observe a  $T_M$  enhancement over the whole temperature range (10 – 100 K). At 10 K we report the highest  $T_M$  value of 15.82  $\mu\text{s}$ . This could be a first indication of an optimisation step towards longer phase memory times for  $^1\text{H}@POSS$  as a potential quantum bit, as already suggested by Mitrikas et al. by changing the isotopes in the cage structure to deuterium<sup>7</sup>.

To further investigate these three systems and the  $T_M$  improvement, we performed ENDOR measurements to gain further insight into the structural arrangement and the interaction with the distant methylene protons of the TMS groups of these three species.

### 3.2 ENDOR investigation

Weiden et al. already presented temperature dependent W-band (95 GHz) ENDOR measurements in 2001 but only at four different temperatures<sup>14</sup>. Therefore, their temperature study is poorly informative and would have required more data points to make valid assumptions about structural properties. In order to gain more insight into the structural properties of our three presented systems, a standard Mims ENDOR pulse sequence was applied.

To understand the relaxation behaviour of a single  $^1\text{H}@POSS$  cage with temperature, we applied the Mims ENDOR pulse sequence on the dissolved powder. Fig.3 illustrates the integral-normalized and temperature dependent ENDOR spectra of the protiated and deuterated THF/toluene (5:1) dissolved powder systems. Fig.3 shows the temperature dependent ENDOR spectra of  $^1\text{H}$  powder dissolved in protiated (blue) and deuterated (orange) solvents. Here, a general broad line is observed for the protiated solutions over the whole temperature range of 40 – 100 K. On the other hand, the deuterated solutions show a different pattern. There, the whole temperature range (40 to 100 K) shows a small splitting similar to the pristine powder of 0.29 MHz together with a small shoulder peak and a larger hyperfine splitting with higher temperature up to 0.62 MHz at 100 K. The grey background of Fig.3 displays the subtraction of the protiated solvent ENDOR spectrum in respect to the deuterated ENDOR spectrum to extract the solvent contribution of solvent hydrogen atoms. The comparison of the integration reveals an overall solvent contribution of 55 to 60 % for all temperatures. This finding already reveals a major contribution of solvent hydrogen atoms regarding the relaxation behaviour and dipolar interaction of the 1s electron

of the paramagnetic hydrogen in the centre of the POSS cage. This further bolsters the overall lower  $T_2$  relaxation times of the protonated  $^1\text{H}@POSS$  cages.

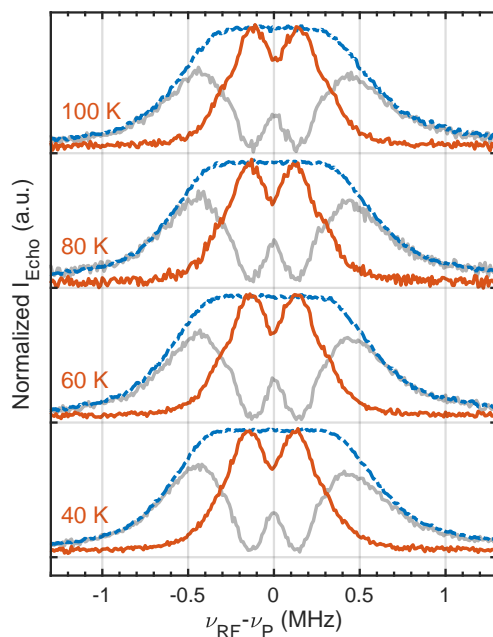


Fig. 3 ENDOR spectra in the temperature range of 40–100 K measured for  $^1\text{H}$  encaged in POSS cages dissolved in protiated (blue) and deuterated (orange) THF/toluene (5:1). The grey background illustrates the subtraction of the protiated solvent ENDOR spectrum in respect to the deuterated ENDOR spectrum to extract the solvent contribution of solvent hydrogen atoms (overall solvent contribution of 55 to 60 %). The ENDOR spectra are centered around the Larmor frequency of  $^1\text{H}$  in Q-band frequency space.

We applied a Mims ENDOR pulse sequence already mentioned above on our pristine powder (see Fig. 4). Upon the first glance there are three temperature regimes visible. At the lowest temperature (40 K) there is a small splitting of 0.28 MHz observed with a low SNR for all acquired ENDOR measurements. This splitting is similar to the measured splitting in deuterated solvents. The following temperature range of 60–100 K reveals a broad signal around the  $^1\text{H}$  Larmor frequency where no splittings can be extracted. In the highest temperature range of 120–240 K small shoulders get visible in the signal similar to bayerite powders investigated by Derouane et al.<sup>15</sup> We attribute this spectral change of the visible splitting to a broad signal towards more tumbling of the corner methyl groups in the silsesquioxane cage structure at higher temperature. The shoulder peaks could also arise from a movement of the central  $^1\text{H}$  towards the edges of the cage which results in a dipolar coupling of the 1s electron with the rotating methyl protons. But this movement can be neglected due to a radial distribution of the Bohr radius of the 1s electron of 0.529 Å<sup>16</sup>. Meanwhile at lower temperature, the cages can

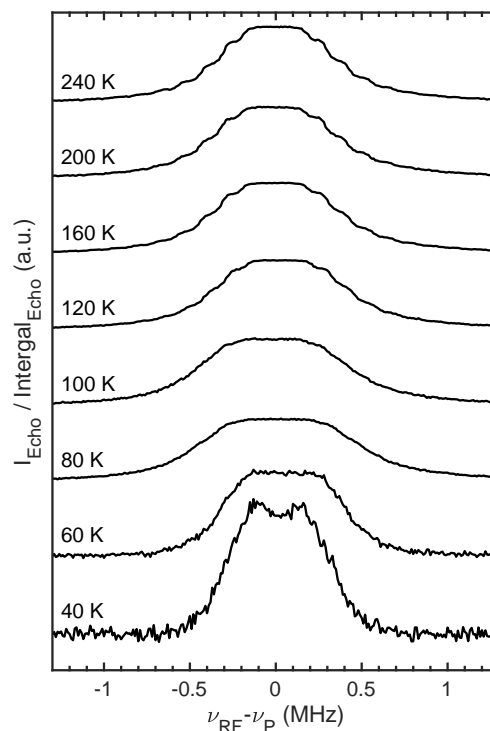
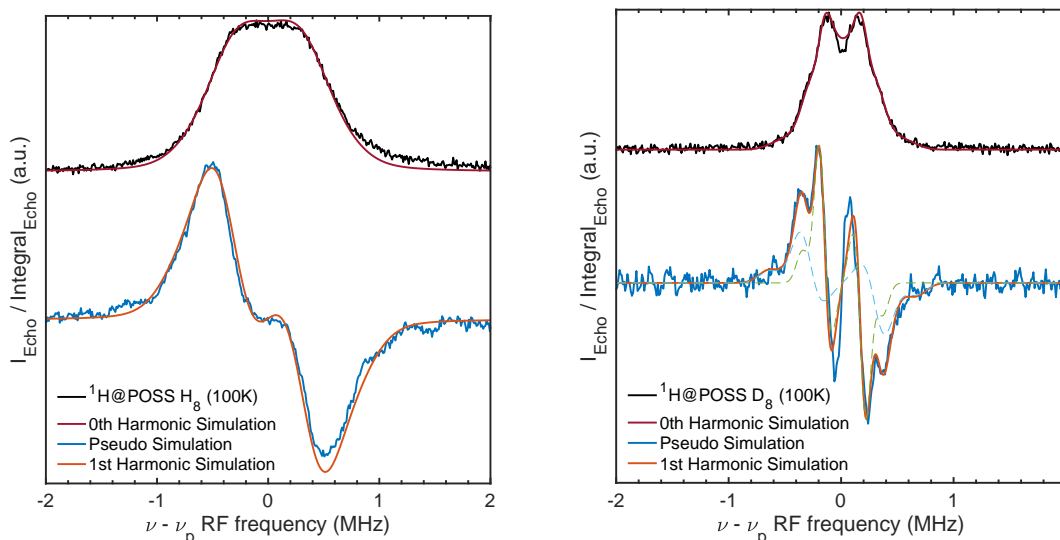


Fig. 4 Integral-normalised ENDOR spectra in the temperature range of 10–240 K measured for  $^1\text{H}$  encaged in POSS cages powder. Here, three temperature regimes are visible. At the lowest temperature (40 K) there is a small splitting of 0.28 MHz observed with a low SNR similar to the measured splitting in deuterated solvents. The following temperature range of 60–100 K reveals a broad signal where no splittings can be extracted. In the highest temperature range of 120–240 K small shoulders get visible possibly arising from a dipolar coupling of the 1s electron with rotating methyl-protons. The ENDOR spectra are centered around the Larmor frequency of  $^1\text{H}$  in Q-band frequency space.

assemble a higher ordered structure and hence reveal a lower FWHM with the observation of the previously mentioned small splitting of the averaged methyl group protons. Brustolon et al. reported a similar behaviour on nitroxide radicals<sup>17</sup>.

To exclude sensitivity problems of our spin system which could be not in equilibrium state before each data acquisition, we applied ENDOR measurements with an additional  $\pi(RF)$  pulse after the original Mims ENDOR sequence which helped in the investigation of  $N@C_{60}$  qubit system to equilibrate by Tyryshkin et al.<sup>18</sup>. Unfortunately, the additional  $\pi(RF)$  pulse in our ENDOR measurements did not resolve the splittings better in our broad signal as postulated.

The ENDOR spectra were then simulated using a pseudo-simulation approach (see Fig. 5). Here, the first derivative of the experimental spectrum is obtained in order to be able to simulate the ENDOR spectrum and to visualize the shoulder peaks already mentioned in Fig. 3. Fig. 5a and 5b show the pseudo-simulated



(a) Experimental (black, top) and simulated (red, top) 100 K ENDOR spectrum of  $^1\text{H}$  encaged in POSS cages dissolved in protiated solvents. The pseudo-simulation of the ENDOR spectrum is displayed below (blue) and the respective simulation (orange).

(b) Experimental (black, top) and simulated (red, top) 100 K ENDOR spectrum of  $^1\text{H}$  encaged in POSS cages dissolved in deuterated THF/toluene (5:1). The pseudo-simulation of the ENDOR spectrum is displayed below (blue) and the respective simulation (orange).

Fig. 5 Experimental (black, top) and simulated (red, top) 100 K ENDOR spectrum of  $^1\text{H}$  encaged in POSS cages dissolved in protiated (left) and deuterated THF/toluene (5:1) (right). The pseudo-simulation of the ENDOR spectra are displayed below (blue) and their respective simulations (orange). The simulation of the deuterated solution also shows both coupling parameters as separate, dashed lines. The ENDOR spectra are centered around the Larmor frequency of  $^1\text{H}$  in Q-band frequency space.

ENDOR spectra for the  $^1\text{H}@POSS$  system dissolved in protiated and deuterated solvents at 100 K. Here, we see a broad signal with one broad coupling derived for the protiated solvated powder with a value of  $A_{iso} = 0.77$  MHz, respectively. In comparison to that, the pseudo-simulated ENDOR spectra for the  $^1\text{H}@POSS$  system dissolved in deuterated solvent at 100 K shows a shoulder peak with couplings of  $A = 0.65$  MHz (37 % contribution) and 0.36 MHz (73 % contribution). The contributions to the sum of the simulation reveals that at 100 K, the dipolar coupling of the 1s electron with methyle group protons can be distributed to two sets of protons. The first group being the hydrogen atoms of methyle groups pointing inwards towards the POSS cage (higher dipolar coupling constant) with a contribution of 37 %, hence eight methyle groups. The other set of protons consists of hydrogen atoms in methyle groups pointing outwards the POSS cage (lower dipolar coupling constant) with a contribution of 73 %, extrapolating to 16 methyle groups. This result postulates a plausible structural description for the dipolar interaction of the 1s electron in the centre with distant nuclei in a single POSS cage at lower temperature.

In order to evaluate the dipolar interaction with distant nuclei at higher temperature, the simulation of the ENDOR spectrum of the pristine powder at 240 K was investigated (see Fig. 6). Here, similarly the pseudo simulated approach was chosen to elucidate the visible shoulder peaks of Fig. 4. The simulation reveals eight

couplings ranging from 0.32 to 2.37 MHz (values given in the SI). The first two dipolar couplings of 0.32 and 0.56 MHz are close to the values obtained for the dipolar couplings of the single cage in deuterated solvents. But that does not explain the higher dipolar coupling values. Since the ENDOR spectrum measured at 240 K was in the pristine powder, intermolecular couplings can occur between methyle groups of other cages pointing towards the face of the cage of the investigated 1s electron. A deeper look into the crystal structure of POSS cages allowed the obtainment of distances of the methyle protons with a hydrogen atom positioned in the centre and one layer surrounding the investigated cage. Fig. 7 illustrates the distances obtained from the crystal structure for the 1944 (27x72) single hydrogen atoms to the centre hydrogen atom (blue points in Fig. 7). The distances obtained from the ENDOR dipolar couplings at 240 K are displayed as green points. Furthermore, in order to visualize the distance dependance of rotating methyle group hydrogens, the averaged distance of three methyle group protons is shown as red points. On the first glance, higher distances are derived from the crystal structure in respect to the distances derived from the ENDOR dipolar couplings. Between 0.4 and 0.5 nm, eight protons have a lower distance to the centre than the 72 intramolecular hydrogen atoms. Upon a deeper investigation of the crystal structure, these eight protons are derived from two methyle groups from neighboring cages pointing towards the face of the centre POSS cage. The other two protons

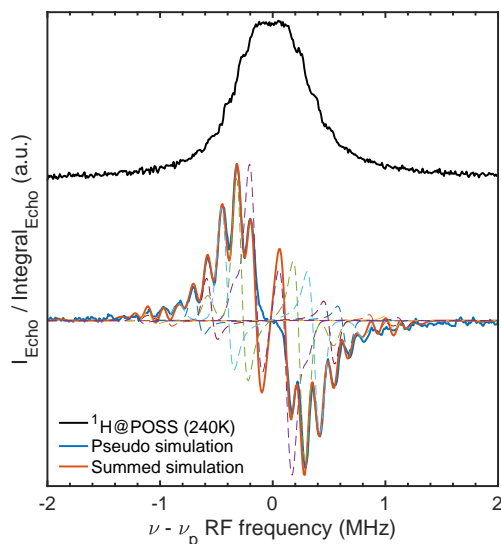


Fig. 6 ENDOR spectrum (black, top) of  $^1\text{H}$  encaged in POSS cages powder at 240 K. The pseudo-simulation of the ENDOR spectrum is displayed below (blue) and the respective simulation (orange). The ENDOR spectrum is centered around the Larmor frequency of  $^1\text{H}$  in Q-band frequency space.

are derived from two single protons from other cages also pointing towards the face of the central cage. This is consistent since the  $1s$  electron has a distribution around the nucleus in the centre and allows for higher couplings towards the distant nuclei in the methyle groups around the corners of the cage. The distances derived from single hydrogen atoms reveal that there is no real dependance visible, since almost every distance from 0.52 to 0.79 nm is covered, resulting in an almost straight line visible in Fig. 7) (orange points). The derivation of distances from averaged methyle groups show a different behaviour. There, it is possible to divide the distances into eight distinct groups. This bolsters our assumption of the contribution of eight dipolar couplings to the experimental ENDOR spectrum. Even though the distances derived from the ENDOR dipolar couplings show smaller values which could be contributed to a distribution of the  $1s$  electron wave function across the centre cage structure, it reveals that mostly eight different groups of protons couple to the  $1s$  electron. Further insight into the crystal structure revealed that these couplings could arise from rotating methyle group protons at the higher temperature of 240 K.

In addition, to compare the different line shapes of the ENDOR spectra for the three systems, Fig. 8 compares the ENDOR spectra obtained at the temperature of 100 K. Both the ENDOR spectra for the powder and for the dissolved powder in protiated THF/toluene show a broad signal at 100 K where no splitting can be extracted. Interestingly, the  $T_M$  is higher for the protiated powder in solution compared to the pristine powder. This should result in a smaller line broadening. But the ENDOR comparison

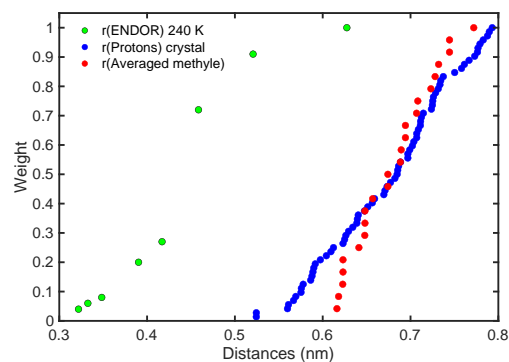


Fig. 7 Comparison of distances obtained from the crystal structure for the 72 single hydrogen atoms (blue points) to the centre hydrogen atom and distances obtained from the ENDOR dipolar couplings at 240 K (green points). The distance dependence of rotating methyle group hydrogens, the averaged distance of three methyle group protons reveals eight groups of distances (red points).

with the powder reveals a wider line broadening. We attribute this to hyperfine couplings of a single  $^1\text{H}$ @POSS cage with protons in the solvent molecules (THF/toluene) which are in near proximity of the surface of the cage structure.

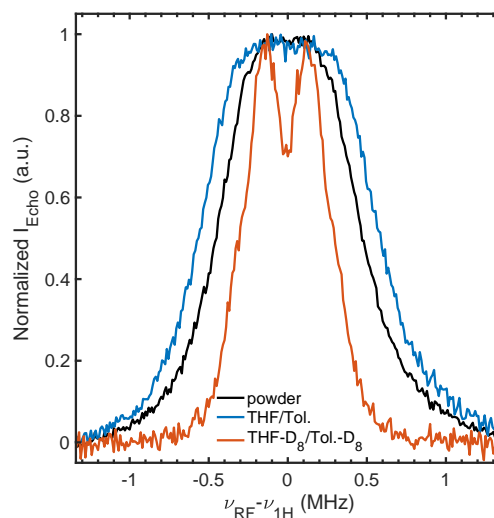


Fig. 8 Comparison of the acquired ENDOR spectra for the pristine powder (black), protiated THF/toluene (5:1) solution (blue) and deuterated THF/toluene (5:1) solution (orange) at a temperature of 100 K.

Comparing this broad signal of the pristine powder and the solution in protiated THF/toluene with respect to the deuterated solvents we see a clear improvement in the lineshape of the ENDOR spectrum where the splitting can be easily extracted with a lower FWHM. We attribute this improvement to less matrix effects with the solvent and less dipolar interactions with distant

nuclei of other cages as proposed for the pristine powder.

#### 4 Conclusion

The three investigated qubit systems described in this paper have been characterized in terms of their potential qubit performance and dipolar interaction of the 1s electron with distant nuclei using several pulsed EPR spectroscopy techniques.

In the beginning, measurements on the phase memory time  $T_M$  were used to study the spin coherence relaxation time behaviour. The postulated  $T_M$  enhancement for the potential qubit system with deuterated environment around the central  $^1H@POSS$  cage could be experimentally verified, thus supporting the future optimization paths towards deuteration of the environment around the 1s electron spin qubit.

The structure was probed by ENDOR spectroscopy to observe the structural transitions with temperature dependence and to investigate the dipolar interaction behaviour with distant nuclei.

The ENDOR spectra for the  $^1H@POSS$  powder show a broad signal surrounded around the Larmor frequency of the  $^1H$  nucleus for couplings to the hydrogen atoms at the corners of the POSS cage structure. At temperatures below 40 K, a small splitting can be derived for a favourable position of the corner hydrogen atoms and little to no thumbing at cryogenic temperatures. Between 40 K and 120 K a transition of the structure in the ENDOR spectra starts to get apparent. The ENDOR spectra for the  $^1H@POSS$  powder begin to show a broad signal in a temperature range higher than 40 K. Shoulder peaks begin to appear at temperatures higher than 120 K presumably for a favourable arrangement of the corner hydrogen atoms averaged in each methyle group with respect to a random orientation in the temperature range of 40 K to 120 K with respect to the external magnetic field  $B_0$ . This behaviour in the ENDOR spectrum could be proven by simulation of the dipolar coupling contributions and extracting the distances out of each contribution. Here, it shows that the distances derived from the ENDOR traces are lower than the distances derived from the crystal structure, presumably because the 1s electron in the centre of the cage has a distribution, thus allowing stronger couplings to the distant nuclei of methyle groups. Movements of methyle groups towards the face of the cage can also occur but are more unlikely due to steric hindrance with other methyle groups.

If the  $^1H@POSS$  qubit is surrounded by solvent molecules, the peak in the ENDOR spectra becomes even broader over the whole temperature range up to 100 K, which could correspond to higher dipolar coupling constants to distant solvent hydrogen atoms.

Replacing the solvent molecules around  $^1H@POSS$  with deuterated solvent molecules resolves the dipolar splitting observed at cryogenic temperatures more, even at temperatures lower than 40 K. These results are consistent with our results for  $T_M$  enhancement at all measured temperatures for the qubit diluted in deuterated solvents. The approach of temperature dependent ENDOR spectra together with ENDOR simulations provide further structural explanations for the  $T_M$  enhancement in the deuterated system.

In conclusion, this multi-method approach with relaxation time measurements and ENDOR spectroscopy together with simulations for structural investigation has proved to be useful in vali-

dating the  $T_M$  enhancement and hence the qubit performance.

Thanks to this work, we have shown that it is very efficient to improve the phase memory time  $T_M$  of a potential qubit system. Further improvements and a deeper look into the relaxation mechanism of spins inside the 1s electron trapped inside a POSS cage in deuterated environments can further increase the qubit efficiency further and lead to even better quantum computers.

#### Author Contributions

H.T.A.W. performed the measurements, processed the experimental data, performed the analysis and drafted the manuscript. M.N., E.S. and R.S. performed pulse EPR measurements. D.S. provided visualizations for the manuscript. J.B. performed CW EPR measurements. G.M. prepared and provided the sample. All authors discussed the results and commented on the manuscript. Project was supervised by G.M. and C.W.M.K. and conceived by C.W.M.K..

#### Conflicts of interest

The authors declare that they have no known competing financial interests or personal relationships that could have appeared to influence the work reported in this paper.

#### Acknowledgements

We thank the workshop of the Saarland University Saarbrücken for supporting this work. This research did not receive any specific grant from funding agencies in the public, commercial, or not-for-profit sectors. EPR spectroscopy was performed on spectrometers purchased with support of the State of Saarland and the German Science Foundation (project number INST 256/535-1).

#### Notes and references

- 1 M. Akhtar, F. Bonus and F. Lebrun-Gallagher, *Nat. Commun.*, 2023, **14**, 1451–1466.
- 2 J. Russell, *IBM Quantum Update: Q System One Launch*, 2019, <https://www.hpcwire.com/2019/01/10/>, Accessed: 2023-09-19.
- 3 M. Wasielewski, M. Forbes, N. Frank, K. Kowalski, G. Scholes, J. Yuen-Zhou, M. Baldo, D. Freedman, R. Goldsmith, T. Goodson and M. Kirk, *Nat. Rev. Chem.*, 2020, **4**, 490–504.
- 4 R. Sasamori, Y. Okaue, T. Isobe and Y. Matsuda, *Science*, 1994, **265**, 1691–1693.
- 5 S. Stoll, A. Ozarowski, R. D. Britt and A. Angerhofer, *J. Magn. Res.*, 2010, **207**, 158–163.
- 6 G. Mitrikas, *Phys. Chem. Chem. Phys.*, 2012, **14**, 3782–3790.
- 7 G. Mitrikas and R. Carmieli, *J. Phys. Chem. C*, 2021, **125**, 9899–9907.
- 8 G. Mitrikas, E. Efthimiadou and G. Kordas, *Phys. Chem. Chem. Phys.*, 2014, **16**, 2378–2383.
- 9 D. M. Murphy and R. D. Farley, *Chem. Soc. Rev.*, 2006, **35**, 249–268.
- 10 M. Paech and R. Stoesser, *J. Phys. Chem. A*, 1997, **101**, 8360–8365.
- 11 A. Schweiger and G. Jeschke, *Principles of Pulse Electron Para-*

- magnetic Resonance*, Oxford University Press, Great Clarendon Street, Oxford OX2 6DP, 2001.
- 12 S. Stoll and A. Schweiger, *J. Magn. Reson.*, 2006, **178**, 42–55.
  - 13 G. Mitrikas, Y. Sanakis and N. Ioannidis, *Appl. Magn. Reson.*, 2020, **51**, 1451–1466.
  - 14 N. Weiden, M. Päch and K. Dinse, *Appl. Magn. Reson.*, 2001, **21**, 507–516.
  - 15 E. G. Derouane and J. C. Vedrine, *J. Chem. Phys.*, 1976, **65**, 927–934.
  - 16 *Physical Chemistry*, ed. P. W. Atkins, J. D. Paula and J. Keeler, Oxford University Press, 2018.
  - 17 M. Brustolon, A. Maniero and U. Segre, *Mol. Phys.*, 1985, **55**, 713–721.
  - 18 A. Tyryshkin, J. Morton, A. Ardavan and S. Lyon, *J. Chem. Phys.*, 2006, **124**, 234508.

### **3.1.2 Short-lived Radicals**

The following two publications illustrate the development of two novel catalytically active nanoparticle systems regarding the degradation of microplastics in an aquatic environment. The catalytic pathway was investigated by trapping the short-lived radicals to long-lived intermediates by the usage of spin traps. The relevant reactive oxygen species could be identified via time dependent CW ESR studies of the long-lived intermediates and furthermore helped in the development of the second nanoparticle system described after the first publication.

3.1.2.1 LaCoO<sub>4</sub> Nanoparticles

Chemical Engineering Journal 429 (2022) 131447



Contents lists available at ScienceDirect

Chemical Engineering Journal

journal homepage: [www.elsevier.com/locate/cej](http://www.elsevier.com/locate/cej)

## Enhanced heterogeneous activation of peroxymonosulfate by Ruddlesden-Popper-type La<sub>2</sub>CoO<sub>4+δ</sub> nanoparticles for bisphenol A degradation

Mohaned Hammad<sup>a,\*</sup>, Baris Alkan<sup>a</sup>, Ahmed K. Al-kamal<sup>a</sup>, Cheolyong Kim<sup>b</sup>, Md Yusuf Ali<sup>a</sup>, Steven Angel<sup>a</sup>, Haakon T.A. Wiedemann<sup>c</sup>, Dina Klippert<sup>c</sup>, Torsten C. Schmidt<sup>b</sup>, Christopher W. M. Kay<sup>c,d</sup>, Hartmut Wiggers<sup>a,e,\*</sup>

<sup>a</sup> IVG, Institute for Combustion and Gas Dynamics – Reactive Fluids, University of Duisburg-Essen, Duisburg, Germany

<sup>b</sup> Instrumental Analytical Chemistry and Centre for Water and Environmental Research, University of Duisburg-Essen, Essen, Germany

<sup>c</sup> Department of Chemistry, Saarland University, Saarbrücken, Germany

<sup>d</sup> London Centre for Nanotechnology, University College London, 17-19 Gordon Street, London WC1H 0AH, United Kingdom

<sup>e</sup> CENIDE, Center for NanoIntegration Duisburg-Essen, University of Duisburg-Essen, Duisburg, Germany

## ARTICLE INFO

## Keywords:

Heterogeneous catalysis  
Spray flame synthesis  
Peroxymonosulfate  
Sulfate radical  
Bisphenol A degradation

## ABSTRACT

The scalable synthesis of stable catalysts for environmental remediation applications remains challenging. Nonetheless, metal leaching is a serious environmental issue hindering the practical application of transition-metal based catalysts including Co-based catalysts. Herein, for the first time, we describe a facile one-step and scalable spray-flame synthesis of high surface area La<sub>2</sub>CoO<sub>4+δ</sub> nanoparticles containing excess oxygen interstitials (+δ) and use them as a stable and efficient catalyst for activating peroxymonosulfate (PMS) towards the degradation of bisphenol A. Importantly, the La<sub>2</sub>CoO<sub>4+δ</sub> catalyst exhibits higher catalytic degradation of bisphenol A (95% in 20 min) and stability than LaCoO<sub>3-x</sub> nanoparticles (60%) in the peroxymonosulfate activation system. The high content of Co<sup>2+</sup> in the structure showed a strong impact on the catalytic performance of the La<sub>2</sub>CoO<sub>4+δ</sub> + PMS system. Despite its high specific surface area, our results showed a very low amount of leached cobalt (less than 0.04 mg/L in 30 min), distinguishing it as a material with high chemical stability. According to the radical quenching experiments and the electron paramagnetic resonance technology, SO<sub>4</sub><sup>-</sup>, ·OH, and <sup>1</sup>O<sub>2</sub> were generated and SO<sub>4</sub><sup>-</sup> played a dominant role in bisphenol A degradation. Moreover, the La<sub>2</sub>CoO<sub>4+δ</sub> + PMS system maintained conspicuous catalytic performance for the degradation of other organic pollutants including methyl orange, rhodamine B, and methylene blue. Overall, our results showed that we developed a new synthesis method for stable La<sub>2</sub>CoO<sub>4+δ</sub> nanoparticles that can be used as a highly active heterogeneous catalyst for PMS-assisted oxidation of organic pollutants.

## 1. Introduction

Bisphenol A (2,2-bis (4-hydroxyphenyl) propane, BPA) is intensively utilized as a key industrial chemical for the production of polycarbonate plastics and epoxy resins in the plastic industry [1]. Unfortunately, a significant amount of BPA is continuously discharged into the environment and detected in food, drinking water, and aquatic animals [2]. BPA mimics estrogenic activity in human and animal bodies causing disruption of the endocrine system through interfering with hormonal

and homeostatic functions [3]. Therefore, the removal of BPA especially from aquatic environments is of great interest.

Recently, the Fenton reaction employing hydroxyl (·OH) and sulfate radicals (SO<sub>4</sub><sup>-</sup>) has attracted increasing interest as a promising method to oxidize organic pollutant in water [4–6]. Compared to the ·OH, SO<sub>4</sub><sup>-</sup> has a longer half-life time, higher standard oxidation potential, and wider pH range applicability, which is more efficient for bisphenol A degradation [7]. Sulfate radicals are typically generated by peroxymonosulfate (PMS) or peroxydisulfate (PDS) activation using heat [8],

\* Corresponding authors at: Institute for Combustion and Gas Dynamics – Reactive Fluids, University of Duisburg-Essen, Carl-Benz-Str. 199, 47057 Duisburg, Germany.

E-mail addresses: [mohaned.hammad@uni-due.de](mailto:mohaned.hammad@uni-due.de) (M. Hammad), [hartmut.wiggers@uni-due.de](mailto:hartmut.wiggers@uni-due.de) (H. Wiggers).

<https://doi.org/10.1016/j.cej.2021.131447>

Received 23 March 2021; Received in revised form 14 July 2021; Accepted 16 July 2021

Available online 10 August 2021

1385-8947/© 2021 Elsevier B.V. All rights reserved.

ultrasound [9], UV [10], electrochemical processes [11], and transition metal ions (e.g., Co, Mn, Cu, Fe, and Ni) [12].

Homogenous transition-metal catalysis is one of the feasible and cost-effective ways to generate  $\text{SO}_4^{\cdot-}$ . Among the transition metals,  $\text{Co}^{2+}$  exhibits the most efficient homogeneous catalyst for PMS activation [13] and is catalytically regenerated during PMS activation, which enhances its catalytic activity [14]. However, Co-based homogeneous activation has serious drawbacks, especially secondary metal-ion pollution and high catalyst consumption [15]. Thus, heterogeneous, Co-based catalysts such as cobalt oxide [16], cobalt-based bimetallic oxide [17,18], and supported cobalt oxide [19] nanoparticles have been investigated for PMS activation. Among them, transition metal-based perovskites ( $\text{ABO}_3$  with B being the transition metal) have attracted increasing attention in heterogeneous catalysis because of their flexibility in chemical composition and their ability for generating oxygen vacancies, thus enabling catalytic redox reactions [20]. More recently, some reports have focused on different transition metals La-based perovskites ( $\text{LaMO}_3$  (M: Co, Cu, Fe, and Ni)) for PMS activation [21]. Particularly,  $\text{LaCoO}_3$  perovskites have been considered being very effective to generate  $\text{SO}_4^{\cdot-}$  from PMS as Co–O– bonds enable a high number of reactive sites for PMS activation [22]. Moreover, the B-site cation deficiency in the  $\text{LaCoO}_{3-\delta}$  perovskite structures enhances their catalytic activity [23]. Although these perovskite catalysts have some advantages such as high catalytic activity, they suffer from metal leaching in the aqueous medium [24]. Thus, it is essential to explore highly stable heterogeneous catalysts for PMS activation.

Compared to transition metal-based perovskites ( $\text{ABO}_3$ ), Ruddlesden-Popper mixed oxides ( $\text{A}_2\text{BO}_4$ ) nanoparticles (RP-MONp) exhibit higher stability and redox ability, because their crystal structure is more opened due to extra space between A-site atoms. They consist of alternating layers of perovskite ( $\text{ABO}_3$ ) and rock salt (AO) [25]. These layered structures possess good thermal stability [26] and show high ionic conductivity. Several studies on RP-based catalysts show that the RP-MONp reveal better oxygen diffusion coefficients and surface exchange than other  $\text{ABO}_3$  perovskite type. They have been reported as catalysts in various heterogeneously catalyzed reactions including oxygen reduction reaction (ORR) and oxygen evolution reaction (OER) [27], photocatalytic water splitting [28], NO and CO removal [29], oxidation of urea and small alcohols [30], as a cathode for a solid oxide electrolysis cell [31], and as a catalyst in the Fenton reaction [32]. In this regard,  $\text{La}_2\text{CoO}_{4+\delta}$  has been selected to be used as a PMS activator since its structure can tolerate excess amounts of oxygen upon oxidation at room temperature up to a  $\delta$  of 0.16 [33]. Moreover, the oxidation state of the B-site cation in this structure can be controlled by tailoring oxygen non-stoichiometry [34]. To summarize,  $\text{La}_2\text{CoO}_{4+\delta}$  is a highly suitable material for advanced catalytic oxidation processes.

Several methods have been demonstrated to synthesize Ruddlesden-Popper mixed oxide catalysts including co-precipitation [35], sol-gel synthesis [36], combustion methods [37], hydrothermal flow synthesis [38], and solid-state reactions [39]. However, all these methods require high-temperature annealing ( $\geq 1000$  °C) at an extended period, which promotes particle growth and sintering, leading to a reduced catalytically active surface area. As an alternative, spray-flame synthesis is an established method to produce non-sintered, homogeneously distributed perovskite nanoparticles down to 10 nm, and even below [40,41]. Surface-sensitive measurements of spray-flame-synthesized  $\text{LaCoO}_3$  nanoparticles show a high content of  $\text{Co}^{2+}$  ions being present at the particles' surface. These results are attributed to the local formation of oxygen-deficient or layered perovskite structures such as  $\text{A}_2\text{BO}_4$  type Ruddlesden-Popper structures, which can stabilize  $\text{Co}^{2+}$  much better than the pure perovskite  $\text{ABO}_3$  [42]. Thus, specific interest is in the targeted formation and investigation of Co-containing Ruddlesden-Popper-type nanoparticles as highly active heterogeneous catalysts.

Herein, the objective of this study is to seek a one-step method for the synthesis of  $\text{La}_2\text{CoO}_{4+\delta}$  nanoparticles using a spray-flame method with the purpose of improving their catalytic performance with a very low

amount of metal leaching to achieve the environmental requirements in respect of organic pollutant degradation. The performance of the catalysts for PMS activation was evaluated in terms of BPA degradation. Moreover, effects of several important parameters such as initial pH value, inorganic anions (such as  $\text{Cl}^-$ ,  $\text{NO}_3^-$ ,  $\text{H}_2\text{PO}_4^-$ ,  $\text{HCO}_3^-$ , etc.), and water bodies (tap water, and drinking water) on their catalytic performances along with the reusability of the  $\text{La}_2\text{CoO}_{4+\delta}$  nanoparticles were also investigated. The radical generation was identified by radical scavenging experiments and electron paramagnetic resonance studies, and a mechanism for PMS activation is proposed.

## 2. Materials and methods

### 2.1. Materials

For the synthesis of  $\text{La}_2\text{CoO}_{4+\delta}$  nanoparticles, La ( $(\text{CH}_3\text{COO})_3 \cdot 1.05 \text{H}_2\text{O}$  (99.9%; Sigma-Aldrich) and Co ( $(\text{CH}_3\text{COO})_2 \cdot 4 \text{H}_2\text{O}$  ( $\geq 98\%$ ; Sigma-Aldrich) were used as the metal precursors while propionic acid (ACS reagent,  $>99.5\%$ ; Sigma-Aldrich), propanol (anhydrous, 99.7%; Sigma-Aldrich), ultrapure DI water ( $18.2 \text{M}\Omega \text{ cm}$  at 25 °C) and ethanol ( $>99.8\%$ ; Sigma-Aldrich) were employed as solvents. 5,5-dimethyl-1-pyrroline N-oxide (DMPO) ( $>97.0\%$ ; TCI), Bisphenol A ( $\geq 99\%$ ), potassium peroxydisulfate, sodium phosphate monobasic ( $\geq 99\%$ ), sodium nitrate ( $\geq 99\%$ ), sodium chloride ( $\geq 99\%$ ), sodium hydrogencarbonate ( $\geq 99\%$ ),  $\beta$ -carotene ( $\geq 95\%$ ), *tert*-butyl alcohol ( $\geq 99.5\%$ ), methylene blue ( $\geq 97\%$ ), rhodamine B ( $\geq 95\%$ ), Acid Orange 7 ( $\geq 98\%$ ) potassium bicarbonate ( $\geq 99.5\%$ ), potassium iodide ( $\geq 90\%$ ), and absolute ethanol were purchased from Sigma Aldrich to be used for the catalytic tests. Sodium hydroxide ( $\geq 97\%$ ) and nitric acid ( $>69\%$ , both VWR International) were used to adjust the pH of the respective solution. All chemicals were used as received without further purification.

### 2.2. Synthesis of $\text{La}_2\text{CoO}_{4+\delta}$ nanoparticles

The spray-flame syntheses of lattice-oxygen-deficient  $\text{LaCoO}_{3-x}$  perovskite and interstitial-oxygen-rich  $\text{La}_2\text{CoO}_{4+\delta}$  Ruddlesden-Popper phases were carried out similar to the process described before [43] (Fig. 1) using precursor solutions and process parameters given in detail in Table S1. Briefly, a precursor solution is transferred to a syringe pump connected to a homemade enclosed reactor, which allows full control of gas flow and pressure. The syringe pump is connected to a hollow needle (0.4 mm inner diameter and 0.7 mm outer diameter) adjusted in the center of a burner nozzle. Oxygen dispersion gas (introduced through an annular gap surrounding the hollow needle) was used to atomize the precursor solution injected into the reactor at a precursor solution flow rate of 3 mL/min. A premixed pilot flame ( $\text{CH}_4/\text{O}_2$ ) surrounding the hollow needle was used to ignite and stabilize the spray-flame while a sheath gas surrounding the flame was used to stabilize the reactor gas flow. The reactor was operated at pressures of 930 and 900 mbar, respectively, adjusted by a valve and a rotary vane pump. The formed particles were collected on a filter membrane.

To investigate the influence of cobalt oxidation states on PMS oxidation, we aimed to synthesize two types of catalysts:  $\text{LaCoO}_3$  perovskites with mostly  $\text{Co}^{3+}$  surface ions, and the newly investigated  $\text{La}_2\text{CoO}_4$  compounds containing a high number of  $\text{Co}^{2+}$  ions. Thus, for the formation of almost stoichiometric  $\text{LaCoO}_3$ , the process and combustion parameters were adjusted to lean conditions using low hydrocarbon chained components as solvent (i.e. propanol and propionic acid), a high volume flow of the  $\text{CH}_4/\text{O}_2$  pilot flame, and a high volume flow of  $\text{O}_2$  dispersion gas. The product is labeled " $\text{LaCoO}_{3-x}$ ". For the new synthesis of  $\text{La}_2\text{CoO}_{4+\delta}$  developed in the course of these investigations, fuel-rich combustion conditions were employed as a strategy to efficiently obtain a cobalt oxidation state of  $\text{Co}^{2+}$  in the nanoparticle product. For this reason, a high carbon chained carboxylic acid was used in the precursor solution as well as lower volume flows of

M. Hammad et al.

Chemical Engineering Journal 429 (2022) 131447

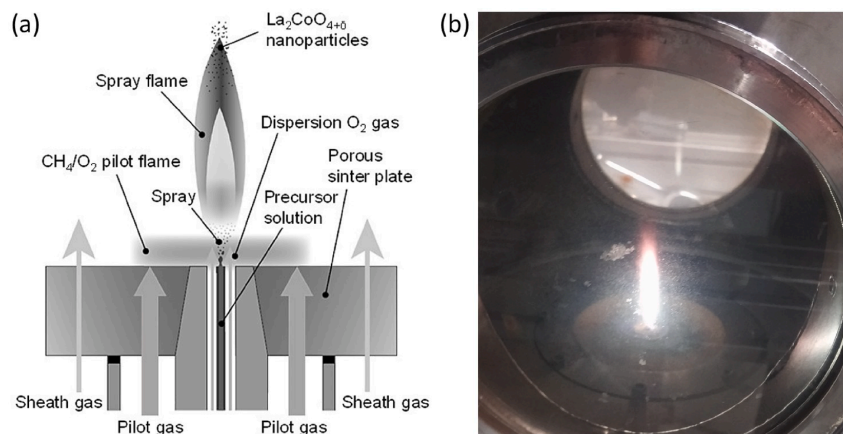


Fig. 1. (a) Schematics of the spray-flame synthesis (adapted from Ref. [43]) and (b) a photo of the spray-flame during nanoparticle synthesis.

the  $\text{CH}_4/\text{O}_2$  pilot flame gases and the  $\text{O}_2$  dispersion gas.

The precursor solution for  $\text{LaCoO}_{3-x}$  was composed of propionic acid mixed with 1-propanol in a glass flask at room temperature and stirred for 10 min. La- and Co-precursors were subsequently added to the solvent mixture and the flask was then heated in a silicon oil bath at  $60^\circ\text{C}$  to dissolve the precursors under constant magnetic stirring for 2 h. The total metal concentration of La and Co was adjusted to 0.45 M and the nominal atomic ratios of La/Co were adjusted to 1. For the precursor solution of  $\text{La}_2\text{CoO}_{4+\delta}$ , a similar procedure was used except that octanoic acid was used as an organic acid and a small amount of water was added to the solvent mixture to appropriately dissolve the La-acetate. The precursor solution was then heated in a silicon oil bath at  $70^\circ\text{C}$  under constant magnetic stirring for 2 h. The total metal concentration of La and Co was adjusted to 0.15 M and the nominal atomic ratios of La/Co were adjusted to 2.

### 2.3. Methods of Characterization

The crystal phases of the samples were determined by X-ray diffraction (XRD) recorded with a PANalytical X-ray diffractometer X'Pert (Netherlands) with a  $\text{Cu K}\alpha$  radiation ( $\lambda = 1.5406 \text{ \AA}$ ). The surface morphology and energy dispersive spectra were analyzed using transmission electron microscopy (TEM, JEM-2200FS, JEOL, Japan). X-ray photoelectron spectroscopy (XPS, VersaProbe II, ULVAC-PHI, Japan with monochromatic  $\text{Al K}\alpha$  light at an emission angle of  $45^\circ$ ) was applied to analyze the surface elemental composition and chemical state of the samples. All measured binding energies were referenced to the  $\text{Cu}2p$  peak at 933 eV. Attenuated total reflectance Fourier transform infrared spectra (ATR-FTIR) were recorded using a Bruker Vertex 80 spectrometer (Bruker, Germany) in the  $400\text{--}4000 \text{ cm}^{-1}$  region. The zeta potential of the catalysts was determined by a Malvern Zetasizer (Malvern Panalytical, United Kingdom). The specific surface areas were measured on a Quantachrome NOVA2200 (Quantachrome GmbH, Germany) analyzer at 77 K by the Brunauer–Emmett–Teller (BET) Nitrogen adsorption/desorption isotherm method.

### 2.4. Catalytic studies and analyses

The catalytic performance of the as-prepared  $\text{La}_2\text{CoO}_{4+\delta}$  nanoparticles was evaluated for PMS activation in terms of BPA degradation. The concentration of BPA was analyzed by high-performance liquid chromatography (HPLC, Shimadzu LC-10AT, Shimadzu Corporation, Japan). The HPLC was equipped with an SPD-M10A diode array detector

(detection wavelength: 230 nm) and a Kinetex C18 reverse-phase column ( $100 \text{ mm} \times 2 \text{ mm}$ ,  $5 \mu\text{m}$ ). The flow rate of the mobile phase consisting of 0.1% formic acid in water and acetonitrile (80:20, v:v) was 0.5 mL/min. In a typical experiment, 2.4 mg catalyst was initially dispersed into 40 mL BPA aqueous solution (40 mg/L) at  $25^\circ\text{C}$  and the resultant suspension was magnetically stirred in dark for 30 min to ensure the establishment of an adsorption/desorption equilibrium between catalyst and BPA before a certain dose of PMS was added. At selected time intervals, 2 mL of the suspension was withdrawn, immediately quenched with 0.5 mL methanol, filtered with a  $0.22 \mu\text{m}$  membrane filter, centrifuged (12000 rpm, 20 min) to remove the particles, and injected into the HPLC vial. 1.0 M solutions of NaOH and  $\text{HNO}_3$  were used to adjust the initial pH. The same operation was repeated with different organic compounds such as methylene blue (MB), rhodamine B (RhB), and acid orange 7 (AO7). The concentrations of MB, RhB, and AO7 were measured by UV–Vis spectroscopy (Varian Cary 400, Varian, Australia) at wavelengths of 664, 553, and 483 nm, respectively. To study the reusability of the  $\text{La}_2\text{CoO}_{4+\delta}$  nanoparticles, the catalyst was collected by centrifugation (Sigma 3-30KS centrifuge, Sigma Laborzentrifugen GmbH, Germany) at 14000 rpm for 10 min, followed by thorough washing with deionized water and then re-dispersed into fresh BPA solution for the next experimental run.

To compare the degradation reaction kinetics of the BPA degradation, pseudo-first-order kinetics reaction rate constants ( $k_{\text{app}}$ ) of the BPA removal were measured according to the following equation:

$$\ln\left(\frac{C_t}{C_0}\right) = -k_{\text{app}}t \quad (1)$$

where  $C_t$  depicts the pollutant concentration at time,  $C_0$  is the initial pollutant concentration,  $k_{\text{app}}$  is the kinetics rate constants, and  $t$  is the time.

The concentration of dissolved metal ions in concentrated nitric acid (60%) was determined by atomic absorption spectroscopy (M–Series, Thermo Electron Corporation, Germany). The total organic carbon (TOC) concentration was analyzed by using a TOC-L total organic carbon analyzer (Shimadzu, Japan) to evaluate the degree of BPA mineralization. To determine the residual concentration of PMS, 100  $\mu\text{L}$  of the suspension was withdrawn at given time intervals, mixed with potassium bicarbonate (5 g/L) and potassium iodide (40 g/L), and then was measured by UV–Vis spectroscopy (Varian Cary 400, Varian, Australia) at a wavelength of 352 nm. To evaluate the contributions of the radical reactions to mineralization, a certain amount of ethanol (EtOH), *tert*-butyl alcohol (TBA), and  $\beta$ -carotene were added to the catalytic system

M. Hamad et al.

Chemical Engineering Journal 429 (2022) 131447

to scavenge  $\text{SO}_4^{\cdot-}$  and  $\cdot\text{OH}$ ,  $\cdot\text{OH}$ , and  $^1\text{O}_2$  respectively. The  $\beta$ -carotene experiment was conducted in 37 mL of acetone and 3 mL of deionized water for dissolving PMS. The intermediates of BPA degradation were identified by an Agilent 1260 Infinity II Liquid Chromatography (LC-MS) system equipped with a 6120 Quadrupole Mass Detector and a Kinetex C18 reverse-phase column (100 mm  $\times$  2 mm, 5  $\mu\text{m}$ ). The mobile phase of LC-MS was the same as HPLC. The generated reactive radicals were measured using the MiniScope MS-5000 electron spin resonance spectrometer (Freiberg Instruments, Germany) with a microwave power of 10 mW and a modulation amplitude of 0.2 G at room temperature. The impedance measurements were performed using an impedance analyzer Solartron 1260 (Solartron Analytical, United Kingdom) with a frequency range of 0.1 Hz – 1 MHz and with an output signal voltage of 100 mV. Gold sputtering was done on both sides of the pellet before the experiment.

### 3. Results and discussion

#### 3.1. Characterization of $\text{La}_2\text{CoO}_{4+\delta}$ nanoparticles

The XRD patterns of the pristine nanoparticles were analyzed to determine crystalline phases of  $\text{La}_2\text{CoO}_{4+\delta}$  and  $\text{LaCoO}_{3-x}$  (Fig. 2). The  $\text{LaCoO}_{3-x}$  diffraction peaks show a good match to a  $\text{LaCoO}_{2.937}$  perovskite phase (Inorganic Crystal Structure Database (ICSD): 153995), while the XRD pattern of  $\text{La}_2\text{CoO}_{4+\delta}$  can be mainly related to a Ruddlesden-Popper type phase of  $\text{La}_2\text{CoO}_{4.13}$  (ICSD: 237238) with a minor content of  $\text{La}(\text{OH})_3$  (ICSD: 31584). Notably, the diffraction peaks of  $\text{La}_2\text{CoO}_{4+\delta}$  appear more broadened compared to those of  $\text{LaCoO}_{3-x}$ , and this finding points out a low degree of crystallinity and/or small crystal sizes of  $\text{La}_2\text{CoO}_{4+\delta}$ . A possible decrease in the crystallinity of the  $\text{La}_2\text{CoO}_{4+\delta}$  phase can be owing to hydrated groups incorporated in its structure as previously reported in Co-based Ruddlesden-Popper type crystals [44].

To investigate the morphology and size distribution of as-prepared nanoparticles, transmission electron microscopy was performed as shown in Fig. 3. For both samples, the count median diameter (CMD) and geometric standard deviation ( $\sigma_g$ ) were determined by fitting the size distribution histograms of about 400 nanoparticles to a lognormal distribution. The CMD and  $\sigma_g$  of  $\text{LaCoO}_{3-x}$  were measured as 17.5 nm

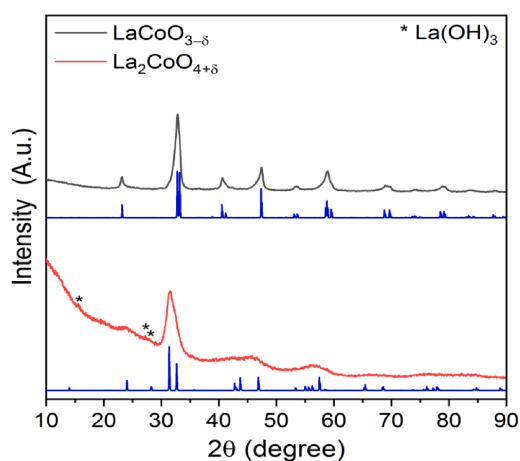


Fig. 2. XRD patterns of as-prepared  $\text{LaCoO}_{3-x}$  and  $\text{La}_2\text{CoO}_{4+\delta}$  nanoparticles. Reference phases are  $\text{La}_2\text{CoO}_{4.13}$  (ICSD no: 237238, blue line),  $\text{LaCoO}_{2.937}$  (ICSD no: 153995, blue line), and  $\text{La}(\text{OH})_3$  (ICSD no: 31584), respectively. (For interpretation of the references to colour in this figure legend, the reader is referred to the web version of this article.)

and 1.5 while those of  $\text{La}_2\text{CoO}_{4+\delta}$  correspond to 10.1 nm and 1.5. Lower particle sizes of  $\text{La}_2\text{CoO}_{4+\delta}$  are also implied from the specific surface areas of  $\text{La}_2\text{CoO}_{4+\delta}$  and  $\text{LaCoO}_{3-x}$  nanoparticles being determined by nitrogen adsorption-desorption isotherms through the BET measurements (Brunauer Emmett Teller) [32]. The specific surface area (SSA) of  $\text{La}_2\text{CoO}_{4+\delta}$  was measured as 89  $\text{m}^2/\text{g}$ , being considerably higher than the SSA of  $\text{LaCoO}_{3-x}$  about 43  $\text{m}^2/\text{g}$ . The lower CMD and higher SSA of  $\text{La}_2\text{CoO}_{4+\delta}$  particles compared to  $\text{LaCoO}_{3-x}$  can be associated with precursor characteristics in that lower concentration of La and Co metals being used in the precursor solution of  $\text{La}_2\text{CoO}_{4+\delta}$  bring about lower nanoparticles sizes and higher SSA of  $\text{La}_2\text{CoO}_{4+\delta}$  (see supplementary material, Table S1). Beside that, the chemical composition of  $\text{LaCoO}_{3-x}$ , being determined by Energy Dispersive X-Ray (EDX) measurements, indicate that their La/Co atomic ratio is close to unity (see supplementary material, Fig. S1), while La/Co atomic ratio of  $\text{La}_2\text{CoO}_{4+\delta}$  was measured about 2.3, being slightly higher than nominal atomic ratios in  $\text{La}_2\text{CoO}_{4+\delta}$ . Excess La content can be owing to small amounts of  $\text{La}(\text{OH})_3$  secondary phase being detected from XRD analyses. Overall, the bulk compositions of  $\text{LaCoO}_{3-x}$  and  $\text{La}_2\text{CoO}_{4+\delta}$  nanoparticles show a good agreement with the expected nominal compositions.

The Surface oxidation state and chemistry of Co and La ions were further investigated using the core-level and satellite X-ray photoelectron spectroscopy (XPS) features of  $\text{Co}2p_{3/2}$  and  $\text{La}3d_{5/2}$  spectra (Fig. 4). In both  $\text{Co}2p$  and  $\text{La}3d$  spectra, lower XPS signals were measured for  $\text{La}_2\text{CoO}_{4+\delta}$  compared to  $\text{LaCoO}_{3-x}$ . This result can be well attributed to the effect of higher content of carbon impurities in  $\text{La}_2\text{CoO}_{4+\delta}$ , which reduces the respective XPS signal of this sample. For  $\text{LaCoO}_{3-x}$ , the intense XPS signals of the  $\text{Co}2p_{3/2}$  at  $\sim 779.3$ , 781.4, and 789.5 eV indicate  $\text{Co}^{3+}$  ions [45], whereas the low-intensity signals of  $\text{Co}2p_{3/2}$  at  $\sim 780.4$ , 782.2, and 785.2 eV can be assigned to the core-level and satellites of  $\text{Co}^{2+}$  ions, respectively [46]. The atomic proportion of surface  $\text{Co}^{3+}/\text{Co}^{2+}$  for  $\text{LaCoO}_{3-x}$  was found as 58/42, which corresponds to a chemical formula of  $\text{LaCoO}_{2.58}$ . At the XPS spectra of  $\text{La}_2\text{CoO}_{4+\delta}$ , the core-level signals of  $\text{Co}^{2+}$  ions show more intense XPS signals relative to those of  $\text{Co}^{3+}$  ions, and a low-intensity peak of metallic Co appears at  $\sim 778.1$  eV. The proportion of  $\text{Co}^{3+}/\text{Co}^{2+}/\text{Co}$  in  $\text{La}_2\text{CoO}_{4+\delta}$  was measured as 40/49/11, confirming reduced oxidation state of cobalt ions in this sample. The  $\text{La}3d$  spectra of  $\text{LaCoO}_{3-x}$  and  $\text{La}_2\text{CoO}_{4+\delta}$  exhibit similar XPS spectra at different binding energies. The core-level and satellite signals of  $\text{La}3d_{5/2}$  signals of  $\text{LaCoO}_{3-x}$  are visible at  $\sim 833.3$  and  $\sim 837.1$  eV with a multiplet splitting of 3.8 eV being in agreement with the  $\text{La}3d$  spectrum of La-based perovskites [47]. Despite showing a similar multiplet splitting,  $\text{La}3d_{5/2}$  signals of  $\text{La}_2\text{CoO}_{4+\delta}$  shift about 1.1 eV towards higher binding energies. This spectral feature can be attributed to Ruddlesden-Popper-type compounds [48]. All in all, XPS analyses of Co and La ions draw attention to a varying content of surface  $\text{Co}^{2+}$  and  $\text{Co}^{3+}$  ions in  $\text{LaCoO}_{3-x}$  and  $\text{La}_2\text{CoO}_{4+\delta}$ , which can govern their catalytic activity for PMS activation.

#### 3.2. Catalytic activity and stability of catalysts

Fig. 5a shows the removal efficiency of BPA for both catalysts and control measurements. The removal of BPA was negligible in the presence of only PMS or catalyst. In the case of the  $\text{La}_2\text{CoO}_{4+\delta}/\text{PMS}$  system, 97% BPA was removed within 30 min, which was higher than that in the  $\text{LaCoO}_{3-x} + \text{PMS}$  system (70%), implying that the catalytic activity of  $\text{La}_2\text{CoO}_{4+\delta}$  is significantly higher than that of  $\text{LaCoO}_{3-x}$ . Furthermore, the catalytic activity of  $\text{La}_2\text{CoO}_{4+\delta}$  was compared to those of other related Co-based catalysts in the literature (Table 1), and the spray-flame synthesized  $\text{La}_2\text{O}_3$  and  $\text{Co}_3\text{O}_4$ , which attained 7% and 45% BPA removal efficiency, respectively, indicating that  $\text{La}_2\text{CoO}_{4+\delta}$  materials show a remarkable improvement for PMS activation.

We attribute the remarkable catalytic enhancement of  $\text{La}_2\text{CoO}_{4+\delta}$  to the high specific surface area (see supplementary material, Fig. S2) and especially the higher surface concentration of  $\text{Co}^{2+}$  compared to  $\text{LaCoO}_{3-x}$  material, as we have shown before (Fig. 4). Moreover, the BPA

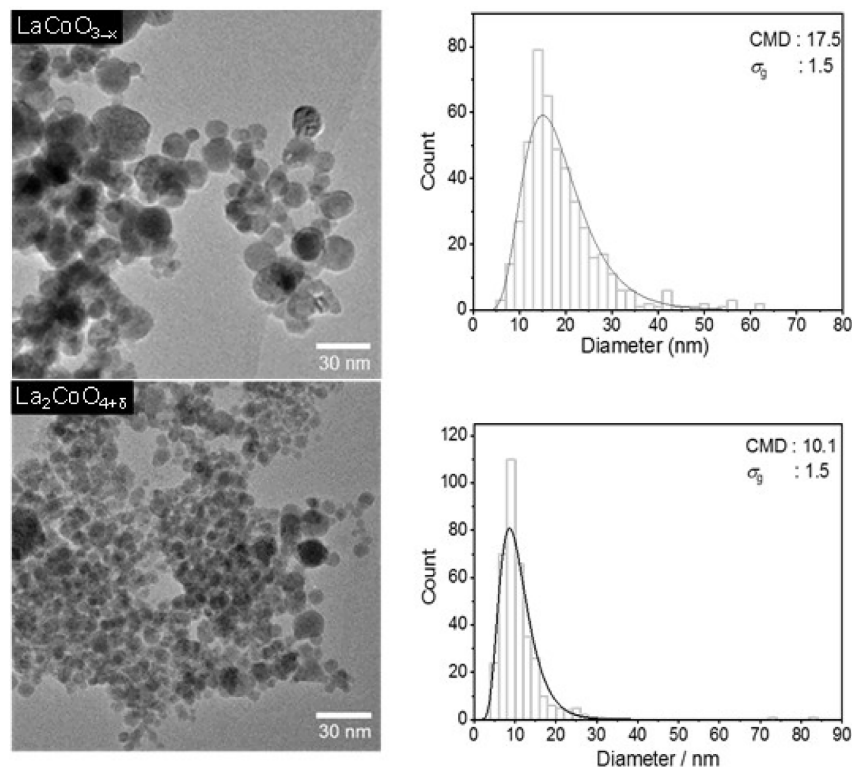


Fig. 3. TEM images of  $\text{LaCoO}_{3-x}$  and  $\text{La}_2\text{CoO}_{4+\delta}$  materials (on the left side) and the respective histograms of their particle sizes fitted to a log-normal particle size distribution (on the right side). Count median particle diameter and geometric standard deviation were abbreviated as a CMD and a  $\sigma_g$ , respectively.

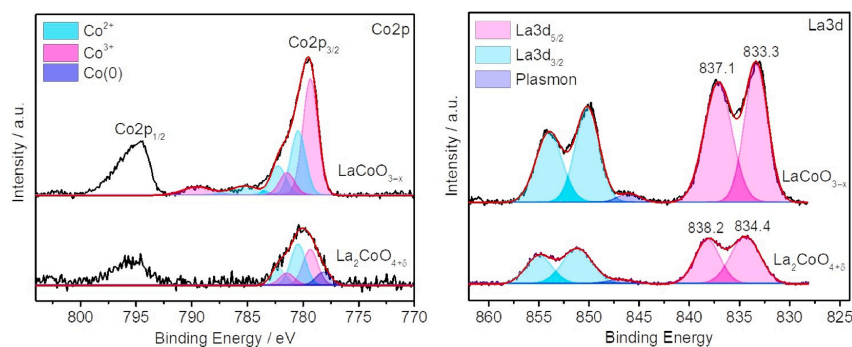


Fig. 4. XPS spectra of Co2p and La3d in  $\text{LaCoO}_{3-x}$  and  $\text{La}_2\text{CoO}_{4+\delta}$ , respectively.

removal in both systems could be well fitted by pseudo-first-order kinetics (see supplementary material, Fig. S3). The  $k_{app}$  of BPA degradation was about  $0.152 \text{ min}^{-1}$  and  $0.03 \text{ min}^{-1}$  for  $\text{La}_2\text{CoO}_{4+\delta}$  and  $\text{LaCoO}_{3-x}$  samples, respectively, confirming that the catalytic performance of the  $\text{La}_2\text{CoO}_{4+\delta}$  catalyst is significantly higher than that of  $\text{LaCoO}_{3-x}$ .

Besides, electrochemical impedance analyses were further performed to investigate the electron transfer behavior of both materials

(see supplementary material, Fig. S4). Obviously, the  $\text{La}_2\text{CoO}_{4+\delta}$  electrode ( $44898 \Omega$ ) exhibited lower charge transfer resistance compared to the  $\text{LaCoO}_{3-x}$  electrode ( $5705 \cdot 10^7 \Omega$ ), suggesting that the electron transfer in the  $\text{La}_2\text{CoO}_{4+\delta}$  structure is more efficient than that in the  $\text{LaCoO}_{3-x}$ , which is favorable for the electron transfer during PMS activation [49].

To support these findings, the variation of residual PMS during the PMS activation in both systems was performed (Fig. 5c). The residual

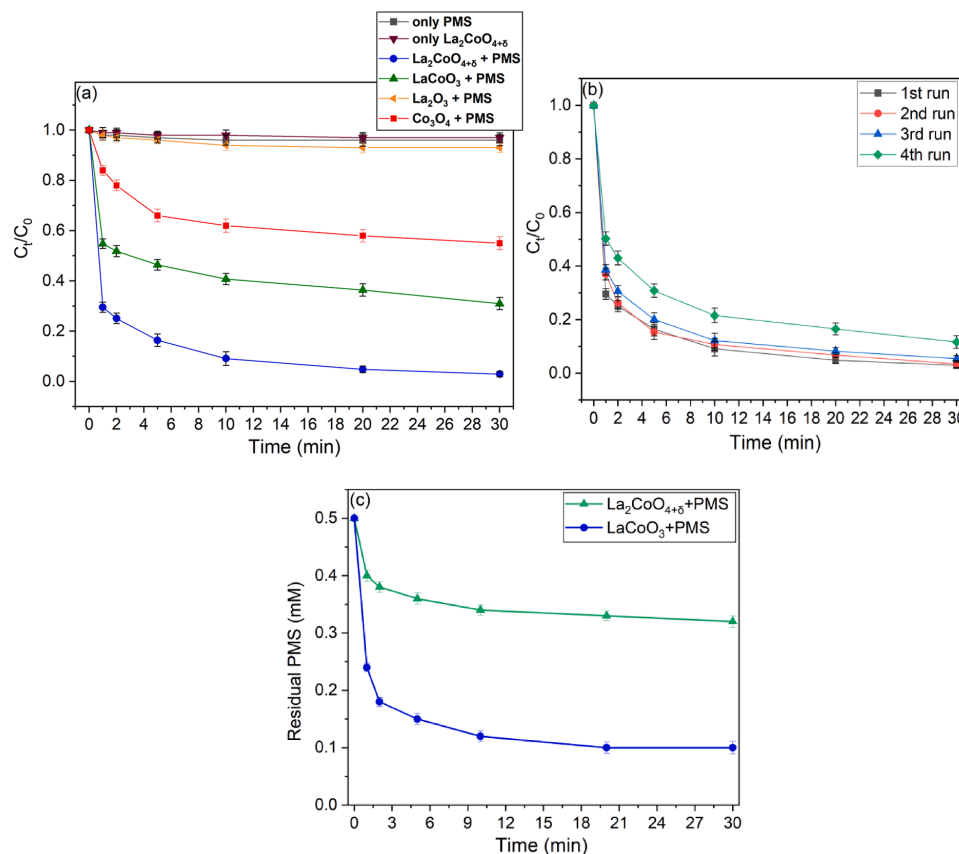


Fig. 5. a) BPA degradation with various catalysts in different reaction systems, b) Stability tests of  $\text{La}_2\text{CoO}_{4+\delta}$ , and c) Residual PMS variation along with the reaction time in different systems. Reaction conditions: (BPA) = 40 mg/L, (PMS) = 0.5 mM; (Catalyst) = 60 mg/L, initial pH = 6.8.

Table 1

Comparison of the BPA degradation by  $\text{La}_2\text{CoO}_{4+\delta}$  in this work with those of other related Co-based catalysts in the literature.

Catalyst	Dosage ( $\text{mg L}^{-1}$ )	BPA conc. ( $\text{mg L}^{-1}$ )	PMS conc (mM)	BPA removal (%)	Time(min)	$k_{app}$ ( $\text{min}^{-1}$ )	Co leaching( $\text{mg L}^{-1}$ )	Refs.
$\text{CoFe}_2\text{O}_{4-x}$	50	30	1	98	30	–	$\approx 1.2$	[50]
$\text{Co}_3\text{O}_4/\text{MXene}$	100	20	1	>99	20	0.3984	$\approx 0.36$	[51]
$\text{Fe}_{0.8}\text{Co}_{2.2}\text{O}_4$	100	20	0.65	95	60	0.049	$\approx 0.36$	[52]
$\text{Fe}_3\text{Co}_7/\text{C}$	100	20	1.3	98	30	0.132	$\approx 3.30$	[53]
$\text{Co}_3\text{O}_4/\text{MOFs}$	100	20	1.6	95	10	0.87	$\approx 0.35$	[54]
$\text{Co}_3\text{O}_4/\text{Bi}_2\text{O}_3$	300	20	0.32	98	30	0.1219	$\approx 0.35$	[55]
$\text{Co}_3\text{O}_4/\text{CC}$	100	10	0.32	>99	10	$\approx 0.52$	$\approx 0.25$	[56]
$\text{La}_2\text{CoO}_{4+\delta}$	60	40	0.5	95	20	0.152	$\approx 0.04$	This work

PMS concentration in a  $\text{La}_2\text{CoO}_{4+\delta}$  + PMS system (0.1 mM) was lower to a  $\text{LaCoO}_3$  + PMS system (0.32 mM), which attributed to about 80 % and 64 % of the initial PMS concentration, respectively, manifesting that the  $\text{La}_2\text{CoO}_{4+\delta}$  + PMS system activates more PMS as a result of fast electron transport from PMS molecules to the  $\text{La}_2\text{CoO}_{4+\delta}$ , and therefore higher BPA degradation is obtained.

To confirm the practicability of the catalyst in the  $\text{La}_2\text{CoO}_{4+\delta}$ /PMS system, the reusability of the  $\text{La}_2\text{CoO}_{4+\delta}$  material was investigated in four cycling experiments. As displayed in Fig. 5b, the reused  $\text{La}_2\text{CoO}_{4+\delta}$  exhibited excellent catalytic performance in the first three reaction runs. However, a decrease in BPA removal to 89% was observed after three

reaction runs, which can be mainly ascribed to the formation of insoluble lanthanum carbonate contaminants on the surface of  $\text{La}_2\text{CoO}_{4+\delta}$ , resulting in the partial deactivation of the catalyst. This structural change of  $\text{La}_2\text{CoO}_{4+\delta}$  catalyst could also be identified by XRD and FTIR. The XRD pattern of the multiple used catalyst shows three additional low-intensity peaks at  $2\theta = 18.4^\circ$ ,  $28^\circ$ , and  $41^\circ$  (Fig. 6a), which can be indexed to the orthorhombic layered structure of  $\text{La}_2(\text{CO}_3)_3 \cdot 1.1 \text{H}_2\text{O}$  [57]. A similar phenomenon was also observed in the FTIR spectra (Fig. 6b). An increased peak intensity around  $730 \text{ cm}^{-1}$  might be ascribed to the formation of  $\text{La}_2(\text{CO}_3)_3 \cdot 1.1 \text{H}_2\text{O}$  [58].

Besides, the mineralization extent of BPA was monitored by the TOC

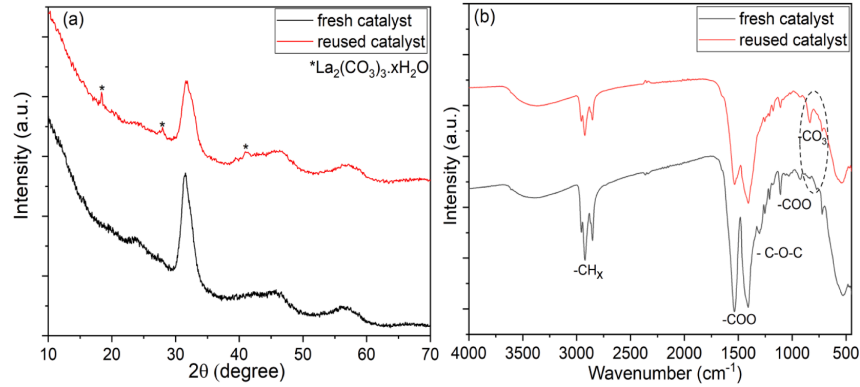


Fig. 6. a) XRD patterns and b) FTIR spectra of fresh and reused  $\text{La}_2\text{CoO}_{4+\delta}$  catalyst.

analyzer. After 30 min, the TOC removals of BPA were 27% and 49% for  $\text{LaCoO}_{3-x}$  and  $\text{La}_2\text{CoO}_{4+\delta}$  materials, respectively, implying the high BPA mineralization in the  $\text{La}_2\text{CoO}_{4+\delta}$  + PMS system. Moreover, the leaching of cobalt and lanthanum ions was further investigated by Atomic

Absorption Spectroscopy (AAS) analysis during the PMS activation. Compared to  $\text{LaCoO}_{3-x}$  (2.6 mg/mL),  $\text{La}_2\text{CoO}_{4+\delta}$  showed less Co leaching (0.04 mg/mL), which attributed to about 4.3% and 0.06% of the initial catalyst concentration, respectively, whereas the concentrations

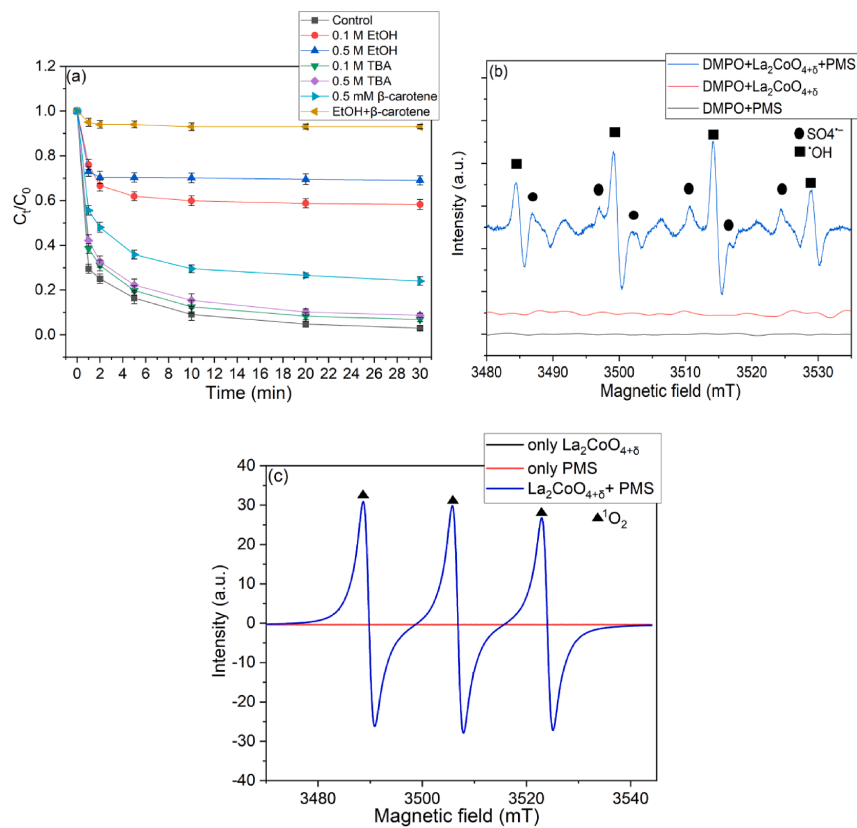


Fig. 7. a) Effect of radical scavengers on BPA degradation in different reaction systems, b) EPR spectra in  $\text{La}_2\text{CoO}_{4+\delta}$ /PMS systems with DMPO, and c) EPR spectra in  $\text{La}_2\text{CoO}_{4+\delta}$ /PMS systems with TEMP as the trapping agent. Reaction conditions: (BPA) = 40 mg/L, (PMS) = 0.5 mM, (Catalyst) = 60 mg/L, (DMPO) = 50 mM, (TEMP) = 20 mM, initial pH = 6.8.

of leached lanthanum for  $\text{LaCoO}_{3-x}$  and  $\text{La}_2\text{CoO}_{4+\delta}$  material were around 6.1 and 0.7 mg/L, respectively, accounting to about 10.2% and 1.17% of the initial catalyst concentration, respectively. We also tested the BPA removal efficiency using the leaching solution under the same conditions (see supplementary material, Fig. S5). The BPA removal on the homogenous system was less than 5%. This suggests that the catalytic activity mainly results from the heterogeneous  $\text{La}_2\text{CoO}_{4+\delta}$ /PMS system. These results showed that the  $\text{La}_2\text{CoO}_{4+\delta}$  catalyst exhibited high stability and very low cobalt leaching, compared to other cobalt-based catalysts used for BPA removal (Table 1) and further cobalt-based perovskite materials [24,59,60].

### 3.3. Reactive species and possible mechanisms

Many reactive oxygen species such as  $\text{SO}_4^{\cdot-}$ ,  $\cdot\text{OH}$ ,  $^1\text{O}_2$ , and  $\text{SO}_5^-$  may be involved in the reaction of BPA degradation [61].  $\text{SO}_5^-$  is less efficient to oxidize BPA due to its lower oxidation potential (0.81 V) compared to  $\text{SO}_4^{\cdot-}$  [62]. To obtain more detailed information, the contribution of different reactive radicals to BPA degradation was investigated by radical quenching experiments employing  $\text{La}_2\text{CoO}_{4+\delta}$ . Ethanol (EtOH) was used to scavenge both  $\text{SO}_4^{\cdot-}$  and  $\cdot\text{OH}$  with a high quenching rate constant of  $k_{\text{EtOH}/\cdot\text{OH}} = (1.2\text{--}2.8) \times 10^9 \text{ M}^{-1} \text{ s}^{-1}$  and  $k_{\text{EtOH}/\text{SO}_4^{\cdot-}} = (1.6\text{--}7.7) \times 10^9 \text{ M}^{-1} \text{ s}^{-1}$ , while *tert*-butyl alcohol (TBA) was employed to scavenge only  $\cdot\text{OH}$  with a reaction rate constant of  $k_{\text{TBA}/\cdot\text{OH}} = (3.8\text{--}7.6) \times 10^9 \text{ M}^{-1} \text{ s}^{-1}$  [63]. Besides, singlet oxygen ( $^1\text{O}_2$ ) might be generated during PMS activation and can be scavenged by  $\beta$ -carotene with a rate constant of  $k_{\beta\text{-carotene}/^1\text{O}_2} = (2\text{--}3.0) \times 10^{10} \text{ M}^{-1} \text{ s}^{-1}$  [64].

As shown in Fig. 7a, the addition of 0.1 M TBA slightly decreased the removal efficiency of BPA from 97% to 95%, and no significant change was observed with the increase of TBA concentration to 0.5 M. In contrast, the BPA removal with the addition of 0.1 M EtOH was significantly declined to about 58% and even stronger inhibition was observed for higher EtOH concentration (0.5 M). However, the BPA removal inhibited by EtOH is incomplete, suggesting that other reactive radicals may be involved in the reaction of BPA degradation. Singlet oxygen ( $^1\text{O}_2$ ) may also be generated during PMS activation and can be scavenged by  $\beta$ -carotene [64]. It can be seen from Fig. 7a that the addition of 0.5 mM  $\beta$ -carotene declined the BPA removal to about 76%, while the addition of  $\beta$ -carotene together with EtOH decreased the BPA degradation in 30 min from 97% to 6%, confirming that  $^1\text{O}_2$  was also generated in  $\text{La}_2\text{CoO}_{4+\delta}$ /PMS system. The quenching tests imply that  $\text{SO}_4^{\cdot-}$  is the primary active radical in the  $\text{La}_2\text{CoO}_{4+\delta}$ /PMS system.

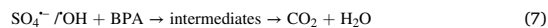
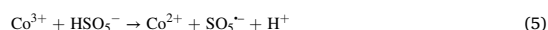
To confirm the generation of reactive radicals from PMS activation, Electron Paramagnetic Resonance (EPR) experiments were conducted using DMPO and TEMP as a radical spin-trapping agent (Fig. 7b). There was no signal peak detected in the presence of PMS alone or of the catalyst alone, indicating that no radicals could be generated with bare PMS and catalyst. However, when  $\text{La}_2\text{CoO}_{4+\delta}$ /PMS were added, characteristic signals for DMPO- $\cdot\text{OH}$  adducts (with hyperfine splitting constants of  $\alpha_{\text{H}} = \alpha_{\text{N}} = 14.8 \text{ G}$ ) and DMPO- $\text{SO}_4^{\cdot-}$  adducts ( $\alpha_{\text{N}} = 13.2 \text{ G}$ ,  $\alpha_{\text{H}} = 9.6 \text{ G}$ ,  $\alpha_{\text{H}} = 1.48 \text{ G}$ ,  $\alpha_{\text{H}} = 0.78 \text{ G}$ ) were observed, confirming that both  $\cdot\text{OH}$  and  $\text{SO}_4^{\cdot-}$  radicals were produced by the  $\text{La}_2\text{CoO}_{4+\delta}$ /PMS system. Thus, we propose that the generation of  $\cdot\text{OH}$  in the  $\text{La}_2\text{CoO}_{4+\delta}$ /PMS system originates from the reaction of  $\text{SO}_4^{\cdot-}$  with the hydroxyl ion (Eq. (2)) or water (Eq. (3)) [65].



Besides, TEMP was selected as the trapping agent to gain more evidence for the generation of the singlet oxygen ( $^1\text{O}_2$ ) by the EPR test. As illustrated in Fig. 7c, the characteristic peak assigned to TEMP- $^1\text{O}_2$  was observed in the  $\text{La}_2\text{CoO}_{4+\delta}$ /PMS system. These results are in good agreement with the quenching experiments, confirming the generation of  $^1\text{O}_2$  in the  $\text{La}_2\text{CoO}_{4+\delta}$ /PMS system.

To further elaborate the mechanism of PMS activation and the roles of La, Co, and O species, the XPS spectra of  $\text{La}_2\text{CoO}_{4+\delta}$  before and after four runs of catalytic experiments were studied. There was no significant change in the La3d spectrum before and after the reaction, suggesting that La is not involved in the PMS activation (see supplementary material, Fig. S6). As depicted in Fig. 8a, the high-resolution Co2p XPS spectra for the fresh and used catalysts can be fitted using five core-level peaks centered at  $\sim 778.2$ , 779.6, 780.4, 781.4, 782.2, and the satellite at  $\sim 786.5 \text{ eV}$ . The binding energies at 780.4 and 782.1 eV can be assigned to  $\text{Co}^{2+}$ , whereas the peak with binding energy positioned at 779.6 eV is assigned to  $\text{Co}^{3+}$  [66]. The shake-up satellite peak located at 786.5 eV indicates the presence of  $\text{Co}^{2+}$  species [66]. While the initial proportions of  $\text{Co}^{3+}/\text{Co}^{2+}/\text{Co}$  were determined as of 40/49/11, they changed to 37/55/8, which indicates the increasing surface concentration of  $\text{Co}^{2+}$  ions, thereby suggesting a redox process  $\text{Co}^{2+} - \text{Co}^{3+} - \text{Co}^{2+}$  at the catalysts' surface. This finding is supported by analyzing the O1s spectra (Fig. 8b). The peaks centered at 528.5, 529.6, 531.2, and 532.3 eV corresponded to oxygen in the lattice ( $\text{O}_{\text{L}}$ ), surface  $\text{O}_2^-/\text{O}^-$ , surface hydroxyl groups (OH), and adsorbed water and carbonates, respectively, and initially accounted for 22, 13, 46, and 19%, respectively [60]. These relative proportions change to 17, 14, 46, and 23% after the catalytic reaction [60]. The decline in the  $\text{O}_{\text{L}}$  can be attributed to the release of oxygen in combination with the reduction of  $\text{Co}^{3+}$  to  $\text{Co}^{2+}$ , suggesting that lattice  $\text{O}_{\text{L}}$  participated in the cobalt redox reaction. The increment of carbonate and water contents can be attributed to the formation of lanthanum carbonate contaminants on the surface of  $\text{La}_2\text{CoO}_{4+\delta}$ .

Based on the above results, a catalysis mechanism of PMS activation by  $\text{La}_2\text{CoO}_{4+\delta}$  is proposed as follows: After the addition of PMS,  $\text{SO}_4^{\cdot-}$  is initially generated by the activation of  $\text{HSO}_5^-$  species on  $\text{La}_2\text{CoO}_{4+\delta}$  (Eq. (4)) and simultaneously some initially generated  $\text{SO}_4^{\cdot-}$  will react with hydroxyl ion or water to generate  $\cdot\text{OH}$  (Eqs. 2–3). These radicals could attack and mineralize the BPA to small organic intermediates and then finally to  $\text{CO}_2$  (Eq. (7)). On the other hand, to keep the charge balance on the  $\text{La}_2\text{CoO}_{4+\delta}$  surface, the lattice oxygen could facilitate the charge transfer to  $\text{Co}^{3+}$  and be released to the system in the form of  $\text{O}_2$  (Eqs. 5–6). Lattice oxygen ions cannot migrate from the bulk to the surface under the atmospheric ambience in the aqueous phase [67,68]. Therefore, the adsorbed oxygen might transform to lattice oxygen due to the high charge and oxygen-ion conductivity [69], which would compensate the surface lattice oxygen to improve catalytic efficiency. Furthermore, since the standard potential value of  $\text{Co}^{2+}/\text{Co}^{3+}$  redox pairs (1.8 V) is higher than that of  $\text{HSO}_5^-/\text{SO}_5^-$  (1.1 V), the reduction of  $\text{Co}^{3+}$  is thermodynamically favorable. Therefore, the regeneration of the catalyst can be achieved by the reverse electron transfer from  $\text{Co}^{3+}$  to  $\text{Co}^{2+}$ .



### 3.4. Effect of reaction parameters on BPA degradation

To select the optimum dosage of  $\text{La}_2\text{CoO}_{4+\delta}$  and PMS concentration, the influence of catalyst dosage and PMS concentration on the BPA removal efficiency was investigated. Moreover, the pH of the medium is one of the important factors for the catalytic stability of  $\text{La}_2\text{CoO}_{4+\delta}$ . Thus, different initial pH values, as well as the effect of the inorganic anions in the process of PMS oxidation, were also investigated as a basis for a practical application of the  $\text{La}_2\text{CoO}_{4+\delta}$  catalyst.

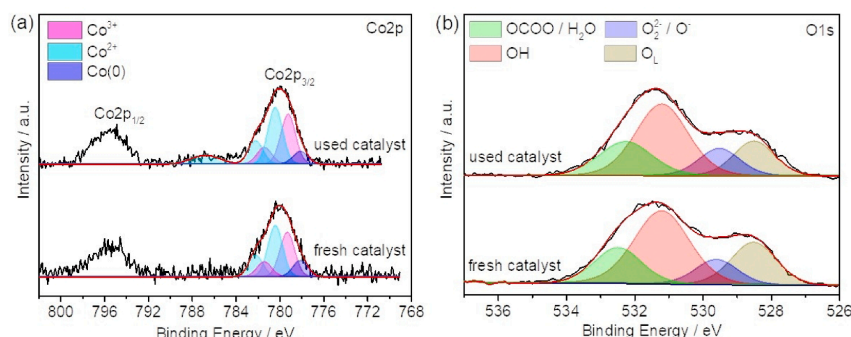
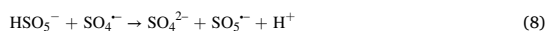


Fig. 8. XPS spectra of (a) Co2p and (b) O1s for fresh and used  $\text{La}_2\text{CoO}_{4+\delta}$  materials.

#### 3.4.1. Effect of catalyst dose and PMS concentration

Not surprisingly, as depicted in Fig. 9a,  $k_{app}$  was enhanced from  $0.046 \text{ min}^{-1}$  to  $0.19 \text{ min}^{-1}$  when the  $\text{La}_2\text{CoO}_{4+\delta}$  loading was increased from between 0.03 and 0.24 g/L. We attribute this to an increasing number of active sites on the surface of  $\text{La}_2\text{CoO}_{4+\delta}$  which are accessible for PMS activation and thus generating more active radicals. The  $k_{app}$  also was increased as the PMS concentration was raised from 0.25 to 2 mM (Fig. 9b), however, it decreased in the case of overdose (4 mM), which was most likely due to the scavenging of  $\text{SO}_4^{\cdot-}$  by the excessive  $\text{HSO}_5^-$  (Eq. (8)) [70].



#### 3.4.2. Effect of initial pH

The initial pH of the reaction solution is also a significant parameter for PMS activation that can affect the interfacial interactions between the catalyst and PMS and is studied in the process of PMS oxidation. Fig. 9c displays the influence of initial pH on BPA removal in the  $\text{La}_2\text{CoO}_{4+\delta}$ /PMS system. It is obvious that the BPA was almost degraded within 30 min over a pH of 5.0 to 8.8. However, when the initial pH of the solution was adjusted to 3.3 and 10.6, the BPA removal efficiency decreased to 50 and 89%, respectively. Since the  $\text{pK}_{a1}$  of PMS is 0 and  $\text{pK}_{a2}$  is 9.4, PMS mainly exists as  $\text{HSO}_5^-$  in the pH range of 0–9.4. The  $\text{pH}_{pzc}$  (pH at the point of zero charges) of  $\text{La}_2\text{CoO}_{4+\delta}$  is determined at around 9.5 (see supplementary material, Fig. S7). Accordingly, when pH is higher than 9.4,  $\text{SO}_5^{2-}$  would replace  $\text{HSO}_5^-$ , which reduces the amount of active reactive species and therefore diminishing the  $\text{La}_2\text{CoO}_{4+\delta}$ /PMS efficiency [71]. Moreover, the electrostatic repulsion interactions between negatively charged  $\text{La}_2\text{CoO}_{4+\delta}$  and PMS species would slow the activation efficiency of PMS, thus the removal efficiency of BPA is reduced. At strong acidic conditions (pH = 3.5), a large number of hydrogen ions  $\text{H}^+$  attached to  $\text{HSO}_5^-$  and form a hydrogen bond, which is unfavorable for the interaction between  $\text{La}_2\text{CoO}_{4+\delta}$  and PMS species. Furthermore, lower pH can result in the leaching of cobalt ions into the solution, resulting in a decrease in the number of catalytic sites (Fig. 9d). The concentration of leached cobalt ions in the acidic solution (pH = 3.5) is 0.8 mg/L and decreased to 0.04 mg/L at pH = 6.8. Therefore, BPA removal efficiency declined significantly at acidic conditions (pH = 3.5).

#### 3.4.3. Effect of co-existing ions

The effect of various anions relevant in aqueous systems (such as  $\text{Cl}^-$ ,  $\text{NO}_3^-$ ,  $\text{H}_2\text{PO}_4^-$ ,  $\text{HCO}_3^-$ , etc.) on the degradation of BPA in  $\text{La}_2\text{CoO}_{4+\delta}$ /PMS was also investigated and is shown in Fig. 9e. Compared to the  $\text{La}_2\text{CoO}_{4+\delta}$ /PMS system, the addition of  $\text{NO}_3^-$  anion did not have a significant impact on BPA degradation. Moreover,  $\text{H}_2\text{PO}_4^-$  and  $\text{HCO}_3^-$

anions exerted an inhibitory effect on BPA degradation while the  $\text{Cl}^-$  anions accelerated the BPA degradation. In the presence of  $\text{H}_2\text{PO}_4^-$ , the degradation of BPA was reduced due to the formation of complex compounds of phosphate-Co during the PMS oxidation system (see supplementary material, Fig. S8), which deactivate the catalytic reactive sites. However,  $\text{HCO}_3^-$  exhibited an inhibitory effect on BPA removal higher than the inhibition caused by  $\text{H}_2\text{PO}_4^-$ . This negative influence might be due to the scavenging effect of  $\text{SO}_4^{\cdot-}$  and  $\cdot\text{OH}$  by  $\text{HCO}_3^-$  in the solution (Eqs. 9–10), which can lead to a decrease in the performance of BPA degradation.



Low concentrations of  $\text{Cl}^-$  (0.01–0.03 M) had a slight inhibitory effect on BPA degradation (see supplementary material, Fig. S9), which may be ascribed to the reaction of  $\text{Cl}^-$  with  $\text{SO}_4^{\cdot-}$  (Eqs. 11–12), producing radicals with lower redox potentials ( $\text{Cl}^{\cdot}$  and  $\text{Cl}_2^{\cdot-}$ ) compared to  $\text{SO}_4^{\cdot-}$ . In contrast, the removal efficiency is enhanced with the addition of  $\text{Cl}^-$  (0.05–0.1 M). The positive influence of  $\text{Cl}^-$  ions on BPA degradation may be ascribed to the generation of a large amount of more effective chlorine species (e.g.  $\text{HOCl}$ ) which participate in BPA degradation because of the reaction with  $\text{HSO}_5^-$  (Eqs. (13)). To further investigate the influence of  $\text{Cl}^-$  on BPA degradation, the catalytic processes in the presence of only PMS were carried out (see supplementary material, Fig. S10). The BPA degradation was significantly enhanced with 0.1 M  $\text{Cl}^-$ , suggest that  $\text{HOCl}$  generated from the reaction of  $\text{Cl}^-$  ions with  $\text{HSO}_5^-$  as a nonradical pathway for BPA degradation. Moreover, the adsorption of BPA with the different  $\text{Cl}^-$  concentrations was also studied (see supplementary material, Fig. S11). 4–6% of BPA was adsorbed by the  $\text{La}_2\text{CoO}_{4+\delta}$  at different  $\text{Cl}^-$  concentrations, indicating that the impact of  $\text{Cl}^-$  on BPA adsorption was almost negligible. Thus, we propose that the accelerated BPA degradation is based on the generation of  $\text{HOCl}$  in the  $\text{La}_2\text{CoO}_{4+\delta}$ /PMS/ $\text{Cl}^-$  system.



#### 3.4.4. Effect of water matrices and different pollutants

The catalytic performance of the  $\text{La}_2\text{CoO}_{4+\delta}$  nanoparticles in degrading different types of organic pollutants is important for its environmental remediation application. Hence, the catalytic activity  $\text{La}_2\text{CoO}_{4+\delta}$  was evaluated with different charge organic pollutants including MB, RhB, and AO7. As shown in Fig. 10a, the removal

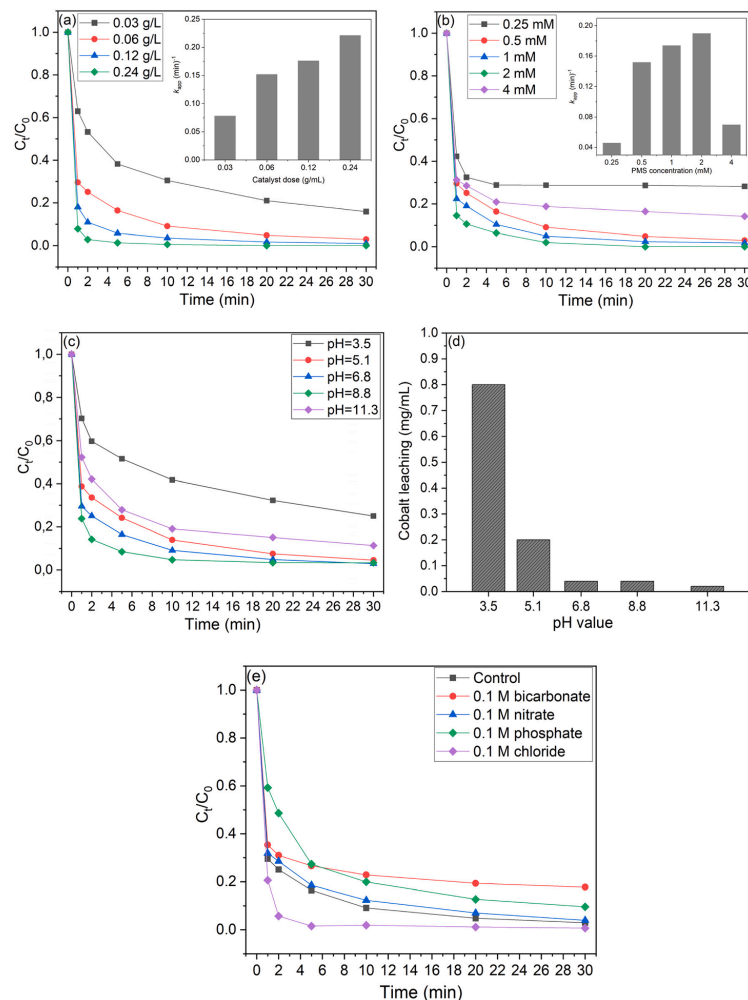


**Fig. 9.** Effects of (a) catalyst loading, (b) PMS dosages, (c) initial pH values and (d) cobalt leaching, and (e) inorganic anions on BPA degradation by  $\text{La}_2\text{CoO}_{4+\delta}/\text{PMS}$ . Reaction conditions: (BPA) = 40 mg/L, (PMS) = 0.5 mM, (Catalyst) = 60 mg/L, initial pH = 6.8.

efficiency of MB, RhB, and AO7 after 30 min was 99%, 90%, and 99%, respectively, proving that the  $\text{La}_2\text{CoO}_{4+\delta}/\text{PMS}$  system could be employed to degrade effectively different kind of organic pollutant. Moreover, to detect the applicability of the  $\text{La}_2\text{CoO}_{4+\delta} + \text{PMS}$  system in real aquatic environments, the effect of various water matrices such as drinking water and tapping water on the catalytic activity of  $\text{La}_2\text{CoO}_{4+\delta}$  was studied. As depicted in Fig. 10b, the removal efficiency of BPA was unremarkably affected in the drinking water sample, whereas the degradation efficiency of BPA was decreased slightly in the tap water sample to 90%. These results suggest that the anions in the water had an insignificant inhibitory effect on the BPA removal.

### 3.5. Possible degradation pathways

To study the degradation pathway of BPA, the degradation intermediates of BPA via the  $\text{La}_2\text{CoO}_{4+\delta}/\text{PMS}$  system were identified by LC-MS (see supplementary material, Fig. S12). According to the mass

spectrometric results (see supplementary material, Table S2), the aromatic and aliphatic intermediates, namely, 2-(4-hydroxyphenyl)-propanol-2-ol, 4-isopropenylphenol, ethanedioic acid, 1,5-hexadiene-3-ol, and trimethylhexane were detected. Mainly, the aromatic ring in BPA is attacked by  $\text{SO}_4^{\cdot-}$  or  $\cdot\text{OH}$  and converted to 2-(4-hydroxyphenyl)-propanol-2-ol [52] and the attack on the tertiary hydroxyl produces 4-isopropenylphenol. Afterwards, the intermediate products were subsequently attacked to form ethanedioic acid, 1,5-hexadiene-3-ol, and trimethylhexane. Finally, the intermediate products were further oxidized and mineralized into  $\text{CO}_2$  and  $\text{H}_2\text{O}$ .

### 4. Conclusions

In summary, we have demonstrated that  $\text{La}_2\text{CoO}_{4+\delta}$  nanoparticles were successfully synthesized via spray-flame synthesis, and applied as novel catalysts for PMS activation. The spray-flame synthesis method has practical advantages such as scalability to produce large amounts of

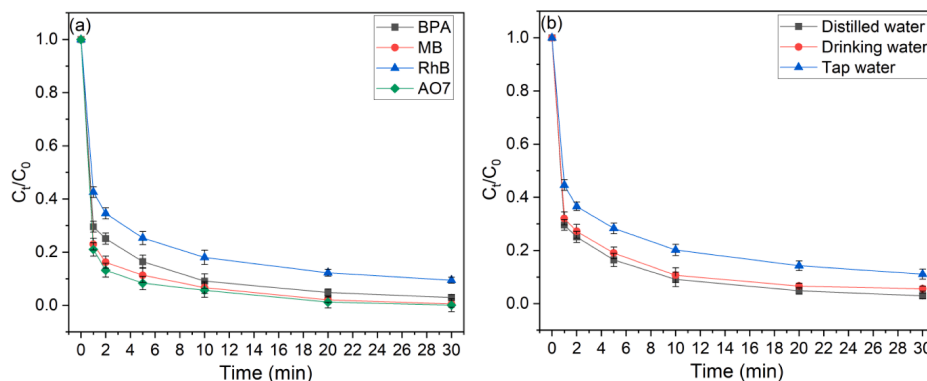


Fig. 10. a) Catalytic activity of  $\text{La}_2\text{CoO}_{4+\delta}$  in the removal of various organics dyes and b) in water matrices.

$\text{La}_2\text{CoO}_{4+\delta}$  nanoparticles in one step without high-temperature annealing, eco-friendliness, and cost-effectivity. Compared to  $\text{LaCoO}_{3-x}$  catalyst,  $\text{La}_2\text{CoO}_{4+\delta}$  nanoparticles exhibit a faster catalytic activity for BPA oxidation and better stability with less cobalt leaching in the presence of PMS. These enhancements were attributed to the lower oxidation state of cobalt, fast regeneration of  $\text{Co}^{2+}$  during PMS activation, and large catalyst particle surface area. Moreover, the removal efficiency maintained 89% after four successive experimental runs. Radicals quenching experiments and electron paramagnetic resonance studies showed that  $\text{SO}_4^{\cdot-}$  played a dominant role during the activation of PMS. In consideration of catalytic activity and costs, this study provides an option to broaden the application of  $\text{La}_2\text{CoO}_{4+\delta}$  catalysts for water treatment by PMS activation.

#### Declaration of Competing Interest

The authors declare that they have no known competing financial interests or personal relationships that could have appeared to influence the work reported in this paper.

#### Appendix A. Supplementary data

Supplementary data to this article can be found online at <https://doi.org/10.1016/j.cej.2021.131447>.

#### References

- [1] C. Erler, J. Novak, Bisphenol A Exposure: Human Risk and Health Policy, *J. Pediatr. Nurs.* 25 (2010) 400–407, <https://doi.org/10.1016/j.pedn.2009.05.006>.
- [2] A. Schechter, N. Malik, D. Haffner, S. Smith, T.R. Harris, O. Paepke, L. Birnbaum, Bisphenol A (BPA) in U.S. Food, *Environ. Sci. Technol.* 44 (24) (2010) 9425–9430, <https://doi.org/10.1021/es102785d>.
- [3] Y. Yoon, P. Westerhoff, S.A. Snyder, E.C. Wert, Nanofiltration and ultrafiltration of endocrine disrupting compounds, pharmaceuticals and personal care products, *J. Memb. Sci.* 270 (2006) 88–100, <https://doi.org/10.1016/j.memsci.2005.06.045>.
- [4] J. Ali, W. Jiang, A. Shahzad, J. Iftikhar, X. Yang, B. Wu, D.T. Oyekunle, W. Jia, Z. Chen, L. Zheng, Z. Chen, Isolated copper ions and surface hydroxyl groups as a function of non-redox metals to modulate the reactivity and persulfate activation mechanism of spinel oxides, *Chem. Eng. J.* 425 (2021), 130679, <https://doi.org/10.1016/j.cej.2021.130679>.
- [5] M. Hammad, P. Fortugno, S. Hardt, C. Kim, S. Salamon, T.C. Schmidt, H. Wende, C. Schulz, H. Wiggers, Large-scale synthesis of iron oxide/graphene hybrid materials as highly efficient photo-Fenton catalyst for water remediation, *Environ. Technol. Innov.* (2020), 101239, <https://doi.org/10.1016/j.eti.2020.101239>.
- [6] S. Guo, H. Wang, W. Yang, H. Fida, L. You, K. Zhou, Scalable synthesis of Ca-doped  $\alpha$ - $\text{Fe}_2\text{O}_3$  with abundant oxygen vacancies for enhanced degradation of organic pollutants through peroxymonosulfate activation, *Appl. Catal. B Environ.* 262 (2020), 118250, <https://doi.org/10.1016/j.apcatb.2019.118250>.
- [7] J. Ali, A. Shahzad, J. Wang, J. Iftikhar, W. Lei, G.G. Aregay, Z. Chen, Z. Chen, Modulating the redox cycles of homogenous Fe(III)/PMS system through constructing electron rich thiomolybdate centres in confined layered double hydroxides, *Chem. Eng. J.* 408 (2021), 127242, <https://doi.org/10.1016/j.cej.2020.127242>.
- [8] Y. Liu, Y. Wang, Q. Wang, J. Pan, J. Zhang, Simultaneous removal of NO and SO<sub>2</sub> using vacuum ultraviolet light (VUV)/heat/peroxymonosulfate (PMS), *Chemosphere.* 190 (2018) 431–441, <https://doi.org/10.1016/j.chemosphere.2017.10.020>.
- [9] Z.-H. Diao, Z.-Y. Lin, X.-Z. Chen, L. Yan, F.-X. Dong, W. Qian, L.-J. Kong, J.-J. Du, W. Chu, Ultrasound-assisted heterogeneous activation of peroxymonosulfate by natural pyrite for 2,4-dichlorophenol degradation in water: Synergistic effects, pathway and mechanism, *Chem. Eng. J.* (2019), 123771, <https://doi.org/10.1016/j.cej.2019.123771>.
- [10] R. Xie, J. Ji, K. Guo, D. Lei, Q. Fan, D.Y.C. Leung, H. Huang, Wet scrubber coupled with UV/PMS process for efficient removal of gaseous VOCs: Roles of sulfate and hydroxyl radicals, *Chem. Eng. J.* 356 (2019) 632–640, <https://doi.org/10.1016/j.cej.2018.09.025>.
- [11] H. Song, L. Yan, Y. Wang, J. Jiang, J. Ma, C. Li, G. Wang, J. Gu, P. Liu, Electrochemically activated PMS and PDS: Radical oxidation versus nonradical oxidation, *Chem. Eng. J.* (2019), 123560, <https://doi.org/10.1016/j.cej.2019.123560>.
- [12] B. Bouzayani, E. Rosales, M. Pazos, S.C. Elaoud, M.A. Sanromán, Homogeneous and heterogeneous peroxymonosulfate activation by transition metals for the degradation of industrial leather dye, *J. Clean. Prod.* 228 (2019) 222–230, <https://doi.org/10.1016/j.jclepro.2019.04.217>.
- [13] G.P. Anipsitakis, D.D. Dionysiou, Radical Generation by the Interaction of Transition Metals with Common Oxidants, *Environ. Sci. Technol.* 38 (13) (2004) 3705–3712, <https://doi.org/10.1021/es035121o>.
- [14] F.J. Rivas, O. Gimeno, T. Borralho, Aqueous pharmaceutical compounds removal by potassium monopersulfate. Uncatalyzed and catalyzed semicontinuous experiments, *Chem. Eng. J.* 192 (2012) 326–333, <https://doi.org/10.1016/j.cej.2012.03.055>.
- [15] J. Wang, S. Wang, Activation of persulfate (PS) and peroxymonosulfate (PMS) and application for the degradation of emerging contaminants, *Chem. Eng. J.* 334 (2018) 1502–1517, <https://doi.org/10.1016/j.cej.2017.11.059>.
- [16] E. Saputra, S. Muhammad, H. Sun, H.-M. Ang, M.O. Tadé, S. Wang, A comparative study of spinel structured  $\text{Mn}_3\text{O}_4$ ,  $\text{Co}_3\text{O}_4$  and  $\text{Fe}_3\text{O}_4$  nanoparticles in catalytic oxidation of phenolic contaminants in aqueous solutions, *J. Colloid Interface Sci.* 407 (2013) 467–473, <https://doi.org/10.1016/j.jcis.2013.06.061>.
- [17] Y. Yao, Y. Cai, G. Wu, F. Wei, X. Li, H. Chen, S. Wang, Sulfate radicals induced from peroxymonosulfate by cobalt manganese oxides ( $\text{CoMn}_3\text{-xO}_4$ ) for Fenton-Like reaction in water, *J. Hazard. Mater.* 296 (2015) 128–137, <https://doi.org/10.1016/j.jhazmat.2015.04.014>.
- [18] A. Jawad, J. Lang, Z. Liao, A. Khan, J. Iftikhar, Z. Lv, S. Long, Z. Chen, Z. Chen, Activation of persulfate by  $\text{CuOx}/\text{Co-LDH}$ : A novel heterogeneous system for contaminant degradation with broad pH window and controlled leaching, *Chem. Eng. J.* 335 (2018) 548–559, <https://doi.org/10.1016/j.cej.2017.10.097>.
- [19] J.C. Espinosa, P. Manickam-Periyaraman, F. Bernat-Quesada, S. Sivanesan, M. Álvaro, H. García, S. Navalon, Engineering of activated carbon surface to enhance the catalytic activity of supported cobalt oxide nanoparticles in peroxymonosulfate activation, *Appl. Catal. B Environ.* 249 (2019) 42–53, <https://doi.org/10.1016/j.apcatb.2019.02.043>.
- [20] J. Zhu, H. Li, L. Zhong, P. Xiao, X. Xu, X. Yang, Z. Zhao, J. Li, Perovskite Oxides: Preparation, Characterizations, and Applications in Heterogeneous Catalysis, *ACS Catal.* 4 (9) (2014) 2917–2940, <https://doi.org/10.1021/cs500606g>.
- [21] K.-Y.-A. Lin, Y.-C. Chen, Y.-F. Lin,  $\text{LaMO}_3$  perovskites ( $\text{M}=\text{Co}$ ,  $\text{Cu}$ ,  $\text{Fe}$  and  $\text{Ni}$ ) as heterogeneous catalysts for activating peroxymonosulfate in water, *Chem. Eng. Sci.* 160 (2017) 96–105, <https://doi.org/10.1016/j.ces.2016.11.017>.
- [22] X. Pang, Y. Guo, Y. Zhang, B. Xu, F. Qi,  $\text{LaCoO}_3$  perovskite oxide activation of peroxymonosulfate for aqueous 2-phenyl-5-sulfobenzimidazole degradation: Effect of synthetic method and the reaction mechanism, *Chem. Eng. J.* 304 (2016) 897–907, <https://doi.org/10.1016/j.cej.2016.07.027>.

M. Hammad et al.

Chemical Engineering Journal 429 (2022) 131447

- [23] P. Liang, D. Meng, Y. Liang, Z. Wang, C. Zhang, S. Wang, Z. Zhang, Cation deficiency tuned LaCoO<sub>3</sub>- $\delta$  perovskite for peroxymonosulfate activation towards bisphenol A degradation, *Chem. Eng. J.* 409 (2021), 128196, <https://doi.org/10.1016/j.cej.2020.128196>.
- [24] X. Duan, C. Su, J. Miao, Y. Zhong, Z. Shao, S. Wang, H. Sun, Insights into perovskite-catalyzed peroxymonosulfate activation: Maneuverable cobalt sites for promoted evolution of sulfate radicals, *Appl. Catal. B Environ.* 220 (2018) 626–634, <https://doi.org/10.1016/j.apcatb.2017.08.088>.
- [25] Y. Takeda, R. Kanno, M. Sakano, O. Yamamoto, M. Takano, Y. Bando, H. Akinaga, K. Takita, J.B. Goodenough, Crystal chemistry and physical properties of La<sub>2-x</sub>Sr<sub>x</sub>NiO<sub>4</sub> (0  $\leq$  x  $\leq$  1.6), *Mater. Res. Bull.* 25 (1990) 293–306, [https://doi.org/10.1016/0025-5408\(90\)90100-G](https://doi.org/10.1016/0025-5408(90)90100-G).
- [26] S.D. Peter, E. Garbowski, N. Guilhaume, V. Perrichon, M. Primet, Catalytic properties of La<sub>2</sub>CuO<sub>4</sub> in the CO + NO reaction, *Catal. Letters.* 54 (1998) 79–84, <https://doi.org/10.1023/A:1019063502409>.
- [27] Y. Huan, S. Chen, R. Zeng, T. Wei, D. Dong, X. Hu, Y. Huang, Intrinsic Effects of Ruddlesden-Popper-Based Bifunctional Catalysts for High-Temperature Oxygen Reduction and Evolution, *Adv. Energy Mater.* 9 (2019) 1901573, <https://doi.org/10.1002/aem.201901573>.
- [28] T. Oshima, T. Yokoi, M. Eguchi, K. Maeda, Synthesis and photocatalytic activity of K<sub>2</sub>CaNaNb<sub>3</sub>O<sub>10</sub>, a new Ruddlesden-Popper phase layered perovskite, *Dalt. Trans.* 46 (32) (2017) 10594–10601, <https://doi.org/10.1039/C6DT04872B>.
- [29] J. Zhu, Z. Zhao, D. Xiao, J. Li, X. Yang, Y. Wu, C.O. Oxidation, N.O. Decomposition, and NO + CO Reduction over Perovskite-like Oxides La<sub>2</sub>CuO<sub>4</sub> and La<sub>2-x</sub>Sr<sub>x</sub>CuO<sub>4</sub>: An MS–TPD Study, *Ind. Eng. Chem. Res.* 44 (2005) 4227–4233, <https://doi.org/10.1021/ie050317d>.
- [30] R.P. Forstlund, C.T. Alexander, A.M. Abakumov, K.P. Johnston, K.J. Stevenson, Enhanced Electrochemical Activities by Substitutional Tuning of Nickel-Based Ruddlesden-Popper Catalysts for the Oxidation of Urea and Small Alcohols, *ACS Catal.* 9 (3) (2019) 2664–2673, <https://doi.org/10.1021/acscatal.8b04103.1021/acscatal.8b04103.s001>.
- [31] J. Choi, S. Park, H. Han, M. Kim, M. Park, J. Han, W.B. Kim, Highly efficient CO<sub>2</sub> electrolysis to CO on Ruddlesden-Popper perovskite oxide with in situ exsolved Fe nanoparticles, *J. Mater. Chem. A* 9 (13) (2021) 8740–8748, <https://doi.org/10.1039/D0TA11328J>.
- [32] H. Chen, Y. Xu, K. Zhu, H. Zhang, Understanding oxygen-deficient La<sub>2</sub>CuO<sub>4</sub>- $\delta$  perovskite activated peroxymonosulfate for bisphenol A degradation: The role of localized electron within oxygen vacancy, *Appl. Catal. B Environ.* 284 (2021), 119732, <https://doi.org/10.1016/j.apcatb.2020.119732>.
- [33] S. Ortatah, J. Ternieden, C. Weidenthaler, Low Temperature Formation of Ruddlesden-Popper-Type Layered La<sub>2</sub>CoO<sub>4</sub> $\pm\delta$  Perovskite Monitored via In Situ X-ray Powder Diffraction, *Eur. J. Inorg. Chem.* 2018 (2018) 5238–5245, <https://doi.org/10.1002/eqic.201801162>.
- [34] X.-K. Gu, E. Nikolla, Design of Ruddlesden-Popper Oxides with Optimal Surface Oxygen Exchange Properties for Oxygen Reduction and Evolution, *ACS Catal.* 7 (9) (2017) 5912–5920, <https://doi.org/10.1021/acscatal.7b01483.1021/acscatal.7b01483.s001>.
- [35] S.-Y. Jeon, M.-B. Choi, H.-N. Im, J.-H. Hwang, S.-J. Song, Oxygen ionic conductivity of La<sub>2</sub>NiO<sub>4</sub>- $\delta$  via interstitial oxygen defect, *J. Phys. Chem. Solids* 73 (2012) 656–660, <https://doi.org/10.1016/j.jpcs.2012.01.006>.
- [36] J. Guo, H. Lou, Y. Zhu, X. Zheng, La-based perovskite precursors preparation and its catalytic activity for CO<sub>2</sub> reforming of CH<sub>4</sub>, *Mater. Lett.* 57 (2003) 4450–4455, [https://doi.org/10.1016/S0167-577X\(03\)00341-0](https://doi.org/10.1016/S0167-577X(03)00341-0).
- [37] C. Jeong, J.-H. Lee, M. Park, J. Hong, H. Kim, J.-W. Son, J.-H. Lee, B.-K. Kim, K. J. Yoon, Design and processing parameters of La<sub>2</sub>NiO<sub>4</sub>- $\delta$ -based cathode for anode-supported planar solid oxide fuel cells (SOFCs), *J. Power Sources* 297 (2015) 370–378, <https://doi.org/10.1016/j.jpowsour.2015.08.023>.
- [38] X. Weng, P. Boldrin, I. Abrahams, S.J. Skinner, J.A. Darr, Direct Syntheses of Mixed Ion and Electronic Conductors La<sub>4</sub>Ni<sub>3</sub>O<sub>10</sub> and La<sub>3</sub>Ni<sub>2</sub>O<sub>7</sub> from Nanosized Coprecipitates, *Chem. Mater.* 19 (18) (2007) 4382–4384, <https://doi.org/10.1021/cm070134c.1021/cm070134c.s001.10.1021/cm070134c.s002>.
- [39] S.J. Kim, T. Akbay, J. Matsuda, A. Takagaki, T. Ishihara, Strain Effects on Oxygen Reduction Activity of Pr<sub>2</sub>NiO<sub>4</sub> Caused by Gold Bulk Dispersion for Low Temperature Solid Oxide Fuel Cells, *ACS Appl. Energy Mater.* 2 (2) (2019) 1210–1220, <https://doi.org/10.1021/acsaem.8b01776.1021/acsaem.8b01776.s001>.
- [40] D. Waffel, B. Alkan, Q.i. Fu, Y.-T. Chen, S. Schmidt, C. Schulz, H. Wiggers, M. Muhler, B. Peng, Towards Mechanistic Understanding of Liquid-Phase Cinnamyl Alcohol Oxidation with tert-Butyl Hydroperoxide over Noble-Metal-Free LaCo<sub>1-x</sub>FexO<sub>3</sub> Perovskites, *Chempluschem* 84 (8) (2019) 1155–1163, <https://doi.org/10.1002/cplu.v84.8.1002/cplu.201900429>.
- [41] S. Angel, J. Neises, M. Dreyer, K. Friedel Ortega, M. Behrens, Y. Wang, H. Arandiyán, C. Schulz, H. Wiggers, Spray-flame synthesis of La(Fe, Co)O<sub>3</sub> nanoperovskites from metal nitrates, *AIChE J.* 66 (1) (2020), <https://doi.org/10.1002/aic.v66.1.1002/aic.16748>.
- [42] B. Alkan, S. Cychy, S. Varhade, M. Muhler, C. Schulz, W. Schuhmann, H. Wiggers, C. Andronescu, Spray-Flame-Synthesized LaCo<sub>1-x</sub>FexO<sub>3</sub> Perovskite Nanoparticles as Electrocatalysts for Water and Ethanol Oxidation, *ChemElectroChem* 6 (16) (2019) 4266–4274, <https://doi.org/10.1002/celec.v6.16.1002/celec.201900168>.
- [43] F. Schneider, S. Suleiman, J. Menser, E. Borukhovich, I. Wlokas, A. Kempf, H. Wiggers, C. Schulz, SpraySyn—A standardized burner configuration for nanoparticle synthesis in spray flames, *Rev. Sci. Instrum.* 90 (8) (2019) 085108, <https://doi.org/10.1063/1.5090232>.
- [44] A. Grimaud, F. Mauvy, J.M. Bassat, S. Fourcade, L. Rocheron, M. Marrony, J. C. Grenier, Hydration Properties and Rate Determining Steps of the Oxygen Reduction Reaction of Perovskite-Related Oxides as H<sub>2</sub>-SOFC Cathodes, *J. Electrochem. Soc.* 159 (6) (2012) B683–B694, <https://doi.org/10.1149/2.101205jes>.
- [45] L. Armelao, M. Bettinelli, G. Bottaro, D. Barreca, E. Tondello, LaCoO<sub>3</sub> Nanopowders by XPS, *Surf. Sci. Spectra.* 8 (1) (2001) 24–31, <https://doi.org/10.1116/11.20010701>.
- [46] M.C. Biesinger, B.P. Payne, A.P. Grosvenor, L.W.M. Lau, A.R. Gerson, R.S.C. Smart, Resolving surface chemical states in XPS analysis of first row transition metals, oxides and hydroxides: Cr, Mn, Fe, Co and Ni, *Appl. Surf. Sci.* 257 (2011) 2717–2730, <https://doi.org/10.1016/j.apusc.2010.10.051>.
- [47] P.H.T. Ngamou, K. Kohse-Höinghaus, N. Bahlawane, CO and ethanol oxidation over LaCoO<sub>3</sub> planar model catalysts: Effect of the thickness, *Catal. Commun.* 12 (2011) 1344–1350, <https://doi.org/10.1016/j.catcom.2011.04.029>.
- [48] S. Pegoraro, M.M. Natile, A. Galenda, A. Glisenti, La<sub>2</sub>CuO<sub>4</sub>Co<sub>0.2</sub>O<sub>4</sub>+ $\delta$  by Pechini Method, *Surf. Sci. Spectra.* 16 (1) (2009) 75–82, <https://doi.org/10.1116/11.20090201>.
- [49] X. Duan, C. Su, L. Zhou, H. Sun, A. Suvorova, T. Odedairo, Z. Zhu, Z. Shao, S. Wang, Surface controlled generation of reactive radicals from persulfate by carbocatalysis on nanodiamonds, *Appl. Catal. B Environ.* 194 (2016) 7–15, <https://doi.org/10.1016/j.apcatb.2016.04.043>.
- [50] L. Wu, Y. Yu, Q. Zhang, J. Hong, J. Wang, Y. She, A novel magnetic heterogeneous catalyst oxygen-defective CoFe<sub>2</sub>O<sub>4</sub>-x for activating peroxymonosulfate, *Appl. Surf. Sci.* 480 (2019) 717–726, <https://doi.org/10.1016/j.apusc.2019.03.034>.
- [51] Y. Liu, R. Luo, Y. Li, J. Qi, C. Wang, J. Li, X. Sun, L. Wang, Sandwich-like Co<sub>3</sub>O<sub>4</sub>/MXene composite with enhanced catalytic performance for Bisphenol A degradation, *Chem. Eng. J.* 347 (2018) 731–740, <https://doi.org/10.1016/j.cej.2018.04.155>.
- [52] X. Li, Z. Wang, B. Zhang, A.I. Rykov, M.A. Ahmed, J. Wang, Fe<sub>3</sub>Co<sub>3</sub>-xO<sub>4</sub> nanocages derived from nanoscale metal-organic frameworks for removal of bisphenol A by activation of peroxymonosulfate, *Appl. Catal. B Environ.* 181 (2016) 788–799, <https://doi.org/10.1016/j.apcatb.2015.08.050>.
- [53] X. Li, A.I. Rykov, B.o. Zhang, Y. Zhang, J. Wang, Graphene encapsulated Fe<sub>3</sub>Co<sub>3</sub> nanocages derived from metal-organic frameworks as efficient activators for peroxymonosulfate, *Catal. Sci. Technol.* 6 (20) (2016) 7486–7494, <https://doi.org/10.1039/C6CY01479FH>.
- [54] C. Wang, H. Wang, R. Luo, C. Liu, J. Li, X. Sun, J. Shen, W. Han, L. Wang, Metal-organic framework one-dimensional fibers as efficient catalysts for activating peroxymonosulfate, *Chem. Eng. J.* 330 (2017) 262–271, <https://doi.org/10.1016/j.cej.2017.07.156>.
- [55] L. Hu, G. Zhang, Q. Wang, Y. Sun, M. Liu, P. Wang, Facile synthesis of novel Co<sub>3</sub>O<sub>4</sub>-Bi<sub>2</sub>O<sub>3</sub> catalysts and their catalytic activity on bisphenol A by peroxymonosulfate activation, *Chem. Eng. J.* 326 (2017) 1095–1104, <https://doi.org/10.1016/j.cej.2017.05.168>.
- [56] R. Luo, C. Liu, J. Li, C. Wang, X. Sun, J. Shen, W. Han, L. Wang, Convenient synthesis and engineering of ultrafine Co<sub>3</sub>O<sub>4</sub>-incorporated carbon composite: towards practical application of environmental remediation, *J. Mater. Chem. A* 6 (8) (2018) 3454–3461, <https://doi.org/10.1039/C7TA11052A>.
- [57] X. Zhang, C. He, L. Wang, J. Liu, M. Deng, Q. Feng, Non-isothermal kinetic analysis of thermal dehydration of La<sub>2</sub>(CO<sub>3</sub>)<sub>3</sub>-3.4H<sub>2</sub>O in air, *Trans. Nonferrous Met. Soc. China* 24 (2014) 3378–3385, [https://doi.org/10.1016/S1003-6326\(14\)63480-4](https://doi.org/10.1016/S1003-6326(14)63480-4).
- [58] M. Dreyer, M. Krebs, S. Najafshirazi, A. Rabe, K. Friedel Ortega, M. Behrens, The Effect of Co Incorporation on the CO Oxidation Activity of LaFe<sub>1-x</sub>CoxO<sub>3</sub> Perovskites, *Catal.* 11 (5) (2021) 550, <https://doi.org/10.3390/catal11050550>.
- [59] S. Lu, G. Wang, S. Chen, H. Yu, F. Ye, X. Quan, Heterogeneous activation of peroxymonosulfate by LaCo<sub>1-x</sub>CuxO<sub>3</sub> perovskites for degradation of organic pollutants, *J. Hazard. Mater.* 353 (2018) 401–409, <https://doi.org/10.1016/j.jhazmat.2018.04.021>.
- [60] C. Su, X. Duan, J. Miao, Y. Zhong, W. Zhou, S. Wang, Z. Shao, Mixed Conducting Perovskite Materials as Superior Catalysts for Fast Aqueous-Phase Advanced Oxidation: A Mechanistic Study, *ACS Catal.* 7 (1) (2017) 388–397, <https://doi.org/10.1021/acscatal.6b02303.1021/acscatal.6b02303.s001>.
- [61] X. Tian, P. Gao, Y. Nie, C. Yang, Z. Zhou, Y. Li, Y. Wang, A novel singlet oxygen involved peroxymonosulfate activation mechanism for degradation of ofloxacin and phenol in water, *Chem. Commun.* 53 (49) (2017) 6589–6592, <https://doi.org/10.1039/C7CC02820B>.
- [62] P. Neta, R.E. Huie, A.B. Ross, Rate Constants for Reactions of Inorganic Radicals in Aqueous Solution, *J. Phys. Chem. Ref. Data.* 17 (3) (1988) 1027–1284, <https://doi.org/10.1063/1.555808>.
- [63] G.P. Anipsitakis, D.D. Dionysiou, Degradation of Organic Contaminants in Water with Sulfate Radicals Generated by the Conjunction of Peroxymonosulfate with Cobalt, *Environ. Sci. Technol.* 37 (20) (2003) 4790–4797, <https://doi.org/10.1021/es0263792>.
- [64] R. Luo, M. Li, C. Wang, M. Zhang, M.A. Nasir Khan, X. Sun, J. Shen, W. Han, L. Wang, J. Li, Singlet oxygen-dominated non-radical oxidation process for efficient degradation of bisphenol A under high salinity condition, *Water Res.* 148 (2019) 416–424, <https://doi.org/10.1016/j.watres.2018.10.087>.
- [65] X. Dong, B. Ren, Z. Sun, C. Li, X. Zhang, M. Kong, S. Zheng, D.D. Dionysiou, Monodispersed CuFe<sub>2</sub>O<sub>4</sub> nanoparticles anchored on natural kaolinite as highly efficient peroxymonosulfate catalyst for bisphenol A degradation, *Appl. Catal. B Environ.* 253 (2019) 206–217, <https://doi.org/10.1016/j.apcatb.2019.04.052>.
- [66] A.F. Lucrédio, G.T. Filho, E.M. Assaf, Co/Mg/Al hydrotalcite-type precursor, promoted with La and Ce, studied by XPS and applied to methane steam reforming reactions, *Appl. Surf. Sci.* 255 (2009) 5851–5856, <https://doi.org/10.1016/j.apusc.2009.01.020>.
- [67] Z. Shao, S.M. Haile, A high-performance cathode for the next generation of solid-oxide fuel cells, *Nature* 431 (7005) (2004) 170–173, <https://doi.org/10.1038/nature02863>.

M. Hammad et al.

Chemical Engineering Journal 429 (2022) 131447

- [68] S. Baumann, F. Schulze-Küppers, S. Roitsch, M. Betz, M. Zwick, E.M. Pfaff, W. A. Meulenber, J. Mayer, D. Stöver, Influence of sintering conditions on microstructure and oxygen permeation of Ba<sub>0.5</sub>Sr<sub>0.5</sub>Co<sub>0.8</sub>Fe<sub>0.2</sub>O<sub>3-δ</sub> (BSCF) oxygen transport membranes, *J. Memb. Sci.* 359 (2010) 102–109, <https://doi.org/10.1016/j.memsci.2010.02.002>.
- [69] M.M. Kuklja, E.A. Kotomin, R. Merkle, Y.A. Mastrikov, J. Maier, Combined theoretical and experimental analysis of processes determining cathode performance in solid oxide fuel cells, *Phys. Chem. Chem. Phys.* 15 (2013) 5443–5471, <https://doi.org/10.1039/C3CP44363A>.
- [70] Y. Huang, C. Han, Y. Liu, M.N. Nadagouda, L. Machala, K.E. O'Shea, V.K. Sharma, D.D. Dionysiou, Degradation of atrazine by ZnxCu<sub>1-x</sub>Fe<sub>2</sub>O<sub>4</sub> nanomaterial-catalyzed sulfite under UV-vis light irradiation: Green strategy to generate SO<sub>4</sub><sup>-•</sup>, *Appl. Catal. B Environ.* 221 (2018) 380–392, <https://doi.org/10.1016/j.apcatb.2017.09.001>.
- [71] Y. Feng, P.-H. Lee, D. Wu, K. Shih, Surface-bound sulfate radical-dominated degradation of 1,4-dioxane by alumina-supported palladium (Pd/Al<sub>2</sub>O<sub>3</sub>) catalyzed peroxymonosulfate, *Water Res.* 120 (2017) 12–21, <https://doi.org/10.1016/j.watres.2017.04.070>.



3.1.2.2 LaCoO<sub>3</sub>/Graphene Nanoparticles

Chemical Engineering Journal 454 (2023) 139900



Contents lists available at ScienceDirect

Chemical Engineering Journal

journal homepage: [www.elsevier.com/locate/cej](http://www.elsevier.com/locate/cej)

## Synthesis of novel LaCoO<sub>3</sub>/graphene catalysts as highly efficient peroxymonosulfate activator for the degradation of organic pollutants

Mohaned Hammad<sup>a,\*</sup>, Steven Angel<sup>c</sup>, Ahmed K. Al-Kamal<sup>c,8</sup>, Anam Asghar<sup>b</sup>, Amin Said Amin<sup>a</sup>, Mena-Alexander Kräenbring<sup>a</sup>, Haakon T.A. Wiedemann<sup>d</sup>, Vineetha Vinayakumar<sup>a</sup>, Md Yusuf Ali<sup>c</sup>, Paolo Fortugno<sup>c</sup>, Cheolyong Kim<sup>b</sup>, Torsten C. Schmidt<sup>b</sup>, Christopher W.M. Kay<sup>d,f</sup>, Christof Schulz<sup>c,e</sup>, Doris Segets<sup>a,e,\*</sup>, Hartmut Wiggers<sup>c,e,\*</sup>

<sup>a</sup> Institute for Combustion and Gas Dynamics – Particle Science and Technology (IVG-PST), University of Duisburg-Essen, Duisburg, Germany

<sup>b</sup> Instrumental Analytical Chemistry and Centre for Water and Environmental Research, University of Duisburg-Essen, Essen, Germany

<sup>c</sup> Institute for Combustion and Gas Dynamics – Reactive Fluids (IVG-RF), University of Duisburg-Essen, Duisburg, Germany

<sup>d</sup> Department of Chemistry, Saarland University, Saarbrücken, Germany

<sup>e</sup> Center for Nanointegration Duisburg-Essen (CENIDE), University of Duisburg-Essen, Duisburg, Germany

<sup>f</sup> London Centre for Nanotechnology, University College London, 17-19 Gordon Street, London WC1H 0AH, United Kingdom

<sup>8</sup> Department of Materials Engineering, University of Al-Mustansiriyah, Baghdad, Iraq

## ARTICLE INFO

## Keywords:

Bisphenol A  
Gas-phase synthesis  
Graphene  
Heterogeneous catalysis  
Peroxymonosulfate

## ABSTRACT

Metal leaching in perovskite-based catalysts during peroxymonosulfate activation processes can severely restrict their application in wastewater treatment. Therefore, enhancing the stability of perovskite nanostructures is crucial to improve catalytic performance and broaden applications but has been rarely achieved so far. We developed a scalable method to synthesize novel stable and environmentally-friendly nanocomposites of LaCoO<sub>3</sub> and few-layer graphene (consisting of roughly-nine layers) for the removal of organic pollutants from wastewater. With abundant oxygen vacancies and synergistic effects between LaCoO<sub>3</sub> and few-layer graphene, the novel LaCoO<sub>3</sub>/graphene catalyst exhibits outstanding catalytic degradation (>99 %) of diclofenac, metoprolol, carbamazepine, and bisphenol A at a high concentration (40 mg/l) in less than 10 min in the peroxymonosulfate activation system, with mineralization of 57, 55, 61, and 62 %, respectively. The LaCoO<sub>3</sub>/graphene catalyst exhibited excellent reusability and high catalytic performance within a wide pH range (3–11). The formation of LaCoO<sub>3</sub>/graphene composites prevents cobalt leaching (0.004 mg/l), stabilizes sub-stoichiometric LaCoO<sub>3</sub> and thus increases the content of Co<sup>2+</sup> in the structure, leading to much higher catalytic activity than that of pure LaCoO<sub>3</sub>. Electron paramagnetic resonance and radical quenching experiments revealed that both radical pathways (SO<sub>4</sub><sup>-•</sup>, <sup>•</sup>OH, and O<sub>2</sub><sup>-•</sup>) and non-radical pathways (<sup>1</sup>O<sub>2</sub>) contribute to bisphenol A degradation and the relative contributions of <sup>•</sup>OH, SO<sub>4</sub><sup>-•</sup>, and <sup>1</sup>O<sub>2</sub>/O<sub>2</sub><sup>-•</sup> were determined to 13.4, 32.6, and 54 % for bisphenol A removal, respectively. Overall, our results indicate that LaCoO<sub>3</sub>/graphene is a promising material towards peroxymonosulfate activation for environmental remediation.

## 1. Introduction

Trace organic pollutants such as industrial chemicals and personal care and pharmaceutical products discharged into the environment have brought serious threats to nature and humans due to their persistence, toxicity, and bioaccumulation [1,2]. Advanced oxidation processes

(AOPs) are considered a promising technology to degrade organic pollutants [3]. The Fenton reaction is a classical AOP method that utilizes iron ions/salts to activate hydrogen peroxide (H<sub>2</sub>O<sub>2</sub>) and produce hydroxyl radicals (<sup>•</sup>OH, oxidative potential 1.9–2.7 V) at acidic pH (2.5–3.5) [4]. However, the traditional Fenton reaction is inherently limited by the narrow range of the working pH, metal leaching, and

\* Corresponding authors at: Institute for Combustion and Gas Dynamics – Particle Science and Technology (IVG-PST), University of Duisburg-Essen, Duisburg, Germany (M. Hammad, D. Segets). Institute for Combustion and Gas Dynamics – Reactive Fluids, University of Duisburg-Essen (IVG-RF), Duisburg, Germany (H. Wiggers).

E-mail addresses: [mohaned.hammad@uni-due.de](mailto:mohaned.hammad@uni-due.de) (M. Hammad), [doris.segets@uni-due.de](mailto:doris.segets@uni-due.de) (D. Segets), [hartmut.wiggers@uni-due.de](mailto:hartmut.wiggers@uni-due.de) (H. Wiggers).

<https://doi.org/10.1016/j.cej.2022.139900>

Received 25 May 2022; Received in revised form 4 October 2022; Accepted 15 October 2022

Available online 21 October 2022

1385-8947/© 2022 Elsevier B.V. All rights reserved.

M. Hammad et al.

Chemical Engineering Journal 454 (2023) 139900

sludge generation during  $H_2O_2$  activation [5]. In the last decade, sulfate radical-based advanced oxidation processes (SR-AOPs) were developed as promising alternatives to the classical Fenton reaction because of their high oxidative potential (2.5–3.1 V), wide pH adaptability (2–9), and long half-life time (30–40 ms) [6]. In order to generate sulfate radicals, peroxydisulfate (PDS), or peroxymonosulfate (PMS), are used most frequently and activated by heat [7], UV or visible light [8], microwave ultrasound [9], electrochemical processes [10], and transition metal ions (e.g., Co, Mn, Cu, and Fe) [11]. In this regard, different transition metal oxide catalysts such as  $Co_3O_4$ ,  $CuFe_2O_4$ ,  $LaCoO_3$ , etc. [12–14], zero-valent metal [15], and carbon-based materials [16] are reported to activate PMS or PDS in refractory chemical degradation processes. Among them, transition metal-based perovskites such as  $LaCoO_3$  (LCO) nanoparticles have received considerable attention in PMS activation because of their structural flexibility, high electronic conductivity, and their ability to create oxygen vacancies [17,18]. Our recent study reveals that the catalytic activity of LCO nanomaterials is significantly higher than that of  $Co_3O_4$  nanoparticles towards PMS activation for bisphenol A degradation [19]. Furthermore, a previous report shows also that the cobalt-based perovskite,  $Ba_{0.5}Sr_{0.5}Co_{0.8}Fe_{0.2}O_{3-\delta}$ , exhibited better redox potential and electrical conductivity than  $Co_3O_4$  nanoparticles for PMS activation [20].  $LaCoO_3$  has been widely used as catalyst in the field of water and ethanol oxidation [21], cyclohexene oxidation [22], catalytic combustion [23], photocatalysis [24], and heterogeneous Fenton reactions [25]. However, the reusability and toxicity of cobalt-based perovskite due to cobalt leaching in aqueous systems severely impeded their practical application in wastewater treatment. Therefore, fabricating stable and environmentally-friendly cobalt-based solid-state catalysts has attracted increasing interest for PMS activation.

For the synthesis of perovskites, various methods have been explored. These methods are usually grouped into different categories [26,27]. One category is known as solid–solid synthesis, including methods such as microwave, combustion, ceramic, and mechanochemistry synthesis. As these methods are usually followed by extended high-temperature calcination to reach the desired crystallographic phase, the final particles typically provide low specific surface areas – with few exceptions (e.g., activated reactive synthesis [28]). In the quest of phase-pure perovskites with high specific surface areas, liquid-based or solution-mediated synthesis has been also explored. This category includes methods such as sol–gel or Pechini processes, or nanocasting (e.g., using soft or hard templates). Nevertheless, these methods are also associated with high-temperature calcination and result the lack of morphology control [29] (e.g., in sol–gel or Pechini methods) or the need of complex removal of templates (e.g., silica in nanocasting methods) and low yields of material [26]. In contrast to these conventional synthesis routes, spray-flame synthesis of perovskites is a method that enables production of phase-pure and high specific surface area materials in a single step [30,31]. Furthermore, this method allows the use of low-cost precursors (e.g., metal nitrates or chlorides) and facilitates the synthesis of high-quality perovskites in a continuous and scalable way [32].

Recently, researchers have attempted to improve the catalytic activity and stability of catalysts by incorporating catalysts on carbonaceous materials such as carbon [33],  $C_3N_4$  [34], carbon quantum dots [35], and graphene derivatives [36]. Comparing with the above mentioned carbonaceous materials, single and few-layer graphene provides high electrochemical stability and high surface area that can be used as adsorbent support for the decomposition of organic pollutants [37]. Xu et al. reported that graphene revealed an improved adsorption capacity for bisphenol A (82 mg/g at 302.15 K) compared to other carbonaceous materials [38]. Due to their high electron mobility and unique optical properties, graphene/semiconductor nanoparticles-based composites have also shown to possess a high photocatalytic activity [39–41]. As reported in one of our previous works, the high surface area of few-layer graphene and the presence of unpaired  $\pi$  electrons in the

graphene structure facilitate a fast transport of the photo-induced electrons between graphene and  $Fe_3O_4$  [42], which improves the degradation efficiency towards methylene blue. Besides, graphene exhibits exciting properties such as mechanical flexibility, chemical stability, and optical transparency [43]. For instance, Wang et al. demonstrated that the catalytic activity of a  $Co_3O_4$ /graphene hybrid in terms of Orange II degradation was 2.5 times faster compared to that of pure  $Co_3O_4$ . Graphene facilitates the electric conductivity of the composite compared to pure  $Co_3O_4$ , and therefore promotes electron transfer between the catalyst and PMS, resulting in increased sulfate radical ( $SO_4^{\cdot-}$ ) generation [44]. However, to the best of our knowledge, there is no report on the application of  $LaCoO_3$ /graphene (LCO/Gr) in PMS activation. This motivates the development of a new strategy for scalable production of LCO/Gr nanostructures for PMS activation. Usually, the incorporation of cobalt-based catalysts in graphene is achieved by hydrothermal [45] or post-impregnating methods [46], which requires additional steps for surface functionalization of nanoparticles and/or graphene-based structures and needs a subsequent chemical reaction step to reduce graphene oxide [47,48]. The hybrids of cobalt-based nanoparticles and graphene can always show low metal leaching [49]. However, the better chemical stability was not based on the low cobalt leaching [50]. In fact, no metal leaching was observed in some metal-free catalysts, but they showed poor chemical stability after PMS activation [51].

The aim of this study is to prepare a stable composite of LCO and few-layer graphene (hereafter referred to as graphene for simplicity), to investigate the contribution of  $LaCoO_3$  and graphene and in particular their interaction with respect to the degradation of pollutants, to understand the physicochemical properties of the novel  $LaCoO_3$ /graphene catalyst, and to propose an activation mechanism for PMS. We demonstrate a convenient and scalable method to prepare stable LCO/Gr nanocomposites. LCO nanoparticles synthesized via spray-flame synthesis are bonded to graphene from scalable microwave-plasma synthesis by a simple ultrasonication technique. This approach follows our previous studies showing that the binding of graphene (30 % w/w) to nanoparticles hinders nanoparticle agglomeration as well as restacking of the graphene sheets [42].

## 2. Materials and methods

### 2.1 Materials

For the synthesis of LCO,  $La(NO_3)_3 \cdot 6H_2O$  (AppliChem Panreac, > 99.0 % purity) and  $Co(NO_3)_2 \cdot 6H_2O$  (Honeywell, > 99.0 % purity) were used as precursors dissolved in a mixture of ethanol (VWR, > 99.9 % purity) and 2-ethylhexanoic acid (2-EHA) (Alfa Aesar, > 99 % purity). 5,5-dimethyl-1-pyrroline N-oxide (>97.0 %; TCI), 2,2,6,6-tetramethyl-4-piperidone ( $\geq 95$  %), bisphenol A ( $\geq 99$  %), diclofenac sodium salt ( $\geq 98$  %), metoprolol tartrate salt ( $\geq 98$  %), carbamazepine ( $\geq 98$  %), potassium peroxymonosulfate (100 %), sodium phosphate monobasic ( $\geq 99$  %), sodium nitrate ( $\geq 99$  %), sodium chloride ( $\geq 99$  %), sodium hydrogencarbonate ( $\geq 99$  %),  $\beta$ -carotene ( $\geq 95$  %), *tert*-butyl alcohol ( $\geq 99.5$  %), *p*-benzoquinone ( $\geq 98$  %), potassium bicarbonate ( $\geq 99.5$  %), and potassium iodide ( $\geq 90$  %) were purchased from Sigma Aldrich for the catalysis tests. Sodium hydroxide ( $\geq 97$  %) and nitric acid (>69 %, both VWR chemical) were used to adjust the pH of the respective solution. All chemicals were used as received without further purification. All gases (argon (Ar), oxygen ( $O_2$ ), methane ( $CH_4$ ), hydrogen ( $H_2$ ), and nitrogen ( $N_2$ )) were supplied from Air Liquide with a purity of 99.5 % or higher. Upper Mississippi River NOM (NOM, 1R110N) was received from International Humic Substances Society (IHSS, Saint Paul, MN, USA) as dry solid extract. NOM stock solutions were prepared by mixing the required concentration of NOM in 50 ml of distilled water containing 0.1 mol/l NaOH with shaking overnight. Afterwards, the solutions were filtered through a polypropylene syringe filter (0.22  $\mu m$ ) and the pH was adjusted to 7 using  $H_3PO_4$ .

M. Hammad et al.

Chemical Engineering Journal 454 (2023) 139900

### 2.2 Synthesis of LCO nanoparticles

The synthesis of LCO nanoparticles was performed using an enclosed spray-flame reactor – described previously [31,52] using the standardized *SpraySyn* burner [53]. For the preparation of the precursor solutions,  $\text{La}(\text{NO}_3)_3 \cdot 6 \text{H}_2\text{O}$  and  $\text{Co}(\text{NO}_3)_2 \cdot 6 \text{H}_2\text{O}$  in a total concentration of 0.2 mol/l were dissolved in a mixture of ethanol (35 vol%) and 2-EHA (65 vol%). By using a syringe pump, the precursor solution was supplied to the reactor at a constant flow rate of 2 ml/min via a capillary surrounded by an annular gap through which  $\text{O}_2$  was supplied at a flow rate of 10 slm as dispersion gas. The atomization of the solution was realized by the shear forces caused by the contact of the high velocity dispersion gas with the solution at the capillary tip. The resulting aerosol was ignited by a premixed flat pilot flame (3 slm  $\text{CH}_4$  and 20 slm  $\text{O}_2$ , stabilized on a sintered bronze plate), coaxially surrounding the spray nozzle. The spray flame was shielded from the reactor walls by a surrounding sheath-gas (140 slm, compressed air). To control the temperature of the off-gas and to minimize the sintering of the nanoparticles, an additional quench gas flow – 200 slm compressed air – was supplied downstream of the spray-flame. The pressure in the reaction chamber was held constant at 970 mbar and the nanoparticles were collected from the reactor off-gas using a membrane filter.

### 2.3 Synthesis of graphene

The synthesis of freestanding few-layer graphene flakes was carried out using a microwave plasma reactor as described before [54]. A microwave antenna (iplas company) was used to focus the microwaves to the center of a quartz tube located in the center of the antenna. Ar (30 slm) and  $\text{H}_2$  (1 slm) were used as plasma gases and to stabilize the centrally introduced precursor gas flow. The plasma was ignited using a 2-kW microwave generator (Muegge, Germany) that operates at a frequency of 2.45 GHz. Ethanol (0.5 ml/min) used as graphene precursor was vaporized at 180 °C and mixed with argon as carrier gas (5 slm) using a controlled evaporation mixing system (CEM W-209-333-P, Bronkhorst). The mixture was fed through a nozzle into the center of the plasma zone. The resulting graphene flakes were collected from a PTFE-coated filter membrane located downstream the reaction zone. The typical production rate of this process is 200 mg/h.

In order to disperse graphene in water and to support the self-assembly with LCO nanoparticles, the graphene surface had to be modified with carboxyl groups. Thus, pristine graphene was stirred in a concentrated mixture of sulfuric and nitric acid (3:1) for a few minutes, collected by centrifugation (12,000 rpm), and washed with de-ionized water for three times. The carboxylated graphene was then dried at 60 °C under vacuum for 24 h.

### 2.4 Reproducible fabrication of LCO/Gr

LCO/Gr nanocomposites were prepared via a controllable ultrasonication-assisted self-assembly process. The LCO/Gr nanocomposites were assembled through an electrostatic interaction between the positively charged LCO (+37.4 mV, pH = 9) and the negatively charged graphene (-40.6 mV, pH = 9). 300 mg carboxylated graphene were dispersed in 60 ml of water by sonication (Hielscher UP200S, 60 % amplitude, 60 % cycle duty (0.6 s pulse rate)) for 30 min. Subsequently, dispersions of LCO (700 mg particles in 100 ml water by sonication) were added to the graphene dispersion under stirring and the obtained mixtures were further sonicated for another 60 min in an ice bath. The final pH of the suspension was 9. The product was collected via centrifugation and dried at 60 °C under vacuum for 24 h.

### 2.5 Materials characterization

Characterization by thermal gravimetric analysis (TGA) was performed with a Netzsch 449 F1 Jupiter at temperatures increasing from

room temperature to 1000 °C with a heating rate of 10 K/min under the flow of synthetic air (250 ml/min). X-ray diffraction (XRD) patterns were recorded in the  $2\theta$  range of 10–80° using a PANalytical X'Pert X-ray diffractometer equipped with a  $\text{Cu K}\alpha$  radiation ( $\lambda = 1.5406 \text{ \AA}$ ). The morphology of the synthesized nanoparticles was acquired with a JEOL JEM-2200FS transmission electron microscope (TEM). Raman spectra were collected using a Renishaw inVia Raman microscope with excitation laser wavelengths of 532 nm (1000–1800  $\text{cm}^{-1}$ ) and 680 nm (100–1000  $\text{cm}^{-1}$ ). The surface composition of the materials was studied by X-ray photoelectron spectroscopy (XPS) using a VersaProbe II (Ulvac-Phi) with monochromatic Al  $\text{K}\alpha$  light at an emission angle of 45°. The specific surface area was analyzed by the Brunauer-Emmett-Teller (BET) method with a Quantachrome NOVA2200 analyzer. The pH point of zero charge ( $\text{pH}_{\text{pzc}}$ ) of the catalysts' dispersion was determined by a Malvern Zetasizer. In order to evaluate the electrochemical behavior of the catalyst, electrochemical impedance spectroscopy (EIS) was performed using a Solartron 1260 in the frequency range between 0.1 Hz and 1 MHz at an applied AC potential value of 100 mV. To that end, the catalyst powder samples were pressed into pellets (thickness between 0.3 and 0.5 mm) by a 5 mm stainless steel die (force: 15 kN, for 15–30 min). Then, the pellets were coated with gold on both sides to improve the contact between the platinum electrodes (size 5 mm). The Hansen solubility (understood here in the context of similarity) parameters (HSP) were determined according to a method reported by Bapat et al. using analytical centrifugation (AC) [55]. Briefly, 1 wt/v% LCO and LCO/Gr dispersions were prepared by 5 min sonication of the powder in the respective probe liquids listed in Table S1. The dispersions were filled into cells and then inserted into the rotor and centrifuged at 2000 rpm for 20 h. AC measurements were performed using a LUMiSizer LS 651 (LUM GmbH, Berlin, Germany) with a wavelength of 410 nm. Reactive radicals spectra were obtained using an electron-spin resonance spectrometer (MiniScope MS-5000, Freiberg Instruments, Germany) and recorded using a microwave power of 10 mW and a modulation amplitude of 0.2 G at room temperature. A mercury intrusion porosimeter (PoreMaster-60, Anton Paar) was used to determine the porosity and pore size distribution. The pore radius ( $r$ ) was determined using the Washburn equation.

$$P = \frac{-2\gamma \cos\theta}{r} \quad (1)$$

Where  $P$  is the pressure,  $\gamma$  is the interfacial energy (surface tension) of mercury and  $\theta$  is the contact angle of mercury with the material. The mercury was intruded into the sample at a rate of 7–28 MPa/min and the pressure ranged from 100 Pa to 400 MPa.

### 2.6 Catalysis studies and analyses

The degradation performance of the as-prepared LCO catalyst was evaluated for BPA degradation. In a typical run, 6 mg catalyst was initially dispersed into 60 ml BPA aqueous solution (40 mg/l) at 25 °C, and the initial pH was adjusted by  $\text{H}_2\text{SO}_4$  and NaOH to different pH values (3–11). The resulting suspension was continuously stirred for 30 min to ensure the establishment of an adsorption/desorption equilibrium between BPA molecules and the as-prepared catalyst before a certain amount of PMS was added. During the experiment, 2 ml of the suspension was withdrawn at given time intervals, immediately quenched with 0.5 ml methanol, centrifuged (12,000 rpm, 20 min) to remove the particles, and the supernatant was injected into a HPLC vial. To evaluate the reusability of the catalyst, the as-prepared nanoparticles were recovered by a centrifuge (12,000 rpm, 20 min), washed with de-ionized water three times, and then re-dispersed into 60 ml BPA aqueous solution for the next use.

Moreover, degradation of DCF, MTP, and CBZ was also investigated to test the catalytic activity of the as-prepared catalyst. To obtain the degradation reaction kinetics of organic pollutants, pseudo-first-order kinetics reaction rate constants ( $k_{\text{app}}$ ) were determined according to

M. Hamad et al.

Chemical Engineering Journal 454 (2023) 139900

the following equation:

$$\ln\left(\frac{C_t}{C_0}\right) = -k_{\text{app}}t \quad (2)$$

Where  $C_t$  depicts the pollutant concentration at time  $t$ ,  $C_0$  is the initial pollutant concentration, and  $k_{\text{app}}$  is the reaction rate constant.

The concentrations of BPA, DCF, MTP, and CBZ were analyzed by high-performance liquid chromatography (HPLC, Shimadzu LC-10AT) with an EVO C18 column (Kinetex 5  $\mu\text{m}$  EVO C18 100  $\text{\AA}$  100  $\times$  3.0 mm, Phenomenex). The flow rate of the mobile phase consisting of 0.1 % formic acid in water and methanol (60:40, v:v) was 0.5 ml/min. To determine the residual concentration of PMS, 100  $\mu\text{l}$  of the suspension was withdrawn at given time intervals, mixed with potassium bicarbonate (5 g/l) and potassium iodide (40 g/l), and then analyzed by UV-vis spectroscopy (Varian Cary 400) at a wavelength of 352 nm [56]. The mineralization rate was determined using a total organic carbon analyzer (TOC-5000A, Shimadzu). The effects of pH, temperature, and co-existing ions (such as  $\text{Cl}^-$ ,  $\text{NO}_3^-$ ,  $\text{H}_2\text{PO}_4^-$ ,  $\text{HCO}_3^-$ , etc.) on the PMS activation of the LCO/Gr composite catalyst were also investigated. To evaluate the reusability of the LCO/Gr nanoparticles, the LCO/Gr catalysts were collected by centrifugation (Sigma 3-30KS centrifuge, Sigma Laborzentrifugen GmbH, Germany) at 14,000 rpm for 10 min, followed by thorough washing with deionized water and re-dispersion into fresh BPA solution for the next experimental run. To identify the dominant reactive radicals in the system, ethanol (EtOH), *tert*-butyl alcohol (TBA), and  $\beta$ -carotene were used as scavengers for  $\text{SO}_4^{\cdot-}$  and  $\cdot\text{OH}$ ,  $\cdot\text{OH}$ , and  $^1\text{O}_2$  respectively. Furthermore, electron paramagnetic resonance (EPR) experiments were performed to identify  $\text{SO}_4^{\cdot-}$  and  $\cdot\text{OH}$ , and  $^1\text{O}_2$ , respectively, using 5,5-dimethyl-1-pyrroline *N*-oxide (DMPO) and 2,2,6,6-tetramethyl-4-piperidin (TEMP) as spin traps. The EPR spectra were measured using a MiniScope MS-5000 electron spin resonance spectrometer (modulation amplitude 0.2 G, microwave power 10 mW). The concentration of dissolved metal ions was determined by atomic absorption spectroscopy (AAS, Thermo Electron Corporation, M-Serie).

### 3. Results and discussion

#### 3.1 Preparation of LCO/Gr nanocomposites

To quantify the amount of adsorbates and carbon in as-synthesized LCO and LCO/Gr nanocomposites, TGA measurements were performed at up to 1000  $^\circ\text{C}$  under synthetic air to decompose residuals on the particle surface as well as graphene (see supplementary material, Fig. S1). The weight loss of the pristine LCO is about 19 % and can be

ascribed to the loss of adsorbates such as water (3 %, 50–170  $^\circ\text{C}$ ) and the oxidation of unburned combustion residuals (16 %, 200–600  $^\circ\text{C}$ ) releasing water and  $\text{CO}_2$ . Compared to the result of as-synthesized LCO, the additional weight loss for LCO/Gr is 32 %, which can be attributed to the oxidation of graphene (300–750  $^\circ\text{C}$ ). Accordingly, the observed graphene weight loss value is in good agreement with the intended composition of the LCO/Gr nanocomposite.

#### 3.2 Structural characterization of LCO/Gr nanocomposites

Raman spectroscopy was employed as a qualitative method to evaluate the purity of the synthesized graphene and to identify the phase composition of the LCO and LCO/Gr nanoparticles (Fig. 1a). The peak at around 650  $\text{cm}^{-1}$  measured for LCO (black graph) matches the Co–O stretching vibration of the  $\text{LaCoO}_3$  phase [57], whereas the Raman spectrum of graphene (red graph) consists of two peaks. The D (1350  $\text{cm}^{-1}$ ) and G (1580  $\text{cm}^{-1}$ ) bands are ascribed to  $\text{sp}^3$  defects and the first-order scattering of  $\text{sp}^2$  carbon atom domains in a 2D hexagonal carbon lattice, respectively. The intensity ratio between the D and G bands ( $I_D/I_G$ ) is a measure of the degree of disorder and defects in the graphene structure [58]. The observed  $I_D/I_G$  ratio of 0.5 is quite low, indicating a very high quality of the as-synthesized few-layer graphene (see supplementary material, Fig. S3a) with a low degree of structural defects. Importantly, there is a significant difference in  $I_D/I_G$  values between the pure few-layer graphene and LCO/Gr composite (0.79, green graph in Fig. 1a). However, when LCO (0.68 g) and graphene (0.32 g) were physically mixed without having been processed to the LCO/Gr nanocomposite in advance, there is almost no change in  $I_D/I_G$  (0.54, blue graph). This provides strong evidence that the deposition of LCO nanoparticles on the graphene nanosheets did introduce defects in the graphene structure due to strong interaction between LCO nanoparticles and graphene sheets.

The crystal structure of LCO, graphene, and LCO/Gr materials was characterized by powder XRD (Fig. 1b). The LCO diffraction peaks (black graph) can be indexed to the rhombohedral  $\text{LaCoO}_3$  perovskite phase (JCPDS Card No. 01-084-0848) [59] and the peak shape is characteristic for nanoparticles with high crystallinity. The mean crystallite sizes calculated from the XRD pattern of LCO and LCO/Gr nanoparticles using Rietveld refinement are 9 and 9.3 nm, respectively (see supplementary material, Fig. S2), which is within the accuracy of the analysis and confirms that the LCO crystallites do not change in structure and size. However, the lattice constants of LCO derived from Rietveld refinement slightly increase with the introduction of LCO to graphene, whereas in case of the physical mixture (LCO + Gr), there is

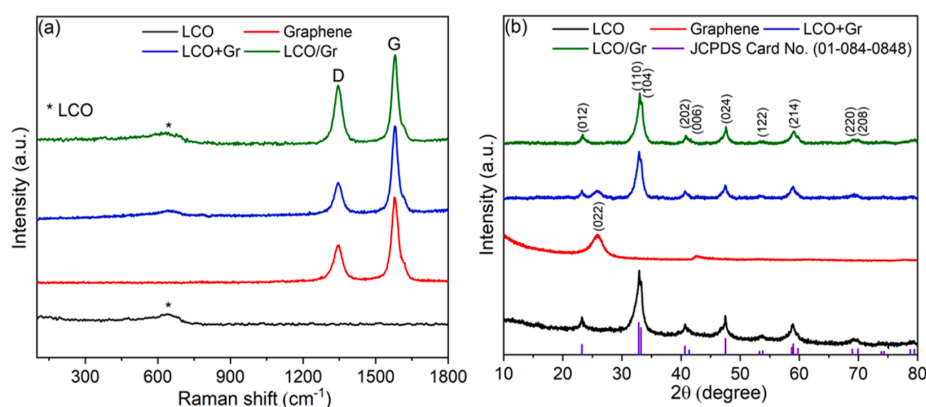


Fig. 1. a) Raman spectra and b) XRD patterns for LCO, graphene, LCO + Gr, and LCO/Gr nanopowders. All Raman spectra were measured with an excitation wavelength of 532 nm (1000–1800  $\text{cm}^{-1}$ ) and 680 nm (100–1000  $\text{cm}^{-1}$ ).

M. Hammad et al.

Chemical Engineering Journal 454 (2023) 139900

no significant change (see [supplementary material, Table S1](#)). We interpret this as a clear indication of chemical interaction between LCO and graphene in the composite material. The weak expansion in the lattice constant of LCO in LCO/Gr (compared to bulk LCO and pristine LCO nanoparticles) can be attributed to the presence of oxygen vacancies as also reported in literature [60,61]. The intense and broad peak of graphene at  $2\theta = 26.2^\circ$  corresponds to the (002) plane of graphene. Interestingly, the characteristic (002) diffraction peak of graphene has almost disappeared in the LCO/Gr nanocomposite compared to the LCO + Gr nanoparticles mixture. This suggests that reduced graphene stacking occurs, most probably due to the coverage of graphene with LCO nanoparticles [44].

The morphology and chemical composition of LCO nanoparticles and LCO/Gr nanocomposites were characterized by TEM and elemental mapping. The sphere-like LCO nanoparticles (mean diameter about 7 nm, see [supplementary material, Fig. S3b](#)) are uniformly distributed, covering almost the entire surface of the graphene sheets in the LCO/Gr

nanocomposite (Fig. 2a). The high-magnification TEM image (Fig. 2b) reveals that all LCO nanoparticles are connected to graphene. The chemical homogeneity of the LCO was evidenced by SEM energy-dispersive X-ray elemental mapping of LCO/Gr (Fig. 2c-g). The EDX analysis was performed to further confirm the composition of the LCO/Gr material and showed that the La/Co ratio is about unity (see [supplementary material, Fig. S3e](#)). Moreover, the high-resolution TEM (HRTEM) image of LCO/Gr further shows the crystal lattice fringes with an interlayer spacing of 0.26 and 0.34 nm, corresponding to the (104) and (002) planes of the rhombohedral  $\text{LaCoO}_3$  perovskite phase and highly crystalline graphene, respectively. This result is consistent with the XRD analysis.

The findings regarding LCO particle size and formation of few-layer graphene are further supported by the results of nitrogen sorption. The mean particle diameter can be calculated from the results with the following formula:

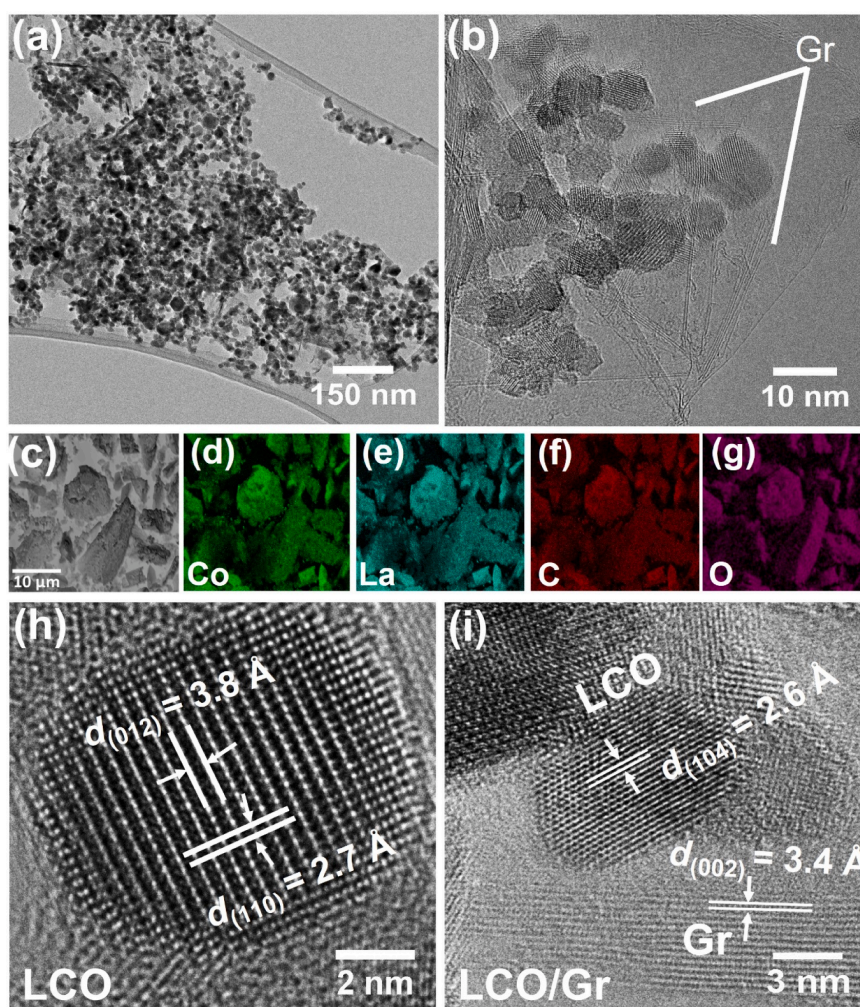


Fig. 2. a) Low-magnification, b) high-magnification TEM image, c-g) SEM image of LCO/Gr composites and the corresponding elemental mapping of cobalt, lanthanum, carbon, and oxygen, and h-i) HRTEM image of LCO and LCO/Gr particles.

M. Hamad et al.

Chemical Engineering Journal 454 (2023) 139900

$$SSA = \frac{6}{\rho d_p} \quad (3)$$

Where SSA is the specific surface area ( $\text{m}^2/\text{g}$ ),  $d_p$  stands for the particle diameter (nm), and  $\rho$  is the density of the analyzed material ( $\text{g}/\text{cm}^3$ ). Assuming spherical and non-aggregated particles, average particle sizes of 8.8 nm were derived from the measured BET surface areas of  $94 \text{ m}^2/\text{g}$ , using a LCO density of  $7.25 \text{ g}/\text{cm}^3$ . The average layer number of graphene can be estimated from the SSA of single-layer graphene ( $2630 \text{ m}^2/\text{g}$ ) versus the measured SSA of graphene. The SSA of graphene was measured as  $300 \text{ m}^2/\text{g}$  and suggests the formation of few-layer graphene with a mean number of nine graphene sheets stacked on top of each other. As expected, the SSA of the LCO/Gr composite was in between and was determined to be  $154 \text{ m}^2/\text{g}$ . Moreover, the pore-size distribution curve of LCO/Gr composite determined by the Washburn equation showed that the pore size distribution is broad with 65 % of the volume accounting for pores in the 2–3 nm range and 35 % in the 6–12 nm range (see supplementary material, Fig. S4). The mesoporous nature of LCO/Gr with high surface area suggests the presence of abundant active sites, which can activate PMS rapidly due to low mass transport resistance [62].

To confirm the surface interaction between LCO nanoparticles and graphene, XPS and FTIR spectroscopy were further studied. The surface chemical composition of LCO and LCO/Gr materials was investigated by XPS analysis (Fig. 3a–b and Fig. S5). Fig. S5a shows the full surface XPS spectra of all samples. The four characteristic peak areas located at

binding energies around 285, 530, 779, and 835 eV belong to C1s, O1s, Co2p, and La3d, respectively. In the surface La3d high-resolution XPS spectra (see supplementary material, Fig. S5d), the spectrum was fitted by peaks at 834 eV and 851.5 eV for  $\text{La}3d_{5/2}$  and  $\text{La}3d_{3/2}$ , respectively, and their corresponding satellite peaks around 837.9 eV and 855.1 eV, which is assigned to  $\text{La}^{3+}$  ions in perovskite structures [63]. Besides, compared to LCO, the La3d peaks of the LCO/Gr was slightly shifted to a higher binding energy, which can be attributed to the interaction between  $\text{LaCoO}_3$  and graphene [64]. The surface Co2p XPS spectrum of LCO was fitted by peaks at 779.7 and 794.5 eV. These are assigned to the  $\text{Co}2p_{3/2}$  and  $\text{Co}2p_{1/2}$  spin-orbital peaks of  $\text{LaCoO}_3$  [65]. The energy difference of the doublet is about 15.2–15.3 eV, which is characteristic for the mixed oxide  $\text{LaCoO}_3$  structure [66]. Besides, small  $\text{Co}2p_{3/2}$  satellite peaks positioned between 785 and 790 eV indicate the presence of a mixed oxidation state of  $\text{Co}^{3+}$  and  $\text{Co}^{2+}$  surface ions. Upon mixing LCO and graphene (LCO + Gr), we could not observe any significant change in the intensity of the satellite peak and the peak position of  $\text{Co}2p_{3/2}$  and  $\text{Co}2p_{1/2}$ . However, compared to LCO + Gr, the surface Co2p XPS spectrum of the LCO/Gr material exhibits peaks at 780.5 eV and 796.4 eV, corresponding to the  $\text{Co}2p_{3/2}$  and  $\text{Co}2p_{1/2}$  states [67]. The increased intensity of the satellite peak around 785 eV along with the shifted peak position of  $\text{Co}2p_{3/2}$  and  $\text{Co}2p_{1/2}$  indicates that a part of the  $\text{Co}^{3+}$  ions was converted to  $\text{Co}^{2+}$  and formed oxygen vacancies ( $\text{O}_{\text{vac}}$ ). In order to evaluate the surface  $\text{O}_{\text{vac}}$  in both LCO and LCO/Gr samples, surface O1s spectra were deconvoluted into three major peaks centered at 528.7, 529.5, and 531.6 eV. This corresponds to surface lattice oxygen ( $\text{O}_L$ ),

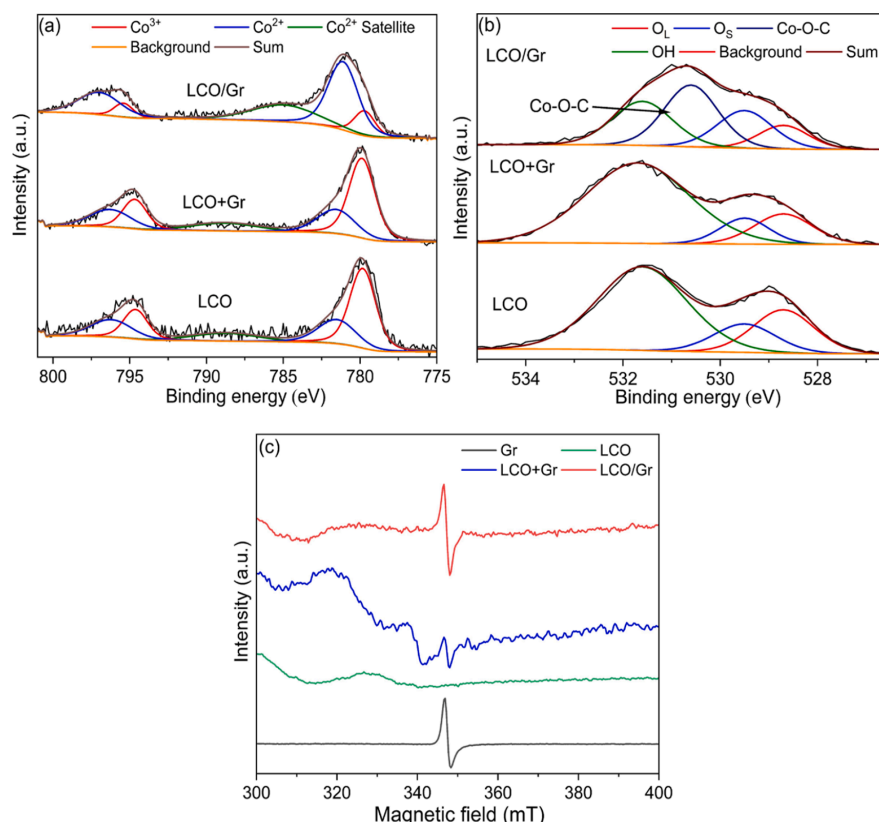


Fig. 3. a) XPS curve fit of Co2p and b) O1s of the LCO, LCO + Gr, and LCO/Gr powder and c) EPR spectra of graphene, LCO, LCO + Gr, and LCO/Gr.

adsorbed oxygen species on the surface vacancy ( $O_s$ ), and surface hydroxyl groups (OH), respectively (Fig. 3b) [68]. The relative concentration of surface  $O_{vac}$  in the LCO/Gr sample was determined to be 23 %, which is higher compared to LCO nanoparticles (15 %) and LCO + Gr (14 %). This confirms the reduced oxidation of cobalt ions in the LCO/Gr sample, further manifesting the formation of  $O_{vac}$ . Interestingly, the new peak centered at 530.4 eV in O1s spectra of LCO/Gr sample confirms the formation of surface Co—O—C bonds (Fig. 3b, highlighted with an arrow). This peak results from the strong surface interaction between LCO and graphene [69]. Details are given in the [supplementary material](#) (Fig. S5). In addition, EPR measurements were carried out to examine unpaired electrons in LCO, graphene, LCO + Gr, and LCO/Gr (Fig. 3c). The broad EPR signal observed for LCO is assigned to the ferromagnetic (FM) clustering of the cobalt ions [70]. For the graphene sample, the narrow signal observed at  $g \approx 2.005$  can be tentatively assigned to the presence of conduction electrons and/or localized sigma “dangling bond” spins associated with defects. In case of the LCO + Gr sample, the broad signal assigned to clustering of cobalt ions is decreased along with the presence of a small narrow signal appearing from the graphene sample. In contrast, the intensity of the narrow signal was increased for the LCO/Gr sample. This confirmed the reduced oxidation of cobalt ions in the LCO/Gr sample and thus further manifests the formation of  $O_{vac}$ .

Furthermore, FTIR spectroscopy was carried out to verify the formation of LCO/Gr nanocomposite (See [supplementary material](#) Fig. S6). In the FTIR spectrum of LCO, the peaks at  $\sim 550$  and  $590\text{ cm}^{-1}$  are assigned to characteristic Co—O stretching vibration and O—Co—O deformation modes of  $LaCoO_3$ , respectively [71], whereas the characteristic peaks at  $845$  and  $1540\text{ cm}^{-1}$ , and  $3200$ – $3600\text{ cm}^{-1}$  are attributed to symmetric and asymmetric  $COO^-$  vibration and O—H stretching vibration [72,73]. However, after the introduction of graphene, the peak intensities of O—H and  $COO^-$  groups decreased significantly, suggesting that the O—H and  $COO^-$  groups are substituted to form a Co—O—C bond between LCO and graphene nanoparticles [74]. This robust interaction between LCO and graphene nanoparticles is assumed to prevent cobalt leaching and mediates fast electron transport through the graphene matrix to the LCO nanoparticles, enhancing their catalytic performance [42]. Besides, new absorption peaks in the  $1380$ – $1470\text{ cm}^{-1}$  range and at  $1640\text{ cm}^{-1}$  are ascribed to aromatic carbon ring vibrations [75] and C=C stretching vibration [76], respectively, confirming the presence of graphene in LCO/Gr. Noteworthy, this result is consistent with TEM, XRD, Raman, and XPS analyses, altogether proving a strong interaction between LCO and graphene and thus the successful formation of a stable LCO/Gr composite.

### 3.3 Electrochemical characterization of LCO/Gr nanocomposites

The interfacial and composite conductivity of the catalyst can affect its catalytic performance. Thus, electrochemical impedance spectroscopy was performed to evaluate the conductivity of the pure LCO catalysts (pressed pellets) and the LCO/Gr nanocomposite. The Argand diagram of LCO (Fig. S7a) shows the typical characteristics of a polycrystalline oxide semiconductor and an equivalent circuit for the grain boundary and bulk conductivity consisting of two R/CPE elements could be fitted to the measured data. The observed conductivity is surprisingly high for a nanocrystalline semiconductor material, whose conductivity is dominated by grain boundary resistances.

The electrical behavior of the composite material (Fig. S7b) is characterized by the very high conductivity of the graphene. All parasitic resistances of our 2-point experimental setup sum up to about 1.2 Ohm, so that essentially Ohmic behavior is observed. Towards higher frequencies (from about 1 kHz) inductive effects appear visibly, which can be fitted by a R/CPE. Compared to the known capacitive behavior, however, the phase angle of this CPE is shifted by about  $180^\circ$  to a capacitor, so that it acts as an inductor. Due to the combination of highly conductive graphene and electrically well-conducting LCO nanoparticles, a very good electrical contact of LCO nanoparticles and

graphene can be assumed here, which we believe greatly promotes the catalytic performance of the LCO/Gr material.

### 3.4 Stability of nanoparticle dispersions

High dispersion stability of the generated catalysts is a key factor to achieve good catalytic activity during PMS activation. Hence, identifying appropriate parameters that distinguish surface characteristics before and after graphene introduction is important. Hansen solubility parameters (HSP) represent surface characteristics and were determined here using analytical centrifuge (AC) experiments [55]. From the AC software (SEPView), we obtain optical transmission profiles (fingerprints) that can be employed to calculate so-called stability trajectories (see [supplementary material](#), Fig. S8-9). These enable to assess the interaction of the particle surface with the continuous phase and thus a categorization of probe liquids into good, uncertain, and poor according to the nanoparticle dispersion stability (see [supplementary material](#), Table S3-S4). As shown in Fig. 4, the dispersion stability of LCO/Gr was analyzed in five probe liquids (water, dimethylformamide, isopropanol, acetonitrile, and *N*-methyl-2-pyrrolidone). In case of LCO, the nanoparticles were well-dispersible in only two probe liquids (acetonitrile and *N*-methyl-2-pyrrolidone). Finally derived HSP values are summarized in the Table 1. The strong difference between LCO and LCO/Gr further corroborates the findings of the previous chapters regarding the successful synthesis of stable LCO/Gr composites.

It needs to be mentioned that for deriving HSP, water was not considered due to its hydrogen bonding capabilities ( $\delta_H = 42\text{ MPa}^{1/2}$ ) and hence its large distance compared to other solvents [77]. However, water is one of the most stable solvents for LCO/Gr, which is important for PMS activation. It is noteworthy to mention that the catalytic reaction was conducted in aqueous medium, suggesting that LCO/Gr might exhibit improved PMS activation compared to LCO which showed a poor dispersibility in water. This leads to agglomeration and sediments, and therefore additionally lowers the catalytic activity. Thus, dispersion studies in water were performed separately employing transmittograms (see [supplementary materials](#), Fig. S10). The LCO/Gr nanoparticles that are dispersed in tap water show the quickest sedimentation due to the presence of inorganic anions that interact with the nanoparticles surface and lead to poor dispersion. In contrast, the LCO/Gr nanoparticles dispersed in deionized water have the best dispersion stability, and even after 330 min, the full particles have not settled. However, when LCO/Gr particles were mixed with PMS, the dispersion stability of LCO/Gr decreased significantly. This can be mainly attributed to a drop from pH 7 to 5 within a few minutes after the addition of PMS (see [supplementary material](#), Fig. S19).

### 3.5 Catalytic performance and stability of catalysts

BPA, an endocrine-disrupting compound, is intensely used for the production of polycarbonate plastics and epoxy resins in the internal coatings of food packaging [78]. As a result of its widespread use, BPA is ubiquitously detected in food, drinking water, aquatic animals, and humans, and it decomposes only slowly under natural conditions [79]. Therefore, the catalytic performance of LCO/Gr was evaluated with regard to the degradation of BPA. 0.1 g/l LCO/Gr and a PMS concentration of 0.5 mmol/l was selected for subsequent experiments. Details are given in the [supplementary material](#) (Section 2, Fig. S11-12).

The catalytic performance of LCO, graphene, and LCO/Gr nanoparticles was studied at pH 7 to understand the synergetic effect between LCO and graphene nanoparticles (Fig. 5a). In the case of either LCO (0.1 g/l) or graphene (0.1 g/l) with PMS, the removal efficiency of BPA achieved 75 % and 30 % within 30 min, respectively. Interestingly, the BPA degradation efficiency of the LCO + Gr + PMS (0.068 g/l LCO + 0.032 g/l graphene) system reached only 80 % within 30 min. In contrast, the LCO/Gr + PMS (0.1 g/l) system showed complete BPA degradation after about 10 min, indicating that the enhanced catalytic

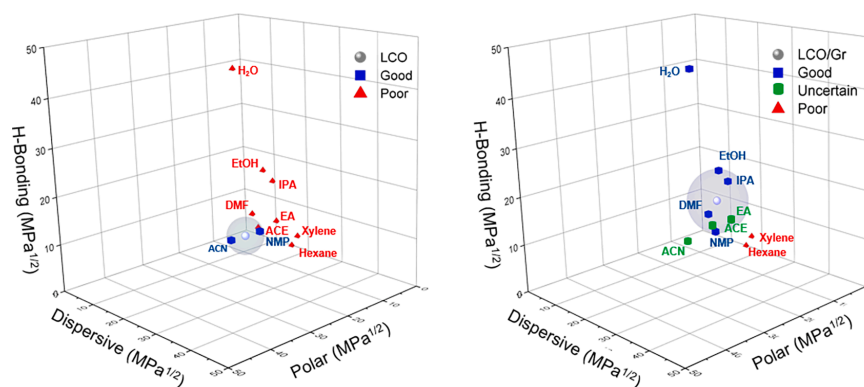


Fig. 4. HSP sphere of LCO (left) and LCO/Gr (right) derived from HSPiP software in Hansen coordinates.

**Table 1**  
HSP of LCO and HSP of LCO/Gr.

Materials	LCO	LCO/Gr
Dispersive interactions $\delta_D$ (MPa <sup>1/2</sup> )	16.7	15.3 – 20.5
Dispersive interactions $\delta_P$ (MPa <sup>1/2</sup> )	15.2	8.4 – 15.4
Dispersive interactions $\delta_H$ (MPa <sup>1/2</sup> )	6.7	11.8 – 14.9
Sphere radius (MPa <sup>1/2</sup> )	4	6.8 – 15.3
Total combinations possible		1024
Combinations chosen for HSP	–	7 out of 8
Outliers	–	1

performance of LCO/Gr is based on a robust interaction between LCO and graphene and the presence of oxygen vacancies, as proven by Raman, XPS, and EPR studies. Based on Equation (2),  $k_{app}$  values of the BPA degradation were calculated as 0.17 and 0.52 min<sup>-1</sup> for LCO and LCO/Gr samples, respectively, confirming that the catalytic performance of the LCO/Gr catalyst is significantly higher than that of pure LCO. We attribute the catalytic enhancement of LCO/Gr to the following features:

- (i) The higher specific surface area of the LCO/Gr composite provides a better accessibility of active sites than pure LCO since the composite supports BPA molecules adsorption through strong  $\pi$ - $\pi$  and hydrogen-bond interaction, leading to faster degradation of BPA.

- (ii) The presence of unpaired  $\pi$  electrons in the LCO/Gr structure facilitates fast electron transport from LCO to PMS molecules through graphene nanosheets, supported by robust Co—O—C interactions that prevent cobalt leaching from LCO/Gr nanoparticles and therefore improve the catalytic performance of LCO/Gr.

The residual PMS concentration was varied during PMS activation in different systems (see [supplementary material, Fig. S13](#)). The concentration of residual PMS in the LCO + PMS and LCO + Gr + PMS system was about 0.27 and 0.23 mmol/l, which attributed to about 54 and 46 % of the initial PMS concentration, respectively. However, in the LCO/Gr + PMS system, the residual PMS concentration declined to about 0.08 mmol/l (16 %). This result suggests that the LCO/Gr + PMS system consumes more PMS which we attribute to the fast electron transport from PMS molecules to the LCO through graphene nanosheets. Therefore, faster BPA degradation is achieved.

The reusability of catalysts is important to determine the catalyst stability for practical applications in water treatment. To confirm the durability of the catalyst in the LCO/Gr + PMS system, five cycling experiments were conducted under identical conditions. As displayed in [Fig. 5b](#), the reused LCO/Gr catalyst presented higher catalytic activity and stability compared to LCO and LCO + Gr in all five reaction runs. The insignificant decrease in BPA removal with LCO/Gr + PMS is due to the mass loss of catalyst after washing during the recycling process. In addition, the mineralization extent of BPA removal was measured for all

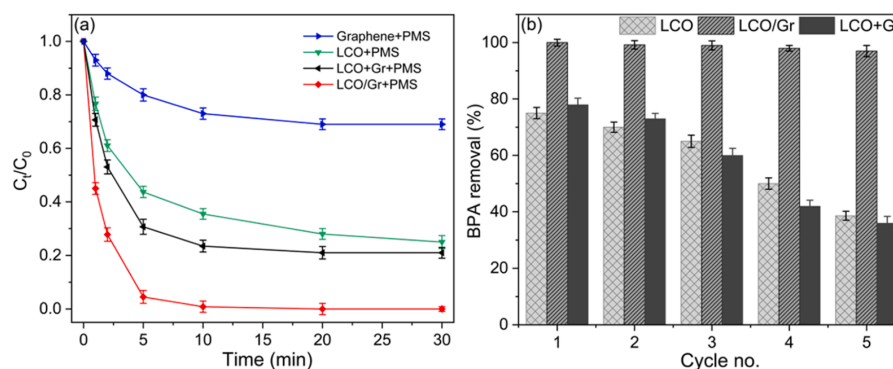


Fig. 5. a) BPA degradation with various catalysts in different reaction systems and b) stability tests of the LCO/Gr + PMS system. Reaction conditions: BPA = 40 mg/l; PMS = 0.5 mmol/l; catalyst = 0.1 g/l; pH = 7.

M. Hammad et al.

Chemical Engineering Journal 454 (2023) 139900

catalytic tests by TOC measurements after 30 min. The TOC removal of BPA was around 35 and 62 % for LCO and LCO/Gr catalysts, respectively, while the TOC removal of BPA for LCO/Gr + PMS remains unabatedly high after five recycling operations (see [supplementary material, Fig. S14](#)). This indicates that the stable LCO/Gr + PMS system exhibits excellent catalytic performance through the multi-cycle process.

As an important catalyst characteristic, leaching of cobalt ions was investigated by AAS analysis during PMS activation. Despite the fact that both LCO + Gr + PMS and LCO + PMS exhibited good catalytic activity, the cobalt leaching amount (2.9 mg/l for LCO + Gr and 3.5 mg/l for LCO) is much higher than that with the LCO/Gr + PMS system (0.004 mg/l), which is clearly below the threshold limit value (0.05 mg/l) set by the World Health Organization (WHO) [80]. To investigate whether the leached cobalt shows some catalytic activity, the BPA removal efficiency using the  $\text{Co}^{2+}$ +PMS system was studied under the same conditions (see [supplementary material, Fig. S15](#)). The BPA removal of the homogeneous  $\text{Co}^{2+}$ +PMS system was less than 4 %, suggesting that the high catalytic performance mainly benefited from the heterogeneous LCO/Gr + PMS system. The unchanged chemical structure of the LCO/Gr catalyst after five runs also supports its high stability (see [supplementary material, Fig. S16](#)). There is no change in the XRD diffraction pattern of the multiply-used catalyst as compared to pristine LCO/Gr. These results indicate that the LCO/Gr system is a much more eco-friendly, efficient, and effective catalyst for practical water treatment applications compared to previously reported heterogeneous carbon-supported catalysts as only a vanishingly small proportion of cobalt is lost with this catalyst material (Table 2).

### 3.6 Reactive species identification

To understand the catalytic mechanism of the LCO/Gr + PMS system, EPR spectra of solutions and XPS spectra of LCO/Gr before and after catalytic experiments were recorded and analyzed. The contribution of different reactive radicals such as  $\text{SO}_4^{\cdot-}$ ,  $\cdot\text{OH}$ ,  $\text{O}_2^{\cdot-}$ , and  $^1\text{O}_2$  for BPA degradation was investigated by adding commonly used radical scavengers like ethanol (EtOH), *tert*-butanol (TBA), *p*-benzoquinone (BQ), and  $\beta$ -carotene (Crt). Here, EtOH was employed to scavenge both  $\text{SO}_4^{\cdot-}$  and  $\cdot\text{OH}$ , TBA was used to quench  $\cdot\text{OH}$  [88], whereas Crt and BQ were chosen as scavengers of  $^1\text{O}_2$  and  $\text{O}_2^{\cdot-}$ , respectively [89].

As depicted in Fig. 6a, the removal rate of BPA was decreased from 100 to 87 % when using 0.1 mol/l EtOH and more inhibition (79 %) was observed with the addition of a high concentration of 0.5 mol/l EtOH. In contrast, no significant change in BPA removal was observed with the addition of 0.1 and 0.5 mol/l TBA. This suggests a minor contribution of  $\text{SO}_4^{\cdot-}$  and  $\cdot\text{OH}$  to BPA degradation. Moreover, the removal efficiency declined to 40 % when adding 5 mmol/l BQ. The addition of a small dose of Crt (0.5 mmol/l) led to a BPA removal efficiency of only 26 %, indicating that  $^1\text{O}_2$  and  $\text{O}_2^{\cdot-}$  are the primary reactive species in the LCO/Gr + PMS system.

The pseudo-first-order constants with the addition of TBA and EtOH were calculated to determine the contribution of different reactive

species in the LCO/Gr + PMS system. The contributions of  $\cdot\text{OH}$  and  $\text{SO}_4^{\cdot-}$  radicals were calculated using the following equations (4–5) [90]:

$$\lambda_{(\cdot\text{OH})} = (k_0 - k_1/k_0) \quad (4)$$

$$\lambda_{(\text{SO}_4^{\cdot-})} = (k_1 - k_2)/k_0 \quad (5)$$

Where  $k_0$  is the rate constant of BPA degradation in LCO/Gr + PMS system without scavenger,  $k_1$  and  $k_2$  are the rates constant for degradation of BPA by  $\cdot\text{OH}$  and  $\text{SO}_4^{\cdot-}$ .

Since  $^1\text{O}_2$  might be generated from the oxidation of  $\text{O}_2^{\cdot-}$ , their common contributions ( $\lambda(\text{O}_2^{\cdot-}/^1\text{O}_2)$ ) were estimated according to the following equation (6) [91]:

$$\lambda_{(\text{O}_2^{\cdot-}/^1\text{O}_2)} = \lambda_{(\text{overall})} - (\lambda_{(\text{SO}_4^{\cdot-})} + \lambda_{(\cdot\text{OH})}) \quad (6)$$

The values of  $k_0$ ,  $k_1$ , and  $k_2$  were calculated as 0.52, 0.45, and 0.28  $\text{min}^{-1}$ , respectively, according to equation (2). As a result, the relative contributions of  $\cdot\text{OH}$ ,  $\text{SO}_4^{\cdot-}$ , and  $^1\text{O}_2/\text{O}_2^{\cdot-}$  in the LCO/Gr + PMS systems were determined to 13.4, 32.6, and 54 %, respectively.

Furthermore, EPR tests using DMPO and TEMP as radical spin-trapping agents for  $\text{SO}_4^{\cdot-}$  and  $\cdot\text{OH}$ , and  $^1\text{O}_2$ , respectively, were carried out to confirm the formation of reactive radicals from PMS activation. As shown in Fig. 6b, when LCO + PMS were added, characteristic signals for DMPO- $\cdot\text{OH}$  adducts (with hyperfine splitting constants of  $\alpha_{\text{H}} = \alpha_{\text{N}} = 14.8$  G) and DMPO- $\text{SO}_4^{\cdot-}$  adducts ( $\alpha_{\text{N}} = 13.2$  G,  $\alpha_{\text{H}} = 9.6$  G,  $\alpha_{\text{H}} = 1.48$  G,  $\alpha_{\text{H}} = 0.78$  G) were observed, demonstrating the generation of both  $\cdot\text{OH}$  and  $\text{SO}_4^{\cdot-}$  radicals by the LCO + PMS system. Similar results were obtained in the LCO + Gr + PMS system with reduced  $\cdot\text{OH}$  and  $\text{SO}_4^{\cdot-}$  signals, due to a decrease in the LCO dosage (0.07 g/l LCO + 0.03 g/l graphene) compared to the LCO system (0.1 g/l). This suggests that there is no interaction between graphene and LCO nanoparticles. However, in case of LCO/Gr + PMS, the appearance of seven-line EPR adducts assigned to 5,5-dimethyl-1-pyrrolidone-2-oxyl (DMPOX) could be indexed to the direct oxidation of DMPO with nonradical species  $^1\text{O}_2$  [92] (Fig. 6b). Additionally, the characteristic triplet signal of the TEMP- $^1\text{O}_2$  adduct ( $\alpha_{\text{N}} = 1.72$  mT) was observed when TEMP was added, confirming the presence of  $^1\text{O}_2$  in the LCO/Gr + PMS system (Fig. 6c). The peak intensity of  $^1\text{O}_2$  in the LCO/Gr + PMS system was significantly higher than that of the LCO + PMS and LCO + Gr + PMS system, suggesting the boosted generation of  $^1\text{O}_2$  which might be attributed to oxygen vacancies. These results are also consistent with the radical scavenging experiments. Hence, it can be concluded that the nonradical pathway ( $^1\text{O}_2$ ) plays a dominant role in the BPA degradation while the radical pathway ( $\text{SO}_4^{\cdot-}$  and  $\cdot\text{OH}$ ) contributes significantly less.

### 3.7 Surface active site identification and possible mechanisms

To investigate the catalytic active sites of LCO/Gr, the activity of LCO/Gr was compared to that of gas-phase synthesized  $\text{Co}_3\text{O}_4$ ,  $\text{La}_2\text{O}_3$ ,  $\text{LaCoO}_3$ , and graphene (see [supplementary material, Fig. S17](#)). The removal efficiency of BPA achieved less than 30 % with  $\text{La}_2\text{O}_3$  + PMS and graphene + PMS, which indicated that the La and C atoms of LCO/

**Table 2**  
Comparison of the BPA removal by LCO/Gr in this work with those of other related carbon-supported catalysts in the literature.

Catalyst	Dosage (mg/l)	BPA conc. (mg/l)	PMS conc (mmol/l)	BPA removal (%)	Time (min)	Metal leaching (mg/l)	References
Fe3C@NCNTs/Gr	100	20	0.65	98	30	(Fe) $\approx$ 0.36	[81]
$\text{Co}_3\text{O}_4$ /MXene	100	20	1	99	20	(Co) $\approx$ 0.36	[82]
CoS/Gr	100	20	0.32	92	8	(Co) $\approx$ 0.52	[83]
$\text{Fe}_3\text{Co}_7$ /Gr	100	20	0.65	98	30	(Co) $\approx$ 3.30	[84]
$\text{Co}_3\text{O}_4$ /MOFs	100	20	1.6	95	10	(Co) $\approx$ 0.35	[85]
$\text{LaFeO}_3$ /GO	500	20	2	100	60	(Fe) $\approx$ 0.24(La) $\approx$ 0.88	[86]
$\text{Co}_3\text{O}_4$ /CC	100	10	0.32	99	10	(Co) $\approx$ 0.25	[87]
LCO/Gr	100	40	0.32	100	10	(Co) $\approx$ 0.004	This work

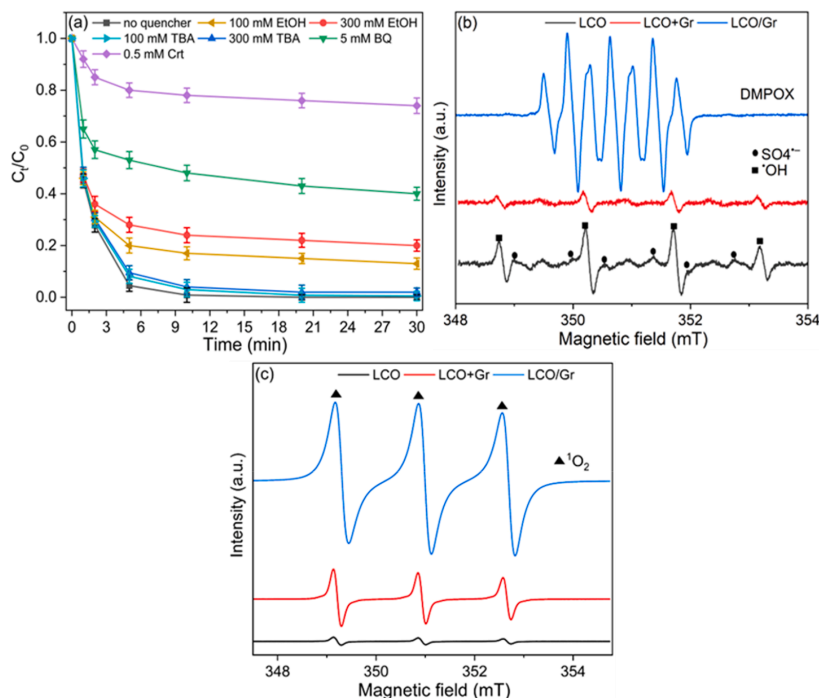


**Fig. 6.** a) Effect of different radical scavengers on the BPA degradation process with LCO/Gr + PMS. EPR spectra using b) DMPO, and c) TEMP as the trapping agent for solutions with PMS, LCO/Gr and LCO/Gr + PMS, respectively. Reaction conditions: BPA = 40 mg/l, PMS = 0.5 mmol/l, catalyst = 0.1 g/l, DMPO = 50 mmol/l, TEMP = 20 mmol/l.

Gr were not the main active sites for BPA removal. In case of  $\text{Co}_3\text{O}_4$  and  $\text{LaCoO}_3$ , the BPA degradation efficiency reached 45 and 75 %, respectively, suggesting that the Co atom in the LCO/Gr catalyst structure can serve as the active center for BPA degradation. To identify the impact of Co in the PMS activation, XPS spectra of LCO/Gr before and after the catalytic reactions were studied. From fitting the spectra shown in Fig. 7a it can be seen that the proportions of  $\text{Co}^{2+}$  and  $\text{Co}^{3+}$  for the fresh catalyst were determined to be 85 and 15 %, while after the catalytic reaction the  $\text{Co}^{3+}$  content increased to 22 %. This indicates that the conversion process in the catalyst occurs at the LCO/Gr surface and  $\text{Co}^{2+}$  may participate in the activation of PMS. It is noteworthy that the addition of citric acid with cobalt-based catalysts during PMS activation can inhibit the degradation process due to the formation of cobalt carboxyl complexes [93]. The addition of 2 mmol/l citric acid decreased the removal efficiency of BPA from 100 to 80 %, and the strong inhibition effect was observed with the increase of citric acid concentration (see supplementary material, Fig. S18), further indicating that Co sites need to be considered as the active sites for PMS activation. Additionally, it has been reported that  $\text{O}_{\text{vac}}$  can promote the bonding and electron transfer of PMS on the catalyst surface [94]. To ascertain the role of  $\text{O}_{\text{vac}}$  on the non-radical mechanism during PMS activation, the change of oxygen content before and after the reaction was analyzed (Fig. 7b). From the O1s spectra, it could be deduced that the percentage of surface oxygen (OS) decreased from 23 to 14 % after the catalytic reaction, suggesting that  $\text{O}_{\text{vac}}$  played a dominant role in BPA degradation and was involved in the generation of  $^1\text{O}_2$ . This finding is supported by analyzing the EPR spectra of fresh and used LCO/Gr catalyst after five reaction runs (Fig. 7c). Compared with fresh LCO/Gr, the EPR signal of the used LCO/Gr was reduced, revealing that  $\text{O}_{\text{vac}}$  participated in PMS activation. Based on the above results, a catalytic mechanism for BPA

degradation by the LCO/Gr + PMS system is suggested including two reaction pathways: A radical ( $\text{SO}_4^{\cdot-}$  and  $\cdot\text{OH}$ ) and a non-radical process ( $^1\text{O}_2$ ). For the radical pathway,  $\text{SO}_4^{\cdot-}$  is generated through a reaction of PMS with the surface  $\text{Co}^{2+}$  of the LCO/Gr material (Equation (7)) and consequently  $\cdot\text{OH}$  is produced from the reaction of  $\text{SO}_4^{\cdot-}$  with the hydroxide ion (Equation (8)) [56]. The produced  $\text{Co}^{3+}$  will react with PMS molecules and convert to  $\text{Co}^{2+}$ , since the standard potential value of the  $\text{Co}^{2+}/\text{Co}^{3+}$  redox pair (1.8 V) is higher than that of  $\text{HSO}_5^-/\text{SO}_5^-$  (1.1 V) (Equation (9)). Thus, the high catalytic performance through the multiple-cycle process can be achieved by the redox reaction of  $\text{Co}^{3+}/\text{Co}^{2+}$ . Moreover, as has been shown in Fig. 7b, a hydroxylation of LCO/Gr occurs, which is attributed to the binding of water molecules to the catalyst surface during PMS activation. Subsequently, these hydroxyl groups will combine with PMS to generate  $\text{SO}_4^{\cdot-}$  (Equation (10)–(11)). The non-radical pathway (creation of  $^1\text{O}_2$ ) is mainly attributed to adsorbed oxygen of metal oxide catalysts [95] and the direct oxidation or recombination of  $\text{O}_2^-$ . Therefore, the generation of  $^1\text{O}_2$  can be attributed to the reaction of adsorbed oxygen species onto the surface vacancy, in which  $\text{O}_{\text{vac}}$  is converted to active oxygen ( $\text{O}^*$ ) leading to the formation of  $^1\text{O}_2$  (Equation (12)–(13)) [96]. Moreover, the quenching test results confirmed that  $\text{O}_2^-$  played a role in BPA degradation as explained before. Thus, another possibility to generate  $^1\text{O}_2$  is the direct oxidation of  $\text{O}_2^-$  that is produced from the reaction of  $\text{O}_2$  via  $\text{O}_{\text{vac}}$  (Equation (14)–(15)). Finally, BPA can be attacked by the generated reactive oxygen species, degrading into small molecular intermediates, and then converting into  $\text{CO}_2$  and  $\text{H}_2\text{O}$  (Equation (16)).



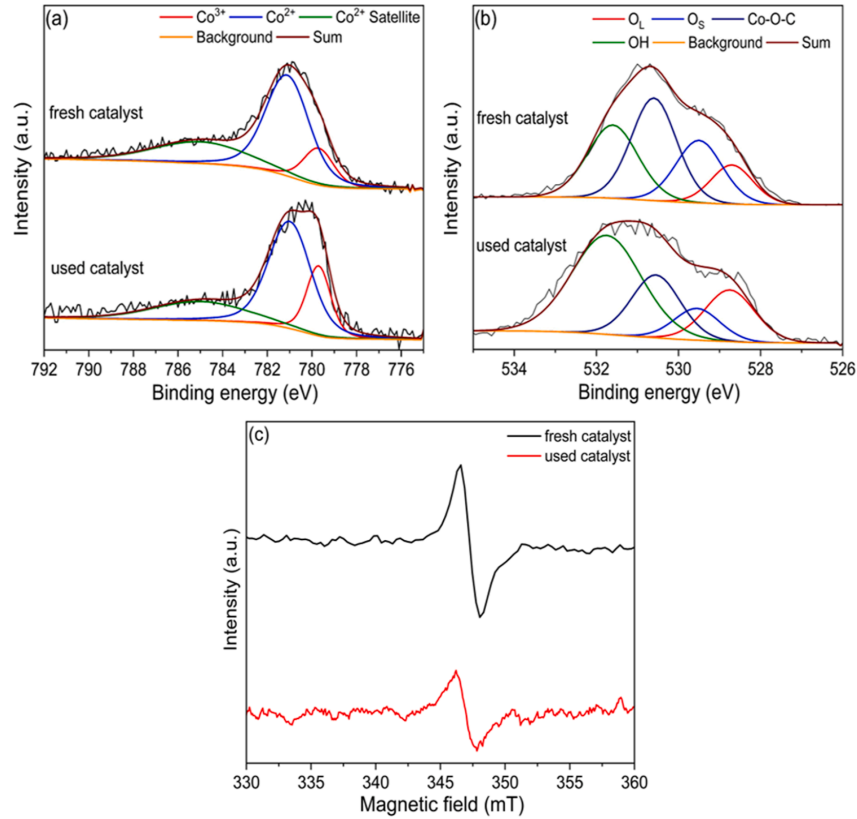
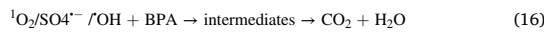
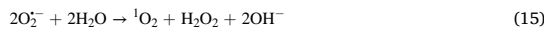
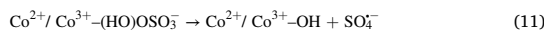
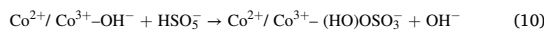


Fig. 7. XPS spectra of (a) Co2p and (b) O1s for fresh and used LCO/Gr nanopowder, and c) EPR spectra of fresh and used LCO/Gr.



### 3.8 Effect of reaction conditions on BPA degradation

#### 3.8.1. Effect of initial pH

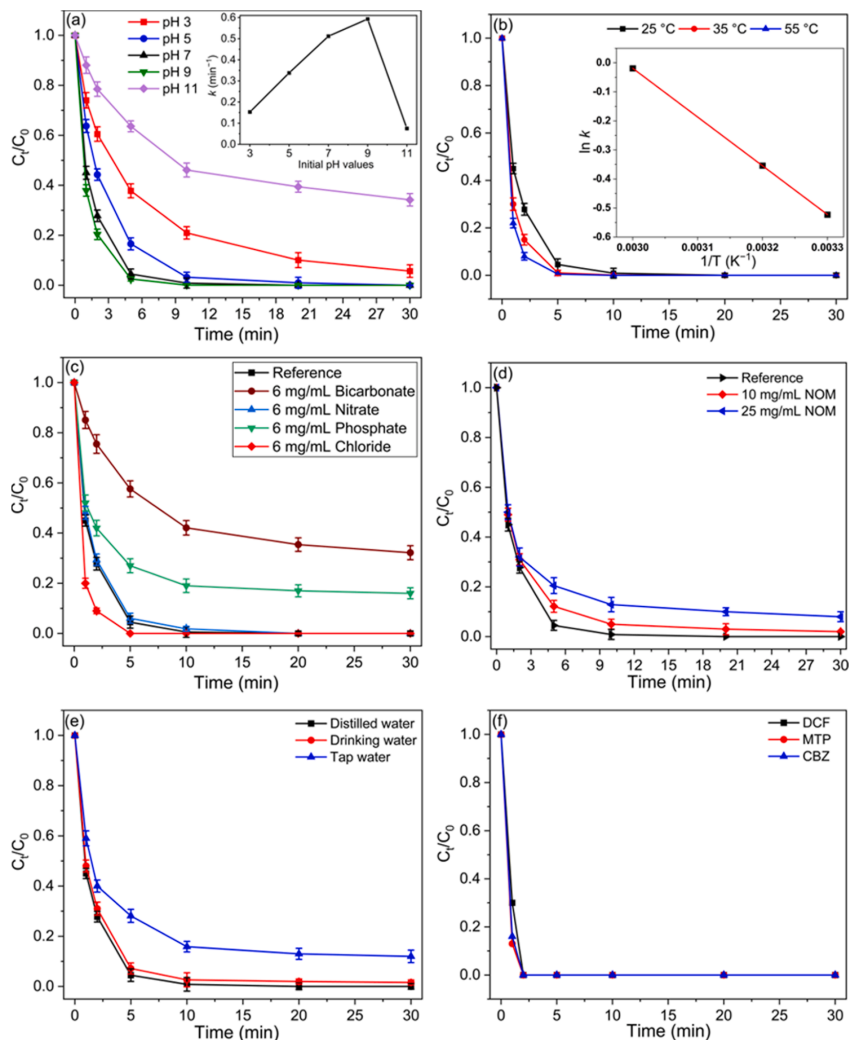
Since changing the pH will affect the surface functional groups of the LCO/Gr material and PMS activation, changing the working pH range is expected to play a crucial role in the catalytic stability of the LCO/Gr material. Thus, the effect of pH on BPA degradation was analyzed ranging from pH = 3.0 to 11.0.

Fig. 8a depicts the influence of the initial pH on BPA removal. It is obvious that the BPA removal efficiency enhanced apparently within 10

min over a pH of 3 to 9 and is decreasing dramatically when the initial pH was adjusted to 11. Accordingly, the pseudo-first order rate constant ( $k_{\text{app}}$ ) of BPA degradation rises from 0.153 to 0.594  $\text{min}^{-1}$  when going from pH = 3 to 9 (see inset Fig. 8a). However, when the initial pH of the solution was adjusted to 11, the  $k_{\text{app}}$  dropped to 0.075  $\text{min}^{-1}$ , which is about eight times lower than that of pH 9. To understand this phenomenon, the pH change with reaction time under different initial pH values during the PMS activation process was studied (see supplementary material, Fig. S19). For initial pH values between 3 and 9, the pH drops sharply within a few minutes after the addition of PMS and decreases only slightly thereafter. For instance, when adjusting the pH to 9, it dropped to 7.5 within 5 min and reached 6.8 after 30 min. In contrast, the pH of the solution with an initial pH of 11 maintained almost stable. This pH is higher than the  $\text{pH}_{\text{pzc}}$  of LCO/Gr nanoparticles (see supplementary material, Fig. S20). Since the  $\text{pK}_{\text{a}1}$  of PMS is 0 and  $\text{pK}_{\text{a}2}$  is 9.4, PMS is present as  $\text{HSO}_5^-$  under the investigated pH range of 0–9.4. Accordingly, for a pH of 11,  $\text{HSO}_5^-$  dissociates into  $\text{SO}_5^{2-}$ , which diminishes the LCO/Gr catalytic efficiency due to the weak oxidative potential of  $\text{SO}_5^{2-}$  [63]. Moreover, a high pH can result in the formation of C–OH, La(OH)<sub>3</sub>, and Co(OH)<sub>2</sub> (see supplementary material, Fig. S21), causing the generation of  $\cdot\text{OH}$  from the reaction of  $\text{SO}_4^-$  with the hydroxide ion (Equation (5)), which also can decrease the catalytic activity of LCO/Gr [97].

#### 3.8.2. Effect of temperature

The effect of reaction temperature on BPA removal with the LCO/Gr



**Fig. 8.** Effects of (a) the initial pH values, (b) temperature, (c) inorganic anions, (d) NOM, and (e) water matrices on BPA degradation by  $\text{La}_2\text{CoO}_{4+6}/\text{PMS}$ , and (f) the catalytic activity of  $\text{LCO}/\text{Gr} + \text{PMS}$  system on the removal of various drugs. Reaction conditions: Drug/BPA = 40 mg/l; PMS = 0.5 mmol/l; catalyst = 0.1 g/l; pH = 7.

+ PMS system was studied at an initial pH of 7. As expected and shown in Fig. 8b, the BPA degradation efficiency was enhanced with increasing reaction temperature. As the reaction temperature increased from 25 to 55 °C, the  $k_{\text{app}}$  ( $1.05 \text{ min}^{-1}$ ) is almost two times higher than at 25 °C ( $0.52 \text{ min}^{-1}$ ). We attribute this result to the fast generation of reactive species by the thermolytic rupture of the O–O bond of PMS. The respective activation energy ( $E_a$ ) was determined from the Arrhenius equation:

$$\ln k_{\text{app}} = \ln A - \frac{E_a}{RT} \quad (17)$$

Where  $A$  is the pre-exponential factor,  $R$  is the universal gas constant ( $8.314 \text{ J mol}^{-1} \text{ K}^{-1}$ ), and  $T$  is the solution temperature. The activation energy  $E_a$  of the  $\text{LCO}/\text{Gr} + \text{PMS}$  system was derived as 14 kJ/mol based on plotting  $\ln k_{\text{app}}$  against  $1/T$  (see inset, Fig. 8b), which is much lower

than the values reported for  $\text{Co}_3\text{O}_4/\text{graphene}$  (26.5 kJ/mol) [98] and  $\text{MnFe}_2\text{O}_4/\text{graphene}$  (25.7 kJ/mol) [99]. These findings imply that the reaction energy barrier for PMS activation is decreased in our  $\text{LCO}/\text{Gr}$  system indicating a higher catalytic activity and performance.

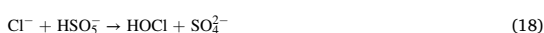
### 3.8.3. Effect of co-existing ions and NOM

Various inorganic anions are ubiquitous in real aquatic environments, which might affect the PMS activation in wastewater treatment as well [19]. Therefore, the effect of various anions relevant in aqueous systems (such as  $\text{Cl}^-$ ,  $\text{NO}_3^-$ ,  $\text{H}_2\text{PO}_4^-$ ,  $\text{HCO}_3^-$ , etc.) on the BPA removal with  $\text{LCO}/\text{Gr}$  nanoparticles was analyzed (Fig. 8c and supplementary material Fig. S22). The comparison of the respective results shows that the  $\text{NO}_3^-$  anion had negligible adverse effects on the BPA degradation, while the  $\text{Cl}^-$  anions had a positive influence on the BPA degradation. The positive effect of  $\text{Cl}^-$  ions on BPA degradation may be attributed to the

M. Hammad et al.

Chemical Engineering Journal 454 (2023) 139900

generation of active chlorine species (e.g. HOCl) which enhance BPA degradation [100] (Equation (18)). Thus, to understand the impact of  $\text{Cl}^-$  on BPA degradation, the BPA removal was analyzed in the presence of only PMS (see [supplementary material, Fig. S23a](#)). The BPA removal efficiency was dramatically enhanced with 6 mg/ml  $\text{Cl}^-$ , suggesting that HOCl was generated as a result of the reaction between PMS and  $\text{Cl}^-$ . Besides, we evaluated the adsorption of BPA by LCO/Gr with the different  $\text{Cl}^-$  concentrations (see [supplementary material, Fig. S23b](#)). As before, 20–23 % of BPA was adsorbed by LCO/Gr at different  $\text{Cl}^-$  concentrations, indicating that the influence of  $\text{Cl}^-$  on BPA adsorption was insignificant. Thus, we propose that the accelerated BPA degradation is based on the generation of HOCl along with  $^1\text{O}_2$  in the LCO/Gr + PMS +  $\text{Cl}^-$  system.



In contrast to  $\text{Cl}^-$  and  $\text{NO}_3^-$ ,  $\text{H}_2\text{PO}_4^-$  exhibits an inhibitory effect on the BPA degradation efficiency because it can chelate with Co and form the Co-phosphate complex (see [supplementary material, Fig. S24](#)), which in turn inhibits the PMS activation. Similarly, the removal efficiency of BPA was decreased with the addition of  $\text{HCO}_3^-$  due to the scavenging effect of  $\text{O}_2^-$ ,  $\text{SO}_4^-$ , and  $\cdot\text{OH}$  by  $\text{HCO}_3^-$  in the system, resulting in a decreased performance of the catalyst [101].

NOM is a constituent of all natural waters and soils and can consume a large number of reactive oxygen species such as  $\text{SO}_4^-$  and  $\cdot\text{OH}$  and block the active site on the catalyst surface during PMS activation [89], resulting in the decreased removal efficiency towards organic contaminants. As depicted in [Fig. 8d](#), the removal rate of BPA was slightly inhibited with the presence of 10 and 25 mg/l NOM. The decrease might be related to the adsorption of NOM on the surface of the catalyst which could reduce the complexation of PMS to generate reactive oxygen species. This is consistent with previous reports showing NOM to have a negligible impact on the performance of nonradical-based systems [102,103].

To evaluate the applicability of the LCO/Gr + PMS system in real aquatic environments, additional BPA removal experiments were conducted in tap and drinking water. The characteristics of tap and drinking water samples are depicted in [Table S5](#). As shown in [Fig. 8e](#), the BPA removal efficiency was insignificantly decreased in the drinking water sample while the BPA degradation efficiency was slightly changed to 90 % in the tap water sample. The results indicate that the inorganic anions in the water have only negligible adverse effects on BPA degradation.

#### 3.8.4. Effect of different pharmaceutical drugs

Moreover, the catalytic performance of the LCO/Gr + PMS system has been tested for different kinds of drugs which is important for wastewater treatment applications. Hence, the catalytic activity of LCO/Gr was evaluated with diclofenac (DCF), metoprolol (MTP), and carbamazepine (CBZ). As shown in [Fig. 8f](#), the degradation of DCF, MTP, and CBZ reaches 100 % after 2 min, implying the exceptionally high catalytic performance of the LCO/Gr + PMS system. The TOC removal of DCF, MTP, and CBZ after 30 min was surprisingly high (57, 55, and 61 %, respectively, see [supplementary material Fig. S25](#)), proving that the LCO/Gr material is a promising catalyst for the use in real wastewater treatment systems.

#### 3.9 Possible degradation pathways

The degradation pathway of BPA via the LCO/Gr + PMS system was investigated and identified by LC-MS (see [supplementary material, Fig. S26](#)). According to the mass spectrometric results, seven intermediates were detected for the BPA degradation using the LCO/Gr + PMS system (see [supplementary material, Table S6](#)). First, BPA is mainly attacked by  $^1\text{O}_2$  to produce phenol and p-isopropyl phenol due to a  $\beta$ -scission of isopropyl between two phenyl groups in BPA [104]. Afterwards, the reaction products are further oxidized to form

hydroquinone and 1-(4-methyl phenyl) ethenone, followed by a subsequent oxidative ring-opening leading to the formation of small-molecule intermediates including penta-1,4-dien-3-one, succinic acid, 1,5-hexadiene-3-ol, and 2-hydroxypropanoic acid. Finally, the small-molecule intermediates are further oxidized and mineralized into  $\text{CO}_2$  and  $\text{H}_2\text{O}$ .

#### 4. Conclusions

In summary, we have demonstrated a robust and scalable method to synthesize LCO/Gr nanocomposites that have been employed as novel catalysts to activate PMS for different pollutants degradation. The developed approach consisting of a spray-flame synthesis method followed by the self-assembling technique has practical advantages such as scalability, reproducibility, easy control of the LCO size, and the subsequent decoration of the graphene nanosheets, eco-friendliness, and cost-effectivity.

The enhanced catalytic activity of the LCO/Gr composite compared to LCO nanoparticles is based on several, especially nano-specific features: First, we observed a synergistic and robust interaction between LCO and graphene, supported by stable Co—O—C interactions, leading to an outstanding BPA degradation efficiency (>99 %) and excellent stability with less cobalt leaching (0.004 mg/l) in the presence of PMS. Secondly, the high surface area of graphene (300 m<sup>2</sup>/g) and the presence of unpaired  $\pi$  electrons in the LCO/Gr structure facilitates a better accessibility of active sites, which is supported by a fast electron transport from LCO to PMS molecules through graphene nanosheets. Thirdly, LCO/Gr has an excellent catalytic activity through the multiple-cycle process (>95 %) and can be utilized over a wide pH range (pH 3–11). Fourthly, the LCO/Gr catalytic system exhibits a very effective removal of different drugs such as diclofenac (>99 %), metoprolol (>99 %), and carbamazepine (>99 %), which are widely detected in municipal and industrial wastewater. Finally, the catalytic efficiency of LCO/Gr is insignificantly reduced in drinking water and tap water samples and showed high resistance to co-existing ions and NOM, proving that the LCO/Gr material is a promising catalyst for subsequent use in real wastewater treatment systems.

#### Declaration of Competing Interest

The authors declare that they have no known competing financial interests or personal relationships that could have appeared to influence the work reported in this paper.

#### Data availability

No data was used for the research described in the article.

#### Acknowledgement

The results are based on work supported by the Mercator Research Center Ruhr (MERCUR) within the DIMENSION project. The authors thank M. Heidelmann from the Interdisciplinary Center for Analytics on the Nanoscale, ICAN, S. Apazeller (IVG UDE), R. Meckenstock (Faculty of Physics, UDE) for the TEM, TGA, and EPR measurements. A.K. Al-Kamal acknowledges the support of the German Academic Exchange Service (DAAD) as well as the IMPRS RECHARGE program of the Max-Planck Society. A.S. Amin gratefully acknowledges financial support from the Federal Ministry for Economic Affairs and Energy (WIPANO funding scheme, project number 03TN0013A). D. Segets thanks the Deutsche Forschungsgemeinschaft (DFG), grant number SE 2526/3-1 and H. Wiggers and C. Schulz thank the DFG through funding within projects 405366241 and 262219004. The authors are grateful to Alexander von Humboldt (AvH) Stiftung, Germany which financially supported this work.

M. Hamad et al.

Chemical Engineering Journal 454 (2023) 139900

## Appendix A. Supplementary data

Supplementary data to this article can be found online at <https://doi.org/10.1016/j.cej.2022.139900>.

## References

- [1] A. Küster, N. Adler, Pharmaceuticals in the environment: scientific evidence of risks and its regulation, *Philos. Trans. R. Soc. Lond. B Biol. Sci.* 369 (2014) 20130587, <https://doi.org/10.1098/rstb.2013.0587>.
- [2] W. Guo, B. Pan, S. Sakkiiah, G. Yavas, W. Ge, W. Zou, W. Tong, H. Hong, Persistent Organic Pollutants in Food: Contamination Sources, Health Effects and Detection Methods, *Int. J. Environ. Res. Public Health* 16 (2019) 4361, <https://doi.org/10.3390/ijerph16224361>.
- [3] J. Wang, S. Wang, Reactive species in advanced oxidation processes: Formation, identification and reaction mechanism, *Chem. Eng. J.* 401 (2020), 126158, <https://doi.org/10.1016/j.cej.2020.126158>.
- [4] A. Fischbacher, C. von Sonntag, T.C. Schmidt, Hydroxyl radical yields in the Fenton process under various pH, ligand concentrations and hydrogen peroxide/Fe(II) ratios, *Chemosphere* 182 (2017) 738–744, <https://doi.org/10.1016/j.chemosphere.2017.05.039>.
- [5] M. Zhang, H. Dong, L. Zhao, D. Wang, D. Meng, A review on Fenton process for organic wastewater treatment based on optimization perspective, *Sci. Total Environ.* 670 (2019) 110–121, <https://doi.org/10.1016/j.scitotenv.2019.03.180>.
- [6] Q. Yang, Y. Ma, F. Chen, F. Yao, J. Sun, S. Wang, K. Yi, L. Hou, X. Li, D. Wang, Recent advances in photo-activated sulfate radical-advanced oxidation process (SR-AOP) for refractory organic pollutants removal in water, *Chem. Eng. J.* 378 (2019), 122149, <https://doi.org/10.1016/j.cej.2019.122149>.
- [7] Y. Liu, Y. Wang, Q. Wang, J. Pan, J. Zhang, Simultaneous removal of NO and SO<sub>2</sub> using vacuum ultraviolet light (VUV)/heat/peroxymonosulfate (PMS), *Chemosphere* 190 (2018) 431–441, <https://doi.org/10.1016/j.chemosphere.2017.10.020>.
- [8] R. Xie, J. Ji, K. Guo, D. Lei, Q. Fan, D.Y.C. Leung, H. Huang, Wet scrubber coupled with UV/PMS process for efficient removal of gaseous VOCs: Roles of sulfate and hydroxyl radicals, *Chem. Eng. J.* 356 (2019) 632–640, <https://doi.org/10.1016/j.cej.2018.09.025>.
- [9] Z.-H. Diao, Z.-Y. Lin, X.-Z. Chen, L. Yan, F.-X. Dong, W. Qian, L.-J. Kong, J.-J. Du, W. Chu, Ultrasound-assisted heterogeneous activation of peroxymonosulfate by natural pyrite for 2,4-dichlorophenol degradation in water: Synergistic effects, pathway and mechanism, *Chem. Eng. J.* 389 (2020) 123771.
- [10] H. Song, L. Yan, Y. Wang, J. Jiang, J. Ma, C. Li, G. Wang, J. Gu, P. Liu, Electrochemically activated PMS and PDS: Radical oxidation versus nonradical oxidation, *Chem. Eng. J.* 391 (2020) 123560.
- [11] B. Bouzayani, E. Rosales, M. Pazos, S.C. Elaoud, M.A. Sanromán, Homogeneous and heterogeneous peroxymonosulfate activation by transition metals for the degradation of industrial leather dye, *J. Clean. Prod.* 228 (2019) 222–230, <https://doi.org/10.1016/j.jclepro.2019.04.217>.
- [12] Z. Li, M. Wang, C. Jin, J. Kang, J. Liu, H. Yang, Y. Zhang, Q. Pu, Y. Zhao, M. You, Z. Wu, Synthesis of novel Co<sub>3</sub>O<sub>4</sub> hierarchical porous nanosheets via corn stem and MOF-Co templates for efficient oxytetracycline degradation by peroxymonosulfate activation, *Chem. Eng. J.* 392 (2020), 123789, <https://doi.org/10.1016/j.cej.2019.123789>.
- [13] S. Chen, J. Deng, C. Ye, C. Xu, L. Huai, J. Li, X. Li, Simultaneous removal of pararsanilic acid and the released inorganic arsenic species by CuFe<sub>2</sub>O<sub>4</sub> activated peroxymonosulfate process, *Sci. Total Environ.* 742 (2020), 140587, <https://doi.org/10.1016/j.scitotenv.2020.140587>.
- [14] S.B. Hammouda, F. Zhao, Z. Safaei, V. Srivastava, D. Lakshmi Ramasamy, S. Iftikhar, S. Kalliola, M. Sillanpää, Degradation and mineralization of phenol in aqueous medium by heterogeneous monopersulfate activation on nanostructured cobalt based-perovskite catalysts ACoO<sub>3</sub> (A=La, Ba, Sr and Ce): Characterization, kinetics and mechanism study, *Appl. Catal. B Environ.* 215 (2017) 60–73.
- [15] J. Cao, L. Lai, B. Lai, G. Yao, X. Chen, L. Song, Degradation of tetracycline by peroxymonosulfate activated with zero-valent iron: Performance, intermediates, toxicity and mechanism, *Chem. Eng. J.* 364 (2019) 45–56, <https://doi.org/10.1016/j.cej.2019.01.113>.
- [16] S. Wang, J. Wang, Kinetics of PMS activation by graphene oxide and biochar, *Chemosphere* 239 (2020), 124812, <https://doi.org/10.1016/j.chemosphere.2019.124812>.
- [17] C. Cheng, S. Gao, J. Zhu, G. Wang, L. Wang, X. Xia, Enhanced performance of LaFeO<sub>3</sub> perovskite for peroxymonosulfate activation through strontium doping towards 2,4-D degradation, *Chem. Eng. J.* 384 (2020), 123377, <https://doi.org/10.1016/j.cej.2019.123377>.
- [18] Y. Wang, Z. Chi, C. Chen, C. Su, D. Liu, Y. Liu, X. Duan, S. Wang, Facet- and defect-dependent activity of perovskites in catalytic evolution of sulfate radicals, *Appl. Catal. B Environ.* 272 (2020), 118972, <https://doi.org/10.1016/j.apcatb.2020.118972>.
- [19] M. Hamad, B. Alkan, A.K. Al-kamal, C. Kim, M.Y. Ali, S. Angel, H.T. A. Wiedemann, D. Klippert, T.C. Schmidt, C.W.M. Kay, H. Wiggers, Enhanced heterogeneous activation of peroxymonosulfate by Ruddlesden-Popper-type La<sub>2</sub>CoO<sub>4+δ</sub> nanoparticles for bisphenol A degradation, *Chem. Eng. J.* 429 (2022) 131447.
- [20] X. Duan, C. Su, J. Miao, Y. Zhong, Z. Shao, S. Wang, H. Sun, Insights into perovskite-catalyzed peroxymonosulfate activation: Maneuverable cobalt sites for promoted evolution of sulfate radicals, *Appl. Catal. B Environ.* 220 (2018) 626–634, <https://doi.org/10.1016/j.apcatb.2017.08.088>.
- [21] B. Alkan, S. Cychy, S. Varhade, M. Muhler, C. Schulz, W. Schuhmann, H. Wiggers, C. Andronescu, Spray-Flame-Synthesized LaCo<sub>1-x</sub>Fe<sub>x</sub>O<sub>3</sub> Perovskite Nanoparticles as Electrocatalysts for Water and Ethanol Oxidation, *ChemElectroChem.* 6 (2019) 4266–4274, <https://doi.org/10.1002/celec.201900168>.
- [22] J. Büker, B. Alkan, Q. Fu, W. Xia, J. Schulwitz, D. Waffel, T. Falk, C. Schulz, H. Wiggers, M. Muhler, B. Peng, Selective cyclohexene oxidation with O<sub>2</sub>, H<sub>2</sub>O<sub>2</sub> and tert-butyl hydroperoxide over spray-flame synthesized LaCo<sub>1-x</sub>Fe<sub>x</sub>O<sub>3</sub> nanoparticles, *Catal. Sci. Technol.* 10 (2020) 5196–5206, <https://doi.org/10.1039/D0CY00906G>.
- [23] H. Chen, W. Cui, D. Li, Q. Tian, J. He, Q. Liu, X. Chen, M. Cui, X. Qiao, Z. Zhang, J. Tang, Z. Fei, Selectively Etching Lanthanum to Engineer Surface Cobalt-Enriched LaCoO<sub>3</sub> Perovskite Catalysts for Toluene Combustion, *Ind. Eng. Chem. Res.* 59 (2020) 10804–10812, <https://doi.org/10.1021/acs.iecr.0c01182>.
- [24] Y. Yamada, K. Yano, D. Hong, S. Fukuzumi, LaCoO<sub>3</sub> acting as an efficient and robust catalyst for photocatalytic water oxidation with persulfate, *PCPP* 14 (2012) 5753–5760, <https://doi.org/10.1039/C2CP00022A>.
- [25] P. Liang, D. Meng, Y. Liang, Z. Wang, C. Zhang, S. Wang, Z. Zhang, Cation deficiency tuned LaCoO<sub>3-δ</sub> perovskite for peroxymonosulfate activation towards bisphenol A degradation, *Chem. Eng. J.* 409 (2021), 128196, <https://doi.org/10.1016/j.cej.2020.128196>.
- [26] X. Huang, G. Zhao, G. Wang, J.T.S. Irvine, Synthesis and applications of nanoporous perovskite metal oxides, *Chem. Sci.* 9 (2018) 3623–3637, <https://doi.org/10.1039/C7SC03920D>.
- [27] S. Royer, D. Duprez, F. Can, X. Courtois, C. Batiot-Dupeyrat, S. Laassiri, H. Alamdari, Perovskites as Substitutes of Noble Metals for Heterogeneous Catalysis: Dream or Reality, *Chem. Rev.* 114 (2014) 10292–10368, <https://doi.org/10.1021/cr500032a>.
- [28] P. Granger, V.I. Parvulescu, S. Kaliaguine, W. Prellier, *Perovskites and Related Mixed Oxides*, Wiley-VCH Verlag GmbH & Co. KGaA, 2016.
- [29] N.T. Thuy, D. Le Minh, Size Effect on the Structural and Magnetic Properties of Nanosized Perovskite <svg style="vertical-align: -4.67647pt; width: 70.75px; id="M1" height="21.1" version="1.1" viewBox="0 0 70.75 21.1" width="70.75" xmlns="http://www.w3.org/2000/svg"><g transform=, Adv. Mater. Sci. Eng. 2012 (2012) 380306. doi: 10.1155/2012/380306.
- [30] B. Alkan, D. Medina, J. Landers, M. Heidelberg, U. Hagemann, S. Salamon, C. Andronescu, H. Wende, C. Schulz, W. Schuhmann, H. Wiggers, Spray-Flame-Prepared LaCo<sub>1-x</sub>Fe<sub>x</sub>O<sub>3</sub> Perovskite Nanoparticles as Active OER Catalysts: Influence of Fe Content and Low-Temperature Heating, *ChemElectroChem.* 7 (2020) 2564–2574, <https://doi.org/10.1002/celec.201902051>.
- [31] S. Angel, J.D. Tapia, J. Gallego, U. Hagemann, H. Wiggers, Spray-Flame Synthesis of LaMnO<sub>3+δ</sub> Nanoparticles for Selective CO Oxidation (SELOX), *Energy Fuels* 35 (2021) 4367–4376, <https://doi.org/10.1021/acs.energyfuels.0c03659>.
- [32] C. Schulz, T. Dreier, M. Fikri, H. Wiggers, Gas-phase synthesis of functional nanomaterials: Challenges to kinetics, diagnostics, and process development, *Proc. Combust. Inst.* 37 (2019) 83–108, <https://doi.org/10.1016/j.proci.2018.06.231>.
- [33] M. Abdul Nasir Khan, P. Kwame Klu, C. Wang, W. Zhang, R. Luo, M. Zhang, J. Qi, X. Sun, L. Wang, J. Li, Metal-organic framework-derived hollow Co<sub>3</sub>O<sub>4</sub>/carbon as efficient catalyst for peroxymonosulfate activation, *Chem. Eng. J.* 363 (2019) 234–246.
- [34] C. Liu, L. Liu, X. Tian, Y. Wang, R. Li, Y. Zhang, Z. Song, B. Xu, W. Chu, F. Qi, A. Ikhlaiq, Coupling metal-organic frameworks and g-C<sub>3</sub>N<sub>4</sub> to derive Fe@N-doped graphene-like carbon for peroxymonosulfate activation: Upgrading framework stability and performance, *Appl. Catal. B Environ.* 255 (2019), 117763, <https://doi.org/10.1016/j.apcatb.2019.117763>.
- [35] W. Han, D. Li, M. Zhang, H. Ximin, X. Duan, S. Liu, S. Wang, Photocatalytic activation of peroxymonosulfate by surface-tailored carbon quantum dots, *J. Hazard. Mater.* 395 (2020), 122695, <https://doi.org/10.1016/j.jhazmat.2020.122695>.
- [36] W. Lin, X. Xie, X. Wang, Y. Wang, D. Segets, J. Sun, Efficient adsorption and sustainable degradation of gaseous acetaldehyde and o-xylene using rGO-TiO<sub>2</sub> photocatalyst, *Chem. Eng. J.* 349 (2018) 708–718, <https://doi.org/10.1016/j.cej.2018.05.107>.
- [37] N. Baig, Ihsanullah, M. Sajid, T.A. Saleh, Saleh, Graphene-based adsorbents for the removal of toxic organic pollutants: A review, *J. Environ. Manage.* 244 (2019) 370–382.
- [38] J. Xu, L. Wang, Y. Zhu, Decontamination of Bisphenol A from Aqueous Solution by Graphene Adsorption, *Langmuir* 28 (2012) 8418–8425, <https://doi.org/10.1021/la301476p>.
- [39] Q. Xiang, J. Yu, M. Janoniec, Graphene-based semiconductor photocatalysts, *Chem. Soc. Rev.* 41 (2012) 782–796, <https://doi.org/10.1039/C1CS15172J>.
- [40] N. Zhang, M.-Q. Yang, S. Liu, Y. Sun, Y.-J. Xu, Waltzing with the Versatile Platform of Graphene to Synthesize Composite Photocatalysts, *Chem. Rev.* 115 (2015) 10307–10377, <https://doi.org/10.1021/acs.chemrev.5b00267>.
- [41] A.V. Karim, A. Selvaraj, Graphene composites in photocatalytic oxidation of aqueous organic contaminants – A state of art, *Process Saf. Environ. Prot.* 146 (2021) 136–160, <https://doi.org/10.1016/j.psep.2020.08.042>.
- [42] M. Hamad, P. Fortugno, S. Hardt, C. Kim, S. Salamon, T.C. Schmidt, H. Wende, C. Schulz, H. Wiggers, Large-scale synthesis of iron oxide/graphene hybrid materials as highly efficient photo-Fenton catalyst for water remediation, *Environ. Technol. Innov.* 21 (2021) 101239.
- [43] U.K. Sur, Graphene: A Rising Star on the Horizon of Materials Science, *Int. J. Electrochem.* 2012 (2012) 1–12.

- [44] C. Wang, P. Shi, X. Cai, Q. Xu, X. Zhou, X. Zhou, D. Yang, J. Fan, Y. Min, H. Ge, W. Yao, Synergistic Effect of Co<sub>3</sub>O<sub>4</sub> Nanoparticles and Graphene as Catalysts for Peroxymonosulfate-Based Orange II Degradation with High Oxidant Utilization Efficiency, *J. Phys. Chem. C* 120 (2016) 336–344, <https://doi.org/10.1021/acs.jpcc.5b10032>.
- [45] V. Murugadoss, P. Panneerselvam, C. Yan, Z. Guo, S. Angaiyah, A simple one-step hydrothermal synthesis of cobaltnickel selenide/graphene nanohybrid as an advanced platinum free counter electrode for dye sensitized solar cell, *Electrochim. Acta* 312 (2019) 157–167, <https://doi.org/10.1016/j.electacta.2019.04.142>.
- [46] F. Yang, J. Mao, S. Li, J. Yin, J. Zhou, W. Liu, Cobalt–graphene nanomaterial as an efficient catalyst for selective hydrogenation of 5-hydroxymethylfurfural into 2,5-dimethylfuran, *Catal. Sci. Technol.* 9 (2019) 1329–1333, <https://doi.org/10.1039/C9CY00330D>.
- [47] M. Khan, M.N. Tahir, S.F. Adil, H.U. Khan, M.R.H. Siddiqui, A.A. Al-warthan, W. Tremel, Graphene based metal and metal oxide nanocomposites: synthesis, properties and their applications, *J. Mater. Chem. A* 3 (2015) 18753–18808, <https://doi.org/10.1039/C5TA02240A>.
- [48] J. Liu, J. Tang, J.J. Gooding, Strategies for chemical modification of graphene and applications of chemically modified graphene, *J. Mater. Chem.* 22 (2012) 12435–12452, <https://doi.org/10.1039/C2JM31218B>.
- [49] Y. Chen, X. Bai, Y. Ji, T. Shen, Reduced graphene oxide-supported hollow Co<sub>3</sub>O<sub>4</sub>/N-doped porous carbon as peroxymonosulfate activator for sulfamethoxazole degradation, *Chem. Eng. J.* 430 (2022), 132951, <https://doi.org/10.1016/j.cej.2021.132951>.
- [50] J. Ye, D. Yang, J. Dai, C. Li, Y. Yan, Confinement of ultrafine Co<sub>3</sub>O<sub>4</sub> nanoparticles in nitrogen-doped graphene-supported macroscopic microspheres for ultrafast catalytic oxidation: Role of oxygen vacancy and ultrasmall size effect, *Sep. Purif. Technol.* 281 (2022), 119963, <https://doi.org/10.1016/j.seppur.2021.119963>.
- [51] Y. Yao, Y. Hu, H. Hu, L. Chen, M. Yu, M. Gao, S. Wang, Metal-free catalysts of graphitic carbon nitride-covalent organic frameworks for efficient pollutant destruction in water, *J. Colloid Interface Sci.* 554 (2019) 376–387, <https://doi.org/10.1016/j.jcis.2019.07.002>.
- [52] S. Hardt, I. Wlokas, C. Schulz, H. Wiggers, Impact of ambient pressure on titania nanoparticle formation during spray-flame synthesis, *J. Nanosci. Nanotechnol.* 15 (2015) 9449–9456, <https://doi.org/10.1166/jnn.2015.10607>.
- [53] F. Schneider, S. Suleiman, J. Menser, E. Borukhovich, I. Wlokas, A. Kempf, H. Wiggers, C. Schulz, SpraySyn—A standardized burner configuration for nanoparticle synthesis in spray flames, *Rev. Sci. Instrum.* 90 (2019) 85108, <https://doi.org/10.1063/1.5090232>.
- [54] A. Münzer, L. Xiao, Y.H. Schelleier, C. Schulz, H. Wiggers, All gas-phase synthesis of graphene: Characterization and its utilization for silicon-based lithium-ion batteries, *Electrochim. Acta* 272 (2018) 52–59, <https://doi.org/10.1016/j.electacta.2018.03.137>.
- [55] S. Bapat, D. Segets, Sedimentation Dynamics of Colloidal Formulations through Direct Visualization: Implications for Fuel Cell Catalyst Inks, *ACS Appl. Nano Mater.* 3 (2020) 7384–7391, <https://doi.org/10.1021/acsnm.0c01467>.
- [56] C. Liang, C.-F. Huang, N. Mohanty, R.M. Kurakalva, A rapid spectrophotometric determination of persulfate anion in ISCO, *Chemosphere* 73 (2008) 1540–1543, <https://doi.org/10.1016/j.chemosphere.2008.08.043>.
- [57] L. Tepech-Carrillo, A. Escobedo-Morales, A. Pérez-Centeno, E. Chigo-Anota, J. F. Sánchez-Ramírez, E. López-Apreza, J. Gutiérrez-Gutiérrez, Preparation of Nanosized LaCoO<sub>3</sub> through Calcination of a Hydrothermally Synthesized Precursor, *J. Nanomater.* 2016 (2016) 6917950, <https://doi.org/10.1155/2016/6917950>.
- [58] M.A. Pimenta, G. Dresselhaus, M.S. Dresselhaus, L.G. Cançado, A. Jorio, R. Saito, Studying disorder in graphite-based systems by Raman spectroscopy, *PCCP* 9 (2007) 1276–1290, <https://doi.org/10.1039/B613962K>.
- [59] T. Ishimoto, Y. Ito, T. Tada, R. Oike, T. Nakamura, K. Amezawa, M. Koyama, Theoretical study on temperature effect of electronic structure and spin state in LaCoO<sub>3</sub> by using density functional theory, *Solid State Ionics* 285 (2016) 195–201, <https://doi.org/10.1016/j.ssi.2015.08.017>.
- [60] F. Cheng, T. Zhang, Y. Zhang, J. Du, X. Han, J. Chen, Enhancing Electrocatalytic Oxygen Reduction on MnO<sub>2</sub> with Vacancies, *Angew. Chemie Int. Ed.* 52 (2013) 2474–2477, <https://doi.org/10.1002/anie.201208582>.
- [61] J. Hu, X. Zeng, G. Wang, B. Qian, Y. Liu, X. Hu, B. He, L. Zhang, X. Zhang, Modulating mesoporous Co<sub>3</sub>O<sub>4</sub> hollow nanospheres with oxygen vacancies for highly efficient peroxymonosulfate activation, *Chem. Eng. J.* 400 (2020), 125869, <https://doi.org/10.1016/j.cej.2020.125869>.
- [62] C. Santhosh, A. Malathi, E. Daneshvar, P. Kollu, A. Bhatnagar, Photocatalytic degradation of toxic aquatic pollutants by novel magnetic 3D-TiO<sub>2</sub>@HPGA nanocomposite, *Sci. Rep.* 8 (2018) 15531, <https://doi.org/10.1038/s41598-018-33818-9>.
- [63] P.H.T. Ngamou, K. Kohse-Höinghaus, N. Bahlawane, CO and ethanol oxidation over LaCoO<sub>3</sub> planar model catalysts: Effect of the thickness, *Catal. Commun.* 12 (2011) 1344–1350, <https://doi.org/10.1016/j.catcom.2011.04.029>.
- [64] C. Lv, H. Chen, M. Hu, T. Ai, H. Fu, Nano-oxides washcoat for enhanced catalytic oxidation activity toward the perovskite-based monolithic catalyst, *Environ. Sci. Pollut. Res.* 28 (2021) 37142–37157, <https://doi.org/10.1007/s11356-021-13354-2>.
- [65] L. Armelao, M. Bettinelli, G. Bottaro, D. Barreca, E. Tondello, LaCoO<sub>3</sub> Nanopowders by XPS, *Surf. Sci. Spectra* 8 (2001) 24–31, <https://doi.org/10.1116/1.20100701>.
- [66] M. Guiotto, M. Pacella, G. Perin, A. Iovino, N. Michelon, M.M. Natile, A. Gilsenti, P. Canu, Washcoating vs. direct synthesis of LaCoO<sub>3</sub> on monoliths for environmental applications, *Appl. Catal. A Gen.* 499 (2015) 146–157, <https://doi.org/10.1016/j.apcata.2015.04.013>.
- [67] Y. Li, L. Liu, Z. Wang, L. Zhou, Y. Lan, C. Chen, Simultaneous oxidation of 4-aminophenylarsonic acid and adsorption of the produced inorganic arsenic by a combination of Co<sub>3</sub>O<sub>4</sub>-La<sub>2</sub>CO<sub>5</sub>@RSCB with peroxymonosulfate, *Chem. Eng. J.* 413 (2021), 127417, <https://doi.org/10.1016/j.cej.2020.127417>.
- [68] S. Dong, Q. Ji, Y. Wang, H. Liu, J. Qu, Enhanced phosphate removal using zirconium hydroxide encapsulated in quaternized cellulose, *J. Environ. Sci.* 89 (2020) 102–112, <https://doi.org/10.1016/j.jes.2019.10.005>.
- [69] S. Yang, Y. Liu, Y. Hao, X. Yang, W.A. Goddard III, X.L. Zhang, B. Cao, Oxygen-Vacancy Abundant Ultrafine Co<sub>3</sub>O<sub>4</sub>/Graphene Composites for High-Rate Supercapacitor Electrodes, *Adv. Sci.* 5 (2018) 1700659, <https://doi.org/10.1002/adv.201700659>.
- [70] T.L. Phan, L.V. Bau, N.V. Khiem, N.X. Phuc, S.C. Yu, ESR study of Sr-doped LaCoO<sub>3</sub> cobaltes, *Phys. Status Solidi.* 242 (2005) 1522–1527, <https://doi.org/10.1002/psb.200440033>.
- [71] C. Sanchez, B. Lebeau, F. Chaput, J.-P. Boilot, Optical Properties of Functional Hybrid Organic-Inorganic Nanocomposites, *Adv. Mater.* 15 (2003) 1969–1994, <https://doi.org/10.1002/adma.200300389>.
- [72] A.M. Salih, M. Bin Ahmad, N.A. Ibrahim, K.Z.H.M. Dahlan, R. Tajau, M. H. Mahmood, W.M.Z.W. Yunus, Synthesis of Radiation Curable Palm Oil-Based Epoxy Acrylate: NMR and FTIR Spectroscopic Investigations, *Molecules* 20 (2015) 14191–14211, <https://doi.org/10.3390/molecules200814191>.
- [73] C. Berthomieu, R. Hienerwadel, Fourier transform infrared (FTIR) spectroscopy, *Photosynth. Res.* 101 (2009) 157–170, <https://doi.org/10.1007/s11120-009-9439-x>.
- [74] G. Zhou, D.-W. Wang, L.-C. Yin, N. Li, F. Li, H.-M. Cheng, Oxygen Bridges between NiO Nanosheets and Graphene for Improvement of Lithium Storage, *ACS Nano* 6 (2012) 3214–3223, <https://doi.org/10.1021/nn300098m>.
- [75] B. Apicella, M. Alfè, R. Barbella, A. Tregrossi, A. Cjajolo, Aromatic structures of carbonaceous materials and soot inferred by spectroscopic analysis, *Carbon* N. Y. 42 (2004) 1583–1589, <https://doi.org/10.1016/j.carbon.2004.02.010>.
- [76] V. Tucureanu, A. Matei, A.M. Avram, FTIR Spectroscopy for Carbon Family Study, *Crit. Rev. Anal. Chem.* 46 (2016) 502–520, <https://doi.org/10.1080/10408347.2016.1157013>.
- [77] S. Abbott, C.M. Hansen, H. Yamamoto, Hansen solubility parameters in practice complete with eBook, software and data, 2013.
- [78] T. Vasiljevic, T. Harner, Bisphenol A and its analogues in outdoor and indoor air: Properties, sources and global levels, *Sci. Total Environ.* 789 (2021), 148013, <https://doi.org/10.1016/j.scitotenv.2021.148013>.
- [79] S. Sharma, S. Basu, N.P. Shetti, M.N. Nadagoda, T.M. Aminabhavi, Microplastics in the environment: Occurrence, perils, and eradication, *Chem. Eng. J.* 408 (2021), 127317, <https://doi.org/10.1016/j.cej.2020.127317>.
- [80] F. Shoushtarian, M. Negahban-Azar, Worldwide Regulations and Guidelines for Agricultural Water Reuse: A Critical Review, *Water*. 12 (4) (2020) 971.
- [81] W. Ma, N. Wang, Y. Du, T. Tong, L. Zhang, K.-Y. Andrew Lin, X. Han, One-step synthesis of novel Fe<sub>3</sub>C/nitrogen-doped carbon nanotubes/graphene nanosheets for catalytic degradation of Bisphenol A in the presence of peroxymonosulfate, *Chem. Eng. J.* 356 (2019) 1022–1031, <https://doi.org/10.1016/j.cej.2018.09.093>.
- [82] Y. Liu, R. Luo, Y. Li, J. Qi, C. Wang, J. Li, X. Sun, L. Wang, Sandwich-like Co<sub>3</sub>O<sub>4</sub>/MXene composite with enhanced catalytic performance for Bisphenol A degradation, *Chem. Eng. J.* 347 (2018) 731–740, <https://doi.org/10.1016/j.cej.2018.04.155>.
- [83] C. Zhu, F. Liu, C. Ling, H. Jiang, H. Wu, A. Li, Growth of graphene-supported hollow cobalt sulfide nanocrystals via MOF-templated ligand exchange as surface-bound radical sinks for highly efficient bisphenol A degradation, *Appl. Catal. B Environ.* 242 (2019) 238–248, <https://doi.org/10.1016/j.apcatb.2018.09.088>.
- [84] X. Li, A.I. Rykov, B. Zhang, Y. Zhang, J. Wang, Graphene encapsulated Fe<sub>3</sub>C<sub>0.4</sub> nanocages derived from metal-organic frameworks as efficient activators for peroxymonosulfate, *Catal. Sci. Technol.* 6 (2016) 7486–7494, <https://doi.org/10.1039/C6CY01479H>.
- [85] C. Wang, H. Wang, R. Luo, C. Liu, J. Li, X. Sun, J. Shen, W. Han, L. Wang, Metal-organic framework one-dimensional fibers as efficient catalysts for activating peroxymonosulfate, *Chem. Eng. J.* 330 (2017) 262–271, <https://doi.org/10.1016/j.cej.2017.07.156>.
- [86] J. Jing, C. Cao, S. Ma, Z. Li, G. Qu, B. Xie, W. Jin, Y. Zhao, Enhanced defect oxygen of LaFeO<sub>3</sub>/GO hybrids in promoting persulfate activation for selective and efficient elimination of bisphenol A in food wastewater, *Chem. Eng. J.* 407 (2021), 126890, <https://doi.org/10.1016/j.cej.2020.126890>.
- [87] R. Luo, C. Liu, J. Li, C. Wang, X. Sun, J. Shen, W. Han, L. Wang, Convenient synthesis and engineering of ultrafine Co<sub>3</sub>O<sub>4</sub>-incorporated carbon composite: towards practical application of environmental remediation, *J. Mater. Chem. A* 6 (2018) 3454–3461, <https://doi.org/10.1039/C7TA11052A>.
- [88] G.P. Anipsitakis, D.D. Dionysiou, Degradation of Organic Contaminants in Water with Sulfate Radicals Generated by the Conjunction of Peroxymonosulfate with Cobalt, *Environ. Sci. Technol.* 37 (2003) 4790–4797, <https://doi.org/10.1021/es0263792>.
- [89] R. Luo, M. Li, C. Wang, M. Zhang, M.A. Nasir Khan, X. Sun, J. Shen, W. Han, L. Wang, J. Li, Singlet oxygen-dominated non-radical oxidation process for efficient degradation of bisphenol A under high salinity condition, *Water Res.* 148 (2019) 416–424, <https://doi.org/10.1016/j.watres.2018.10.087>.
- [90] X. Zhou, C. Luo, M. Luo, Q. Wang, J. Wang, Z. Liao, Z. Chen, Z. Chen, Understanding the synergistic effect from foreign metals in bimetallic oxides for PMS activation: A common strategy to increase the stoichiometric efficiency of

M. Hamad et al.

Chemical Engineering Journal 454 (2023) 139900

- oxidants, *Chem. Eng. J.* 381 (2020), 122587, <https://doi.org/10.1016/j.cej.2019.122587>.
- [91] C. Tan, X. Jian, L. Su, X. Lu, J. Huang, J. Deng, W. Chu, Kinetic removal of acetaminophen and phenacetin during LED-UV365 photolysis of persulfate system: Reactive oxygen species generation, *Chemosphere* 269 (2021), 129337, <https://doi.org/10.1016/j.chemosphere.2020.129337>.
- [92] C. Chen, F. Li, H.-L. Chen, M.G. Kong, Interaction between air plasma-produced aqueous  $1O_2$  and the spin trap DMPO in electron spin resonance, *Phys. Plasmas* 24 (10) (2017) 103501.
- [93] X. Peng, J. Wu, Z. Zhao, X. Wang, H. Dai, Y. Wei, G. Xu, F. Hu, Activation of peroxymonosulfate by single atom Co-N-C catalysts for high-efficient removal of chloroquine phosphate via non-radical pathways: Electron-transfer mechanism, *Chem. Eng. J.* 429 (2022), 132245, <https://doi.org/10.1016/j.cej.2021.132245>.
- [94] X. Tian, P. Gao, Y. Nie, C. Yang, Z. Zhou, Y. Li, Y. Wang, A novel singlet oxygen involved peroxymonosulfate activation mechanism for degradation of ofloxacin and phenol in water, *Chem. Commun.* 53 (2017) 6589–6592, <https://doi.org/10.1039/C7CC02820B>.
- [95] T. Zhang, Y. Ding, H. Tang, Generation of singlet oxygen over Bi(V)/Bi(III) composite and its use for oxidative degradation of organic pollutants, *Chem. Eng. J.* 264 (2015) 681–689, <https://doi.org/10.1016/j.cej.2014.12.014>.
- [96] E.-T. Yun, J.H. Lee, J. Kim, H.-D. Park, J. Lee, Identifying the Nonradical Mechanism in the Peroxymonosulfate Activation Process: Singlet Oxygenation Versus Mediated Electron Transfer, *Environ. Sci. Technol.* 52 (2018) 7032–7042, <https://doi.org/10.1021/acs.est.8b00959>.
- [97] Q. Wang, Y. Shao, N. Gao, W. Chu, J. Chen, X. Lu, Y. Zhu, N. An, Activation of peroxymonosulfate by  $Al_2O_3$ -based  $CoFe_2O_4$  for the degradation of sulfachloropyridazine sodium: Kinetics and mechanism, *Sep. Purif. Technol.* 189 (2017) 176–185, <https://doi.org/10.1016/j.seppur.2017.07.046>.
- [98] Y. Yao, Z. Yang, H. Sun, S. Wang, Hydrothermal Synthesis of  $Co_3O_4$ -Graphene for Heterogeneous Activation of Peroxymonosulfate for Decomposition of Phenol, *Ind. Eng. Chem. Res.* 51 (2012) 14958–14965, <https://doi.org/10.1021/ie301642g>.
- [99] Y. Yao, Y. Cai, F. Lu, F. Wei, X. Wang, S. Wang, Magnetic recoverable  $MnFe_2O_4$  and  $MnFe_2O_4$ -graphene hybrid as heterogeneous catalysts of peroxymonosulfate activation for efficient degradation of aqueous organic pollutants, *J. Hazard. Mater.* 270 (2014) 61–70, <https://doi.org/10.1016/j.jhazmat.2014.01.027>.
- [100] H.V. Lutz, N. Kerlin, T.C. Schmidt, Sulfate radical-based water treatment in presence of chloride: Formation of chlorate, inter-conversion of sulfate radicals into hydroxyl radicals and influence of bicarbonate, *Water Res.* 72 (2015) 349–360, <https://doi.org/10.1016/j.watres.2014.10.006>.
- [101] W. Duan, J. He, Z. Wei, Z. Dai, C. Feng, A unique Si-doped carbon nanocatalyst for peroxymonosulfate (PMS) activation: insights into the singlet oxygen generation mechanism and the abnormal salt effect, *Environ. Sci. NANO* 7 (2020) 2982–2994, <https://doi.org/10.1039/D0EN00848F>.
- [102] A. Shahzad, J. Ali, J. Iftikhar, G.G. Aregay, J. Zhu, Z. Chen, Z. Chen, Non-radical PMS activation by the nanohybrid material with periodic confinement of reduced graphene oxide (rGO) and Cu hydroxides, *J. Hazard. Mater.* 392 (2020), 122316, <https://doi.org/10.1016/j.jhazmat.2020.122316>.
- [103] S. Yang, P. Wu, J. Liu, M. Chen, Z. Ahmed, N. Zhu, Efficient removal of bisphenol A by superoxide radical and singlet oxygen generated from peroxymonosulfate activated with  $FeO$ -montmorillonite, *Chem. Eng. J.* 350 (2018) 484–495, <https://doi.org/10.1016/j.cej.2018.04.175>.
- [104] S. Wang, J. Tian, Q. Wang, F. Xiao, S. Gao, W. Shi, F. Cui, Development of  $CuO$  coated ceramic hollow fiber membrane for peroxymonosulfate activation: a highly efficient singlet oxygen-dominated oxidation process for bisphenol a degradation, *Appl. Catal. B Environ.* 256 (2019), 117783, <https://doi.org/10.1016/j.apcatb.2019.117783>.

### **3.1.3 Light-induced Radicals**

The last subsection of the chemical sciences illustrates an example on the usage of TR-EPR spectroscopy. Here, a diamagnetic porphyrine system will undergo a transition to a triplet state by short laser pulses. By using a broad range of EPR techniques (TR-EPR, 3p-ESEEM, ED-TR-EPR, Davies ENDOR and inversion recovery) the magnetic properties of the triplet state of the described aluminum-porphyrine system could be investigated. The findings derived here can also be applied to other metal-porphyrine systems.



## 3.1.3.1 Aluminum Porphyrine TR-EPR

Journal of Magnetic Resonance 353 (2023) 107515



Contents lists available at ScienceDirect

Journal of Magnetic Resonance

journal homepage: [www.elsevier.com/locate/jmr](http://www.elsevier.com/locate/jmr)

## The electronic structure and dynamics of the excited triplet state of octaethylaluminum(III)-porphyrin investigated with advanced EPR methods

Angelo Carella<sup>a,1</sup>, Susanna Ciuti<sup>a,1</sup>, Haakon T.A. Wiedemann<sup>b</sup>, Christopher W.M. Kay<sup>b,c</sup>, Arthur van der Est<sup>d</sup>, Donatella Carbonera<sup>a</sup>, Antonio Barbon<sup>a,\*</sup>, Prashanth K. Poddutoori<sup>e</sup>, Marilena Di Valentin<sup>a,\*</sup><sup>a</sup> Department of Chemical Sciences, University of Padova, Via Marzolo 1, 35131 Padova, Italy<sup>b</sup> Department of Chemistry, Saarland University, Campus B 2.2, 66123 Saarbrücken, Germany<sup>c</sup> London Centre for Nanotechnology, University College London, 17-19 Gordon Street, London WC1H 0AH, UK<sup>d</sup> Department of Chemistry, Brock University, 1812 Sir Isaac Brock Way, St. Catharines, Ontario, Canada<sup>e</sup> Department of Chemistry & Biochemistry, University of Minnesota Duluth, 1038 University Drive, Duluth, MN 55812, USA

## ARTICLE INFO

## Article history:

Received 21 April 2023

Revised 14 June 2023

Accepted 18 June 2023

Available online 22 June 2023

## ABSTRACT

The photoexcited triplet state of octaethylaluminum(III)-porphyrin (**AIOEP**) was investigated by time-resolved Electron Paramagnetic Resonance, Electron Nuclear Double Resonance and Electron Spin Echo Envelope Modulation in an organic glass at 10 and 80 K. This main group element porphyrin is unusual because the metal has a small ionic radius and is six-coordinate with axial covalent and coordination bonds. It is not known whether triplet state dynamics influence its magnetic resonance properties as has been observed for some transition metal porphyrins. Together with density functional theory modelling, the magnetic resonance data of **AIOEP** allow the temperature dependence of the zero-field splitting (ZFS) parameters, D and E, and the proton  $A_{zz}$  hyperfine coupling (hfc) tensor components of the methine protons, in the zero-field splitting frame to be determined. The results provide evidence that the ZFS, hfc and spin-lattice relaxation are indeed influenced by the presence of a dynamic process that is discussed in terms of Jahn-Teller dynamic effects. Thus, these effects should be taken into account when interpreting EPR data from larger complexes containing **AIOEP**.

© 2023 Published by Elsevier Inc.

## 1. Introduction

Porphyrin derivatives are among the most versatile molecules in nature. Examples are the chlorophylls, employed in photosynthesis for solar energy conversion, and the hemes, used in respiration for oxygen transport and as electron carriers in oxidation and reduction catalytic reactions. In addition to their biological significance, porphyrin derivatives are also used extensively for a variety of applications such as artificial photosynthesis [1–3], dye-sensitized solar cells [4,5], molecular electronics and photonics [6,7], molecular catalysis [8,9] and photodynamic therapy [10]. The versatility of the porphyrins arises from the extended  $\pi$ -conjugation of the tetrapyrrole ring, its ability to bind a wide variety of substituents on its periphery and various elements in

its center. The  $\pi$ -conjugation makes the porphyrins ideal for photochemical applications because it results in strong absorption of visible light and comparatively long excited singlet state lifetimes. Substituents on the periphery can be used to shift the absorption wavelengths and control the solubility properties. The element bound at the center of the tetrapyrrole ring can act as a catalytic site and influences the oxidation and reduction potentials of the conjugated  $\pi$ -system. Insertion of an Al(III) ion, for example, gives the porphyrin properties that make it a good redox active photosensitizer in supramolecular systems for artificial photosynthesis [1]. Such complexes can be constructed by attaching electron donors, acceptors and/or chromophores on opposite faces of the porphyrin ring via a covalent ester or ether linkage on one face and a Lewis acid–base coordination bond on the opposite face. The axial covalent bonding can also be used to form co-facial porphyrin dimers that mimic the special pair chlorophyll dimers found in natural photosynthesis [11].

Recently, we studied the excited state properties of one such dimer in which Al(III) octaethylporphyrin (**AIOEP**, Fig. 1) was

\* Corresponding authors.

E-mail addresses: [antonio.barbon@unipd.it](mailto:antonio.barbon@unipd.it) (A. Barbon), [marilena.divalentin@unipd.it](mailto:marilena.divalentin@unipd.it) (M. Di Valentin).<sup>1</sup> Angelo Carella and Susanna Ciuti have contributed equally.

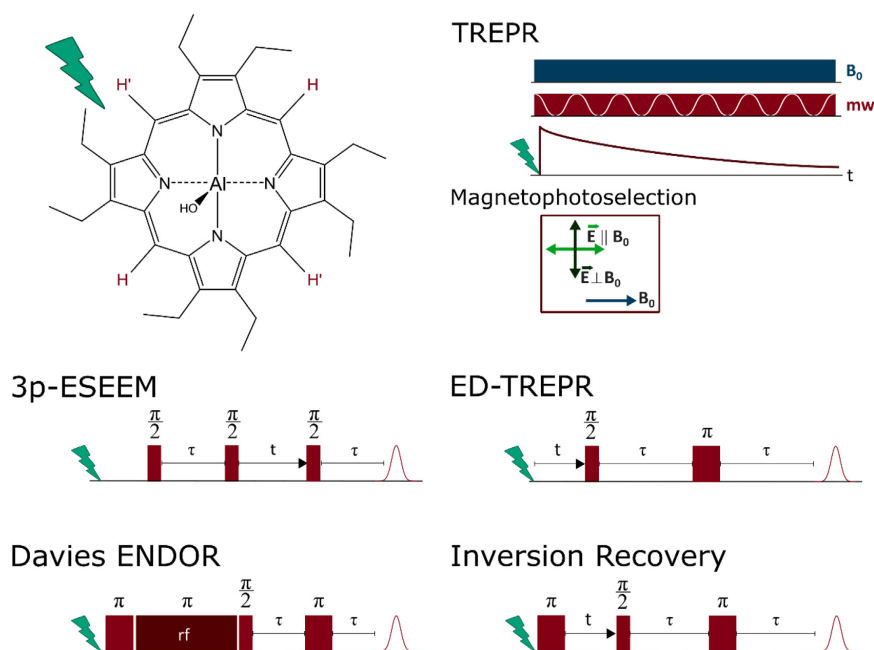


**Fig. 1.** Top left: chemical structure of **AIOEP**, where the two sets of equivalent methine protons are indicated. Top right: schematic representation of the Time-Resolved EPR (TREPR) experiment, including the use of linearly polarized light for magnetophotoselection. Bottom: pulse sequences of the experiments performed in this work: 3-pulse Electron Spin Echo Envelope Modulation (3p-ESEEM), Davies Electron Nuclear Double Resonance (ENDOR), Echo-Detected Time Resolved EPR (ED-TREPR) and Inversion Recovery.

linked to a phosphorus porphyrin [12]. The Time-Resolved Electron Paramagnetic Resonance (TREPR) spectra of this complex showed interesting solvent dependent changes in the zero-field splitting (ZFS), which we ascribed to changes in the charge-transfer character of its delocalized triplet state. For such investigations, information on the behaviour of the triplet state of the corresponding porphyrin monomers can be invaluable to help distinguish between local dynamic effects within the monomers versus delocalization effects in larger multi-porphyrin complexes. The EPR characterization can be particularly useful in understanding the behaviour of the triplet state, but the data on main group porphyrins such as **AIOEP** is sparse. Thus, we have undertaken a detailed study of the magnetic properties of **AIOEP** using several time-resolved and pulsed electron paramagnetic resonance (EPR) methods.

TREPR, Electron-Spin Echo (ESE) techniques and pulsed Electron Nuclear Double Resonance (ENDOR), when coupled with photoexcitation, are ideally suited for investigating the electronic structure and dynamics of chromophores in their triplet state [13–17].

From the spin-polarized triplet state TREPR spectra it is possible to extract information about the zero-field splitting (ZFS) tensor and the triplet-sublevel dependence of the intersystem crossing rates. The ZFS parameters  $D$  and  $E$  are sensitive indicators of the spatial extension and symmetry of the excited triplet state, and the spin polarization properties are a fingerprint for the mechanism of its formation [15]. The time-evolution of the TREPR spectrum and specific ESE pulse sequences, *i.e.*, inversion recovery and echo-detected TREPR (ED-TREPR), can also be used to obtain information on spin dynamics and kinetic properties of the triplet spin sublevels [18,19].

Photoselective TREPR is an excellent method for quantitative determination of the relative orientation of the triplet-state ZFS axes and the optical absorption transition dipole moments [20–22]. It also allows these axes to be fixed in the molecule if the orientation of one of them is known or can be determined *in silico*.

Additional and more specific information about the unpaired electron spin distribution is obtained from the interaction of the triplet state with magnetic nuclei of the molecule, *i.e.* the electron-nuclear hyperfine couplings (hfc). The isotropic hfc ( $a_{\text{iso}}$ ) reflects the unpaired electron spin density at the respective nucleus and the anisotropy of the hyperfine tensor ( $\mathbf{T}$ ) is determined by the dipolar coupling between the electron and nuclear magnetic moments and hence it depends on the molecular geometry in the vicinity of the nucleus. However, the splitting of the EPR transitions due to the hfc is not usually resolved in triplet-state EPR powder spectra. Thus, to determine the hfc more advanced methods like ENDOR and Electron Spin Echo Envelope Modulation (ESEEM) experiments are required [23–27]. If the hfc of several nuclei in different parts of the cofactor(s) can be determined and assigned to specific nuclei, the spin density distribution of the triplet state in the molecule is revealed. Pulse ENDOR and ESEEM combined with pulsed laser excitation at low temperatures are well suited for this purpose, since these hyperfine spectroscopies can take full advantage of the large electron spin polarization of the chromophore in the triplet state [28,29] compared to continuous light excitation and continuous wave-ENDOR methods.

The core of a metalloporphyrin is a tetrapyrrole ring with  $D_{4h}$  symmetry. Its lowest excited triplet state is doubly degenerate with  $^3E_u$  symmetry [30,31] and hence, its ZFS tensor is axially symmetric and the four methine protons at the meso positions are

magnetically equivalent (see Fig. 1). However, static distortions and vibronic coupling can break the symmetry and lift the degeneracy of the triplet states. This results in a loss of the axial symmetry of the ZFS tensor and inequivalence of these protons. If the energy difference between the two lowest triplet states is small enough to allow thermally induced transitions between them, averaging of the magnetic interactions in the two states occurs. If the rate of the transitions is higher than the frequency difference between interactions in the two states, the ZFS becomes axially symmetric and the hyperfine coupling to the four methine protons is the same. If transition rate is slower than the frequency difference, the ZFS tensor remains rhombic, and the four protons are not equivalent. This effect is known as the dynamic Jahn-Teller effect [32–35] and leads to changes in the rhombicity of the ZFS tensor and the hyperfine couplings as a function of temperature. The size of this effect depends on subtle details of the porphyrin structure and is difficult to predict *a priori*.

Here, we employ a range of light-induced EPR techniques to investigate in detail the triplet state of **AIOEP**. We show that the ZFS tensor obtained from the TREPR spectra becomes increasingly axial with increasing temperature as has been observed previously for Mg and Zn porphyrins [36,37], and has been interpreted as due to a dynamic Jahn-Teller effect. ENDOR and ESEEM measurements reveal that the hyperfine couplings to the methine protons are also strongly temperature dependent as expected from the proposed dynamic Jahn-Teller effect. However, in contrast to the Mg and Zn porphyrins, the presence of axial ligands in **AIOEP** plays an important role in the orientation dependence of the spin–lattice relaxation and temperature dependence of the hyperfine couplings.

## 2. Results

### 2.1. TREPR and pulse EPR: ZFS parameters, spin polarization and spin–lattice relaxation

In this section we present X-band TREPR results for the triplet state of **AIOEP** in a glass-forming solvent at  $T = 10$  K and 80 K. From the spin polarization patterns and magnetophotoselection data, the ZFS parameters and the orientation of the principal axes of the ZFS tensor with respect to the optical transition dipole moments have been obtained at the two temperatures. The spectral dependence of the spin polarization decay gives insight into the orientation dependence of the spin–lattice relaxation.

Fig. 2 shows a comparison between the X-band TREPR spectra of **AIOEP** in the glass phase of a 3:1 mixture of 2-methyltetrahydrofuran: dichloromethane (MeTHF:DCM) at 10 and 80 K. The spectra are extracted from the 2D data sets in a time window around the maximum of the EPR signal and are the weighted sum ( $I_{\parallel} + 2I_{\perp}$ ) of spectra taken with the polarization of the excitation beam parallel ( $I_{\parallel}$ ) and perpendicular ( $I_{\perp}$ ) to the magnetic field to remove any photoselection effects. Simulations of the triplet spectra are shown in Fig. 2 (dashed spectra) and the parameters obtained from them are presented in Table 1. The simulations do not yield the signs of  $D$  and  $E$  directly but only the absolute value and therefore we report only the absolute values. However, both parameters been taken as positive based on self-consistent field theory (CASSCF) calculations and on the ENDOR data that will be discussed below. With this sign choice, the relative population rates  $p_x$  and  $p_y$  are equal and larger than  $p_z$ , as previously reported

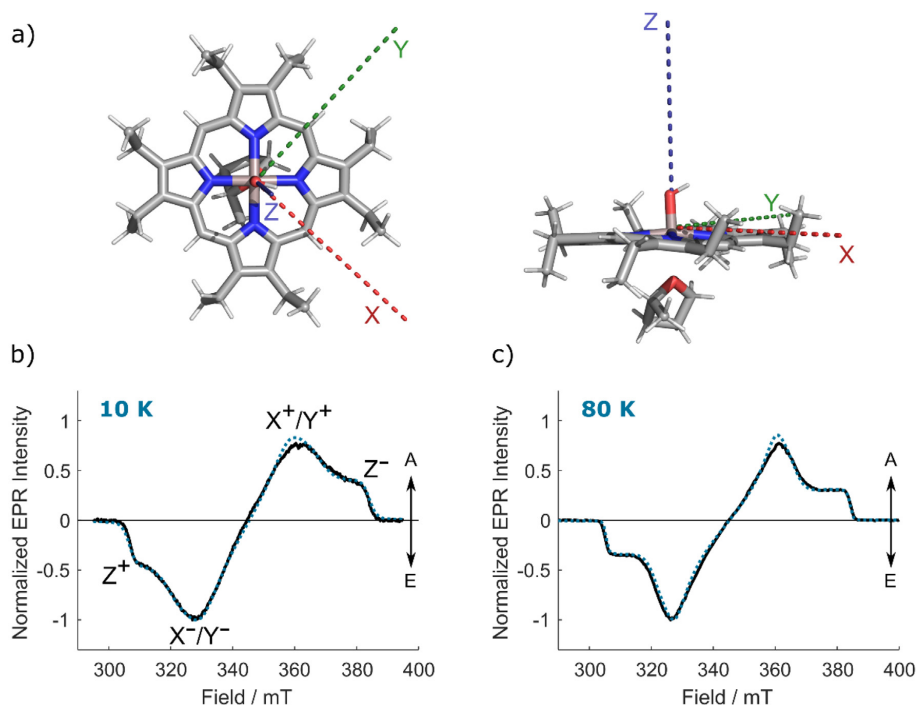


**Fig. 2.** (a) Top and side view of the orientation of the ZFS tensor principal axes ( $x = \text{red}$ ,  $Y = \text{green}$ ,  $Z = \text{blue}$ ) in the **AIOEP** molecular frame, including a solvent molecule (MeTHF), obtained from Density Functional Theory (DFT) calculations. Experimental (black, solid) and simulated (blue, dashed) triplet state TREPR spectrum of **AIOEP** in a glassy 3:1 mixture of MeTHF:DCM, recorded at 80 K (b) and at 10 K (c). Simulation parameters are reported in Table 1. (For interpretation of the references to colour in this figure legend, the reader is referred to the web version of this article.)

**Table 1**

ZFS parameters  $D$  ( $\pm 8$  MHz) and  $E$  ( $\pm 5$  MHz), relative triplet sublevel populations\* ( $\pm 0.05$ ), and spin–lattice relaxation time constant ( $\pm 1$   $\mu$ s at 10 K and  $\pm 0.2$   $\mu$ s at 80 K) derived from simulation of the TREPR spectra at 80 K and 10 K. For the decay constants, see text.

	$P_x:P_y:P_z$	$ D $ (MHz)	$ E $ (MHz)	$T_{1x}$ ( $\mu$ s)	$T_{1y}$ ( $\mu$ s)	$T_{1z}$ ( $\mu$ s)
10 K	0.43: 0.42: 0.15	1092	100	17	17	14
80 K	0.42: 0.39: 0.19	1105	61	0.8	0.8	0.6

\*The population ratios correspond to  $D, E > 0$  as predicted by CASSCF-NEVPT computations [12] and confirmed by the ENDOR data presented below.

[12]. It is apparent from the spectra in Fig. 2 and the parameters in Table 1 that the relative population rates, and hence the polarization patterns, are essentially the same at 10 and 80 K. Similarly, the total width of the spectrum, which is determined by the ZFS parameter  $D$ , is not strongly affected by the temperature and is only  $\sim 1\%$  larger at 80 K. In contrast, the value of  $E$  obtained from the simulations is reduced by  $\sim 40\%$  at 80 K compared to 10 K, although the ZFS tensor remains orthorhombic. In the literature a decrease in  $|E|$  with increasing temperature, observed in related porphyrins, has been ascribed to dynamic Jahn-Teller averaging [33]. We note that for the  $X^+/Y^+$  transitions the experimental signal is always slightly less intense than the simulation for all recorded spectra while the  $X^-/Y^-$  intensity is reproduced. This indicates that absorptive  $X^+/Y^+$  transitions are weaker than the emissive  $X^-/Y^-$  for these orientations and hence, the spin system displays weak net emissive polarization. We have shown previously that such net polarization can be generated by back-and-forth transitions between two triplet states with ZFS axes related to one another by a rotation about the z-axis [38,39]. Such a situation can occur in porphyrins if the degeneracy of the lowest triplet state is lifted slightly due to the Jahn-Teller effect and thermally activated transitions between the two states can take place.

To further characterize the triplet state ZFS tensor, we carried out magnetophotoselection experiments. Fig. 3 shows the TREPR spectra of AIOEP in the glass phase of a 3:1 mixture of MeTHF:DCM at 80 K with the plane of the laser polarization parallel (red spectrum) and perpendicular (blue spectrum) to the magnetic field. The transitions at 544 nm (Fig. 3b) and at 576 nm (Fig. 3c), corresponding to the two Q-bands of the electronic absorption spectrum, were used for excitation. Since the experimental setup assured the same excitation conditions for the two polarization orientations, the spectra are displayed without renormalization and show an evident magnetophotoselection effect, with enhanced X and Y triplet transitions with the parallel orientation and enhanced Z transitions with the perpendicular orientation. Neither the magnetophotoselection effect nor the ZFS parameters show any significant wavelength dependence. Simulations of the spectra

were carried out using the parameters given in Table 1 and include the relative orientation of the ZFS axis system and the electric transition dipole moments as variable parameters. The simulations show that the transition dipole moment(s) and the X and Y principal axes of the ZFS tensor lie in the same plane. Complete active space CASSCF calculations predict that the  $Q_x$  and  $Q_y$  optical transitions are degenerate [12], suggesting that the two Q-bands observed in the spectrum are part of a vibrational progression [40]. This means that the  $Q_x$  and  $Q_y$  transitions cannot be excited separately, and hence it is only possible to determine that the X and Y principal axes of the ZFS tensor lie in the same plane as the  $Q_x$  and  $Q_y$  transitions but not their orientations within the xy plane. The calculations also predict that the two transition dipole moments are orthogonal to one another and lie in the porphyrin plane as do the X and Y axes of the calculated ZFS tensor, in agreement with the magnetophotoselection result.

Triplet state kinetics, including dynamic and relaxation processes, can be investigated by analysis of the time evolution of the spin polarization. The time dependence of the TREPR signals represents the motion of the magnetization in the rotating frame and depends on spin-relaxation, precession of the magnetization about the effective field and decay of the excited triplet state. In the limit of low microwave power and for a long-lived triplet state with  $T_1 \gg T_2$ , the decay of the polarization determined by the TREPR experiments is dominated by  $T_1$  [41]. Alternatively, ED-TREPR and inversion recovery pulse experiments can be carried out to estimate the spin–lattice relaxation time.

Before collecting a full time/field dataset for kinetic analysis, we measured several transients at field positions corresponding to the ZFS canonical orientations to check for possible distortion due to response time limitations of the cavity. When these transients were fit as a sum of simple exponentials, the lifetime of one of the components was close to the response time of the critically-coupled cavity. Therefore, we decided to reduce the response time of the cavity by over-coupling it to reduce its Q-factor. To determine what Q-factor gave an undistorted signal, we used the ED-TREPR signal as a reference. The ED-TREPR method (Fig. 1) is

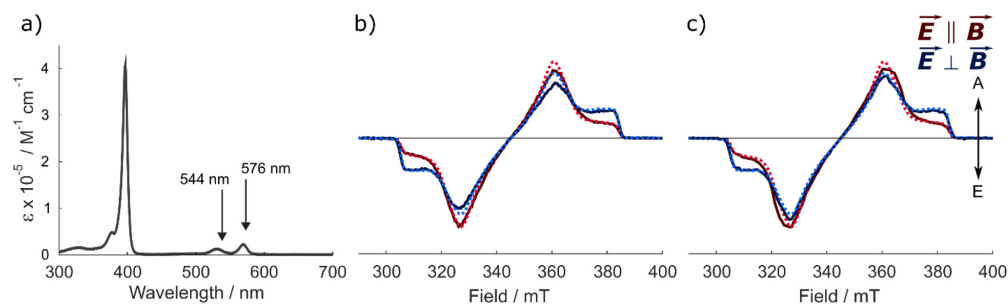


**Fig. 3.** Magnetophotoselection and wavelength dependence of the triplet state TREPR spectra of AIOEP. (a) UV/VIS absorption spectrum for AIOEP in DCM at room temperature. (b) Experimental (solid) and simulation (dashed) triplet state TREPR spectrum of AIOEP in a glassy 3:1 mixture of MeTHF:DCM, recorded at 80 K, after photoexcitation at 544 nm with light linearly polarized parallel (red) and perpendicular (blue) to the magnetic field. (c) Corresponding TREPR spectra of AIOEP after photoexcitation at 576 nm. All other parameters are the same as panel b). Simulation parameters are reported in Table 1. (For interpretation of the references to colour in this figure legend, the reader is referred to the web version of this article.)

characterized by excellent time resolution at the cost of lower signal intensity and long acquisition time. At several field points corresponding to the principal orientations ZFS tensor we confirmed that the TREPR transients collected with the cavity over-coupled were undistorted with respect to the corresponding

ED-TREPR transients (see Figs. S1 and S2). We then collected a full time/field dataset for analysis.

The dataset and its simulation are summarized in Fig. 4. In Fig. 4a, the calculated full time/field TREPR dataset is compared with the experimental dataset at 80 K. Fig. 4b shows the triplet

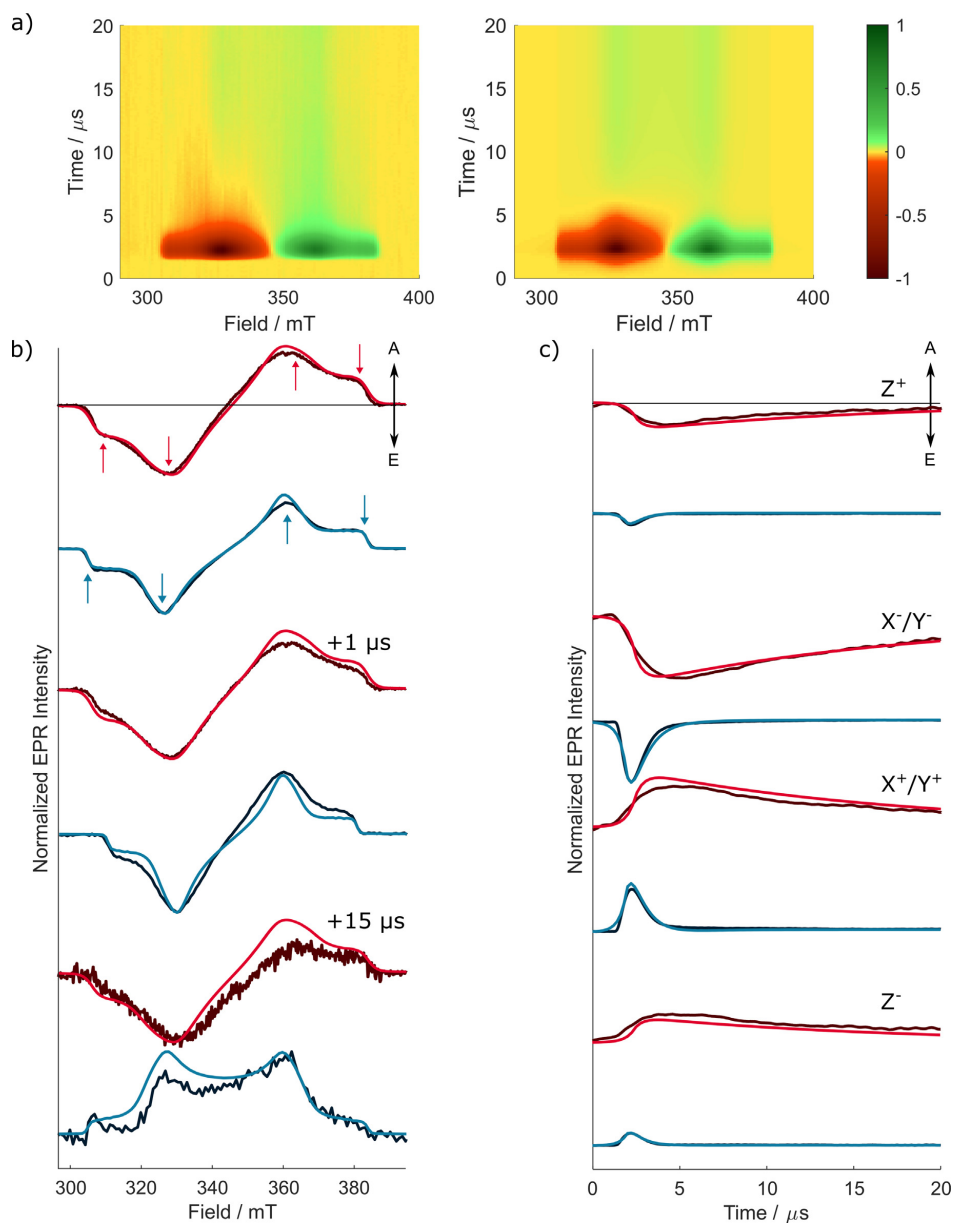


**Fig. 4.** (a) Experimental (left) and simulated (right) contour plots of the 2D TREPR data for the triplet state of **AIOEP** in a glassy 3:1 mixture of MeTHF:DCM, recorded at 80 K. The corresponding 2D TREPR data at 10 K is reported in Fig. S1. (b) Variation of the TREPR spectra at 10 K (dark red) and 80 K (dark blue) at different delays from the maximum of the signal (0, 1, 15  $\mu$ s) and corresponding simulation (light red and blue, respectively). (c) Time evolution of the TREPR signal at 10 K and 80 K measured with an over-coupled resonator, recorded at the canonical ZFS turning points (indicated by the arrows) and the corresponding simulations, colour code as in (b). Simulation parameters are reported in Table 1. (For interpretation of the references to colour in this figure legend, the reader is referred to the web version of this article.)

powder spectra at selected time delays after flash (DAF) with the corresponding simulations. Time traces at selected field positions indicated by the red arrows in Fig. 4b are shown in Fig. 4c. To better facilitate comparison of the evolution of the dataset at 10 K and 80 K, data at the two temperatures are shown together in Fig. 4b and c. The simulations at 80 K are shown in dark blue and those at 10 K are in red. As can be seen in Fig. 4b, at 80 K (dark blue), the early detected spectrum with polarization *eee/aaa* (*e*: emissive, *a*: absorptive) for the three feature pairs evolves to a purely absorptive spectrum at 15  $\mu$ s, with a lineshape close to that expected for a Boltzmann population distribution. In contrast, at 10 K, the shape of the spectrum remains almost unchanged also after 15  $\mu$ s.

The simulation of the time evolution of the intensity was obtained considering the time variation of the population by solving the master equation [42,43], in which both the spin–lattice relaxation time  $T_1$ , and the decay to the ground state were considered as described in the Materials and Methods section (Eq. (2)). In this treatment the time dependence of the signal is assumed to arise only from the time dependence of the populations of the stationary states of the Hamiltonian. The microwave field is not explicitly included, and precession of the magnetization is ignored. Such a treatment is valid for slowly decaying signals measured with low microwave power. In this case, the off-resonant and coherent contributions that decay within a few tens of ns are not resolved and only exponential decay of the signal by  $T_1$  relaxation and/or decay to the ground state is observed. To ensure that these conditions were met, we compared  $T_1$  values obtained by model fitting with the values obtained from the ED-TREPR and ESE inversion-recovery experiments at the canonical transitions (see Fig. S2) and found that they are in good agreement. The kinetic parameters derived from the simulations of full time/field TREPR dataset are reported in Table 1. The slowest component of the signal decay is found to be on the order of a few hundreds of  $\mu$ s, as evaluated for example from the ED-TREPR traces and is similar to the room temperature lifetime of the AIOEP triplet state (86  $\mu$ s) [11]. The faster components observed in the time window of the TREPR experiments (20  $\mu$ s) can therefore be ascribed to  $T_1$  relaxation and can be used to discuss dynamical effects on the molecule.

The strong temperature dependence of the  $T_1$  relaxation is expected since modulation of the highly anisotropic ZFS by either molecular and/or electronic motion provides an effective  $T_1$  relaxation mechanism that can account for the experimental observations. It has been shown that if a second low-lying triplet state is thermally accessible and has ZFS axes that are rotated with respect to the lowest excited triplet state, temperature dependent spin–lattice relaxation caused by the modulation of the ZFS is observed [44]. Since we observe temperature dependent changes in the ZFS parameters (Table 1) and the lowest triplet state of AIOEP is (nearly) degenerate, the change in the relaxation rate is likely due to modulation of the ZFS as would be expected from the dynamic Jahn-Teller effect.

## 2.2. ENDOR and ESEEM: Hyperfine structure

Experimental studies of the spin-polarized triplet state of AIOEP by TREPR are complemented by pulse ENDOR and ESEEM measurements to provide more detailed information about the unpaired electron spin distribution at specific positions of the macrocycle. The bridging methine protons at the four meso positions are characterized by large negative spin densities and can serve as sensitive probes.

The significant anisotropy of the triplet state ZFS tensor, in comparison to that of the hfc, allows orientation-selective hyperfine spectroscopy to be performed and provides the orientation of the

hfc tensor components ( $A_{ii}$ ) relative to the ZFS tensor axes, which include the Fermi-contact  $a_{iso}$  and the dipolar interaction component  $T_{ii}$  ( $A_{ii} = a_{iso} + T_{ii}$ ). Excitation is performed at the turning points of the triplet spectrum where the external field is mainly parallel to one of the ZFS canonical axes. In addition, in contrast to doublet states, the ENDOR spectra of triplet states allow direct determination of the signs of the hfc (see Fig. 5) if the sign of the ZFS parameter  $D$  is known. Analogous considerations apply to ESEEM, as the periodic modulation of the local field experienced by the electron spin provides information about the hyperfine frequencies if the hyperfine principal axes deviate from the ZFS tensor axes.

Fig. 5a shows the splitting of the spin energy levels of the triplet state at high field ( $B_0$ ) for the three canonical orientations X, Y, and Z. In the diagram, the ZFS  $D$  parameter has been chosen to be positive, as expected for  $\pi$ - $\pi^*$  triplet states of porphyrin derivatives [15] and confirmed by magnetophotoselection experiments and published CASSCF calculations for AIOEP [12]. In Fig. 5b the spin energy levels are shown for the hyperfine interaction of the triplet spin ( $S = 1$ ) with one proton spin ( $I = 1/2$ ) in the high-field limit. As an example, we consider the triplet spin energy levels for the Z canonical orientation, which include the first-order hyperfine interaction  $A_{ZZ}$  in the ZFS frame. A small interaction is assumed ( $A/2 < \nu_H$ ). In the ENDOR spectrum, a strong and narrow line is expected at the Larmor frequency,  $\nu_H$ , arising from the  $M_S = 0$  manifold, and a further ENDOR transition occurs either at higher or lower frequency depending on the sign of the hyperfine interaction tensor element.

The two ENDOR resonance frequencies according to the triplet ENDOR resonance condition [13] are:

$$\nu_{\text{ENDOR}} = |\nu_H - M_S A_{ZZ}| \quad (1)$$

For the  $Z^+$  transition of a triplet state with  $D > 0$ , the ENDOR lines from the  $M_S = +1$  manifold occur on the low (if  $A_{ZZ} > 0$ ) or high (if  $A_{ZZ} < 0$ ) frequency side with respect to the Larmor frequency of the proton,  $\nu_H$ . The opposite situation is encountered for the  $Z^-$  transition, where the lines correspond to the  $M_S = -1$  manifold.

ENDOR experiments of porphyrin triplet states performed with the magnetic field positioned at  $Z^+$  or  $Z^-$  in the EPR spectrum are selective for molecules oriented with their molecular ( $\pi$ ) plane perpendicular to  $B_0$ , leading to a strong orientational selection and single crystal-like ENDOR spectra [45]. For methine protons, which are located in the plane of the  $\pi$ -system (see Fig. 1), the hfc tensor component along the Z ZFS axis ( $A_{ZZ}$ ) corresponds to a very good approximation to the corresponding principal component of the hfc tensor [46], see Fig. S4.

The Q-band  $^1\text{H}$  Davies ENDOR spectrum of the triplet state of AIOEP in the glass phase of a 3:1 mixture of MeTHF:DCM, recorded at the  $Z^-$  canonical field position ( $T = 10$  K), is shown in Fig. 6a. In the corresponding inset, the echo-detected spectrum is reported to highlight the working field position. The ENDOR spectrum is plotted versus  $\nu - \nu_H$  so that the proton Larmor frequency peak appears at zero. The ENDOR peaks corresponding to negative hyperfine components, as expected for the  $A_{ZZ}$  components of the methine protons as they are  $\alpha$ -protons, occur at lower frequencies with respect to the Larmor frequency for this specific EPR transition. Indeed, two broad ENDOR lines, which can be assigned to two distinct sets of methine protons based on the sign of the hfc, are present in the low-frequency region of the spectrum, as highlighted in the deconvolution of the spectrum. The corresponding hfc are reported in Table 2.

The assignment is further corroborated by DFT calculations using the PBE-D3 functional and the def2-TZVP basis set. The orientation of the ZFS principal axes in the molecular frame from previously published CASSCF calculations [12] was used with the hyperfine tensor from the DFT calculations to obtain the values  $A_{ZZ}$  given in Table 2. The calculations were repeated for several

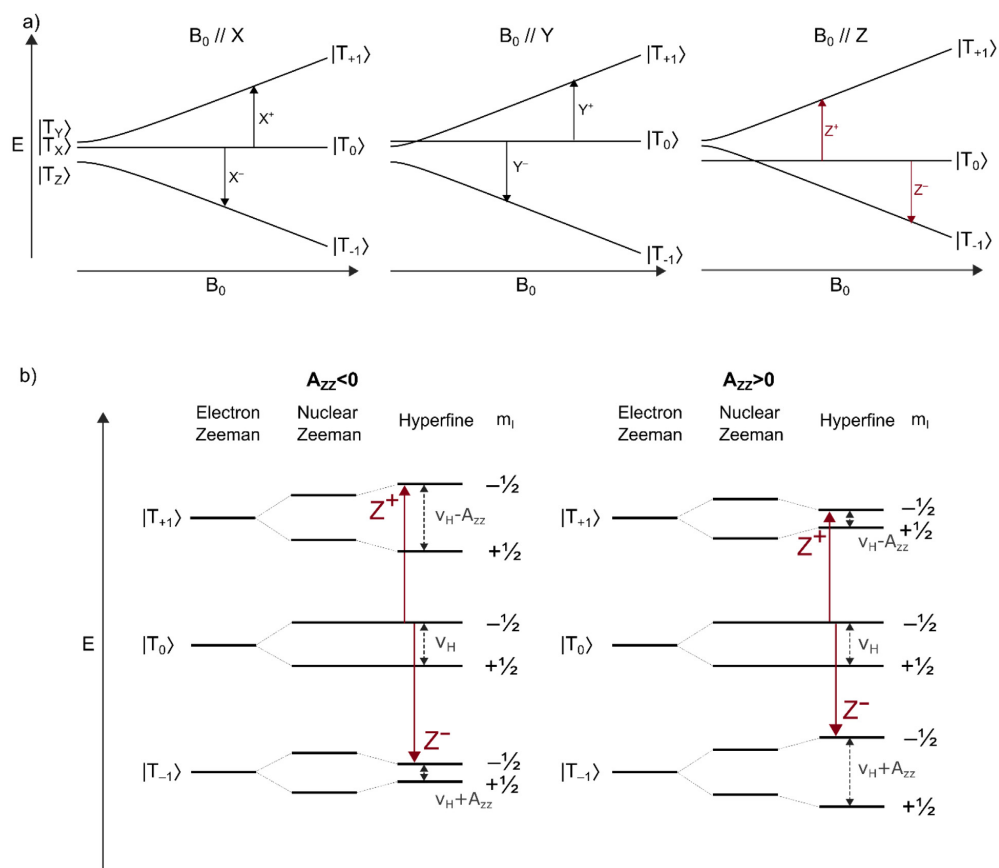


**Fig. 5.** (a) Energy diagram of the triplet spin sublevels as a function of the magnetic field  $b_0$ , for  $D > 0$  and  $E > 0$ , with the field vector parallel to each of the principal axes of the ZFS tensor. The arrows indicate the two allowed canonical EPR transitions according to the selection rule  $\Delta M_s = \pm 1$ . (b) Energy scheme of a triplet state coupled to a single proton  $^1\text{H}$  ( $I = 1/2$ ) for  $B_0$  parallel to the Z ZFS axis and positive and a negative hyperfine coupling constant  $A_{zz}$ . The red arrows indicate the EPR transition for  $m_i = -1/2$ ; those for  $m_i = +1/2$  are omitted. The dark grey arrows (dashed) indicate the ENDOR transitions. Note that the electron spin and ZFS energies are not to scale. (For interpretation of the references to colour in this figure legend, the reader is referred to the web version of this article.)

different conformers of the ethyl substituents but no significant effects were observed for the hfcs of the methine or ethyl protons (see Table S1). The corresponding ENDOR lines of the latter appear as a weak shoulder on the free proton line. The calculated values of  $A_{zz}$ , reported in Table 2, refer to two distinct cases: a six-coordinate geometry of Al(III), involving both the covalently bound hydroxyl group and a coordinated solvent molecule (MeTHF) or five-coordinate geometry involving only the hydroxyl group. The optimized structures in the triplet state with and without solvent coordination are shown in Fig. S4 in the Supporting Information. Calculations confirm the inequivalence of the methine protons and show that their hfcs strongly depend on the solvent coordination of Al(III). Better agreement between the calculated and experimental hfcs at 10 K is obtained when a coordinated solvent molecule is included in the DFT calculation.

In the ENDOR experiments measured with the field set to the positions of the X and Y canonical transitions, a variety of orientations with respect to the magnetic field are excited, which broadens the lines and complicates the corresponding spectrum. In Fig. S5 of the Supporting Information, the Q-band  $^1\text{H}$  Davies ENDOR

spectra, recorded for AIOEP in the triplet state at the  $Y^+$  canonical field position, are reported and the broad  $A_{YY}$  contributions of the methine protons are simulated, showing a satisfactory agreement with DFT calculations.

ENDOR experiments at higher temperatures were precluded by short relaxation times, therefore X-band 3p-ESEEM experiments were performed at 80 K in the glass phase of a 3:1 mixture of MeTHF:DCM to investigate the temperature dependence of the hfcs. The 3p-ESEEM frequency spectrum and the simulation at the  $Z^+$  canonical field position are shown in Fig. 6b. In the corresponding inset, the echo-detected spectrum is reported in order to highlight the working field position. The ESEEM spectrum is plotted versus  $\nu - \nu_H$  so that the proton Larmor frequency peak appears at zero. In addition to this peak, the spectrum in Fig. 6b shows proton hyperfine peaks around 5 MHz and strong  $^{14}\text{N}$  peaks around -10 MHz. The  $^{14}\text{N}$  region is dominated by the double-quantum frequency of the  $M_s = 0$  manifold, as shown previously for Zn porphyrins [47,48]. As in the ENDOR experiments, the position of the proton hyperfine peaks relative to the free proton line depends on the sign of the hyperfine coupling and the value of

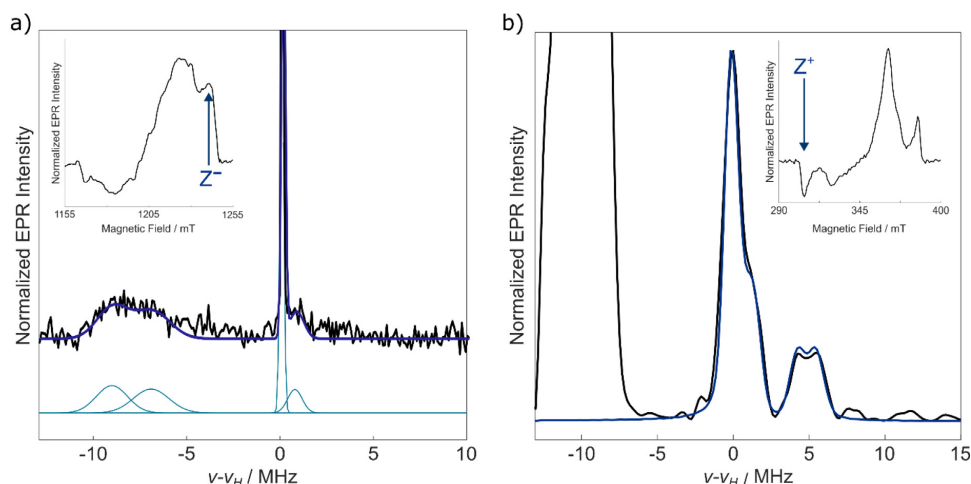


**Fig. 6.** (a) Triplet state Davies ENDOR spectrum of **AIOEP** in a glassy 3:1 mixture of MeTHF:DCM (black), recorded at 10 K and at Q-band; the overall best fit (blue) and the relative Gaussian deconvolution (light blue) are also shown. The resonance field corresponds to the  $Z^-$  ZFS canonical transition, as indicated by the arrow in the field-swept ESE spectrum shown in the inset. (b) Triplet state 3p-ESEEM frequency spectrum of **AIOEP** in a glassy 3:1 mixture of MeTHF:DCM (black), recorded at 80 K and at X-band; the simulation is shown in blue. The resonance field corresponds to the  $Z^+$  ZFS canonical transition as indicated by the arrow in the field-swept ESE spectrum shown in the inset. The hyperfine parameters are reported in Table 2. (For interpretation of the references to colour in this figure legend, the reader is referred to the web version of this article.)

**Table 2**

$A_{zz}$  in MHz for the methine protons of **AIOEP** in the triplet state, obtained from ENDOR experiments at 10 K ( $\pm 0.5$  MHz), 3p-ESEEM experiments at 80 K ( $\pm 0.2$  MHz) and DFT calculations.

$A_{zz}$ (MHz)	Solvent	Methine	Methine*
ENDOR	MeTHF/DCM 3:1	-9.2	-6.7
3p-ESEEM	MeTHF/DCM 3:1	-5.9	-4.3
DFT	MeTHF	-8.54	-6.91
	No solvent	-5.70	-5.15

\* The methine protons are indicated in Fig. 1.

$M_S$ . For the ESEEM experiment shown in Fig. 6b, the low field canonical transition was selected since the  $^{14}\text{N}$  and the negative  $^1\text{H}$  hfcs will appear on opposite sides of the proton Larmor frequency line and can, therefore, be easily distinguished. The peaks near 5 MHz can be assigned to the methine protons, since they are the only ones with significant negative  $^1\text{H}$  hfcs in **AIOEP**. As can be seen in Fig. 6b, the peak near 5 MHz is broad and shows some structure suggesting that the methine protons are probably not equivalent. In the fitted spectrum, it has been modelled as two sets of protons, but the two peaks are not clearly resolved in the spectrum. As can be seen in Table 2, the methine proton hfcs obtained from the 80 K ESEEM experiment are significantly smaller than those at 10 K. Comparison with the hfcs from DFT calculations suggests that this may be the result of weaker coordination of the solvent at 80 K.

### 3. Discussion and conclusions

To a first approximation, the electronic structure of metalloporphyrins such as **AIOEP** can be modelled as a porphine ring with  $D_{4h}$  symmetry (Fig. 7). Using this model, the lowest triplet state of porphyrins with substituents in the  $\beta$ -pyrrolic positions is described as an  $a_{1u}(\pi) \rightarrow e_g(\pi^*)$  excitation and is doubly degenerate with  $^3E_u$  symmetry [30,31]. However, this degeneracy may be lifted by Jahn-Teller distortion of the plane of the molecule and/or asymmetry of the environment. As shown in Fig. 7, an in-plane distortion,

which changes the ring symmetry from  $D_{4h}$  to  $D_{2h}$ , lifts the degeneracy of the  $^3E_u$  state generating  $^3B_{2u}$  and  $^3B_{3u}$  states. The values of E are equal and opposite in these two states, while D is the same. Depending on the temperature and the energy difference and barrier between these two states, back-and-forth transitions between them can occur resulting in a dynamic Jahn-Teller effect. If the transition rate is fast enough the ZFS tensor is averaged, and it becomes axial.

In the case of **AIOEP**, the axial ligands break the  $D_{4h}$  symmetry and the lowest triplet state is not truly degenerate. Thus, it is perhaps more correct to refer to the distortions as a *pseudo* Jahn-Teller effect, but we will not use this term in keeping with the majority of the literature. While the idealized model shown in Fig. 7 should describe the general behaviour of the **AIOEP** triplet state, some deviations can be expected. For example, it is possible that in the two low-lying triplet states the values of E might not be exactly equal and opposite. Jahn-Teller distortions involving the axial ligands are also possible. These have been reported to influence the spin relaxation properties of six-coordinate Fe(III) porphyrins [49] and could also potentially play a similar role in **AIOEP**. They could also lead to differences in the values of D and the directions of the ZFS Z-axes in the two low-lying triplet states.

The analysis of the isotropically excited TREPR spectra, extracted from the 2D dataset at short delay after the laser pulse when the electron spin polarization is largest, shows that the ZFS tensor is orthorhombic ( $E \neq 0$ ) in the temperature range under investigation (10–80 K), but there is a decrease in the rhombicity of the ZFS tensor at higher temperature ( $\lambda = |E/D|$  are  $0.092 \pm 0.005$  and  $0.055 \pm 0.005$  at 10 K and 80 K, respectively), which suggests the presence of a dynamic Jahn-Teller effect. The triplet spin sub-level populations remain essentially constant over the temperature range. In the specific case of the in-plane populations ( $p_x$  and  $p_y$ ), their values are similar and therefore the amount of information on the Jahn-Teller effect that may be derived from a change of these parameters is limited. In Mg and Zn porphyrins, the Jahn-Teller averaging at temperatures around 80 K can be complete or only partial depending on the type of substituents and the coordinating properties of the solvent [36,37].

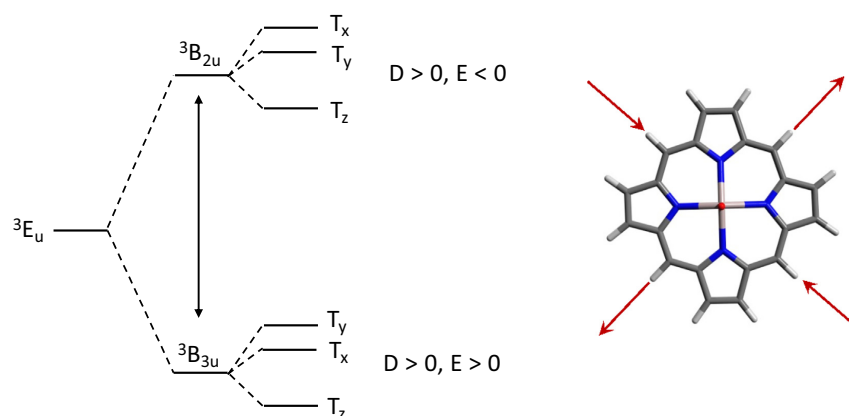


**Fig. 7.** Influence of a static Jahn-Teller distortion of an idealized porphyrin ring with  $D_{4h}$  symmetry on the triplet state energy levels [31]. Distortion of the ring as indicated by the red arrows lifts the degeneracy of the  ${}^3E_u$  state. The  ${}^3B_{2u}$  state has been placed lowest in energy based on the positive value of  $E$  obtained from CASSCF calculations of AIOEP. (For interpretation of the references to colour in this figure legend, the reader is referred to the web version of this article.)

The dynamic Jahn-Teller effect can also make an important contribution to the spin-lattice  $T_1$  relaxation [50,51]. As discussed above, the relaxation rate  $1/T_1$  increases by nearly an order of magnitude at 80 K compared to 10 K (Table 1). A similar temperature dependence has also been reported for Zn(II) tetratraphenylporphyrin and other Zn analogues [36,37]. For Zn porphyrins, the Jahn-Teller distortion consists of alternate elongation of the molecule along each of the two perpendicular in-plane symmetry axes, resulting in a reduction the symmetry from  $D_{4h}$  to  $D_{2h}$ , as shown in Fig. 7. The two forms are symmetry-related [35] and strong anisotropic relaxation is produced when they can exchange by a thermally activated interconversion that acts as a pseudorotation, in which the Z-axis of the ZFS tensor is preserved, but the X and Y principal directions are exchanged. The process of interconversion then provides a contribution to the spin-lattice relaxation, which is dependent on the interconversion rate and the value of  $E$ , that is a measure of the ZFS anisotropy in the XY plane [39]. As a consequence, the time-dependence of the triplet spectra is characterized by a strongly anisotropic temperature dependent relaxation behaviour with the X and Y ZFS components relaxing more rapidly than the Z transition at higher temperature.

In AIOEP, the spin-lattice relaxation does not show the strong orientation dependence observed in Zn porphyrins. As can be seen in kinetic parameters obtained from simulation of the time-evolution of the triplet spectrum (Table 1) the  $T_1$  values are essentially the same for all three canonical orientations but are much shorter at 80 K than at 10 K. This reduction in  $T_1$  is not accompanied by any substantial change in the ZFS parameter  $D$ . Since modulation of the ZFS is expected to be the main mechanism for  $T_1$  relaxation and is known to be responsible for the relaxation of the X and Y components in Zn porphyrins, the data suggest that modulation of the Z component also occurs in AIOEP but that its average value is essentially unaffected. An obvious difference between the Zn porphyrins and AIOEP is the presence of axial ligands in the latter. An out-of-plane Jahn-Teller distortion has been implicated in the relaxation properties of axially coordinated Fe(III)-substituted porphyrins [49] and we speculate that this may also be responsible for the temperature dependent relaxation of the Z component in AIOEP. Unlike the in-plane motions that cause interconversion of the X and Y components and a reduction in  $E$ , out-of-plane motions involving the axial ligands could modulate  $D$  without changing its average value or the orientation of the z-axis.

Magnetic interactions other than the ZFS can also be affected by Jahn-Teller distortions. For example, in Cu(II) complexes, the dynamic Jahn-Teller effect has been observed as a vibronic averaging of the  $g$  and  $A$  tensors [52–54], but these effects have never been investigated in porphyrin systems. For this reason, we performed both pulse ENDOR and ESEEM experiments on AIOEP at 10 and 80 K, respectively. ENDOR was not feasible at 80 K since the electronic relaxation times are too short to use a radio frequency pulse with the appropriate length in the ENDOR sequences, while the relaxation conditions are still favourable for the 3p-ESEEM experiment. The fast detection scheme of ESEEM allows the mapping of proton ENDOR frequencies at higher temperatures. Usually, ESEEM is used to detect nuclei with a small gyromagnetic ratio, but proton ESEEM can be useful when a temperature dependence is investigated. Furthermore, single crystal-like ESEEM may be possible for photoexcited triplet states by recording ESEEM spectra at the magnetic fields relative to the Z features. The limitation of ESEEM is that traces need to be recorded outside of the hyperfine tensor canonical directions: if the ZFS and hyperfine frames are collinear a very weak, or null, modulation amplitude is expected if ESEEM is recorded at the Z-resonant field positions. This can, however, be overcome by moving the resonance field slightly to select resonant molecules having a tilt angle (*i.e.*,  $\sim 20^\circ$ ) with respect to the principal orientations of the hyperfine tensor [29].

Hyperfine spectroscopy on AIOEP allows detection of the hfcs of the methine protons, which are characterized by a large, negative isotropic contribution and a strongly anisotropic dipolar contribution, as shown by DFT calculations. The  $A_{zz}$  component, in the ZFS frame, was detected both at 10 K and at the higher temperature by excitation near the Z triplet transition. ENDOR spectra obtained from excitation near the Y transitions show a severe broadening of the lines that can be ascribed to incomplete orientation selection and/or slow Jahn-Teller interconversion rate between slightly different triplet states.

Two different hfcs corresponding to two different sets of methine protons have been detected in both the 80 K ESEEM and 10 K ENDOR spectra. The inequivalence of the four methine proton is predicted by DFT calculations and has also been reported for the free-base porphine [55,56]. A single signal from the meso protons should only occur if the porphyrin ring has four-fold symmetry. The comparison of the ENDOR and ESEEM spectra shows that at

80 K the frequency difference between the two methine proton lines is reduced as is the average of the two frequencies. Since the hfcs at 80 K are close to the calculated values without a coordinated solvent molecule, we speculate that distortion of the molecule in the axial direction may occur and that a triplet state with weaker coordination of the solvent becomes accessible at higher temperature. This is also consistent with the strong reduction in the spin–lattice relaxation time at 80 K compared to 10 K.

There are very few reports of the averaging of hyperfine couplings in Jahn–Teller systems [52,54], and the data in the literature have been collected mostly at very low temperatures where the spin–lattice relaxation time is sufficiently long to be measured and where the Jahn–Teller dynamics are very slow. In addition, most of the ENDOR studies of porphyrins in the literature have been carried out on *meso*-substituted porphyrins [21,47,56,57] compared to the  $\beta$ -substituted porphyrin reported here. Elucidation of the electronic structure of  $\beta$ -substituted metalloporphyrins is particularly important since substituents are only found at these positions in naturally occurring porphyrins and chlorins. The data presented here confirm that bridging methine protons are characterized by a rather large negative spin density, as predicted by DFT calculations and in agreement with the large methine hfcs reported for free-base porphine [55].

The spin density distribution on the nuclei is closely related to the electronic wavefunction, since it probes the coefficients of the atomic orbitals contributing to the HOMO and LUMO where the two unpaired electrons are localized. Tuning of the hfcs and consequently of the spin density distribution is not easily achieved in porphyrins and an active role is probably played by the coordination chemistry of Al(III) which produces subtle distortion effects of the macrocycle. This finding complements the characterization of the dynamic behavior of Al porphyrins, showing that the coordination properties of Al(III) can produce strong effects in terms of the electronic structure and consequently on the reactivity and photochemical properties of the tetrapyrrole macrocycle.

In contrast to the large body of EPR and Optically Detected Magnetic Resonance investigations yielding D and E parameters, which are integral properties of the triplet wavefunction and depend on its overall spatial distribution, there are only a limited number of studies on the hyperfine structure of the triplet state of porphyrins resolved by hyperfine spectroscopy [21,47,56–60]. Similar to TREPR, pulsed ENDOR and ESEEM of photo-excited triplet states take advantage of their large spin polarization. The light-induced polarization of triplet spin label/probes has been shown to provide an important increase in sensitivity for dipolar spectroscopy and distance determination [61–63]. The same reasoning should apply to hyperfine spectroscopy which take full advantage of the large electron spin polarization of the triplet state compared to the corresponding application to radical cations and anions, while probing the electron distribution of both the HOMO and the LUMO in the same experiment.

In summary, the magnetic and dynamic parameters of AIOEP in the triplet state were determined using the complete gamut of light-induced advanced EPR techniques and complemented with theoretical methodologies, providing a reliable and detailed picture of the electronic structure and assessing the symmetry of a representative member of this important class of heterocyclic tetrapyrrolic compounds. The data indicate the involvement of a dynamic Jahn–Teller effect that leads to partial averaging of the magnetic parameters at higher temperature. The data also suggest that axial ligands can play an important role in the Jahn–Teller dynamics. The effect on the hyperfine interaction of the methine protons and on the anisotropy of the spin–lattice relaxation both point towards distortion of the axial coordination bond that modulates Z component of the ZFS and the spin density at the *meso* positions of the porphyrin ring. This detailed picture underlines

that, in the presence of Al(III) coordination, the porphyrin triplet state is characterized by unique properties when compared to other metalloporphyrins, which are commonly employed in diverse applications including artificial photosynthesis.

## 4. Materials and methods

### 4.1. Sample preparation

The synthesis of the porphyrin has been described previously [11]. Samples were prepared dissolving the porphyrin in the solvents of choice. Samples were prepared in a 3:1 mixture of MeTHF:DCM with a concentration of about 500  $\mu$ M. TR-EPR and pulse experiments (ESEEM, ED-TREPR, Inversion Recovery) were additionally performed on a sample prepared in a 9:1 mixture of MeOH: glycerol at the same concentration. X-band samples were prepared inserting the solution inside 4 mm o.d. quartz tubes which were sealed under vacuum after few freeze–pump–thaw cycles. Q-band samples were prepared in a glovebox, inserting the solution inside 1.6 mm o.d. quartz tubes which were sealed under vacuum after a few freeze–pump–thaw cycles.

### 4.2. EPR measurements

EPR measurements at 80 K were performed on a Bruker Elexsys E580 spectrometer and operating at X-band and equipped with a dielectric MD5 resonator. Photoexcitation was obtained using a Quantel Rainbow Nd:YAG pulsed laser equipped with second and third harmonic modules and with an optical paramagnetic oscillator (OPOTECH) for irradiation at variable wavelength within the visible, working at 10 Hz, with pulse length of 5 ns and an energy of 3–5 mJ/pulse. Temperature stability was assured by an Oxford CF935 dynamic continuous-flow cryostat cooled with liquid nitrogen and controlled by Oxford ITC503 units.

TREPR spectra were obtained by accumulating typically 100–120 traces of the unmodulated EPR signal coming out from the diode detector after a 6 MHz bandwidth preamplification stage. The digitalization of the traces was performed by externally connected LeCroy digital oscilloscopes (series 9300). The cavity was maintained either in critically coupled condition or with a Q-value lower by a factor of 0.5 ca. to have a faster time response. Field-independent time traces contributions, deriving from the cavity and obtained as averaged off-resonance high field and low field traces, were subtracted.

The microwave power was near 0.2 mW. Magnetophotoselection experiments were performed by irradiating the sample with polarized laser pulses, with the electric field either parallel or perpendicular to the static magnetic field. The rotation of the polarization plane of the light was obtained with a half waveplate and a linear polarizer was added for a better control of the polarization.

Evolution of the magnetization with time was also recorded by pulse methods, measuring the 2-pulse echo intensity for variable delays between the laser flash and the first pulse (ED-TREPR). The delay between the pulses was set to 300 ns and a  $\pi/2$  pulse of 16 ns was used. The inversion recovery experiment was performed by applying the sequence laser-DAF-( $\pi$ )- $t_1$ -( $\pi/2$ )- $t_2$ -( $\pi$ )- $t_2$ , increasing the time  $t_1$  starting from a value of 300 ns with increments of 100 ns. The DAF was 56 ns; a  $\pi/2$  pulse of 16 ns was used.

3p-ESEEM experiments were performed by applying the echo sequence laser-DAF-( $\pi/2$ )- $t_1$ -( $\pi/2$ )- $t_2$ -( $\pi/2$ )- $t_1$ . The DAF was 200 ns, delay  $t_1$  was set to 180 ns, while the initial  $t_2$  to 300 ns. After removal of the decaying component, the spectrum was then obtained by application of a Hamming function followed by zero-filling to 1024 points and Fourier transform of the signal. In order to cope with the variation of the modulation depth as a function of

the molecular orientation, which alters the ESEEM lineshape, the 3p-ESEEM spectrum was simulated with EasySpin [64] using the experimental parameters and four protons with the hfc value as indicated in Table 2.

For EPR measurements at 10 K, a closed-cycle cryostat (Cryogenic CF VTC) in a helium atmosphere was used for temperature control. Pulsed optical excitation at 10 K was provided by a Nd:YAG laser (Spectra-Physics Quanta-Ray INDI PS 51/52) equipped with a second harmonic module, a pulse width of approximately 6 ns, a pulse energy of 3–5 mJ and a shot repetition rate of 20 Hz.

X-Band TREPR experiments at 10 K were performed on an Elexsys E580 X-Band Pulse Spectrometer system and a dielectric resonator (Bruker ER 4118X-MD5). Q-Band EPR measurements at 10 K were performed on a Bruker Elexsys E580 Super Q-FT spectrometer equipped with an EN5107D2 resonator. Q-band ENDOR measurements were performed applying the Davies ENDOR sequence laser-DAF- $(\pi)$ - $(\pi_{rf})$ - $(\pi/2)$ - $t$ - $(\pi)$ . The DAF was 500 ns, delay  $t$  was set to 400 ns. 40 ns long gaussian-shaped pulses with different amplitudes were employed along with an 11  $\mu$ s RF pulse amplified using a Bruker 250 W RF amplifier. The values of the proton hfc's along the principal axes of the ZFS tensor were determined by Gaussian deconvolution of the ENDOR spectra.

#### 4.3. TREPR simulations

The simulation of the time evolution of the magnetization after its generation by population of the molecular triplet state of **AIOEP** by intersystem crossing was performed by solving the master equation reported in Refs. [42,43]. The master equation accounts for the decay to the ground state of the triplet, the spin lattice relaxation time and the reaching of the Boltzmann population distribution between levels in the absence of decay processes. For each field position, the on-resonance/off-resonance contributions were calculated by the appropriate integration over the possible relative orientations of the triplet molecule and of the external magnetic field as

$$I(B_0, t) = \sum_{\pm} \iint G[B_{res\pm}(\vartheta, \varphi) - B_0] \cdot \Delta P_{\pm}(\vartheta, \varphi, t) \sin\vartheta d\vartheta d\varphi \quad (2)$$

where  $G[B_{res\pm}(\vartheta, \varphi) - B_0]$  is a line shape function,  $B_{res}$  is the resonance field at a given orientation  $(\vartheta, \varphi)$  of the magnetic field  $B_0$ , and  $\Delta P_{\pm}(\vartheta, \varphi, t)$  is the non-Boltzmann population differences between the two resonant states. The resonance fields were calculated upon diagonalization of the Hamiltonian  $H = \mu_B \mathbf{S} \cdot \mathbf{g} \cdot \mathbf{B}_0 + \mathbf{S} \cdot \mathbf{D} \cdot \mathbf{S}$ , where  $\mathbf{D}$  is the dipolar tensor. The calculation was performed by programming Eq. (2) in MATLAB<sup>™</sup> and using a least square fitting routine to fit the signal intensity to the experimental dataset.

#### 4.4. DFT calculations

The hfc's for **AIOEP** were calculated using ORCA 5.0.2 [65,66]. The structure was first constructed using the program Avogadro [67] from the X-ray crystal structure data of a related porphyrin [68] and then subjected to energy minimization using the UFF force field either with or without a coordinated MeTHF molecule [69]. The geometry of the triplet state was then optimized in ORCA using the PBE functional [70] and the def2-TZVP basis set [71] with the D3 dispersion correction [72]. The resolution of identity approximation [73] was used to speed up the calculations. A single point calculation was then performed using the EPRNMR module of Orca to determine the hfc's. The obtained hyperfine tensors were rotated into the ZFS principal axis frame obtained from CASSCF computations the details of which are described elsewhere [12].

#### Data availability

All data are available in the manuscript or in the Supporting Information

#### Declaration of Competing Interest

The authors declare that they have no known competing financial interests or personal relationships that could have appeared to influence the work reported in this paper.

#### Acknowledgements

S.C., A.B. and M.D.V. gratefully acknowledge the Interdepartmental Centre Giorgio Levi Cases for Energy Economics and Technology (Biomolecular DSSCs Project) for financial support. A.C. would like to thank Department of Chemical Sciences of the University of Padua for a Nexus project scholarship and Prof. C. W. M. Kay for the opportunity to work at Saarland University. AvdE acknowledges support from NSERC (Discovery Grant 2015-04021). This work was made possible by the facilities of the Shared Hierarchical Academic Research Computing Network (SHARCNET: [www.sharcnet.ca](http://www.sharcnet.ca)) and Compute/Calcul Canada. This work was supported by the Chancellor's Faculty Small Grant - University of Minnesota Duluth to PKP. EPR spectroscopy at Saarland University was performed on spectrometers purchased with support of the State of Saarland and the German Science Foundation (project number INST256/535-1).

#### Appendix A. Supplementary material

Supplementary material to this article can be found online at <https://doi.org/10.1016/j.jmr.2023.107515>.

#### References

- [1] N. Zarrabi, P.K. Poddutoori, Aluminum(III) porphyrin: A unique building block for artificial photosynthetic systems, *Coord. Chem. Rev.* 429 (2021), <https://doi.org/10.1016/j.ccr.2020.213561>.
- [2] E. Nikoloudakis, I. López-Duarte, G. Charalambidis, K. Ladomenou, M. Ince, A.G. Coutsolelos, Porphyrins and phthalocyanines as biomimetic tools for photocatalytic H<sub>2</sub> production and CO<sub>2</sub> reduction, *Chem. Soc. Rev.* 51 (2022) 6965–7045, <https://doi.org/10.1039/D2CS00183G>.
- [3] S. Fukuzumi, Y.-M. Lee, W. Nam, Bioinspired artificial photosynthesis systems, *Tetrahedron* 76 (2020), <https://doi.org/10.1016/j.tet.2020.131024>.
- [4] M. Borgström, E. Blart, G. Boschloo, E. Mukhtar, A. Hagfeldt, L. Hammarström, F. Odobel, Sensitized Hole Injection of Phosphorus Porphyrin into NiO: Toward New Photovoltaic Devices, *J. Phys. Chem. B* 109 (2005) 22928–22934, <https://doi.org/10.1021/jp054034a>.
- [5] P.K. Poddutoori, J.M. Thomsen, R.L. Milot, S.W. Sheehan, C.F.A. Negre, V.K.R. Garapati, C.A. Schmuttenmaer, V.S. Batista, G.W. Brudvig, A. van der Est, Interfacial electron transfer in photoanodes based on phosphorus(V) porphyrin sensitizers co-deposited on SnO<sub>2</sub> with the Ir(III)Cp<sup>+</sup> water oxidation precatalyst, *J. Mater. Chem. A* 3 (2015) 3868–3879, <https://doi.org/10.1039/C4TA07018F>.
- [6] P. Zwick, D. Dulić, H.S.J. van der Zant, M. Mayor, Porphyrins as building blocks for single-molecule devices, *Nanoscale* 13 (2021) 15500–15525, <https://doi.org/10.1039/D1NR04523G>.
- [7] D. Dini, M.J.F. Calvete, M. Hanack, Nonlinear Optical Materials for the Smart Filtering of Optical Radiation, *Chem. Rev.* 116 (2016) 13043–13233, <https://doi.org/10.1021/acs.chemrev.6b00033>.
- [8] F. Leng, H. Liu, M. Ding, Q.-P. Lin, H.-L. Jiang, Boosting Photocatalytic Hydrogen Production of Porphyrinic MOFs: The Metal Location in Metalloporphyrin Matters, *ACS Catal.* 8 (2018) 4583–4590, <https://doi.org/10.1021/acscatal.8b00764>.
- [9] J. Jiang, K.L. Materna, S. Hedström, K.R. Yang, R.H. Crabtree, V.S. Batista, G.W. Brudvig, Antimony Complexes for Electrocatalysis: Activity of a Main-Group Element in Proton Reduction, *Angew. Chem. Int. Ed.* 56 (2017) 9111–9115, <https://doi.org/10.1002/anie.201704700>.
- [10] P. Agostinis, K. Berg, K.A. Cengel, T.H. Foster, A.W. Girotti, S.O. Gollnick, S.M. Hahn, M.R. Hamblin, A. Juzeniene, D. Kessel, M. Korbelik, J. Moan, P. Mroz, D. Nowis, J. Piette, B.C. Wilson, J. Golab, Photodynamic therapy of cancer: An update, *CA Cancer J. Clin.* 61 (2011) 250–281, <https://doi.org/10.3322/caac.20114>.

- [11] N. Zarrabi, B.J. Bayard, S. Seetharaman, N. Holzer, P. Karr, S. Ciuti, A. Barbon, M. Di Valentin, A. Van Der Est, F. D'Souza, P.K. Poddutoori, A charge transfer state induced by strong exciton coupling in a cofacial  $\mu$ -oxo-bridged porphyrin heterodimer, *Phys. Chem. Chem. Phys.* 23 (2021) 960–970, <https://doi.org/10.1039/d0cp05783e>.
- [12] S. Ciuti, J. Toninato, A. Barbon, N. Zarrabi, P.K. Poddutoori, A. van der Est, M. Di Valentin, Solvent dependent triplet state delocalization in a co-facial porphyrin heterodimer, *Phys. Chem. Chem. Phys.* 24 (2022) 30051–30061, <https://doi.org/10.1039/D2CP04291F>.
- [13] W. Lubitz, Pulse EPR and ENDOR studies of light-induced radicals and triplet states in photosystem II of oxygenic photosynthesis, *Phys. Chem. Chem. Phys.* 4 (2002) 5539–5545, <https://doi.org/10.1039/B206551G>.
- [14] W. Lubitz, F. Lendzian, R. Bittl, Radicals, Radical Pairs and Triplet States in Photosynthesis, *Acc. Chem. Res.* 35 (2002) 313–320, <https://doi.org/10.1021/ar000084g>.
- [15] S. Richert, C.E. Tait, C.R. Timmel, Delocalisation of photoexcited triplet states probed by transient EPR and hyperfine spectroscopy, *J. Magn. Reson.* 280 (2017) 103–116, <https://doi.org/10.1016/j.jmr.2017.01.005>.
- [16] S. Weber, EPR Transient, EMagRes, John Wiley & Sons, Ltd, 2017, pp. 255–270, <https://doi.org/10.1002/9780470034590.emrstm1509>.
- [17] C.E. Tait, M.D. Krzyaniak, S. Stoll, Computational tools for the simulation and analysis of spin-polarized EPR spectra, *J. Magn. Reson.* 349 (2023), <https://doi.org/10.1016/j.jmr.2023.107410>.
- [18] T.S. Lin, Electron spin echo spectroscopy of organic triplets, *Chem. Rev.* 84 (1984) 1–15, <https://doi.org/10.1021/cr00059a001>.
- [19] M. Di Valentin, S. Ceola, E. Salvadori, G. Agostini, G.M. Giacometti, D. Carbonera, Spectroscopic properties of the peridinin involved in chlorophyll triplet quenching in high-salt peridinin-chlorophyll  $\alpha$ -protein from Amphidinium carterae as revealed by optically detected magnetic resonance, pulse EPR and pulse ENDOR spectroscopies, *Biochimica et Biophysica Acta (BBA) – Bioenergetics* 1777 (2008) 1355–1363, <https://doi.org/10.1016/j.bbabi.2008.06.006>.
- [20] A. Toffoletti, Z. Wang, J. Zhao, M. Tommasini, A. Barbon, Precise determination of the orientation of the transition dipole moment in a Bodipy derivative by analysis of the magnetophotoselection effect, *Phys. Chem. Chem. Phys.* 20 (2018) 20497–20503, <https://doi.org/10.1039/c8cp01984c>.
- [21] A. Barbon, M.G. Dal Farra, S. Ciuti, M. Albertini, L. Bolzonello, L. Orian, M. Di Valentin, Comprehensive investigation of the triplet state electronic structure of free-base 5,10,15-tetrakis(4-sulfonatophenyl)porphyrin by a combined advanced EPR and theoretical approach, *J. Chem. Phys.* 152 (2020), <https://doi.org/10.1063/1.5131753>.
- [22] S. Ciuti, A. Carella, A. Lucetti, M. Tommasini, A. Barbon, M. Di Valentin, Insights into the phototautomerism of free-base 5, 10, 15, 20-tetrakis(4-sulfonatophenyl) porphyrin, *Photochem. Photobiol. Sci.* (2023), <https://doi.org/10.1007/s43330-023-00413-5>.
- [23] M.D. Kemple, ENDOR of Triplet State Systems in Solids, in: M.M. Dorio, J.H. Freed (Eds.), *Multiple Electron Resonance Spectroscopy*, Springer US, Boston, MA, 1979, pp. 409–436, [https://doi.org/10.1007/978-1-4684-3441-5\\_12](https://doi.org/10.1007/978-1-4684-3441-5_12).
- [24] C. Gemperle, A. Schweiger, Pulsed electron-nuclear double resonance methodology, *Chem. Rev.* 91 (1991) 1481–1505, <https://doi.org/10.1021/cr00007a011>.
- [25] K. Möbius, A. Savitsky, High-Field EPR Spectroscopy on Proteins and their Model Systems: Characterization of Transient Paramagnetic States, *R. Soc. Chem.* (2008), <https://doi.org/10.1039/9781847559272>.
- [26] L. Kulik, W. Lubitz, Electron-nuclear double resonance, *Photosynth. Res.* 102 (2009) 391–401, <https://doi.org/10.1007/s1120-009-9401-y>.
- [27] J.R. Harmer, Hyperfine spectroscopy-ENDOR, *EMagRes* 5 (2016) 1493–1514, <https://doi.org/10.1002/9780470034590.emrstm1515>.
- [28] J. Niklas, A. Agostini, D. Carbonera, M. Di Valentin, W. Lubitz, Primary donor triplet states of Photosystem I and II studied by Q-band pulse ENDOR spectroscopy, *Photosynth. Res.* 152 (2022) 213–234, <https://doi.org/10.1007/s1120-022-00905-y>.
- [29] M. Di Valentin, C.E. Tait, E. Salvadori, L. Orian, A. Polimeno, D. Carbonera, Evidence for water-mediated triplet-triplet energy transfer in the photoprotective site of the peridinin-chlorophyll  $\alpha$ -protein, *Biochimica et Biophysica Acta (BBA) – Bioenergetics* 1837 (2014) 85–97, <https://doi.org/10.1016/j.bbabi.2013.07.005>.
- [30] J.H. van der Waals, W.G. van Dorp, T.J. Schaafsma, Electron spin resonance of porphyrin excited states, in: *The Porphyrins*, Vol. IV, Academic Press, 1979, pp. 257–312, <https://research.wur.nl/en/publications/electron-spin-resonance-of-porphyrin-excited-states> (accessed June 10, 2023).
- [31] S.R. Langhoff, E.R. Davidson, M. Gouterman, W.R. Leenstra, A.L. Kwiram, Zero field splitting of the triplet state of porphyrins. II, *J. Chem. Phys.* 62 (2008) 169–176, <https://doi.org/10.1063/1.430249>.
- [32] M. Gouterman, Angular Momentum, Magnetic Interactions, Jahn-Teller and Environment Effects in Metalloporphyrin Triplet States, *Ann. N. Y. Acad. Sci.* 206 (1973) 70–83, <https://doi.org/10.1111/j.1749-6632.1973.tb43205.x>.
- [33] P.J. Angiolillo, J.M. Vanderkooi, Electron paramagnetic resonance of the excited triplet state of metal-free and metal-substituted cytochrome c | Elsevier Enhanced Reader, (n.d.), [https://doi.org/10.1016/S0006-3495\(95\)80433-9](https://doi.org/10.1016/S0006-3495(95)80433-9).
- [34] B.M. Hoffman, M.A. Ratner, Jahn-Teller effects in metalloporphyrins and other four-fold symmetric systems, (n.d.), *Mol. Phys.* 35 (1978) 901–925, <https://doi.org/10.1080/00268977800100671>.
- [35] K.A. Nguyen, R. Pachter, Jahn-Teller triplet excited state structures and spectra of zinc complexes of porphyrin and phthalocyanine: A density functional theory study, *J. Chem. Phys.* 118 (2003) 5802–5810, <https://doi.org/10.1063/1.1540627>.
- [36] P.J. Angiolillo, J.M. Vanderkooi, The Photoexcited Triplet State as a Probe of Chromophore-Protein Interaction in Myoglobin, *Biophys. J.* 75 (1998) 1491–1502, [https://doi.org/10.1016/S0006-3495\(98\)74068-8](https://doi.org/10.1016/S0006-3495(98)74068-8).
- [37] P.J. Angiolillo, V.-S.-Y. Lin, J.M. Vanderkooi, M.J. Therien, EPR Spectroscopy and Photophysics of the Lowest Photoactivated Triplet State of a Series of Highly Conjugated (Porphinato)Zn Arrays, *J. Am. Chem. Soc.* 117 (1995) 12514–12527, <https://doi.org/10.1021/ja00155a015>.
- [38] M.G.D. Farra, C. Martin, E. Bergantino, Y.E. Kandraschkin, A. van der Est, M. Di Valentin, Electron spin polarization transfer induced by triplet-radical interactions in the weakly coupled regime, *Phys. Chem. Chem. Phys.* 22 (2020) 19982–19991, <https://doi.org/10.1039/D0CP03565C>.
- [39] Y.E. Kandraschkin, M. Di Valentin, A. van der Est, Reversible triplet energy hopping in photo-excited molecules: A two-site model for the spin polarization, *J. Chem. Phys.* 153 (2020), <https://doi.org/10.1063/5.0022164>.
- [40] S. Ciuti, A. Barbon, M. Bortolus, A. Agostini, E. Bergantino, C. Martin, M. Di Valentin, D. Carbonera, Neuroglobin Provides a Convenient Scaffold to Investigate the Triplet-State Properties of Porphyrins by Time-Resolved EPR Spectroscopy and Magnetophotoselection, *Appl. Magn. Reson.* 53 (2022) 1031–1042, <https://doi.org/10.1007/s00723-021-01421-3>.
- [41] R. Furrer, P. Fajara, C. Lange, D. Stehlik, H.M. Vieth, W. Vollmann, Transient ESR nutation signals in excited aromatic triplet states, *Chem. Phys. Lett.* 75 (1980) 332–339, [https://doi.org/10.1016/0009-2614\(80\)80526-4](https://doi.org/10.1016/0009-2614(80)80526-4).
- [42] Z. Wang, A. Toffoletti, Y. Hou, J. Zhao, A. Barbon, B. Dick, Insight into the drastically different triplet lifetimes of BODIPY obtained by optical/magnetic spectroscopy and theoretical computations, *Chem. Sci.* 12 (2021) 2829–2840, <https://doi.org/10.1039/D0SC05494A>.
- [43] C.J. Winscom, Analysis of Spin Polarisation Transients in Periodically Photo-excited Triplet States, *Zeitschrift Für Naturforschung A* 30 (1975) 571–582, <https://doi.org/10.1515/zna-1975-0301>.
- [44] P.J.F. Verbeek, A.I.M. Dicker, J. Schmidt, Spin–lattice relaxation processes in photo-excited triplet states through a rotation of the spin axes on thermal excitation, *Chem. Phys. Lett.* 56 (1978) 585–590, [https://doi.org/10.1016/0009-2614\(78\)89047-2](https://doi.org/10.1016/0009-2614(78)89047-2).
- [45] B.M. Hoffman, V.J. DeRose, P.E. Doan, R.J. Gurbiel, A.L.P. Houseman, J. Telsner, Metalloenzyme Active-Site Structure and Function through Multifrequency CW and Pulsed ENDOR, in: L.J. Berliner, J. Reuben (Eds.), *EMR of Paramagnetic Molecules*, Springer US, Boston, MA, 1993, pp. 151–218, [https://doi.org/10.1007/978-1-4615-2892-0\\_4](https://doi.org/10.1007/978-1-4615-2892-0_4).
- [46] A. Agostini, D.M. Palm, F.-J. Schmitt, M. Albertini, M. Di Valentin, H. Paulsen, D. Carbonera, An unusual role for the phytol chains in the photoprotection of the chlorophylls bound to Water-Soluble Chlorophyll-binding Proteins, *Sci. Rep.* 7 (2017) 7504, <https://doi.org/10.1038/s41598-017-07874-6>.
- [47] C.E. Tait, P. Neuhäus, H.L. Anderson, C.R. Timmel, Triplet State Delocalization in a Conjugated Porphyrin Dimer Probed by Transient Electron Paramagnetic Resonance Techniques, *J. Am. Chem. Soc.* 137 (2015) 6670–6679, <https://doi.org/10.1021/jacs.5b03249>.
- [48] C.E. Tait, P. Neuhäus, H.L. Anderson, C.R. Timmel, D. Carbonera, M. Di Valentin, HYSCORE on Photoexcited Triplet States, *Appl. Magn. Reson.* 46 (2015) 389–409, <https://doi.org/10.1007/s00723-014-0624-5>.
- [49] R. Quinn, J.S. Valentine, M.P. Byrn, C.E. Strouse, Electronic structure of low-spin ferric porphyrins: a single-crystal EPR and structural investigation of the influence of axial ligand orientation and the effects of pseudo-Jahn-Teller distortion, *J. Am. Chem. Soc.* 109 (1987) 3301–3308, <https://doi.org/10.1021/ja00245a019>.
- [50] S.K. Hoffmann, J. Goslar, W. Hilczner, M.A. Augustyniak, M. Marciniak, Vibronic Behavior and Electron Spin Relaxation of Jahn–Teller Complex  $\text{Cu}(\text{H}_2\text{O})_6^{2+}$  in  $(\text{NH}_4)_2\text{Mg}(\text{SO}_4)_2 \cdot 6\text{H}_2\text{O}$  Single Crystal, *J. Phys. Chem. A* 102 (1998) 1697–1707, <https://doi.org/10.1021/jp971834f>.
- [51] S.K. Hoffmann, J. Goslar, W. Hilczner, R. Kaszyński, M.A. Augustyniak-Jabłokow, Electron spin relaxation of the Jahn-Teller  $\text{Cu}(\text{H}_2\text{O})_6^{2+}$  complex in  $\text{Cs}_2\text{Zn}(\text{SO}_4)_2 \cdot 6\text{H}_2\text{O}$  crystals, *Solid State Commun.* 117 (2001) 333–336, [https://doi.org/10.1016/S0038-1098\(00\)00464-6](https://doi.org/10.1016/S0038-1098(00)00464-6).
- [52] B.L. Silver, D. Getz, ESR of  $\text{Cu}^{2+}(\text{H}_2\text{O})_6$ . II. A quantitative study of the dynamic Jahn-Teller effect in copper-doped zinc Tutton's salt, *J. Chem. Phys.* 61 (1974) 638–650, <https://doi.org/10.1063/1.1681940>.
- [53] M.J. Riley, M.A. Hitchman, A.W. Mohammed, Interpretation of the temperature dependent g values of the  $\text{Cu}(\text{H}_2\text{O})_6^{2+}$  ion in several host lattices using a dynamic vibronic coupling model, *J. Chem. Phys.* 87 (1987) 3766–3778, <https://doi.org/10.1063/1.452932>.
- [54] S. Kiczka, S.K. Hoffmann, J. Goslar, L. Szczepanska, Electronic structure, Jahn-Teller dynamics and electron spin relaxation of two types of octahedral  $\text{Cu}(\text{II})$  complexes in cadmium formate dihydrate  $\text{Cd}(\text{HCOO})_2 \cdot 2\text{H}_2\text{O}$ . EPR and ESE studies, *Phys. Chem. Chem. Phys.* 6 (2004) 64–71, <https://doi.org/10.1039/B311063J>.
- [55] W.G. van Dorp, M. Soma, J.A. Kooter, J.H. van der Waals, Electron spin resonance in the photo-excited triplet state of free base porphyrin in a single crystal of n-octane, *Mol. Phys.* 28 (1974) 1551–1568, <https://doi.org/10.1080/00268977400102801>.
- [56] C.W.M. Kay, The Electronic Structure of the Photoexcited Triplet State of Free-Base (Tetraphenyl)porphyrin by Time-Resolved Electron-Nuclear Double Resonance and Density Functional Theory, *J. Am. Chem. Soc.* 125 (2003) 13861–13867, <https://doi.org/10.1021/ja036278j>.
- [57] C.W.M. Kay, M. Di Valentin, K. Möbius, A time-resolved Electron Nuclear Double Resonance (ENDOR) study of the photoexcited triplet state of free-base

- tetraphenylporphyrin, *Sol. Energy Mater. Sol. Cells* 38 (1995) 111–118, [https://doi.org/10.1016/0927-0248\(94\)00219-3](https://doi.org/10.1016/0927-0248(94)00219-3).
- [58] V. Hamacher, J. Wrachtrup, B. von Maltzan, M. Plato, K. Möbius, EPR and ENDOR study of porphyrins and their covalently linked dimers in the photoexcited triplet state, *Appl. Magn. Reson.* 4 (1993) 297–319, <https://doi.org/10.1007/BF03162504>.
- [59] C.E. Tait, P. Neuhaus, M.D. Peeks, H.L. Anderson, C.R. Timmel, Transient EPR Reveals Triplet State Delocalization in a Series of Cyclic and Linear  $\pi$ -Conjugated Porphyrin Oligomers, *J. Am. Chem. Soc.* 137 (2015) 8284–8293, <https://doi.org/10.1021/jacs.5b04511>.
- [60] A.J. Redman, G. Moise, S. Richert, E.J. Viero, W.K. Myers, M.J. Therien, C.R. Timmel, EPR of Photoexcited Triplet-State Acceptor Porphyrins, *J. Phys. Chem. C* 125 (2021) 11782–11790, <https://doi.org/10.1021/acs.jpcc.1c03278>.
- [61] M. Di Valentin, M. Albertini, E. Zurlo, M. Gobbo, D. Carbonera, Porphyrin Triplet State as a Potential Spin Label for Nanometer Distance Measurements by PELDOR Spectroscopy, *J. Am. Chem. Soc.* 136 (2014) 6582–6585, <https://doi.org/10.1021/ja502615n>.
- [62] M. Di Valentin, M. Albertini, M.G. Dal Farra, E. Zurlo, L. Orian, A. Polimeno, M. Gobbo, D. Carbonera, Light-Induced Porphyrin-Based Spectroscopic Ruler for Nanometer Distance Measurements, *Chem. – Eur. J.* 22 (2016) 17204–17214, <https://doi.org/10.1002/chem.201603666>.
- [63] A. Bertran, K.B. Henbest, M. De Zotti, M. Gobbo, C.R. Timmel, M. Di Valentin, A. M. Bowen, Light-Induced Triplet-Triplet Electron Resonance Spectroscopy, *J. Phys. Chem. Lett.* 12 (2021) 80–85, <https://doi.org/10.1021/acs.jpclett.0c02884>.
- [64] S. Stoll, A. Schweiger, EasySpin, a comprehensive software package for spectral simulation and analysis in EPR, *J. Magn. Reson.* 178 (2006) 42–55, <https://doi.org/10.1016/j.jmr.2005.08.013>.
- [65] F. Neese, The ORCA program system, *WIREs Comput. Mol. Sci.* 2 (2012) 73–78, <https://doi.org/10.1002/wcms.81>.
- [66] F. Neese, Software update: the ORCA program system, version 4.0, *WIREs Comput. Mol. Sci.* 8 (2018) e1327, <https://doi.org/10.1002/wcms.1327>.
- [67] M.D. Hanwell, D.E. Curtis, D.C. Lonie, T. Vandermeersch, E. Zurek, G.R. Hutchison, Avogadro: an advanced semantic chemical editor, visualization, and analysis platform, *J. Cheminf.* 4 (2012) 17, <https://doi.org/10.1186/1758-2946-4-17>.
- [68] R. Guillard, A. Zrineh, A. Tabard, A. Endo, B.C. Han, C. Lecomte, M. Souhassou, A. Habbou, M. Ferhat, K.M. Kadish, Synthesis and spectroscopic and electrochemical characterization of ionic and sigma-bonded aluminum(III) porphyrins. Crystal structure of methyl(2,3,7,8,12,13,17,18-octaethylporphinato)aluminum(III), (OEP)Al(CH<sub>3</sub>), *Inorg. Chem.* 29 (1990) 4476–4482, <https://doi.org/10.1021/ic00347a029>.
- [69] A.K. Rappe, C.J. Casewit, K.S. Colwell, W.A. Goddard, W.M. Skiff, UFF, a full periodic table force field for molecular mechanics and molecular dynamics simulations, *J. Am. Chem. Soc.* 114 (1992) 10024–10035, <https://doi.org/10.1021/ja00051a040>.
- [70] J.P. Perdew, K. Burke, M. Ernzerhof, Generalized Gradient Approximation Made Simple, *Phys. Rev. Lett.* 77 (1996) 3865–3868, <https://doi.org/10.1103/PhysRevLett.77.3865>.
- [71] F. Weigend, R. Ahlrichs, Balanced basis sets of split valence, triple zeta valence and quadruple zeta valence quality for H to Rn: Design and assessment of accuracy, *Phys. Chem. Chem. Phys.* 7 (2005) 3297, <https://doi.org/10.1039/b508541a>.
- [72] S. Grimme, J. Antony, S. Ehrlich, H. Krieg, A consistent and accurate *ab initio* parametrization of density functional dispersion correction (DFT-D) for the 94 elements H–Pu, *J. Chem. Phys.* 132 (2010), <https://doi.org/10.1063/1.3382344>.
- [73] R.A. Kendall, H.A. Früchtl, The impact of the resolution of the identity approximate integral method on modern *ab initio* algorithm development, *Theor. Chem. Acta* 97 (1997) 158–163, <https://doi.org/10.1007/s002140050249>.

## 3.2 Contributions to Physical Science

In this section, the spectrometer setup, MW resonators in particular, are more thoroughly investigated. The first publication focuses in the optimization of a MW ESR resonator, where a simulational approach was used to simulate the  $B_1$  magnetic field inside a dielectricum. Here, three optimized MW resonator setups were developed and described thoroughly, shining light on the interaction between MW's and the sample of interest. The findings demonstrate a high degree of correlation between the simulated and experimental data, providing a robust framework for future optimizations of MW resonators. The next publication builds up on the previous findings on MW resonators. The research revealed unexpected results regarding the coupling situation of a MASER (microwave amplification by the stimulated emission of radiation), challenging previously held assumptions in the field. The described methods in the publications range from CW ESR methods, TR-EPR measurements and pulsed ESR methods.



## 3.2.1 Microwave Resonators

### 3.2.1.1 High Performance MW Resonators

Journal of Magnetic Resonance 354 (2023) 107519



Contents lists available at ScienceDirect

Journal of Magnetic Resonance

journal homepage: [www.elsevier.com/locate/jmr](http://www.elsevier.com/locate/jmr)



## Towards high performance dielectric microwave resonators for X-band EPR spectroscopy

Haakon T.A. Wiedemann<sup>a,\*</sup>, Stefan Ruloff<sup>a</sup>, Rudolf Richter<sup>a</sup>, Christoph W. Zollitsch<sup>a,b,c</sup>, Christopher W.M. Kay<sup>a,b</sup>

<sup>a</sup> Department of Chemistry, Saarland University, Saarbrücken 66123, Saarland, Germany

<sup>b</sup> London Centre of Nanotechnology, University College London, London WC1H 0AH, United Kingdom

<sup>c</sup> Department of Physics & Astronomy, University College London, London WC1E 6BT, United Kingdom

#### ARTICLE INFO

##### Keywords:

Microwave resonators  
X-band  
EPR resonators  
CW EPR  
Transient EPR  
Pulse EPR  
B<sub>1</sub>-field homogeneity  
Transient nutations  
Spin relaxation

MSC:  
0000  
1111

#### ABSTRACT

Microwave (MW) resonators in Electron Paramagnetic Resonance (EPR) spectroscopy concentrate the MW magnetic field ( $B_1$ ) at the sample and separate the MW electric field from the sample. There are numerous experimental methods in EPR spectroscopy which all impose different requirements on MW resonators (e.g. high or low quality factor, MW conversion, and  $B_1$ -field homogeneity). Although commercial spectrometers offer standardized MW resonators for a broad application range, newly emerging and highly-specialized research fields push these spectrometers to or beyond their sensitivity limits. Optimizing the MW resonator offers one direct approach to improve the sensitivity. Here we present three low-cost optimization approaches for a commercially available X-band (9–10 GHz) MW resonator for three experimental purposes (continuous-wave (CW), transient and pulse EPR). We obtain enhanced MW conversion factors for all three optimized resonators and higher quality factors for two optimized resonators. The latter is important for CW and transient EPR. Furthermore, we fabricated a resonator which features an extended area of homogeneous  $B_1$ -field and, hence, improved pulse EPR performance. Our results demonstrate that small changes to a commercial MW resonator can enhance its performance in general or for specific applications.

#### 1. Introduction

Electron paramagnetic resonance (EPR) spectroscopy is a key analytical tool in a variety of different research fields ranging from photoexcited (triplet) states [1], quantum physics [2], and materials science [3] to biological processes [4] and clinical research [5].

An essential component of an EPR spectrometer is the microwave (MW) resonator [6]. A variety of dedicated developed MW resonators are available for the most common EPR frequency band (9–10 GHz, X-band), optimized for different purposes such as maximum sensitivity [7,8], small sample size [9,10], or high time-resolution (large bandwidth) [11,12]. In all cases, at the sample, the magnetic component of the MW field is maximized and the electric component is minimized in order to reduce losses due to absorption [13].

All EPR methods require resonators that efficiently convert MW power  $P$  into an oscillating magnetic field  $B_1 = 2 \cdot B_1^{\text{eff}} \cos(\omega t)$  of high-magnitude  $B_1^{\text{eff}}$  at the sample. This characteristic is described by the

MW conversion efficiency  $\Lambda = B_1/\sqrt{P}$  [14]. For this purpose, many resonators utilise dielectric rings or metallic loop-gap structures, housed inside a metal cavity. These concentrate the magnetic field in a confined region, thereby increasing the (typically weak) spin-to-field interaction significantly [15]. Commercially available dielectric resonators often use sapphire ( $\text{Al}_2\text{O}_3$ ) for this purpose [16,17].

Recently, Syryamina et al. showed that changing the shape of the dielectric resonator from cylindrical to concave can enhance the  $B_1$  homogeneity and hence, improve pulsed EPR performance [18]. Their study was carried out with a Bismuth germanate ( $\text{Bi}_4\text{Ge}_3\text{O}_{12}$ ) crystal.

The quality factor or  $Q$ -factor is a characteristic property defined as  $Q = \nu_{\text{res}}/\Delta\nu$  [19] and quantifies the relation of stored energy in respect to energy losses per microwave cycle. For continuous wave (CW) EPR high  $Q$ -factors are required to attain high signal-to-noise ratios, whereas for pulsed EPR the quality factor is required to be low in order to have a high bandwidth to accommodate short MW pulses [20,21].

In this work, we present three novel and easily reproducible MW

\* Corresponding author.

E-mail address: [haakon.wiedemann@uni-saarland.de](mailto:haakon.wiedemann@uni-saarland.de) (H.T.A. Wiedemann).

<https://doi.org/10.1016/j.jmr.2023.107519>

Received 21 December 2022; Received in revised form 27 June 2023; Accepted 28 June 2023

Available online 14 July 2023

1090-7807/© 2023 Elsevier Inc. All rights reserved.

resonator optimizations for three experimental applications (CW, transient (TR) EPR and pulsed EPR). In our designs we kept the metal cavity unchanged, but replaced metallic parts with copper and reduced the volume of Teflon supports which hold the dielectric ring inside the cavity. This approach allowed us to optimize  $Q$ -factors, MW conversion factors and  $B_1$  field homogeneity. Furthermore, we fabricated two alternative sapphire resonators (1) a shorted but wider resonator and (2) a novel concave resonator similar to that of Syryamina et al. [18].

## 2. Experimental

### 2.1. EPR measurements

All EPR experiments were carried out on an X-band Bruker ELEXSYS E580 EPR spectrometer at room temperature. We used the Bruker X-band standard ER 4118 X-MD5 resonator (referred to below as Asymmetric Long, AL) in comparison with our newly fabricated resonators. For CW experiments, we used a weak pitch (WP) sample and a standard protocol in order to estimate the signal-to-noise ratio (SNR) [22]. Moving a sample of bisdiphenylene- $\beta$ -phenyl allyl (BDPA, dimensions: 0.1 mm  $\times$  0.1 mm  $\times$  0.07 mm) through the MW resonators, we qualitatively extracted their  $B_1$  magnetic field profiles. All experimental conditions and used pulse sequences are available in the supporting information.

TR EPR experiments were performed on the triplet state of a small pentacene crystal in a  $p$ -terphenyl matrix (1.8 mm  $\times$  1.2 mm  $\times$  1.8 mm) excited at 532 nm by a Spectra-Physics OPO pulse laser INDI-HG-20S Nd:YAG (30 mJ average energy). The pentacene crystal was fixed inside a small quartz tube to maintain an identical position upon changing resonators.

Pulsed EPR measurements were carried out with a  $\gamma$ -irradiated silicon dioxide (e-prime) sample rod (length: 14 mm, diameter: 1 mm). The e-prime sample rod was positioned inside a quartz tube supported by two Teflon rods.

### 2.2. Full wave electromagnetic simulations

The electromagnetic field simulations were performed by using the full-wave electromagnetic software *CST Studio Suite 2021-Student Edition*, which is freely available online [23]. The software uses the finite element method (FEM) to solve numerically Maxwell's equations inside a 3D geometry. The 3D resonator models were designed using the exact dimensions of all four dielectric resonators. All simulations were calculated with the frequency domain solver and hexahedral meshes because of its robustness for complex geometries. A drawback of this mesh type is that no lossy materials can be simulated leading to idealized  $Q$ -factors and MW field distributions. In addition, each model was simplified slightly in the optimization process to further improve the simulation performance (see Fig. 1). The symmetry and boundary conditions were chosen to focus on the  $TE_{015}$  mode of the resonator at X-band<sup>1</sup>. The resonance frequencies and field distributions were simulated with and without EPR tubes inside of the cavity for comparison.

### 2.3. Technical description

Fig. 1 shows a schematic cross section of the MD5 probehead in the SL (symmetric long) configuration. Fig. 2 shows the MW resonator package, which is housed inside the metal shield of the MD5 probehead. Every resonator is held by two Teflon holders (triangular prisms in light grey, see Fig. 2) and together they are sandwiched between two metal end caps. These caps are closing the cylindrical metal shield at the top and bottom (bronze in Fig. 2). The different sapphire rings are positioned in the center of every package (light blue in Fig. 2). All resonators

were held in the cavity body of the MD5 probehead (see Fig. 1). For reference, all experiments were performed with the originally configured Bruker ER 4118 X-MD5 resonator (Asymmetric Long, AL, shown in Fig. 2(a)). The AL resonator consists of nickel-silver alloy end caps with a cylindrical Teflon holder at the top of the package and a triangular prism Teflon holder at the bottom. The sapphire resonator is 13 mm long, has an outer diameter of 10 mm and an inner diameter of 5.1 mm to fit standard EPR tubes.

The first step of optimization was done by changing the material of the outer metal caps (Ni-Ag alloy to copper) and varying the shape of the Teflon holders to a symmetrical shape through triangular prisms with less Teflon on both ends (Symmetric Long, SL, shown in Fig. 2(b)) while keeping the same dielectrical resonator (sapphire descriptions listed in Table 1). Furthermore, we wanted to investigate the impact of changing the size of the dielectric resonator. By decreasing the height of the resonator, while maintaining the resonance frequency through increasing its outer diameter, the mode volume is decreased and the  $B_1$  field is enhanced (Symmetric Compact, SC, shown in Fig. 2(d)). Our third approach changed the shape of the dielectric insert to improve the  $B_1$  field homogeneity (Symmetric Diabolo, SD, shown in Fig. 2(c)). All described sapphires were machined to our specifications by Agate Products Limited, UK.

## 3. Results and discussion

### 3.1. Optimization strategy

We began our optimizations by performing finite element simulations of different MW resonator layouts to find the most suitable configuration. In the second step we manufactured the resonators and in a final step we verified their performance experimentally. The simulation models are motivated by the idea of improving the  $Q$ -factor and the  $B_1$  field homogeneity inside of the dielectric resonators through geometric adjustment inside the original Bruker probehead [18,24–26].

The first simulation model is the SL resonator, which is most similar to the AL resonator (see Fig. 2a) but with lighter and symmetrical Teflon holders. The asymmetrical placement of the sapphire ring inside of the AL's metal shield by two distinct Teflon holders (see Fig. 2b) shifts the maximum magnitude of the  $B_1$  field towards the top metal end cap resulting in deformed field distributions and higher losses due to e.g. higher eddy currents in the shield's walls [27] (see Fig. 3a and b). Since the loss tangent  $\tan\delta$  of Teflon [28,29] is approximately one order of magnitude larger than that of sapphire [30,31] at room temperature, the total losses of the resonator are decreased and hence the  $Q$ -factor is increased by the design of thinner Teflon holders (see Table 2). This symmetrical positioning of the sapphire ring and the use of lighter Teflon holders is maintained for the following simulation models.

The second simulation model was motivated by the work of Syryamina et al. [18], demonstrating that shaping the dielectric resonator itself leads to a transition from a sine-function like  $B_1$  field distribution to a more uniform distribution similar to Helmholtz coils (see Fig. 2c). In a standard – cylindrical – dielectric resonator, the electric field density reaches its maximum at the center of the shell of the dielectric ring and consequently the magnetic field density is maximal at the center of the resonator (see Fig. 3b). To generate approximately a magnetic field distribution similar to Helmholtz coils, the radius of the dielectric ring must change over the height of the dielectric resonator. To this end, we choose a circular hyperboloid<sup>2</sup> shape for the dielectric resonator labeling it symmetric Diabolo (SD)<sup>3</sup>. The SD is modelled easily by rotating the curve  $R(z) = \sqrt{4/H_{sap}^2(R_{max}^2 - R_{min}^2)z^2 + R_{min}^2}$  along the symmetry/ $z$ -axis of a given cylindrical sapphire ring ( $H_{sap}$ : height,  $R_{max}$ : radius at the

<sup>1</sup> For more additional information see supporting information.

<sup>2</sup> Also called hyperboloid of revolution.

<sup>3</sup> Dielectric circular hyperBOLoid = DIABOLO.

H.T.A. Wiedemann et al.

Journal of Magnetic Resonance 354 (2023) 107519

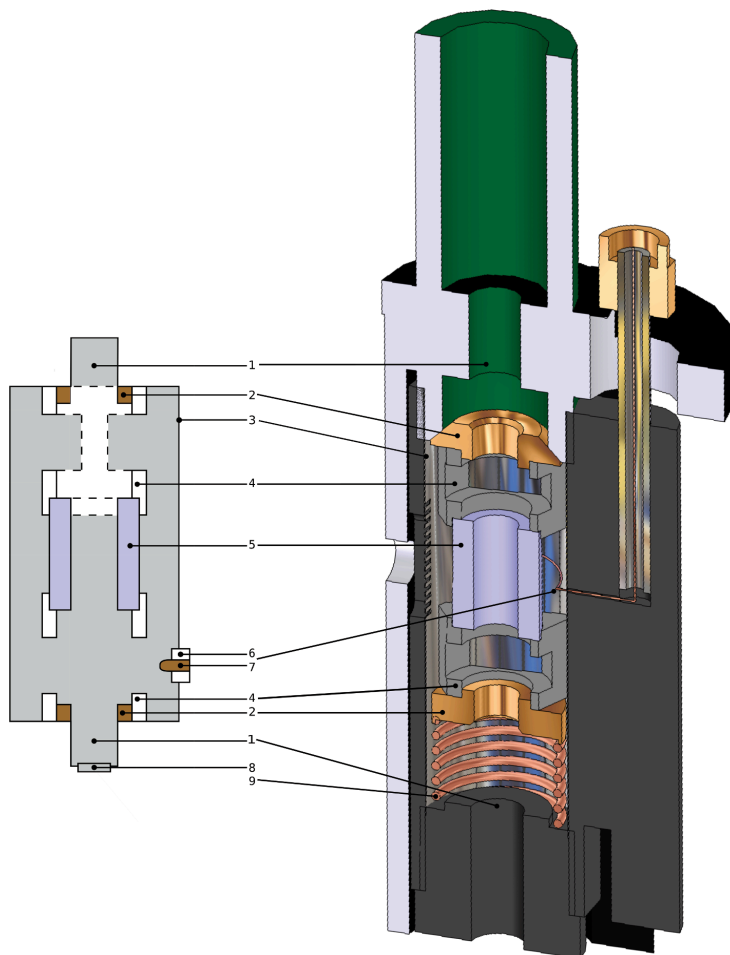


**Fig. 1.** Cross section of the simplified 3D model of the SL resonator inside the MD5 probehead. The basic structures and exploded views of all resonators are further described below (see Fig. 2)). 1 - edge of the cylindrical outer cavity (top: green, bottom: black), 2 - metal end caps (orange), 3 - inner surface of the flexline resonator body including the illumination window, 4 - prism-like, low loss PTFE holder (white; black dashed lines sketch the 3D cross section of the holder), 5 - SL sapphire ring (blue), 6 - coaxial input to the coupling antenna (white), 7 - center conductor of the coaxial input coupling antenna (bronze), 8 - output coupling iris used in simulations (light grey, black), 9 - copper spring to ensure tight alignment of the inner parts (bronze).

edge,  $R_{min}$ : radius at the center). The CST simulations give a  $B_1$  field homogeneity with a flat plateau in axial as well as radial direction with a standard EPR tube (ID = 4 mm, OD = 5 mm) inserted in the dielectric resonator for the parameter values:  $H_{spp} = 13$  mm,  $D_{max} = 13.80$  mm,  $D_{min} = 8.55$  mm (see Fig. 3c). Comparison of the top row a,b and c in Fig. 3 shows that the maximum of the electric field distribution is distorted along the axis of the dielectric resonator, leading to a maximum on each side. This extends the region of homogeneous  $B_1$  field in the axial direction but also to a slightly less homogeneous field in the radial direction, because of the squeezed electric field (see Fig. 3 bottom row of a, b and c).

The third simulation model is the SC resonator, which is less than half the height of the other sapphire rings. Since the metal shield dimensions are kept constant, the diameter of the sapphire ring has to be increased to keep its resonance frequency in the X-band region. Due to this shape, the electric field distribution is squeezed in axial and stretched in radial direction (see Fig. 3 2a/b and 2d). An analysis of the magnetic field distribution reveals that in contrast to the field homogeneity of the SD resonator, the MW field has no plateau but it has a local minimum in the center radial direction of the sapphire ring with two maxima in

opposite radial directions. However in the axial direction the  $B_1$  field distribution is still like a sine-function as for the SL and AL.

### 3.2. Quality factors and resonance frequencies

The first descriptive measurements of the fabricated resonators are power reflection measurements, using a vector network analyzer (MS64122B VNA, Anritsu). The measured and simulated resonance frequencies  $\nu_{Res}^m$  and  $\nu_{Res}^s$  as well as the empty quality factors  $Q_{empty}$  and filled quality factors  $Q_F$  (4 mm quartz tube inside a 5 mm quartz tube) are given in Table 2<sup>4</sup>. Acquired baselines were corrected by a linear fit to accurately determine the frequencies  $-3$  dB at each side of  $\nu_{Res}^m$ . In our designs, we kept the shield length constant but first changed the metal caps of commercially available EPR resonators from a nickel-silver alloy to copper because copper exhibits a smaller skin depth [32]. Subsequently, we substituted the asymmetric Teflon holders with symmetric

<sup>4</sup> The annotations empty and filled in  $\nu_{Res,0}^m$  and  $\nu_{Res,F}^m$  describe whether there is a sample tube in the resonator.

H.T.A. Wiedemann et al.

Journal of Magnetic Resonance 354 (2023) 107519

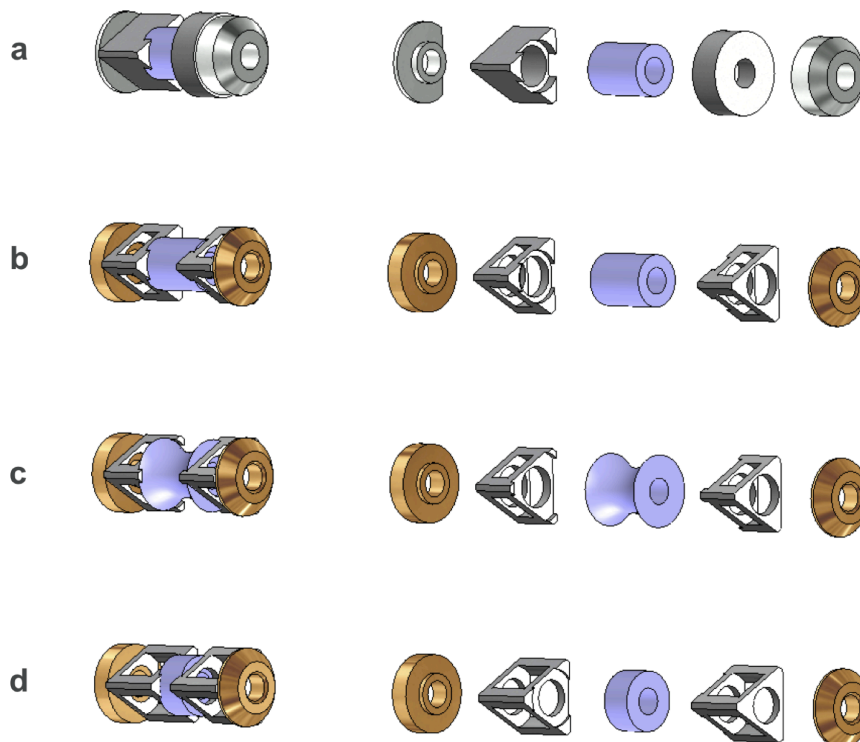


Fig. 2. Schematics of the resonators (a) AL resonator, (b) SL resonator, (c) SD resonator and (d) SC resonator with exploded view of each resonator package on the right side. The metal holders are colored in light brown for copper and silver for Ag-Ni-alloy. The Teflon holders are colored in light grey and the dielectric sapphires in blue.

**Table 1**

Dimensions of the different dielectric sapphire ring resonators in mm. To characterize the exact shape of the SD, a minimal and a maximal width is required due to its concave cross-section.

Resonator	AL	SL	SD	SC
Height		13	13	6
Width		10	13.8 (edge)	11.4
		8.6 (center)		
Inner diameter		5.1	5.1	5.1

ones (SL resonator) since first measurements of power reflection curves showed that less Teflon and symmetric holders give an improved  $Q$ -factor.

The resonance frequencies of all resonators lie within the X-band frequency range of 9–10 GHz. The comparison of the measured and simulated resonance frequencies in Table 2 yields a maximum relative error of 1.2% for the SD resonator, which corresponds to a frequency shift of 120 MHz. This small frequency deviation most likely result from assuming a simplified model in the simulation and the limited range of model options of the used CST student version. Also for this reason no simulated  $Q$ -factors are given since the absolute values are not realistic, however the relative values can be used to compare the different resonator models.

The measured  $Q$ -factor of the AL resonator (4761) is in good agreement with the literature value of 4000, given by Bruker [33]. In comparison, the resonator packages with our optimizations show increased  $Q$ -factors from SL (7046) to SC (8956). This corresponds to our first

hypothesis that by changing the material of the metal caps and redesigning the Teflon holders already reduces the MW losses inside the resonator significantly. Although the  $Q$ -factor is reduced with the SD (2123), we note that it is favorable for pulsed EPR purposes [20,21], and that it is much less affected by the EPR tube.

### 3.3. CW EPR

#### 3.3.1. SNR

To estimate the SNR, a standard protocol with WP was carried out [22]. The reference measurement for the AL resonator with a SNR of 298 is in good agreement with the SNR of 300 given by Bruker (see Table 2). For the other resonators, the SNR of the SL and SC are higher with values of 378 and 397, respectively. The SD resonator exhibits a lower SNR of 171. We attribute this rise in SNR of the SC and SL in the better conversion of MW power into effective  $B_1$  field inside both resonators (see next section). The lower SNR of the SD resonator most likely originates from the less effective conversion of MW power inside the resonator which is further supported by the smaller  $Q$ -factor. This is discussed in more detail in the following section.

#### 3.3.2. $B_1$ field homogeneity

The  $B_1$  field homogeneity of all four resonators was quantified by two experimental and one theoretical method. The first method is based on EPR spectroscopy: a point sample of BDPA is moved along the symmetry axis of the resonator at 0.5 mm intervals and the signal amplitude recorded. The second is the perturbing sphere method [34,35], in which a metallic sphere is moved along the symmetry axis of the resonator at

H.T.A. Wiedemann et al.

Journal of Magnetic Resonance 354 (2023) 107519

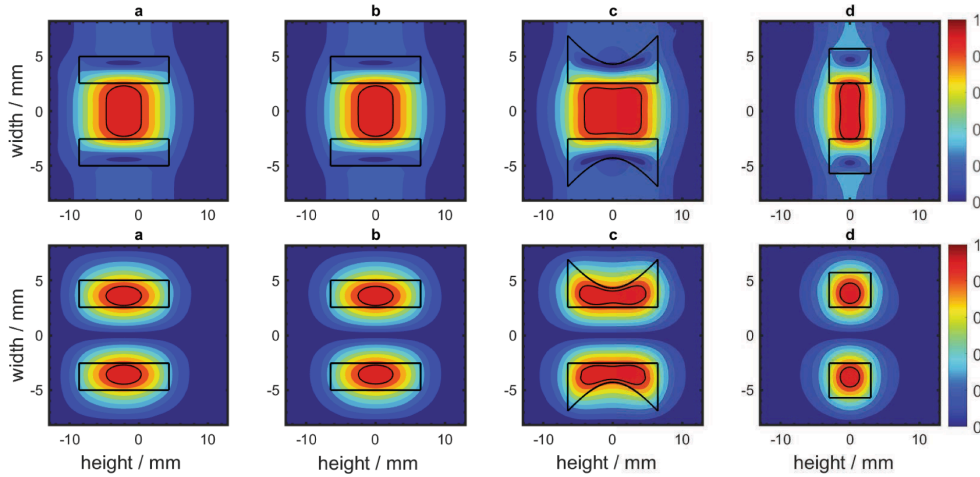


**Fig. 3.** Normalized magnitude of the magnetic (top row) and electric (bottom row) field distributions inside the cross-section of the different sapphire ring resonators (AL = a; SL = b; SD = c; SC = d). On the right handside of each plot is the bottom metal end cap with the coupling antenna and on the left is the top metal end cap. The contour levels at 0.9 are highlighted in black and the black rectangular black lines represent the cross sections of the different sapphire rings. The Teflon holders, metal end caps, coupling antenna as well as the inserted EPR tubes, which are present in models, are not shown in these plots. The contour plots show the broadening and narrowing of the field distribution along different directions depending on the actual shapes of the sapphire rings.

**Table 2**

Quality factors, resonance frequencies (in GHz) and SNR of WP for all resonators.  $\nu_{Res,0}^m$  and  $\nu_{Res,F}^m$  represent empty and filled resonator.

Resonator	$\nu_{Res,0}^m$	$\nu_{Res,0}^f$	$\nu_{Res,F}^m$	$\nu_{Res,F}^f$	$Q_{empty}$	$Q_F$	S/N ratio
AL	9.69	9.71	9.52	9.55	4761	2098	298
SL	9.70	9.73	9.53	9.56	7046	2229	378
SD	9.97	9.85	9.79	9.69	2123	1761	171
SC	9.84	9.91	9.70	9.78	8956	2375	397

0.5–1 mm intervals. The experimental results were then compared with the predicted electromagnetic field distributions, which give the  $B_1$  field homogeneity, derived from CST.

For the  $B_1$  field homogeneity measurement via BDPA, the resonator was maintained at critical coupling for all positions. Fig. 4 shows both the experimentally determined normalized EPR signal amplitude and the simulated  $B_1$  field profiles as a function of the relative BDPA position inside the resonators. As the signal intensity is proportional to the magnitude of the  $B_1$  field, we are able to determine the  $B_1$  field profile [36] (see Fig. 4 left). As the sample moves through the resonator the signal intensity increases until the sample reaches the point of maximal  $B_1$  field intensity, after which it decreases again.

For the perturbing sphere method, we performed similar measurements. A small brass sphere of 0.3 mm diameter was placed inside a small EPR tube (OD = 2 mm, ID = 0.9 mm, shown in the supplementary material) and fixed with quartz wool at a specified position. The tube was centered along the symmetry axis of the sapphire ring and moved by a stepper motor driven inside the cavity. The EPR tube was moved back and forth in 0.5–1 mm steps inside the different resonator configurations. After each step the resonance frequency was measured with a VNA. The metal sphere interacts with the electromagnetic field of the resonator, resulting in different shifts of the resonance frequency for different sphere positions. If the sphere is moved along the axis with zero electric field (which is approximately true for the  $TE_{01,6}$  mode near the symmetry axis), the resonance shift is solely induced by the  $B_1$  field contribution. In this case the  $B_1$  field distribution can be extracted from the shift by the following equation [18,34,37,35]:

$$B_1^2 = \frac{\mu_0 Q_0 P_m f^2 - f_0^2}{2\pi^2 r^3 f_0^3}, \quad (1)$$

where  $\mu_0$  is the free-space permeability,  $Q_0$  is the intrinsic quality factor of the resonator,  $r$  is the radius of the brass sphere,  $P_m$  is the effective input power being dissipated in the cavity and  $f_0$  and  $f$  are the non-perturbed and perturbed resonance frequencies. Eq. (1) assumes that the metallic sphere is nearly diamagnetic and not ferromagnetic which is the reason brass is used. The resonator was critically coupled when the brass sphere entered the resonator shield, hence we can approximate the input power  $P_m$  by the output power of the VNA. Fig. 5 illustrates the determined  $B_1^2$  field profiles measured by the perturbing sphere method and it matches the results of the other two methods.

We compare the experimental data of both methods with the simulated  $B_1$  field profiles from CST simulations (see Fig. 3) along the symmetry axis of the resonator (see Fig. 4 right) and determine the relative deviations in MSZ and FWHM (see Table 3). Moreover, we extracted the quantitative deviations in MSZ and FWHM by comparing the BDPA  $B_1$  field homogeneity measurement with the simulation and used the perturbing sphere method only to validate our BDPA  $B_1$  field homogeneity experiments since the experimental methods should provide similar results. A qualitative comparison of both experimental methods shows that the shape is similar for all four resonator configurations (depicted in Fig. 5). The experimental  $B_1$  field profile of the AL, SL and SC resonator determined via BDPA exhibit a small shift from the centre of the resonators (approx. 1 mm).

With respect to the original configuration AL, the  $B_1$  profile of the SL is shifted towards the center by 0.2 mm. This must be a systematic error in the measurement setup since the physical boundary conditions of the resonators require the field distribution of the  $TE_{01,6}$  mode to be an even function in terms of the center of the resonator except for the AL resonator<sup>5</sup>. We extract the full width at half maximum (FWHM) by fitting the

<sup>5</sup> The deviation of the resonator coupling was less than 1%.

<sup>6</sup> The maximum magnetic field has to be in the center of the dielectric resonator because of the symmetric boundary conditions of the cavity.

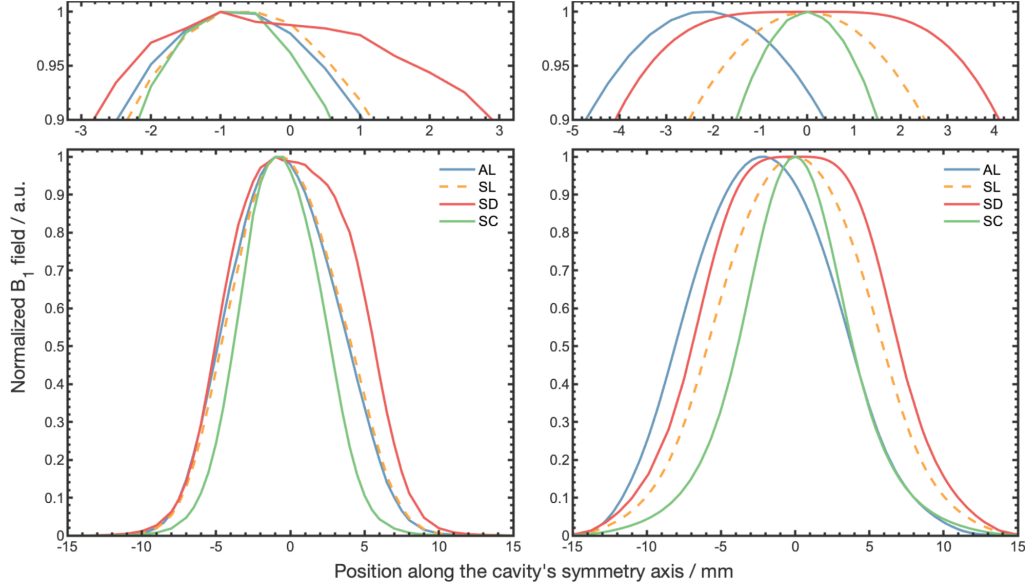


**Fig. 4.** Experimental (left) and simulated (right)  $B_1$  profiles of all presented resonators taken along their symmetry axes. Upper inset: Zoomed center part (> 90%) of the diagram showing the maximal signal zone. The simulated field distributions are broader than the experimental ones because of the idealized boundary condition and the neglect of losses in the simulation. In addition all fields are centered around the origin besides of the AL that matches the physical BC in contrast to the measurement.

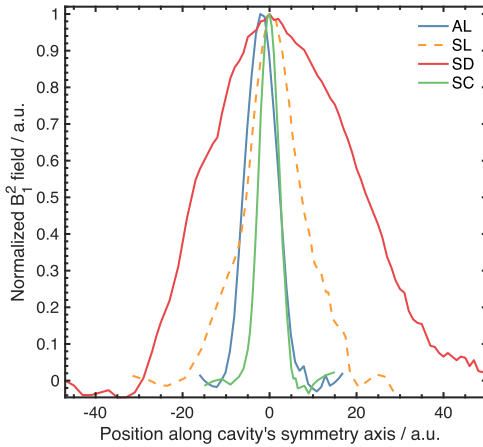


**Fig. 5.**  $B_1^2$  profiles of all resonators along their symmetry axes determined by the perturbing sphere method, using a brass sphere with a diameter of 0.3 mm and a maximum step width of 1 mm. In addition to the other two methods shown in Fig. 4 the MSZ and FWHM of the  $B_1$  profiles can be ordered from largest to smallest: SD-SL-AL-SC.

profiles of the AL, SL and SC, using a one-term Gaussian function (see Table 3). We find that the SL, with a FWHM of  $8.4 \pm 0.2$  mm, is marginally wider than the AL with a FWHM of  $8.3 \pm 0.2$  mm. Interestingly, the areas of highest  $B_1$  field intensities are of similar magnitude except for the SD. To characterize this we define a region around the maximum  $B_1$  field, maximum signal zone (MSZ), where the relative change is smaller than 98%. The shorter SC resonator exhibits a

**Table 3**

Homogeneous zones at maximum signal intensity (> 98%, in mm) MSZ, calculated FWHM (in mm, FWHM were obtained using a one-term gaussian fit model and errors were obtained by extracting the statistical error margin out of the fit), relative deviations of the homogeneous zones at maximum signal intensity (> 98%, MSZ)  $\delta\epsilon_{MSZ}^m$  (%) and the calculated FWHM  $\delta\epsilon_{FWHM}^m$  (%) referenced to the AL resonator for both experimental (exponent 'm') and simulated data (exponent 's').

Resonator	MSZ	FWHM	$\delta\epsilon_{MSZ}^m$	$\delta\epsilon_{MSZ}^s$	$\delta\epsilon_{FWHM}^m$	$\delta\epsilon_{FWHM}^s$
AL	1.5	8.3(2)	0	0	0	0
SL	1.5	8.4(2)	0	2.98	1.21	6.01
SD	2.5	10.7(4)	66.67	125.54	28.92	24.29
SC	1.2	6.3(1)	-20.00	-43.20	-24.10	-30.85

narrower profile with a FWHM of  $6.3 \pm 0.1$  mm.

In contrast, the  $B_1$  profile of the SD resonator is well centered at the resonator center and shows the widest FWHM ( $10.7 \pm 0.4$  mm) [38] and more than double the MSZ (2.5 mm) with respect to the SC resonator.

We compare the experimental data with the simulated data and determine the relative deviations in MSZ and FWHM (see Table 3). The relative deviations of the MSZ and the FWHM are calculated for both experimental (BDPA) and simulated data with respect to the AL resonator [39]. The simulated data are within the same order of magnitude as the experimental data, where the simulations provide higher values than the measurements in general. Note that the simulated MSZ is approximately twice as large as the experimental one, except for the SL resonator. The FWHM data shows a better agreement between simulation and experiment. We attribute this discrepancy to the assumption of ideal conditions for the CST simulations, especially the treatment of lossy materials as lossless ones and a limited simulation power.

H.T.A. Wiedemann et al.

Journal of Magnetic Resonance 354 (2023) 107519

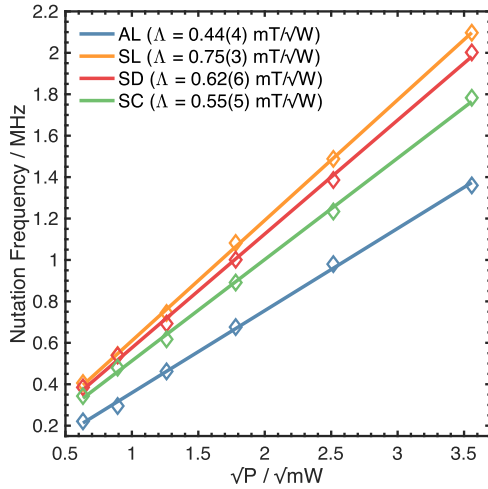


Fig. 6. Linear fitted dependency of the nutation frequency against the MW power with conversion factors of presented resonators. Nutation frequencies were taken from the transient nutations of the low-field emissive line.

#### 3.4. Transient EPR

The MW conversion efficiency  $\Lambda$  is calculated directly from the transient nutation frequency  $\omega_{\text{Nut}}$  of the photoexcited triplet state of pentacene hosted in a *p*-terphenyl matrix (1.8 mm  $\times$  1.2 mm) and is positioned tightly in an EPR quartz tube. The triplet state is generated by pulsed laser excitation. The transient nutation curves were measured at the maximum emissive resonance of pentacene (low-field) [40]. In order to obtain the transient nutation frequency  $\omega_{\text{Nut}}$  the nutation curves are converted to frequency space by Fast Fourier transformation (FFT) [13]. Before FFT, the starting point was set to the first maximum of the transient oscillation and a Hamming window was applied<sup>7</sup>. Fig. 6 shows the nutation frequency as a function of the square root MW power. The slope of  $\omega_{\text{Nut}}$  gives the conversion factor:  $\Lambda = \omega_{\text{Nut}}/(\gamma_e \sqrt{2} \sqrt{P})$  [40].

The conversion factors obtained are listed in Table 4. The AL resonator with  $0.44 \pm 0.04$  mT/ $\sqrt{W}$ , which is in good agreement with the conversion factor of  $0.42$  mT/ $\sqrt{W}$  stated by Bruker [33], is outperformed by all optimized resonators which show a higher conversion of MW into  $B_1$  field (see Table 4). For the SL and SD resonator we find values of  $0.75 \pm 0.03$  mT/ $\sqrt{W}$  and  $0.62 \pm 0.06$  mT/ $\sqrt{W}$ , respectively. The conversion factor of the SC resonator is  $0.55 \pm 0.05$  mT/ $\sqrt{W}$ .

Additionally we calculated the magnetic mode volume  $V_m$  of the driven  $TE_{01\delta}$  mode of the presented CST resonator models (the resonant length for the  $TE_{01\delta}$  mode is less than  $\lambda_g/2$ , where  $\lambda_g$  is the guide wavelength of the  $TE_{01}$  dielectric waveguide mode, the symbol  $\delta = 2L/\lambda_g < 1$  is used to denote the  $z$  variation of the resonant mode) [41]. The mode volume of a resonant mode is a measure of the physical extent of the mode inside the resonator [42]. It is given by the ratio of the stored  $B_1$  field energy within the cavity to the maximum  $B_1$  field energy density  $V_m = \int_{V_{\text{cov}}} |\mathbf{B}_1(\mathbf{r})|^2 dV / \max_{r \in V_{\text{cov}}} (|\mathbf{B}_1(\mathbf{r})|^2)$ . Since the simulated magnetic field profiles are broader than the measured ones due to the idealized boundary conditions, the calculated mode volumes in Table 4 represent an upper limit of the realistic mode volumes of the resonators. Nevertheless, the relative order of the mode volumes should be preserved in the comparison of experimental and simulated data as indicated in

<sup>7</sup> For more additional information see supporting information.

Table 4

Slopes (in MHz/ $\sqrt{mW}$ ), evaluated conversion factors  $\Lambda$  (in mT/ $\sqrt{W}$ ) and simulated magnetic mode volumes  $V_m$  (in  $\text{cm}^3$ ) of presented resonators (errors were obtained by extracting the statistical error margin out of the fit).

Resonator	AL	SL	SD	SC
Slope	0.39(4)	0.58(3)	0.55(6)	0.49(5)
$\Lambda$	0.44(4)	0.75(3)	0.62(6)	0.55(5)
$V_m$	0.359	0.356	0.456	0.298

Table 3. The calculated mode volumes show that the SL has a slightly smaller mode volume than the AL and that the SC has the overall smallest mode volume.

We attribute the improved  $\Lambda$  for the smaller SC to the smaller mode volume. The pentacene crystal fits very well in the shorter dielectric ring resonator, while in the longer versions the filling factor is smaller. Note, that for bigger samples the SC resonator would be worse than the longer resonators. This underlines the main advantage of the SC resonator, as it excels for small samples [19]. Compared to the other two resonators, SL and SD, the SC resonator is worse in the conversion efficiency. We attribute this to a local minimum of the  $B_1$  field along the radial axis inside the resonator, indicating a smaller field inside the SC resonator (also visible the upper part of Fig. 3d) and hence, a worse conversion factor.

#### 3.5. Pulsed EPR

Finally we investigated the relaxation behaviour of spins within the resonator using pulsed EPR.

In order to compare the performance for pulsed EPR within each resonator, we measured the coherence time  $T_2$ , using a standard Hahn echo sequence and a one-term exponential decay function (exception: stretched exponential decay function for SC, and discussed below). Additionally, transient recordings of a Hahn echo of a standard  $\gamma$ -irradiated silicon (e-prime) sample rod were recorded and fitted with a simple one-term Gaussian fit to obtain  $\sigma$  and hence, the  $T_2^*$  relaxation time. Both sets of parameters are listed in Table 5 below.

Hahn echo experiments were carried out in order to determine the spin-spin relaxation time,  $T_2$ . The relaxation data is displayed in Fig. 7.

The  $T_2$  relaxation times are similar for all resonators, indicating that none of our resonator optimizations induces a negative effect on the intrinsic spin-spin interactions. The relaxation curve of the SC resonator was fitted with a stretched exponential (stretch factor: 0.88) because there is an observable turning point visible after the first few microseconds (see Fig. 7) which can be attributed to a spin diffusion mechanism because the e-prime sample rod is reaching out of the efficient  $B_1$  field.

The electron spin echos are shown in Fig. 8 where the normalized intensity is plotted against time. The echo is the widest for the SC resonator with a  $T_2^*$  of  $410 \pm 4$  ns. The AL and SL resonator have a similar  $T_2^*$  with  $292 \pm 2$  and  $261 \pm 3$  ns, respectively. The narrowest echo is observed with the SD resonator with a  $T_2^*$  of  $199 \pm 2$  ns.

The resulting  $T_2^*$  values (see Table 5) indicate a reciprocal dependence of active EPR sample volume or mode volume (see Table 4). The SC resonator with the smallest mode volume shows the longest  $T_2^*$  and is the shortest for the SD resonator, which features the largest mode volume, due to the extended  $B_1$  field. The e-prime sample rod extends

Table 5

$T_2^*$  ( $\mu\text{s}$ ) of the echos and  $T_2$  ( $\mu\text{s}$ ) of presented resonators (errors were obtained by extracting the statistical error margin out of the fit).

Resonator	AL	SL	SD	SC
$T_2^*$	0.29(2)	0.26(3)	0.20(2)	0.41(4)
$T_2$	21.11(8)	20.22(6)	21.42(8)	22.38(4)

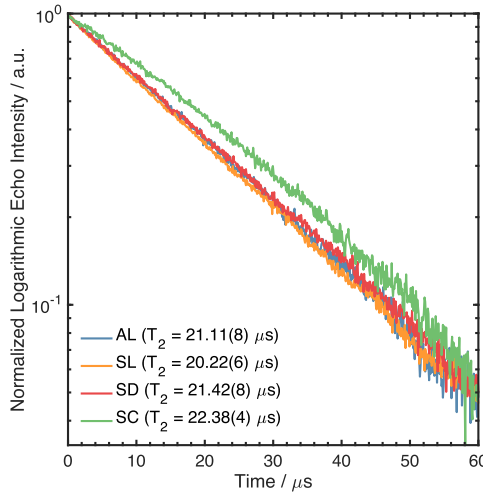


**Fig. 7.**  $T_2$  relaxation curves of e-prime inside the AL resonator (blue), SL resonator (orange), SC resonator (green) and SD resonator (red) by using the following delayed Hahn-Echo sequence:  $(\pi)/2 - \tau + t_1 - (\pi) - \tau + t_2 - \text{echo}$ ;  $(\pi)/2 = 12$  ns,  $(\pi) = 24$  ns,  $\tau = 4$   $\mu$ s,  $t_1 = 48$  ns,  $t_2 = 96$  ns. Other experimental conditions:  $T = 290$  K, averages: 100, shot repetition time: 5 ms, shots per point: 10, Field and MW frequency dependant on selected resonator (information upon request).

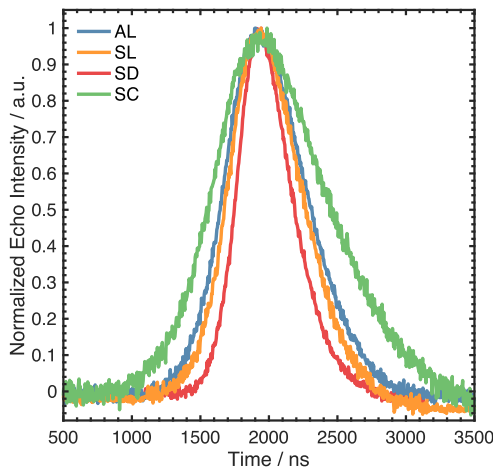


**Fig. 8.** Electron spin echos of e-prime inside the AL resonator (blue), SL resonator (orange), SC resonator (green) and SD resonator (red) by using the following Hahn-Echo sequence:  $(\pi)/2 - \tau - (\pi) - \tau - \text{echo}$ ;  $(\pi)/2 = 12$  ns,  $(\pi) = 24$  ns,  $\tau = 4$   $\mu$ s. Other experimental conditions:  $T = 290$  K, averages: 100, shot repetition time: 5 ms, shots per point: 10, Field and MW frequency dependant on selected resonator (information upon request).

beyond the dimensions of all resonators. Together, this suggests that the extracted  $T_2^*$  times are limited by the  $B_0$  field homogeneity of the magnet system used in our experiments. A larger area within an inhomogeneous static magnetic field  $B_0$  would lead to a larger field gradient and a wider spectral distribution of spins. A shorter  $T_2^*$  suggests a broader distribution in frequency space. This supports the conclusion that the SD

resonator has larger region of homogeneous  $B_1$  field and in return probes a larger area of the sample which is exposed to more  $B_0$  field inhomogeneities.

In this experiment we only probe the part of the sample which is within the mode volume of the resonator. Correspondingly, the larger the mode volume, the larger is the region of the sample that gives an EPR response. Any inhomogeneities in the static  $B_0$  field result in a field gradient across the sample region. The  $T_2^*$  is directly influenced by such  $B_0$  inhomogeneities, where a larger inhomogeneity corresponds to a shorter  $T_2^*$  time. As the SD resonator features the largest homogeneous  $B_1$  field region and the largest mode volume, it is more sensitive to inhomogeneities in the  $B_0$  field and thus the shortest  $T_2^*$  times are observed.

#### 4. Discussion and conclusion

This study was stimulated by the observation of the asymmetric arrangement of the commercially available resonator, AL. We optimized the symmetry by designing new Teflon holders and metal caps. The three resonators (SC, SL and SD) described here combine low-cost optimizations and exhibit enhanced EPR performance for three experimental applications (CW, transient and pulsed EPR). and by investigating the influence of the dielectric sapphire ring shape.

The resonance frequencies of all fabricated resonators possess a  $\nu_{Res}$  within the commonly used frequency band, X-band (9–10 GHz). The Q-factors of the SL and SC resonator were optimized to higher values, 7046 and 8956 respectively, in order to obtain better CW EPR performance. The SD resonator exhibits a lower quality factor (2123) more favorable for pulsed and transient EPR experiments.

Measurements of the MW conversion factors showed that all three resonators have enhanced MW conversion into effective  $B_1$  field. Even though the mode volume and the Q-factor of the SL resonator are only marginally better than that of the AL resonator, it outperforms the AL resonator in MW conversion to effective  $B_1$  field which we attribute to a more symmetric resonator topology and lower MW losses through copper metal end caps instead of Ni-Ag alloy end caps. To qualitatively study the  $B_1$  field homogeneity, the EPR signal of a point sample as a function of its position inside the resonator was measured. The expected  $B_1$  profile of the SD resonator similar to Syriamina et al. was experimentally confirmed and hence, supports the chosen optimization route to concave shaped dielectric resonators.

Finally, pulsed EPR was used to observe the relaxation behaviour of spins inside each resonator. The extracted  $T_2$  times from all resonators are of similar values, demonstrating that our optimizations have no negative effects on  $T_2$  measurements. We find that the  $T_2^*$  time shows a reciprocal dependence on the mode volume, being the longest for the SC resonator and the shortest for the SD resonator. We attribute this to  $B_0$  field inhomogeneities in our magnet system, which, however, corroborates the extended homogeneous  $B_1$  field region of the SD resonator. In addition, the  $T_2^*$  relaxation times allow  $B_0$  inhomogeneities in EPR spectrometer magnets to be investigated. Due to its smaller mode volume, which is compensated by a higher Q-factor and MW conversion factor giving rise to a higher SNR the SC is better suited for smaller samples than the other designs.

To conclude, we demonstrated that a cost-efficient enhancement of commercially available resonators, without the need to design a completely new probeheads, is possible, and expect that this study will provide impetus in the ongoing quest for higher sensitivity in EPR spectroscopy.

#### Author contributions

H.T.A.W. performed the measurements, processed the experimental data, performed the analysis and drafted the manuscript. S.R. performed the theoretical calculations and simulations and the perturbing sphere

H.T.A. Wiedemann et al.

Journal of Magnetic Resonance 354 (2023) 107519

measurements. R.R. prepared the technical drawings of the resonators and made the visualizations. All authors discussed the results and commented on the manuscript. Project was supervised by C.W.Z. and C.W.M.K. and conceived by C.W.M.K..

#### Declaration of Competing Interest

The authors declare the following financial interests/personal relationships which may be considered as potential competing interests: [Christopher William Michael Kay reports financial support was provided by Engineering and Physical Sciences Research Council. Haakon Tassilo Adam Wiedemann reports administrative support was provided by Saarland University.]

#### Data availability

Data will be made available on request.

#### Acknowledgements

We are indebted to Stefanie Porger and Jens Wiegert, who machined the components of the resonators. Both are members of the highly skilled team in the engineering workshop of the Department of Physical Chemistry at Saarland University. We thank the Saarland university and the EPSRC EP/S000690/1 grant for financial support.

#### Appendix A. Supplementary material

Supplementary data associated with this article can be found, in the online version, at <https://doi.org/10.1016/j.jmr.2023.107519>.

#### References

- [1] C. Hintze, U. Steiner, M. Drescher, Photoexcited triplet state kinetics studied by electron paramagnetic resonance spectroscopy, *Chem. Phys. Chem.* 18 (2017) 6–16.
- [2] D. Park, G. Feng, R. Rahimi, J. Baugh, R. Laflamme, Randomized benchmarking of quantum gates implemented by electron spin resonance, *J. Magn. Reson.* 267 (2016) 68–78.
- [3] J. Niklas, O. Poluektov, Charge transfer processes in opv materials as revealed by epr spectroscopy, *Adv. Energy Mater.* 7 (2017) 1602226.
- [4] T. Stich, W. Myers, R. Britt, Paramagnetic intermediates generated by radical s-adenosylmethionine (sam) enzymes, *Accounts Chem. Res.* 47 (2014) 2235–2243.
- [5] A. Samouilov, D. Komarov, S. Petryakov, A. Iosilevich, J.L. Zweier, Development of an l-band resonator optimized for fast scan epr imaging of the mouse head, *Magn. Res. Med.* 86 (2021) 2316–2327.
- [6] G. Annino, M. Cassettari, I. Longo, Dielectric resonators in esr: Overview, comments and perspectives, *Appl. Magn. Reson.* 16 (1999) 45–62.
- [7] Y. Twig, E. Suhovoy, A. Blank, Sensitive surface loop-gap microresonators for electron spin resonance, *Rev. Sci. Instrum.* 81 (2010) 104703.
- [8] M. Simenas, J. O'Sullivan, C.W. Zollitsch, O. Kennedy, M. Seif-Eddine, I. Ritsch, M. Hülsmann, M. Qi, A. Godt, M.M. Roessler, G. Jeschke, J.J. Morton, A sensitivity leap for x-band epr using a probehead with a cryogenic preamplifier, *J. Magn. Reson.* 322 (2021) 106876.
- [9] R.R. Mett, J.W. Sidabras, J.R. Anderson, C.S. Klug, J.S. Hyde, Rutile dielectric loop-gap resonator for x-band epr spectroscopy of small aqueous samples, *J. Magn. Res.* 307 (2019) 106585.
- [10] D. Thomas, C. Wendt, W. Francisz, J. Hyde, Saturation transfer epr spectroscopy on spin-labeled muscle fibers using a loop-gap resonator, *Biophys. J.* 43 (1) (1983) 131–135.
- [11] R. Tschaggelar, F. Breitgoff, O. Oberhänsli, High-bandwidth q-band epr resonators, *Appl. Magn. Reson.* 48 (2017) 1273–1300.
- [12] P. Spindler, P. Schops, W. Kallies, S. Glaser, T. Prisner, Perspectives of shaped pulses for epr spectroscopy, *J. Magn. Reson.* 280 (2017) 30–45.
- [13] S. Kiss, A. Rostas, L. Heidinger, N. Spengler, M. Meissner, N. MacKinnon, E. Schleicher, S. Weber, J. Korvink, A microwave resonator integrated on a polymer microfluidic chip, *J. Magn. Res.* 270 (2016) 169–175.
- [14] S. Weber, *Transient epr*, *eMagRes* 6 (2017) 255–269.
- [15] N. Abhyankar, A. Agrawal, J. Campbell, T. Maly, P. Shrestha, V. Szalai, Recent advances in microresonators and supporting instrumentation for electron paramagnetic resonance spectroscopy, *Rev. Sci. Instrum.* 93 (10) (2022) 101101.
- [16] N.A. Shtin, J.M.L. Romero, E. Prokhorov, Theory of fundamental microwave absorption in sapphire, *J. Appl. Phys.* 106 (2009) 104115.
- [17] M.Y. Ivanov, V.A. Nadolinny, E.G. Bagryanskaya, Y.A. Grishin, M.V. Fedin, S. L. Veber, Bismuth germanate as a perspective material for dielectric resonators in epr spectroscopy, *J. Magn. Res.* 271 (2016) 83–89.
- [18] V.N. Syryamina, A.G. Matveeva, Y.V. Vasiliev, A. Savitsky, Y.A. Grishin, Improving b1 field homogeneity in dielectric tube resonators for epr spectroscopy via controlled shaping of the dielectric insert, *J. Magn. Res.* 311 (2020) 106685.
- [19] D. Barr, S. Eaton, G. Eaton, Workshop on quantitative EPR, in: *Proceedings of the 31st Annual International EPR Symposium, 2008*, <https://portfolio.du.edu/downloaditem/220701>, accessed: 2023/07/13 20:10:30.
- [20] R. Narkowicz, D. Suter, I. Niemeyer, Scaling of sensitivity and efficiency in planar microresonators for electron spin resonance. review of scientific instruments, *Rev. Sci. Instrum.* 79 (2008) 084702.
- [21] Y.S. Yap, H. Yamamoto, Y. Tabuchi, M. Negoro, A. Kagawa, M. Kitagawa, Strongly driven electron spins using a ku band stripline electron paramagnetic resonance resonator, *J. Magn. Res.* 232 (2013) 62–67.
- [22] J. Möser, K. Lips, M. Tseytlin, G. Eaton, S. Eaton, A. Schnegg, Using rapid-scan epr to improve the detection limit of quantitative epr by more than one order of magnitude, *J. Magn. Res.* 281 (2017) 17–25.
- [23] <https://www.3ds.com/products-services/simulia/products/cst-studio-suite/student-edition/>, accessed: 2023/07/13 20:10:30.
- [24] R.R. Mett, W. Francisz, J.S. Hyde, Axially uniform resonant cavity modes for potential use in electron paramagnetic resonance spectroscopy, *Rev. Sci. Instrum.* 72 (11) (2001) 4188–4200.
- [25] J.S. Hyde, R.R. Mett, Epr uniform field signal enhancement by dielectric tubes in cavities, *Appl. Magn. Reson.* 48 (11) (2017) 1185–1204.
- [26] J.S. Hyde, J.W. Sidabras, R.R. Mett, Uniform field resonators for epr spectroscopy: A review, *Cell Biochem. Biophys.* 77 (1) (2019) 3–14.
- [27] Y. Xu, J. Yao, Electron magnetic resonance principles, in: *Electron Magnetic Resonance Principles*, De Gruyter, 2019, Ch. 1.2.2, pp. 8–9.
- [28] S. Rajesh, V. Nisa, K. Murali, R. Raheesh, Microwave dielectric properties of ptfe/rutile nanocomposites, *J. Alloys Comp.* 477 (1–2) (2009) 677–682.
- [29] L. Wall, *Fluoropolymers*. new york-london-sydney-toronto: Wiley-interscience, 1972.
- [30] L. Jin, M. Pfender, N. Aslam, P. Neumann, S. Yang, J. Wrachtrup, R.-B. Liu, Proposal for a room-temperature diamond maser, *Nat. Commun.* 6 (1) (2015) 1–8.
- [31] M.T. Sebastian, Dielectric Materials for Wireless Communication, Elsevier, 2010.
- [32] A. Wheeler, Formulas for the skin effect, *Proc. I.R.E.* 30 (1942) 412–424.
- [33] R. Weber, Bruker biospin corporation, in: *ELEXSYS E 580 Pulse EPR Spectrometer User Manual*, 2001, p. 278.
- [34] L.C. Maier Jr, J. Slater, Field strength measurements in resonant cavities, *J. Appl. Phys.* 23 (1) (1952) 68–77.
- [35] J.W. Sidabras, E.J. Reijerse, W. Lubitz, Uniform field re-entrant cylindrical te 01 u cavity for pulse electron paramagnetic resonance spectroscopy at q-band, *Appl. Magn. Reson.* 48 (11–12) (2017) 1301–1314.
- [36] G. Eaton, S. Eaton, D. Barr, R. Weber, *Quantitative Epr*, Springer Science & Business Media, 2010.
- [37] H. Klein, *Basic concepts i* (1992).
- [38] Due to the special shape of this profile we extracted the fwhm just by finding the points at half maximum.
- [39] The relative deviation for the msz used here is defined as  $\delta\epsilon_{MSZ}(\%) = \frac{MSZ_i - MSZ_{BO}}{MSZ_{BO}} \cdot 100\%$ , where  $msz_1$  is given for the sl, sd and sc resonator. the calculation for the fwhm is analogous.
- [40] M. Schröder, D. Rauber, C. Matt, Pentacene in 1,3,5-tri(1-naphthyl)benzene: A novel standard for transient epr spectroscopy at room temperature, *Appl. Magn. Reson.* (2021) 1–10.
- [41] D. Pozar, *Microwave engineering fourth edition* (2012).
- [42] J. Breeze, K.-J. Tan, B. Richards, J. Sathian, M. Oxborrow, N.M. Alford, Enhanced magnetic purcell effect in room-temperature masers, *Nat. Commun.* 6 (1) (2015) 1–6.



## 3.2.1.2 MASER Resonator

# communications physics

ARTICLE

<https://doi.org/10.1038/s42005-023-01418-3>

OPEN

## Maser threshold characterization by resonator Q-factor tuning

Christoph W. Zollitsch <sup>1,2,3</sup>✉, Stefan Ruloff<sup>1</sup>, Yan Fett <sup>1</sup>, Haakon T. A. Wiedemann <sup>1</sup>, Rudolf Richter<sup>1</sup>, Jonathan D. Breeze <sup>2</sup> & Christopher W. M. Kay <sup>1,3</sup>✉

Whereas the laser is nowadays an ubiquitous technology, applications for its microwave analog, the maser, remain highly specialized, despite the excellent low-noise microwave amplification properties. The widespread application of masers is typically limited by the need of cryogenic temperatures. The recent realization of a continuous-wave room-temperature maser, using NV<sup>-</sup> centers in diamond, is a first step towards establishing the maser as a potential platform for microwave research and development, yet its design is far from optimal. Here, we design and construct an optimized setup able to characterize the operating space of a maser using NV<sup>-</sup> centers. We focus on the interplay of two key parameters for emission of microwave photons: the quality factor of the microwave resonator and the degree of spin level-inversion. We characterize the performance of the maser as a function of these two parameters, identifying the parameter space of operation and highlighting the requirements for maximal continuous microwave emission.

<sup>1</sup>Department of Chemistry, Saarland University, Saarbrücken 66123, Germany. <sup>2</sup>Department of Physics & Astronomy, University College London, Gower Street, London WC1E 6BT, UK. <sup>3</sup>London Centre for Nanotechnology, University College London, 17-19 Gordon Street, London WCH1 0AH, UK. ✉email: [c.zollitsch@ucl.ac.uk](mailto:c.zollitsch@ucl.ac.uk); [christopher.kay@uni-saarland.de](mailto:christopher.kay@uni-saarland.de)

## ARTICLE

COMMUNICATIONS PHYSICS | <https://doi.org/10.1038/s42005-023-01418-3>

The first maser system was realized using ammonia molecules in the gas phase<sup>1</sup> and applications for signal amplifiers, frequency standards or as spectrometers were subsequently proposed. However, the need for cryogenic and/or high vacuum environments restricted miniaturization and integration towards more general applications. Maser research and development was mainly focused on low-noise microwave receiving systems for deep-space antenna networks<sup>2</sup>, and several other maser systems based on ruby<sup>3</sup>, atomic hydrogen<sup>4</sup> or Rydberg atoms<sup>5</sup> were realized. These systems were all still subject to the same restrictions and the focus on fundamental research into masers declined. The field was reinvigorated upon the realization of a room-temperature pulsed maser in an optically pumped crystal of pentacene-doped *p*-terphenyl, placed inside a high quality factor microwave resonator<sup>6–8</sup>. Here, masing was achieved not only without the need of cryogenics or a high-vacuum environment, but also with easily accessible optical pump rates. Shortly afterwards, a proposal for a continuous-wave room-temperature maser in optically spin polarized, negatively charged nitrogen vacancy (NV<sup>-</sup>) centers in diamond<sup>9</sup> and its consecutive experimental realization<sup>10</sup> followed. The excellent low-noise amplification properties of the maser have been demonstrated in recent work<sup>11–13</sup> and has found application in enhanced quantum sensing of molecular spin ensembles<sup>14</sup>. The search for other solid-state maser materials, such as SiC<sup>15</sup> has continued, and an application in quantum technology by creating a maser system based on Floquet states in Xe atoms<sup>16</sup> has also been reported.

With the increased focus on room-temperature solid-state masers a quantitative experimental characterization of the parameter space of operation supplements the current endeavors to optimize the performance of such systems. Understanding the behavior of the maser performance, defined by the level-inversion of the spin ensemble and the loaded *Q*-factor  $Q_L$  of the resonator, can lead to higher output power maser systems. To guarantee reproducibility and maximize the power output of maser-based technologies, a complete understanding of the system parameter space, including the minimal requirements to surpass the masing threshold, is required.

Here, we present an experimental setup that we exploited to investigate the maser performance of a NV<sup>-</sup> spin ensemble hosted in diamond as a function of the resonator quality factor and the degree of spin level-inversion. In the resulting maser threshold diagram, we can clearly identify the threshold for maser action, thereby obtaining a set of experimental boundary conditions for the optimal operation of a maser system. Additionally, our optimized setup yields the highest continuous-wave maser output power reported to date.

## Results and discussion

**Experimental setup.** We use a cylindrical dielectric ring resonator made of sapphire to deliver/detect resonant microwaves to/from the NV<sup>-</sup> centers contained in the diamond host. A key parameter for the continuous maser emission is the loaded *Q*-factor,  $Q_L$ , of the resonator, which is defined by  $1/Q_L = 1/Q_{\text{int}} + 1/Q_{\text{ext}}$  with the internal *Q*-factor,  $Q_{\text{int}}$ , and the external *Q*-factor,  $Q_{\text{ext}}$ . Although sapphire dielectric resonators exhibit low dielectric losses<sup>17</sup>, radiative losses typically dominate and prevent high internal quality factors. Hence, to suppress radiative losses the resonator is placed inside a metal cavity. The cavity design is further constrained by two conditions: (i) it has to fit between the poles of our electromagnet system, which gives the static magnetic field  $B_0$  used to tune the energy levels of the NV<sup>-</sup> spins via the Zeeman interaction, and (ii) the resonance frequency of the cavity containing the sapphire ring is required to be within the

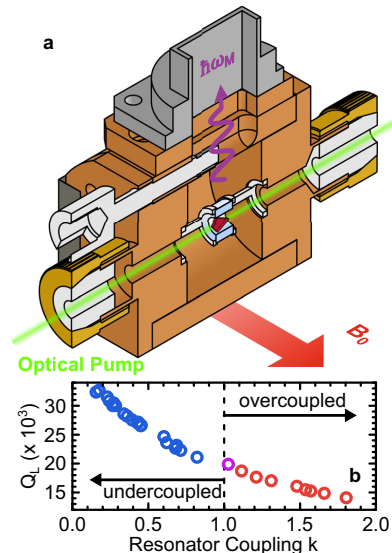


**Fig. 1** Schematic cross-section of the microwave cavity-resonator setup.

**a** Microwave cavity, holding the sapphire ring resonator. The schematic shows half of the cavity to reveal the interior. The light blue sapphire ring is held by two Teflon holders. On the top is the iris coupled waveguide port. The coupling to the resonator is adjusted by a Teflon screw with a metal ring at its tip. The 532 nm optical pump laser is aligned along the symmetry axis of the cylindrical resonator, while the static magnetic field  $B_0$  is perpendicular to it. Finally, the diamond sample is placed inside the resonator. **b** Loaded *Q*-factor as a function of the resonator coupling, showing the full range of coupling, with the diamond sample in the resonator.

9–10 GHz (X-band) frequency range, to allow a fast pre-characterization of the NV<sup>-</sup> spin ensemble by conventional electron spin resonance (ESR). To this end, we designed a cylindrical cavity made of oxygen-free high-thermal conductivity copper, plated with thin layers of (first) silver and (second) gold to prevent oxidation of the metal surfaces, thereby minimizing additional resistive losses.

Figure 1a shows a 3D schematic of the fully assembled cavity cut at a symmetry plane to reveal the interior. The cavity has sample entries at opposite ends of the cylinder symmetry axis for sample and optical access. In the center of the cavity the resonator is held in place by two wire-frame Teflon holders. The holders are machined to have minimal volume in order to minimize additional dielectric losses. Microwave power is coupled in and out via a single waveguide iris port on the top. This port represents the external quality factor  $Q_{\text{ext}}$  and together with  $Q_{\text{int}}$  the resonator coupling  $k = Q_{\text{int}}/Q_{\text{ext}}$  is defined.  $k$  is controlled via a Teflon screw with a metal ring at its tip. Changing the coverage of the iris by the metal ring allows a continuous change<sup>18</sup> from over-coupled to under-coupled: the regimes where  $Q_L$  is dominated by external losses or intrinsic losses, respectively. Figure 1b shows the achievable  $Q_L$  as a function of  $k$  for our resonator-cavity system, loaded with the diamond sample. The resonator parameters are extracted from microwave reflection measurements, using a vector network analyzer. By fitting the microwave reflection as a function of frequency with a Lorentzian model function the parameters for resonance frequency, resonator coupling and internal quality factor are determined. A

description of the model function can be found in the methods section. We use the  $TE_{01\delta}$  mode for our experiments, where the electric field is mostly contained in the sapphire ring and the magnetic field is mostly focused in the bore. Without a sample, the sapphire resonator has a resonance frequency  $\omega_{\text{res}}/2\pi = 9.25$  GHz and the  $Q_L = 42,500$  when fully under-coupled. We define the resonator as fully under-coupled when  $k = 0.0027$ , where the Iris is no longer covered by the metal tip of the Teflon screw. Here,  $Q_L$  remains unchanged upon further extraction of the screw. For detailed cavity and resonator dimensions see Supplementary Note 4<sup>19</sup>.

**Maser working principles.** The process of continuous emission of microwave photons from the  $NV^-$  centers is schematically shown in Fig. 2a, c. The diamond hosting the  $NV^-$  centers is placed inside a high-Q resonator, which is highly under-coupled ( $k \ll 1$ ). The resonator may be pictured in analog to its optical counterpart the laser, with one perfectly reflective mirror and one weakly transmitting mirror. The latter represents the iris coupled single microwave port on the microwave cavity.

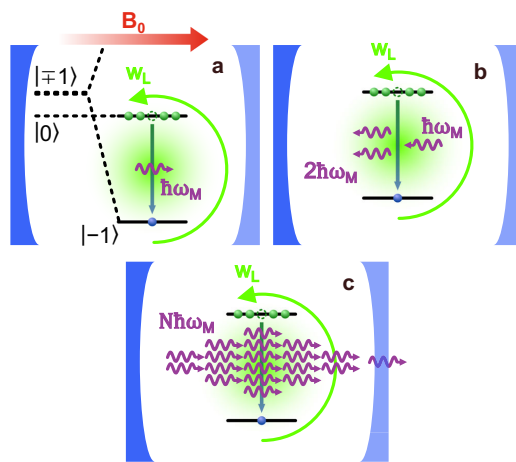
The applied static magnetic field  $B_0$  lifts the degeneracy of the  $|\pm 1\rangle$  states and, tunes the  $|-1\rangle$  state energetically below the  $|0\rangle$  state such that the splitting  $\hbar\omega_M$  is resonant with the microwave resonator frequency. The experiment is performed only on one sub-set of  $NV^-$  centers which are aligned with the external magnetic field  $B_0$ . This provides the shown level structure, having the largest Zeeman splitting of the energy levels and consequently the largest initial population difference at Boltzmann equilibrium. By illuminating the  $NV^-$  centers continuously with a 532 nm laser, the spin populations which are initially at Boltzmann equilibrium are predominately pumped into the  $|0\rangle$  state<sup>20</sup>, resulting in a level-inversion (see Fig. 2a). A description of the optical spin polarization process is found in Supplementary

Note 2<sup>19</sup>. Finally, the laser polarization is required to be aligned along the  $NV^-$  defect axis to achieve most efficient pump rates<sup>21,22</sup>.

To trigger a collective stimulated emission, an initial photon with  $\hbar\omega_M$  is required. This is provided either by an externally applied seeding photon, due to spontaneous emission or thermal photons (see Fig. 2b). From this point an avalanche of stimulated photons is created, forming a coherent microwave field inside the resonator (see Fig. 2c). If the laser pump rate is sufficient to maintain the level inversion and the resonator loaded quality factor is high enough to support a large enough coherent microwave field, continuous microwave emission is achieved.

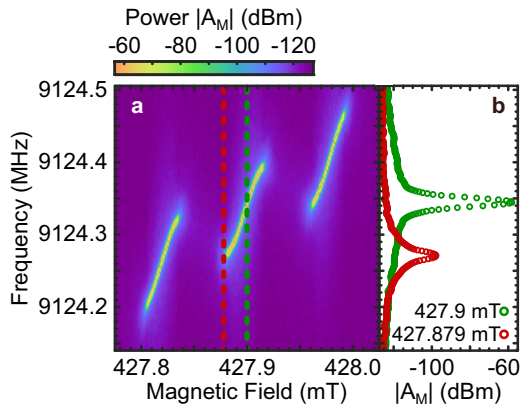
**NV defect axis alignment.** In our experimental setup, the diamond sample is held inside a quartz ESR tube, supported between two additional quartz tubes fitted inside the first one. The tube is inserted into the cavity and positioned such that the diamond is located at the center of the sapphire ring where the magnetic component of the microwave field is largest. The cavity with sample is mounted between the poles of an electromagnet system. We connect either a conventional ESR spectrometer, a vector network analyzer or a spectrum analyzer to the microwave port of the cavity, to perform low-power microwave spectroscopy of the  $NV^-$  spin transitions or to study the maser emission. A goniometer is attached to the sample tube, allowing a precise rotation of the quartz tube containing the diamond with respect to the static magnetic field. Conventional ESR as a function of  $B_0$  and rotation angle is performed to find an orientation of the diamond where the defect axis of a sub-set of  $NV^-$  centers is mostly parallel to the applied magnetic field. For such an orientation the  $NV^-$  spins feature an energy level scheme of the electronic ground state as schematically shown in Fig. 2a and the states  $|0\rangle$  and  $|\pm 1\rangle$  can be considered pure. This can be characterized by the frequency/magnetic field splitting between the low-field ( $|0\rangle \rightarrow |+1\rangle$ ) and high-field ( $|0\rangle \rightarrow |-1\rangle$ ) transitions corresponding to twice the zero-field splitting  $D$ . Away from this alignment the states become mixed, resulting in a smaller splitting than  $2D$  between the two allowed transitions<sup>23,24</sup> and a smaller maximal achievable spin polarization. Without laser illumination, we find a maximal splitting of about 205 mT or 5.762 GHz, agreeing well with twice the zero-field splitting,  $D$ , of  $NV^-$  centers in diamond.

**Maser emission spectrum characterization.** Having optimized the orientation of the  $NV^-$  centers, we characterize the performance of our maser setup by analyzing the microwave emission spectrum. Figure 3a shows the color encoded maser emission power  $|A_M|$  as a function of frequency and static magnetic field for a laser pump rate  $w_L = 430$  s<sup>-1</sup> and with the resonator fully under-coupled,  $Q_L \approx Q_{\text{int}}$ , which gives a loaded quality factor  $Q_L$  of 33,500. The three bright lines represent the maser emission of the three <sup>14</sup>N hyperfine transitions of the  $NV^-$  centers oriented along  $B_0$ . In this configuration, we achieve a maximum maser emission power of  $-56.5$  dBm. The maser emission shows a finite frequency-magnetic field dispersion, where the maser power is maximal in the center of the line. This is illustrated in Fig. 3b which depicts the maser emission power as a function of frequency for two fixed magnetic fields. The dispersion results from the hybridization of the microwave resonator mode and the resonant  $NV^-$  transition. The resonator resonance frequency  $\omega_{\text{res}}/2\pi = 9.12$  GHz lies at the center of the middle maser emission line. The inverted spin population causes a dispersive shift of the resonator frequency to lower frequencies for the lower magnetic field emission line and respectively to a shift to higher frequencies for the higher magnetic field emission line. The



**Fig. 2 Schematic of the maser emission process. a–c** The blue mirrors are the optical analog of a high-Q microwave resonator, with one mirror being fully reflective (dark blue) and one weakly transmissive (light blue); **(a)** Energy states of the  $NV^-$  spin ensemble aligned along  $B_0$ . The  $|-1\rangle$  state is tuned below the  $|0\rangle$  state by the Zeeman interaction, while the optical pump generates a population inversion and spins spontaneously emit microwaves. **b** Spontaneously emitted or thermally stimulated microwaves can stimulate the emission of additional microwaves. **c** For sufficiently large optical pump rates and a high  $Q_L$  coherent microwave emission is established.

## ARTICLE

COMMUNICATIONS PHYSICS | <https://doi.org/10.1038/s42005-023-01418-3>

**Fig. 3 Maser emission spectrum.** **a** Maser emission power  $|A_M|$ , in logarithmic units, as a function of frequency and static magnetic field at  $w_L = 430 \text{ s}^{-1}$  and  $Q_L$  of about 33,500. **b**  $|A_M|$  as a function of frequency for two different magnetic field values, indicated by the red and green dashed lines in (a).

maser dispersion can be described via a Tavis-Cummings model with an inverted spin polarization, where the frequency range covered by the maser emission lines increases with increasing inversion.

In order to determine the dependency of the maser output on the laser pump rate  $w_L$  and the loaded quality factor  $Q_L$ , both were varied systematically. The latter is dependent on the resonator coupling  $k$  which is controlled by the iris screw. Figure 4a shows the peak maser power  $|A_M|$  of the central maser line as a function of  $w_L$  (from  $165 \text{ s}^{-1}$  to  $695 \text{ s}^{-1}$ ) and  $Q_L$  (from 14,000 to 33,500). Note, that after each change of  $w_L$  we wait 45 min before starting measurements to allow the diamond to reach a thermal equilibrium (see Supplementary Note 1 for details<sup>19</sup>). For low loaded quality factors, i.e., an over-coupled resonator, there is no microwave emission for all laser pump rates studied and the signal amplitude is represented by the noise floor of the spectrum analyzer. Note that critical resonator coupling ( $k = 1$ ) is achieved at  $Q_L \approx 20,000$ , marking the transition between over- and under-coupling<sup>25</sup>. With increasing  $Q_L$  a weak microwave emission is observed for moderate to high laser pump rates. Here, the emission spectrum is broad and governed by the amplification of thermal photons residing in the resonator<sup>9</sup>. In this region, the resonator losses are still too high to allow the build-up of sufficient stimulated photons for continuous masing. For  $Q_L > 26,000$  and  $w_L > 400 \text{ s}^{-1}$  the rate of stimulated emission exceeds the losses in the resonator and the spin system, and continuous masing is established. Figure 4b shows the evolution of the peak maser power as a function of the loaded quality factor for two different laser pump rates. Upon passing the threshold  $Q_L$  of 26,000,  $|A_M|$  increases until reaching an onset of saturation for the highest  $Q_L$ , where the final level of saturation depends on the laser pump rate. A  $Q_L$  larger than 26,000 further promotes the stimulated microwave emission, thus reducing the threshold laser pump rate required. For a fully under-coupled resonator with  $Q_L = 33,500$ , continuous microwave emission is already achieved for  $w_L > 200 \text{ s}^{-1}$ . Figure 4c shows the peak maser power  $|A_M|$  as a function of the laser pump rate  $w_L$  at two different loaded quality factors of the resonator. The peak maser power increases with increasing laser pumping, reflecting the achieved level-inversion. Consequently, for the largest  $Q_L$  and highest  $w_L$ , which

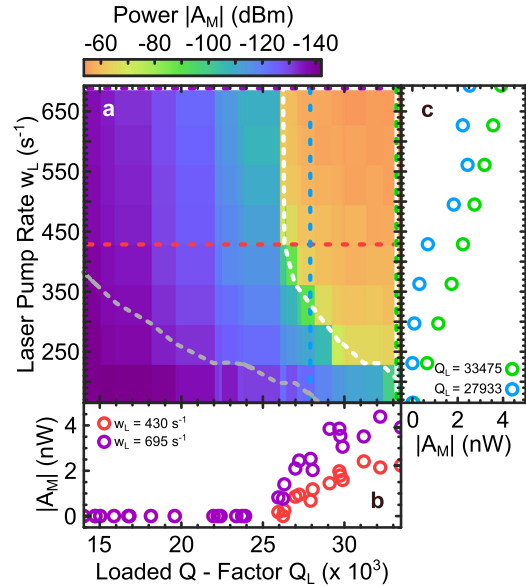


**Fig. 4 Maser threshold diagram.** **a** Maximal maser emission power  $|A_M|$ , in logarithmic units, of the central hyperfine maser transition line as a function of laser pump rate  $w_L$  and the loaded quality factor  $Q_L$  of the resonator. The white and gray dashed lines represent the theoretical threshold for masing, with and without temperature effects, respectively. **b**  $|A_M|$  as a function of  $Q_L$  for two  $w_L$  indicated by the purple and red dashed lines in (a). **c**  $|A_M|$  as a function of  $w_L$  at two  $Q_L$  indicated by the blue and green dashed lines in (a).

guarantees a stable microwave field inside the resonator and the largest level inversion, respectively, the highest maser power of  $-54.1 \text{ dBm}$  is achieved. This is an improvement of more than three orders of magnitude in maser power over the initial report on a  $\text{NV}^-$ -based maser in ref. <sup>10</sup> with reported  $-90.3 \text{ dBm}$ . The threshold laser pump rate  $w_{th}$  for masing can be derived from the steady-state Heisberg equations of motion based on the coupled resonator-spin ensemble Tavis-Cummings model, including dissipative channels for the resonator and spins, and is given by<sup>9,10,26</sup>

$$w_{th} = \frac{\eta}{T_1 \left( \frac{g_0^2 N}{\kappa_0 \gamma} - 1 \right)}. \quad (1)$$

Here,  $T_1$  is the effective longitudinal relaxation time of the  $\text{NV}^-$  spins,  $g_0$  gives the strength of the magnetic dipole coupling between a single spin and a single microwave photon<sup>27</sup>,  $N$  is the absolute number of spins per hyperfine transition and per  $\text{NV}^-$  defect axis and  $\kappa_0$  and  $\gamma$  are the resonator and spin loss rates (HWHM), respectively. We estimate  $g_0/2\pi$  by finite element simulations of the magnetic field profile inside the sapphire ring resonator<sup>28</sup> to an average value of  $0.244 \text{ Hz}$  and determine  $\gamma/2\pi$  and  $N$  via low-power microwave spectroscopy of the low-field transition ( $|0\rangle \rightarrow |+1\rangle$ ) to  $530.8 \text{ kHz} \pm 7.7 \text{ kHz}$  and  $2.32 \times 10^{13}$ , respectively. A detailed derivation of these system parameters is found in Supplementary Note 3<sup>19</sup>. The resonator loss rate is defined through  $Q_L$  as  $\kappa_0 = \omega_{res}/2Q_L$ , which we control by changing the resonator coupling. The scaling factor  $\eta$  modifies the optical pump rate defined for a two-level system within the framework of the Tavis-Cummings model to take all seven energy levels involved in the pumping of a single  $\text{NV}^-$  spin into account.

We extract  $\eta = 14.05$  from the calculated spin-level inversion as a function of  $w_L$ <sup>9,10</sup>, by solving the set of optical pump rate equations in the steady-state<sup>29</sup>. For  $T_1$  we explicitly take the influence of an optical pump into account. In addition to polarizing spins, the pump leads to excessive heating of the diamond, which decreases the  $T_1$  time<sup>30</sup>. We determine  $T_1$  for each  $w_L$ , finding 5.2 ms for low  $w_L$  and a minimum of 1.5 ms for the highest  $w_L$ , where a detailed description of the  $T_1$  dependence on  $w_L$  is given in Supplementary Note 1<sup>19</sup>. The white dashed line in Fig. 4a gives the masing threshold  $w_{th}$  as a function of the loaded quality factor and is in excellent agreement with the experimentally found threshold of our maser, when acknowledging the reduction of the relaxation time due to high pump rates. For comparison, we include the expected threshold for a fixed  $T_1 = 5.2$  ms (gray dashed line), demonstrating the significant influence of laser heating.

### Conclusion

To summarize, our characterization setup allows the resonator coupling to be continuously and precisely adjusted between over- and under-coupled in conjunction with the optical pump rate. This permits the detailed study of the performance of the maser as a function of the rate of stimulated emission and the degree of level-inversion. Control of these parameters enabled the first experimental verification of the maser threshold equation over a wide parameter space. Thus, the regions of microwave emission below the detection limit, thermal photon amplification and continuous masing could be identified in a NV<sup>-</sup> diamond maser.

Our results highlight an efficient operation of the maser is in the highly under-coupled regime. Clearly, this limits the maser output power as only a small fraction of the microwaves in the weakly coupled resonator can exit. For applications, a higher output is essential and, hence, a larger coupling to the resonator is required. The resulting threshold diagram suggests that either higher pump rates or a resonator with a higher  $Q_{int}$  will enable a larger coupling of the resonator. However, higher pump rates not only require bulky laser systems but cause the sample to heat up. We demonstrate that the  $T_1$  relaxation time is shortened, thus reducing the spin inversion. Indeed, it is clear for our results that pump rates can be reduced to a level where small (e.g., <1 W) laser diodes can be employed instead. Therefore, increasing the Q factor of the resonator is a more viable approach, although it is necessary to point out that this will decrease the bandwidth<sup>11</sup>. Finally, the optimized design yielded an increase of the maximal maser output of more than three orders of magnitude compared to the initial report on a NV<sup>-</sup>-based maser from -90.3 dBm to -54.1 dBm<sup>10</sup>. We attribute this mainly to an improved heat management of the diamond sample to limit a reduction in  $T_1$  time and consequently limit the increase of the masing threshold. Thus it provides not only a blueprint for solid-state based maser systems and but also sets a benchmark for future characterization and optimization studies.

### Methods

**Diamond sample.** Our diamond sample is of rhombic shape with its long axis having about 5 mm, its short axis having about 4 mm and a thickness of 1 mm. The diamond consists of natural abundance carbon and we estimate the total number of NV<sup>-</sup> to  $2.78 \times 10^{14}$  or 0.16 ppm (see Supplementary Note 3 for details on the number of spins estimate<sup>19</sup>). At room temperature and no optical pump the NV<sup>-</sup> feature a  $T_2 = 25$   $\mu$ s, determined by pulsed ESR.

**Laser pumping.** We use a 532 nm *Coherent Verdi V-5* laser to optically pump the spin population of the NV<sup>-</sup> centers. The laser

features a spot size of about 4 mm and hits the diamond sample on its flat edge, an area of about 4 mm  $\times$  1 mm. We determine the laser pump rate as  $w_L = \sigma P_{pump}/A_{pump} h \omega_{pump}$  (ref. 10), with the one-photon absorption cross-section for NV<sup>-</sup> centers  $\sigma = 3.1 \times 10^{-21}$  m<sup>2</sup>, the pump laser power  $P_{pump}$ , the laser spot area  $A_{pump}$  and the laser frequency  $\omega_{pump}$ .

**Microwave spectroscopy.** We study the microwave emission from the maser with a Keysight N9020B MXA 10 Hz to 44 GHz spectrum analyzer. To improve the SNR we pre-amplify the maser signal, using a Mini Circuits Low Noise Amplifier ZX60-06183LN + prior detection by the spectrum analyzer. The low power microwave spectroscopy was carried out using an Anritsu vector network analyzer MS46122B 1 MHz to 43.5 GHz. For conventional ESR measurements a Bruker EMXplus spectrometer is used.

**Resonator coupling.** We determine the microwave resonator coupling  $k$  by measuring the microwave reflection as a function of frequency with a VNA, far detuned from the NV<sup>-</sup> centers. We fit the magnitude of the reflection scattering parameter  $|S_{11}|$  of the resonator for different positions of the Iris screw, using a Lorentzian model function derived from an equivalent circuit model, which depends on  $k$ <sup>31</sup>.

$$|S_{11}| = A \left| \frac{k - 1 - iQ_{int} \left( \frac{\omega}{\omega_{res}} - \frac{\omega_{res}}{\omega} \right)}{k + 1 + iQ_{int} \left( \frac{\omega}{\omega_{res}} - \frac{\omega_{res}}{\omega} \right)} \right| \quad (2)$$

In addition, we can extract the internal quality factor  $Q_{int}$  and via the relation for the resonator coupling  $k = Q_{int}/Q_{ext}$  the external Q-factor  $Q_{ext}$  and hence the loaded quality factor  $Q_L$ , as well as the resonator frequency  $\omega_{res}$  and its loss rate  $\kappa_0$ .

### Data availability

The data that supports the findings of this study is available upon reasonable request.

Received: 20 March 2023; Accepted: 5 October 2023;

Published online: 14 October 2023

### References

- Gordon, J. P., Zeiger, H. J. & Townes, C. H. The maser—new type of microwave amplifier, frequency standard, and spectrometer. *Phys. Rev.* **99**, 1264–1274 (1955).
- Reid, M., Clauss, R., Bathker, D. & Stelzried, C. Low-noise microwave receiving systems in a worldwide network of large antennas. *Proc. IEEE* **61**, 1330–1335 (1973).
- Makhov, G., Kikuchi, C., Lambe, J. & Terhune, R. W. Maser action in ruby. *Phys. Rev.* **109**, 1399–1400 (1958).
- Goldenberg, H. M., Kleppner, D. & Ramsey, N. F. Atomic hydrogen maser. *Phys. Rev. Lett.* **5**, 361–362 (1960).
- Moi, L. et al. Rydberg-atom masers. i. a theoretical and experimental study of super-radiant systems in the millimeter-wave domain. *Phys. Rev. A* **27**, 2043–2064 (1983).
- Oxborrow, M., Breeze, J. D. & Alford, N. M. Room-temperature solid-state maser. *Nature* **488**, 353–356 (2012).
- Breeze, J. et al. Enhanced magnetic purcell effect in room-temperature masers. *Nat. Commun.* **6**, 6215 (2015).
- Salvadori, E. et al. Nanosecond time-resolved characterization of a pentacene-based room-temperature maser. *Sci. Rep.* **7**, 41836 (2017).
- Jin, L. et al. Proposal for a room-temperature diamond maser. *Nat. Commun.* **6**, 8251 (2015).
- Breeze, J. D., Salvadori, E., Sathian, J., Alford, N. M. & Kay, C. W. M. Continuous-wave room-temperature diamond maser. *Nature* **555**, 493–496 (2018).
- Sherman, A. et al. Diamond-based microwave quantum amplifier. *Sci. Adv.* **8**, eade6527 (2022).

## ARTICLE

COMMUNICATIONS PHYSICS | <https://doi.org/10.1038/s42005-023-01418-3>

12. Koppenhöfer, M., Groszkowski, P., Lau, H.-K. & Clerk, A. Dissipative superradiant spin amplifier for enhanced quantum sensing. *PRX Quantum* **3**, 030330 (2022).
13. Jiang, M. et al. Floquet spin amplification. *Phys. Rev. Lett.* **128**, 233201 (2022).
14. Wu, H. et al. Enhanced quantum sensing with room-temperature solid-state masers. *Sci. Adv.* **8**, eade1613 (2022).
15. Gottscholl, A. et al. Superradiance of spin defects in silicon carbide for maser applications. *Front. Photonics* **3**, 886354 (2022).
16. Jiang, M., Su, H., Wu, Z., Peng, X. & Budker, D. Floquet maser. *Sci. Adv.* **7**, eabe0719 (2022).
17. Shtin, N. A., Romero, J. M. L. & Prokhorov, E. Theory of fundamental microwave absorption in sapphire ( $\alpha$ -al<sub>2</sub>o<sub>3</sub>). *J. Appl. Phys.* **106**, 104115 (2009).
18. Accatino, L. & Bertin, G. Design of coupling irises between circular cavities by modal analysis. *IEEE Trans. Microw. Theory Tech.* **42**, 1307–1313 (1994).
19. For additional information see: Supplementary Material: Maser Threshold Characterization by Resonator Q-Factor Tuning.
20. Robledo, L., Bernien, H., Sar, Tvd & Hanson, R. Spin dynamics in the optical cycle of single nitrogen-vacancy centres in diamond. *N. J. Phys.* **13**, 025013 (2011).
21. Fu, K.-M. C. et al. Observation of the dynamic jahn-teller effect in the excited states of nitrogen-vacancy centers in diamond. *Phys. Rev. Lett.* **103**, 256404 (2009).
22. Doherty, M. W. et al. The nitrogen-vacancy colour centre in diamond. *Phys. Rep.* **528**, 1–45 (2013).
23. Mrozek, M. et al. Longitudinal spin relaxation in nitrogen-vacancy ensembles in diamond. *EPJ Quantum Technol.* **2**, 22 (2015).
24. Jeong, K. et al. Understanding the magnetic resonance spectrum of nitrogen vacancy centers in an ensemble of randomly oriented nanodiamonds. *J. Phys. Chem. C* **121**, 21057–21061 (2017).
25. Göppl, M. et al. Coplanar waveguide resonators for circuit quantum electrodynamics. *J. Appl. Phys.* **104**, – (2008).
26. Kolobov, M. I., Davidovich, L., Giacobino, E. & Fabre, C. Role of pumping statistics and dynamics of atomic polarization in quantum fluctuations of laser sources. *Phys. Rev. A* **47**, 1431–1446 (1993).
27. Haroche, S. & Raimond, J.-M. *Exploring the quantum. Atoms, cavities and photons. Reprint of the 2006 hardback ed.* (Oxford Graduate Texts. Oxford: Oxford University Press., 2013).
28. Oskooli, A. F. et al. Meep: a flexible free-software package for electromagnetic simulations by the fdtd method. *Comput. Phys. Commun.* **181**, 687–702 (2010).
29. Sherman, A., Buchbinder, L., Ding, S. & Blank, A. Performance analysis of diamond-based masers. *J. Appl. Phys.* **129**, 144503 (2021).
30. Jarmola, A., Acosta, V. M., Jensen, K., Chemerisov, S. & Budker, D. Temperature- and magnetic-field-dependent longitudinal spin relaxation in nitrogen-vacancy ensembles in diamond. *Phys. Rev. Lett.* **108**, 197601 (2012).
31. Wang, P. et al. Novel method to measure unloaded quality factor of resonant cavities at room temperature. *Nucl. Sci. Tech.* **29**, 50 (2018).

**Acknowledgements**

This study is supported by EPSRC through EP/S000690/1 and EP/S000798/2 and the Royal Society through URF/R1\191297. We greatly acknowledge the work and expertise

of the workshop personnel Stefanie Porger and Jens Wiegert at the University of Saarland for building the cavity and components for it.

**Author contributions**

S.R., R.R. and C.W.M.K. designed and optimized the resonator. The experimental setup and its automation was realized by S.R., Y.F., H.T.A.W., C.W.Z. and C.W.M.K. C.W.Z. performed the experiments and the data analysis with input from J.D.B. and C.W.M.K. C.W.Z. supported by C.W.M.K. wrote the manuscript with input from all authors. C.W.Z., J.D.B. and C.W.M.K. conceived the study.

**Funding**

Open Access funding enabled and organized by Projekt DEAL.

**Competing interests**

The authors declare no competing interests.

**Additional information**

**Supplementary information** The online version contains supplementary material available at <https://doi.org/10.1038/s42005-023-01418-3>.

**Correspondence** and requests for materials should be addressed to Christoph W. Zollitsch or Christopher W. M. Kay.

**Peer review information** *Communications Physics* thanks the anonymous reviewers for their contribution to the peer review of this work. A peer review file is available.

**Reprints and permission information** is available at <http://www.nature.com/reprints>

**Publisher's note** Springer Nature remains neutral with regard to jurisdictional claims in published maps and institutional affiliations.



**Open Access** This article is licensed under a Creative Commons Attribution 4.0 International License, which permits use, sharing, adaptation, distribution and reproduction in any medium or format, as long as you give appropriate credit to the original author(s) and the source, provide a link to the Creative Commons license, and indicate if changes were made. The images or other third party material in this article are included in the article's Creative Commons license, unless indicated otherwise in a credit line to the material. If material is not included in the article's Creative Commons license and your intended use is not permitted by statutory regulation or exceeds the permitted use, you will need to obtain permission directly from the copyright holder. To view a copy of this license, visit <http://creativecommons.org/licenses/by/4.0/>.

© The Author(s) 2023

### **3.3 Contributions to Biological Science**

The last section showcases an example on the usage of ESR spectroscopy to unravel structural information from a conformational shift of a membrane protein in different environments. Previous proposals of a contribution of the hairpin protein upon protein partitioning could be experimentally proven. This interdisciplinary study showcases the importance of connecting theoretical findings with experimental validations. The use of the described power saturation ESR technique could provide important information on the structural properties of the protein of interest. This work serves as a leading example for other structural questions regarding the arrangement of proteins in a particular environment.



### 3.3.1 Membrane Proteins

#### 3.3.1.1 Structural Rearrangement of Hairpin Protein

nature communications



Article

<https://doi.org/10.1038/s41467-024-48843-8>

# Hairpin protein partitioning from the ER to lipid droplets involves major structural rearrangements

Received: 28 January 2024

Accepted: 15 May 2024

Published online: 27 May 2024

Check for updates

Ravi Dhiman<sup>1,6</sup>, Rehani S. Perera<sup>1,6</sup>, Chetan S. Poojari<sup>2,6</sup>,  
Haakon T. A. Wiedemann<sup>3</sup>, Reinhard Kappl<sup>4</sup>, Christopher W. M. Kay<sup>3,5</sup>,  
Jochen S. Hub<sup>2</sup> & Bianca Schrul<sup>1</sup>✉

Lipid droplet (LD) function relies on proteins partitioning between the endoplasmic reticulum (ER) phospholipid bilayer and the LD monolayer membrane to control cellular adaptation to metabolic changes. It has been proposed that these hairpin proteins integrate into both membranes in a similar monotopic topology, enabling their passive lateral diffusion during LD emergence at the ER. Here, we combine biochemical solvent-accessibility assays, electron paramagnetic resonance spectroscopy and intra-molecular crosslinking experiments with molecular dynamics simulations, and determine distinct intramembrane positionings of the ER/LD protein UBXD8 in ER bilayer and LD monolayer membranes. UBXD8 is deeply inserted into the ER bilayer with a V-shaped topology and adopts an open-shallow conformation in the LD monolayer. Major structural rearrangements are required to enable ER-to-LD partitioning. Free energy calculations suggest that such structural transition is unlikely spontaneous, indicating that ER-to-LD protein partitioning relies on more complex mechanisms than anticipated and providing regulatory means for this trans-organelle protein trafficking.

Lipid droplets (LDs) are ubiquitous cytoplasmic organelles with key roles in cellular physiology. They dynamically balance the storage and consumption of the majority of metabolic energy in the form of neutral lipids such as triglycerides and sterol-esters. The fundamental importance of LDs in lipid metabolism is reflected by their implication in numerous pathologies including hallmark metabolic diseases of contemporary times, such as diabetes and obesity<sup>1–3</sup>, but the molecular mechanisms of their biogenesis, function, and turnover remain incomplete. LDs originate from the endoplasmic reticulum (ER), where triglyceride synthesis and accumulation trigger the budding of an LD from the cytoplasmic leaflet of the ER membrane. They ultimately consist of a hydrophobic neutral lipid core, which is encapsulated by a

phospholipid monolayer<sup>2,4,5</sup>. Hence, as they do not separate two aqueous compartments by a phospholipid bilayer, LDs are an exception to the general principle of organelle architecture.

This unique organelle architecture has consequences for the establishment of the LD proteome. The surface of LDs is decorated with a variety of proteins including regulatory enzymes with central functions in lipid metabolism<sup>6</sup> but due to the aliphatic neutral lipid core, transmembrane-spanning proteins with soluble domains on both sides of the membrane are excluded from LDs<sup>4,7,8</sup>. While some proteins target the LDs from the cytosol and associate with the LD monolayer in a peripheral fashion, e.g., via amphipathic helices or lipid moieties, many LD proteins are first inserted into the ER bilayer membrane and

<sup>1</sup>Medical Biochemistry and Molecular Biology, Center for Molecular Signaling (PZMS), Faculty of Medicine, Saarland University, 66421 Homburg/Saar, Germany. <sup>2</sup>Theoretical Physics and Center for Biophysics, Saarland University, 66123 Saarbrücken, Germany. <sup>3</sup>Physical Chemistry and Chemistry Education, Saarland University, 66123 Saarbrücken, Germany. <sup>4</sup>Department of Biophysics, Center for Integrative Physiology and Molecular Medicine (CIPMM), Faculty of Medicine, Saarland University, 66421 Homburg/Saar, Germany. <sup>5</sup>London Centre for Nanotechnology, University College London, WC1H 0AH London, UK. <sup>6</sup>These authors contributed equally: Ravi Dhiman, Rehani S. Perera, Chetan S. Poojari. ✉ e-mail: [bianca.schrul@uks.eu](mailto:bianca.schrul@uks.eu)

## Article

<https://doi.org/10.1038/s41467-024-48843-8>

then partition to the phospholipid monolayer of the LDs<sup>8</sup>. The latter follow the so-called ER to LD (ERTOLD) pathway and stably integrate into both membranes in a monotopic topology, meaning that they expose all soluble domains towards the cytosol and adopt a hairpin topology. Importantly, many of these proteins not only pass through the ER en route to the LD but execute distinct functions in both organelles. UBXD8, for example, contributes to ER-associated protein degradation in the ER membrane, while on LDs, it modifies the activity of ATGL, the rate-limiting enzyme for triglyceride hydrolysis<sup>9–21</sup>. Yet, the intrinsic properties of UBXD8 that control its partitioning remain elusive.

Proteins that co-exist in the ER and LDs must cope with distinct biophysical membrane environments; namely, compared to the ER bilayer, the LD monolayer exhibits increased hydrophobicity and reveals more frequent phospholipid packing defects<sup>12–14</sup>. Pataki et al. provided the first structural insight into how ER/LD-localized proteins can associate with both types of membranes<sup>15</sup>. By combining biochemical solvent-accessibility experiments with molecular dynamics (MD) simulations, they identified an amphipathic helix in DHRS3, which stably anchors the protein at the membrane-solvent interface of bilayer and monolayer membranes. They proposed that amphipathic interfacial alpha helices are conserved among several ER/LD proteins<sup>15</sup>. However, many ER/LD-localized proteins, such as UBXD8 and AUP1, adopt a hairpin topology in which a hydrophobic segment penetrates into the membrane in a loop-like fashion<sup>16–18</sup>. An appealing model is that such hairpin proteins are embedded into only the outer leaflet of the ER bilayer membrane, which would enable them to partition to the LD monolayer membrane during LD biogenesis, potentially by lateral diffusion<sup>19</sup> (Fig. 1a). A recent model, however, suggests that late ERTOLD cargos cannot cross the proteinaceous seipin barrier at LD biogenesis sites and, instead of accumulating on nascent LDs, target mature LDs via bilayer-LD membrane stalks<sup>20</sup>. This suggests that different modes of membrane partitioning must exist. Since hydrophobic hairpin domains establish different interactions with phospholipid bilayers and the LD environment, they likely possess dynamic and transient configurations and differences in the free energy of these interactions could impact the bilayer-to-monolayer partitioning of monotopic proteins<sup>9</sup>. Indeed, a recent simulation-based approach on the membrane-embedded motifs of the *Drosophila melanogaster* proteins GPAT4 and ALG14 suggests that at least some hairpin proteins are inserted into the ER bilayer membrane in an energetically disfavored orientation and that partitioning to the LD monolayer membrane lowers the free energy and energetic constraints of the proteins<sup>21</sup>. However, experimental systems to assess the intramembrane positioning of monotopic membrane proteins in both types of membranes are sparse, which limits mechanistic understanding of the differential partitioning between them.

Here, we combine biochemical solvent-accessibility assays and intramolecular crosslinking experiments with atomistic MD simulations and establish electron paramagnetic resonance (EPR) spectroscopy workflows to determine the intramembrane positioning of the ERTOLD protein UBXD8 in both, ER bilayer and LD monolayer membranes. Our work reveals that UBXD8 adopts distinct and stable conformations in both membranes and that ER-to-LD protein partitioning relies on more complex mechanisms than initially anticipated.

## Results and discussion

### UBXD8<sub>53-153</sub> inserts into ER bilayer and LD monolayer membranes

In order to assess how LD-destined hairpin proteins are embedded into ER bilayer and LD monolayer membranes, we employed UBXD8 as a model hairpin protein. To precisely map the membrane-embedded region of UBXD8 in both types of membranes, we probed the solvent-accessibility of individual amino acids by PEGylation of single cysteine mutants. To focus on the membrane-embedded domain of UBXD8

without additional influence of the functional UBXD8 domains such as the UBA and UBX domains, which are exposed to the cytosol, we used the truncated version UBXD8<sub>53-153</sub>, which is naturally cysteine-free and was previously shown to be sufficient for correct ER membrane integration in a monotopic topology (Fig. 1b)<sup>17</sup>. It consists of the hydrophobic domain (aa 91–111), which is essential for ER membrane insertion of UBXD8<sup>11,17</sup> and considered to constitute the membrane-embedded hairpin domain of UBXD8, plus additional flanking regions. An N-terminal opsin (op) tag encodes an N-linked glycosylation consensus site that, in case of translocation into the ER lumen, results in a molecular mass shift of 2 kDa due to the addition of an N-linked glycan. The absence of glycosylation, therefore, serves as a readout for the correct membrane integration of UBXD8<sub>53-153</sub> in a monotopic topology. To verify by live-cell microscopy that UBXD8<sub>53-153</sub> is also sufficient to correctly target to LDs in cells, we fused opUBXD8<sub>53-153</sub> to mCherry. As expected, transiently expressed opUBXD8<sub>53-153</sub>mCherry localized to the ER as well as to LDs in oleate-treated cells (Fig. 1b). Likewise, biochemical fractionation and density gradient centrifugation revealed that transiently expressed opUBXD8<sub>53-153</sub>mCherry resides in the membrane and LD fractions (Fig. 1c). Importantly, isolated opUBXD8<sub>53-153</sub>mCherry-containing LDs were virtually free of cytosolic and ER-resident proteins indicating that these LD fractions can be employed to assess the membrane topology of opUBXD8<sub>53-153</sub>mCherry exclusively in LD monolayer membranes (Fig. 1c).

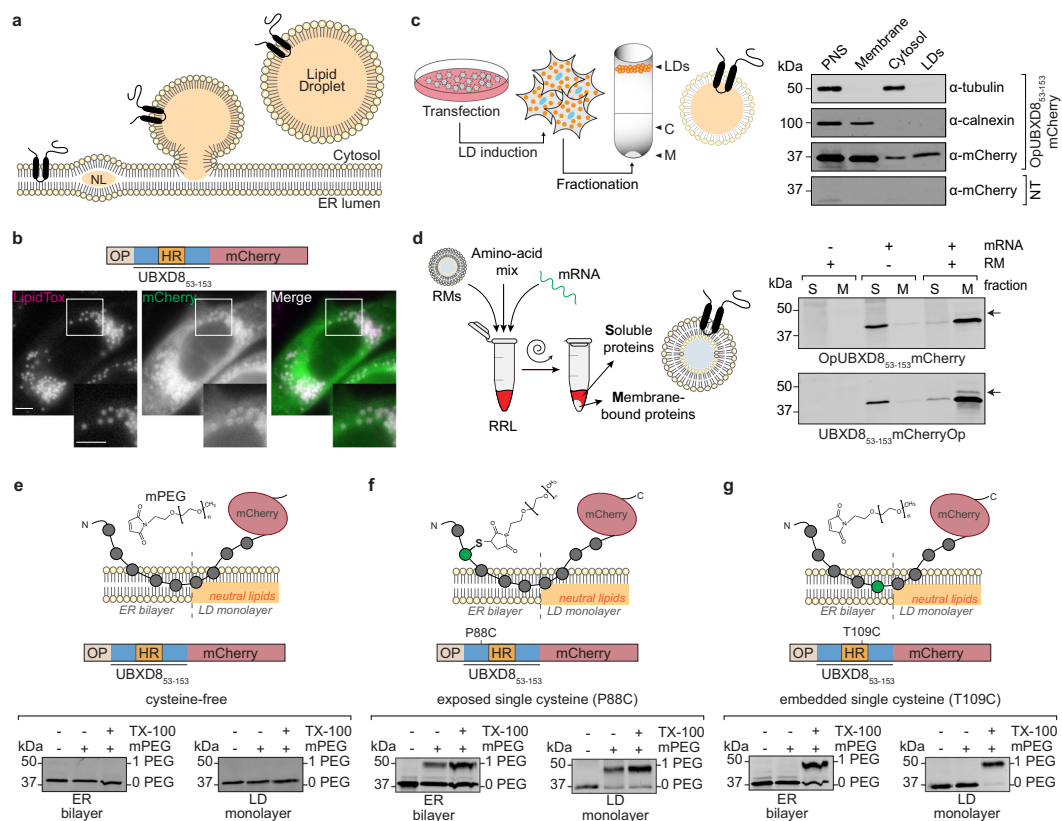
In order to guarantee that we can also assess the membrane topology of opUBXD8<sub>53-153</sub>mCherry exclusively in ER bilayer membranes, we employed previously established in vitro translation systems in which newly translated opUBXD8<sub>53-153</sub>mCherry is inserted into ER-derived rough microsomes (RMs) (Fig. 1d)<sup>17</sup>. When opUBXD8<sub>53-153</sub>mCherry was translated in presence of RMs, it was specifically enriched in the ER membrane fractions upon centrifugation, while it remained soluble in the supernatant when no RMs were present during translation (Fig. 1d). Similarly, when adding the opsin tag to the C-terminus of the protein and translating UBXD8<sub>53-153</sub>mCherryOP in vitro, the majority of the protein was specifically enriched in the membrane fraction when RMs were present during the translation (Fig. 1d). Importantly, less than 2% of the population was accessible to N-linked glycosylation (arrows in Fig. 1d), demonstrating that more than 98% of UBXD8<sub>53-153</sub>mCherry was correctly inserted into RMs in a monotopic topology. Therefore, these RMs can be employed to specifically assess the membrane-embedding of UBXD8 in ER bilayer membranes. Together, these results show that ER-derived RMs as well as LDs isolated from cells can be employed to assess the topology of opUBXD8<sub>53-153</sub>mCherry in two distinct physicochemical environments.

### PEGylation-based solvent-accessibility probing enables mapping of the UBXD8 topology in ER bilayer and LD monolayer membranes with amino acid resolution

In order to probe the intramembrane positioning of UBXD8 in ER bilayer as well as in LD monolayer membranes, we established a solvent-accessibility method based on PEGylation. The PEGylation assay exploits the unique side-chain chemistry of the amino acid cysteine and has been used in the past to monitor the topology of membrane proteins<sup>15,22</sup>. In a reducing environment, the maleimide moiety of membrane-impermeable methoxypolyethylene glycol maleimide (mPEG) reacts covalently with the free thiol (-SH) group of the exposed cysteine, thereby adding an extra molecular weight to the protein that results in a mobility shift upon SDS-PAGE. Cysteines embedded within the membrane remain inaccessible to PEGylation (Fig. 1e–g, top panels).

As a proof-of-concept, we first introduced a single cysteine mutation either outside of the hydrophobic region of UBXD8 (P88C) or within the predicted hydrophobic hairpin region (T109C) by site-directed mutagenesis. opUBXD8<sub>53-153</sub>mCherry is naturally cysteine-

## Article

<https://doi.org/10.1038/s41467-024-48843-8>


**Fig. 1 | Establishment of a PEGylation-based solvent-accessibility assay for opUBXD8<sub>53-153</sub>mCherry single cysteine mutants in ER bilayer and LD monolayer membranes.** **a** Schematic depicting LD biogenesis from the ER membrane. ERTOLD hairpin proteins are considered to integrate first into the cytosolic leaflet of the ER membrane in a monotopic topology, which presumably enables them to partition from the ER bilayer to the LD monolayer membrane during LD biogenesis. NL neutral lipids. **b** Dual localization of opUBXD8<sub>53-153</sub>mCherry to the ER and LDs. Top: Schematic outline of the opsin (op) and mCherry-tagged opUBXD8<sub>53-153</sub>mCherry construct. HR hydrophobic region. Bottom: Fluorescence micrographs of oleate-treated cells transfected with opUBXD8<sub>53-153</sub>mCherry representative for 3 independent experiments. LipidTox marks LDs. Scale bar: 10 μm. **c** Isolation of opUBXD8<sub>53-153</sub>mCherry-containing LDs from cells. Left: Schematic outline for isolation of UBXD8-containing LDs. Right: immunoblot of post-nuclear supernatant (PNS), membranes (M), cytosol (C), and LD fractions derived from oleate-treated cells expressing OpUBXD8<sub>53-153</sub>mCherry using anti-calnexin (ER-resident protein), anti-tubulin (cytosolic protein) and anti-mCherry antibodies. Non-transfected cells (NT) serve as specificity control for the antibody. Data are representative for 3 independent experiments. **d** Integration of opUBXD8<sub>53-153</sub>mCherry into rough microsomes (RMs). Left: Schematic outline of co-

translational protein insertion into RMs employing *in vitro* translation of UBXD8 mRNAs in rabbit reticulocyte lysate (RRL) with subsequent fractionation into soluble and membrane-inserted proteins by centrifugation. Right: Immunoblot of soluble (S) and membrane-inserted (M) fractions derived from *in vitro* translations reactions using anti-mCherry antibodies (representative for  $n = 3$  independent experiments). mRNA encoding either opUBXD8<sub>53-153</sub>mCherry or UBXD8<sub>53-153</sub>mCherryOP and RMs were added to the reaction as indicated. Arrows indicate glycosylated forms of the respective proteins. **e-g** opUBXD8<sub>53-153</sub>mCherry single cysteine mutants can be PEGylated in ER bilayer and LD monolayer membranes, respectively. Only solvent-exposed cysteines are accessible to mPEG forming covalent adducts, while bilayer-embedded cysteines are not reactive with mPEG. Bottom: Proof-of-concept immunoblots probed with anti-mCherry antibodies after PEGylation reaction on RM-inserted and LD-inserted opUBXD8<sub>53-153</sub>mCherry single cysteine mutants as indicated. Non-PEGylated proteins are indicated by (0 PEG) and PEGylated proteins by (1 PEG). Triton X-100. Quantifications for multiple replicates of these experiments are shown in Fig. 2c.

free and is therefore expected to be non-reactive to mPEG. Indeed, upon co-translational insertion of these opUBXD8<sub>53-153</sub>mCherry versions into RMs, no labeling by mPEG, and hence no apparent shift in the molecular weight was detected for cysteine-free, wild-type opUBXD8<sub>53-153</sub>mCherry upon immunoblotting (0 PEG) (Fig. 1e). However, the cysteine at position 88 was covalently modified by mPEG resulting in an apparent molecular weight shift upon SDS-PAGE (1 PEG) (Fig. 1f), which indicates that it is exposed. In contrast, the cysteine at position 109 remained inaccessible to mPEG and only became

modified upon solubilization of the membranes with Triton X-100 (Fig. 1g), indicating that this amino acid is embedded into the ER bilayer.

To assess the solvent-accessibility in LD monolayer membranes, we expressed the individual cysteine mutants in cells followed by the induction of LDs with oleate supplementation. LDs were isolated from the cells by biochemical subcellular fractionation and subjected to PEGylation to probe the topology of opUBXD8<sub>53-153</sub>mCherry in LD monolayer membranes. Similar results were obtained for the



## Article

<https://doi.org/10.1038/s41467-024-48843-8>

and R119C) close to the C-terminal membrane-solvent interface (P<sub>123</sub>-D<sub>124</sub>), which suggests that these amino acids are partially solvent-exposed and therefore presumably close to the membrane surface.

We note that three cysteine mutants (P102C, I113C, F114C) remained inaccessible to PEGylation even upon solubilization of the membranes with Triton X-100. We exemplarily tested whether the cysteine at position 102 becomes accessible to PEGylation after solubilizing the membranes with different concentrations of SDS but were unable to detect any labeling with mPEG (Supplementary Fig. 1). The absence of labeling in the presence of either Triton X-100 or SDS suggests that the cysteines at these positions are located in a region where the opUBXD8<sub>53-153</sub>mCherry secondary structure arrangement restricts the accessibility of mPEG and that care should be taken when interpreting the PEGylation efficiency at these positions.

Taken together, these PEGylation data confirm a monotopic hairpin topology of UBXD8 in the ER bilayer membrane and, furthermore, indicate that the membrane-embedded domain of UBXD8 is longer than initially assumed. While amino acids L<sub>91</sub>-L<sub>111</sub> within the hydrophobic region were shown to be essential for the membrane integration of UBXD8<sup>117</sup>, our solvent-accessibility data indicate that the bona fide hairpin region is comprised of 29 amino acids (W<sub>94</sub>-R<sub>122</sub>) that are embedded in the bilayer membrane.

In order to determine the membrane-embedding of opUBXD8<sub>53-153</sub>mCherry in LD monolayer membranes, we expressed the individual cysteine mutants in cells followed by the induction of LDs with oleate supplementation. LDs were isolated from the cells by biochemical subcellular fractionation and subjected to PEGylation to probe the topology of opUBXD8<sub>53-153</sub>mCherry in LD monolayer membranes (Fig. 2b, c). The N- and C-termini of the opUBXD8<sub>53-153</sub>mCherry, as well as the membrane-solvent interface regions, showed similar relative PEGylation in LD monolayers as in ER bilayers, indicating that the overall topology of UBXD8 is similar on both types of membranes. However, major differences were observed in the hairpin region (W<sub>94</sub>-R<sub>122</sub>), which was overall more solvent-exposed in the LD monolayer than in ER bilayer membranes. Interestingly, every third to fourth amino acid in the hairpin region was partially solvent-exposed in a periodic pattern, which suggests an  $\alpha$ -helical structure positioned close to the membrane-solvent interface (Fig. 2b, c). Overall, our PEGylation data support a hairpin topology model for UBXD8 in ER bilayer and LD membranes and revealed that UBXD8 is differentially positioned and more solvent-exposed in the LD monolayer membrane.

#### MD simulations reveal differential intramembrane positioning of UBXD8 in bilayer and monolayer membranes

Since the biochemical solvent-accessibility assay does not provide direct information on the structural arrangement and the intramembrane positioning of the membrane-embedded region, we employed atomistic molecular dynamics (MD) simulations. Ab initio protein structure prediction suggested a monotopic topology for UBXD8<sub>80-128</sub>, which we used as a starting structure in two different phospholipid bilayer simulation systems. First, we deeply inserted this peptide into a palmitoyl-oleoyl-sn-glycero-phosphocholine (POPC) bilayer membrane. Unbiased MD simulations of 2  $\mu$ s revealed that UBXD8<sub>80-128</sub> can adopt a deeply inserted V-shaped, monotopic topology with several striking characteristics (Fig. 3a): A central proline (P102) is positioned in a kink region separating two short antiparallel helices. A neighboring central arginine (R104) snorkels to the phospholipid headgroups on the opposing side of the membrane thereby potentially tethering the peptide deep inside the bilayer membrane. Two tyrosine pairs are positioned next to each other in the two opposing helices in the midplane of the bilayer membrane, which is unusual since tyrosines are typically found at the membrane-solvent interface in transmembrane helices<sup>23,24</sup>. Five charged amino acids (arginines 85, 89, 115, 119, and 122) at the membrane-solvent interfaces snorkel to the surface of

the cytoplasmic leaflet thereby potentially anchoring the peptide in a monotopic topology.

In contrast, when we integrated the UBXD8<sub>80-128</sub> peptide only partially into the POPC bilayer at the beginning of the simulation, the positioning of UBXD8<sub>80-128</sub> was significantly altered compared to the deep-V inserted state (Fig. 3b and Supplementary Fig. 2): The membrane-solvent interfaces remained largely unchanged but the tilt angle of the peptide within the membrane plane changed dramatically, from -80 degrees to -30 degrees, resulting in a shallow positioning of the peptide and allowing the central arginine R104 to snorkel to the upper surface of the monolayer membrane, potentially anchoring it here. The V-shape of the peptide was now in a more open conformation with a larger distance between the two helices. Together, these simulation results suggest that UBXD8 can in principle adopt two different conformations in bilayer membranes.

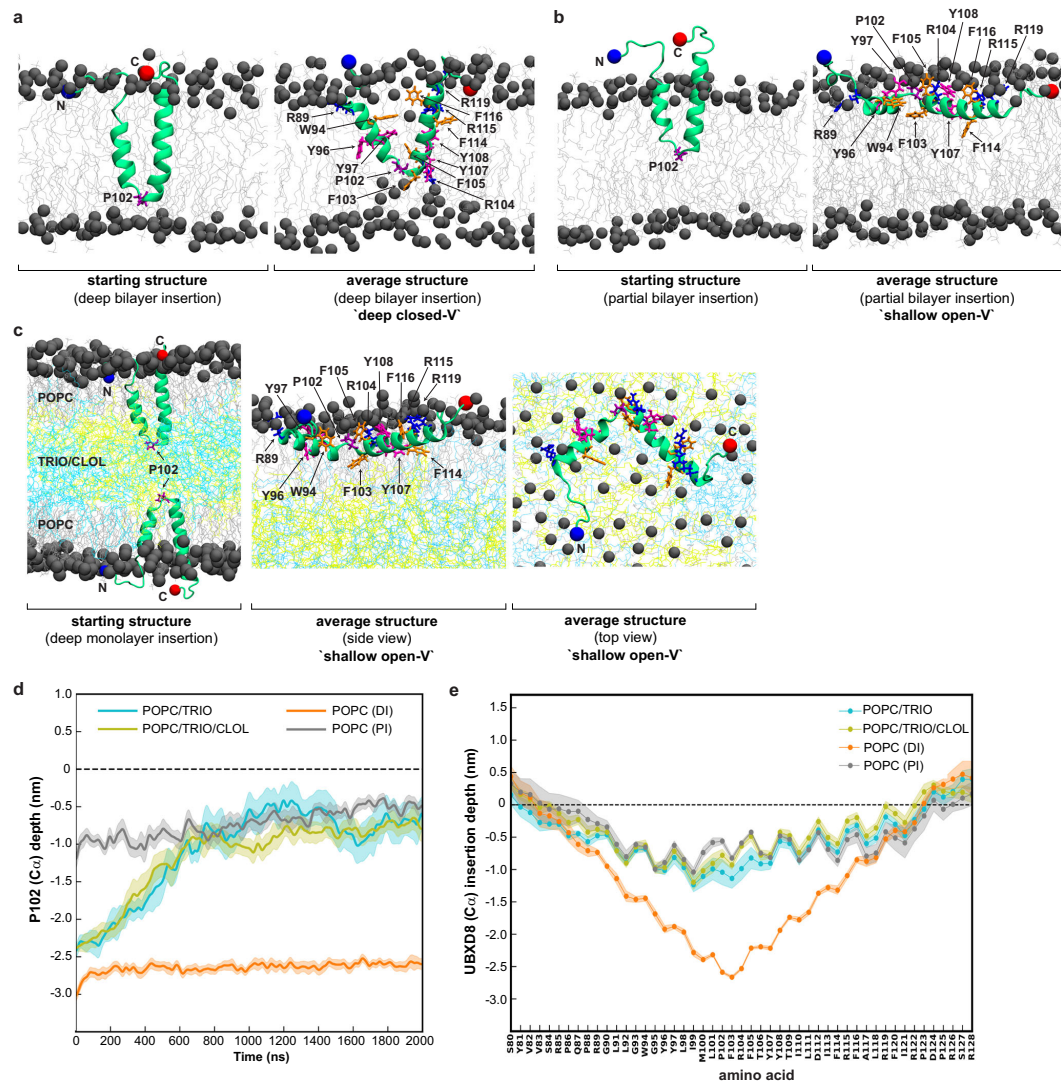
In order to assess the intramembrane positioning of UBXD8 in LD monolayer membranes, we deeply inserted UBXD8<sub>80-128</sub> into a trilayer setup with a central slab of neutral lipids (either triolein alone or a mixture of triolein and cholesteryl oleate) sandwiched between two POPC monolayers (Fig. 3c). However, within 1  $\mu$ s of simulation, the central P102 traversed from the neutral lipid core to the phospholipid monolayer surface (Fig. 3d), likely because polar interactions between the neutral lipids and UBXD8<sub>80-128</sub> are insufficient for stabilizing a deeply inserted closed V-shaped topology at the LD surface. The transition led to a stable topological arrangement of UBXD8 very similar to that observed in the bilayer simulations when UBXD8<sub>80-128</sub> was only partially inserted into the membrane at the beginning of the simulations (compare Fig. 3b-e and Supplementary Fig. 2). In the average structure, UBXD8<sub>80-128</sub> was in a shallow and open-angled position on the LD monolayer membrane.

Based on these simulations, two different scenarios are conceivable: First, UBXD8 may integrate into ER bilayer and LD monolayers in a similar, open-angled, and shallow manner. Second, UBXD8 is deeply inserted in a closed V-shaped topology into the ER bilayer membrane and undergoes major structural transitions during ER-to-LD partitioning. Direct comparison of the biochemical solvent-accessibility data (Fig. 2b, c) with the calculated penetration depths of the individual amino acids into monolayer and bilayer membranes as assessed by MD simulations (Fig. 3e) reveals that the deep-V insertion state in the bilayer and the open-shallow conformation in the LD monolayer, thus scenario number two, would be in best agreement with the experimental evidence obtained by solvent-accessibility probing.

#### Intramolecular crosslinking confirms angle opening of UBXD8 during ER-to-LD partitioning

In order to address whether UBXD8 indeed undergoes major structural rearrangements during ER-to-LD partitioning, we performed intramolecular crosslinking experiments. Our MD simulations revealed that UBXD8 adopts a more open conformation in the LD monolayer compared to the deep-V conformation in the ER bilayer. From the MD simulations, the C $\alpha$  atoms in L91 and L118, which are located on opposite sides of the two antiparallel  $\alpha$ -helices close to the membrane-solvent interface (Fig. 4a), exhibited distances of -20 Å in bilayer versus -36 Å in LD monolayer membranes (Fig. 4b). If true, amino acids at this position should be accessible to intramolecular crosslinking when in the closed conformation in the ER bilayer but resistant to intramolecular crosslinking when in an open conformation on the LD. We, therefore, generated the double-cysteine mutant opUBXD8<sub>53-153</sub>L91C\_L118C\_mCherry and subjected it to intramolecular crosslinking with the membrane-permeable, homo-functional crosslinker bismaleimido-hexane (BMH) (Fig. 4c). Because intramolecular crosslinking adducts are often hard to resolve and to detect upon SDS-PAGE, we combined the crosslinking experiments with our PEGylation assay. In the absence of crosslinking, both cysteines are

## Article

<https://doi.org/10.1038/s41467-024-48843-8>

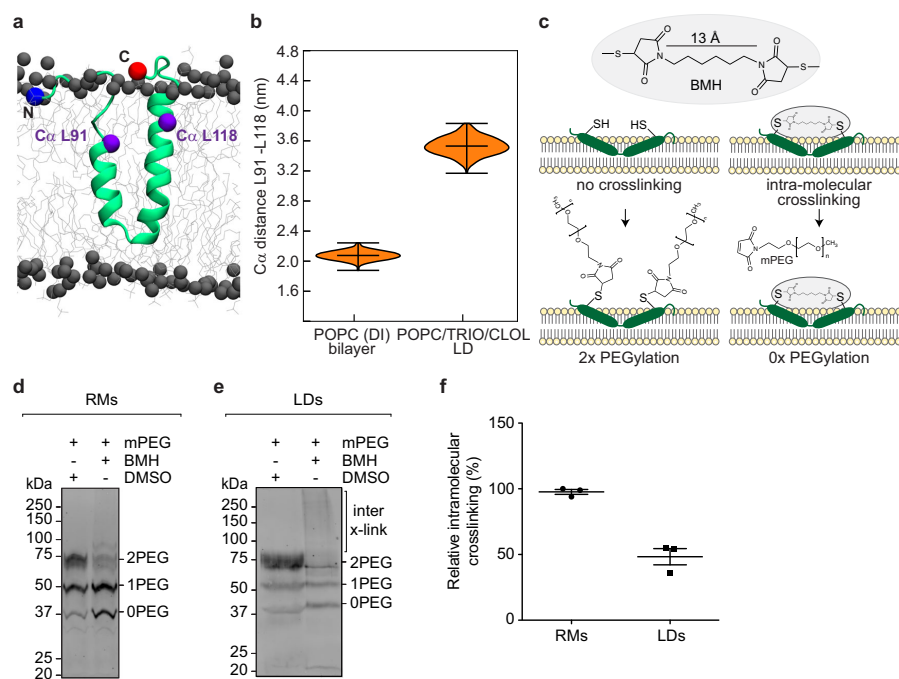
**Fig. 3 | Atomic MD simulations reveal intramembrane positioning of UBXD8 in bilayer and monolayer membranes.** **a** Atomistic MD simulations of UBXD8<sub>80-128</sub> in a POPC bilayer membrane with a deeply inserted starting structure. Left: Starting structure Right: average structure after 2  $\mu$ s. **b** Atomistic MD simulations of UBXD8<sub>80-128</sub> in a POPC bilayer membrane with a partially inserted starting structure. Left: Starting structure Right: average structure after 2  $\mu$ s. **c** Atomistic MD simulations of UBXD8<sub>80-128</sub> in a POPC-triolein/cholesteryl-oleate-POPC trilayer system mimicking the LD monolayer membrane. Left: Starting structure; Middle: side view of average structure after 2  $\mu$ s; Right: top view of average structure after 2  $\mu$ s; **d** Center of mass distances of the C $\alpha$  atom in P102 of UBXD8<sub>80-128</sub> and the P atom in the phospholipid headgroup (dotted line) during

the simulation time of 2  $\mu$ s, and upon UBXD8<sub>80-128</sub> insertion into POPC bilayers or into trilayer systems as indicated. PI partially inserted, DI deeply inserted, TRIO Triolein, CLOL (cholesteryl-oleate). **e** Center of mass distances of amino acid C $\alpha$  atoms in UBXD8<sub>80-128</sub> and the P atom in the phospholipid headgroup (dotted line) in the average structures obtained after 2  $\mu$ s simulations. UBXD8<sub>80-128</sub> was inserted into POPC bilayers or into trilayer systems as indicated. Max. penetration into bilayer is -2 nm and into monolayer is -1 nm. Five independent simulations with the CHARMM36m force field over 2  $\mu$ s were performed. For **(d)** and **(e)**: Lines and shaded areas show mean and  $\pm$ SEM, respectively ( $n = 5$  simulations). Source data are provided as a source data file.

expected to remain accessible to PEGylation upon membrane-solubilization, which would result in the detection of 2-fold PEGylated protein species. In contrast, intramolecular crosslinking of these two cysteines would render them inaccessible to subsequent PEGylation, which would result in the enrichment of non-PEGylated

protein species (Fig. 4c). Indeed, we observed that RM-inserted opUBXD8<sub>53-153</sub>L91C\_L118C\_mCherry can be PEGylated twice (Fig. 4d, lane 1), which confirms that both cysteines are accessible to mPEG upon Triton X-100 solubilization of the membranes. Interestingly, significantly less PEGylation is detected upon the addition of the

## Article

<https://doi.org/10.1038/s41467-024-48843-8>


**Fig. 4 | Intramolecular crosslinking provides experimental evidence for angle opening of UBXD8 during ER-to-LD partitioning.** **a** Positioning of the amino acids L91 and L118 within the atomistic starting structure of UBXD<sub>80-128</sub> that were mutated to a cysteine pair in opUBXD<sub>83-153</sub>L91C\_L118C\_mCherry. C $\alpha$  atoms are highlighted as purple spheres. **b** Violin plots of distances between the C $\alpha$  atoms of amino acids L91 and L118 in MD simulations in different membrane systems as shown in Figs. 3a, c, respectively. DI deeply inserted, TRIO Triolein, CLOL (cholesterol-oleate). Vertical bars indicate median and maximum/minimum values of the distributions ( $n = 5$  simulations). **c** Schematic representation to illustrate the principle of the combined intramolecular crosslinking - PEGylation assay. For clarity, a double-cysteine-containing peptide is only schematically depicted in a bilayer membrane and does not particularly reflect closed or open conformations of UBXD8 in different types of membranes. **d, e** Immunoblots using anti-mCherry antibodies showing intramolecular crosslinking/PEGylation experiments of

opUBXD<sub>83-153</sub>L91C\_L118C\_mCherry in either RMs (**d**) or in isolated LDs from cells (**e**). Non-PEGylated protein species (0 PEG) as well as species with one mPEG (1 PEG) or two mPEG (2PEG) molecules attached, are indicated. High molecular weight adducts derived from *inter*-molecular crosslinking of opUBXD<sub>83-153</sub>L91C\_L118C\_mCherry on LDs are indicated (inter x-link). **f** Quantification of relative opUBXD<sub>83-153</sub>L91C\_L118C\_mCherry intramolecular crosslinking efficiencies in RMs versus LDs. From experiments as shown in (**d, e**), bands corresponding to non-PEGylated/intramolecularly crosslinked OpUBXD<sub>83-153</sub>L91C\_L118CmCherry (0 PEG) were quantified. The relative increase in these bands upon addition of crosslinker (lane 2 versus negative DMSO control in lane 1) was calculated from three independent experiments and the values were normalized to the highest value, which was set to 100%. Scatter plots show the mean values with SEM from three independent experiments as well as the individual values for each replicate. Source data are provided as a source data file.

crosslinker and the non-PEGylated population (0 PEG) is strongly enriched (Fig. 4d, lane 2). This shows that in ER bilayer membranes, L91C and L118C are sufficiently close positioned to allow crosslinking with a 13 Å spacer-length crosslinker, which is in accordance with our MD simulations revealing a closed deep-V intramembrane positioning of UBXD8 in bilayer membranes (Figs. 3a and 4b). In contrast, when we expressed opUBXD<sub>83-153</sub>L91C\_L118C\_mCherry in cells and subjected the isolated LDs to this analysis, less intramolecular crosslinking was observed (Fig. 4e). Also in LD membranes, L91C and L118C were accessible to PEGylation in the absence of crosslinker (Fig. 4e, lane 1 “2PEG”). However, upon the addition of a crosslinker, the non-PEGylated population (0 PEG) did not increase (compare lanes 1 and 2 “0 PEG” in Fig. 4d, e, respectively). This indicates that L91C and L118C were not efficiently crosslinked to each other in the LD environment. Of note, the 2-fold PEGylated population was also diminished upon the addition of a crosslinker (Fig. 4e, compare lanes 1 and 2 “2PEG”), which appears counterintuitive at first glance because the non-crosslinked amino acids L91C and L118C should remain accessible to PEGylation. Instead, several high molecular weight adducts were detectable, which are most likely *inter*-molecular crosslinking

adducts of opUBXD<sub>83-153</sub>L91C\_L118C\_mCherry, either forming homooligomers or hetero-oligomers with other endogenous proteins on LDs (Fig. 4e, lane 2 “inter x-link”). Quantification revealed that intramolecular crosslinking of L91C and L118C in LD monolayer membranes was reduced by approximately 50% compared to crosslinking in ER bilayer membranes (Fig. 4f). Together, these results indicate that UBXD8 indeed adopts a more open conformation in LD monolayers than in ER bilayer membranes.

#### cwEPR spectroscopy confirms deeper membrane penetration of UBXD8 in phospholipid bilayers than in LD monolayer membranes

In order to experimentally determine the insertion depth of UBXD8 in bilayer and monolayer membranes, respectively, we established continuous-wave electron paramagnetic resonance (cwEPR) spectroscopy workflows of UBXD8 in different biomimetic model membranes. We purified several recombinant S- and His-tagged single cysteine mutants of UBXD<sub>71-132</sub> to homogeneity and subjected them to site-directed MTSL spin-labeling (Fig. 5a). The recombinant and spin-labeled UBXD8 peptides (MTSL-sUBXD<sub>71-132</sub>His) were reconstituted

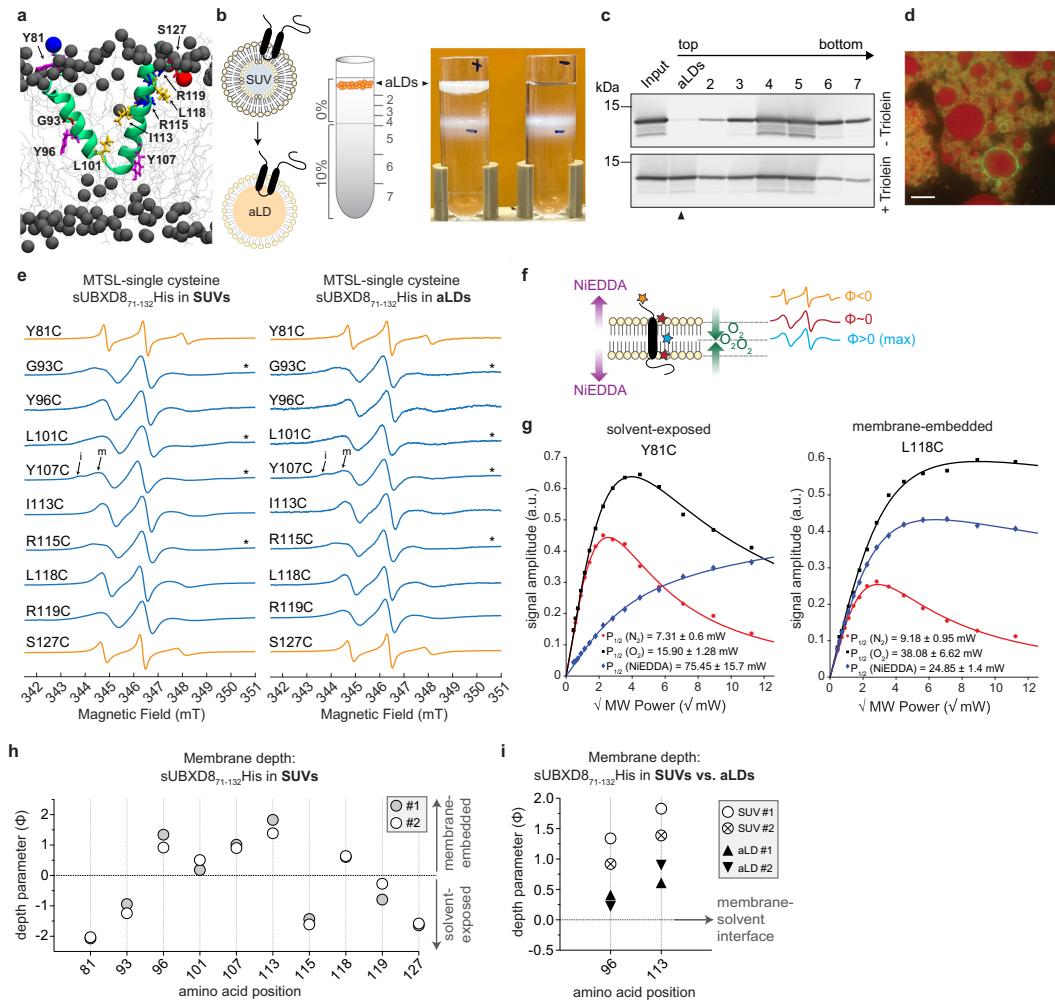


**Fig. 5 | cwEPR spectroscopy confirms deeper membrane penetration of UBXD8 in phospholipid bilayers than in LD monolayer membranes.** **a** Average atomistic MD simulation structure of UBXD8<sub>80-128</sub> in a POPC bilayer (as in Fig. 3a) indicating amino acids that were substituted for single cysteines for cwEPR analyses. **b** Left: Schematic outline of proteo-aLDs generation from proteo-SUVs and isolation by density gradient centrifugation. Right: photograph showing density gradients after centrifugation with floating aLDs when triolein was present during the reconstitution (+). (-): negative control without triolein. **c** Immunoblot analysis of proteo-aLDs isolation by density gradient fractionation as indicated in (b) using anti-S-tag antibodies. Top: negative control without triolein. Arrowhead indicates MTSL-labeled sUBXD8<sub>71-132</sub>His S127C in the top floating aLD fraction when triolein was present during the reconstitution. Representative for  $n = 3$  independent experiments. **d** Fluorescence micrograph of the top floating aLDs fraction as shown in (b) upon reconstitution of Atto488-labeled sUBXD8<sub>71-132</sub>His T130C (green). LipidTox Red marks the neutral lipid core (red). Scale bar: 10  $\mu\text{m}$ . Representative for  $n = 3$  independent experiments. **e** First derivative absorption cwEPR spectra of MTSL spin-labeled sUBXD8<sub>71-132</sub>His single cysteine mutants in POPC/DOPS SUVs (left) and aLDs (right). Spectra were normalized by the height of the central EPR line. Asterisks mark spectra with additional shoulders in the low-field region indicating immobile (i) and mobile (m) motional components. **f** Schematic illustration of how

the spin-label positioning in a membrane protein affects the line shape of cwEPR spectra and the membrane depth parameter ( $\Phi$ ). Solvent-exposed: orange; membrane-associated: red; membrane-embedded: blue. In the bilayer midplane, the O<sub>2</sub> concentration is the highest (green), while NIEDDA is gradually excluded from the membrane (purple). **g** Exemplary EPR power saturation plots of MTSL spin-labeled sUBXD8<sub>71-132</sub>His Y81C and L118C single cysteine mutants reconstituted into SUVs. The peak-to-peak amplitude of the central EPR line was plotted against the square root of the applied microwave power. Power saturation curves were measured under three conditions: nitrogen gas as control (red circles), molecular O<sub>2</sub> (black squares), and NIEDDA (blue diamonds).  $P_{1/2}$  values were obtained after curve fitting and are indicated with SEM. **h** Membrane depth parameter ( $\Phi$ ) analysis of MTSL spin-labeled sUBXD8<sub>71-132</sub>His single cysteine mutants in SUVs using cwEPR power saturation analyses ( $n = 2$  independent experiments). Positive  $\Phi$ : membrane-embedding; negative  $\Phi$ : solvent exposure. **i** Membrane depth parameter ( $\Phi$ ) analysis of MTSL spin-labeled sUBXD8<sub>71-132</sub>His Y96C and I113C reconstituted into either SUVs or aLDs using cwEPR power saturation analyses ( $n = 2$  independent experiments).  $\Phi$  close to 0: proximity to solvent-membrane interface. Results for SUVs are duplicates from (h) for direct comparison with aLDs. Source data are provided as a source data file.

## Article

<https://doi.org/10.1038/s41467-024-48843-8>

into small unilamellar vesicles (SUVs), which serve as a mimetic for ER bilayer membranes (Supplementary Fig. 3). These proteo-SUVs were then used to generate artificial LDs (aLDs) containing MTSL-sUBXD8<sub>71-132</sub>His peptides. Upon mixing of proteo-SUVs with triolein and after density gradient centrifugation, aLDs could be isolated from the top fraction of the gradient (Fig. 5b). Immunoblot analyses confirmed the presence of sUBXD8<sub>71-132</sub>His in this fraction if triolein was present during the reconstitution. Without the addition of triolein, sUBXD8<sub>71-132</sub>His-containing SUVs were only detected in the lower fractions 2–7 of the gradient (Fig. 5c) confirming that the floating LD fraction was virtually free of bilayer-embedded sUBXD8<sub>71-132</sub>His. In order to confirm that the floating aLDs are intact and homogeneously covered by the protein, we reconstituted an Atto488-labeled sUBXD8<sub>71-132</sub>His single cysteine variant<sup>25</sup> into aLDs and examined the top floating fraction by fluorescence microscopy (Fig. 5d).

All MTSL-sUBXD8<sub>71-132</sub>His single cysteine mutants that were reconstituted into either SUV bilayer membranes or into aLDs displayed cwEPR spectra with a good signal-to-noise ratio, indicating efficient spin-labeling of the proteins (Fig. 5e). The line shape of the individual cwEPR spectra primarily provides information about the mobility of the spin labels and therefore about the local environment of the labeled residues (Fig. 5f orange, red, blue line shapes). Spin-labeling of sUBXD8<sub>71-132</sub>His mutants Y81C and S127C resulted in sharp and narrow spectral lines, (orange line shapes with smaller peak-to-peak linewidth in Fig. 5e) which is indicative of a high mobility, and hence solvent exposure at these positions. In contrast, the cwEPR spectra of all other spin-labeled sUBXD8<sub>71-132</sub>His mutants (G93C, Y96C, L101C, Y107, I113C, R115C, L118C, and R119C) showed broad lines, which indicates more restricted mobility and presumably membrane-embedding (blue line shapes with larger peak-to-peak linewidth in Fig. 5e). Consistently, spin labels at positions Y81C and S127C have overall lower rotational correlation times (RCTs), hence faster motion than spin labels that are positioned within the hairpin region of sUBXD8 (Supplementary Fig. 4a). Thus, the cwEPR results are consistent with our solvent-accessibility assays (Fig. 2) and with our MD simulations (Fig. 3).

Note that the spin-labeled sUBXD8<sub>71-132</sub>His mutants G93C, L101C, Y107C, and R115C exhibited two motional components in the low-field region of their cwEPR spectra (spectra marked with asterisks in Fig. 5e and explicitly marked immobile “i” and mobile “m” for sUBXD8<sub>71-132</sub>His\_Y107C). Indeed, exemplary simulation of the cwEPR spectrum of sUBXD8<sub>71-132</sub>His\_Y107C revealed one mobile component possessing a lower RCT (2.2 ns in SUVs and 2.1 ns in aLDs) and another more immobile component with a higher RCT (5.6 ns in SUVs and aLDs) (Supplementary Fig. 4b). Such distinct motional components may either derive from two distinct rotamer conformations, or they may experience two distinct environments<sup>26,27</sup>. In particular, they may reflect heterogeneous interactions at the membrane-solvent interface or may be caused by their proximity to bulky amino acids such as W94, Y108, F114, and F116 (see also Fig. 3). Importantly, the overall line shape of the cwEPR spectra and the RCTs were similar for the spin-labeled proteins in SUVs and in aLDs indicating that recombinant MTSL-sUBXD8<sub>71-132</sub>His peptides are correctly reconstituted in a monotopic topology in both biomimetic model membranes.

For a quantitative assessment of the membrane penetration depth of sUBXD8 in SUV bilayer and in aLD monolayer membranes, respectively, we employed cwEPR power saturation experiments. The membrane insertion depths of spin labels attached to specific sites of membrane proteins can be studied through the acquisition of cwEPR spectra over a range of microwave powers and using the accessibility of two different paramagnetic relaxing agents to the spin label. To assess the spin-label location, molecular oxygen (O<sub>2</sub>) was used as a lipid-soluble paramagnetic relaxant, whereas NiEDDA served as a water-soluble paramagnetic relaxant. Pure non-paramagnetic nitrogen gas was utilized as the control environment

to measure the intrinsic relaxation rate of the spin label. These chemical agents have inverse concentration gradients in the lipid bilayer membrane with a higher O<sub>2</sub> concentration in between the two leaflets of the phospholipid bilayer compared to outside of the bilayer and vice versa for NiEDDA<sup>26,28,29</sup> (Fig. 5f). Figure 5g depicts exemplarily the cwEPR power saturation plots for spin-labeled sUBXD8<sub>71-132</sub>His mutants Y81C and L118C in SUVs. The respective P<sub>1/2</sub> values indicate that the spin labels in these proteins are differentially relaxed by NiEDDA and O<sub>2</sub>, suggesting that Y81C is more solvent-exposed than L118C. Calculating the depth parameter ( $\Phi$ ) by using the collision frequency of the MTSL spin-label with either O<sub>2</sub> or NiEDDA provides a quantitative metric for the membrane penetration depth of individual amino acid positions. Positive  $\Phi$  values indicate membrane-embedding and the highest  $\Phi$  value corresponds to the midplane of the phospholipid bilayer. Negative  $\Phi$  values indicate solvent exposure of the spin-label.  $\Phi$  values close to 0 indicate that the spin-label is close to the membrane-solvent interface (Fig. 5f)<sup>26,28,30</sup>.

We calculated the depth parameter for all ten sUBXD8<sub>71-132</sub>His single cysteine mutants in SUVs and detected two hydrophilic moieties (negative  $\Phi$ ) flanking one hydrophobic core (positive  $\Phi$ ) with a local minimum at L101C ( $\Phi$  close to zero) (Fig. 5h and Supplementary Fig. 5). This pattern is characteristic and expected for a monotopic protein topology in which Y81C and S127C are most solvent-exposed, and G93C, L118C, and R119C are closer to the membrane-solvent interface. Y96C, Y107C, and I113C have the highest membrane depth parameter, while L101C has a depth parameter close to 0. This indicates that Y96C, Y107C, and I113C are positioned in the midplane of the phospholipid bilayer, while L101C is positioned close to the opposing membrane-solvent interface. Of note, R115C also exhibited a negative depth parameter, which in theory would suggest that it is located outside of the membrane. This, however, seems unlikely because the amino acids in direct proximity (I113 and L118) are clearly membrane-embedded. This apparent discrepancy could be explained by a model in which the three arginines in the C-terminal end of the hydrophobic domain (R115, R119, R122) attract water molecules into the membrane, which would allow NiEDDA to enter the membrane at this position to relax the spin-label at position R115. Indeed, our MD simulations indicate that water molecules are dragged into the membrane at the C-terminal membrane-solvent interface of sUBXD8 and accumulate here at the inner side of the V-shaped helix (Supplementary Fig. 5c). L118C is located at the outer side of the helix and points towards the hydrophobic phospholipid acyl chains, explaining why L118C exhibits a positive depth parameter, while R115C and R119C exhibit negative depth parameters. Together, these cwEPR data strongly indicate that sUBXD8 is deeply embedded into the phospholipid bilayer, which is consistent with the MD simulations revealing the deep-V intramembrane positioning of sUBXD8 (see Fig. 3a).

In order to assess whether the membrane penetration depth of sUBXD8 is altered in LD monolayer membranes, we performed cwEPR power saturation experiments with MTSL-labeled sUBXD8<sub>71-132</sub>His single cysteine mutants that were reconstituted into aLDs (Fig. 5i and Supplementary Fig. 5b). We selected the mutants Y96C and I113C as they showed the highest membrane depth parameter in SUV bilayers. If the model that sUBXD8 undergoes major structural rearrangements from a “deep-V” to an “open-shallow” positioning during ER-to-LD partitioning is correct, Y96C and I113C are expected to show the biggest differences in depth parameters when comparing SUV- and aLD-embedded proteins, as they would reposition from the midplane of the bilayer (most positive  $\Phi$ ) to the membrane-solvent interface ( $\Phi$  close to zero). Indeed, we reproducibly determined lower membrane depth parameters for sUBXD8<sub>71-132</sub>His Y96C and I113C in aLDs, which strongly suggests that these amino acid positions are closer to the membrane-solvent interface in LD monolayers than in phospholipid bilayers (Fig. 5i).

## Article

<https://doi.org/10.1038/s41467-024-48843-8>**Free-energy calculations suggest that additional factors are required to assist the conformational transition of UBXD8 at the bilayer-LD interface**

Our biochemical assays, cwEPR spectroscopic analyses, and MD simulation data strongly indicate that UBXD8 is differentially positioned in ER bilayer compared to LD monolayer membranes, which furthermore suggests that UBXD8 has to undergo major structural rearrangements during bilayer-to-monolayer partitioning. This contrasts with the previous assumption that LD-destined hairpin proteins are inserted only into the cytoplasmic leaflet of the ER bilayer membrane, which would enable their passive lateral diffusion from the ER bilayer to the LD monolayer during LD biogenesis. While such a lateral diffusion mechanism is plausible for proteins that associate with both types of membranes via amphipathic interfacial  $\alpha$ -helix membrane anchors such as DHRS3<sup>15</sup>, our data clearly show a distinct mode of membrane integration for UBXD8, which is deeply embedded into the ER bilayer and requires structural rearrangements to allow partitioning to the LD monolayer in a shallow conformation.

To demonstrate the importance of different UBXD8 conformations for bilayer-to-monolayer partitioning, we next employed coarse-grained MD simulations of a small triolein/cholesteryl oleate lens in continuity with a POPC bilayer membrane, mimicking a nascent LD from the ER membrane (Fig. 6a). When we inserted UBXD8<sub>80-128</sub> into the POPC bilayer in the open-shallow conformation, the peptide readily partitioned to the LD surface where it accumulated, resulting in the formation of an asymmetric LD lens (Fig. 6a, top panel). These results are in agreement with previous experimental data that indicated that the presence of UBXD8 proteins on biomimetic LDs alters the surface tension of the LD leaflet substantially<sup>25</sup>. However, when UBXD8<sub>80-128</sub> was inserted into the POPC bilayer in its deep-V conformation, no partitioning to the LD surface could be observed within 5  $\mu$ s. Instead, UBXD8<sub>80-128</sub> remained in its deeply inserted state over the simulation time and diffused in the bilayer plane with a preference for the bilayer-LD rim interface (Fig. 6a, bottom panel). This confirms that UBXD8<sub>80-128</sub> initially adopting the deep-V conformation may partition into the LD monolayer only after a deep-V to open-shallow transition.

To test whether the deep-V to open-shallow transition occurs spontaneously, or whether it requires assistance by other proteins, we carried out additional atomistic MD simulations. We used pulling simulations to drive UBXD8<sub>80-128</sub> embedded in a POPC bilayer from a deep to a shallow conformation and vice versa (Fig. 6b, c), and we used umbrella sampling simulations to estimate the free-energy costs corresponding to the transitions along the two pulling directions (Fig. 6e). Both, during the deep-to-shallow transition and vice versa, we observed the formation of energetically unfavorable large water defects as the charged amino acids cross the hydrophobic membrane core. Thus, in the absence of additional proteins, as simulated here, the transitions require a very high cost of free energy in the order of 100 kJ/mol, similar to the high costs for forming aqueous defects across POPC membranes<sup>31,32</sup>. To test whether these transitions are energetically more favorable near the rim of an LD lens, we repeated the simulations with UBXD8<sub>80-128</sub> in a simulation system with a small LD embedded in a POPC bilayer (Fig. 6d). However, the free-energy costs required to pull the peptide across a planar POPC bilayer or across the LD rim are similarly high (Fig. 6e). This suggests that both states of UBXD8 are energetically stable and long-lived and that a transition between them is unlikely to occur spontaneously without the help of additional proteins.

A recently proposed model depicts that some ERTOLD pathway proteins partition from the ER to LDs early, presumably during LD biogenesis, while other proteins partition to LDs only at later stages potentially via membrane stalks that are formed between the ER bilayer and mature LDs. Here, seipin seems to act as a gatekeeper and

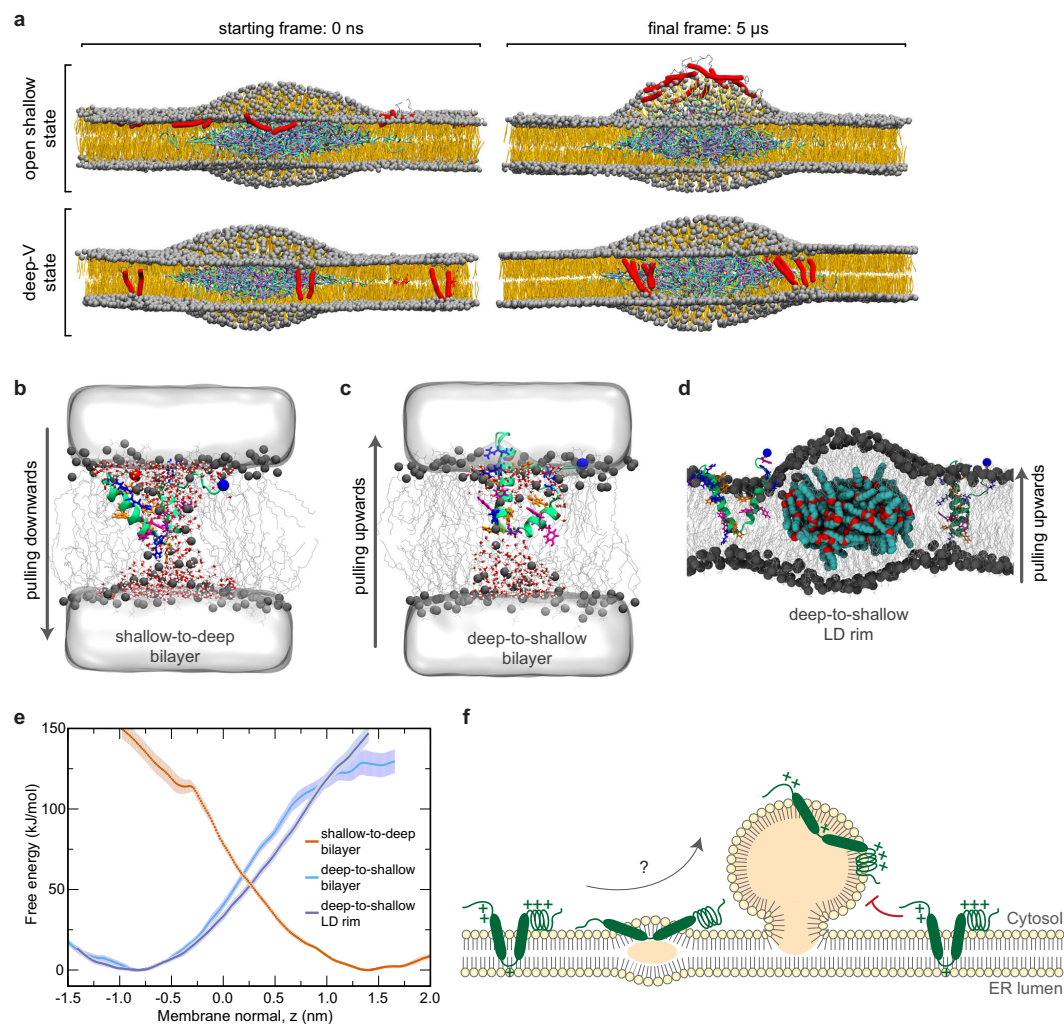
restricts late ERTOLD proteins such as GPAT4 from partitioning to LDs during the early stages<sup>30</sup>. Seipin is a transmembrane protein that forms large oligomeric complexes in the ER bilayer membrane. It concentrates neutral lipids via a hydrophobic element on the luminal domain that protrudes into the ER bilayer<sup>33-35</sup>, while the transmembrane domains form a cage-like structure<sup>36,37</sup> that assists in neutral lipid nucleation and may help constrict the bud neck of the lipid droplet<sup>38-40</sup>. Interestingly, UBXD8 is considered an early ERTOLD protein<sup>20</sup> and it is tempting to speculate that the distinct intramembrane positioning that we observed for UBXD8 in bilayer and LD monolayer membranes allows UBXD8 to pass the seipin barrier at LD biogenesis sites, and furthermore, that seipin might play an active role in enabling the transition of UBXD8. It will be important to test this model in future studies and to decipher why late ERTOLD proteins cannot cross the seipin barrier. It is conceivable that these proteins undergo different transitions during membrane partitioning. Indeed, based on previous MD simulation studies, the hairpin proteins GPAT4 and Alg14 appear to embed deeply into phospholipid bilayers in a similar fashion as we observed it for UBXD8. However, and in contrast to UBXD8, a central arginine in GPAT stays deeply embedded in the LD environment, where it coordinates with water molecules in the neutral lipid lens<sup>21</sup>. Proteins with such an intramembrane positioning and that are not transitioning from a deep-V to an open-shallow conformation could potentially be restricted to pass the seipin barrier at LD biogenesis sites.

To conclude, a combination of biochemical assays, in silico modeling, and cwEPR spectroscopy allowed us to determine a *hitherto* unknown and distinct intramembrane positioning of a monotopic hairpin protein in both, ER bilayer and LD monolayer membranes. Importantly, the establishment of advanced biochemical and EPR spectroscopy-based approaches enabled us to dissect different models that were suggested by MD simulations. Assessment of the solvent-accessibility, the membrane penetration depth, and the intramolecular arrangement of UBXD8 in both types of membranes with amino acid resolution unequivocally revealed a deep integration of the protein in a V-shape topology in ER bilayer membranes and an open-angled, shallow positioning in LD monolayer membranes. Free-energy calculations provided mechanistic insight into the protein partitioning process between these membranes and suggest that UBXD8, and potentially other hairpin proteins, needs to undergo unexpected major structural rearrangements during ER-to-LD protein partitioning (Fig. 6f). These transitions are more complex than initially anticipated and may provide a mechanistic basis for controlling quantitative ER-to-LD partitioning. This is of particular relevance for membrane proteins that fulfill distinct functions in the ER and on LDs and that do not only transiently pass the ER en route to LDs. These proteins usually co-exist in both organelles and passive depletion from the ER would pose the risk of misbalancing their subcellular functional abundance. Our work provides an important structural framework to identify the collective physicochemical features governing ER-to-LD partitioning and regulating this trans-organelle protein trafficking.

**Methods****Reagents and antibodies**

Canine pancreatic rough microsomes were a kind gift from Prof. B. Dobberstein and stored at 2 eq/ $\mu$ l in RM buffer (250 mM sucrose, 50 mM Hepes/KOH pH 7.6, 50 mM KOAc, 2 mM Mg(OAc)<sub>2</sub>, 1 mM dithiothreitol (DTT)). Primary antibodies: rabbit anti-mCherry (Invitrogen, PA534974, 1:5000), rabbit anti-calnexin (Enzo Life Sciences, ADI-SPA-865-F, 1:2000), mouse anti-tubulin (Sigma-Aldrich, T6199-100UL, 1:10,000), rabbit anti-his-tag (Cell Signaling, 23655, 1:2,000) and mouse anti-S-peptide (Invitrogen, MA1-981, 1:3000). IRDye conjugated secondary antibodies against rabbit (680LT, 926-6802L, 1:20,000) and mouse (800CW, 926-32210, 1:15,000) were obtained from LiCor Biosciences.

## Article

<https://doi.org/10.1038/s41467-024-48843-8>


**Fig. 6 | Free-energy calculations suggest that additional factors are required to assist the conformational transition of UBXD8 at the bilayer-LD interface.**

**a** MARTINI-based coarse-grained simulation of a bilayer-embedded LD lens consisting of triolein/cholesteryl oleate. Upper panel: UBXD<sub>80-128</sub> was integrated into the bilayer in its shallow conformation as assessed by atomistic simulations. After 5  $\mu$ s, the peptides have partitioned to the LD monolayer surface where they accumulate. Lower panel: When inserted into the bilayer in the deep-V state as suggested by atomistic simulations, UBXD<sub>80-128</sub> accumulates at the bilayer-LD rim but does not transition to the LD surface within 5  $\mu$ s. **b, c** All-atom pulling simulations reveal high free-energy costs involved in pulling the shallow-open state of

UBXD<sub>80-128</sub> downwards (**b**) or the deep-V state upwards (**c**) within a planar POPC bilayer membrane. **d** All-atom simulation system of a minimal LD-bilayer system used for pulling the deep-V-inserted UBXD<sub>80-128</sub> along the LD rim towards the open-shallow conformation. **e** Graphs comparing free-energy profiles during MD pulling experiments of UBXD<sub>80-128</sub> in planar bilayers versus at the LD rim as derived from (**b-d**). Shaded areas show SEM derived by bootstrapping from the set of 33 umbrella histograms. **f** Revised model for the intramembrane positioning of UBXD8 in ER bilayer versus LD monolayer membranes indicating that structural rearrangements are required for enabling the partitioning. Positive charges are indicated by "+". Source data are provided as a source data file.

### Plasmids

To generate plasmids encoding opUBXD<sub>853-153</sub> that is C-terminally fused to mCherry, we first PCR amplified mCherry cDNA using primers encoding EcoRI and KpnI restriction sites followed by ligation into pCDNA3.1(-). UBXD<sub>853-153</sub> was amplified from pCDNA3.1(-) opUBXD8s as described in ref. 17 using a forward primer encoding an XbaI restriction site and an N-terminal opsin tag (MGPNFYVPFSNKTG) and a reverse primer encoding an EcoRI restriction site. The digested PCR fragment

was ligated into pCDNA3.1(-) mCherry. For generating C-terminally opsin-tagged UBXD<sub>853-153</sub>mCherryOp, the opsin-tagged mCherry was generated by PCR using a forward primer encoding an EcoRI site and a reverse primer encoding the opsin tag followed by a KpnI restriction site. Digested PCR fragments were cloned into pCDNA3.1(-). PCR amplified UBXD<sub>853-153</sub> was cloned upstream of mCherryOp using XbaI and EcoRI restriction sites. pCDNA3.1(-) opUBXD<sub>853-153</sub>mCherry was used as a DNA template to generate the single cysteine mutant library

## Article

<https://doi.org/10.1038/s41467-024-48843-8>

through site-directed mutagenesis via primer-extension overlap PCR with primer pairs harboring the respective mutation (Supplementary Table 1), followed by *DpnI* digestion and transformation into chemically competent *E. coli* (DH5 $\alpha$ ) cells. All plasmids were verified by DNA sequencing (Eurofins, Germany) prior to use.

To generate plasmids encoding GST-3C-sUBXD8<sub>71-132</sub>His for bacterial expression, UBXD8<sub>71-132</sub> was amplified from pCDNA3.1(-)opUBXD8<sub>53-153</sub>mCherry carrying individual single cysteine substitutions at position (Y81C, G93C, Y96C, L101C, Y107C, I113C, R115C, L118C, R119C, S127C) using a forward primer encoding a BamHI restriction site and a reverse primer encoding a NotI restriction site and a 6-histidine (His) tag. The digested PCR fragments were ligated into the prokaryotic expression vector pGEX6P encoding a human rhinovirus (HRV) 3C protease recognition site between the glutathione S-transferase (GST) and S-peptide tag. The GST-3C-sUBXD8<sub>71-132</sub>His\_T130C expressing construct was described previously<sup>25</sup>. A full list of all plasmids generated in this study is available in Supplementary Table 2. Plasmids and full sequences are available upon request.

**Cell culture and transfection**

HeLa Kyoto cells<sup>17</sup> were cultured at exponential growth in Dulbecco's Modified Eagle Medium (DMEM) containing 4.5 g/l glucose and glutamine (Gibco), supplemented with 10% (v/v) fetal bovine serum (Biobrom AG), in a 37 °C temperature-controlled humidified incubator with 5% CO<sub>2</sub>. Cells were regularly screened for the absence of mycoplasma. For transient transfection, Polyethylenimine (PEI 25 K, Polysciences, cat. no.23966-2) was used with a DNA-PEI ratio of 1:4. LD biogenesis was induced 24 h after transfection by treating the cells with 200  $\mu$ M oleic acid (Sigma-Aldrich) complexed with 0.2% fatty acid-free bovine serum albumin (BSA, Sigma-Aldrich) in DMEM including 10% FBS for 16 h.

**Fluorescence microscopy**

For live-cell imaging, HeLa Kyoto cells (100,000) were seeded onto 35-mm glass-bottom dishes (14 mm micro-well, 1.5 cover glass, Cellvis) and transfected after 24 h at a confluency of approx. 50%. 24 h post-transfection, cells were oleate-treated for 16 h, then washed twice with PBS, and LDs stained with HCS LipidTOX green (1:1000, Invitrogen).

For fluorescence imaging of aLDs containing Atto488-labeled sUBXD8<sub>71-132</sub>His\_T130C, floated proteo-aLDs were incubated with LipidTOX Deep red (1:1000, Invitrogen) to stain the neutral lipid core.

Images were acquired using a Zeiss AxioObserver.Z1/7 inverted microscope, using a Plan-Apochromat oil objective (63 $\times$ , NA 1.4) with appropriate filter sets. For each image, 15 individual z-sections with a step size of 0.25  $\mu$ m were collected using a Rolera EM-C<sup>2</sup> camera (QImaging). Images were pseudo-colored and maximum intensity z-projection was generated using Fiji software. Adobe Photoshop and Illustrator were used for cropping and assembling the final images.

**Cellular fractionation of LDs**

Cellular fractionation was essentially conducted as described in ref. 17. In brief, transfected and oleate-treated cells from three 10 cm dishes were washed once with ice-cold PBS and harvested by scraping into ice-cold PBS. Pelleted cells (500  $\times$  g for 5 min at 4 °C) were resuspended in ice-cold hypotonic lysis medium (HLM; 20 mM Tris/HCl, pH 7.5, 1 mM EDTA) supplemented with Complete EDTA-free protease inhibitor cocktail (Roche), 1 mM phenylmethylsulfonyl fluoride (PMSF) and 250 mM sucrose, and incubated on ice for 20 min. Cells were lysed by 26 passages through a 27G 1<sup>1/2</sup> syringe needle. Cellular debris and nuclei were removed by centrifugation at 3000  $\times$  g for 10 min at 4 °C. The resulting post-nuclear supernatant (PNS) was brought to 20% sucrose by adding ice-cold HLM buffer containing 60% sucrose and transferred to the bottom of an ultracentrifuge tube (Beckman, Ultraclear II  $\times$  35 mm). Thereafter, ice-cold HLM buffer was gently layered over the PNS. After centrifugation at 172,000  $\times$  g for 1 h in a TLS-55 rotor (Beckman Coulter) at 4 °C, the buoyant opaque LD fraction was

collected using a tube slicer (Beckman). Isolated LD was either used directly for downstream analyses (see below) or further processed for assessing the fractionation quality by immunoblotting. In the latter case, also the cytosolic fraction and membrane-containing pellet were collected from the gradient by pipetting. LDs were solubilized in 2% Triton X-100 for 20 min at 65 °C and proteins precipitated with 10% TCA followed by two washes in ice-cold acetone.

**In vitro transcription/ In vitro translation**

Capped mRNAs were synthesized in vitro from purified PCR products using the T7 RiboMax express large-scale RNA production system supplemented with m7G cap analog (Promega). mRNAs were treated with RNase-free DNase I (Promega) and subjected to column purification using Microspin G-25 columns (GE Healthcare). Purified mRNAs were translated in vitro using rabbit reticulocyte lysate (RRL, Promega) supplemented with complete amino acid mix (Promega) and in the presence of canine pancreatic rough microsomes for 45 min at 30 °C in a thermomixer with shaking at 450 rpm. The reaction was terminated by adding 2.5 mM puromycin (5 min at 30 °C) with shaking at 450 rpm, after which soluble proteins (fraction S) and membrane fraction (M) were collected upon ultracentrifugation in a TLA-100 rotor (100,000  $\times$  g, 5 min, 4 °C) through a sucrose cushion (500 mM sucrose, Hepes/KOH, pH 7.6, 150 mM KOAc, 2 mM Mg(OAc)<sub>2</sub>, 1 mM TCEP). The membrane fraction (M) after solubilization in PEG buffer was again centrifuged through a sucrose cushion (100,000  $\times$  g, 10 min, 4 °C). For analysis by SDS-PAGE and quantitative immunoblotting, soluble proteins (fraction S) were subjected to ammonium sulfate precipitation, whereas the membrane fraction (M) was resuspended in Laemmli buffer directly. For solvent-accessibility assays, pelleted membranes were resuspended in PEG buffer (50 mM Hepes/KOH, pH 7.0, 150 mM NaCl, 1 mM EDTA, 10 mM Maltose, 1 mM TCEP).

**PEGylation-based solvent-accessibility assays with RMs and LDs**

For sulfhydryl labeling with methoxypolyethylene glycol maleimide (mPEG, 5 kDa, Sigma-Aldrich) in ER bilayer membranes, RMs containing newly synthesized single cysteine UBXD8 variants were resuspended in PEG buffer and divided into three 10  $\mu$ l sample. To determine the maximum PEGylation efficiency for each UBXD8 single cysteine mutant, one sample was solubilized with 1% (v/v) Triton X-100 before subjecting it to PEGylation. For PEGylation, samples were incubated with 2 mM mPEG for 30 min on ice. DMSO incubation served as a negative control in one sample. The reactions were quenched with 10 mM DTT for 10 min on ice.

For PEGylation on LDs, UBXD8 variants were transiently expressed in HeLa Kyoto cells, and LDs were isolated after 16 h treatment with oleate. Isolated LDs from three 10 cm dishes were divided into three 100  $\mu$ l samples. Each sample was first treated with 1 mM TCEP for 5 min on ice and subsequently subjected to PEGylation by treatment with 2 mM mPEG for 1 h on ice. One sample was solubilized with 2% Triton X-100 before subjecting it to PEGylation to determine maximum PEGylation efficiency and one sample was treated with DMSO only as a negative control. The reactions were quenched with 10 mM DTT for 10 min on ice. Proteins were solubilized in 2% (v/v) Triton X-100 and subjected to trichloroacetic acid (TCA) precipitation. All protein samples were subjected to SDS-PAGE and quantitative immunoblotting. For each UBXD8 single cysteine mutant, relative PEGylation efficiency was determined by the percentage of PEGylated UBXD8 species in its native, membrane-embedded environment versus the maximum PEGylation after membrane extraction by Triton X-100, which was set to 100%.

**Intramolecular crosslinking in RMs and LDs**

For chemical crosslinking, the protocol was adapted from ref. 41. Amino acids L91 and L118 in the hydrophobic region of opUBXD8<sub>53-153</sub>mCherry were substituted to cysteines (L91C and L118C) by site-

## Article

<https://doi.org/10.1038/s41467-024-48843-8>

directed mutagenesis. For assessing intramolecular crosslinking of opUBXD8<sub>53-153</sub>L91C\_L118C\_mCherry in RMs, mRNAs were generated in vitro and the proteins translated in RRL. After terminating the translation with 2.5 mM puromycin (5 min at 30 °C) and centrifugation at 13,000 × *g* for 5 min, RMs were added to the reaction post-translationally for 30 min. Membranes containing opUBXD8<sub>53-153</sub>L91C\_L118C\_mCherry were collected by two cycles of ultracentrifugation in a TLA-100 rotor (100,000 × *g*, 10 min, 4 °C) through a sucrose cushion (500 mM sucrose, Hepes/KOH, pH 7.6, 150 mM KOAc, 2 mM Mg(OAc)<sub>2</sub>, 1 mM TCEP), resuspended in PEG buffer (50 mM Hepes/KOH, pH 7.0, 150 mM NaCl, 1 mM EDTA, 10 mM Maltose, 1 mM TCEP) and divided into two 10 μl aliquots. One aliquot was treated with 500 μM 1,6-Bismaleimido-hexane (BMH, Thermo-Scientific), and the other with DMSO as a negative control for 1 h on ice. The reactions were quenched with 10 mM DTT for 10 min on ice and membranes were collected by ultracentrifugation (100,000 × *g*, 30 min, 4 °C) through a sucrose cushion (500 mM sucrose, Hepes/KOH, pH 7.6, 150 mM KOAc, 2 mM Mg(OAc)<sub>2</sub>) without reducing agents. Membranes were resuspended in 10 μl PBS containing 1 mM TCEP and solubilized with 1% Triton X-100 for 10 min on ice. The solubilized membrane fractions were subjected to PEGylation by treatment with 2 mM PEG-Mal for 30 min on ice. The reactions were quenched with 10 mM DTT for 10 min on ice and thereafter mixed with Laemmli buffer and subjected to SDS-PAGE and quantitative immunoblotting.

For assessing intramolecular crosslinking in LDs, opUBXD8<sub>53-153</sub>L91C\_L118C\_mCherry was transiently expressed in HeLa Kyoto cells, LD biogenesis induced by oleate-treatment and LDs isolated from three 10-cm culture dishes. Isolated LDs suspended in ice-cold HLM buffer were divided into two 150 μl aliquots. After reduction with 1 mM TCEP for 10 min on ice, one sample was treated with 500 μM BMH, the other one with DMSO as a negative control for 1 h on ice. The reactions were quenched with 4 mM DTT for 10 min on ice. After diluting with Triton X-100 (2%) to a DTT concentration below 0.5 mM the samples were subjected to PEGylation by treatment with 2 mM PEG-Mal for 1 h on ice. After quenching with 10 mM DTT for 10 min on ice, proteins were TCA precipitated and subjected to SDS-PAGE and quantitative immunoblotting.

To calculate relative intramolecular crosslinking, bands corresponding to non-PEGylated opUBXD8<sub>53-153</sub>L91C\_L118C\_mCherry (0 PEG) were quantified in DMSO control and BMH crosslinking samples by densitometry (LiCor Image Studio software) whereas band intensities in the DMSO control were set to 100%. For comparison of intramolecular crosslinking efficiencies in RMs versus LDs (*n* = 3 each), all values were then normalized to the highest relative crosslinking value in RMs (set to 100%).

### Quantitative Immunoblotting

After SDS-PAGE, proteins were transferred onto nitrocellulose membranes using the Trans-Blot Turbo transfer system (Bio-Rad). 5% non-fat dry milk in TBS-T was used for blocking and antibody dilution. IRDye coupled secondary antibodies were used for signal detection in 700 nm and 800 nm channels using the Odyssey CLx imaging system (LiCor) and band intensities were quantified by densitometry using Image Studio Lite software (LiCor). Uncropped scans of all immunoblots are shown in Supplementary Fig. 6.

### Atomistic MD simulations

The starting structure of UBXD8<sub>80-128</sub> was modeled as a monotopic topology using the ab initio protein structure prediction tool QUARK<sup>42,43</sup>. The N- and C- terminal segments S<sub>80</sub>-R<sub>89</sub> and P<sub>123</sub>-R<sub>128</sub> respectively were modeled as disordered regions and the central segment G<sub>90</sub>-R<sub>122</sub> as alpha-helix with a kink at P102. The predicted structure agrees with previous protease protection assays, which confirmed that UBXD8 adopts a monotopic topology in lipid membranes<sup>17</sup>.

For MD simulations in bilayer membranes, the peptide structure generated from QUARK was processed using CHARMM-GUI server<sup>44</sup> and described using CHARMM36m (WYF) parameters<sup>45,46</sup>. The N- and C- terminal ends were capped with ACE and NME neutral groups respectively and inserted into a POPC (CHARMM36 lipids<sup>47</sup>) bilayer at varying depths. The UBXD8<sub>80-128</sub> POPC bilayer system was next solvated with the CHARMM-modified TIP3P water model, and the system charge was neutralized by adding Cl<sup>-</sup> counter ions. The solvated systems were subjected to energy minimization using the steepest descent algorithm to remove atomic clashes and several short position-restrained equilibrations were carried out using the CHARMM-GUI server<sup>44</sup> generated molecular dynamics parameter (mdp) files. During equilibration, the temperature of 310 K was controlled using the Berendsen thermostat<sup>48</sup> with a time constant of 1.0 ps, and the pressure was regulated using the Berendsen barostat<sup>48</sup> with a semi-isotropic coupling scheme with a time constant of 5.0 ps. The reference pressure of 1.0 bar was maintained in the x-y and z directions. The Verlet cutoff-scheme is used for neighbor list search with a cutoff distance of 1.2 nm. The non-bonded coulombic and Van-der-Waals interactions were computed using the particle-mesh Ewald method<sup>49,50</sup> and cutoff methods respectively, with a cutoff distance of 1.2 nm. Covalent bonds involving hydrogen atoms were constrained using the LINCS algorithm<sup>51</sup>. For the final production run, all restraints were removed, the thermostat was switched to the Nose-Hoover scheme<sup>52,53</sup> and the barostat to Parrinello-Rahman scheme<sup>54,55</sup>. All other parameter settings were the same as those used during equilibration. The production runs were carried out for 2 μs with an integration time step of 2 fs and the output was saved every 100 ps. All simulations were carried out using the GROMACS 2020.2 simulation package<sup>56</sup>.

The trilayer setup used to model an LD monolayer system contained a central slab with neutral lipids triolein (TRIO) and cholesterol oleate (CLOL) sandwiched between two POPC monolayers. The trilayer was prepared by first equilibrating a POPC bilayer patch, then translating the POPC monolayers in the z-direction to create a large box, and finally a neutral lipid patch consisting of either TRIO or TRIO/CLOL (1:1) was translated to the center of the enlarged box. The neutral lipid patches were prepared using the PACKMOL<sup>57</sup> program and GROMACS<sup>56</sup>. The CHARMM36 force field<sup>47</sup> parameters for TRIO and CLOL are based on Olarte et al.<sup>21</sup> and were provided by the corresponding authors. The built trilayer systems (POPC/TRIO and POPC/TRIO/CLOL) were energy minimized to remove any atomic clashes, followed by short equilibration to compress the simulation box in the z-direction. During equilibration, the temperature of 310 K was controlled using the Berendsen thermostat<sup>48</sup> with a time constant of 1.0 ps, and pressure was regulated using the Berendsen barostat<sup>48</sup> coupled to a semi-isotropic coupling scheme with a time constant of 20.0 ps. The box was compressed in the z-direction with a reference pressure of 1.0 bar in the x-y-direction and 1000.0 bar in the z-direction to speed up the process. During the compression simulation, phosphorous atoms and the terminal POPC tail atoms were position restrained in the x-y plane to prevent undesired flipping. Following compression, the systems were solvated with TIP3P water and re-equilibrated for 1 microsecond without any restraints. Here the Nose-Hoover thermostat<sup>52,53</sup> (tau<sub>t</sub> = 1.0 ps) and Parrinello-Rahman barostat were used<sup>54,55</sup> (tau<sub>p</sub> = 5.0 ps). The reference pressure was set to 1 bar in x-y and z-direction.

To the above equilibrated trilayer systems, UBXD8<sub>80-128</sub> was inserted at varying depths using a method described previously<sup>58</sup> and the system charge was neutralized by adding Cl<sup>-</sup> counter ions. The energy minimization, equilibration, and production runs were carried out using the same parameters described for the bilayer simulations. The final production run was performed for 2 μs. All analyses were performed for the last 500 ns of the trajectory using GROMACS tools, data were plotted using matplotlib and images were rendered using VMD tool<sup>59</sup>. Table 1 summarizes all simulation systems.

## Article

<https://doi.org/10.1038/s41467-024-48843-8>**Table 1 | The table lists the systems simulated**

Simulation type	Membrane-peptide system	Lipid composition	Monolayer thickness (nm)	No. of repeats	Total simulation time ( $\mu$ s)
Conventional simulations	Bilayer – partial insertion (PI)	POPC	-	5	10
	Bilayer – deep insertion (DI)	POPC	-	5	10
	Monolayer – DI / PI	POPC:TRIO	4	5	10
	Monolayer – DI / PI	POPC:TRIO:CLOL	4	5	10
Umbrella Sampling	Bilayer – DI (Upward Pulling)	POPC	-	1	3.3
	Bilayer – DI (Downward Pulling)	POPC	-	1	3.3
	LD – DI (Upward Pulling)	POPC:TRIO	-	1	1.45
Bilayer-LD partitioning	Deep-V peptide conformation	POPC:TRIO:CLOL	-	1	5
	Shallow-open peptide conformation	POPC:TRIO:CLOL	-	1	5

**Umbrella sampling simulations of UBXD8 membrane translocation**

To estimate the free-energy costs required for UBXD8<sub>80-128</sub> transition from the deep-V to the open-shallow state, or vice versa, we carried out umbrella sampling (US) simulations (Table 1). Free energies were estimated across the flat membrane (Fig. 6b, c) and along the edge of the minimal lipid droplet model (Fig. 6d). The reaction coordinate for pulling the peptide was defined by the center of mass of Arg104 at the tip of the UBXD8<sub>80-128</sub> hairpin structure relative to the center of mass of POPC atoms projected onto the normal (z coordinate). The deeply inserted UBXD8<sub>80-128</sub> in the POPC membrane system (see Fig. 3a, average structures) served as a starting structure for downward and upward pulling across the flat membrane. The initial pulling was performed over 100 ns with pull rate and force constant set to 0.032 nm/ns and 4000 kJ mol<sup>-1</sup> nm<sup>-2</sup> respectively. From pulling simulations, 33 equally spaced US windows (spacing 0.1 nm) were extracted and simulated for 100 ns in each window with a force constant of 1000 kJ mol<sup>-1</sup> nm<sup>-2</sup>.

For pulling UBXD8<sub>80-128</sub> along the edges of the lipid droplet, we set up a system as shown in Fig. 6d. Briefly, an equilibrated POPC bilayer (398 POPC lipids) was split by moving the monolayers apart by -6 nm in the z-direction (membrane normal). The gap between the two monolayers was filled with 55 TRIO lipids. Next, the system was energy minimized using the steepest descent method, followed by equilibration during which the system was compressed in the z-direction to bring the separated monolayers close to each other. The temperature of 310 K was maintained using the Berendsen thermostat<sup>48</sup> with a time constant of 1 ps, while the pressure of 1 bar along x-y directions and 1000 bar in the z-direction using a semi-isotropic Berendsen pressure coupling scheme with a time constant of 5 ps. To avoid lipid flipping during compression in the z-direction, POPC lipid P atom and terminal C atoms of lipid tails were position restrained in the x-y directions with a force constant of 1000 kJ mol<sup>-1</sup> nm<sup>-2</sup>. In addition, attractive layer-shaped flat-bottomed restraints were applied in the x-direction on all the atoms of TRIO lipids with a radius of 3 nm and a force constant of 100 kJ mol<sup>-1</sup> nm<sup>-2</sup>, and in the z-direction on oxygen atoms of TRIO lipids with a radius of 1.2 nm and a force constant of 100 kJ mol<sup>-1</sup> nm<sup>-2</sup>. The TRIO lipid phase as thus periodic in the y-direction only, thereby forming an LD-to-bilayer rim along the y-direction. The equilibration run was carried for 2 ns. Following equilibration, the system was subjected to the production run with the velocity rescale thermostat<sup>49</sup> and using a pressure of 1 bar maintained using a semi-isotropic Parrinello-Rahman pressure coupling scheme<sup>54,55</sup> with a time constant of 5 ps. Position restraints on POPC lipids were removed, while still maintaining the layer-shaped flat-bottomed restraints on TRIO lipids to maintain the LD shape. The production run was carried out for 1  $\mu$ s, with the integration time step set to 2 fs. The final structure from the production run was used to insert two UBXD8<sub>80-128</sub> peptides in the closed deep-V conformation using the method described by Javanainen et al.<sup>58</sup>, such that one UBXD8<sub>80-128</sub> peptide was located near each of

the LD-to-bilayer rims. The system charge was neutralized by replacing water molecules with counter Cl<sup>-</sup> ions. The energy minimization was performed using the steepest descent method, followed by a production run for 2  $\mu$ s using the above production simulation parameters.

The final structure from the production simulation was used for pulling UBXD8<sub>80-128</sub> along the edges of the lipid droplet, using the reaction coordinate described above. Both UBXD8<sub>80-128</sub> were pulled simultaneously over 100 ns with pull rate and force constant set to 0.032 nm/ns and 4000 kJ mol<sup>-1</sup> nm<sup>-2</sup> respectively. From the pulling simulations, 29 equally spaced US windows (spacing 0.1 nm) were taken. Each window was simulated for 50 ns or 100 ns for the LD or bilayer systems, respectively, with a force constant of 1000 kJ mol<sup>-1</sup> nm<sup>-2</sup>. All simulations were carried out using the GROMACS 2021 software package<sup>56</sup>. The free-energy profiles (also called potentials of mean force, PMFs) were calculated using GROMACS wham module<sup>61</sup> and the errors were estimated using the bootstrap method<sup>62</sup>. For analysis, the first 20 ns or 40 ns were removed from each US window for the LD or bilayer systems, respectively.

**Coarse-grained simulations of bilayer-LD partitioning**

To investigate UBXD8<sub>80-128</sub> partitioning from the bilayer to the LD, coarse-grained (CG) MD simulations were performed (Table 1). The CG partitioning simulations were set up using the Martini 2.0 force field<sup>63-66</sup>. Briefly, an equilibrated POPC bilayer (3200 POPC lipids) was split by moving the monolayers apart by -6 nm along the z-direction (membrane normal). The gap between the two monolayers was filled with 160 TRIO and 160 CLOL lipids. Next, the system was energy minimized using the steepest descent method, followed by equilibration during which the system was compressed in the z-direction to bring the separated monolayers close to each other. The temperature of 310 K was maintained using the Berendsen thermostat<sup>48</sup> with a time constant of 1 ps, while the pressure of 1 bar along x-y directions and 1.001 bar in the z-direction was maintained using a semi-isotropic Berendsen pressure coupling scheme with a time constant of 5 ps. In addition, lipid phosphate beads were position restrained in the x-y directions with a force constant of 100 kJ mol<sup>-1</sup> nm<sup>-2</sup> and cylindrical flat-bottom restraints were applied to TRIO/CLOL lipids with a radius of 10 nm and a force constant of 10 kJ mol<sup>-1</sup> nm<sup>-2</sup>. The equilibration run was carried out for 10 ns. Following equilibration, the system was subjected to a production run with the velocity rescaling thermostat<sup>49</sup> and pressure of 1 bar along x-y and z directions was maintained using a semi-isotropic Parrinello-Rahman pressure coupling scheme<sup>54,55</sup> with a time constant of 12 ps. Position restraints on lipid phosphate beads were removed, while still maintaining the flat-bottom cylindrical restraints on TRIO/CLOL lipids to maintain the LD radius. The production run was carried out for 3  $\mu$ s, with the integration time step set to 20 fs.

The final structure from the production run was used to insert UBXD8<sub>80-128</sub> peptides. The most populated (average) UBXD8<sub>80-128</sub>

## Article

<https://doi.org/10.1038/s41467-024-48843-8>

conformation from the cluster analysis (see Fig. 3a, b average structures) were back mapped from atomistic to coarse-grained representation using martinize script<sup>65</sup>. The coarse-grained UBXD8<sub>80-128</sub> peptides (5 peptides) were inserted in either closed deep-V or shallow-open conformation using the method described by Javanainen et al.<sup>58</sup> The system charge was neutralized by replacing water molecules with counter Cl<sup>-</sup> ions. The energy minimization was performed using the steepest descent method, followed by a production run for 5  $\mu$ s using the above production simulation parameters. All simulations were carried out using the GROMACS 2021 software package<sup>66</sup>.

#### Expression, purification, and spin-labeling of GST-3C-sUBXD8<sub>71-132</sub>His cysteine variants

Protein expression of GST-3C-sUBXD8<sub>71-132</sub>His single cysteine variants (Y81C, G93C, Y96C, L101C, Y107C, I113C, R115C, L118C, R119C, S127C, T130C) was induced in *E. coli* Rosetta star (BL21 DE3 star + pRARE) (Novagen) by the addition of 0.025 mM IPTG at an OD<sub>600</sub> of ~0.6<sup>25</sup>. After incubation for 2 h at 37 °C and 220 rpm, cells were harvested by centrifugation (4420  $\times$  g at 4 °C for 10 min), washed with ice-cold PBS, and re-centrifuged. The cell pellet was resuspended in lysis buffer (50 mM Tris/HCl pH 8.0, 150 mM NaCl, 1 mM EDTA) supplemented with fresh protease inhibitor cocktail (Pepstatin A, Chymostatin, Antipain, 0.010 mg/ml each), 1 mM PMSF, 0.25 mg/ml lysozyme and incubated for 40 min at 4 °C. Upon addition of 1 mM MgCl<sub>2</sub> and 0.025 U/ $\mu$ l Benzonase the cell lysate and incubated for another 20 min at 4 °C before sonication for 5 min (50% power level, 7 cycles) with a Bandelin Sonotrode VS70T in a Bandelin Sonopuls sonicator on ice. After centrifugation at 17,000  $\times$  g for 1 h at 4 °C, the pellet was resuspended in solubilization buffer (50 mM HEPES/KOH pH 7.6, 300 mM NaCl, 0.07 mM EDTA) supplemented with fresh protease inhibitor cocktail, 1 mM PMSF, 2 mM DTT, 1% (w/v) DDM and rotated overnight at 4 °C. After centrifugation at 17,000  $\times$  g for 1 h at 4 °C, the supernatant was diluted 1:1 with protease buffer (50 mM Tris/HCl, pH 7.0, 150 mM NaCl, 1 mM EDTA) and incubated with GSH-Sepharose beads (Cytiva) for 1 h at 4 °C. After washing the column with protease buffer supplemented with 1 mM DTT and 0.2% DDM, the GST-tag of the protein was cleaved-off and eluted by incubating the beads with 30.4 ng/ml homemade GST-tagged HRV 3C protease in protease buffer supplemented with 1 mM DTT and 0.2% DDM for 2 h at RT.

For MTSL labeling, the eluted protein was buffer exchanged to protease buffer using 30,000 MWCO filters (Sartorius Vivaspin™ 20) to remove DTT and concentrate. MTSL spin-label (Bertin Bioreagent, 250 mM in methanol) was added to the concentrated protein in ~50-fold molar excess, followed by nitrogen gas purging, sealing, and incubation overnight at 4 °C. For removal of the free label, the MTSL-labeled protein was diluted with His wash buffer (50 mM Tris/HCl pH 8.0, 300 mM NaCl, 20 mM Imidazole, fresh 0.1% DDM), and incubated with Ni-NTA agarose resin (Qiagen) for 1 h at 4 °C. After washing the column with His wash buffer, the spin-labeled protein was eluted with elution buffer (50 mM Tris/HCl pH 8.0, 300 mM NaCl, 250 mM Imidazole, fresh 0.1% DDM) and buffer exchanged to labeling buffer (50 mM HEPES/KOH pH 7.0, 150 mM NaCl, 1 mM EDTA, 5% glycerol) supplemented with 0.1% DDM and concentrated using 30,000 MWCO filters (Sartorius Vivaspin™ 20).

For Atto488 labeling of sUBXD8<sub>71-132</sub>His T130C, the eluted protein after (HRV) 3C protease cleavage was buffer exchanged to His wash buffer, and incubated with Ni-NTA agarose resin (Qiagen) for 1 h at 4 °C. After washing the column with His wash buffer, the protein was eluted with elution buffer and buffer exchanged to labeling buffer containing 0.1% DDM. 1 mM TCEP was added to the concentrated protein followed by adding 1.3-fold molar excess of Atto488 (Atto-Tec) and incubation at 4 °C overnight in the dark. Atto488-labeled protein was then again buffer exchanged to labeling buffer containing 0.1% DDM and concentrated.

#### Reconstitution of purified labeled sUBXD8<sub>71-132</sub>His cysteine variants into SUVs

For reconstitution of purified labeled sUBXD8<sub>71-132</sub>His cysteine variants into 10 mM POPC/DOPS (9:1) liposomes, the protocol was adapted from Puza et al.<sup>25</sup>. In brief, liposomes were prepared by mixing chloroform solutions of 1-palmitoyl-2-oleyl-*sn*-glycero-phosphocholine (POPC) and 1,2-dioleoyl-*sn*-glycero-3-phospho-L-serine (DOPS) in a 9:1 molar ratio with a final concentration of 10 mM. The lipids mixture was dried under a gentle stream of nitrogen gas in a thermomixer at 60 °C at 800 rpm. To remove any leftover chloroform, the lipids were further dried in a desiccator under a vacuum pump (Welch) in the EndDruk program for 1 h at RT. The dried lipid film was hydrated in reconstitution buffer 1 (20 mM HEPES/KOH, pH 7.4, 150 mM NaCl, 5% (v/v) glycerol) and incubated for 30 min at 60 °C and 1200 rpm in a thermomixer. Thereafter, the mixture was sonicated at 60 °C for 20 min in a water bath sonicator (VWR USC900D ultrasonic cleaner, 200 W ultrasonic) at power level 9.

For the reconstitution, the liposomes were solubilized in reconstitution buffer 1 and a final concentration of 0.5% (w/v) DDM. Solubilized liposomes were mixed with the purified, labeled protein in a 1:400 molar ratio of protein to lipid and with a final DDM concentration of 0.2%. After 10 min incubation at RT, the protein-lipid mixture was incubated twice with Bio-Beads SM-2 (Bio-Rad) (pre-washed with methanol followed by milli-Q water and reconstitution buffer 1) for 1.5 h at RT to remove the detergent. For generation of proteo-SUVs, the reconstituted proteo-liposomes were extruded through Avanti PC membranes (Whatman) with a pore size of 0.4  $\mu$ m and 0.1  $\mu$ m with 21 extrusions for each membrane using an Avestin LiposoFast™ mini-extruder. Extruded proteo-SUVs were concentrated using 30,000 MWCO filter units. Dynamic light scattering (Malvern Zetasizer Nano S) confirmed a homogeneous size distribution of proteo-SUVs around 120 nm.

To confirm whether proteins were efficiently reconstituted into liposomes, a gradient fractionation was performed. The extruded proteo-SUVs were mixed with 50% (v/v) Opti-prep (Sigma-Aldrich) in reconstitution buffer 1 (20 mM HEPES/KOH, pH 7.4, 150 mM NaCl, 5% (v/v) glycerol), and overlaid with 30% (v/v) Opti-prep in reconstitution buffer 1, and reconstitution buffer 2 (20 mM HEPES/KOH, pH 7.4, 150 mM NaCl, 1% (v/v) glycerol). Upon centrifugation in a swinging bucket rotor (SW41 Ti) at 230,335  $\times$  g for 16 h at 4 °C in a Beckman Coulter Optima LE-80K ultracentrifuge, 1 ml fractions were collected by pipetting from top to bottom and analyzed by immunoblotting.

#### Reconstitution of purified sUBXD8<sub>71-132</sub>His single cysteine variants into artificial LDs

For preparation of proteo-aLD in 1.5 ml centrifugation tubes, a 10 mg/ml triolein (Sigma) stock solution in chloroform was dried in a desiccator under vacuum for 1 h at RT followed by drying with N<sub>2</sub> gas and overlaid with proteo-SUVs in reconstitution buffer 1 at final molar ratio of phospholipids from the SUVs to triolein of 1:2 according to Wang et al.<sup>67</sup>.

After incubation overnight at 4 °C, samples were sonicated in a water bath sonicator (VWR USC900D ultrasonic cleaner, 200 W ultrasonic) for 2 min, power level 9, at 30 °C. For gradient fractionation, samples were brought to 10% (w/v) sucrose concentration reconstitution buffer 1, overlaid with reconstitution buffer 1 in thin wall tubes (Beckman Coulter 7/16 X 1-3/8 in Ultra Clear™ tube), and centrifuged at 173,400  $\times$  g in a TLS-55 rotor for 2 h at 4 °C in a benchtop ultracentrifuge (Beckman Coulter Optima™ MAX-XP). Floating aLDs (approx. 300  $\mu$ l) were fractionated using a tube slicer (Beckman Coulter) and subjected to cwEPR spectroscopy and microscopy. The remaining gradient was collected in fractions of three 100  $\mu$ l and three 500  $\mu$ l fractions from top to bottom by pipetting and analyzed by immunoblotting using anti-S-tag antibodies in 3% BSA. For cwEPR power saturation experiments, aLDs collected by tube slicing were

## Article

<https://doi.org/10.1038/s41467-024-48843-8>

further concentrated by flotation in a capillary (Hirschmann ringcap® capillary) using a capillary centrifuge (Hermle Z 233 M-2).

**Continuous-wave (cw) EPR spectroscopy measurements**

cwEPR experiments for 10 MTSL-labeled sUBXD8<sub>71-132</sub>His single cysteine variants in POPC/DOPS SUVs and POPC/DOPS/triolein aLDs were performed at RT (298 K) on a Bruker X-band EMXplus spectrometer operating at 9.4 GHz equipped with an ER4123D resonator (Bruker Biospin GmbH, Ettlingen, Germany). Each spectrum was acquired under 20 mW microwave power, 100 kHz modulation frequency, 0.2 mT modulation amplitude, 12 ms conversion time, 10.24 ms time constant, 60 dB receiver gain, 30 s field scans, 343.7 mT central field and sweep width of 10 mT. Samples were placed in a glass capillary tube (Hirschmann ringcap®) with a volume of 50 µL and data acquisition was performed with signal averaging of 50 scans. Each experiment was repeated for at least three biological replicates. Plots of cwEPR spectra were generated using MATLAB software. For simulating cwEPR spectra and the determination of the rotational correlation times (RCTs), we used the Easyspin toolbox (version 5.2.36) developed by Stefan Stoll and Arthur Schweiger<sup>68</sup>.

**cwEPR power saturation studies and membrane depth parameter analysis**

cwEPR power saturation measurements were performed for each mutant to determine the membrane insertion depth of sUBXD8<sub>71-132</sub>His into POPC/DOPS SUV bilayer and POPC/DOPS/triolein artificial lipid droplet monolayer membranes on the same EPR spectrometer. 5 µL of MTSL labeled sUBXD8<sub>71-132</sub>His single cysteine mutants reconstituted into either SUVs or artificial LDs were loaded into a TPX gas permeable capillary tube (Bruker). EPR spectra were collected using a modulation amplitude of 0.2 mT, 343.6 mT central field, sweep width of 6 mT, receiver gain of 60 dB, 30 s field scans, modulation frequency of 100 kHz. Power saturation measurements were performed with microwave power varying from 0.2 to 126.2 mW (2–30 dB in 2 dB steps) at room temperature with signal averaging of 5–10 scans. Each experiment was repeated for two biological replicates.

The power saturation curves for all selected sites in UBXD8 were obtained under three conditions: (1) equilibrated with the hydrophobic paramagnetic reagent 21% O<sub>2</sub> (air), (2) equilibrated with non-paramagnetic nitrogen gas as a control to measure the intrinsic relaxation rate of the spin-label and (3) equilibrated with hydrophilic paramagnetic reagent NiEDDA (50 mM) under nitrogen atmosphere. O<sub>2</sub> gas and NiEDDA were used as paramagnetic relaxants with different membrane permeability. The water-soluble paramagnetic NiEDDA was synthesized as previously described<sup>28,29</sup>. In brief, 0.005 mol of ethylenediamine-N,N'-diacetic acid (EDDA) (Merck) were completely dissolved in distilled water and 0.005 mol of Ni(OH)<sub>2</sub> (Merck) were added. The resulting milky green solution was allowed to mix and dissolve completely by rotating a round bottom flask in a water bath at 55 °C overnight. This solution was stirred further at RT overnight. The solution was filtered using a 0.2 µm pore size polyethersulfone bottle top filter to a clean bottle to remove undissolved material. The filtered solution was dried in a round bottom flask immersed in a 40 °C water bath under vacuum using a rotational evaporator. The slightly wet solid was scraped to the bottom of the flask and washed with methanol to remove the remaining Ni(OH)<sub>2</sub> or EDDA. The solid was then completely dried under vacuum overnight and the NiEDDA was scraped off to a falcon. A 100 mM NiEDDA stock solution was made in milli-Q water. An aliquot of NiEDDA stock solution with 100 mM concentration was dried under vacuum in an Eppendorf tube and SUV and aLD samples were mixed to reach a final NiEDDA concentration of 50 mM. SUV samples with NiEDDA were freeze-thawed in liquid N<sub>2</sub> ten times and aLD samples with 50 mM NiEDDA were incubated overnight at 4 °C to ensure that NiEDDA is equally distributed. Before performing each measurement, samples were purged for 30 min at a moderate flow rate

with either in-house supply of compressed air for condition (1) or with high purity N<sub>2</sub>(g) for conditions (2) and (3).

Generation of power saturation plots, data fitting, and analysis was performed using MATLAB software. Power saturation curves were plotted for the peak-to-peak amplitude of the central EPR line ( $M_1 = 0$ ) as a function of the square root of the incident microwave power ( $P$ ). The data points were then fitted using a Matlab script according to the following Eq. (1):

$$A = I\sqrt{P} \left[ 1 + \left( 2^{1/\varepsilon} - 1 \right) P/P_{1/2} \right]^{-\varepsilon} \quad (1)$$

$A$  is the peak-to-peak amplitude of the central EPR line,  $I$  is a scaling factor,  $P$  is the microwave power, and  $P_{1/2}$  is the microwave power where the amplitude of the central EPR line is reduced to half of its unsaturated value.  $\varepsilon$  is a measure of the homogeneity of saturation of the resonance line.  $\varepsilon$  equals 1.5 for a homogeneous saturation curve and 0.5 for an inhomogeneous saturation curve. It is approximately 1.5 under N<sub>2</sub>(g) for natural relaxation conditions and decreases with higher collision rates<sup>28,29</sup>.

The depth parameter was calculated using the following Eq. (2) where  $P_{1/2}(\text{Oxygen})$ ,  $P_{1/2}(\text{Nitrogen})$ , and  $P_{1/2}(\text{NiEDDA})$  are the corresponding power values where the EPR central line amplitude is reduced to half of its hypothetical unsaturated value (derived from extrapolation of the linear part of the saturation curves)<sup>28,29</sup>.

$$\phi = \ln \left[ \frac{\Delta P_{1/2}(\text{Oxygen})}{\Delta P_{1/2}(\text{NiEDDA})} \right] = \ln \left[ \frac{P_{1/2}(\text{Oxygen}) - P_{1/2}(\text{Nitrogen})}{P_{1/2}(\text{NiEDDA}) - P_{1/2}(\text{Nitrogen})} \right] \quad (2)$$

**Reporting summary**

Further information on research design is available in the Nature Portfolio Reporting Summary linked to this article.

**Data availability**

Data generated in this study is provided in the Figures and the Supplementary Information. In addition, MD simulation systems (structures, topologies, MD parameter, and force field files) and original cwEPR data generated in this study were deposited to Zenodo.org (<https://doi.org/10.5281/zenodo.11036547>)<sup>69</sup>. Source data are provided with this paper.

**Code availability**

All MD simulations were conducted using open-source code, and citations for the relevant code are provided in the manuscript. MATLAB code used for cwEPR analyses was deposited to Zenodo.org (<https://doi.org/10.5281/zenodo.11036547>)<sup>69</sup>.

**References**

- Zechner, R. FAT FLUX: enzymes, regulators, and pathophysiology of intracellular lipolysis. *EMBO Mol. Med.* **7**, 359–362 (2015).
- Zadoorian, A., Du, X. & Yang, H. Lipid droplet biogenesis and functions in health and disease. *Nat. Rev. Endocrinol.* **19**, 443–459 (2023).
- Krahmer, N., Farese, R. V. Jr. & Walther, T. C. Balancing the fat: lipid droplets and human disease. *EMBO Mol. Med.* **5**, 905–915 (2013).
- Olzmann, J. A. & Carvalho, P. Dynamics and functions of lipid droplets. *Nat. Rev. Mol. Cell Biol.* **20**, 137–155 (2019).
- Walther, T. C., Chung, J. & Farese, R. V. Jr. Lipid droplet biogenesis. *Annu Rev. Cell Dev. Biol.* **33**, 491–510 (2017).
- Xu, S., Zhang, X. & Liu, P. Lipid droplet proteins and metabolic diseases. *Biochim. Biophys. Acta Mol. Basis Dis.* **1864**, 1968–1983 (2018).

## Article

<https://doi.org/10.1038/s41467-024-48843-8>

7. Bersuker, K. & Olzmann, J. A. Establishing the lipid droplet proteome: Mechanisms of lipid droplet protein targeting and degradation. *Biochim. Biophys. Acta* **1862**, 1166–1177 (2017).
8. Olarte, M. J., Swanson, J. M. J., Walther, T. C. & Farese, R. V. Jr. The CYTOLD and ERTOLD pathways for lipid droplet-protein targeting. *Trends Biochem. Sci.* **47**, 39–51 (2022).
9. Xu, Y., Liu, Y., Lee, J. G. & Ye, Y. A ubiquitin-like domain recruits an oligomeric chaperone to a retrotranslocation complex in endoplasmic reticulum-associated degradation. *J. Biol. Chem.* **288**, 18068–18076 (2013).
10. Olzmann, J. A., Richter, C. M. & Kopito, R. R. Spatial regulation of UBXD8 and p97/VCP controls ATGL-mediated lipid droplet turnover. *Proc. Natl Acad. Sci. USA* **110**, 1345–1350 (2013).
11. Suzuki, M. et al. Derlin-1 and UBXD8 are engaged in dislocation and degradation of lipidated ApoB-100 at lipid droplets. *Mol. Biol. Cell* **23**, 800–810 (2012).
12. Prevost, C. et al. Mechanism and determinants of amphipathic helix-containing protein targeting to lipid droplets. *Dev. Cell* **44**, 73–86.e74 (2018).
13. Kim, S. & Swanson, J. M. J. The surface and hydration properties of lipid droplets. *Biophys. J.* **119**, 1958–1969 (2020).
14. Chorlay, A., Foret, L. & Thiam, A. R. Origin of gradients in lipid density and surface tension between connected lipid droplet and bilayer. *Biophys. J.* **120**, 5491–5503 (2021).
15. Pataki, C. I. et al. Proteomic analysis of monolayer-integrated proteins on lipid droplets identifies amphipathic interfacial alpha-helical membrane anchors. *Proc. Natl Acad. Sci. USA* **115**, E8172–E8180 (2018).
16. Zehmer, J. K., Bartz, R., Liu, P. & Anderson, R. G. Identification of a novel N-terminal hydrophobic sequence that targets proteins to lipid droplets. *J. Cell Sci.* **121**, 1852–1860 (2008).
17. Schrul, B. & Kopito, R. R. Peroxin-dependent targeting of a lipid-droplet-destined membrane protein to ER subdomains. *Nat. Cell Biol.* **18**, 740–751 (2016).
18. Stevanovic, A. & Thiele, C. Monotopic topology is required for lipid droplet targeting of ancient ubiquitous protein 1. *J. Lipid Res.* **54**, 503–513 (2013).
19. Dhiman, R., Caesar, S., Thiam, A. R. & Schrul, B. Mechanisms of protein targeting to lipid droplets: a unified cell biological and biophysical perspective. *Semin. Cell Dev. Biol.* **108**, 4–13 (2020).
20. Song, J. et al. Identification of two pathways mediating protein targeting from ER to lipid droplets. *Nat. Cell Biol.* **24**, 1364–1377 (2022).
21. Olarte, M. J. et al. Determinants of Endoplasmic Reticulum-to-Lipid Droplet Protein Targeting. *Dev. Cell* **54**, 471–487.e477 (2020).
22. Howe, V., Chua, N. K., Stevenson, J. & Brown, A. J. The regulatory domain of squalene monooxygenase contains a re-entrant loop and senses cholesterol via a conformational change. *J. Biol. Chem.* **290**, 27533–27544 (2015).
23. Ulmschneider, M. B. & Sansom, M. S. Amino acid distributions in integral membrane protein structures. *Biochim. Biophys. Acta* **1512**, 1–14 (2001).
24. Killian, J. A. & von Heijne, G. How proteins adapt to a membrane-water interface. *Trends Biochem. Sci.* **25**, 429–434 (2000).
25. Puza, S. et al. Lipid droplets embedded in a model cell membrane create a phospholipid diffusion barrier. *Small* **18**, e2106524 (2022).
26. Klug, C. S. & Feix, J. B. Methods and applications of site-directed spin labeling EPR spectroscopy. *Methods Cell Biol.* **84**, 617–658 (2008).
27. Bagneris, C. et al. Role of the C-terminal domain in the structure and function of tetrameric sodium channels. *Nat. Commun.* **4**, 2465 (2013).
28. Altenbach, C., Greenhalgh, D. A., Khorana, H. G. & Hubbell, W. L. A collision gradient method to determine the immersion depth of nitroxides in lipid bilayers: application to spin-labeled mutants of bacteriorhodopsin. *Proc. Natl Acad. Sci. USA* **91**, 1667–1671 (1994).
29. Oh, K. J., Altenbach, C., Collier, R. J. & Hubbell, W. L. Site-directed spin labeling of proteins. Applications to diphtheria toxin. *Methods Mol. Biol.* **145**, 147–169 (2000).
30. Yu, L. et al. CW-EPR studies revealed different motional properties and oligomeric states of the integrin beta1a transmembrane domain in detergent micelles or liposomes. *Sci. Rep.* **5**, 7848 (2015).
31. Hub, J. S. & Awasthi, N. Probing a continuous polar defect: a reaction coordinate for pore formation in lipid membranes. *J. Chem. Theory Comput.* **13**, 2352–2366 (2017).
32. Roesel, D., Eremchev, M., Poojari, C. S., Hub, J. S. & Roke, S. Ion-induced transient potential fluctuations facilitate pore formation and cation transport through lipid membranes. *J. Am. Chem. Soc.* **144**, 23352–23357 (2022).
33. Prasanna, X. et al. Seipin traps triacylglycerols to facilitate their nanoscale clustering in the endoplasmic reticulum membrane. *PLoS Biol.* **19**, e3000998 (2021).
34. Zoni, V. et al. Seipin accumulates and traps diacylglycerols and triglycerides in its ring-like structure. *Proc. Natl Acad. Sci. USA* **118**, e2017205118 (2021).
35. Renne, M. F., Corey, R. A., Ferreira, J. V., Stansfeld, P. J. & Carvalho, P. Seipin concentrates distinct neutral lipids via interactions with their acyl chain carboxyl esters. *J. Cell Biol.* **221**, e202112068 (2022).
36. Klug, Y. A. et al. Mechanism of lipid droplet formation by the yeast Sei1/Ldb16 Seipin complex. *Nat. Commun.* **12**, 5892 (2021).
37. Arlt, H. et al. Seipin forms a flexible cage at lipid droplet formation sites. *Nat. Struct. Mol. Biol.* **29**, 194–202 (2022).
38. Kim, S. et al. Seipin transmembrane segments critically function in triglyceride nucleation and lipid droplet budding from the membrane. *eLife* **11**, e75808 (2022).
39. Yan, R. et al. Human SEIPIN binds anionic phospholipids. *Dev. Cell* **47**, 248–256.e4 (2018).
40. Salo, V. T. et al. Seipin facilitates triglyceride flow to lipid droplet and counteracts droplet ripening via endoplasmic reticulum contact. *Dev. Cell* **50**, 478–493.e9 (2019).
41. Tu, L., Khanna, P. & Deutsch, C. Transmembrane segments form tertiary hairpins in the folding vestibule of the ribosome. *J. Mol. Biol.* **426**, 185–198 (2014).
42. Xu, D. & Zhang, Y. Ab initio protein structure assembly using continuous structure fragments and optimized knowledge-based force field. *Proteins* **80**, 1715–1735 (2012).
43. Xu, D. & Zhang, Y. Toward optimal fragment generations for ab initio protein structure assembly. *Proteins* **81**, 229–239 (2013).
44. Lee, J. et al. CHARMM-GUI input generator for NAMD, GROMACS, AMBER, OpenMM, and CHARMM/OpenMM simulations using the CHARMM36 additive force field. *J. Chem. Theory Comput.* **12**, 405–413 (2016).
45. Huang, J. et al. CHARMM36m: an improved force field for folded and intrinsically disordered proteins. *Nat. Methods* **14**, 71–73 (2017).
46. Khan, H. M., MacKerell, A. D. Jr. & Reuter, N. Cation-pi interactions between methylated ammonium groups and tryptophan in the CHARMM36 additive force field. *J. Chem. Theory Comput.* **15**, 7–12 (2019).
47. Klauda, J. B. et al. Update of the CHARMM all-atom additive force field for lipids: validation on six lipid types. *J. Phys. Chem. B* **114**, 7830–7843 (2010).
48. Berendsen, H. J. C. & Postma, J. P. M. Gunsteren WFV, DiNola A, Haak JR. Molecular dynamics with coupling to an external bath. *J. Chem. Phys.* **81**, 3684–3690 (1984).

## Article

<https://doi.org/10.1038/s41467-024-48843-8>

49. Darden, T. A., York, D. M. & Pedersen, L. G. Particle mesh Ewald: An N-log(N) method for Ewald sums in large systems. *J. Chem. Phys.* **98**, 10089–10092 (1993).
50. Essmann, U. et al. A smooth particle mesh Ewald method. *J. Chem. Phys.* **103**, 8577–8593 (1995).
51. Hess, B., Bekker, H., Berendsen, H. J. C. & Fraaije, J. G. E. M. LINCS: a linear constraint solver for molecular simulations. *J. Comput. Chem.* **18**, 1463–1472 (1997).
52. Hoover, W. G. Canonical dynamics: equilibrium phase-space distributions. *Phys. Rev. A Gen. Phys.* **31**, 1695–1697 (1985).
53. Nosé, S. A molecular dynamics method for simulations in the canonical ensemble. *Mol. Phys.* **100**, 191–198 (2002).
54. Parrinello, M. & Rahman, A. Polymorphic transitions in single crystals: a new molecular dynamics method. *J. Appl. Phys.* **52**, 7182–7190 (1981).
55. Parrinello, M. & Rahman, A. Crystal structure and pair potentials: a molecular-dynamics study. *Phys. Rev. Lett.* **45**, 1196–1199 (1980).
56. Abraham, M. J. et al. GROMACS: high performance molecular simulations through multi-level parallelism from laptops to super-computers. *SoftwareX* **1–2**, 19–25 (2015).
57. Martinez, L., Andrade, R., Birgin, E. G. & Martinez, J. M. PACKMOL: a package for building initial configurations for molecular dynamics simulations. *J. Comput. Chem.* **30**, 2157–2164 (2009).
58. Javanainen, M. & Martinez-Seara, H. Efficient preparation and analysis of membrane and membrane protein systems. *Biochim. Biophys. Acta* **1858**, 2468–2482 (2016).
59. Humphrey, W., Dalke, A. & Schulten, K. VMD: visual molecular dynamics. *J. Mol. Graph.* **14**, 33–38 (1996). 27–38.
60. Bussi, G., Donadio, D. & Parrinello, M. Canonical sampling through velocity rescaling. *J. Chem. Phys.* **126**, 014101 (2007).
61. Kumar, S., Rosenber, J. M., Bouzida, D., Swendsen, R. H. & Kollman, P. A. THE weighted histogram analysis method for free-energy calculations on biomolecules. I. The method. *J. Comput. Chem.* **13**, 1011–1021 (1992).
62. Hub, J. S., de Groot, B. L. & van der Spoel, D. g\_wham—a free weighted histogram analysis implementation including robust error and autocorrelation estimates. *J. Chem. Theory Comput.* **6**, 3713–3720 (2010).
63. Marrink, S. J., de Vries, A. H. & Mark, A. E. Coarse grained model for semiquantitative lipid simulations. *J. Phys. Chem. B* **108**, 750–760 (2004).
64. Marrink, S. J., Risselada, H. J., Yefimov, S., Tieleman, D. P. & de Vries, A. H. The MARTINI force field: coarse grained model for biomolecular simulations. *J. Phys. Chem. B* **111**, 7812–7824 (2007).
65. de Jong, D. H. et al. Improved parameters for the Martini coarse-grained protein force field. *J. Chem. Theory Comput.* **9**, 687–697 (2013).
66. Monticelli, L. et al. The MARTINI coarse-grained force field: extension to proteins. *J. Chem. Theory Comput.* **4**, 819–834 (2008).
67. Wang, Y. et al. Construction of nanodroplet/adiposome and artificial lipid droplets. *ACS Nano* **10**, 3312–3322 (2016).
68. Stoll, S. & Schweiger, A. EasySpin, a comprehensive software package for spectral simulation and analysis in EPR. *J. Magn. Reson.* **178**, 42–55 (2006).
69. Dhiman, R. et al. Hairpin protein partitioning from the ER to Lipid Droplets involves major structural rearrangements. [Data set] Zenodo. <https://doi.org/10.5281/zenodo.11036547> (2024).

## Acknowledgements

We are grateful to David Mick and Mike Renne for critical feedback during the manuscript preparation and thank Louisa Krauß, Lisa Friedmann, Martin Leibrock, Silke Guthörl, and Nikolina Mitreska for excellent technical assistance. This work was supported by funding from the Deutsche Forschungsgemeinschaft (DFG) within the Collaborative Research Center 1027 with the grants CRC1027 project B7 to J.S.H. and CRC1027 project C9 to B.S. This work was additionally supported by the DFG via grant INST 256/539-1 to J.S.H. and INST 256/535-1 to C.W.M.K.

## Author contributions

Conceptualization, B.S.; Methodology, R.D., C.S.P., R.S.P., R.K., C.W.M.K., J.S.H., and B.S.; Investigation, R.D., C.S.P., R.S.P., and H.T.A.W.; Visualization, R.D., C.S.P., R.S.P., H.T.A.W., and B.S.; Supervision, R.K., C.W.M.K., J.S.H., and B.S.; Funding acquisition, C.W.M.K., J.S.H., and B.S.; All authors jointly wrote the manuscript and agreed on the final version. R.D., R.S.P., and C.S.P. contributed equally to this work.

## Funding

Open Access funding enabled and organized by Projekt DEAL.

## Competing interests

The authors declare no competing interests.

## Additional information

**Supplementary information** The online version contains supplementary material available at <https://doi.org/10.1038/s41467-024-48843-8>.

**Correspondence** and requests for materials should be addressed to Bianca Schrul.

**Peer review information** *Nature Communications* thanks Sharon Ruthstein and the other, anonymous, reviewer(s) for their contribution to the peer review of this work. A peer review file is available.

**Reprints and permissions information** is available at <http://www.nature.com/reprints>

**Publisher's note** Springer Nature remains neutral with regard to jurisdictional claims in published maps and institutional affiliations.

**Open Access** This article is licensed under a Creative Commons Attribution 4.0 International License, which permits use, sharing, adaptation, distribution and reproduction in any medium or format, as long as you give appropriate credit to the original author(s) and the source, provide a link to the Creative Commons licence, and indicate if changes were made. The images or other third party material in this article are included in the article's Creative Commons licence, unless indicated otherwise in a credit line to the material. If material is not included in the article's Creative Commons licence and your intended use is not permitted by statutory regulation or exceeds the permitted use, you will need to obtain permission directly from the copyright holder. To view a copy of this licence, visit <http://creativecommons.org/licenses/by/4.0/>.

© The Author(s) 2024



# Chapter 4

## Conclusion

The conclusion of this scientific thesis will be separated into two chapters describing the general conclusion in the first part derived from the scientific contributions of this thesis to the scientific fields of chemistry, physics and biology. Secondly, every distinct project will be discussed regarding the applied ESR technique.

### 4.1 First section of the Conclusion

As already mentioned in the motivational part in the beginning of this thesis, the aim of this PhD thesis was the investigation of a series of interdisciplinary, scientific challenging questions. The investigations in the field of chemical sciences started with the characterization of novel stable radicals such as a novel inorganic, paramagnetic aluminum complex. Time dependent CW ESR spectra could confirm the formation of the aluminum radical species [101]. Moreover, an optimized oxide nanoparticle synthesis route for  $\text{TiO}_2$  and  $\text{Nb}_2\text{O}_5$  nanoparticles with a low-cost mechanochemical reduction could be examined in later studies [102]. Another unpublished manuscript is incorporated and deals with the dipolar coupling between a 1s electron of a hydrogen atom and its neighbouring nuclei. The temperature dependant ENDOR measurements provide important insights into intra- and intermolecular interactions. After these studies, the research focus switched towards short-lived radicals and developments on catalytically active nanoparticles starting off with CW ESR spin trap experiments exploring the radical formation pathway of novel  $\text{LaCoO}_4$  and  $\text{LaCoO}_4/\text{graphene}$  nanoparticles. In order to distinguish the different generated reactive oxygen species during catalysis, an orthogonal approach under usage of different spin traps was used. Hence, the activity and the catalytical reaction pathway in the first few minutes could be described [31, 103]. A more advanced approach to investigate the magnetic and dynamic parameters of a light-induced species could be described afterwards. Here, aluminum embedded in a porphyrine framework could be analyzed for a potential application in artificial photosynthesis [104]. Temperature dependent transient EPR measurements, as well as temperature dependent, multi-frequency ENDOR measurements, were employed in the investigation.

The next project goes more into detail in the physical properties of ESR resonators in the realm of physics. The optimization of a commercially available ESR resonator was based on a logical approach after opening up the ESR resonator and revealing that the resonator topology was unsymmetric and could be optimized for different experimental tasks [105]. Hence, the scientific work around the resonator optimization centered not solely on the optimization of the current resonator setup. Further deeper knowledge on the generation of the magnetic field inside the MW resonator was implemented to build up completely new resonator topologies for several experimental challenges. The knowledge of this project helped in the investigation of the coupling parameters needed for the MASER resonator project. Here, it could be shown that a resonator setup needs to be in the undercoupled regime in order for the MASER to amplify microwaves, not in overcoupled conditions, as previously thought [106].

Directing towards the scientific realm of structural biology, power saturation ESR studies were employed in the later part of this scientific thesis to differentiate two different structural arrangements of a protein model system in different environments. Here, spin-labelling, as well as CW ESR studies, were conducted in collaboration with the working group of Schrul *et al.* at the campus in Homburg to allow important experimental evidence for postulated structural rearrangements by MD simulations [23].

After combination of all these projects, the timeline of this scientific PhD thesis can be summarized as starting with novel, stable radicals in the realm of chemistry and then switching the focus on the CW ESR spin trap investigation of short-lived radicals induced by catalytically active nanoparticles. Later studies on the optimization of the experimental setup, MW resonators and a MASER resonator in particular, could delve more in detail in the physical science of magnetic resonance. Afterwards, more advanced techniques (transient EPR, ENDOR, pulsed ESR) were employed to investigate magnetic and kinetic properties of inorganic complexes as well as a metalloporphyrine system. Further outreach to biological samples yielded important insight to structural arrangements of a protein model system and showed the versatility of magnetic resonance in the biological science.

In sum, this PhD thesis incorporates important, interdisciplinary scientific studies in the realms of chemistry, physics and biology with a wide variety of applications. All described scientific projects are published in journals available for a broad range of researchers of all scientific fields.

## 4.2 Second section of the Conclusion

The theoretical description of this thesis explained several techniques used in ESR spectroscopy. Mainly, CW ESR, spin trap experiments, power saturation, transient EPR and pulsed ESR techniques (relaxation times, ENDOR, PELDOR) were demonstrated. In the following, the collection of the scientific projects and the usage of the respective ESR technique are discussed.

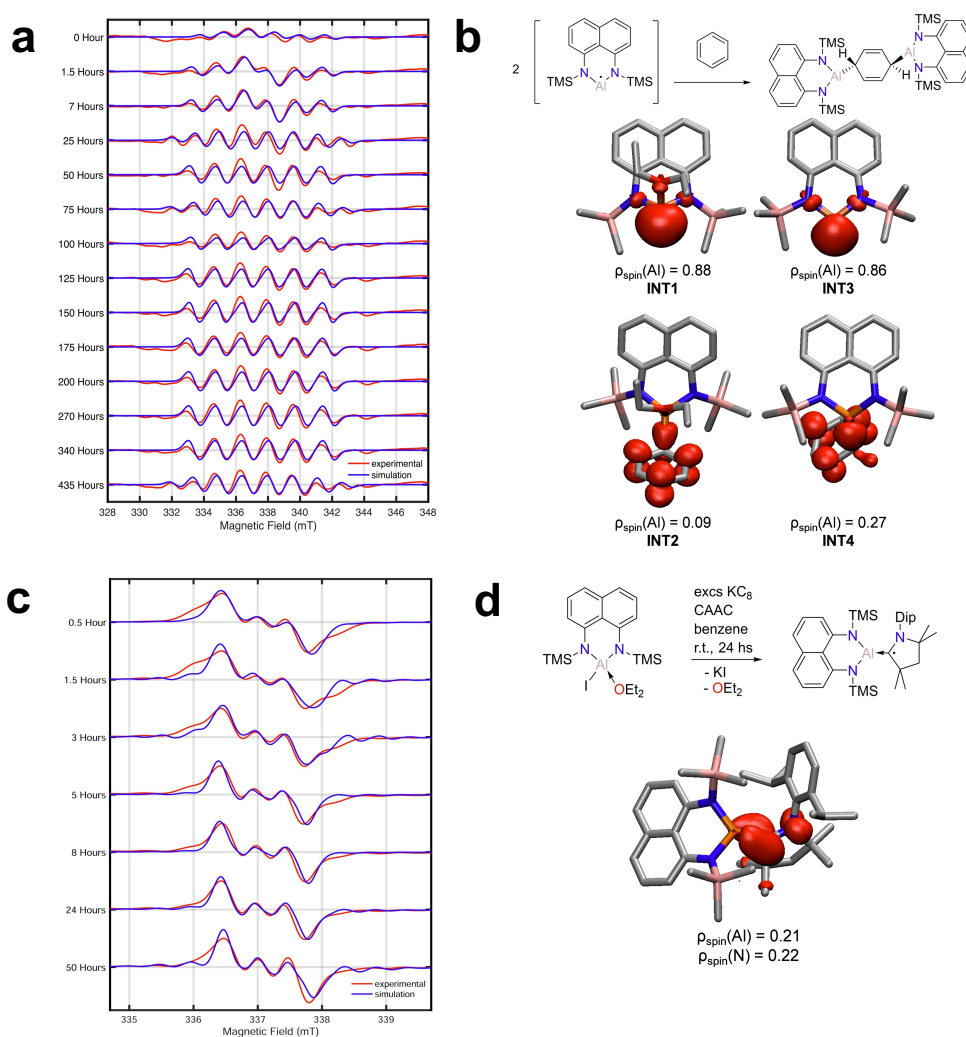


**Fig. 4.1** (a) Time dependent ESR spectra of the benzene activation reaction with the aluminum complex. (b) Scheme of the reaction with benzene (upper part) and spin density plots of the reaction intermediates INT 1–4. (c) Time dependent ESR spectra of the benzene activation reaction with an aluminum complex in the presence of CAACDip at various time intervals. (d) Reaction scheme of the reaction with benzene (upper part) and spin density plots of the resulting CAAC-coordinated radical. [101]

In a collaboration project with a working group of the Saarland University, Andrada *et al.*, a series of CW ESR spectra on the activation of benzene by an aluminum (II) complex could be recorded and simulated (Fig. 4.1 (a)). The reaction scheme is shown in Fig. 4.1 (b). Here, DFT (density functional theory) calculations have demonstrated that the reaction pathway follows a birch-type reduction process, where benzene gets activated by the radical species shown on the left side of the scheme. The reaction intermediates with their respective spin densities and Mulliken spin-density plots responsible for the activation of benzene INT 1-4 are illustrated below the scheme in Fig. 4.1 (b, H atoms have been omitted for clarity).

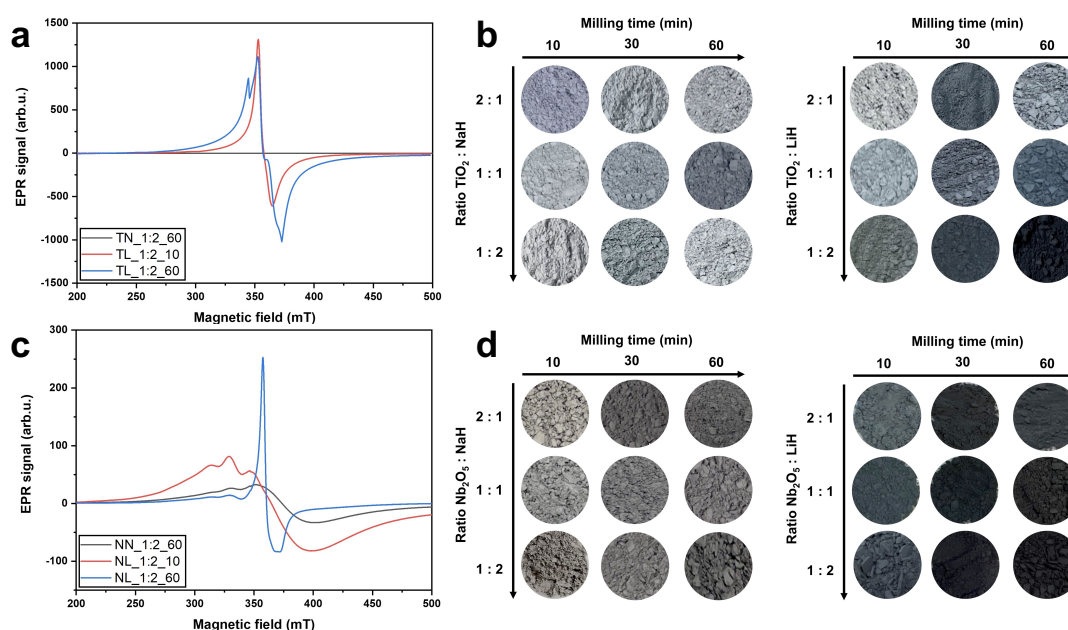


**Fig. 4.2** Low temperature (5 K) CW ESR spectra of reduced TiO<sub>2</sub> (a) and Nb<sub>2</sub>O<sub>5</sub> (c) nanoparticles under usage of different reducing agents (TN = TiO<sub>2</sub> with NaBH<sub>4</sub>, TL = TiO<sub>2</sub> with LiAlH<sub>4</sub>, NN = Nb<sub>2</sub>O<sub>5</sub> with NaBH<sub>4</sub> and NL = Nb<sub>2</sub>O<sub>5</sub> with LiAlH<sub>4</sub> after 10 and 60 minutes). The right side shows the powder colours of the reduced TiO<sub>2</sub> (b) and Nb<sub>2</sub>O<sub>5</sub> (d) nanoparticles in relation to the milling time, as well as the oxide to reducing agent ratio. [102]

In a similar manner, reduced TiO<sub>2</sub> and Nb<sub>2</sub>O<sub>5</sub> nanoparticles (Fig. 4.2) could be investigated. Here, TiO<sub>2</sub> and Nb<sub>2</sub>O<sub>5</sub> nanoparticles underwent reduction with different reducing agents while simultaneously prolonging the milling time (demonstrated in Fig. 4.2 (b) and (d)). The resulting low temperature (5 K) CW ESR spectra revealed paramagnetic oxygen vacancies  $V_0$ , as well as Ti<sup>3+</sup> and other lower valence Ti species (Fig. 4.2 (a)), as documented for many oxide materials [107]. The formation of unpaired electrons during the mechanochemical reduction of TiO<sub>2</sub> with LiH could be confirmed, while the NaH-mediated reduction of TiO<sub>2</sub> only showed a weak intensity signal. To differentiate the

different ball milling times, the peak areas of the reduced oxides were compared. As expected, for samples obtained after prolonged milling, the peak area below the ESR signal increases with milling time, indicating more paramagnetic centres [108]. The longer the milling time, the more  $\text{Ti}^{4+}$  ions are reduced to  $\text{Ti}^{3+}$ , which is accompanied by the formation of oxygen vacancies or the intercalation of Li, also yielding a darker colour (shown in Fig. 4.2 (b)). The formation of unpaired electrons during the mechanochemical reduction of  $\text{Nb}_2\text{O}_5$  with LiH/NaH could be confirmed as well (Fig. 4.2 (c)), but with lower intensities and peak areas and thus, fewer paramagnetic species.

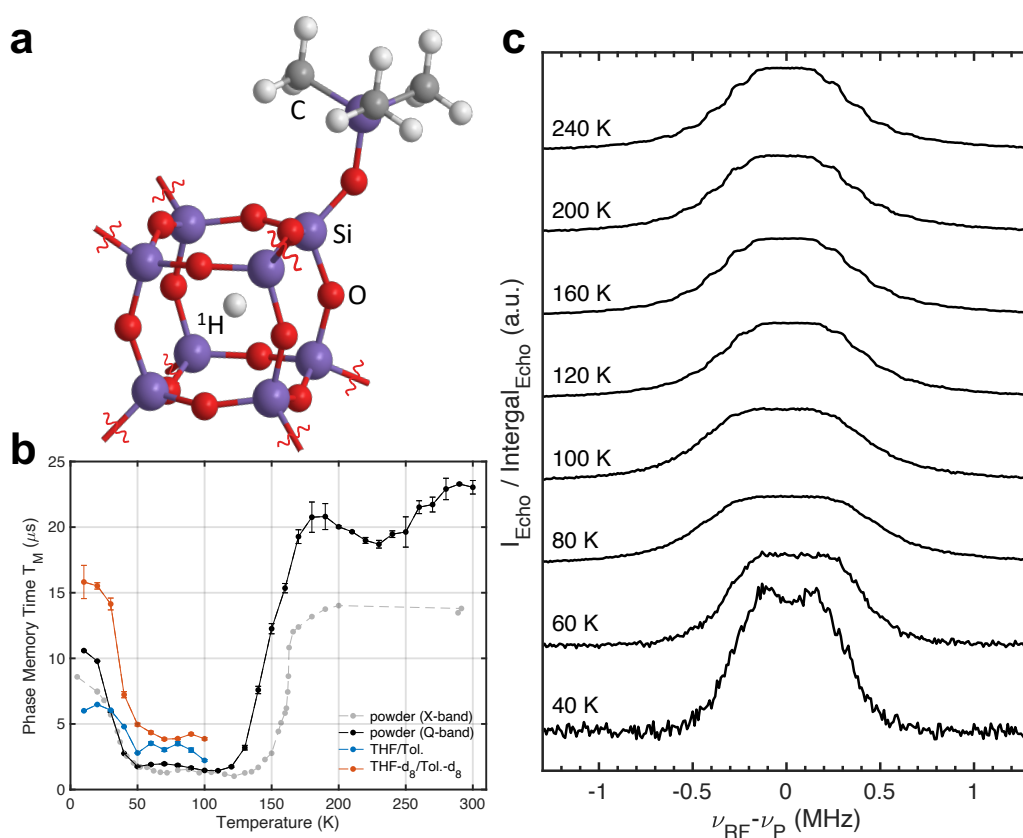


**Fig. 4.3** (a) Molecular structure of  $^1\text{H}@$ POSS, where only one trimethylsilyl (TMS) corner of the cage structure is shown (H = hydrogen (white), C = carbon (grey), O = oxygen (red), Si = silicon (purple)). (b) Temperature dependent phase memory time  $T_M$  of the three investigated systems (powder (X-band, grey), powder (Q-band, black), protiated solvation (blue) and deuterated solvation (orange)) (c) ENDOR spectra in the temperature range of 40 – 240 K measured for  $^1\text{H}@$ POSS powder. The ENDOR spectra are centered around the Larmor frequency of  $^1\text{H}$  in Q-band frequency space.

The next study describes a system where structural properties could be linked to its relaxation behaviour. An advanced ESR technique, ENDOR, was used in the study of a quantum bit (qubit) molecule. The molecular scheme depicted in Fig. 4.3(a) shows atomic

hydrogen ( $^1\text{H}$ ) encaged in polyhedral oligosilsesquioxanes (POSS) cages [73, 72, 74]. Here, the motivation to measure temperature dependent ENDOR spectra derived from the need to combine the function of this possible qubit candidate (long phase memory time  $T_M$ ) with its structural properties [109]. First experiments revealed a  $T_M$  enhancement upon placing the  $^1\text{H@POSS}$  molecule in deuterated environment at low temperatures (orange curve in Fig. 4.3(b)).

Fig. 4.3(c) shows experimentally acquired Mims-ENDOR spectra of  $^1\text{H@POSS}$ . The scientific work around the  $^1\text{H@POSS}$  molecule revealed that placing the molecular structure in deuterated environment (here: deuterated THF and toluene), led to a further prolongation of  $T_M$ . In order to understand the mechanism behind it we employed temperature dependent ENDOR measurements to investigate the structural mechanism upon  $T_M$  relaxation time enhancement. These ENDOR measurements revealed a direct evidence for the contribution of several factors in the  $T_M$  enhancement. One significant parameter was proven to be the rotation of the hydrogen atoms of the methylgroups in the corners of each cage. This resulted in a dipolar coupling between the wavefunction of the electron located in the central hydrogen atom with the averaged, centered hydrogen position of each methyle group at higher temperatures. Furthermore, ENDOR measurements at higher temperatures in the pristine powder revealed the contribution of intermolecular dipolar couplings between cages in the near proximity which could cause shorter relaxation times and thus, a worse qubit performance. Taken these facts into consideration, this study revealed a necessity of the investigation of the structure leading to a deeper understanding of the phase memory time  $T_M$ .



**Fig. 4.4** Reaction pathway of the activation of peroxymonosulfate (PMS) via  $\text{La}_2\text{CoO}_{4+\delta}$  nanoparticles. In the beginning, sulfate radicals and singlet oxygen are formed with subsequent formation of hydroxide radicals in aqueous environment. TEMP is used as radical scavenger for singlet oxygen, while DMPO is used as radical scavenger for  $\text{OH}^-$ - and  $\text{SO}_4^-$ -radicals.

Moving on with the investigation of short-lived radicals, spin trap experiments were employed to investigate the catalytic activity of novel nanoparticles. As an example for a scientific contribution with the usage of spin traps, DMPO and TEMP were used as spin traps to investigate the radical formation pathway of the peroxymonosulfate activation using  $\text{La}_2\text{CoO}_{4+\delta}$  (LCO) nanoparticles in the Bisphenol A degradation [31].

Bisphenol A (BPA) is a key compound in the production of polycarbonate [31]. A significant amount of BPA is discharged into the environment during the polycarbonate production and BPA is detected as microplastic in food, drinking water and aquatic animals [110]. The removal of BPA is therefore of great interest because BPA mimics estrogenic activity in human and animal bodies causing disruption of the endocrine system [111]. The motivation to develop nanoparticles as a way to degrade BPA arised through studies of Fenton reactions. Here, the formation of hydroxide and sulfate radicals has attracted increasing interest as a promising method to oxidize organic pollutants in water [103, 112, 113]. The postulated reaction pathway from earlier studies is depicted in Fig. 4.4 and was confirmed by spin trap ESR studies [31].

The next scientific work was carried out on a light-induced radical system. Fig. 4.5 (a) and (b) display the investigated light-induced radical porphyrine system from the aerial and side view. Here, the aluminum is located slightly above the porphyrine ring plane. Fig. 4.5 (c) shows the light-induced Davies ENDOR spectrum of the short-lived radical in Q-band frequencies (33 - 35 GHz) with the field-swept ESE (Electron Spin Echo) spectrum as inset (with the chosen field position for the ENDOR spectrum marked with an arrow) in the upper left corner. Fig. 4.5 (d) demonstrates the respective X-band frequency (9 - 10 GHz) light-induced 3p-ESEEM (3-pulse Electron Spin Echo Envelope Modulation) spectrum together with the field-swept ESE (Electron Spin Echo) spectrum as inset (with the chosen field position for the ENDOR marked with an arrow) in the upper left corner. There, the magnetic and dynamic parameters of AIOEP in the triplet state were determined using the complete range of advanced light-induced EPR techniques and complemented with theoretical methodologies. The results provide a reliable and detailed picture of the electronic structure and assessing the symmetry of a representative member of this important class of heterocyclic tetrapyrrolic compounds. The data indicate the involvement of a dynamic Jahn-Teller effect that leads to partial averaging of the magnetic parameters at higher temperatures. The data also suggest that axial ligands can play an important role in the Jahn-Teller dynamics [104].

These examples highlight the versatility of CW ESR experiments in the investigation of the formation of certain radicals (spin trap experiments and time dependent CW ESR spectra at the aluminum complex) and transient EPR in the investigation of light-induced radi-

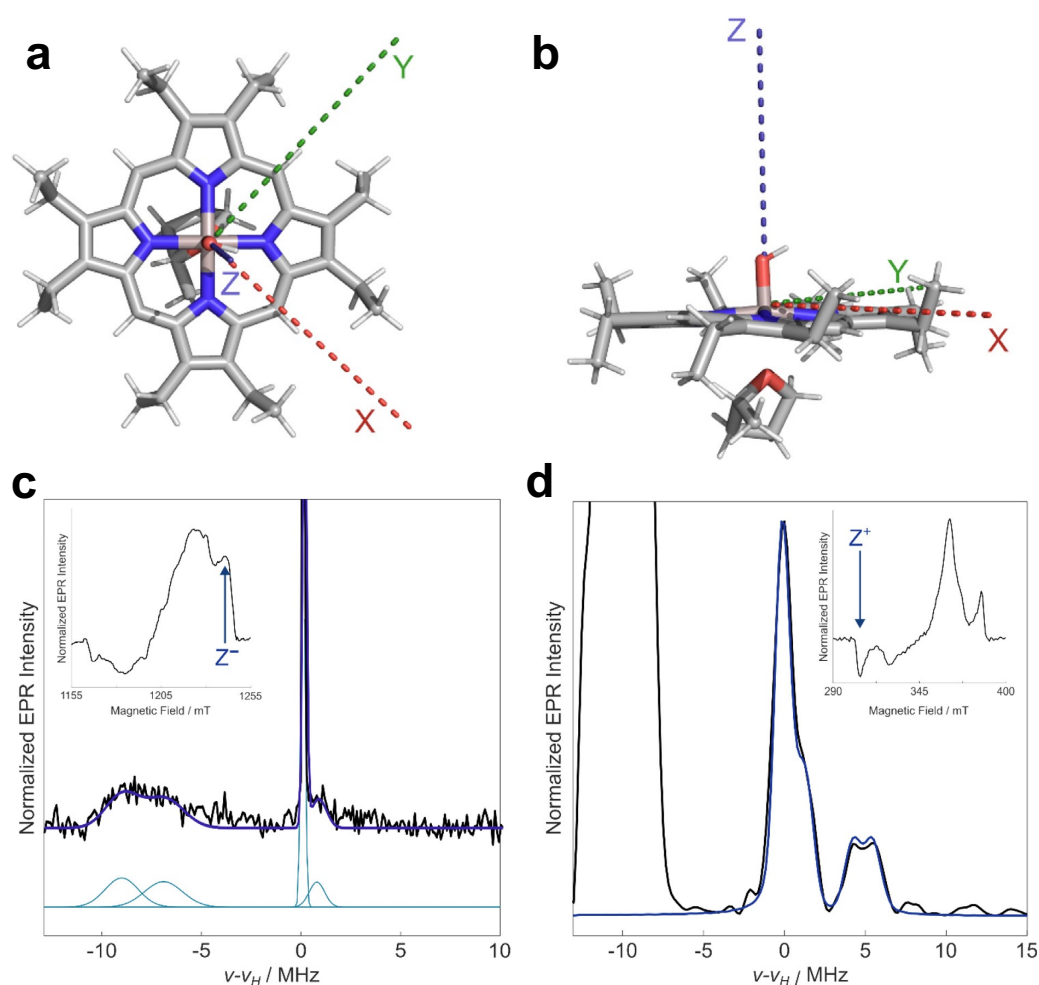


**Fig. 4.5** Top- (a) and side-view (b) of the molecular structure of octaethylaluminum(III)-porphyrin (AIOEP) (aluminum (purple), hydrogen (white), carbon (grey), oxygen (red), nitrogen (blue)). (c) Triplet state Davies ENDOR spectrum of AIOEP (10 K, Q-band, black); the overall best fit (blue) and the relative Gaussian deconvolution (light blue) are also shown. The resonance field corresponds to the  $Z^-$  ZFS canonical transition, as indicated by the arrow in the field-swept ESE spectrum shown in the inset (upper left corner). (d) Triplet state 3p-ESEEM frequency spectrum of AIOEP (80 K, X-band, black); the simulation is shown in blue. The resonance field corresponds to the  $Z^+$  ZFS canonical transition as indicated by the arrow in the field-swept ESE spectrum shown in the inset (upper left corner). [104]

cal systems. Furthermore, the performance of several reducing agents ( $\text{NaBH}_4$  and  $\text{LiAlH}_4$ ) in the generation of catalytically active oxide nanoparticles ( $\text{TiO}_2$  and  $\text{Nb}_2\text{O}_5$  nanoparticles) via low-cost mechanochemical reduction of metal oxides has been thoroughly investigated, making its application to other oxide nanoparticles possible.[114–118].

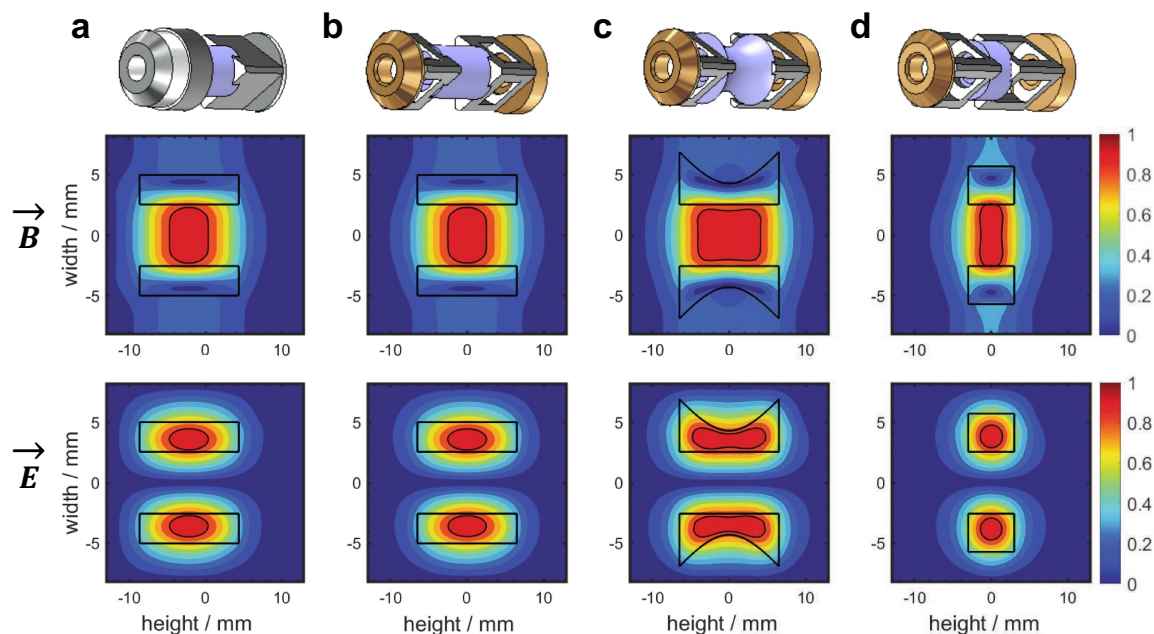


**Fig. 4.6** Scientific work on the optimization of X-band MW resonators. (Top row) Schemes of the Bruker Original MW resonator Asymmetric Long (AL, a) and three anticipated MW resonator optimizations Symmetric Long (SL, b), Symmetric Diaboloic (SD, c) and Symmetric Concave (SC, d). Contour plots of the normalized magnitude of the magnetic (Central row,  $\vec{B}$ ) and electric (Bottom row,  $\vec{E}$ ) field distributions inside the cross-section of the different sapphire ring resonators (AL = a; SL = b; SD = c; SC = d). On the right handside of each plot is the bottom metal end cap with the coupling antenna and on the left is the top metal end cap. The contour plots show the broadening and narrowing of the field distribution along different directions depending on the actual shapes of the sapphire rings. [105]

Simultaneously, the MW resonator optimization of the original setup in a commercially available ESR spectrometer setup (Fig. 4.6 (a) top row) yielded three optimized resonator topologies useful for different scientific tasks (Fig. 4.6 (b), (c) and (d)). Deeper insight and simulations on the generation of the MW  $B_1$  magnetic field led to the development of novel sapphire shapes for several experimental challenges (depicted in Fig. 4.6 central row).

Furthermore, an example on how the spin-spin relaxation time  $T_2$  can be used in a scientific workflow was described in addition to the derivation of MW conversion to effective  $B_1$  magnetic field inside the sapphire resonators. The electric component of MW field generation could be minimized ((depicted in Fig. 4.6 bottom row). A multi-experimental approach was chosen to bolster the theoretical predictions depicted in Fig. 4.6 [105]. The findings derived from this scientific work furthermore laid the ground

work in the evaluation of the coupling situation in a MASER resonator described by Zollitsch *et al.* [106].

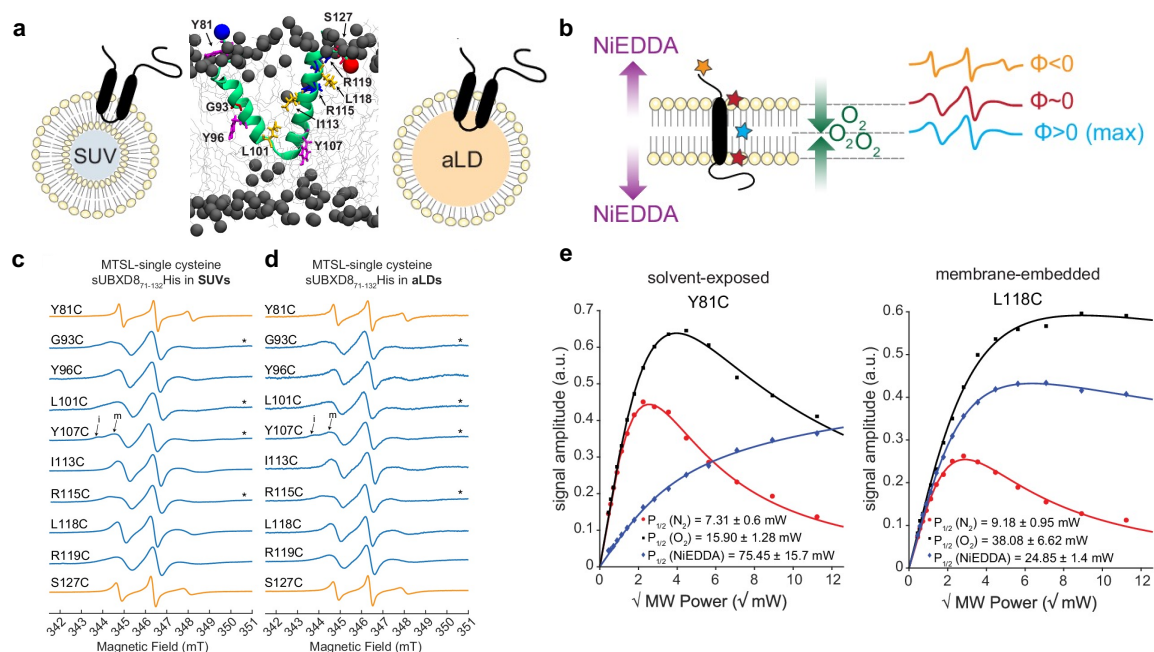


**Fig. 4.7** (a) Average atomistic MD simulation structure of the UBXD8 hairpin membrane protein indicating spin-labelled amino acids (81-127) in two environments: SUVs (single unilamellar vesicles, left) and aLDs (artificial lipid droplets, right). (b) Schematic illustration of how the spin-label positioning in a membrane protein affects the line shape of CW ESR spectra and the membrane depth parameter ( $\Phi$ , Solvent-exposed: orange; membrane-associated: red; membrane-embedded: blue). First derivative absorption CW ESR spectra of MTSL spin-labeled UBXD8<sub>81-127</sub> single cysteine mutants in SUVs (c) and aLDs (d). Asterisks mark spectra with additional shoulders in the low-field region indicating immobile (i) and mobile (m) motional components. (e) Exemplary ESR power saturation plots of MTSL spin-labeled Y81C and L118C single cysteine mutants reconstituted into SUVs. The peak-to-peak amplitude of the central ESR line was plotted against the square root of the applied microwave power (three conditions: nitrogen gas control (red circles), molecular O<sub>2</sub> (black squares) and NiEDDA (blue diamonds)). [23]

In addition to novel chemical molecules and physical optimizations of the experimental setup, the structure of biological samples was investigated. Structural rearrangements in biological systems on the molecular level are challenging to investigate without freezing the proteins of interest with cryo-EM techniques. An alternative approach to allow structural answers can be employed by the power saturation ESR technique.

Fig. 4.7 (a) demonstrates the schematic of a protein model system (UBXD8 hairpin membrane protein) embedded into a bilayer of lipid membranes (single unilamellar vesicles SUVs, Fig. 4.7 (a, left) or artificial lipid droplets aLDs, Fig. 4.7 (a, right). If the

spin-label of the protein is attached to the outer part of the membrane protein (depicted in Fig. 4.7 (c) and (d)), the resulting ESR spectrum will display three narrow lines due to a higher mobility (fast rotational correlation time, RCT). If the spin label is membrane associated or membrane embedded, the ESR spectrum gets broader as a result of a more restricted mobility (slow RCT) [23].

Depending on the spin-label position throughout the protein the spin-label can interact differently with relaxing agents ( $O_2$  or NiEDDA depicted in Fig. 4.7 (b)) and hence, allow statements on the structure of the investigated protein. The postulation of a structural rearrangement could therefore be confirmed by extracting the depth parameter. The depth parameter is negative for solvent exposed spin labels, since they can interact and relax due to the water-soluble NiEDDA which has a higher concentration in the surrounding solvent (yellow star in Fig. 4.7 (b)). On the other hand, oxygen can penetrate the bilayer and is accumulated in the midplane of the bilayer, giving rise to positive depth parameters (blue star in Fig. 4.7 (b)). For spin labels positioned directly at the membrane, the depth parameter is close to zero (red star in Fig. 4.7 (b)). Hence, extracting the depth parameter for two different membrane environments (exemplarily shown in Fig. 4.7 (e)) yields important experimental evidence for the postulated rearrangement by MD simulations [23]. Additionally, PELDOR measurements are in progress to deliver further confirmation of the experimental evidence derived by power saturation studies.

In summary, the described published peer-reviewed works offer a range of CW ESR methods and setup optimizations up to more advanced techniques, such as transient EPR and pulsed ESR techniques. These techniques have been applied to challenging issues through the chemical, physical and biological fields of science and offer a great contribution to the scientific community of magnetic resonance.



# Chapter 5

## Scientific Contributions

### 5.1 Publications of Haakon T.A. Wiedemann in peer-reviewed Journals

- (1) M. Hammad, B. Alkan, A. K. Al-kamal, C. Kim, M. Y. Ali, S. Angel, H. T. A. Wiedemann and C. W. M. Kay, Enhanced heterogeneous activation of peroxymonosulfate by Ruddlesden-Popper-type  $\text{La}_2\text{CoO}_{4+\delta}$  nanoparticles for bisphenol A degradation, *Chemical Engineering Journal*, 429, **2022**, 131447.
- (2) M. Hammad, S. Angel, A. K. Al-Kamal, A. Asghar, A. S. Amin, M. Kräenbring, H. T. A. Wiedemann and C. W. M. Kay, Synthesis of novel  $\text{LaCoO}_3$ /graphene catalysts as highly efficient peroxymonosulfate activator for the degradation of organic pollutants, *Chemical Engineering Journal*, 454, **2023**, 139900.
- (3) D. Mandal, T. I. Demirer, T. Sergeieva, B. Morgenstern, H. T. A. Wiedemann, C. W. M. Kay and D. M. Andrada, Evidence of Al(II) Radical Addition to Benzene, *Angewandte Chemie*, **2023**, e202217184.
- (4) A. Michaely, O. Janka, E. C. J. Gießelmann, R. Haberkorn, H. T. A. Wiedemann, C. W. M. Kay and G. Kickelbick, Black Titania and Niobia within Ten Minutes - Mechanochemical Reduction of Metal Oxides with Alkali Metal Hydrides, *Chemistry—A European Journal*, **2023**, e202300223.
- (5) A. Carella, S. Ciuti, H. T. A. Wiedemann, C. W. M. Kay, A. van der Est, D. Carbonera, A. Barbon, P. K. Poddutoori, and M. D. Valentin, The electronic structure and dynamics of the excited triplet state of octaethylaluminum (III)-porphyrin investigated with advanced EPR methods, *Journal of Magnetic Resonance*, **2023**, p.107515.
- (6) H. T. A. Wiedemann, S. Ruloff, R. Richter, C. W. Zollitsch, and C. W. M. Kay, Towards high performance dielectric microwave resonators for X-band EPR spectroscopy, *Journal of Magnetic Resonance*, **2023**, p.107519.

- (7) C. W. Zollitsch, S. Ruloff, Y. Fett, H. T. A. Wiedemann, R. Richter, J. D. Breeze, C. W. M. Kay, Maser threshold characterization by resonator Q-factor tuning, *Communication Physics*, **2023**, 6, 295.
- (8) R. Dhiman, R. S. Perera, C. S. Poojari, H. T. A. Wiedemann, R. Kappl, C. W. M. Kay, J. S. Hub, and B. Schrul, Hairpin protein partitioning from the ER to lipid droplets involves major structural rearrangements, *Nature Communications*, 15, 1, **2024**, 4504.

## 5.2 Contributions of Haakon T.A. Wiedemann at Scientific Conferences

- (1) H. T. A. Wiedemann, S. Ruloff, R. Richter, C. W. Zollitsch and C. W. M. Kay, Ways to high performance EPR (Electron Paramagnetic Resonance) resonators, *43rd FGMR Annual Discussion Meeting*, **2022**, (Karlsruhe, Germany).
- (2) H. T. A. Wiedemann, D. Klippert, M. Hammad and C. W. M. Kay, Reactive oxygen species (ROS) detection via spin traps - How does it work?, *PARACAT Workshop: Electron Paramagnetic Resonance in Catalysis*, **2022**, (Athens, Greece).
- (3) H. T. A. Wiedemann, M. Neuberger, C. W. Zollitsch and C. W. M. Kay, Applications of Continuous Wave and Pulsed Electron Paramagnetic Resonance Spectroscopy, *PhD Day Saarland University*, **2023**, (Saarbrücken, Germany).
- (4) H. T. A. Wiedemann, M. Neuberger, R. Schank, G. Mitrikas and C. W. M. Kay, Pulse-EPR and ENDOR (Electron Nuclear Double Resonance) Studies on atomic Hydrogen in different Matrices, *9th EFEPR EPR Summer School*, **2023**, (Geneva, Switzerland).
- (5) H. T. A. Wiedemann, S. Ruloff, R. Richter, C. W. Zollitsch and C. W. M. Kay, Towards high performance EPR (Electron Paramagnetic Resonance) resonators, *The 57th Annual International Meeting of the ESR Spectroscopy Group of the Royal Society of Chemistry*, **2024**, (Warwick, United Kingdom).
- (6) H. T. A. Wiedemann, M. Neuberger, J. N. Bach, D. Schroeder, E. Steuer, R. Schank, G. Mitrikas and C. W. M. Kay, Temperature dependent Pulse-EPR and ENDOR (Electron Nuclear Double Resonance) Studies on Atomic Hydrogen in different Matrices, *18th International Symposium on Spin and Magnetic Field Effects in Chemistry and Related Phenomena (Spin Chemistry Meeting 2024)*, **2024**, (Kobe, Japan).

### 5.3 Other Contributions of Haakon T.A. Wiedemann

- (1) H. T. A. Wiedemann, M. Neuberger, J. N. Bach, D. Schroeder, E. Steuer, R. Schank, G. Mitrikas and C. W. M. Kay, Temperature-dependent pulsed Electron Paramagnetic Resonance (EPR) and Electron-Nuclear-Double-Resonance (ENDOR) studies on atomic hydrogen in different matrices, *Unpublished manuscript*, **2024**.
- (2) M. Hammad, S. Angel, A.K. Al-kamal, A. Asghar, M. Kräenbring, A. Amin, H. T. A. Wiedemann, A. S. Amin, V. Vinayakumar, T. C. Schmidt, C. W. M. Kay, D. Segets, H. Wiggers, Spray-flame synthesis of LaCo<sub>0.2</sub>Mn<sub>0.8</sub>O<sub>3</sub> for peroxy monosulfate activation towards efficient degradation of carbamazepine, *Unpublished manuscript*, **2024**.
- (3) H. Haldar, S. Das, H. T. A. Wiedemann, K. Beuthert, C. W. M. Kay, S. Dehnen, C. B. Yildiz, M. Majumdar, Tetra-cationic Distibane stabilized by Bis(alpha-iminopyridine) and its Reactivity, *Unpublished manuscript*, **2024**.



# References

- [1] H.T.A. Wiedemann. Optimierung der stimulierten Emission bei den Stickstoff-Leerstellen eines Diamanten, 2018. unpublished Bachelorthesis.
- [2] Wolfgang Demtröder. *Experimentalphysik 3 - Atome, Moleküle und Festkörper*. Springer Verlag, 2005.
- [3] A. Schweiger and G. Jeschke. *Principles of pulse electron paramagnetic resonance*. Oxford University Press, Great Clarendon Steet, Oxford OX2 6DP, UK, 2001.
- [4] Bruker. *Xenon Guide: An EPR Primer*. Bruker, 2017.
- [5] M. Symons. *Chemical and Biochemical Aspects of Electron-Spin Resonance Spectroscopy*. Van Nostrand Reinhold Company Ltd., 1978.
- [6] G. Wedler. *Lehrbuch der physikalischen Chemie*. Wiley-VCH Verlag, 2007.
- [7] B.C. Hall. *Lie Groups, Lie Algebras, and Representations: An Elementary Introduction, Graduate Texts in Mathematics*, volume 222. Springer, 2015.
- [8] H. Friebolin and C. M. Thiele. *Ein- und zweidimensionale NMR-Spektroskopie*. Wiley-VCH Verlag, 2013.
- [9] P. Neugebauer. *Developpement d'un Spectrometre de Resonance Paramagnetique Electronique Haute Frequence / Haut Champ Heterodyne fonctionnant autour de 285 GHz*. PhD thesis, University Grenoble, France, 2010.
- [10] P.W. Atkins and J. de Paula. *Physikalische Chemie*. Wiley-VCH Verlag, 2013.
- [11] C. Altenbach, D.A. Greenhalgh, H.G. Khorana, and W.L. Hubbell. *Proc. Natl. Acad. Sci. USA*, 91:1667–1671, 1994.
- [12] A. Ball, R. Nielsen, M.H. Gelb, and B.H. Robinson. *Proc. Natl. Acad. Sci. USA*, 96:6637–6642, 1999.
- [13] M. Barranger-Mathys and D.S. Cafiso. *Biochemistry*, 35:498–505, 1996.
- [14] Y. Lin, R. Nielsen, D. Murray, W.L. Hubbell, and C. Mailer. *Science*, 279:1925–1929, 1998.
- [15] Z. Qin and D.S. Cafiso. *Biochemistry*, 35:2917–2925, 1996.
- [16] S.L. Wertz, Y. Savino, and D.S. Cafiso. *Biochemistry*, 35:11104–11112, 1996.
- [17] B. Bersch, M. R. Groves, J. P. Klare, A. E. Torda, and D. O. de Orué Lucana. *Systems Biology of Free Radicals and Antioxidants - Applications of Structural Biology and Bioinformatics in the Investigation of Oxidative Stress-Related Processes*, volume 196. Springer-Verlag Berlin Heidelberg, 2014.

- [18] A.A. Frazier, M.A. Wisner, N.J. Malmberg, K.G. Victor, and G.E. Fanucci. *Biochemistry*, 41:6282–6292, 2002.
- [19] A.A. Frazier, C.R. Roller, J.J. Havelka, A. Hinderliter, and D.S. Cafiso. *Biochemistry*, 42:96–105, 2003.
- [20] S.C. Kohout, S. Corbalan-Garcia, J.C. GomezFernandez, and J.J. Falke. *Biochemistry*, 42:1254–1265, 2002.
- [21] N.J. Malmberg, D.R. Van Buskirk, and J.J. Falke. *Biochemistry*, 42:13227–13240, 2003.
- [22] C. W. M. Kay, B. Mennenga, H. Görisch, and R. Bittl. *PNAS*, 103:5267–5272, 2006.
- [23] R. Dhiman, R.S. Perera, C.S. Poojari, H.T.A. Wiedemann, R. Kappl, C.W.M. Kay, J.S. Hub, and B. Schrul. *Nat. Comm.*, 15:4504, 2024.
- [24] K.J. Oh, C. Altenbach, R.J. Collier, and W.L. Hubbell. *Methods Mol. Biol.*, 145:147–169, 2000.
- [25] M.J. Davies and C.L. Hawkins. *Rad. Biolog. Med.*, 36:1072–1086, 2004.
- [26] G. Huang, C. Wang, C. Yang, P. Guo, and H. Yu. *Environ. Sci. Technol.*, 51:12611–12618, 2017.
- [27] P.L. Zamora and F.A. Villamena. *J. Phys. Chem. A*, 116:7210–7218, 2012.
- [28] B.C. Gilbert, N.M. Atherton, and M.J. Davies. *Electron Paramagnetic Resonance*. The Royal Society of Chemistry, 16th edition, 1998.
- [29] W. He, Y. Liu, W. G. Wamer, and J. Yin. *Journal of Food and Drug Analysis*, 22(1):49–63, 2014.
- [30] F.A. Menezes, J.G. Oliveira, and A.O. Guimaraes. *Appl. Magn. Res.*, 55:335–355, 2024.
- [31] M. Hammad, B. Alkan, A.K. Al-kamal, C. Kim, Md Y. Ali, S. Angel, H.T.A. Wiedemann, D. Klippert, T. Schmidt, C.W.M. Kay, and H. Wiggers. *Chem. Eng. J.*, 429:131447, 2023.
- [32] S.S. Kim and S.I. Weissman. *J. Magn. Reson.*, 24:167, 1976.
- [33] C.W.M. Kay, G. Elger, and K. Möbius. *Chem. Phys. Chem.*, 1:3999–4002, 1999.
- [34] C.W.M. Kay. *J. Am. Chem. Soc.*, 125:13861–13867, 2003.
- [35] A. Kawai and K. Shibuya. *J. Photochem. Photobiol. C: Photochem. Rev.*, 7:89–103, 2006.
- [36] D. Barr, S.S. Eaton, and G.R. Eaton. *Booklet: Workshop on Quantitative EPR*. Breckenridge, Colorado, 2008.
- [37] A. Merchanka, A. Savitsky, W. Lubitz, and K. Möbius. *J. Phys. Chem. B*, 114:14364, 2010.

- [38] D. Nohr, S. Franz, R. Rodriguez, B. Paulus, L.O. Essen, S. Weber, and E. Schleicher. *Biophys. J.*, 111:301, 2016.
- [39] M. Fuki, H. Murai, H. Tachikawa, and Y. Kobori. *J. Phys. Chem. B*, 120:4365, 2016.
- [40] B. Ferlez, W. Dong, R. Siavashi, K. Redding, H.J.M. Hou, J.H. Golbeck, and A. van der Est. *J. Phys. Chem. B*, 119:13714, 2015.
- [41] F. Conti, L. Panzella, A. Napolitano, M. d'Ischia, and A. Toffoletti. *Spectroscopy*, 24:289–295, 2010.
- [42] A. van der Est and P.K. Poddutoori. *Appl. Magn. Reson.*, 44:301, 2013.
- [43] Y.E. Kandrashkin, P.K. Poddutoori, and A. van der Est. *Appl. Magn. Reson.*, 47:511, 2016.
- [44] M.T. Colvin, A.B. Ricks, A.M. Scott, D.T. Co, and M.R. Wasielewski. *J. Phys. Chem. A*, 116:1923, 2012.
- [45] M. Fathalla, J.C. Barnes, R.M. Young, K.J. Hartlieb, S.M. Dyar, S.W. Eaton, A.A. Sarjeant, D.T. Co, M.R. Wasielewski, and J.F. Stoddart. *Chem. Eur. J.*, 20:14690, 2014.
- [46] G. Zhu, Y. Wang, H. Fu, X. Xu, Z. Cui, X. Ji, and G. Wu. *Spectrochim. Acta A*, 137:148, 2015.
- [47] S.M. Dyar, E.A. Margulies, B.A. Horwitz, K.E. Brown, M.D. Krzyaniak, and M.R. Wasielewski. *J. Phys. Chem. B*, 119:13560, 2015.
- [48] C.E. Tait, P. Neuhaus, M.D. Peeks, H.L. Anderson, and C.R. Timmel. *J. Am. Chem. Soc.*, 137:8284, 2015.
- [49] T. Miura, M. Aikawa, and Y. Kobori. *J. Phys. Chem. Lett.*, 5:30, 2014.
- [50] T. Miura, A. Kageyama, S. Torii, and H. Murai. *J. Phys. Chem. B*, 114:14550, 2010.
- [51] F. Kraffert, R. Streyleuthner, S. Albrecht, D. Neher, M.C. Scharber, R. Bittl, and J. Behrends. *J. Phys. Chem. C*, 118:28482, 2014.
- [52] M. Schröder, D. Rauber, and C. Matt. Pentacene in 1,3,5-tri(1-naphthyl)benzene: A novel standard for transient epr spectroscopy at room temperature. *Appl. Magn. Reson.*, pages 1–10, 2021.
- [53] S. Weber. Transient EPR. *eMagRes*, 6(2):255–269, 2017.
- [54] J. Schmidt, D.J. van den Heuvel, A. Henstra, T.S. Lin, and W.T. Wenckebach. *Pure and Appl. Chem.*, 64:859–863, 1992.
- [55] A.J. Vanstrien and J. Schmidt. *Chem. Phys. Lett.*, 70:513–517, 1980.
- [56] C.E. Avalos, S. Richert, E. Socie, G. Karthikeyan, G. Casano, G. Stevanato, D.J. Kubicki, J.E. Moser, C.R. Timmel, M. Lelli, A.J. Rossini, O. Ouari, and L. Emsley. *J. Phys. Chem. A*, 124:6068–6075, 2020.

- [57] S.H. Chan, H.K. Lee, Y.M. Wang, N.Y. Fu, X.M. Chen, Z.W. Cai, and H.N.C. Wong. *Chem. Commun.*, 1:66–68, 2005.
- [58] F.A. Sperlich. *Electron Paramagnetic Resonance Spectroscopy of Conjugated Polymers and Fullerenes for Organic Photovoltaics*. PhD thesis, Universität Würzburg, 2013.
- [59] D. Lubert-Perquel, E. Salvadori, and M. Dyson. *Nat. Commun.*, 9:4222, 2018.
- [60] H.C. Torrey et al. *Phys. Rev.*, 76:1059–1068, 1949.
- [61] I.I. Rabi, N.F. Ramsey, and J. Schwinger. *Rev. mod. phys.*, 26:167–171, 1954.
- [62] P.W. Atkins, K.A. McLauchlan, and P.W. Percival. *Mol. Phys.*, 25(2):281–296, 1973.
- [63] D. Wolf. *Spin temperature and nuclear spin relaxation in matter*. Clarendon press 2. Aufl., Oxford, 1979.
- [64] K. Laukenmann. *Zeitaufgelöste EPR-Untersuchungen an lichtinduzierten Radikalpaaren in photosynthetischen Modellsystemen*. PhD thesis, Universität Freiburg, 1999.
- [65] J.H. Moore and N.D. Spencer. *Encyclopedia of chemical physics and physical chemistry*, volume 3. Institutes of Physics Publishing, 2001.
- [66] A.J. Hoff. *Advanced EPR: Applications in biology and biochemistry*. Elsevier Science, 2012.
- [67] S.Z. Kiss, A.M. Rostas, L. Heidinger, N. Spengler, M.V. Meissner, N. MacKinnon, E. Schleicher, S. Weber, and J.G. Korvink. *J. Magn. Res.*, 270:169–175, 2016.
- [68] T. Biskup. *Frontiers in Chemistry*, 7, 2019.
- [69] Z. Wang and A. Toffoletti et al. *Chem. Sci.*, 12:2829, 2021.
- [70] S. Richert and C. Tait et al. *J. Magn. Res.*, 280:103–116, 2017.
- [71] David M. Pozar. *Microwave Engineering*. John Wiley and Sons, Inc., 2012.
- [72] G. Mitrikas. *Phys. Chem. Chem. Phys.*, 14:3782–3790, 2012.
- [73] G. Mitrikas, E.K. Efthimiadou, and G. Kordas. *Phys. Chem. Chem. Phys.*, 16:2378–2383, 2014.
- [74] G. Mitrikas and R. Carmieli. *J. Phys. Chem. C*, 125:9899–9907, 2021.
- [75] H. Kurreck, B. Kirste, and W. Lubitz. *Angew. Chem. Int. Ed.*, 23:173–194, 1984.
- [76] D. J. Lowe. *Prog. Biophys. molec. Biol.*, 57:1–22, 1992.
- [77] D. Goldfarb and S. Stoll. *EPR Spectroscopy: Fundamentals and Methods*. John Wiley and Sons Ltd., 16 edition, 2018.
- [78] C. Gmeiner, G. Dorn, F.H.T. Allain, G. Jeschke, and M. Yulikov. *Phys. Chem. Chem. Phys.*, 19:28360–28380, 2017.

- [79] D. Papaianou, S. Geibel, M.B.A. Kunze, C.W.M. Kay, and G. Waksman. *Prot. Sci.*, 25:627–637, 2016.
- [80] P. Widder, J. Schuck, D. Summerer, and M. Drescher. *Phys. Chem. Chem. Phys.*, 22:4875–4879, 2020.
- [81] D. Nohr, R. Rodriguez, S. Weber, and E. Schleicher. *Front. Mol. Biosci.*, 2:1–16, 2015.
- [82] B. Joseph, E.A. Jaumann, A. Sikora, K. Barth, T.F. Prisner, and D.S. Cadiso. *Nature Protocols*, 14:2344–2369, 2019.
- [83] C. Bagneris, P.G. DeCaen, B.A. Hall, C.E. Naylor, D.E. Calpham, C.W.M. Kay, and B. A. Wallace. *Nat. Comm.*, 4:1–10, 2013.
- [84] S. Brandon, A.H. Beth, and E.J. Hustedt. *J. Magn. Res.*, 218:93–104, 2012.
- [85] G. Jeschke. *Chem. Phys. Chem.*, 3:927–932, 2002.
- [86] O. Schiemann, C.A. Heubach, D. Abdullin, K. Ackermann, M. Azarkh, E.G. Bagryanskaya, M. Drescher, B. Endeward, J.H. Freed, L. Galazzo, D. Goldfarb, T. Hett, L.E. Hofer, L.F. Ibanez, E.J. Hustedt, S. Kucher, I. Kuprov, J.E. Lovett, A. Meyer, S. Ruthstein, S. Saxena, S. Stoll, C.R. Timmel, M. Di Valentin, H.S. Mchaourab, T.F. Prisner, B.E. Bode, E. Bordignon, M. Bennati, and G. Jeschke. *J. Am. Chem. Soc.*, 143(43):17875–17890, 2021.
- [87] G. Jeschke and Y. Polyhach. *Phys. Chem. Chem. Phys.*, 9:1895–1910, 2007.
- [88] M. Pannier, S. Veit, A. Godt, G. Jeschke, and H.W. Spiess. *J. Magn. Reson.*, 213:316–325, 2011.
- [89] S.K. Misra and H.R. Salahi. *Physica B: Condensed Matter*, 625:413511, 2022.
- [90] A.D. Milov and Y.D. Tsvetkov. *Appl. Magn. Reson.*, 12:495–504, 1997.
- [91] A.D. Milov, A.B. Ponomarev, and Y.D. Tsvetkov. *Chem. Phys. Lett.*, 110:67–72, 1984.
- [92] R.A. Stein, A.H. Beth, and E.J. Hustedt. *Methods Enzymol.*, 563:531–567, 2015.
- [93] Y. Polyhach, E. Bordignon, R. Tschaggelar, S. Gandra, A. Godt, and G. Jeschke. *Phys. Chem. Chem. Phys.*, 14:10762–10773, 2012.
- [94] M. Srivastava J.H. Freed. *J. Phys. Chem. Lett.*, 8:5648–5655, 2017.
- [95] S.G. Worswick, J.A. Spencer, G. Jeschke, and I. Kuprov. *Sci. Adv.*, 4:eaat5218, 2018.
- [96] H.T.A. Wiedemann. Continuous Wave (CW) EMX X-band EPR spectrometer, 2024. University of Saarland Saarbrücken.
- [97] H.T.A. Wiedemann. Pulsed X-band E580 EPR spectrometer, 2024. University of Saarland Saarbrücken.
- [98] H.T.A. Wiedemann. Pulsed Q-band SuperQ E580 EPR spectrometer, 2024. University of Saarland Saarbrücken.

- [99] Cryogenic Limited. Cryogen-Free Temperature Cryostat for EPR (CF VTC for EPR) Manual, 2015.
- [100] H.T.A. Wiedemann. Pulsed laser setup on the optical table, 2024. University of Saarland Saarbrücken.
- [101] D. Mandal, T. I. Demirer, T. Sergeieva, B. Morgenstern, H. T. A. Wiedemann, C. W. M. Kay, and D. M. Andrada. *Angew. Chem. Int. Ed.*, page e202217184, 2023.
- [102] A. Michaely, O. Janka, E.C.J. Giesselmann, R. Haberkorn, H.T.A. Wiedemann, C.W.M. Kay, and G. Kickelbick. *Chem. Eur. J.*, page e202300223, 2023.
- [103] M. Hammad, P. Fortugno, S. Hardt, C. Kim, S. Salamon, T.C. Schmidt, H. Wende, C. Schulz, and H. Wiggers. *Environ. Technol. Innov.*, page 101239, 2020.
- [104] A. Carella, S. Ciuti, H.T.A. Wiedemann, C.W.M. Kay, A.v.d. Est, D. Carbonera, A. Barbon, P.K. Poddutoori, and M.D. Valentin. *J. Magn. Res.*, 353:107515, 2023.
- [105] H.T.A. Wiedemann, S. Ruloff, R. Richter, C.W. Zollitsch, and C.W.M. Kay. *J. Magn. Res.*, 354:107519, 2023.
- [106] C.W. Zollitsch, S. Ruloff, Y. Fett, H.T.A. Wiedemann, R. Richter, J.D. Breeze, and C.W.M. Kay. *Comm. Phys.*, 6:295, 2023.
- [107] Y. Su, J. Lang, L. Li, K. Guan, C. Du, L. Peng, D. Han, and X. Wang. *J. Am. Chem. Soc.*, 135:11433–11436, 2013.
- [108] G. Ou, Y. Xu, B. Wen, R. Lin, B. Ge, Y. Tang, Y. Liang, C. Yang, K. Huang, D. Zu, R. Yu, W. Chen, J. Li, H. Wu, L.M. Liu, and Y. Li. *Nat. Commun.*, 9:1302, 2018.
- [109] M. Wasielewski, M. Forbes, N. Frank, K. Kowalski, G. Scholes, J. Yuen-Zhou, M. Baldo, D. Freedman, R. Goldsmith, T. Goodson, and M. Kirk. *Nat. Rev. Chem.*, 4:490–504, 2020.
- [110] A. Schechter, N. Malik, D. Haffner, S. Smith, T.R. Harris, O. Paepke, and L. Birnbaum. *Environ. Sci. Technol.*, 44:9425–9430, 2010.
- [111] Y. Yoon, P. Westerhoff, S.A. Snyder, and E.C. Wert. *J. Memb. Sci.*, 270:88–100, 2006.
- [112] J. Ali, W. Jiang, A. Shahzad, J. Ifthikar, X. Yang, B. Wu, D.T. Oyekunle, W. Jia, Z. Chen, L. Zheng, and Z. Chen. *Chem. Eng. J.*, 425:130679, 2021.
- [113] S. Guo, H. Wang, W. Yang, H. Fida, L. You, and K. Zhou. *Appl. Catal. B Environ.*, 262:118250, 2020.
- [114] N. Cox, W. Ames, B. Epel, L. V. Kulik, L. Rapatskiy, F. Neese, J. Messinger, K. Wieghardt, and W. Lubiz. *Inorg. Chem.*, 50:8238–8251, 2011.
- [115] K.M. Sharples, E. Carter, C.E. Hughes, K.D.M. Harris, J.A. Platts, and D.M. Murphy. *Phys. Chem. Chem. Phys.*, 15:15214–15222, 2013.
- [116] G. Rao, A.B. Altman, A.C. Brown, L. Tao, T.A. Stich, J. Arnold, and R.D. Britt. *Inorg. Chem.*, 58:7978–7988, 2019.

- 
- [117] G.E. Cutsail. *Dalton Trans.*, 49:12128–12135, 2020.
- [118] Y. Kutin, J. Reitz, P.W. Antoni, A. Savitsky, D.A. Pantazis, M. Kasanmascheff, and M.M. Hansmann. *J. Am. Chem. Soc.*, 143:21410–21415, 2021.



# Appendix A

## Supporting Information

### Used Software

For all data plots and data evaluation, the *MATLAB* version 23.2.0.2428915 (R2023b) was used. All displayed ESR spectra simulations were acquired with the *Easyspin* Toolbox version 6.0.0. Data, Matlab-Code as well as ESR simulation scripts will be made available on request.

